DISTRIBUTION OF DISTRICT-SCALE HYDROTHERMAL ALTERATION, VEIN ORIENTATIONS AND WHITE MICA COMPOSITIONS IN THE HIGHLAND VALLEY COPPER DISTRICT, BRITISH COLUMBIA, CANADA: IMPLICATIONS FOR THE EVOLUTION OF PORPHYRY CU-MO SYSTEMS

by

Guillaume Lesage

B.Sc., Université Laval, 2008
M.Sc., University of Alberta, 2011

A THESIS SUBMITTED IN PARTIAL FULFILLMENT OF
THE REQUIREMENTS FOR THE DEGREE OF

DOCTOR OF PHILOSOPHY

in

THE FACULTY OF GRADUATE AND POSTDOCTORAL STUDIES

(Geological Sciences)

THE UNIVERSITY OF BRITISH COLUMBIA

(Vancouver)

February 2020

The following individuals certify that they have read, and recommend to the Faculty of Graduate and Postdoctoral Studies for acceptance, the dissertation entitled:

Distribution of district-scale hydrothermal alteration, vein orientations and white mica compositions in the Highland Valley Copper district, British Columbia, Canada: Implications for the evolution of Porphyry Cu-Mo systems

submitted by Guillaume Lesage in partial fulfillment of the requirements for

the degree of Doctor of Philosophy

in Geological Sciences

Examining Committee:

Craig Hart
Supervisor

Gregory Dipple
Supervisory Committee Member

Kenneth Hickey
Supervisory Committee Member

Erik Eberhardt
University Examiner

Bern Klein
University Examiner

Abstract

This thesis presents a multi-layer lineament mapping method that integrates topography, geophysical data and geological observations to interpret faults at surface, and demonstrates how magnetic intensity data can be used to estimate the dip of fault-related magnetic anomalies by performing 2D inverse modeling along profiles extracted from a magnetic intensity grid. Dip modeling of magnetic anomalies created in a synthetic 3D magnetic susceptibility model shows that the method is accurate to better than 5° for input dips >60°. Comparison between fault orientations modeled from magnetic data and measured in the field in the Guichon Creek batholith (GCB) confirms that the methodology can be successfully applied to brittle faults in real, albeit relatively simple geological environments.

Alteration mapping across the Highland Valley Copper (HVC) district defined zones of K-feldspar-bearing and muscovite-bearing veins, and later and more extensive zones of veins bearing sodic-calcic and propylitic mineral assemblages. A palinspastic reconstruction of the GCB to its Late Triassic geometry shows that: 1) potassic alteration forms a westerly-elongated ~12 x 2 km zone that overlaps with the Valley–Lornex and Highmont deposits, 2) sodic-calcic alteration forms discontinuous zones that cover an area ~17 km by 11 km (southwest) and <1 km (northeast), and 3) propylitic alteration is ubiquitous but a 10 km diameter zone of higher vein intensity (>5 cm/m) is located in the center of the batholith. Permeability within the batholith was dominantly the result of local stresses induced by magma or magmatic fluid overpressure (i.e., radial aplite and K-feldspar-bearing vein patterns around porphyry deposits), and by thermal contraction (i.e., sodic-calcic and propylitic veins perpendicular and parallel to intrusive contacts). The Late Triassic regional sinistral stress regime

only locally contributed to the batholith-scale permeability along favourably-oriented west to west-northwest-trending structures.

White mica compositional variations, determined by short-wave infrared (SWIR) spectroscopy, define footprints associated with porphyry mineralization. Sodic-calcic and propylitic alteration are characterized by a zone of increased muscovitic white mica abundance that is detectable within 3 km of the HVC deposits, and a zone of increased phengitic white mica abundance detectable to distances up to ~5 km from the HVC deposits.

Lay Summary

Porphyry deposits are a major source of copper and molybdenum in the world. New deposit discoveries are required to sustain the increasing demand for these. A better understanding of the geological controls on the district-scale alteration, or footprint, surrounding porphyry deposits can help focus exploration efforts and result in new discoveries. The Highland Valley Copper district, hosted in the Guichon Creek batholith near Kamloops, British Columbia, has consistently produced copper and molybdenum since 1962 from four porphyry deposits. The district-scale footprint of these deposits, however, is poorly understood. This research presents a new structural framework for the present-day Guichon Creek batholith and reconstructs the batholith to identify the structural setting under which the porphyry deposits formed during the Late Triassic. The project also defines the spatial extent and mineralogy of the porphyry-related alteration in the district, and offers insight into the implications of this research for global porphyry deposit exploration.

Preface

The data and interpretations presented in this thesis are the results of my own work, which was carried out between 2014 and 2019 at the Mineral Deposit Research Unit (MDRU) at the University of British Columbia (UBC). Research supervisor Craig J.R. Hart (UBC), UBC researchers Peter Winterburn and Robert G. Lee, and Lakehead University researcher Pete Hollings, provided supervision, advice, suggestions and editorial co-authorship on manuscripts. William A. Morris (McMaster University) also provided suggestions and editorial co-authorship on one manuscript. This research was conducted as part of the Canada Mining Innovation Council (CMIC) Footprints Project sponsored by the Natural Sciences and Engineering Research Council of Canada (NSERC) as well as by industry sponsors. The CMIC Footprints network includes 42 researchers from 24 universities across Canada and 45 industry collaborators from 27 mining, exploration and service companies (https://cmic-footprints.laurentian.ca/). This network was formed to develop holistic district-scale mineral deposit models for disseminated gold (Canadian Malartic), basinal uranium (McArthur River - Millennium), and porphyry copper deposits (Highland Valley Copper). Teck Resources Limited was the site sponsor for the porphyry Cu site, which is the focus of this thesis. My research peers at the study site were Michael D'Angelo (M.Sc., Lakehead University), Rachel Chouinard (M.Sc., UBC), Christophe Grenon (M.Sc., École Polytechnique), Andrea Reman (M.Sc., University of Waterloo), Kevin Byrne (Ph.D., University of Alberta, kevin.byrne@teck.com), and Philip Lypaczewski (Ph.D., University of Alberta, lypaczew@ualberta.ca). Kevin and Philip provided raw data for this research project, but did not participate in the interpretation of the results. Similarly, I provided raw data and rock samples for each of their doctoral research project. Kevin, Philip and I agreed to focus on different aspects of the porphyry footprint for our respective theses in order to avoid overlap between the three research projects. Kevin's research focused on the whole rock geochemistry, the epidote and prehnite mineral chemistry, as well as the stable and radiogenic isotope footprint of the Highland Valley Copper porphyry systems. Philip's research, on the other hand, focused on the hyperspectral imaging of alteration minerals (e.g., biotite, chlorite, epidote, kaolinite, prehnite, tourmaline, and white mica) across several ore deposit types including Highland Valley Copper (copper), Canadian Malartic (gold), and McArthur River (uranium). My own contribution is detailed below.

The study site was geographically divided into two domains for the mapping and rock sampling. Data collected during the mapping included outcrop magnetic susceptibility, alteration paragenesis, and vein orientation, mineralogy, thickness and density per meter. I collected data and samples in the southwest domain, whereas Kevin Byrne was responsible for the northeast domain. Field work was conducted between 2014 and 2016. Mapping results were integrated to produce district-scale lithology and alteration maps. Samples were shared between us. Rock samples were used to collect petrography, whole rock geochemistry, mineral chemistry, short-wave infrared (SWIR), and physical property data.

The objectives of the research presented in this thesis were devised by me in collaboration with Kevin Byrne, Craig J.R. Hart, Pete Hollings, and Sarah A. Gleeson (GFZ-Potsdam, formerly University of Alberta). The research herein is paper-based and is presented in five chapters that include an introduction (Chapter 1), three paper manuscripts (Chapters 2, 3, and 4), and a conclusion (Chapter 5). Thesis chapters are accompanied by supplementary material presented in Appendices A to F. Each paper manuscript presents original work that addresses a specific research objective of the thesis. The redundancy of some background information was inevitable in order to produce stand-alone manuscripts. I provided the original ideas, acquired all data, wrote the content, and designed all tables and figures for each manuscript (unless otherwise specified). Contributions from co-authors are detailed below.

Chapter 2 is titled "*Interpreting regional 3D fault networks from integrated geological and geophysical data sets: An example from the Guichon Creek batholith, British Columbia*" and was published in the Journal of Structural Geology in 2019. I am the lead author, I conducted the field work and I carried out the geological modeling presented in the manuscript. The geophysical modeling presented was done by me in collaboration with co-author William A. Morris. Other co-authors, which include Kevin Byrne, Randolph J. Enkin (Geological Survey of Canada), Robert G. Lee, Reza Mir (Laurentian University), and Craig J.R. Hart provided technical advice and editorial suggestions during the development of the manuscript, but did not contribute to the interpretation of the results. The manuscript presents a new 3D structural interpretation of the Guichon Creek batholith based on geological observations made in the field and on geophysical modeling, primarily of magnetic intensity data.

Chapter 3 is titled "*District-scale extent of hydrothermal alteration and vein orientations in the Highland Valley Copper district, British Columbia: Implications for permeability controls in porphyry Cu-Mo systems*" and is intended for publication in an international peer-reviewed journal. I am the lead author on the manuscript and conducted all analysis and interpretation of data. Mapping and vein orientation data were collected by me (~50%) and Kevin Byrne (~50%). Feldspar staining was also completed by me and Kevin Byrne at the UBC. Co-authors include Kevin Byrne, Robert G. Lee, and Craig

J.R. Hart. Co-authors and Richard Tosdal (PicachoEx LLC) provided technical advice and editorial suggestions during manuscript preparation, but did not contribute to the interpretation of the results. The manuscript describes the distribution alteration minerals and vein orientations in the Guichon Creek batholith, presents a palinspastic reconstruction of the batholith based upon the work published in Chapter 2, and discusses the structural controls on syn-mineralization permeability. Supplementary data for this manuscript are presented in Appendix A and B.

Chapter 4 is titled "*Infrared spectra and chemistry of hydrothermal white mica in the Highland Valley Copper district, British Columbia: Implications for its use as a vector toward porphyry mineralization*" and is intended for publication in an international peer-reviewed journal. I am the lead author and conducted all interpretation of data for this manuscript. Philip Lypaczewski collected the hyperspetral SWIR data at the University of Alberta, processed the raw data and provided Al-OH wavelength maps of every rock sample collected by Kevin Byrne and me during the geological mapping. Philip did not use these data in his own research project. Rietveld Refinement analyses were conducted at the UBC by Mati Raudsepp. I conducted all other analyses at the UBC, which include Terraspec® SWIR measurements on sample slabs and EPMA analyses of white mica. Co-authors, which include Kevin Byrne, Philip Lypaczewski, Robert G. Lee, and Craig J.R. Hart provided technical advice and editorial suggestions during manuscript preparation, but did not contribute to the interpretation of the results. The manuscript describes the spatial distribution of hydrothermal white mica SWIR characteristics and mineral composition throughout the Guichon Creek batholith, and discusses the implications of these data for porphyry deposit models and for mineral exploration. Supplementary data for this manuscript are presented in Appendix C to F.

Table of Contents

List of Tables

List of Figures

Acknowledgements

I would like to thank my supervisor Craig Hart for giving me the opportunity to join the Mineral Deposit Research Unit (MDRU) for this research project. I am also thankful for the guidance provided by others: Peter Winterburn, Pete Hollings, and Robert Lee. Sadly Peter died before this thesis was completed. Thanks to Al Lewis and Roger Beckie for participating in my candidacy examination. Thanks to Greg Dipple, Ken Hickey, Erik Eberhardt, and Bern Klein for taking the time to read this thesis and for participating in the final doctoral examination.

This research would not have been possible without the support of the Natural Sciences and Engineering Council of Canada (NSERC) and of the Canada Mining Innovation Council (CMIC) through the NSERC Collaborative Research and Development Program. Thanks to Teck Resources Limited for granting access to historical Highland Valley Copper (HVC) data and for providing field support during the mapping campaigns. More specifically, I would like to thank Teck geologists James Stemler, Gerald Grubisa, John Ryan, Catherine Ryan, Semyon Martynenko and Miguel Alfaro for their support. I would also like to thank Shell Canada for awarding me a Graduate Mapping Prize and SRK Consulting Canada for granting me a graduate scholarship through the UBC Department of Earth, Ocean and Atmospheric Sciences.

Thanks to all my field assistants for their good company and their hard work: Mike D'Angelo, Jonas Silveira, Antonio Celis, and Alex Colyer. Thanks also to my fellow CMIC Footprints graduate student Kevin Byrne. Working with you was great and I always appreciated the opportunity to exchange ideas with you. Thanks to SRK Consulting Canada geologists Wayne Barnett and Julia Kramer for their time and advice. Thanks to Randolph Enkin from the GSC for his help and his enthousiasm. Thanks to Bill Morris, Dick Tosdal and John Dilles for their invaluable insights and for tirelessly answering all my questions. I thank all my fellow researchers, staff and students from the MDRU for their support.

I thank all my past mentors and teachers for helping me become the geologist I am today: Georges Beaudoin, Réjean Hébert, Jeremy Richards, Rael Lipson, Ross Sherlock, Alina Gaibor, Peter Dunkley, and so many others. All the opportunities these people gave me have lead to the completion of this PhD project.

Finally, thanks to all my friends and family for their emotional support over the last few years. This research project was hard work, but I stayed grounded because of you. Thank you Mr. Mugatu, my faithful furry friend for your company during the writing process. Philippe, when I was 18 you said you wanted me to become a doctor so I could take care of you when you get old. I suppose you meant another kind of doctor, but here it is anyway.

Katie, you were always there for me when I needed. Thank you for putting up with my moods and for your unconditional love. I look forward to all of our next adventures together.

“There is no such thing as the unknown. Only things temporarily hidden, temporarily not understood.”

Captain James T. Kirk

Chapter 1. Introduction

1.1. Project rationale

Mineral deposit models are the result of the integration of the scientific community's current understanding of the characteristics of mineral deposits, their environment of formation and the processes involved in their formation (e.g., Cox and Singer, 1986; Goodfellow, 2007, and references therein). These models play an important role in understanding how mineral deposits form, and are crucial for mineral exploration because they can help predict where mineralized zones might be located. A model for a specific deposit type is built by studying and integrating the characteristics of typical mineralized zones of this type of deposit. These mineralization-centric models describe the characteristics of the central, typically economic part of hydrothermal systems, and can help predict the distribution of ores at the deposit scale, but they typically lack the larger scale perspective required to make them an effective exploration tool beyond the limits of ore bodies.

Porphyry-type deposits, which account for approximately 69% of Cu and 95% of Mo worldwide production, and are important sources of other metals such as Au, Ag, W, Pt and Pd (Sinclair, 2007; Singer, 2017), form as a result of the flow of a significant volume (10 to >100 km^3) of hot metal-rich hydrothermal fluids exsolved from a large underlying magma chamber (e.g., Burnham, 1979; Cline and Bodnar, 1991; Shinohara and Hedenquist, 1997; Cloos, 2001; Richards, 2011). When the flow of these magmatic fluids is focused into a relatively small area, intense fluid-rock interactions and changes in fluid temperature, pH and composition can result in the precipitation of sufficient metal-bearing minerals to form economically-mineralized zones, or ore deposits. Porphyry Cu deposits are characterized by relatively low to moderate grade (i.e., 0.3–2.0 % Cu), but by large tonnages (i.e., >100 million to billions of tonnes of ore) (John et al., 2010; Mudd et al., 2013).

The high temperature of the magma and magmatic fluids induce convective flow of heated external fluids in the brittle crust (meteoric fluids or sedimentary brines; e.g., Cathles, 1977; Weis, 2015). Hydrothermal fluids flow through the host rocks beyond the limits of the economic mineralization and continue to circulate after the metals have been precipitated. As a consequence of this, hydrothermal fluids react with a volume of rock that is much larger than that of the economic deposit itself. Changes to the original host rock caused by fluid-rock interactions include geological, mineralogical, geochemical and physical property changes. The footprints of a mineral deposit are the detectable and measureable results of all of these changes.

The porphyry Cu deposit model has been greatly improved since its first publication in 1970 by Lowell and Guilbert (e.g., Lowell and Guilbert, 1970; Sillitoe, 1972; Gustafson and Hunt, 1975; Brimhall, 1977; Dilles and Einaudi, 1992; Proffett, 2003; Richards, 2003; Masterman et al., 2005; Sinclair, 2007; Seedorff et al., 2008; Richards, 2009; John et al., 2010; Sillitoe, 2010; Lang et al., 2013; Cooke et al., 2014a), and significant advances to the understanding of the porphyry deposit footprint have been made over the last few years, particularly in the areas of mineral chemistry (e.g., Alva Jimenez, 2011; Cohen, 2011; Cooke et al., 2014b; Wilkinson et al., 2015), whole rock lithogeochemistry and short-wave infrared spectroscopy (e.g., Greenlaw, 2014; Halley et al., 2015). The size of a porphyry deposit footprint is dependent on the volume of hydrothermal fluids involved in its formation. The current understanding of the farthest components of the footprint of porphyry deposits is that it can be tracked up to approximately five kilometers laterally from a mineralized center (e.g., white mica chemistry, Cohen, 2011; chlorite chemistry, Wilkinson et al., 2015; epidote chemistry, Byrne, 2019). The hypothesis behind this research project is that the footprint of porphyry Cu deposits extends beyond what is currently documented in mineral deposit models.

Research presented herein was conducted in the Highland Valley Copper (HVC) district located 54 km southwest of Kamloops, British Columbia, a globally significant porphyry district hosted in the Late Triassic Guichon Creek batholith (GCB) (Mortimer et al., 1990; D'Angelo et al., 2017). The HVC district contains five porphyry Cu-Mo systems: Bethlehem, Valley, Lornex, Highmont, and J.A. (McMillan, 1985; Byrne et al., 2013). Mining in the HVC district began in 1962 (Casselman et al., 1995) and is still ongoing, with current reserves of 535 million tonnes of ore grading 0.30% Cu, measured resources are 499 million tonnes grading 0.30% Cu, and indicated resources are 672 million tonnes grading 0.24% Cu (Teck Resources Limited, 2019).

This thesis presents the results of research on the controls on fracture permeability and hydrothermal fluid flow that result in porphyry-related alteration, and of the effects of fluid-rock interactions on the mineralogical and chemical properties of the of host rocks and minerals that surround porphyry Cu deposits beyond the limits of economic mineralization.

1.2. The porphyry deposit model

1.2.1. Origin, characteristics and evolution of magmatic fluids in porphyry systems

Typical porphyry deposit-generating magmas are alkalic to calc-alkalic magmas that contain between 2 and 4 weight percent water, whereas typical granodiorites may only contain up to 0.6 weight percent water located in hydrous minerals such as hornblende or biotite (Burnham, 1981). This difference between magma and crystalline rock water contents results from the exsolution of an aqueous phase of magmatic fluid during magma crystallization (Lorenz et al., 1994). Studies show that a magma chamber volume of roughly 50 km^3 would be large enough to produce sufficient magmatic fluids to form a porphyry Cu deposit, however the formation of a giant porphyry deposit would require a magma chamber of at least 500 km^3 (e.g., Dilles, 1987; Cline and Bodnar, 1991; Shinohara and Hedenquist, 1997; Cloos, 2001; Cathles and Shannon, 2007; Sillitoe, 2010).

The magnitude of magmatic fluid volume increase that results from exsolution is dependent upon the initial water content of the magma and inversely dependent upon the depth at which the exsolution process takes place (Burnham, 1985). Magmatic fluid volume increase eventually leads to supralithostatic fluid pressures in the uppermost parts of the magma chamber (cupolas), where the buoyant fluids ascend and concentrate. The expansion of the ascending fluids to shallower crustal levels initiates brittle failure of the host rock and fractures the roof of the magma chamber. This fracturing process rapidly and significantly increases the open space volume available for the contents of the magma chamber (e.g., up to 12% at 3.3 km, Burnham, 1985), which causes rapid decompression of the magma and leads to further exsolution of magmatic fluids (second boiling). This sequence of events may be repeated several times as the crystallizing magma seals the chamber and causes pressures to rise, each time increasing the number and size of the fractures above the magma chamber, and potentially injecting dikes and breccias along larger fractures.

The orientation of fractures formed under a tectonic regime characterized by a large far-field differential stress typically forms a simple pattern with a dominant orientation (e.g., Titley et al., 1986; Lindsay et al., 1995; Wilson et al., 2007; Houston and Dilles, 2013). In some porphyry deposits, however, local stresses caused by supralithostatic magmatic fluid pressures, which push the magma chamber roof upward and outward, are greater than the far-field stresses and the resulting fractures form a characteristic radial fracture pattern around the source of the overpressure (e.g., Cornejo et al., 1997; Tosdal and Richards, 2001; Proffett, 2003; Garcia-Cuison, 2010). Permeability along these fractures is maintained as long as there is a pressure/temperature gradient causing upward fluid flow. The overpressured magmatic fluids flow mainly upwards through the hydrofractured crust due to the pressure gradient, but also outwards and into regional fracture-controlled permeability over distances potentially greater than 5 km. The flow of magmatic fluids displaces the ambient external fluids that are under hydrostatic pressure, which ultimately creates a magmatic-hydrothermal convection cell (e.g., Cathles, 1977, 1981; Cathles et al., 1997). When the magmatic fluid pressure decreases, the fluid flow ceases and the temperature drops, mineral precipitation (predominantly quartz) causes fractures to seal and permeability to plummet. Retrograde quartz solubility between 500°C and 350°C can however maintain permeability as the system cools down. In these cases, external fluids such as meteoric fluids, seawater and/or sedimentary brines can flow into and along fractures near the cooling magmatic source, get heated, circulate, and cause late sodic-calcic and propylitic alteration (e.g., Dilles and Einaudi, 1992; Byrne, 2019).

To form a porphyry Cu deposit the parental magma from which the magmatic fluids are exsolved must be metal-rich, sulfur-rich and oxidized. High sulfur and metal content can be achieved through injection of mafic magmas to the parental chamber (e.g., Keith et al., 1997; Hattori and Keith, 2001; Maughan et al., 2002; Halter et al., 2005; Zajacz and Halter, 2009). High oxygen fugacity ensures that the sulfur is present as SO_2 rather than H_2S, which prevents chalcophile elements such as Cu from being extracted from the magma into magmatic sulfide blebs, thus allowing the chalcophyle elements to concentrate into the subsequently exsolved aqueous phase (e.g., Burnham and Ohmoto, 1980; Candela and Holland, 1986; Dilles, 1987; Cline and Bodnar, 1991; Candela, 1992; Candela and Piccoli, 2005; Richards, 2005).

At high pressure at depths > 5 km, the exsolved magmatic fluid is a single phase supercritical fluid with a salinity of 2–10 wt.% NaCl equiv. (Rusk et al., 2004; Rusk et al., 2008; Sillitoe, 2010). Above 4 km, in the environment where most porphyry deposits typically form, the fluid separates into a hypersaline brine that contains between 35 and 70 wt.% NaCl equivalent in which Fe, Zn, Pb, Mn and Mo become concentrated, and a low-salinity vapor in which Cu, Au, Ag, As, S, Sb, Te and B are more compatible and become concentrated (e.g., Cline and Bodnar, 1991; Fournier, 1999; Heinrich et al., 1999; Heinrich, 2005; Pokrovski et al., 2005; Williams-Jones and Heinrich, 2005; Simon et al., 2007; Audétat et al., 2008; Pokrovski et al., 2008; Pudack et al., 2009).

Where fluid flow is concentrated above the cupolas of magma chambers and large volumes of fluid react with the host rock, cooling the fluid down, changes in fluid chemistry provoke sulfide mineral precipitation. Precipitation of Cu-Fe sulfides is a function of three main factors: (1) temperature, (2) availability of sulfur, and (3) pH (Hemley et al., 1992). Metal solubility in the fluid significantly decreases between 550°C and 250°C, which is the temperature window in which the bulk of the copper-bearing sulfide minerals precipitate in a porphyry Cu environment (Hemley et al., 1992). The reactions that lead to copper-bearing sulfide mineral precipitation are described by equations 1 to 6 below. The main reaction is equation 1.

$$Cu^{+} + Fe^{2+} + 2\ H_2S + \tfrac{1}{4}\ O_2 \Leftrightarrow CuFeS_2 + 3\ H^{+} + \tfrac{1}{2}\ H_2O \qquad \text{(Eq. 1)}$$

At temperatures >350°C in the potassic core of porphyry systems (Seedorff et al., 2005), decomposition of ferromagnesian minerals (e.g., alteration of hornblende to biotite) follows an equation of the style of equation 2. The wide compositional range of hornblende may affect the exact reaction equation (Brimhall et al., 1985). Alteration of hornblende to biotite consumes sulfuric acid (i.e., raises the fluid pH), produces silica that precipitates as quartz in veins, and increases the concentration of Ca^{2+} and Fe^{2+} in the fluid, which makes Fe available for sulfide precipitation and drives equation 1 to the right. Because of this, sulfide minerals in altered rocks are typically located in mafic sites where Fe is more readily available, and mafic rocks tend to have higher copper grades than more felsic rocks because of their higher Fe content (e.g., Langton et al., 1982; John et al., 2010).

$$\text{Hornblende} + K_2SO_4 + H_2SO_4 \Leftrightarrow \text{Biotite} + \text{Quartz} + \text{anhydrite} \qquad \text{(Eq. 2)}$$

At temperatures <400°C, SO_2 disproportionates to form sulfuric acid and hydrogen sulfide following equation 3, which lowers the fluid pH and provides H_2S for equation 1, and thus promotes sulfide precipitation (e.g., Holland, 1965;

Ohmoto and Rye, 1979; Einaudi et al., 2003; Field et al., 2005; Chambefort et al., 2008). As a result of equation 3, hydrothermal alteration caused by magmatic fluids at temperatures <400°C is mainly driven by acid-buffering hydrolytic alteration of feldspars to white micas (i.e., muscovite, illite, phengite, and paragonite) and clays, which forms alteration assemblages such as sericitic, intermediate argillic and advanced argillic (Seedorff et al., 2005).

$$4\ SO_2 + 4\ H_2O = 3\ H_2SO_4 + H_2S \Leftrightarrow 3\ HSO_4^- + 3\ H^+ + H_2S \qquad \text{(Eq. 3)}$$

Equations 4 to 6 show that the alteration of K-feldspar, albite and anorthite to white mica consumes H^+ (i.e., raises the fluid pH) and produces quartz. By increasing the fluid pH, these equations also significantly reduce metal solubility by driving equation 1 to the right, which causes further sulfide precipitation.

$$1½\ KAlSi_3O_8 + H^+ \Leftrightarrow ½\ KAl_2(AlSi_3)O_{10}(OH)_2 + 3\ SiO_2 + K^+ \qquad \text{(Eq. 4)}$$

$$1½\ NaAlSi_3O_8 + H^+ + ½\ K^+ \Leftrightarrow ½\ KAl_2(AlSi_3)O_{10}(OH)_2 + 3\ SiO_2 + 1½\ Na^+ \qquad \text{(Eq. 5)}$$

$$1½\ CaAl_2Si_2O_8 + 2\ H^+ + K^+ \Leftrightarrow KAl_2(AlSi_3)O_{10}(OH)_2 + 1½\ Ca^+ \qquad \text{(Eq. 6)}$$

1.2.2. Zonation of porphyry-related alteration

Porphyry systems characteristically display large hydrothermal alteration halos with strong lateral and vertical zoning. Hydrothermal alteration within and near the economically mineralized zones is typically easily recognizable and has been well documented in the past, but peripheral alteration is often very subtle and difficult to detect.

As rising magmatic fluids cool and become more and more acidic due to equation 3, the hydrothermal alteration assemblages formed in porphyry systems are typically, from deepest to shallowest and oldest to youngest: 1) potassic centered on the mineralizing intrusion(s), 2) sericitic (also referred to as phyllic), and 3) advanced argillic alteration (Figure 1.1) (e.g., Seedorff et al., 2005; Sillitoe, 2010; Halley et al., 2015). The degree of superposition of these assemblages, however, is a function of the amount of collapse and telescoping that took place during the evolution of the system (Gustafson and Hunt, 1975). If minimal telescoping takes place, there can be a gap of 0.5 to 1 km between the potassic and advanced argillic zones (Sillitoe, 2010).

Potassic alteration takes place early at depth and at temperatures between 350 and 700°C, proximal to and within the porphyry mineralizing intrusions (Brimhall, 1977; Seedorff et al., 2005). The typical potassic assemblage is K-feldspar, biotite, quartz, anhydrite and magnetite (Gustafson and Hunt, 1975). Biotite is the dominant alteration mineral in mafic rocks such as basalt due to the greater abundance of Fe in these rocks compared to more felsic rocks such as granodiorites and quartz monzonites. In the latter, K-feldspar is the dominant alteration mineral. Magnetite typically forms in mafic sites along with secondary biotite because of the availability of Fe liberated by the alteration of hornblende. Veins formed during potassic alteration are characterized by quartz-poor sulfide-bearing veinlets with selvages that may contain magnetite, biotite, K-feldspar and locally fine-grained white mica (e.g., early dark micaceous veins, Meyer, 1965; Brimhall, 1977; Rusk et al., 2008; early halo veins, Proffett, 2009), and by sulfide-bearing granular quartz veins with narrow K-feldspar selvages (A-type veins) or without selvages (B-type veins; Gustafson and Hunt, 1975). Quartz veins in the potassic zone can either form a stockwork or sets of sheeted veins, and may locally constitute up 25 to 60% of the rock in the most heavily veined areas in and around early porphyry intrusions (e.g., Gustafson and Hunt, 1975; Osatenko and Jones, 1976). In many porphyry deposits the potassic alteration zone has a barren core at depth where the fluid temperature was too

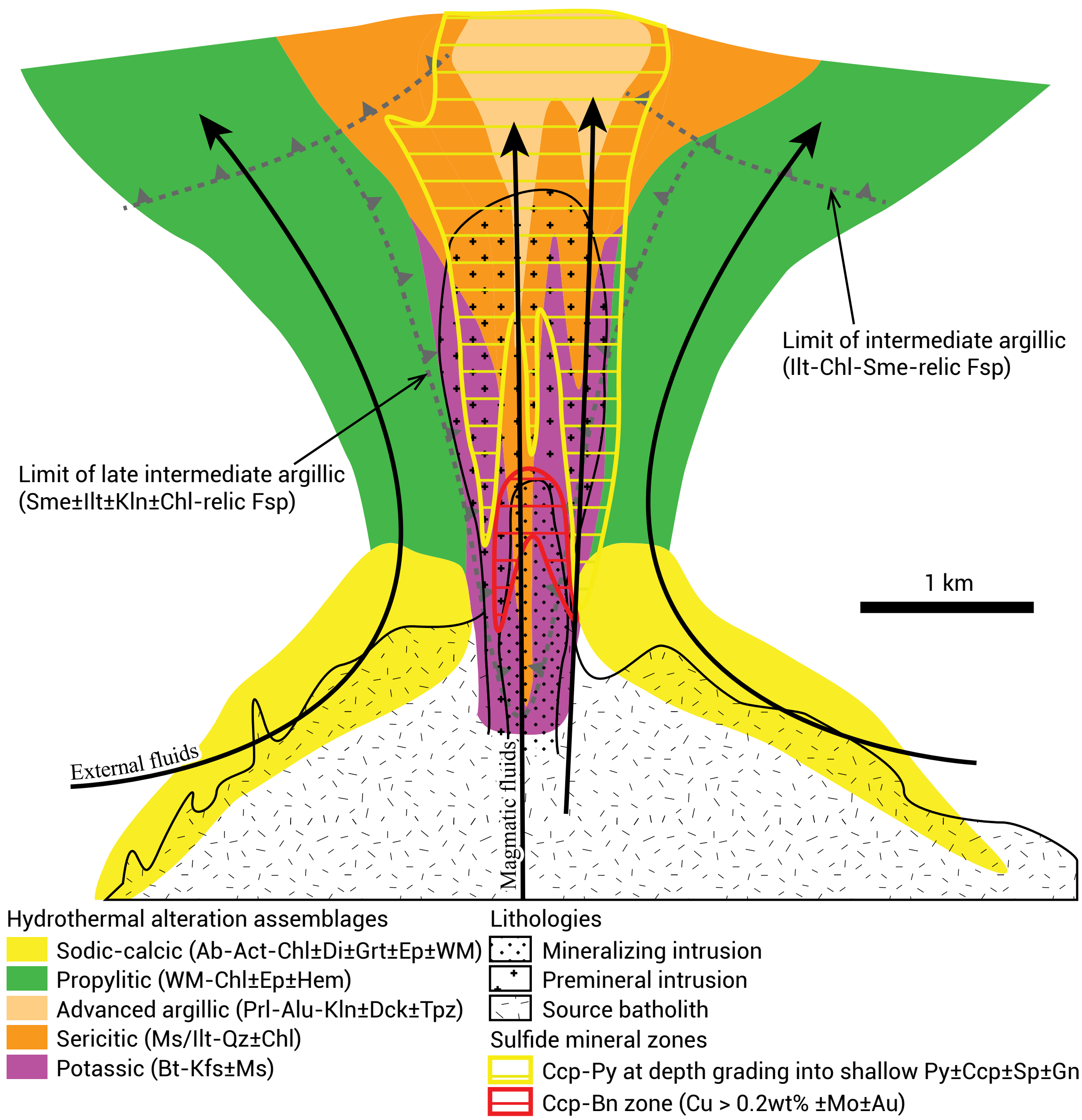

Figure 1.1. Schematic vertical cross-section of a typical porphyry Cu magmatic-hydrothermal system showing distribution of alteration assemblages and sulfide minerals (modified from Halley et al., 2015). Scale is an approximation. Abbreviations: Ab = albite, Act = actinolite, Alu = alunite, Bn = bornite, Bt = biotite, Ccp = chalcopyrite, Chl = chlorite, Dck = dickite, Di = diopside, Ep = epidote, Gn = galena, Grt = garnet, Hem = hematite, Ilt = illite, Kfs = K-feldspar, Kln = kaolinite, Ms = muscovite, Prl = pyrophyllite, Py = pyrite, Qz = quartz, Sp = sphalerite, Tpz = topaz, WM = fine-grained white mica.

high to allow precipitation of sulfide minerals. The upper part of the potassic zone is generally associated with a chalcopyrite–bornite zone that typically transitions outwards to a chalcopyrite–pyrite zone (e.g., Gustafson and Hunt, 1975).

Sericitic alteration is generally located above potassic alteration, but may also partially to completely overprint it depending on the degree of telescoping. This alteration is characterized by abundant pyrite precipitation, and by a series of hydrolytic reactions in which mafic minerals are altered to chlorite, and feldspars are altered to fine-grained white mica and quartz at temperatures between 300 and 550°C (Seedorff et al., 2005). Sericitic alteration is typically structurally-controlled and forms alteration selvages around quartz ± sulfide-bearing veins (D-type veins) or fractures with no vein material (Gustafson and Hunt, 1975). Selvage thickness varies between a few millimeters and several meters depending on the intensity of fluid–rock interaction. D-type veins may extend several kilometers away from mineralized zones both laterally and vertically (i.e., up to 3 km vertically at Yerington, Dilles, 1987; up to 10 km lateraly at Butte, Rusk et al., 2008; up to 4 km laterally at Valley, Alva Jimenez, 2011).

The shallowest alteration assemblage in porphyry systems is generally advanced argillic alteration. This assemblage is characterized by quartz, pyrophyllite, dickite, kaolinite, and alunite and forms at temperatures <360°C (Seedorff et al., 2005). Advanced argillic alteration typically transitions from structurally-controlled at depth to large barren lithocaps near the surface that can cover 10 km^2 or up to 100 km^2 in extreme cases, and can be up to 1 km thick (Sillitoe, 2010). Because of its location in the system and of the nature of its mineralogy, advanced argillic alteration tends to be recessive and may be eroded by the time the porphyry deposits are at the surface.

Intermediate argillic alteration typically forms late in the alteration paragenesis and occurs when meteoric fluids and magmatic fluids interact at temperatures <200°C, which causes hydrolytic alteration of the host rock to form minerals such as fine-grained white mica, smectite, kaolinite, montmorillonite and chlorite (e.g., Sillitoe, 1993, 2000; Seedorff et al., 2005; Halley et al., 2015).

Propylitic alteration forms on the distal margins of the system where heated external fluids or spent magmatic fluids cause metasomatic reactions to take place at low to moderate temperatures (i.e., 200–350°C; Digel and Gordon, 1995; Dilles et al., 2000; Bird and Spieler, 2004; Seedorff et al., 2005). Propylitic alteration is generally interpreted to be coeval with higher-temperature potassic alteration (Sillitoe, 2010). Three sub-facies of propylitic alteration may be present in porphyry systems (Norman et al., 1991; Cooke et al., 2014a): an inner zone of higher-temperature minerals that contains actinolite, an intermediate zone characterized by chlorite–epidote, and an outer lower-temperature zone characterized by chlorite–calcite–prehnite–zeolites. Propylitic alteration is typically weakly to moderately developed and only involves minor mass transfer of elements (Cooke et al., 2014a; Byrne, 2019).

Syn to post-mineralization sodic-calcic alteration typically occurs at a similar depth or deeper than potassic alteration, near the top of the source batholith and on the margins of the mineralizing intrusions (Figure 1.1) (e.g., Dilles and Einaudi, 1992; Dilles et al., 2000; Halley et al., 2015). This alteration is generally late in the evolution of the system and takes place as the magmatic fluid pressure and temperature decline and non-magmatic fluids such as seawater or sedimentary brines flow through the existing fracture-controlled permeability and are heated to temperatures between 300 and 450°C (e.g., Dilles and Einaudi, 1992; Dilles et al., 2000; Byrne, 2019). The metasomatism caused by these heated fluids adds Na and Ca and removes K and Fe from the host rock. At temperatures >400°C the dominant alteration minerals are albite and actinolite, with minor garnet, diopside, tourmaline and titanite, whereas at temperatures <400°C the dominant minerals are albite, epidote, chlorite, and minor fine-grained white mica (e.g., Carten, 1986; Dilles and Einaudi, 1992; Seedorff et al., 2005). Sodic-calcic alteration is generally sulfide and metal-poor, though magnetite and/or hematite may locally be present.

1.3. The Highland Valley Copper district: previous work and geological summary

The five porphyry Cu systems of the HVC district (i.e., Bethlehem, J.A., Valley, Lornex and Highmont) are hosted in the GCB (McMillan, 1985; Byrne et al., 2013; D'Angelo et al., 2017), a large 30 x 65 km north-northwest-elongated composite calc-alkaline batholith that intruded the Nicola Group volcanosedimentary package (Preto, 1979; Beatty et al., 2006; McMillan et al., 2009; Schiarizza, 2017) during the Late Triassic (Mortimer et al., 1990; D'Angelo et al., 2017). The Nicola Group is part of the exotic Quesnel island arc terrane (Stanley and Senowbari-Daryan, 1999; Nelson et al., 2013).

Voluminous Late Triassic arc magmatism (i.e., ~210 to ~195 Ma) formed several batholiths in the southern Quesnel terrane (e.g., Guichon Creek, Granite Mountain, Thuya, Takomkane; Figure 1.2) and generated three sub-parallel belts of porphyry systems (Preto, 1979; Logan and Mihalynuk, 2014; Schiarizza, 2014) that host most of the large deposits in the Canadian Cordillera (Logan

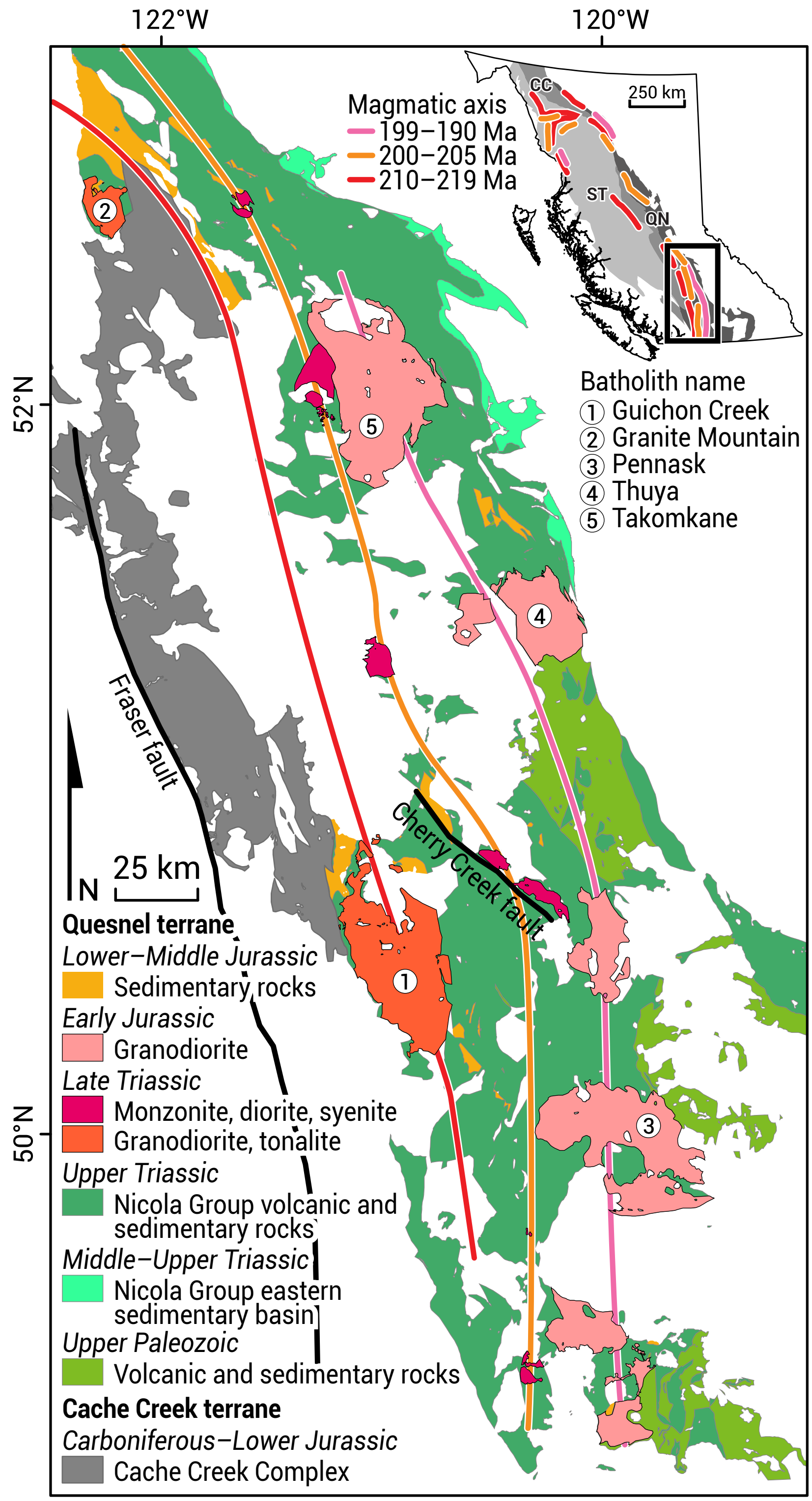

Figure 1.2. Simplified map of southern British Columbia showing rocks from the Cache Creek and Quesnel terranes, and the linear traces of Late Triassic to Early Jurassic arc intrusions (modified from Logan and Mihalynuk, 2014; Schiarizza, 2014; Cui et al., 2017). Terrane abbreviations: CC = Cache Creek, QN = Quesnel, ST = Stikine. Coordinates are in WGS1984.

and Mihalynuk, 2014). The HVC porphyry deposits are part of the oldest and westernmost of the three porphyry system belts (Figure 1.2).

The GCB is compositionally zoned from mafic older marginal facies to felsic younger central facies (Figure 1.3) (Carr, 1966; Northcote, 1969; McMillan, 1976b, 1985; Byrne et al., 2013; D'Angelo et al., 2017). The oldest magmatic episode, which intruded between 211.0 ± 0.2 Ma and 210.4 ± 0.4 Ma, formed the Border, Guichon and Chataway intrusive facies and is characterized by equigranular diorites, granodiorites and rare gabbros. A second magmatic episode, which intruded between 209.8 ± 0.3 Ma and 208.6 ± 0.2 Ma, formed the Bethlehem, Skeena and Bethsaida intrusive facies and is characterized by equigranular to weakly porphyritic granodiorites and monzogranites. Two volumetrically smaller younger units, a mineralized fine-grained equigranular granodiorite stock at Valley called the “Salt and Pepper” (S&P) Bethsaida facies and a post-mineralization quartz-rich quartz–feldspar-porphyritic dike at Highmont, may be part of a third magmatic episode and were respectively dated at 208.2 ± 0.2 Ma and 207.0 ± 0.2 Ma (U-Pb zircon, D'Angelo et al., 2017).

Gravity and seismic models of the GCB (Ager et al., 1973; Roy and Clowes, 2000) suggest that: 1) the batholith forms a flattened funnel-shaped intrusive body with steep eastern and western contacts and shallow northern and southern contacts, 2) it has a steeply-plunging feeder zone located below the porphyry systems, and 3) it is tilted by ~12–15° to the northeast. Post-emplacement tilting of the GCB is supported by aluminium-in-hornblende barometry, which shows that exposed rocks from the southern half of the GCB formed at depths between 3.7 and 7.4 km, whereas rocks from the northern half of the batholith formed at depths ranging from 2.6 to 4.8 km (D'Angelo, 2016).

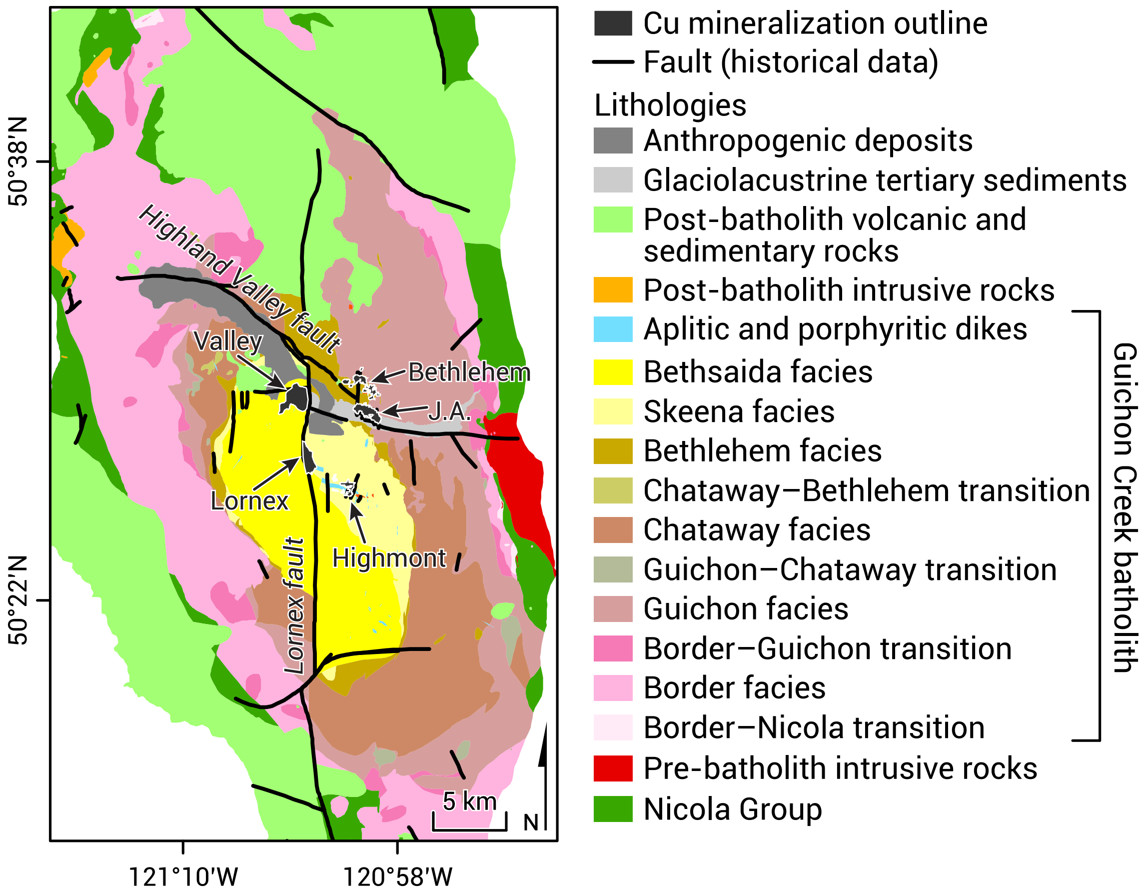

Figure 1.3. Geological map of the Guichon Creek batholith showing the location of the five known Highland Valley Copper porphyry centers and the position of fault traces as interpreted prior to the current study (modified from McMillan et al., 2009).

Porphyry Cu mineralization in the HVC district was emplaced during at least two main hydrothermal episodes (Byrne et al., 2013). The Bethlehem and J.A. deposits formed during the first hydrothermal episode at ~209 Ma. The two deposits are mainly hosted in the Bethlehem facies near the Guichon–Bethlehem facies contact, and were formed prior to the intrusion of the Skeena and Bethsaida facies. The Valley, Lornex and Highmont deposits were subsequently emplaced between ~208 Ma and ~207 Ma, as shown by Re-Os dating of molybdenite from Valley, Lornex and Highmont (Ash et al., 2006; D'Angelo et al., 2017). The Highmont deposit is hosted in the Skeena facies, the Lornex deposit is hosted at the contact between the Skeena and Bethsaida facies, and the Valley deposit is hosted in the Bethsaida facies (Figure 1.3). The Valley and Lornex deposits are interpreted to have formed as a single porphyry system (Allen and Richardson, 1970; Hollister et al., 1975), that was later dismembered by post-mineralization brittle faulting.

After the accretion of the Quesnel terrane onto the western margin of the North American continent during the Middle Jurassic (Nixon et al., 1993), the tectonic regime changed from sinistral transpression to dextral transpression during the mid-Cretaceous to Eocene period (Nelson and Colpron, 2007; Nelson et al., 2013). This dextral structural regime is expressed in the GCB as dextral offset of lithological contacts and porphyry Cu mineralized zones across north-trending faults. The Lornex fault, which offsets the Valley and Lornex deposits by approximately 3.5 km (Hollister et al., 1975), records the largest post-mineralization dextral displacement in the district (Figure 1.3). Additionally, Tertiary extension is expressed as normal displacement along the west-northwest to northwest-trending Highland Valley fault (McMillan, 1976b), and caused the formation of a basin now filled with up to 300 m of pre-glacial and glacial sediments under which the J.A. deposit is buried (Figure 1.3) (Bobrowsky et al., 1993).

Hydrothermal alteration within the HVC porphyry deposits was studied in detail in the 1970s and 1980s, but few studies have been published since then (Byrne et al., 2013, and references therein). The Bethlehem and J.A. deposits are characterized by weakly mineralized biotite-dominant potassic alteration, well-mineralized fine-grained white mica–chlorite sericitic alteration, and post-mineralization sodic-calcic alteration that remobilized Cu mineralization, particularly at depth (Briskey and Bellamy, 1976; McMillan, 1976a; Briskey, 1980; Alva Jimenez, 2011; Byrne et al., 2013). The Valley and Lornex deposits both have a central zone of intense early barren quartz stockwork veins with K-feldspar alteration selvages, which transition outward to weakly mineralized K-feldspar ± quartz ± chalcopyrite ± bornite veins (Osatenko and Jones, 1976; Waldner et al., 1976; McMillan, 1985; Byrne et al., 2013). The Highmont deposit also contains K-feldspar ± quartz ± chalcopyrite ± bornite veins, although these veins are less abundant than at Valley and Lornex (Bergey et al., 1971; Reed and Jambor, 1976). Minor biotite alteration of primary hornblende is present at all three deposits. Copper mineralization at Valley, Lornex and Highmont is dominantly hosted in well-mineralized quartz–bornite–chalcopyrite ± molybdenite veins with selvages of coarse-grained grey paragonitic muscovite, quartz and minor calcite (Osatenko and Jones, 1976; Reed and Jambor, 1976; Waldner et al., 1976; Alva Jimenez, 2011). Thick banded quartz–chalcopyrite–molybdenite ± pyrite veins with extensive fine to coarse-grained grey muscovite selvages are generally present at the margins of the deposits (McMillan, 1985). Sodic-calcic alteration characterized by albite–chlorite ± actinolite ± titanite ± epidote ± tourmaline and rare diopside and garnet is weak at Valley but locally strong at Lornex and Highmont (Alva Jimenez, 2011; Byrne et al., 2017). Complex cross-cutting relationships indicate that sodic-calcic alteration occurred after potassic alteration, but both before and after the formation of quartz–sulfide-bearing veins with coarse-grained muscovite. Chapter 3 of this thesis provides detailed descriptions of the mineralization and hydrothermal alteration at each HVC porphyry deposit based on historical work and observations made during this study.

A first description of district-scale alteration at HVC was provided by Casselman et al. (1995), who briefly described the distribution of “green sericite” and chlorite veins across the district. This work, however, only characterized vein intensity as weak or moderate–strong, and no other data was presented.

Prior to the CMIC Footprints Project, only one recent study focused on hydrothermal alteration at the district-scale at HVC (Alva Jimenez, 2011). The study characterized the compositional variations in white mica and chlorite from the transitional potassic-sericitic to sericitic alteration assemblages within the Bethlehem deposit and along a transect between the Valley deposit and the Alwin Cu occurrence located approximately 4 km to the west of Valley. Alva Jimenez (2011) concluded that white mica from within the Valley deposit is high-temperature sodium-rich (i.e., paragonitic) muscovite, whereas white mica from the margins of the Valley deposit and from the Alwin Cu occurrence is phengitic muscovite.

One other graduate thesis that focused on alteration in the HVC district was recently completed as part of the CMIC Footprint Project. Kevin Byrne completed a Ph.D. thesis that investigated the magnetic susceptibility signature of hydrothermal alteration (Byrne et al., 2019), as well as the whole rock lithogeochemistry, the epidote and prehnite mineral geochemistry, and the stable (H, O, C, and B) and radiogenic (Sr) isotope signature of the various HVC alteration assemblages, with a particular focus on sodic-calcic and propylitic alteration (Byrne et al., 2017; Byrne, 2019). Byrne (2019) concluded that sodic-calcic alteration at HVC formed from heated seawater-derived fluids, which locally mixed with magmatic fluids within and next to the deposits. The study also determined that water and calcite addition to the host rock by porphyry-related alteration form a lithogeochemical footprint that can be detected up to 6 km away from porphyry Cu mineralization. Similarly, pathfinder trace elements (e.g., As, Ge, Mn, Pb, Sb, Zn) interpreted to be sourced from cooling magmatic fluids can be detected up to 6 km and 8 km from porphyry Cu mineralization in epidote and prehnite mineral chemistry, respectively.

1.4. Research objectives

The aim of this study is to 1) interpret the present-day batholith-scale structural framework of the GCB in order to restore it to its Late Triassic configuration, 2) determine the district-scale mineralogy and the spatial extent of each alteration assemblage formed as a result of porphyry-related hydrothermal fluid flow, 3) establish what are the structural controls on fracture permeability and hydrothermal fluid flow during porphyry mineralization in a batholithic environment, and 4) identify, for each alteration assemblage, the district-scale variations in white mica composition that characterize the porphyry Cu deposit footprint.

1.4.1. What is the present-day GCB structural framework?

Displacement along brittle faults may significantly complicate the geology of an area, therefore documenting the location and geometry of these faults is important in order to reconstruct the geological setting within which the mineral deposits present in an area were formed. The ~3.5 km post-mineralization dextral displacement along the Lornex fault in the HVC district is one such example (Allen and Richardson, 1970; Hollister et al., 1975) that significantly affected the spatial distribution of porphyry Cu mineralization and hydrothermal alteration assemblages across the HVC district. Previous structural studies of the HVC district mainly focused on the Lornex and Highland Valley faults because of their strong topographic expression and their proximity to the porphyry systems (e.g., Hollister et al., 1975; McMillan, 1976b, 1985). A few studies have focused on the structural setting within individual porphyry deposits (e.g., Lornex deposit, Waldner et al., 1976; Bethlehem deposit, Briskey et al., 1981), however studies that focus on the structural architecture of the entire GCB are lacking. The known faults in the GCB prior to this study are shown in Figure 1.3. A new structural framework interpretation of the entire GCB is presented in Chapter 2 and is the first step required to produce an accurate palinspastic reconstruction of the batholith to show the spatial distribution of hydrothermal alteration assemblages and vein orientations across the HVC district during the Late Triassic.

1.4.2. What is the mineralogy and district-scale spatial extent of each alteration assemblage formed as a result of porphyry-related hydrothermal fluid flow?

Porphyry systems generate vast amounts of hot fluids that flow convectively through the surrounding host rocks (e.g., Cathles, 1977; Burnham, 1979; Cline and Bodnar, 1991; Weis, 2015). These fluids interact with the rocks and change their mineralogy and chemistry. Different alteration minerals form through fluid-rock interactions depending on the rock and fluid characteristics, such as temperature and pH (e.g., Meyer and Hemley, 1967; Titley, 1982). Studies that documented the distal alteration that surrounds porphyry Cu deposits, however, are few and are generally restricted to within 5 km vertically and laterally from Cu mineralization (e.g., Halley et al., 2015). To improve upon the current understanding of the porphyry Cu deposit footprint, Chapter 3 of this thesis defines the footprint of porphyry systems beyond the limits of copper mineralization by systematically characterizing the paragenesis, mineralogy, intensity and spatial distribution of all the hydrothermal alteration assemblages present across the HVC district to distances >10 km from the deposits.

1.4.3. What are the structural controls on fracture permeability and hydrothermal fluid flow during porphyry mineralization in a batholithic environment?

The spatial extent of hydrothermal alteration is controlled by the capacity of the hydrothermal fluids to move away from the heat source and react with the host rocks. Hydrothermal fluid flow in the brittle crust is primarily controlled by host rock fracture permeability (Ingebritsen and Manning, 2010; Ingebritsen, 2012; Weis et al., 2012). The mechanisms that generate fracture permeability are influenced by regional tectonic stresses (e.g., Tosdal and Richards, 2001; Houston and Dilles, 2013) as well as local stresses (e.g., Burnham and Ohmoto, 1980; Bergbauer and Martel, 1999; Fournier, 1999). Vein and fracture orientations in typical porphyry environments have been studied in the past at several deposits (e.g., Sierrita-Esperanza, Titley et al., 1986; Yerington, Carten et al., 1988; Bingham Canyon, Gruen et al., 2010; Butte, Houston and Dilles, 2013), however studies that systematically investigate porphyry-related vein orientations at the district-scale are lacking. Chapter 3 of this thesis analyses vein orientations across the GCB for each alteration assemblage in order to determine what mechanisms generated fracture permeability and how these mechanisms evolved through time.

1.4.4. What are, for each alteration assemblage, the district-scale variations in white mica composition that characterize the porphyry Cu deposit footprint?

White mica minerals form in high and low-temperature porphyry-related hydrothermal alteration assemblages (e.g., Seedorff et al., 2005), so understanding their compositional variations across porphyry systems can be a powerful tool to vector towards the porphyry deposits. Significant advances have been made in the use of short-wave infrared (SWIR) spectroscopy, using shifts in the wavelength of the Al-OH absorption feature in the 2180–2220 nm range (e.g., Duke, 1994), to recognize compositional variations in white mica alteration minerals and to map gradients in hydrothermal fluid composition, temperature and pH (e.g., Thompson et al., 1999; Halley et al., 2015). These studies, however, have focused primarily on white mica compositional variations within 5 km of porphyry Cu mineralization in assemblages such as transitional potassic-sericitic to sericitic (Alva Jimenez, 2011; Benavides, 2018), sericitic or phyllic (Harraden et al., 2013; Uribe-Mogollon and Maher, 2018), or sericitic to intermediate argillic (Cohen, 2011; Graham et al., 2018). Studies of white mica as part of the propylitic or sodic-calcic alteration assemblages at the district scale are lacking. Chapter 4 of this thesis investigates the variations in white mica composition from all alteration assemblages across the HVC district to distances >10 km from the porphyry deposits.

1.5. Research approach

1.5.1. Field mapping

Lithology and alteration mapping for this research project was undertaken as a collaboration between the author and fellow CMIC student Kevin Byrne. To avoid an overlap of the research and to optimize the regional coverage, field work was divided and samples were shared between the two Ph.D. research projects. Five transects, each approximately 10–14 km in length and 2.5–3.5 km wide, were mapped at 1:10,000 scale across the GCB between 2014 and 2016. Transects start at one of the HVC porphyry deposits and end near the outer margin of the GCB. The area located within 3–4 km to the southwest of the Valley deposit was mapped at 1:5,000 scale. Open pit benches were also mapped at 1:5,000 scale in the Valley, Lornex and Highmont deposits. The total area mapped is approximately 225 km^2.

Structural measurements for fault, dikes and veins were recorded using the right hand rule: for each plane the bearing of the strike and dip angle to the right of the strike were recorded. Vein intensity, expressed in centimeters of vein and altered selvage per meter of rock (cm/m), was also measured at each vein location. A total of 1647 orientation measurements were collected. In addition, 563 vein orientations were provided by Teck Resources Limited ("Teck"). A total of 739 rock samples that contain hydrothermal alteration were collected on a grid pattern every 250 m for areas mapped at 1:5,000 scale and every 500 m for areas mapped at 1:10,000 scale. Rock slabs were cut from every sample for further analyses (e.g., feldspar staining, SWIR spectroscopy). Rocks samples collected by the author are stored at the University of British Columbia, whereas samples collected by Kevin Byrne are stored at Teck's Highland Valley Copper mine site.

1.5.2. Fault modeling and GCB reconstruction

Structural mapping in areas where there is a paucity of outcrops is challenging because brittle faults are typically very susceptible to erosion, and direct observation of faults in the field may not be possible. A solution to this challenge is the use of geophysical techniques to interpret the geometry of faults. These techniques provide information collected remotely and indirectly about the bedrock geology at depth. Magnetic surveys, which are among the most commonly used geophysical techniques (e.g., Reford and Sumner, 1964; Nabighian et al., 2005; Purucker and Clark, 2011), provide district-scale magnetic intensity data that can be used to interpret the location and dip of faults because brittle faulting processes typically result in a lowered magnetic susceptibility in faulted rocks compared to the surrounding host rocks Henkel and Guzman (1977).

In Chapter 2 of this thesis, the surface expression of faults was identified via lineament analysis using a multi-layered approach similar to the approach of Sánchez et al. (2014). Fault dips were subsequently modeled by performing simple 2D inverse modeling along profiles extracted from the HVC district reduced-to-pole magnetic intensity grid perpendicularly across the interpreted faults. Fault strikes and dips were also measured in the field where available. A new batholith-scale 3D structural interpretation of the GCB based on the results of the lineament analysis and on the modeled and measured fault orientations is then presented.

Chapter 3 of this thesis uses the new GCB structural framework interpretation presented in Chapter 2 to produce a palinspastic reconstruction of the batholith. The spatial distribution of vein orientations and intensities in the reconstructed GCB is then used to identify the mechanisms that generated fracture-controlled permeability for each alteration assemblage.

1.5.3. Feldspar staining

After each slab was etched using hydrofluoric (HF) acid, sodium cobaltinitrate and amaranth were used to respectively stain K-feldspar crystals yellow and calcic plagioclase crystals red (Gabriel and Cox, 1929; Bailey and Stevens, 1960; Laniz et al., 1964; Lyons, 1971; Norman, 1974). Feldspar staining highlighted the effect of hydrothermal alteration on feldspar mineralogy: for example addition of K-feldspar by potassic alteration, removal of K-feldspar by sodic-calcic alteration, or white mica alteration of primary plagioclase.

1.5.4. Analytical methods

Short-wave infrared analyses and feldspar staining was performed on the same slabs to better constrain the alteration assemblage present in each sample. Infrared reflectance spectra were collected using a Specim SisuROCK™ hyperspectral scanner, as well as an ASD TerraSpec® portable mineral analyzer. Chapter 4 presents a comparison of the effectiveness of each technique at identifying district-scale compositional variations in white mica using the Al-OH absorption feature wavelength (~2200 nm). Thirteen representative samples from each alteration assemblage were also selected for electron microprobe analyses (EPMA) to determine the major and minor element composition of white mica alteration minerals. Finally, quantitative X-ray diffraction analyses (i.e., Rietveld refinement) were conducted on four clay-bearing samples with intermediate argillic alteration in order to characterize their mineralogy. All data generated during this study are presented in Appendix A to F.

Chapter 2. Interpreting regional 3D fault networks from integrated geological and geophysical data sets: An example from the Guichon Creek batholith, British Columbia

2.1. Introduction

Brittle faults cut through earlier-formed rocks and displacement along them may significantly complicate the geology of an area. Documenting the location and geometry of faults is therefore an essential element of all geological mapping programs. Defining fault geometry is also an essential step in most 3D geological modeling software packages used in mineral exploration and mining, such as Leapfrog Geo™, GeoModeller™, and Paradigm GOCAD®. In order to make a geological model that is as accurate as possible, these software packages all require the user to define the location and geometry of faults prior to modeling lithologies.

Direct field observations and measurements are required to confirm the location and geometry of a fault, but structural mapping in areas where bedrock exposures are sparse or lacking make such objectives problematic. Another challenge is that the apparent dip of a fault in outcrop may not be representative of the dip of the same fault at depth. Using remote and indirect methods such as geophysical techniques to interpret the geometry of faults offers a solution to these challenges because such techniques provide information about the bedrock geology at depth. Magnetic surveys, which map lateral changes in total magnetic intensity, are among the most commonly used geophysical techniques because they can be conducted over large areas, quickly and at relatively low costs, and data can be processed on personal computers at low cost (e.g., Reford and Sumner, 1964; Nabighian et al., 2005; Purucker and Clark, 2011).

Many previous studies that interpreted structural features in magnetic data sets were fairly simple 2D efforts that emphasized linear magnetic discontinuities or breaks (i.e., lineaments) to interpret lithological contacts or faults at the surface (e.g., Gunn et al., 1997; Sánchez et al., 2014; Brethes et al., 2018), or more complex attempts to model sub-surface geology with forward or inverse 3D modeling techniques (e.g., Jessell and Valenta, 1996; Jessell, 2001). A comprehensive discussion of the potential impacts of structures on magnetic intensity patterns was presented by Jessell (2002), which examined fold geometries, fault displacements and fault zone alteration. The results reported in Jessell (2002) were derived from NODDY™, a forward modelling software package that allows geologists and geophysicists to create synthetic 3D geological models and investigate the geophysical signatures that these models might produce.

In most previous studies the modeling attempted to explain the magnetic intensity patterns in terms of lithological variations without a specific focus on 3D fault geometry (e.g., Spicer et al., 2011; Mahmoodi et al., 2017). However, magnetic intensity data also contain information about faults because brittle faulting processes typically result in a lowered magnetic susceptibility in faulted rocks Henkel and Guzman (1977). Betts et al. (2015), for example, showed that magnetic intensity data often contain kinematic indicator patterns like those recognized by structural geologists in outcrops, but their study did not discuss the geometry of faults at depth.

In this paper we present a simple approach to integrate direct field measurements of fault geometry with indirect estimates of fault geometry derived from aeromagnetic surveys, with the objective to develop a 3D fault network at a regional or district scale. Our approach combines 1) multi-layer

2D lineament mapping to identify potential faults at the surface (Sánchez et al., 2014) with 2) dip modeling from magnetic intensity data for brittle faults that are represented by a lower magnetic susceptibility compared to the surrounding country rock, and 3) integration of strike and dip measurements from exposed structures as a ground-truthing measure, where available. With this method, dip direction and dip angle can be modeled for each fault by representing the faults as low magnetic susceptibility tabular bodies that extend to depth. The input data for each fault-model computation is a profile extracted from a reduced-to-pole (RTP) magnetic intensity grid. Extracted profiles are oriented perpendicular to linear low magnetic anomalies that are interpreted to be faults.

To test the validity of the approach, we used NODDY™ to create a synthetic 3D magnetic susceptibility model that contains linear low magnetic anomalies with known dip and then computed a magnetic intensity grid from the 3D magnetic susceptibility input model. The width and magnetic susceptibility of the low magnetic anomalies remained constant, but their dip was set at 5° increments. We then extracted profiles from the magnetic intensity grid derived from the model and solved for the best fit dip for each anomaly. After we confirmed the viability of our methodology, we applied the approach to the magnetic intensity grid from the Guichon Creek batholith in British Columbia to test its applicability and demonstrate the generation of an internally-consistent batholith-scale 3D fault network.

2.2. Characteristics of faults

2.2.1. Magnetic susceptibility

The primary magnetization of rocks is influenced by lithological processes (i.e., magmatic or depositional) and is mainly dependent on the magnetite-ulvöspinel solid solution mineral content (Grant, 1985; Clark, 1997; Clark, 1999). A large range of geological processes such as metamorphism, hydrothermal alteration or weathering/oxidation may overprint the primary magnetization and modify the bulk magnetic susceptibility of rocks by either adding or removing magnetite (Marshall and Cox, 1972; Lapointe et al., 1984; Grant, 1985; Lapointe et al., 1986; Latham et al., 1989; Airo, 2002; Chevrier et al., 2006; Airo and Mertanen, 2008; Mitchinson et al., 2013). As first reported by Henkel and Guzman (1977), brittle faulting results in the development of fracture zones that are commonly characterized by elongate low magnetic anomalies that form from the oxidation of magnetite to less magnetic minerals such as hematite or goethite in these highly permeable zones. Linear or curvilinear magnetic features of lower intensity than the surrounding area in a magnetic grid can therefore be interpreted as magnetite-destructive lineaments that correspond to fault zones.

2.2.2. Topography

Fault damage zones are commonly more vulnerable to erosion than the surrounding country rock because of their fractured nature and the presence of clay minerals, gouge and water (e.g., Wallace and Morris, 1979), which contribute to more rapid weathering. The location of a fault plane's intersection with the topographic surface (i.e., fault trace) can therefore be interpreted by mapping linear valleys, provided that the geological significance of these valleys can be assessed using other data sets, such as geophysical or geological data sets.

2.3. Guichon Creek batholith geology

The Guichon Creek batholith ~54 km southwest of the city of Kamloops is a Late Triassic intrusion that hosts the five major porphyry Cu-Mo mineralized systems of the Highland Valley Copper district (McMillan, 1985; Byrne et al., 2013; D'Angelo et al., 2017). The mineralized systems at Highland Valley Copper include the actively producing Valley, Lornex, and Highmont open pits, the formerly producing Bethlehem open pits, and the undeveloped and buried J.A. center (Teck Resources Limited, 2018; Figure 2.1). The Valley and Lornex orebodies are interpreted to have formed as a single porphyry system, which were subsequently cut and offset by the Lornex fault (Allen and Richardson, 1970; Hollister et al., 1975).

The Guichon Creek batholith is a large (30 x 65 km) concentrically zoned composite calc-alkaline body (Figure 2.1). Older mafic marginal facies (i.e., diorite to quartz monzonite or granodiorite; Border facies, Guichon and Chataway subfacies of the Highland Valley facies) transition into younger, more felsic facies (i.e., granodiorite; Bethlehem, Skeena and Bethsaida facies) towards the center of the batholith (Northcote, 1969; McMillan, 1976a; Casselman et al., 1995; McMillan et al., 2009; D'Angelo et al., 2017). Average magnetic susceptibility values for each intrusive facies, measured on outcrops characterized as fresh or having weak hydrothermal alteration, range from 46.7 x 10^{-3} SI for the outermost Border facies to 18.7 x 10^{-3} SI for the central Bethsaida facies (Table 2.1). In general the magnetic susceptibility values decrease towards the center of the batholith, consistent with the observed decrease in magnetite content from the older Border to the younger Bethsaida facies (D'Angelo, 2016).

Multiple studies conducted over the past fifty years have characterized the geometry (Ager et al., 1973; Roy and Clowes, 2000) and petrogenesis (D'Angelo et al., 2017, and references therein) of the Guichon Creek batholith, the age and style of porphyry-related hydrothermal alteration (Byrne et al., 2013, and

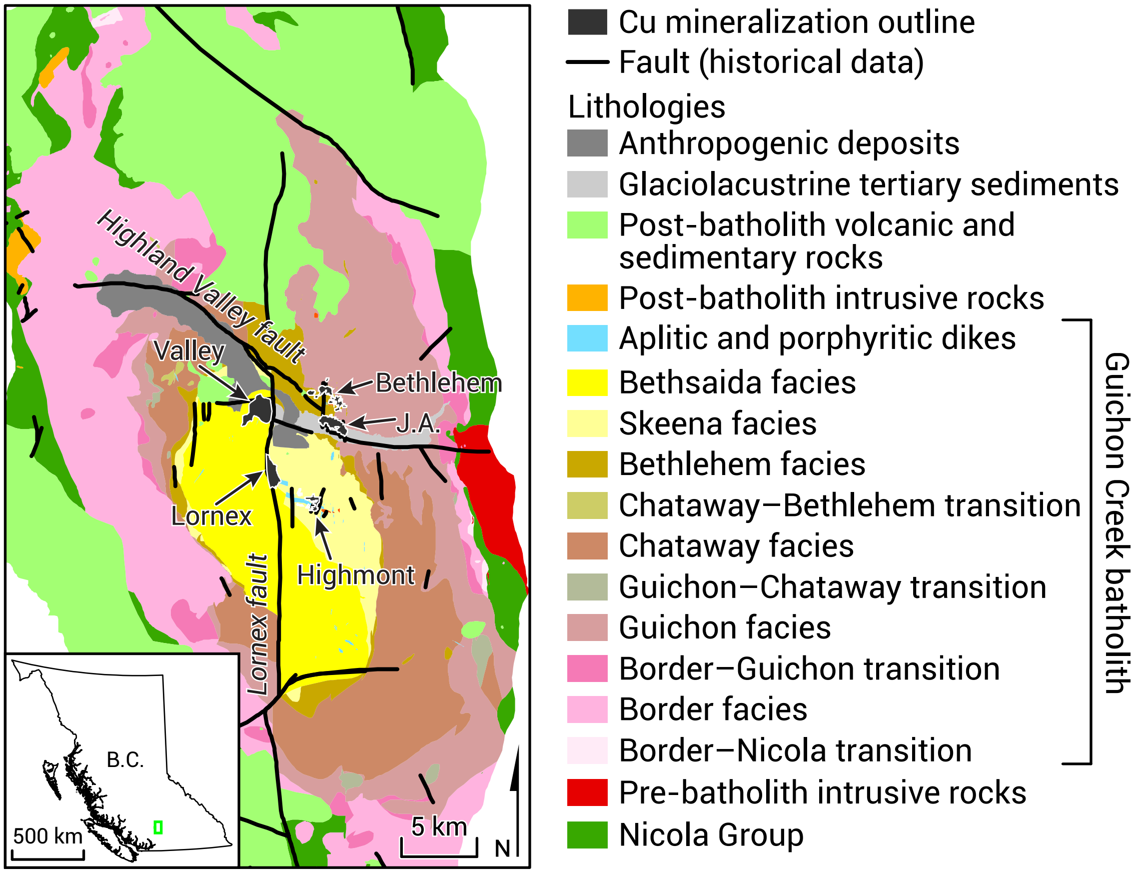

Figure 2.1. Geological map of the Guichon Creek batholith showing the location of the five known Highland Valley Copper porphyry centers and the fault traces for the district prior to this study (modified from McMillan et al., 2009). Inset shows the outline of British Columbia and the location of the study area (green rectangle).

Table 2.1. Average magnetic susceptibility for the least altered outcrop locations of the six main intrusive facies of the Guichon Creek batholith. Abbreviations: Mag susc = magnetic susceptibility, stdev = standard deviation.

Intrusive facies	Number of samples	Mag susc average (10^{-3} SI)	Mag susc stdev (10^{-3} SI)
Border	33	46.7	13.3
Guichon	99	36.7	8.2
Chataway	50	31.2	6.8
Bethlehem	15	26.1	5.3
Skeena	48	23.4	6.6
Bethsaida	189	18.7	4.3

references therein) and the structural setting at the individual porphyry systems (e.g., Waldner et al., 1976; Briskey et al., 1981). Few studies have focused, however, on the structural architecture of the batholith (Hollister et al., 1975; McMillan, 1976a), and geometric information in the literature concerning faults is lacking. The known faults in the Guichon Creek batholith prior to this study are shown in Figure 2.1.

Previous structural studies have mainly focused on the Lornex and Highland Valley faults because of their strong topographic expression and their proximity to the porphyry systems (Figure 2.1). The Lornex fault is exposed in the Valley and the Lornex open pits. Its dip varies from steeply east-dipping in the Valley open pit (Casselman et al., 1995) to steeply west-dipping in the Lornex open pit (Waldner et al., 1976). The J.A. system is interpreted to have been down-thrown by the Highland Valley fault, a west-northwest-trending fault that is inferred to dip ~80° toward the north, and was covered by sediments during Tertiary extension (Hollister et al., 1975; McMillan, 1976b).

2.4. Data sets

To better constrain the geometry of faults in the Guichon Creek batholith, we first use a multi-layer approach, similar to the methodology used by Sánchez et al. (2014), to interpret the location of lineaments that correspond to fault traces. The data sets used are: 1) drill hole data, 2) historical geological and structural mapping, 3) new geological and structural mapping done by the authors, 4) airborne magnetic intensity data (reduction to pole: RTP; first vertical derivative of RTP: RTP1VD), and 5) topography.

2.4.1. Geological data

There is a paucity of direct geological observations of faults in the Guichon Creek batholith due to the combination of poor outcrop abundance and the recessive nature of faults. Good-quality data for the locations and dips of faults in open pits and defined by drilling (un-oriented core) contribute to the new geological map of the batholith proposed in to this study, but are spatially limited to the porphyry centers. District-scale faults exposed in open pits include the Lornex and Yellow fault in the Valley pit, and the Lornex fault in the Lornex pit, whereas faults intersected by several drill holes include the Lornex, Highland Valley, Huestis, Spud, Trojan, Yubet and Yellow faults (Table 2.2). In addition to geological data from literature and provided by Teck Resources Limited ("Teck") (Figure 2.1), geological mapping that focused on lithology, hydrothermal alteration and structure was conducted between 2014 and 2016 along five transects across the Guichon Creek batholith. Each transect is approximately 10–14 km long and 2.5–3.5 km wide. The transects start at one of the known porphyry systems and end near the outer margin of the batholith. Data collected during the mapping includes the location and description of fault zones, and strike and dip measurements of fault and fracture planes.

2.4.2. Aeromagnetic survey

The Guichon Creek batholith is a high plateau with rounded hills and deep valleys. Elevation across the district varies from 210 meters in the Thompson River valley west of the batholith to 2260 meters in the peaks above the plateau. The Highland Valley Copper district aeromagnetic data were collected by fixed-wing aircraft in 1997 for Teck along east-west flight lines at a nominal spacing of 250 m. The magnetic data were reprocessed in 2015 for the Natural Sciences

Table 2.2. Guichon Creek batholith fault trace interpretation summary.

Fault name	Fault ID (Fig. 3E)	Trend	Lineament present in dataset: Magnetic intensity	Topography	Drilling	Mapping (CMIC / Teck)	Mapping (historical)	Reliability index
Aberdeen	1	N	1	1	0	1	0.5	3.5
Alamo	2	NNW	1	0	0	1	0.25	2.25
Barnes Creek	3	NW	1	1	0	0	0.25	2.25
BX	4	NNW	1	1	0	1	0	3
Cleveland	5	N	1	0	0	0	0	1
Gaza	6	NW	1	0.5	0	0	0	1.5
Guichon Creek	7	NNW	1	1	0	1	0.5	3.5
Highland Valley North	8	W	0	1	1	0	0.5	2.5
Highland Valley South	9	W	0	1	0	0	0.5	1.5
Huestis	10	N	0	0	1	0	0.5	1.5
JD	11	NE	1	1	0	1	0	3
King	12	N	1	1	0	0.5	0.25	2.75
Lornex (middle segment)	13	N	1	1	1	1	0.5	4.5
Lornex (north segment)	14	N	1	1	0	0	0.5	2.5
Lornex (south segment)	15	N	1	1	0	0.5	0.5	3
Prince	16	NE	1	1	0	0	0	2
Queen	17	NNW	1	0.5	0	0	0	1.5
Royal	18	NNE	1	0	0	0	0	1
Skuhun Creek	19	NE	1	1	0	0.5	0.5	3
Spatsum	20	NE	1	1	0	0	0	2
Spud	21	N	1	0	1	0	0.5	2.5
Tam	22	NW	1	1	0	0	0	2
Trojan	23	NNE	1	0.5	1	1	0.5	4
West Boundary	24	NNW	1	1	0.5	0.5	0.5	3.5
West Highmont	25	NNE	1	0.5	0	1	0	2.5
Yellow	26	NNE	0.5	1	1	1	0.5	4
Yubet	27	N	1	0.5	1	0	0.25	2.75

and Engineering Research Council (NSERC) of Canada and Canada Mining Innovation Council (CMIC) supported Mineral Exploration Footprints project.

The data were gridded using the minimum curvature algorithm of Geosoft Oasis montaj®, which generates the smoothest possible surface that fits all the data available. Oasis montaj® is a software package that provides tools for processing and interpretation of geophysical and geochemical data. A grid cell size of 50 m was used, which is appropriate for the 250 m flight line spacing. The height of the sensor above the ground ranged from 59 m to 761 m, with a mean of 185 m. Magnetic signal amplitude varies as a function of the cube of the distance between the source and the sensor. Hence the magnetic data collected by a loose drape (i.e., variable sensor–ground distance) aeromagnetic survey over areas with large topographic fluctuations such as the Guichon Creek batholith will contain some signal that is the result of the varying sensor–ground separation (Luyendyk, 1997; Ugalde and Morris, 2008; Hinze et al., 2013). To compensate for the varying sensor–ground effect on the observed magnetic intensity data, a correction to a uniform flight height of 110 m was applied to the data using the Geosoft Oasis montaj® Compudrape™ algorithm. Locally, the Compudrape™ correction produced some minor corruption of the observed signal, so following the drape correction the data were compared to data from north-south tie-lines and microlevelled to remove discrepancies. It should be noted that the Compudrape™ correction does not account for the effect of the topographic surface itself, which also produces a signal because of the strong magnetic contrast at the ground–air interface (Grauch and Campbell, 1984; Ugalde and Morris, 2008). Abrupt changes in topographic slopes may therefore introduce magnetic anomalies, positive or negative, in the observed magnetic intensity. This issue was considered during the fault trace interpretation.

A reduction to pole (RTP) filter was calculated by removing the modern inclination and declination of the study area from the data, which transforms the dipolar magnetic anomalies caused by induced magnetization into monopolar anomalies that become centered directly over their source (Baranov and Naudy, 1964). The RTP 1st vertical derivative (RTP1VD) filter was obtained by calculating the rate of change of the RTP grid with respect to the z direction, which enhances shorter wavelengths to highlight shallow structures such as faults, but also enhances noise (Nabighian, 1984).

The Highland Valley Copper aeromagnetic data cover the entire Guichon Creek batholith and are essentially contiguous because they were collected at a uniform flight line spacing. Additionally, the east-west orientation of the flight lines is nearly orthogonal to the major fault trend in the area so the magnetic intensity data collected are optimal for resolving north-trending magnetic anomalies caused by faults. This data set is therefore chosen as base layer for the fault trace interpretation.

2.4.3. Topographic data

For this study we use Shuttle Radar Topography Mission (SRTM) topographic data. For compatibility this data was also gridded at 50 m cell size using the minimum curvature algorithm of Geosoft Oasis montaj®. Other sources of topographic information such as air photograph-derived Canada DEM products or ASTER satellite imagery provided similar results, but in both cases it was found that they contained unmapped regions and/or datum shifts related to separate satellite passes. Topographic images can also be constructed from data collected during aeromagnetic surveys (Morris et al., 2009). However, in the case of the Highland Valley Copper aeromagnetic survey the steep slopes and aircraft elevation changes degraded the quality of the retrievable elevation data.

2.5. Methodology

2.5.1. Fault trace interpretation

The use of linear features to map faults and related structural elements has a long history under the term lineament mapping (e.g., Hobbs, 1904; Lattman, 1958). Objective lineament mapping approaches provide an automated and unbiased way to identify lineaments, whereas subjective approaches depend on the skill of the interpreter and involve geological knowledge. Both objective and subjective approaches to lineament mapping are used in this study: lineaments are first identified by an objective approach and then reviewed by the authors to ensure that the identified features are of geological significance.

The objective lineament mapping approach chosen for this study is based on a method developed by Blakely and Simpson (1986) and successfully used to identify magnetic lineaments in synthetic magnetic data sets by Lee et al. (2012). The analysis is performed in Geosoft Oasis montaj® using the GridPeaks™ algorithm. The approach compares the value of each cell in a grid with the value of the eight adjacent cells (i.e., along the row, column, and both diagonals) and identifies all the cells for which grid values are lower in any two directions. This process outlines ridges of local maxima in the grid. Since the lineaments of interest for the fault trace interpretation are magnetic low anomalies (i.e., troughs of local minima), the RTP magnetic intensity grid is multiplied by a factor -1, which converts magnetic minima into maxima, and the GridPeaks™ approach is applied to the new grid to identify the RTP grid troughs.

Although the location of cells that are not part of a linear low magnetic anomaly may be identified by this method, a number of lineaments containing several adjacent cells are identified (Figure 2.2A). These lineaments are interpreted as faults because they represent zones of low magnetic intensity that have higher intensity on both sides away from the anomaly, regardless of whether the background level is similar on both sides or not. Intrusive contacts are ruled out as an explanation for the identified lineaments because the lineaments resulting from such contacts would represent a transition zone between two different

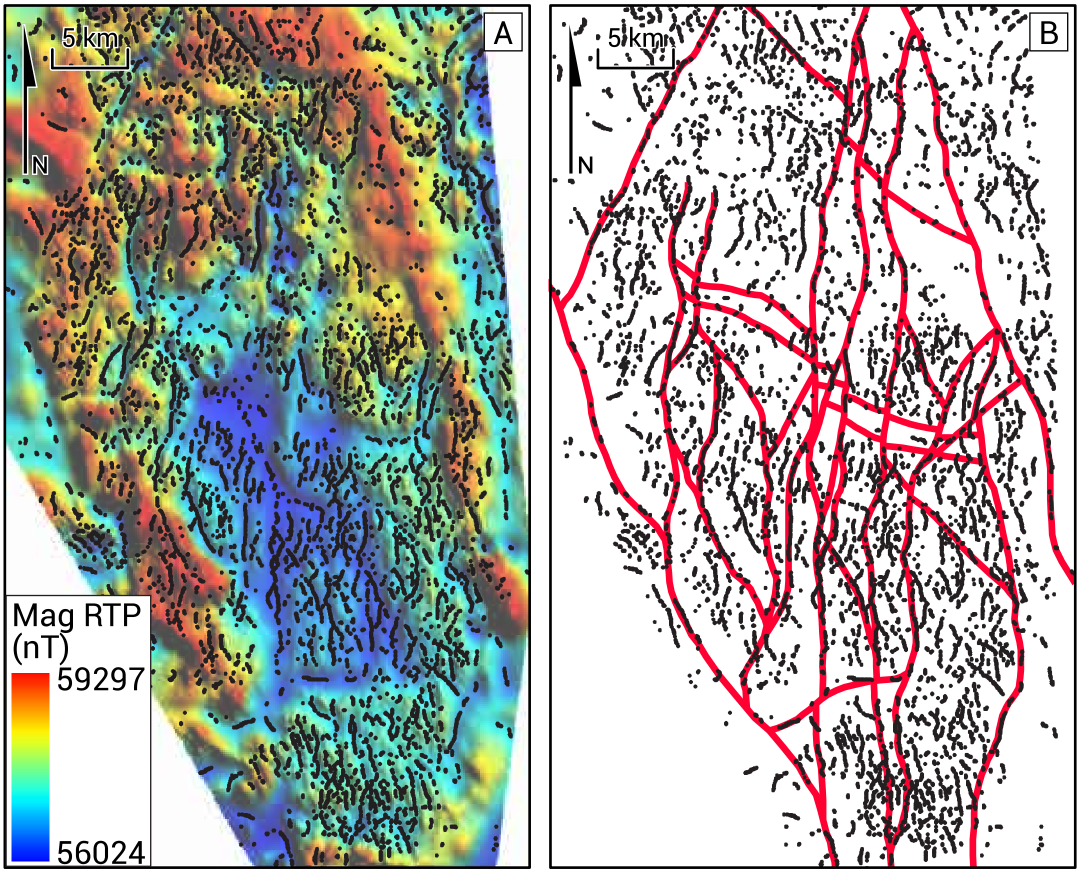

Figure 2.2. Maps showing the location of all cells from the RTP magnetic intensity grid for which at least two of their eight adjacent cells have a higher magnetic intensity (black dots) underlain by: A) the RTP magnetic intensity grid and B) the new fault trace interpretation (red lines).

magnetic intensity levels, but would not include a lower magnetic intensity zone along the contact itself. Unless geological data confirms the presence of a fault, lineaments that directly overlap with abrupt slope changes are also discarded because they are interpreted to result from the shape of the topographic surface itself. In addition to the fault-related lineaments identified from the magnetic data, other faults that do not coincide with magnetic lineaments but are known from previous geological work in the Guichon Creek batholith (e.g., the Highland Valley faults) are integrated into the fault trace interpretation. This explains the presence of some fault traces in Figure 2.2B that do not correspond to linear low magnetic anomalies.

Because the Guichon Creek batholith area is structurally complex, only faults with a total along-strike continuity >4 km in the various data sets are included as meaningful contributors to the fault network. Fault segments <4 km are included in the fault network if they are interpreted to be part of faults that have been segmented by younger faults and the total length of the combined segments is >4 km.

To provide a measure of geological confidence to support the existence of the interpreted faults, the other datasets are checked for the presence of the faults and a reliability index is calculated for each fault following a method similar to (Figure 2.3; Sánchez et al., 2014). To calculate the reliability index, each fault is attributed a maximum score of 1 per data set in which it occurs, except for the historical map data set where mapped faults are given a maximum score of 0.5. A score of 1 per data set indicates that the entire lineament corresponds to a strong anomaly, whereas lower scores indicate that only segments of the lineament correspond to an anomaly. A score of 0 per data set indicates that no positive evidence is observed for a lineament, i.e., no anomaly is present or no data is available. Faults are given a positive score for the geological data sets (i.e., drilling, and historical and recent mapping) if a fault has been directly observed in the field or if there is a significant lithological change across the lineaments interpreted as faults from other data sets (i.e., topography and magnetic intensity). Because five data sets were considered, including the historical map data, the maximum reliability index value possible in this study is 4.5. No lineaments are rejected because of a low reliability index value, however, geological confidence in lineaments that have a reliability index of ≤1 is low and further investigation in the field is recommended in order to confirm these lineaments as faults.

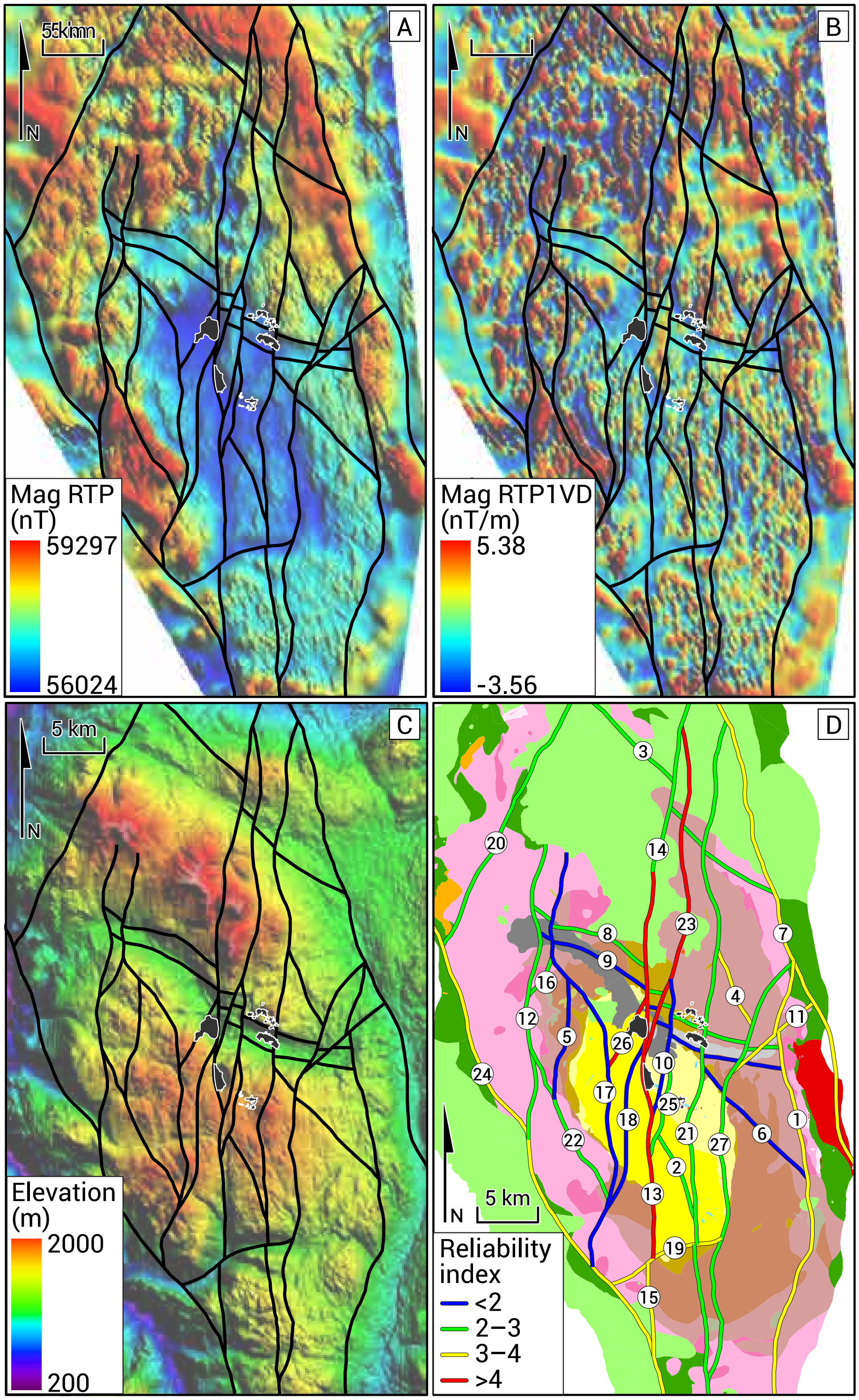

Figure 2.3. Maps showing the data layers used for lineament mapping: A) RTP magnetic intensity grid, B) RTP1VD grid, C) SRTM topographic data, and D) geological map with newly interpreted fault traces (modified from McMillan et al., 2009). New fault traces are coloured according to their reliability index value, and circled numbers refer to fault names (see Table 2.2). Lithology legend provided in Figure 2.2.

The presence of mutually cross-cutting faults (e.g., in an “X” pattern) implies that displacement was synchronous along both fault planes, which requires a significant redistribution of volume within each fault blocks (Odonne and Massonnat, 1992). Although mutually cross-cutting faults are possible in nature (Horsfield, 1980; Odonne and Massonnat, 1992), Ferrill et al. (2000, 2009) demonstrated that sequential, alternating displacements along interacting faults is more likely because no volume redistribution is required in this scenario. To avoid mutually cross-cutting faults in the lineament mapping, lineaments that correspond to older faults are terminated against lineaments that correspond to younger faults. The relative timing of the interpreted lineaments is determined based on geological observations where available (e.g., a fault that offsets hydrothermal alteration is younger than a fault that contains alteration along its plane), and on the along-strike continuity of the lineaments in the various datasets.

2.5.2. Fault dip modeling

To provide additional dip data for where the strike and dip of faults cannot be measured due to cover or to unexposed faults, we perform simple inverse modeling of a series of 2D profiles extracted from the sensor elevation-corrected RTP magnetic intensity grid perpendicularly across the interpreted fault traces. The dip modeling is carried out in Geosoft Oasis montaj® using the PotentQ™ approach outlined below.

Magnetic intensity profiles are extracted between two local maxima with a central magnetic low corresponding to the fault. A regional background field, estimated from data away from faults, is subtracted from each profile. Faults are approximated as dipping tabular bodies in order to more realistically represent them as damage zones as opposed to single slip planes. The upper and lower bounds of the tabular body are flat, and the sides are parallel to each other. The upper surface is set to a fixed height of 110 meters below the sensor, which is the ground level based on the drape correction used.

Fault damage zones may contain a complex assortment of discrete slip surfaces, gouge, and variably fractured rock (Wallace and Morris, 1979; Cox and Scholz, 1988; Childs et al., 1997) and as a result likely have a heterogeneous magnetic susceptibility. However, as described above the processes involved in the formation of damage zones all tend to lower the magnetic susceptibility of rocks (Henkel and Guzman (1977), so to simplify modeling the tabular body that represents a fault damage zone is attributed a homogeneous magnetic susceptibility signature that is lower than the background field. The tabular body output parameters that are iteratively adjusted by the software during the modeling are: location (i.e., the x-y coordinates for the center of the body), geometry (i.e., the dip and width), and magnetic susceptibility. The strike output parameter, which is fixed during the modeling, is perpendicular to the strike of the 2D profile.

The quality of the fit between the observed and the modeled magnetic intensity profiles is assessed by calculating the root-mean-square deviation (RMSD), which represents the prediction error and is the square root of the average of squared differences between measured and modeled points in the magnetic intensity profile. A RMSD value of 0 would indicate a perfect fit between the measured and modeled magnetic intensity profiles. There is no fixed threshold limit to determine an acceptable RMSD because it is a measure of accuracy that is dependent on the scale of the data used in the analysis (Hyndman and

Koehler, 2006). For this study, RMSD values higher than two standard deviations above the mean of the population are considered too high and are rejected.

2.5.2.1. Synthetic data test

To determine the validity of the dip modeling approach, we construct a synthetic 3D magnetic susceptibility model using NODDY™ (Jessell, 2002). We choose a 50 m cell size for the model, the same cell size as the Highland Valley Copper aeromagnetic data. In this model, we create linear low magnetic anomalies at 5° dip increments between 50° and 90° (e.g., Figure 2.4A). The magnetic susceptibility is progressively reduced from the edges to the center of the anomalies to simulate the pattern of susceptibility reduction that might be observed from the weakly fractured margins to the highly fractured center of symmetrical fault damage zones. Because the model cell size is 50 m, the width of the low magnetic anomalies is fixed at 500 m in order to provide a minimum of 10 points where the magnetic susceptibility reduction relative to background is recorded. For this exercise, a background magnetic susceptibility set at 25 x 10^{-3} SI is gradually reduced by two orders of magnitude to 0.25 x 10^{-3} SI at the center of the anomalies following a Gaussian curve, as shown in Figure 2.5. This range of magnetic susceptibility values was chosen to approximate the range of magnetic susceptibility of the Guichon Creek batholith rocks. After 5% random signal is added to the synthetic 3D model, a magnetic intensity grid is computed using a vertical magnetic field (e.g., Figure 2.4B). The magnetic intensity grid varies from background values of approximately 600 nT to 200 nT in the center of the anomalies. Magnetic profiles are extracted from the grid, and the dip of the low magnetic anomalies is solved using the tabular body approach outlined above (e.g., Figure 2.4C).

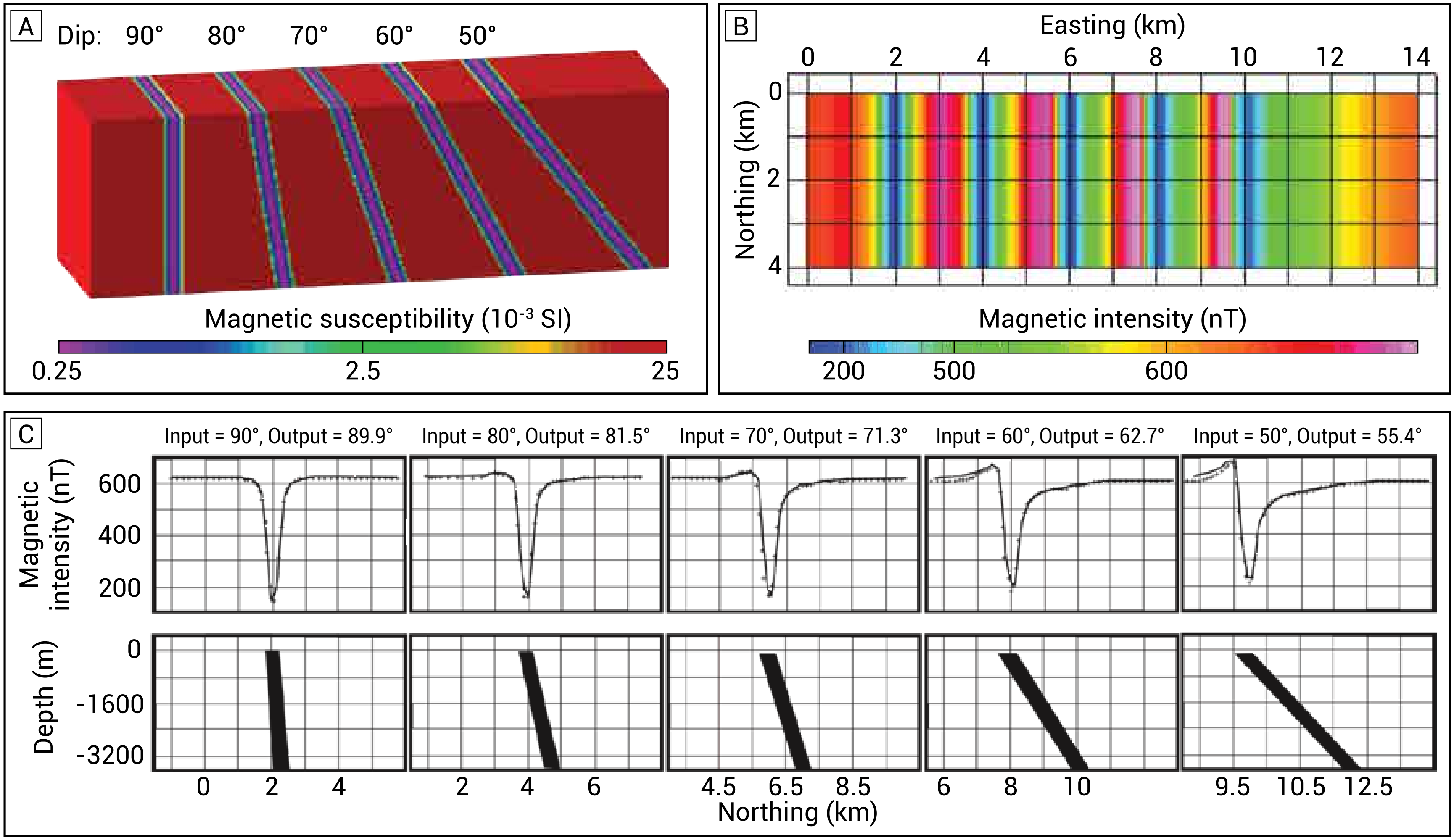

Figure 2.4. Example of magnetic intensity profile modeling workflow applied to low magnetic anomalies of known dip: A) 3D magnetic susceptibility model showing anomalies that dip 50°–90°, B) plan view of the magnetic intensity grid computed from (A), and C) dips modeled along magnetic intensity profiles extracted from the magnetic grid computed in (B).

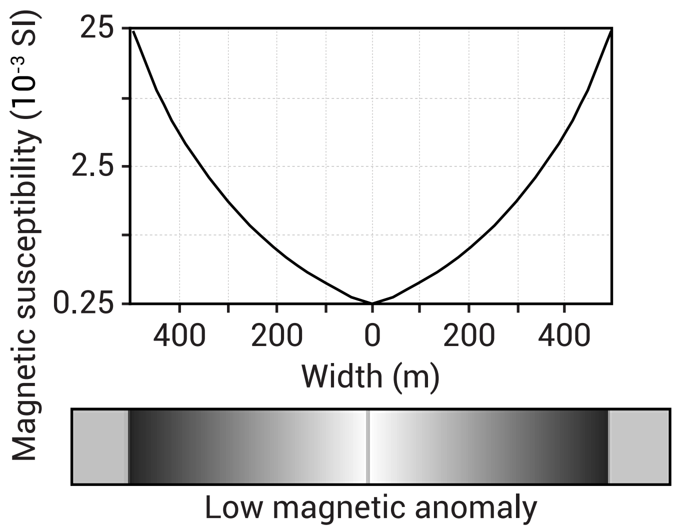

Figure 2.5. Gaussian pattern of magnetic susceptibility reduction from background field (25 x 10-3 SI) to a minimum of 0.25 x 10-3 SI at the center of a 500 meter-wide low magnetic anomaly. This pattern is used to define linear low magnetic anomalies in a synthetic 3D magnetic susceptibility model.

To test the repeatability of the approach, at every 10° increments two additional 2D profiles are extracted from the grid at different locations along-strike of the anomalies and solved. To assess the influence of fault strike on the dip modeling approach, we generate and solve the anomaly dips for two synthetic 3D model versions: one with north-trending and one with west-trending low magnetic anomalies.

2.5.3. 3D fault network modeling

For dip modeling of magnetite-destructive faults in the Guichon Creek batholith, multiple 2D profiles are extracted from the RTP magnetic intensity grid along each fault trace (i.e., lineament) to account for along-strike dip variation. The strikes derived from the orientation of the extracted 2D magnetic intensity profiles and the associated modeled dips are imported as "planar structural data" into the Leapfrog Geo™ v. 4.0 software package. Leapfrog Geo™ is a widely used 3D modeling software that uses implicit modeling and mathematical tools to generate 3D surfaces and build complex geological models. Surface structural measurements are also imported as “planar structural data” into Leapfrog Geo™.

In Leapfrog Geo™, the following steps are taken for each fault: 1) the fault trace is digitized as a polyline (i.e., a series of control points) on the topography surface, 2) a mesh (i.e., 3D surface) is created that must pass through all the control points of the polyline, and 3) the imported “planar structural data” are added to the resulting mesh. When structural data is added to a mesh, the 3D surface is compelled by the software to honour the strike and dip of the data points when in their vicinity. Finally, relative timing between the various faults is honoured by terminating older fault meshes against younger fault meshes.

2.6. Results

2.6.1. Synthetic 3D data

Dips modeled from the synthetic 3D model are within 6° of the input dips for north-trending anomalies and within 8° of the input dips for west-trending anomalies (Figure 2.6A). Two modeled dips are rejected because their RMSD values, respectively 226 and 213 nT (Figure 2.6B), is above the RMSD cut-off of two standard deviations above the mean (standard deviation = 40 nT, mean = 77 nT). Both rejected results are for input dips of 50°: one from a north-trending anomaly and one from a west-trending anomaly. Within the 60°–90° input dip range, modeled dips are consistently within 5° of the input dips, and vertical anomalies are consistently within <1° of the input dip. Modeled dips are consistently steeper than input dips. A linear regression of input dips versus modeled dips shows that the data are well correlated, with R^2 values of 0.99 for both anomaly trends (Figure 2.6A). The difference increases with decreasing

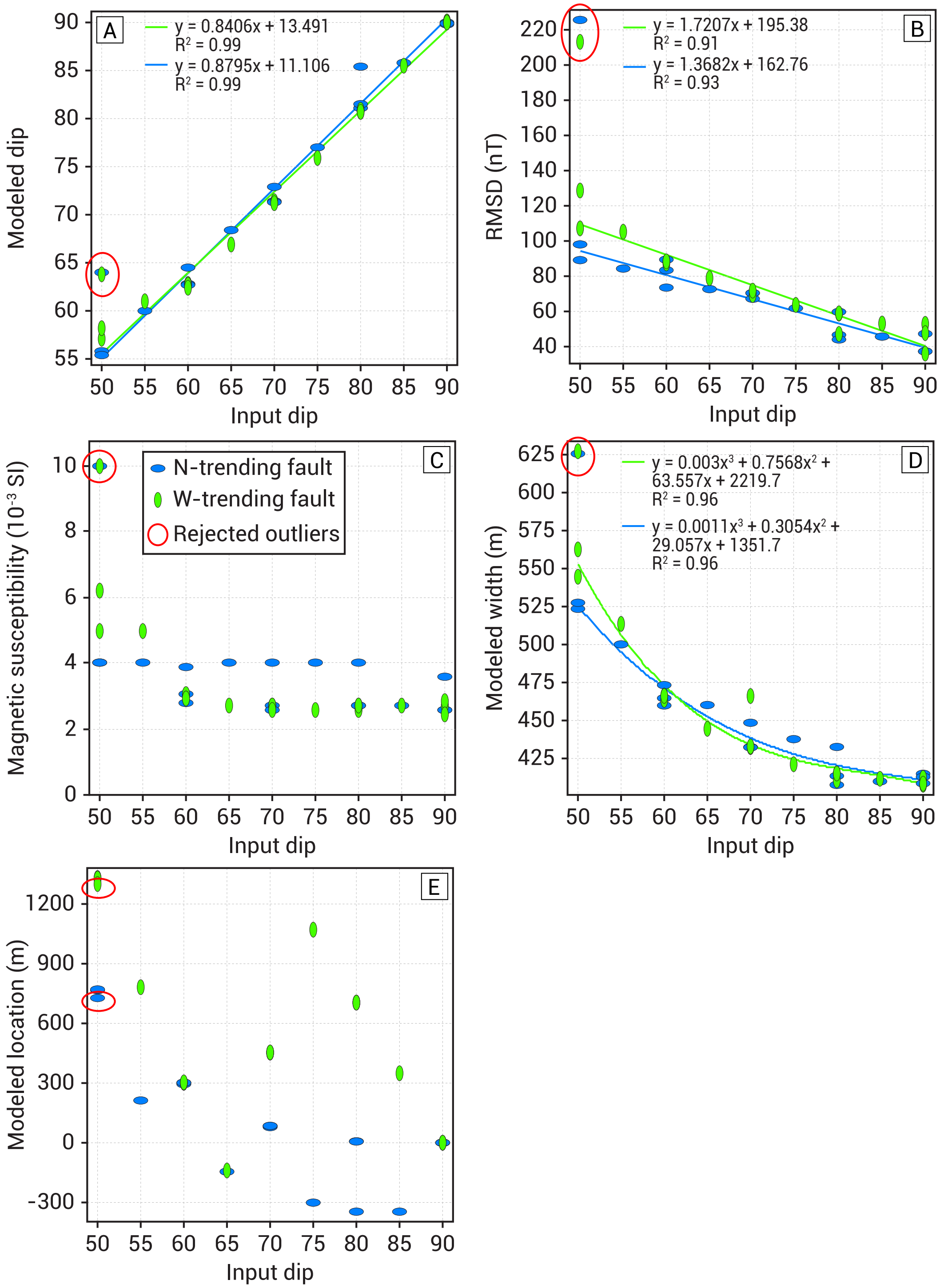

Figure 2.6. Results of dip modeling of linear low magnetic anomalies of known geometry. Model output values are plotted against input dips: A) modeled dip, B) root-mean-square deviates (RMSD), C) magnetic susceptibility in the modeled tabular body, D) width of the modeled tabular body, and E) location of the center of the modeled tabular body. Models that have an RMSD value higher than two standard deviations above the mean of the population are considered too high and are rejected.

input dips, which indicates that vertical anomalies are modeled more accurately than shallowly-dipping anomalies.

The computed solution for the dip of the modeled tabular body comes from the shape and amplitude of the anomaly on the magnetic intensity profile. If the applied magnetic field is vertical, as is the case in our synthetic model or in reduced-to-pole magnetic data, the magnetic intensity at any location is a function of the magnetic susceptibility of the rocks below said location. The shape and amplitude of low magnetic intensity anomalies is dependent on the alignment between the applied magnetic field (i.e., vertical) and the geometry of the low magnetic susceptibility zone. Vertical low magnetic susceptibility zones, which are perfectly aligned with the applied magnetic field, results in symmetrical low magnetic intensity anomalies of maximum amplitude (Figure 2.4C). Anomaly profiles associated with dipping low magnetic susceptibility zones are asymmetrical and have a smaller amplitude because of the misalignment between the long axis of the low susceptibility zone and the applied magnetic field. As the dip of low magnetic susceptibility zones decreases, the misalignment with the applied magnetic field increases, which leads to increasing asymmetry and decreasing amplitude of the resulting magnetic intensity anomaly (Figure 2.4C). Weaker anomalies and more complex magnetic signal with decreasing dip negatively affects the modeling fit (i.e., RMSD) and the accuracy of the dip modeling method.

The magnetic susceptibility of the modeled tabular bodies ranges between 2.5×10^{-3} and 6.2×10^{-3} SI (Figure 2.6C). These values are higher than the minimum magnetic susceptibility of 0.25×10^{-3} SI set in the center of the magnetic anomalies in the input model. This is a consequence of the pattern of magnetic susceptibility used to define the anomalies in the synthetic 3D magnetic susceptibility model, which is not an instantaneous change from the background level of 25 x 10^{-3} SI to the minimum of 0.25 x 10^{-3} SI but rather is a gradual reduction from of 25 x 10^{-3} SI to 0.25 x 10^{-3} SI at the center of the anomalies with intermediate values between the two (Figure 2.5). The modeled tabular body magnetic susceptibility is higher than 0.25 x 10^{-3} SI because it is a composite of all the susceptibility values along the 2D profile over the width of the tabular body.

The modeled width of the tabular body increases with decreasing input dips (Figure 2.6D). The data for both north-trending and west-trending anomalies follow trends that can be well defined by a cubic function, as indicated by R^2 values of 0.96 for both trends. The input low magnetic anomaly width is fixed at 500 m, however, modeled tabular body widths for vertical anomalies range from 408 m to 415 m. The smaller modeled tabular body widths compared to input anomaly widths is also a consequence of the pattern of magnetic susceptibility reduction used to define the anomalies in the input model (Figure 2.5). The model approximates a fault damage zone as a tabular zone of uniformly low magnetic susceptibility, whereas the input model simulates a damages zone by progressively decreasing the magnetic susceptibility toward the center of the anomaly. Based on the pattern of magnetic susceptibility used to define the anomalies, this indicates that the method can identify vertical features defined by a magnetic susceptibility contrast greater than approximately 75%.

The location of the center of the tabular body is the parameter obtained from the 2D magnetic intensity profile modeling that shows the most scattering (Figure 2.6E). No clear trend can be identified in the data but modeled locations are generally positive, which means that they are located on the dipping side of the anomalies. Vertical anomaly locations are the most accurately modeled regardless of the anomaly trend, i.e., consistently within 1 m of the input location. At shallower input dips, however, modeled locations are less accurate: distances from the input location are up to 770 m for north-trending anomalies and up to 1330 m for west-trending anomalies at input dips of 50°. When magnetic anomalies of all dips are considered, modeled locations are on average 373 m away from the center of the anomaly, with a standard deviation of 365 m.

2.6.2. Guichon Creek batholith fault trace interpretation

Brittle faulting in the Guichon Creek batholith resulted in faulted rocks that exhibit abundant fractures (Figure 2.7A) and surface exposures of friable rocks with pervasive oxidation (Figure 2.7B) that have a lower magnetic susceptibility compared to non-faulted rocks of the same lithology. The cumulative frequency plot of the arithmetic mean of outcrop magnetic susceptibility values shows that faulted rocks consistently have a lower susceptibility than non-faulted rocks of similar lithologies (Figure 2.7C). Another factor that can significantly contribute to lowering the magnetic susceptibility of rocks in the Guichon Creek batholith is the intensity of porphyry-related hydrothermal alteration (Byrne et al., 2017), so only the least hydrothermally altered outcrops are plotted in Figure 2.7C (i.e., weak alteration or less).

Based on lineament mapping, the new fault network proposed for the Guichon Creek batholith comprises 25 faults (Table 2.2). The proposed faults are displayed with the various data sets used for the calculation of the reliability index in Figure 2.3. Reliability index values, a measure of geological confidence in the interpreted faults, range from 4.5 to 1. Four faults have a reliability index

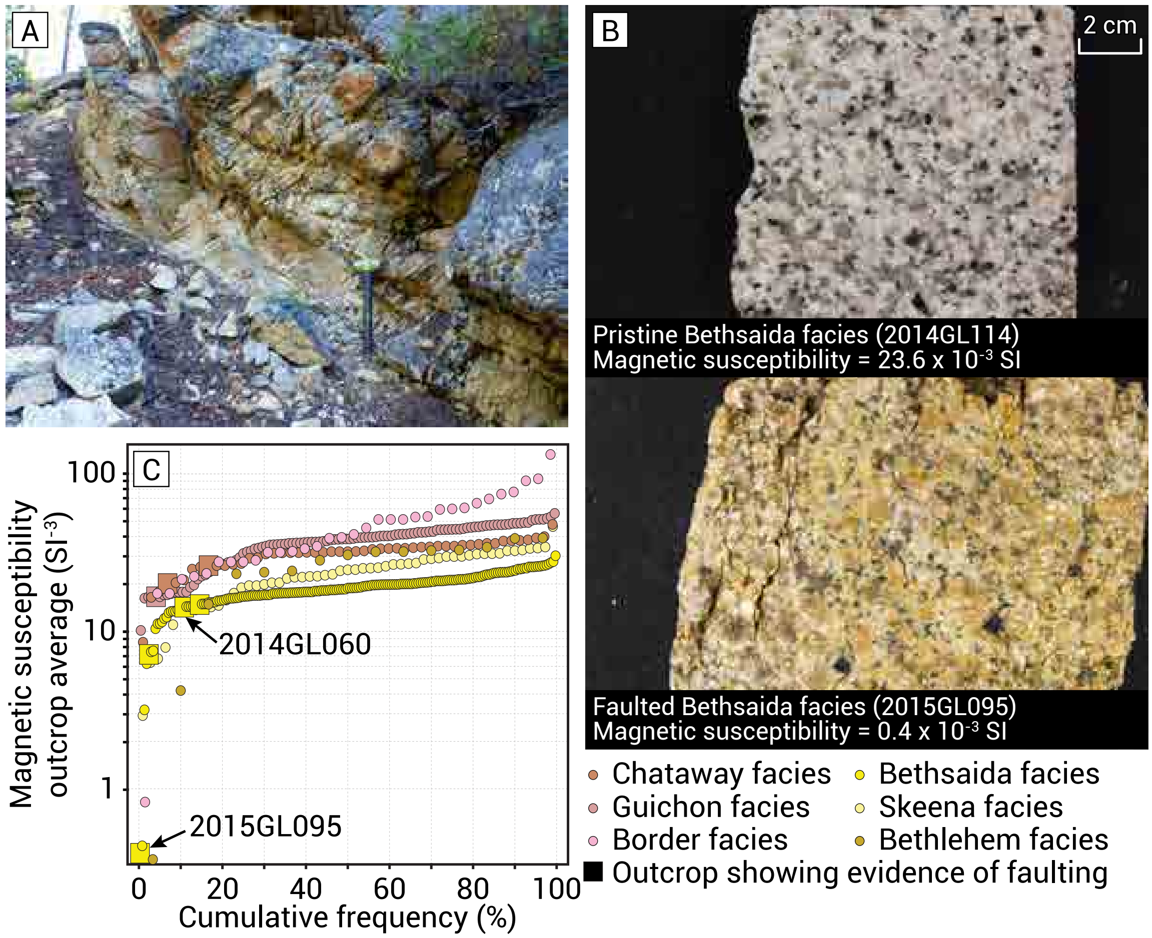

Figure 2.7. A) Photo of faulted outcrop (location 2014GL060), B) comparison of pristine rock (above; sample 2014GL114) versus faulted rock (below; 2015GL095) of the same lithology (Bethsaida facies) at the same scale showing abundant fractures and oxidation that results in significantly lower magnetic susceptibility in the faulted rock, and C) cumulative frequency plot showing average outcrop magnetic susceptibility for the six main intrusive facies of the Guichon Creek batholith. Only outcrops with porphyry-related hydrothermal alteration characterized as weak or less are plotted. Within each intrusive facies, outcrops affected by faulting have magnetic susceptibility values within the lowest quartile of the population.

lower than 2. Faults with low reliability indices generally lie outside of the area mapped for this study or where there is no drilling data available.

2.6.3. Guichon Creek batholith 3D interpretation

A total of 81 magnetic intensity profiles are extracted from the Highland Valley Copper RTP magnetic intensity grid to model the dip of the interpreted faults

(Figure 2.8A). The modeling results are accepted if the fit between the observed and modeled data is good. Output data parameters selected for further analysis are strike (i.e., perpendicular to the 2D profile), modeled dip, and easting and northing coordinates for the center of the modeled tabular body (Table 2.3). The data is imported in Leapfrog Geo™ v. 4.0 as "planar structural data". The coordinates derived from the magnetic intensity profile modeling are not very accurate (Figure 2.6F) and do not include elevation. Consequently, once imported into Leapfrog Geo™ the data points are projected onto the topography surface and each data point is manually moved to the nearest location on the appropriate fault trace identified by the lineament analysis. Data points are moved an average of 342 m with a standard deviation of 343 m, which is comparable to the distances obtained from the synthetic data modeling.

Forty-seven strike and dip measurements corresponding to the interpreted fault zones are selected from the mapping data on the basis of proximity to the faults and having a good confidence level (Table 2.4). These data are also imported in Leapfrog Geo™ as "planar structural data". Figure 2.8 shows the location and orientation of the combined measured and modeled orientations.

To build the final 3D fault network, the fault traces are digitized onto the topography surface and meshes are generated for each fault. The measured and modeled structural data are then added to the appropriate fault meshes to compel the 3D surfaces to follow the correct strike and dip in the vicinity of the data points. Finally, the relative timing of faults determined during the lineament mapping is respected and older fault meshes are terminated against younger fault meshes (Figure 2.8C).

There is excellent consistency in strike and dip values modeled at different locations along the same fault (Figure 2.8B and C), and a significant overlap

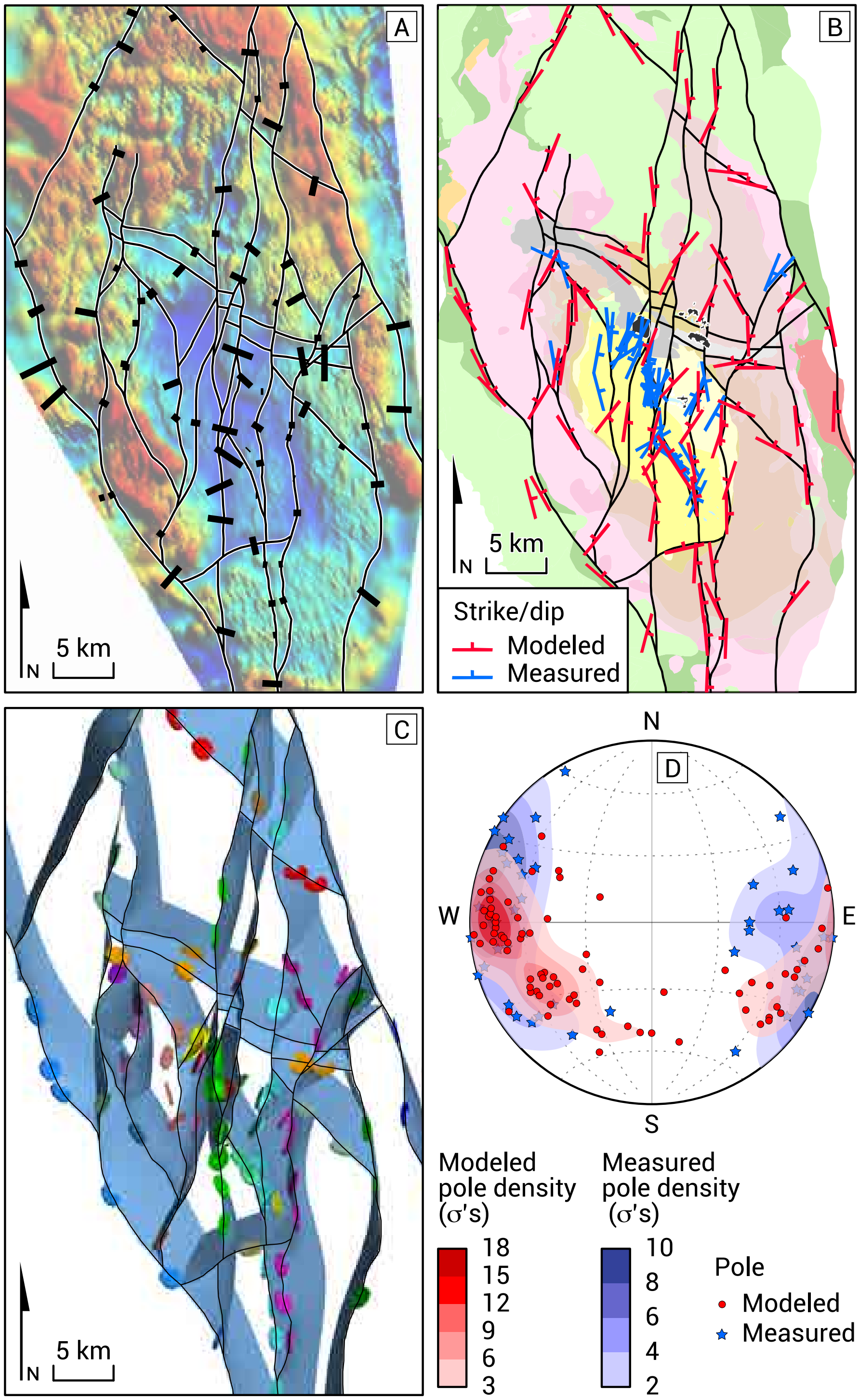

Figure 2.8. A) Map of the RTP magnetic intensity grid showing the new fault traces and the location of the extracted 2D profiles used to model fault dips, B) map of the Guichon Creek batholith geology showing the new fault traces and the location of strikes and dips measured at the surface and modeled using magnetic data, C) plan view of the final 3D fault network interpretation with the measured and modeled strikes and dips shown as disks, and D) equal area stereonet displaying poles to measured and modeled fault orientations.

Table 2.3. Strikes and dips modeled using the Highland Valley Copper aeromagnetic data. Abbreviation: HV = Highland Valley. Modeled Easting and Northing columns are the output values obtained from the modeling, whereas Final Easting, Northing and Elevation are the coordinates used to generate the 3D fault network. Coordinates in UTM NAD1983 Zone 10.

Fault name F	Modeled easting (m)	Modeled northing (m)	Final easting (m)	Final northing (m)	Final elev (m)	Distance moved (m)	Strike	Dip
Aberdeen	652013	5572181	651331	5572383	1182	712	219	52
Aberdeen	650966	5597107	650987	5597240	1195	135	223	60
Aberdeen	651745	5586339	651861	5586379	1372	122	355	72
Aberdeen	652743	5581494	652668	5581508	1256	76	356	88
Alamo	642073	5582746	642145	5582590	1586	172	327	52
Alamo	642001	5584384	641185	5584210	1615	834	328	82
Barnes Creek	638227	5617674	638250	5617920	1242	247	326	38
Barnes Creek	647446	5606256	647615	5606727	1227	501	283	49
Barnes Creek	647030	5609112	646014	5607669	1271	1765	276	51
Barnes Creek	635774	5620257	635965	5620397	1059	237	333	57
BX	645279	5599799	645574	5600100	1399	421	329	63
BX	645973	5596891	646656	5597167	1408	737	330	66
Cleveland	632656	5594895	632868	5594828	1508	222	2	48
Cleveland	633119	5596720	632954	5596724	1545	165	178	63
Cleveland	631640	5591496	631928	5591436	1586	295	189	82
Cleveland	631838	5591238	631878	5591100	1610	144	10	85
Gaza	649790	5584623	649783	5584815	1428	192	297	56
Gaza	646676	5587728	646727	5588026	1512	302	294	57
Guichon Creek	654553	5587738	655040	5587569	973	515	2	75
Guichon Creek	654462	5594663	654291	5594498	1026	238	169	89
HV North	637552	5600793	637420	5601041	1512	281	292	66
HV North - HV South	646514	5591727	646387	5591845	1221	173	260	32
HV North - HV South	648315	5591551	648249	5591475	1215	101	270	51
HV South	636250	5599217	636815	5599474	1254	621	313	51
King	631378	5616012	631269	5616058	1362	119	317	52
King	630023	5588269	629976	5588503	1406	239	211	54
King	629777	5605248	629906	5605198	1424	138	332	65
King	631234	5608991	631008	5609141	1749	271	201	73
King	628536	5595778	629356	5595946	1384	837	11	80
Lornex Central	640372	5583778	639581	5583854	1577	795	213	40
Lornex Central	639608	5581275	639837	5581625	1417	419	335	63
Lornex Central	639703	5578584	639948	5578366	1215	328	8	69
Lornex Central	639921	5606010	639947	5606210	1768	202	354	71
Lornex Central	640048	5586040	639585	5586054	1616	463	194	76
Lornex Central	639304	5602318	639283	5602338	1718	29	4	82
Lornex Central - Huestis	641120	5592517	639192	5593018	1402	1992	201	68
Lornex North	642158	5617362	641930	5617446	1228	243	5	78
Prince	631087	5599430	631204	5599337	1461	149	29	49
Queen	635643	5589840	636358	5589863	1612	715	338	29
Queen	633906	5597424	633845	5597611	1455	196	321	61
Queen	635972	5587013	636095	5586928	1652	149	38	66
Queen	634034	5597270	634054	5597375	1447	107	318	66
Queen	634725	5577376	634787	5577113	1412	270	219	72
Royal	637611	5586614	637655	5586628	1600	46	8	79
Skuhun Creek	642486	5576420	642282	5576440	1144	205	257	57
Spatsum	632386	5620631	632670	5620438	1114	343	23	61
Spatsum	631737	5617791	631543	5618268	1123	515	208	63
Spatsum	629185	5614524	629407	5614703	1512	285	215	76
Spud	644265	5596588	644447	5596466	1508	219	26	26

Table 2.3. Strikes and dips modeled using the Highland Valley Copper aeromagnetic data. Abbreviation: HV = Highland Valley. Modeled Easting and Northing columns are the output values obtained from the modeling, whereas Final Easting, Northing and Elevation are the coordinates used to generate the 3D fault network. Coordinates in UTM NAD1983 Zone 10. Cont'd

Fault name F	Modeled easting (m)	Modeled northing (m)	Final easting (m)	Final northing (m)	Final elev (m)	Distance moved (m)	Strike	Dip
Spud	644020	5611415	644534	5611197	1262	558	26	47
Spud	644185	5568992	644313	5568994	1477	128	355	57
Spud	643991	5564953	644409	5564711	1403	483	2	63
Spud	642687	5580573	643373	5580547	1549	686	352	69
Spud	642979	5583264	643151	5583384	1612	209	349	70
Spud	642762	5586266	642677	5586474	1686	225	214	72
Spud	643145	5589230	643671	5589207	1623	526	0	75
Spud	644998	5614636	645064	5614422	1464	224	356	76
Spud	643959	5571624	643991	5571672	1487	57	353	77
Spud	643413	5574848	643403	5574958	1392	111	3	78
Tam	632823	5586040	632826	5585971	1573	69	327	63
Trojan	642794	5613497	642828	5613501	1501	34	355	61
Trojan	642355	5601014	642160	5601329	1653	371	220	73
Trojan - Huestis	641190	5598637			0	0	27	81
West Boundary	624577	5591158	625624	5591347	897	1064	334	33
West Boundary	635590	5573817	635607	5574023	843	206	311	36
West Boundary	625834	5588702	626520	5589441	894	1009	317	49
West Boundary	630640	5580602	630615	5580875	1375	274	331	52
West Boundary	624427	5595866	624389	5595817	703	62	328	56
West Boundary	624351	5595942	624244	5596419	649	488	335	57
West Boundary	640118	5569264	639482	5569043	1027	673	15	82
West Boundary	623124	5599825	622986	5599651	688	222	353	85
West Boundary	629831	5580373	629831		0	0	345	89
West Highmont	641716	5590124	641304	5590127	1556	412	223	71
Yubet	644905	5571877	644953	5571954	1451	91	335	55
Yubet	644692	5574865	644800	5575083	1370	244	353	62
Yubet	645802	5582004	645789	5581877	1574	128	198	73
Yubet	647789	5593658	647820	5593770	1299	117	358	75
Yubet	645625	5586418	645601	5586417	1589	24	2	79
Yubet	645376	5585393	645326	5585180	1595	219	18	81
Yubet	646084	5579146	646063	5579034	1424	114	359	82
Yubet	645451	5568907	645443	5568703	1490	204	182	83

between the modeled and measured strikes and dips (Figure 2.8D). The lack of modeled strike and dip data for some faults near the center of the batholith (e.g., NNE-striking Yellow fault) is because the magnetic contrast between the faulted rocks and the surrounding country rocks is too small. The low magnetic susceptibility of the host granodiorite (i.e., Bethsaida facies) combined with the presence of magnetite-destructive hydrothermal alteration near the porphyry systems (Lesage et al., 2016; Vallée et al., 2017; Byrne et al., 2019) hindered dip modeling along the 2D profiles because the contrast between the magnetic intensity of the country rock and the fault-related low magnetic anomalies was too small.

2.7. Discussion

The aim of this study is to provide a simple methodology to obtain information about the geometry of brittle faults from topographic and magnetic data sets. The applicability of the proposed approach is evaluated below based on the results of modeling of synthetic data and of the Guichon Creek batholith data.

The modeling of a synthetic magnetic intensity grid that contains linear low magnetic anomalies of known geometry has established that the quality of the fit between the modeled and observed magnetic intensity profiles is consistently good (i.e., low RMSD), and that modeled dips are accurate at input dips >50°. The orientation of magnetic anomalies did not affect the quality of the modeling results. For fault dips below 50^{o} the synthetic model results do not yield a close approximation (i.e., within 5^{o}) of the input model. Because the RMSD and the difference between the input and modeled dip increase with decreasing input dip (Figure 2.6A and B), the method is better suited for modeling of steep anomalies than shallow anomalies and is therefore best suited for strike-slip and extensional tectonic regimes. The width and location output parameters obtained from the magnetic intensity profile modeling are not accurate, however, although they vary systematically relative to the input dips (Figure 2.6D and E). We do not recommend using these output parameters for the construction of a 3D fault network.

For magnetic data collected in the field (i.e., airborne or ground surveys), the accuracy of the dip modeling method is also dependent on the spacing and

Table 2.4. Strikes and dips measured at surface outcrops. Abbreviation: HV = Highland Valley. Coordinates in UTM NAD1983 Zone 10.

Fault name	Station ID	Easting (m)	Northing (m)	Elev (m)	Description	Strike	Dip
Alamo	2015GL048	641850	5583209	1590	Fault	320	70
Alamo	2015GL048	641876	5583258	1595	Fault	325	80
Alamo	2015GL049	641806	5583806	1626	Heavily fractured zone	320	75
Alamo	2015GL050	641414	5583814	1601	Fault	320	60
Alamo	2015GL050	641449	5583790	1602	Fault	305	65
Cleveland	2014GL140	631670	5591837	1535	Heavily fractured zone	350	75
Huestis	2015GLLornex	639922	5589597	1438	Fault	215	80
Huestis	2015GLLornex	640031	5589638	1438	Fault	200	40
HV South	2014GL227	631209	5600707	1349	Fault	295	45
Lornex Central	2015GLLornex	639641	5589501	1417	Fault	140	80
Lornex Central	2015GLLornex	639741	5589524	1417	Fault gouge	355	90
Lornex Central	2015GLLornex	639856	5589567	1438	Fault gouge	185	85
Lornex Central	2015GLLornex	638992	5589826	1434	Fault breccia	175	60
Lornex Central	2015GLLornex	639057	5589745	1434	Fault breccia	185	45
Lornex Central	2015GLLornex	639091	5589698	1434	Fault breccia	180	45
Lornex Central	2015GLLornex	639128	5589629	1434	Fault breccia	195	75
Lornex Central	2015GLLornex	639170	5589564	1434	Fault breccia	160	50
Lornex Central	2015GLLornex	639249	5589503	1434	Fault gouge	160	72
Lornex Central	2015GLLornex	638996	5589820	1434	Fault breccia	175	60
Lornex Central	2015GLLornex	639014	5589790	1434	Fault breccia	190	70
Lornex Central	2015KB244	639633	5591542	1445	Fault zone	0	75
Lornex Central	2015KB250A	639686	5591903	1405	Fault zone	10	80
Queen	2014GL060	636476	5594107	1565	Fault	5	65
Queen	2014GL077	635280	5592310	1667	Fault	10	62
Queen	2014GL112	635434	5589313	1732	Heavily fractured zone	345	85
Queen	2014GL221	632383	5599461	1420	Heavily fractured zone	343	90
Queen	2015GL094	636170	5594549	1427	Fault gouge	355	60
Royal	2014GL021	637898	5591872	1633	Fault breccia	205	77
Spud	2015GL059	642926	5583710	1631	Fault	330	80
Spud	2015GL073	643407	5581177	1572	Fault	25	60
Spud	2015GL081	643590	5580198	1508	Fault	25	70
Spud	2015KB216	644272	5590052	1524	Fault zone	350	70
Spud	2015KB222	643028	5588921	1629	Heavily fractured zone	200	80
Spud	2015KB227	643345	5588498	1678	Heavily fractured zone	30	90
West Highmont	2015GL012	640105	5586190	1636	Heavily fractured zone	175	65
West Highmont	2015GL092	639876	5584881	1574	Fault breccia	60	85
West Highmont	2015GL092	639884	5584911	1581	Fault breccia	35	90
Yellow	2014GL013	637318	5592584	1627	Fault breccia	237	74
Yellow	2014GL037	636843	5592633	1699	Heavily fractured zone	210	90
Yellow	2015GLValley	637711	5593901	1265	Fault	25	80
Yellow	2015GLValley	637753	5594055	1265	Shear	20	65
Yellow	2015GLValley	637813	5594070	1265	Fault	5	85
Yellow	2015GLValley	638400	5593757	1250	Fault gouge	205	80
Yellow	2015GLValley	638405	5593756	1250	Fault gouge	185	90
Yubet	2015KB065	650463	5599003	1140	Fault zone	42	75
Yubet	2015KB070	649808	5599011	1246	Fault zone	22	75
Yubet	2015KB209	645022	5587268	1648	Heavily fractured zone	30	80

orientation of the survey flight lines. Magnetic signal is only measured along flight lines, so interpolation is required between lines in order to generate a magnetic intensity grid that provides an even coverage of data for effective interpretation. The minimum curvature algorithm used to interpolate the data assumes a smooth fit between the various flight lines, which may not be the case in reality. Data quality along flight lines is therefore better than between lines, and the interpolated grid is a simplified representation of data with a heterogeneous spatial resolution.

The dip modeling method outlined in this study is most effective when magnetic intensity profiles are extracted along the survey flight lines where the gridded values most closely represent the data. Flight line spacing is therefore a limitation of the proposed method, i.e., surveys with wider line spacing require more interpolation to generate a grid, and when applied to these grids the method may only be able to accurately model the dip of very large fault zones.

The shape of magnetic anomalies on profiles extracted from a grid between flight lines may contain errors introduced by the grid interpolation procedure. When interpolated, sharply-defined thin linear high magnetic features (e.g., mafic dikes) or low magnetic features (e.g., faults) that are orthogonal or oblique to the survey flight lines can produce a "bead"-like signature along-strike of the anomaly in the resulting grid. Such gridding artefacts are particularly common for anomalies that have a width smaller that the flight line spacing. In turn, when profiles are extracted from the interpolated part of the grid these gridding artefacts could adversely affect the accuracy of the modeled dips. For this study the flight line spacing was 250 m, so interpolation of the data produced a grid at a 50 m cell size with only limited data corruption. Also, in this case the data was collected along east-west-oriented flight lines, which is nearly orthogonal to the predominant fault orientation. This flight line configuration is optimal in order to most accurately define the shape of north-trending linear low magnetic anomalies. Additionally, pre-existing anisotropy or heterogeneity in the magnetic properties of the rock can introduce error into the analysis and hinder fault dip modeling. It is essential that it be possible to recognize background magnetic intensity levels on either side of the interpreted fault location. The methodology is most effective for simple structural environments with homogeneous magnetic rock properties in the hanging wall and footwall of brittle faults.

The Guichon Creek batholith is an ideal location to apply the methodology because of its relatively simple geology and homogenously magnetic crystalline rocks. Comparison of the strike and dip modeling results with measured values at the surface across the batholith confirms that the technique can successfully be applied to real geological environments, as evidenced by the strong overlap between modeled and measured orientations in Figure 2.8D. A potential biais towards steep faults may be present in both data sets shown in Figure 2.8D., however, because of the difficulty to model the dip of shallow magnetite-destructive zones, as well as to the likely underrepresentation of shallow faults in the Guichon Creek batholith mapping data due to the “rolling hill” topography of the area, where shallow-dipping features are less likely to outcrop.

The similarity of the fault orientations in the proposed Guichon Creek batholith fault network compared to well-studied structures in southern British Columbia provides an additional validation. The proposed fault network is dominantly composed of north to north-northwest-trending and northwest-trending faults, which are respectively parallel to the ~300 km-long Fraser fault, located ~30 km west of the Guichon Creek batholith (Schiarizza et al., 1996; Gabrielse et al., 2006), and to the ~50 km-long Cherry Creek fault, located ~20 km to the northeast of the Guichon Creek batholith (Ewing, 1981). The Fraser fault is a strike-slip fault system that bounds the Cache Creek and Quesnel terranes along which upwards of 100 km of dextral displacement has taken place since the mid-Cretaceous (Wyld et al., 2006).

The results of synthetic data modeling indicate that a low magnetic anomaly is successfully detected when the contrast between the background magnetic susceptibility and the magnetic susceptibility in the anomaly is greater than 75%. A smaller susceptibility contrast between an anomaly and the background field leads to less accurate dip estimates. The methodology is therefore more effective in terranes characterized by highly magnetic lithologies (e.g., mafic rocks).

Although untested, we postulate that the presented method may also be applicable to linear high magnetic anomalies, provided that the magnetic susceptibility contrast between the background field and the anomaly is sufficiently large (>75%). Consequently, the method may also be suitable for modeling the dip of magnetic high or low anomalies caused by other planar geological features such as dikes, tilted sills, dipping stratigraphy, magnetite-rich faults, or elongated magnetite-bearing hydrothermal alteration zones.

2.8. Conclusions

The use of 2D profiles extracted from a magnetic intensity grid to model the dip of low magnetic susceptibility zones can predict their dip to better than 5° in the case of synthetic data at dips >60°. The methodology can be used to successfully build 3D fault networks in geological environments where faults are brittle and dominantly steeply dipping, as evidenced by the Guichon Creek batholith case study, with the assumption that brittle faults have a lower magnetic susceptibility than their surrounding country rock (Henkel and Guzman, 1977; Lapointe et al., 1984; Clark, 1997; Maidment et al., 2000). The application of the methodology, however, may be problematic in complex geological environments where rocks may have pre-existing magnetic anisotropies or heterogeneities.

The 3D structural framework of an area can be determined or improved by integrating sound geological knowledge, multi-layer 2D surface lineament mapping, and simple 2D inverse modeling along profiles extracted from a magnetic intensity grid perpendicular to linear low magnetic anomalies that are interpreted as faults. The presented approach is a valuable tool to enhance the 3D structural understanding, especially in areas where contiguous geological data is lacking but geophysical data is available, such as in areas where mineral exploration is at an early stage or in partially covered terrain where fault exposure is limited. Magnetic intensity data used in the workflow can be collected rapidly by airborne surveys over large areas and at relatively low cost (e.g., Nabighian et al., 2005). The approach leverages commonly available remotely sensed magnetic and topographic data sets and can be completed on personal computers to interpret a preliminary fault network that can be used as a predictive tool to help target areas to visit during surface mapping campaigns.

Chapter 3. District-scale extent of hydrothermal alteration and vein orientations in the Highland Valley Copper district, British Columbia: Implications for permeability controls in porphyry Cu-Mo systems

3.1. Introduction

The economically-mineralized parts of porphyry systems, referred to as orebodies, account for approximately 69% of Cu and 95% of Mo worldwide production, and are important sources of other metals such as Au, Ag, W, Pt and Pd (Sinclair, 2007; Singer, 2017). These orebodies are characterized by relatively low to moderate grade (i.e., 0.3–2.0 % Cu), but their large tonnages (i.e., >100 million to billions of tons of ore) make them attractive exploration targets (John et al., 2010; Mudd et al., 2013). The large amount of metal contained in porphyry systems requires the presence at depth of a large magma chamber from which a significant volume of metal-rich magmatic fluids can be exsolved (e.g., Burnham, 1979; Cline and Bodnar, 1991; Shinohara and Hedenquist, 1997; Cloos, 2001; Richards, 2011). At typical depths of porphyry system formation (<4–6 km; e.g., Seedorff et al., 2005), the high temperature of the magma and magmatic fluids induce convective flow of heated external fluids (meteoric fluids or sedimentary brines; e.g., Cathles, 1977; Weis, 2015), which can result in vast volumes of altered but barren rock outside the mineralized system.

Understanding the district-scale expressions, or footprints, of mineral deposits is a key factor in improving the success rate of mineral exploration. This is especially important because a large proportion of the easily identifiable mineral deposits around the world have been found over the last ~65 years, and as a result mineral exploration is becoming increasingly focused on areas of covered terrains and/or at significant (>500 m) depths (Witherly, 2012). Many studies have documented the deposit-scale zonation and paragenesis of hydrothermal alteration processes (e.g., Lowell and Guilbert, 1970; Gustafson and Hunt, 1975; Brimhall, 1977; Dilles and Einaudi, 1992; Proffett, 2003; Masterman et al., 2005; Seedorff et al., 2008; Lang et al., 2013), and the deposit-scale orientation of veins and fractures (e.g., Titley et al., 1986; Carten et al., 1988; Gruen et al., 2010; Houston and Dilles, 2013), which are typical of porphyry systems. Similarly, significant advances in the understanding of the porphyry deposit footprints have been made over the last several years in the areas of mineral chemistry (e.g., Alva Jimenez, 2011; Cohen, 2011; Cooke et al., 2014; Wilkinson et al., 2015), whole rock lithogeochemistry and short-wave infrared spectroscopy (e.g., Greenlaw, 2014; Halley et al., 2015) to distances of up to 5 km from the deposits. However, studies that focus on the porphyry deposit footprint >5 km from the deposits, and on the structural controls on hydrothermal fluid flow and the resulting vein orientations at the district scale are lacking.

The flow of hydrothermal fluids in the brittle crust is controlled by host rock fracture permeability (Ingebritsen and Manning, 2010; Ingebritsen, 2012; Weis et al., 2012). The location and orientation of fractures depends on a combination of factors that includes regional tectonic stresses (e.g., Tosdal and Richards, 2001; Houston and Dilles, 2013) and local stresses (e.g., Burnham and Ohmoto, 1980; Bergbauer and Martel, 1999; Fournier, 1999).

Porphyry systems are genetically linked to the emplacement of intrusive stocks and dikes that exhibit porphyritic textures. These typically form in clusters at depths of 1–6 km above voluminous calc-alkaline or alkaline, intermediate to felsic batholiths, which were emplaced and crystallized at depths of 5–10 km in convergent settings above subduction zones (e.g., Sillitoe, 1972; Tosdal and

Richards, 2001; Richards, 2003; Seedorff et al., 2005; Richards, 2011; Audétat et al., 2012). Regional tectonic stresses and crustal-scale faults play an important role in focusing magmatism in these settings (e.g., Hutton, 1988; Petford and Atherton, 1992; Richards, 2001). This causes batholiths, and overlying porphyry system clusters, to form along linear arc-parallel belts that range up to thousands of kilometers in length and may include several large deposits (e.g., Sillitoe and Perelló, 2005; Sillitoe, 2010).

The Highland Valley Copper (HVC) district in southern British Columbia (Figure 1), located approximately 54 km southwest of Kamloops and ~42 km northwest of Merritt, forms part of such a linear belt of porphyry systems in the southern Quesnel terrane (Logan and Mihalynuk, 2014; Schiarizza, 2014). The district is hosted in the Late Triassic calc-alkaline Guichon Creek batholith (GCB) and contains five porphyry Cu-Mo systems: Bethlehem, Valley, Lornex, Highmont, and J.A. Mining at HVC took place at Bethlehem between 1962 and 1982, and began at Lornex in 1972, at Highmont in 1980, and at Valley in 1982 (Casselman et al., 1995). Combined production from all pits at HVC (Table 1) prior to 1984 was 384 million tonnes grading 0.43% Cu (McMillan, 1985), and was 1115 million tonnes grading 0.35% Cu between 1986 and the end of 2011 (Graden, 2012). Current reserves are 535 million tonnes of ore grading 0.30% Cu, measured resources are 499 million tonnes grading 0.30% Cu, and indicated resources are 672 million tonnes grading 0.24% Cu (Teck Resources Limited, 2019).

Previous studies of hydrothermal alteration and mineralization at HVC were mainly focused on individual porphyry systems (e.g., Briskey and Bellamy, 1976; McMillan, 1976b; Osatenko and Jones, 1976; Reed and Jambor, 1976; Waldner et al., 1976; McMillan, 1985; Byrne et al., 2013, and references therein). Only two

Table 3.1. Summary of mined ore, mineral reserves and resources in the Highland Valley Copper district.

<table>
<tr><th rowspan="2">Deposit</th><th colspan="3">Ore mined (pre-1984)[1]</th><th colspan="3">Ore mined (1986–2011)[2]</th><th colspan="3">Reserves[3]</th><th colspan="3">Measured resources[3, 4]</th><th colspan="3">Indicated resources[3, 4]</th></tr>
<tr><th>Tonnage (Mt)</th><th>Cu (%)</th><th>Mo (%)</th><th>Tonnage (Mt)</th><th>Cu (%)</th><th>Mo (%)</th><th>Tonnage (Mt)</th><th>Cu (%)</th><th>Mo (%)</th><th>Tonnage (Mt)</th><th>Cu (%)</th><th>Mo (%)</th><th>Tonnage (Mt)</th><th>Cu (%)</th><th>Mo (%)</th></tr>
<tr><td>Bethlehem</td><td>105.9</td><td>0.50</td><td>-</td><td>-</td><td>-</td><td>-</td><td>-</td><td>-</td><td>-</td><td>-</td><td>-</td><td>-</td><td>-</td><td>-</td><td>-</td></tr>
<tr><td>J.A.</td><td>-</td><td>-</td><td>-</td><td>-</td><td>-</td><td>-</td><td>-</td><td>-</td><td>-</td><td>-</td><td>-</td><td>-</td><td>-</td><td>-</td><td>-</td></tr>
<tr><td>Valley</td><td>15.6</td><td>0.51</td><td>-</td><td rowspan="3">1115</td><td rowspan="3">0.35</td><td rowspan="3">0.009</td><td rowspan="3">535</td><td rowspan="3">0.30</td><td rowspan="3">0.007</td><td rowspan="3">499</td><td rowspan="3">0.30</td><td rowspan="3">0.008</td><td rowspan="3">672</td><td rowspan="3">0.24</td><td rowspan="3">0.009</td></tr>
<tr><td>Lornex</td><td>228.0</td><td>0.42</td><td>0.159</td></tr>
<tr><td>Highmont</td><td>34.7</td><td>0.21</td><td>0.032</td></tr>
</table>

[1]McMillan (1985), [2]Graden (2012), [3]Teck Resources Limited (2019), [4]Resources are exclusive of reserves.

studies include descriptions of district-scale alteration: Alva Jimenez (2011) studied the mineral chemistry of white mica and chlorite in the immediate vicinity of the Bethlehem system and along a 4 km transect between the Valley system the Alwin Cu occurrence to the west; and Casselman et al. (1995) briefly described the distribution of "green sericite" and chlorite veins across the district, but only characterized their intensity as weak or moderate–strong. To more fully characterize the mineralogy, paragenesis, and distribution of hydrothermal alteration products formed during porphyry mineralization in the HVC district, the geometry and mineralogy of deposit-scale alteration present at each porphyry system were summarized from previous studies, and new alteration mapping, feldspar staining and petrography were undertaken across the district to distances >10 km from the deposits.

Additionally, past studies indicated that post-mineralization dextral displacement along north-trending faults offset lithologies and deposits at HVC (e.g., Hollister et al., 1975; McMillan, 1976a). A new fault network interpretation for the GCB has been developed and used to build a palinspastic reconstruction of the batholith. This reconstruction also enables restoration of alteration zones as well as dike and vein orientation patterns to their original geometry. Fault, aplite, porphyritic dike and vein orientation, as well as vein intensity across the district are then used to identify the controls on permeability at the time of porphyry mineralization.

3.2. Regional geology

The GCB intruded the exotic Quesnel terrane, which formed as an island arc off the western coast of Ancestral North America and is part of the Peri-Laurentian realm of the Canadian Cordillera (Reid, 1985; Stanley and Senowbari-Daryan, 1999; Colpron and Nelson, 2011; Nelson et al., 2013). Final accretion of the Quesnel terrane onto the North American continent occurred during the Middle Jurassic (Nixon et al., 1993), following closure and obduction of the Cache Creek ocean beneath the Quesnel terrane (Mihalynuk et al., 1994). The convergent tectonics caused crustal thickening in the Quesnel terrane that reached a maximum during the Early Jurassic (Mihalynuk et al., 1999).

Late Triassic voluminous arc magmatism, which created the contemporaneous Quesnel and Stikine terranes, also generated most of the large porphyry systems in the Canadian Cordillera (Logan and Mihalynuk, 2014). In the southern Quesnel terrane, three sub-parallel belts of porphyry systems were formed between ~210 and ~195 Ma, with metal assemblages ranging from Cu-Mo±Au in the west to Cu-Au in the east (Preto, 1979; Logan and Mihalynuk, 2014; Schiarizza, 2014). The Late Triassic GCB (Mortimer et al., 1990; D'Angelo et al., 2017) is part of the oldest and westernmost of the three porphyry system belts (Figure 3.1) that intruded the Nicola Group volcanic and sedimentary rocks (Preto, 1979; Beatty et al., 2006; Schiarizza, 2017), which formed in a submarine environment above an east-dipping subduction zone (Mortimer, 1987; Ghosh, 1995). Norian basaltic to andesitic lava flow deposits and pyroclastic rocks in

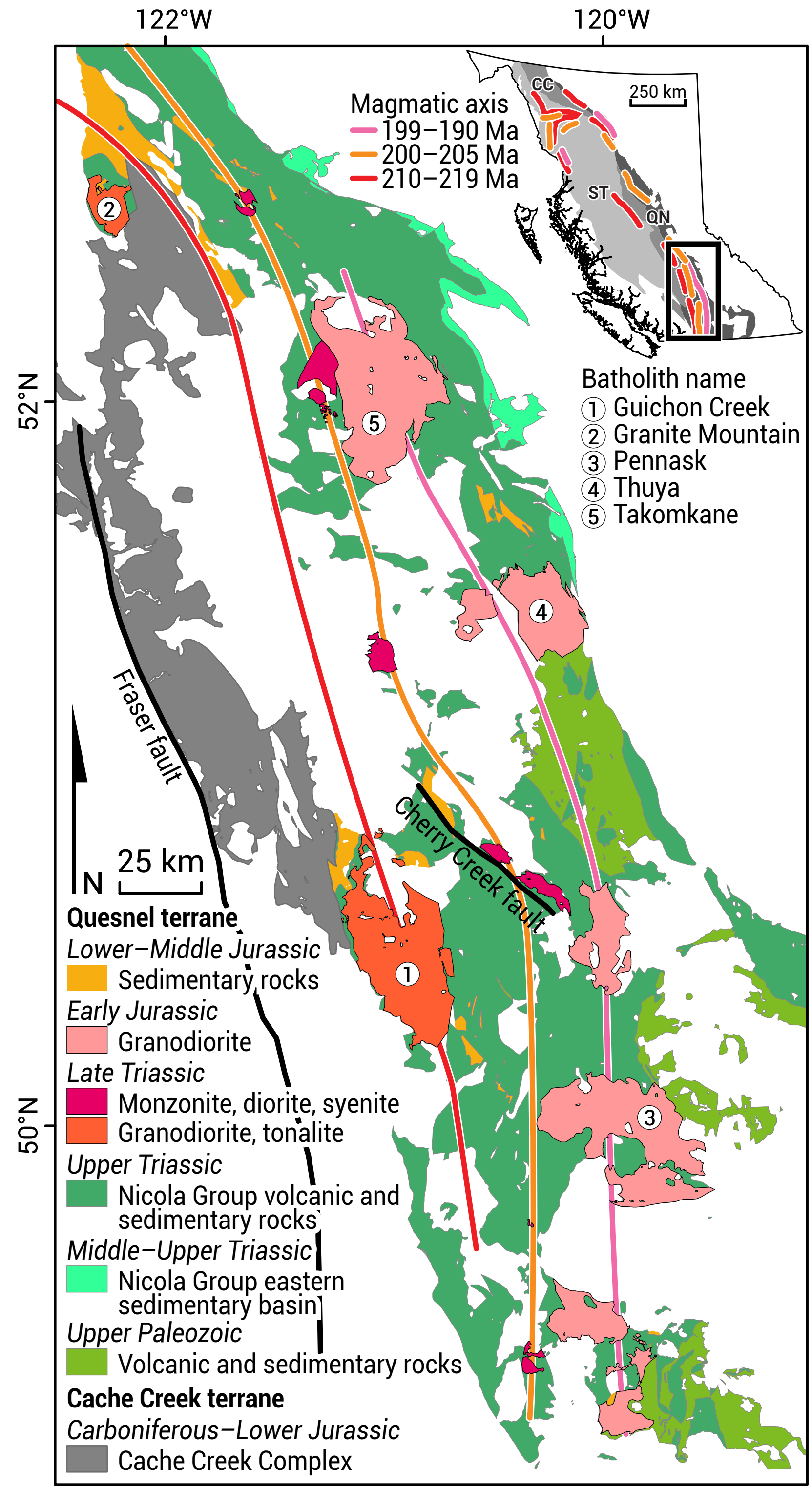

Figure 3.1. Simplified map of southern British Columbia showing rocks from the Cache Creek and Quesnel terranes, and the linear traces of Late Triassic to Early Jurassic arc intrusions (modified from Logan and Mihalynuk, 2014; Schiarizza, 2014; Cui et al., 2017). Terrane abbreviations: CC = Cache Creek, QN = Quesnel, ST = Stikine. Coordinates are in WGS1984.

the Merritt (Preto, 1979) and Kamloops (Beatty et al., 2006) areas indicate that there was active volcanism at the time of the GCB emplacement.

Following accretion of the Quesnel terrane onto the Ancestral North American margin, the tectonic regime in southern British Columbia transitioned from sinistral transpression (Nelson and Colpron, 2007) and crustal thickening to dextral transpression from the mid-Cretaceous to the Eocene period. This is recorded by large-scale dextral displacements along major transcurrent structures such as the ~300 km-long north to north-northwest-trending Fraser fault (~30 km west of the GCB; Schiarizza et al., 1996; Gabrielse et al., 2006), and the ~50 km-long northwest-trending Cherry Creek fault (~20 km northeast of the GCB; Ewing, 1981). The Fraser fault is a strike-slip fault system that currently juxtaposes the Cache Creek and Quesnel terranes along which upwards of 100 km of dextral displacement has taken place since the mid-Cretaceous (Wyld et al., 2006).

3.3. GCB geology

The GCB intruded the Late Triassic Nicola Group volcanosedimentary package and forms a large 30 x 65 km north-northwest-trending irregularly-shaped ellipsoid (Figure 3.2). The batholith is a composite calc-alkaline intrusion that has geochemical similarities to the western Nicola Group volcanic rocks and is interpreted to represent part of their plutonic root (Mortimer, 1987; Ghosh, 1995). The batholith is unconformably overlain by volcanic and sedimentary rocks of the mid-Cretaceous Spences Bridge Group to the southwest, the Eocene Kingsvale Group to the south, and the Jurassic Ashcroft Formation and Eocene Kamloops Group to the north (McMillan et al., 2009).

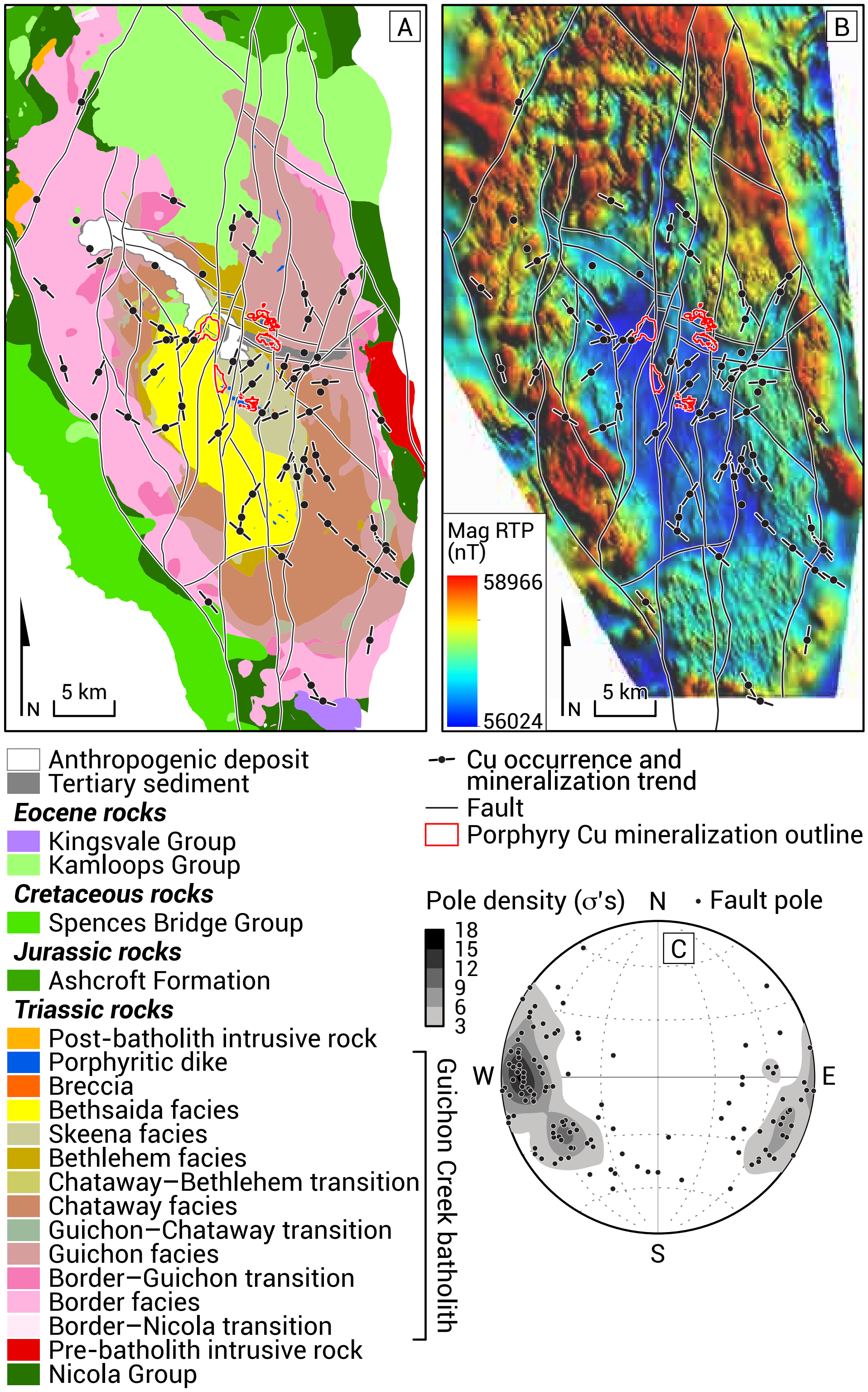

Figure 3.2. A) Geological map of the Guichon Creek batholith showing the location of porphyry Cu mineralization and of small Cu occurrences, B) reduced to pole (RTP) aeromagnetic grid, and C) stereonet showing fault pole orientation. Lithology map modified from McMillan et al. (2009) and batholith-scale fault network and fault orientation data from (Lesage et al., 2019).

Interpretations from gravity and seismic data indicate that the batholith forms a flattened funnel-shaped body with steeply-dipping eastern and western contacts, and northern and southern contacts that dip shallowly inwards toward a steeply-plunging feeder zone located below the porphyry systems (Ager et al., 1973; Roy and Clowes, 2000). Aluminium-in-hornblende barometry shows that exposed rocks from the southern half of the GCB formed at depths between 3.7 and 7.4 km, whereas rocks from the northern half of the batholith formed at depths ranging from 2.6 to 4.8 km (D'Angelo, 2016). These data are consistent with post-emplacement tilting to the northeast of ~12–15° predicted from the gravity and seismic models (Ager et al., 1973; Roy and Clowes, 2000). The depths are also consistent with the stratigraphic thickness estimates of 3–6 km for the Nicola Group rocks in the Quesnel terrane (Preto, 1979).

In the GCB, the mid-Cretaceous to Eocene dextral structural regime displaced lithological contacts and porphyry deposits across north-trending faults. The largest dextral displacement in the district is ~3.5 km and was recorded on the Lornex fault (Hollister et al., 1975). The Lornex fault offsets the Valley and Lornex deposits, which are interpreted to have formed as a single porphyry system (Allen and Richardson, 1970; Hollister et al., 1975), and the dip of the fault varies between steeply west-dipping in the Lornex open pit (Waldner et al., 1976) and steeply east-dipping in the Valley open pit (Casselman et al., 1995).

Late Paleocene–Eocene transtension is also recorded by west-northwest to northwest-trending normal faults such as the Highland Valley fault, which down-threw the structural block that contains the J.A. porphyry system and caused the formation of a basin that was filled with up to 300 m of pre-glacial and glacial sediments (McMillan, 1976b; Bobrowsky et al., 1993). Quaternary sediments at HVC include mid-Wisconsinan or older glaciofluvial and glaciolacustrine sediments that infilled deep valleys, younger till that formed a blanket of variable thickness over the area, and local post-glacial fluvial and lacustrine sediments (Bobrowsky et al., 1993; Plouffe and Ferbey, 2015; Ferbey et al., 2016).

The GCB formed from two distinct pulses of magmatism that generated concentric compositional zones from mafic older marginal facies to felsic younger central facies (Figure 3.2A) (Carr, 1966; Northcote, 1969; McMillan, 1976a, 1985; Byrne et al., 2013; D'Angelo et al., 2017). U-Pb dating of zircons from each intrusive facies by D'Angelo et al. (2017) detailed the formation of the batholith. The first magmatic pulse consists of equigranular diorite, granodiorite and rare gabbro (Border facies, and Guichon and Chataway subfacies of the Highland Valley facies) and intruded between 211.0 ± 0.2 Ma and 210.4 ± 0.4 Ma. The younger magmatic pulse comprises equigranular to weakly porphyritic granodiorite and monzogranite (Bethlehem, Skeena and Bethsaida facies) and intruded between 209.8 ± 0.3 Ma and 208.6 ± 0.2 Ma. A seventh unit, a fine-grained equigranular granodiorite named the "Salt and Pepper" (S&P) Bethsaida facies (Byrne et al., 2013), occurs as stocks and dikes deep in the Valley pit and was dated at 208.2 ± 0.2 Ma.

3.3.1. Late dikes

Aplite dikes, as well as pre, syn and post-mineralization porphyritic dikes have been documented at every porphyry system and at several other Cu occurrences across the GCB (D'Angelo et al., 2017, and references therein). Timing of dike intrusion relative to other lithologies, and to Cu mineralization, has mainly been determined from cross-cutting relationships. These relationships indicate that the porphyritic dikes at Bethlehem and J.A. formed prior to the porphyritic dikes at Valley, Lornex and Highmont (Byrne et al., 2013; D'Angelo et al., 2017). Only one isotopic age determination is available from the porphyritic dikes, and comes from a post-mineralization, quartz-rich, quartz–feldspar-porphyritic dike at the Highmont deposit. This dike cross-cuts syn-mineralization quartz–feldspar–biotite-porphyritic dikes and yielded an age of 207.0 ± 0.2 Ma (U-Pb zircon, D'Angelo et al., 2017). The geochemical compositions of porphyritic dikes in the HVC porphyry systems indicate that they evolved from the same magma source as the Bethlehem and Bethsaida facies of the batholith (D'Angelo et al., 2017).

Porphyritic dike orientation varies significantly between the HVC porphyry systems. Porphyritic dikes in the Bethlehem system are dominantly north-trending and vertical to steeply west-dipping. At J.A., the main porphyritic body trends northwest and intruded along the Guichon–Bethlehem facies contact (McMillan, 1976b). The Bethsaida facies at Valley and the Skeena facies at Lornex and Highmont are cross-cut by west-northwest-trending pre-mineralization quartz–feldspar–biotite to post-mineralization quartz-rich quartz–feldspar-porphyritic dikes. The dikes are steeply north-dipping at Valley (McMillan, 1985), and are vertical to steeply north-dipping at Lornex and Highmont (Reed and Jambor, 1976). Pre to post-mineralization porphyritic dikes at Lornex and Highmont form a 60 to 240 m-wide, west-northwest-trending dike complex, referred to as the Gnawed Mountain Porphyry dike (Reed and Jambor, 1976; Byrne et al., 2013).

Porphyritic dikes are spatially associated with magmatic-hydrothermal breccias. Breccia spatial association, geometry, and clast populations indicate that breccia formation is related to dike emplacement. Breccia cements include a mixture of tourmaline and specular hematite. Breccias are volumetrically significant at Bethlehem and in and around Highmont, whereas they do not occur at Valley and Lornex (Byrne et al., 2013). The presence of sulfide minerals in the hydrothermal breccia cement, and the presence of veined or altered clasts indicate that the breccia formation was contemporaneous with porphyry mineralization.

Aplite dikes are characterized by K-feldspar, plagioclase and quartz, with rare biotite or magnetite. Aplites typically exhibit a fine-grained graphic texture, although a porphyritic texture with plagioclase phenocrysts is locally present in wider dikes. Cross-cutting relationships indicate that aplite dikes were emplaced late to post-mineralization at Bethlehem and pre-mineralization at Valley (Osatenko and Jones, 1976; Byrne et al., 2013). Aplite dikes have not been dated.

3.4. Methodology

3.4.1. Mapping

In order to identify the district-scale porphyry-related alteration assemblages and their spatial distribution, geological mapping at 1:10 000 scale was focused along five transects across the GCB from 2014 to 2016. The work was conducted as part of the Natural Sciences and Engineering Research Council (NSERC) of Canada and Canada Mining Innovation Council (CMIC) supported Mineral Exploration Footprints project (Lesher et al., 2017). Each transect is approximately 10–14 km in length and 2.5–3.5 km wide, starts at one of the known porphyry systems and ends near the outer margin of the batholith. The total area mapped is approximately 225 km^2. Bench mapping was conducted in the southwestern portion of the Valley open pit, in the southern quarter of the Lornex open pit, and in the Highmont open pits. The areas located within 3–4 km to the southwest of Valley and the open pit benches were mapped at a scale of 1:5,000.

Structural measurements for aplites, porphyritic dikes, and veins were recorded using the right hand rule, whereby for each plane the bearing of the strike and dip angle to the right of the strike are recorded. A total of 139 dike orientations were measured (Appendix A). Vein orientation, frequency and width, and vein and selvage mineralogy were systematically recorded at every outcrop. Because alteration selvages adjacent to veins are symmetrical, selvage width was recorded on one side between the vein margin and the limit of visible alteration. Vein occurrence and spacing at the outcrop scale varies significantly; some areas of an outcrop may have several closely-spaced veins whereas other areas completely lack veins. To minimize this issue, vein frequency per meter was recorded for each vein set on the longest outcrop exposure possible, perpendicular to the vein strike. Vein intensity, expressed in centimeters of vein and altered selvage per meter of rock (cm/m), gives a measure of the intensity of fluid-rock interactions and was calculated by multiplying the vein frequency by the vein thickness and total selvage thickness on either side of the vein.

In addition to the data collected during this mapping campaign, historical vein mineralogy and orientation data collected by Teck Resources Limited ("Teck") geologists between 2012 and 2014 were made available for the study. A total of 1461 vein orientations were measured by the authors, and 563 vein orientations were selected from the data set provided by Teck on the basis of sufficient metadata available (Appendix B). Structural data were plotted on Schmidt equal area stereonets and pole density contours were calculated using a modified Kamb method with exponential smoothing for two standard deviation contour intervals (Vollmer, 1995).

3.4.2. Feldspar staining

Rock samples were collected in a grid pattern approximately every 500 m along the mapped transects. Slabs were cut from each sample perpendicular to the vein orientation. Each slab was stained in order to highlight the effect of hydrothermal alteration on feldspar mineralogy. Staining was performed in three steps: slabs were 1) etched in a bath of hydrofluoric (HF) acid for one minute, 2) dipped into an amaranth solution for five seconds, and 3) dipped into a sodium cobaltinitrate solution for 30 seconds. Slabs were rinsed and dried between each step. Sodium cobaltinitrate stains K-feldspar crystals yellow, whereas amaranth stains calcic feldspar crystals red (Gabriel and Cox, 1929; Bailey and Stevens, 1960; Laniz et al., 1964; Lyons, 1971; Norman, 1974). Other calcic minerals, such as calcite or prehnite, may also be stained by the amaranth to various shades of red (Norman, 1974). Although other calcic minerals are present in the HVC as part of the hydrothermal alteration footprint, they typically occur within veins so they are easily distinguished from the magmatic calcic feldspars.

3.4.3. Fault interpretation and palinspastic reconstruction

Post-mineralization fault offsets can significantly affect the spatial distribution of porphyry-related hydrothermal alteration products. The effects of ~3.5 km of mid-Cretaceous to Eocene dextral displacement along the Lornex fault is one such example (Hollister et al., 1975). A palinspastic reconstruction of the GCB was undertaken to restore the spatial distribution of the HVC district-scale alteration assemblages to their original geometry.

Previous work on the structural architecture of the GCB mainly focused on the Lornex and Highland Valley faults because of their strong topographic expressions and proximity to the porphyry systems (e.g., Hollister et al., 1975; McMillan, 1976a, 1985). To perform an accurate reconstruction, a new fault network for the entire GCB was constructed that includes all faults with along-strike continuity >4km (Figure 3.2) (Lesage et al., 2019). A multi-layered approach, similar to the approach developed by Sánchez et al. (2014), was used to map linear features that correspond to the intersection of fault planes with the topographic surface (i.e., fault traces) and ensure that the identified features are of geological significance. Data sets used for the fault interpretation include: 1) Shuttle Radar Topography Mission (SRTM) topographic data, 2) drill hole data, where available, 3) historical geological and structural mapping, 4) new geological and structural mapping done by the authors (Figure 3.2A), 5) induced polarization resistivity data, and 6) airborne reduced to pole (RTP) magnetic intensity data (Figure 3.2B). Fault orientations were measured in the field where available, but these data are sparse because faults are typically recessive features that are infilled with the extensive glacial cover in the area. To provide additional orientation constraints, (Lesage et al., 2019) modeled the strikes and dips of faults in several locations using the magnetic intensity data (Figure 3.2C).

The presence of mutually cross-cutting faults (e.g., in an "X" pattern) implies that displacement was synchronous along both fault planes, which requires a significant redistribution of volume within each fault blocks (Odonne and Massonnat, 1992). Although mutually cross-cutting faults are possible in nature (Horsfield, 1980; Odonne and Massonnat, 1992), sequential or alternating displacements along interacting faults is more likely because it requires no volume redistribution (Ferrill et al., 2000; Ferrill et al., 2009). To avoid mutually cross-cutting faults in the proposed interpretation, the relative timing of the faults is determined based on geological observations and on the along-strike continuity of the corresponding linear features in the various datasets. Older faults are terminated against younger faults.

3.5. Cu mineralization in the GCB

3.5.1. HVC porphyry systems

Mineralization at the five porphyry systems in the HVC district was emplaced during at least two main hydrothermal episodes (Byrne et al., 2013). The deposit-scale alteration assemblages and timing relationships described below are compiled from previous studies (McMillan, 1985; Byrne et al., 2013) and observations from this study. The deposit-scale alteration characteristics are used as a framework to determine the HVC district-scale alteration assemblages and paragenetic sequence. Deposit geometry is also a potentially important characteristic, because deposit elongation may be the result of preferential fluid pathway orientation and as such reflect the syn-mineralization stress regime. Table 3.2 presents the mineral name abbreviations used in figures and tables below, and Table 3.3 summarizes the porphyry system characteristics.

The first hydrothermal episode was the formation of the Bethlehem porphyry system at ~209 Ma. Copper mineralization at Bethlehem post-dates intrusion of the Bethlehem facies of the GCB, but pre-dates the Skeena and Bethsaida facies. Based on their similar characteristics, the Bethlehem and J.A. systems, both of which straddle the Guichon–Bethlehem facies contact, are interpreted to be coeval. The Valley, Lornex and Highmont porphyry systems were subsequently emplaced between ~208 Ma (Lornex and Highmont systems; D'Angelo et al., 2017) and ~207 Ma (Valley system: Ash et al., 2006), as indicated by Re-Os ages from molybdenite. Host rocks at Valley, Lornex and

Table 3.2. List of mineral abbreviations (from Whitney and Evans, 2010).

Abbreviation	Mineral name
Ab	Albite
Act	Actinolite
Bn	Bornite
Bt	Biotite
Cal	Calcite
Ccp	Chalcopyrite
Cct	Chalcocite
Chl	Chlorite
Di	Diopside
Ep	Epidote
Fsp	Feldspar
Grt	Garnet
Hbl	Hornblende
Hem	Hematite
Kfs	K-feldspar
Kln	Kaolinite
Mag	Magnetite
Mol	Molybdenite
Ms	Muscovite
Pl	Plagioclase
Prh	Prehnite
Py	Pyrite
Qz	Quartz
Spec	Specular hematite
Ttn	Titanite
Tur	Tourmaline
Vrm	Vermiculite
WM	White mica

Highmont are respectively the Bethsaida, Skeena and Bethsaida, and Skeena facies.

3.5.1.1. Bethlehem

Three deposits (i.e., Huestis, Jersey and Iona) comprise the west-northwest-elongated Bethlehem porphyry system. Early hydrothermal alteration at Bethlehem consists of a potassic assemblage characterized by weakly mineralized quartz veins with secondary biotite and K-feldspar selvages (Briskey, 1980; Alva Jimenez, 2011). Potassic alteration was followed by quartz vein-controlled to weakly pervasive chlorite and fine-grained white mica alteration. Both alteration assemblages contain Cu mineralization. Post-

Table 3.3. Summary of the HVC porphyry system characteristics.

Deposit	Host facies	Dike facies [timing relative to Cu mineralization]	Geometry of orebody	Vein / Selvage minerals	Geometry of faults
Bethlehem	Guichon Bethlehem (near contact)	Fsp-Hbl-Bt-phyric [pre] Fsp-Qz-phyric [late to post] Aplites [post]	Associated with Guichon–Bethlehem contact WNW-trending long axis Steeply N-dipping Locally pipe-like	Qz-Bt-Bn±Ccp / Bt Bn±Ccp / Kfs Qz-Ccp-Py / fine Ms Ccp±Bn / Chl Qz-Ep / Chl-Ab±Act	Abundant small faults N-trending Subvertical to steeply W-dipping Post-mineralization
J.A.	Guichon Bethlehem J.A. porphyry stock	Qz-Fsp-phyric [pre]	Associated with Guichon–Bethlehem contact WNW-trending long axis Minor NE-trending zones extending from main zone	Qz±Bt-Ccp±Bn / Kfs±Bt (weakly mineralized) Ccp-Bn±Mo / fine Ms Qz-Ccp±Bn / fine Ms Qz-Ep / Chl±Ab-Ep	Two fault orientations described: WNW and NE-trending Post-mineralization
Valley	Bethsaida Salt & Pepper Bethsaida stock	Aplites [pre] Qz-Fsp-Bt-phyric [pre] Qz-Fsp-phyric (phenocryst poor) [pre] Qz-Fsp-phyric [pre to syn]	NW-trending long axis Subvertical to steeply NE-dipping Sharp gradients in Cu grade along NE direction	Qz / Kfs (barren core) Qz-Bn-Ccp±Mo / Kfs Qz-Bn-Ccp±Mo / coarse Ms Qz-Ccp-Py-Mo / fine to coarse Ms	Lornex fault to the east (N-trending, steeply E-dipping) Yellow fault to the west (NE-trending, ~80°E dip) Abundant small NNW-trending, moderately E-dipping faults
Lornex	Skeena Bethsaida	Aplites [pre] Qz-Fsp-Bt-phyric [pre] Qz-Fsp-phyric [pre to syn] Qz-Fsp-phyric (Qz-rich) [post]	NW-trending long axis Steeply NE-dipping Sharp gradients in Cu grade along NE direction	Qz (barren) Qz-Bn-Ccp±Mo / Kfs Ab / Ab-Act-Ttn Chl±Ab / Chl±Ab-Ep Qz-Bn-Ccp±Mo / coarse Ms Qz-Ccp-Py-Mo / fine to coarse Ms	Lornex fault to the west (50 m, N-trending, ~75° W-dipping) Faulted Skeena–Bethsaida contact (20 m, N-trending, subvertical) Abundant N-trending, W-dipping faults west of the Lornex fault
Highmont	Skeena	Aplites [pre] Qz-Fsp-Bt-phyric (Gnawed Mountain) [pre] Qz-Fsp-phyric [pre to syn] Qz-Fsp-phyric (Qz-rich) [post]	Located on both sides of (and partially hosted in) the Gnawed Mountain Porphyry WNW-trending long axis Minor NNE-trending zones extending from main zone to the NE	Qz-Bn-Ccp±Mo / Kfs Ab / Ab-Act-Ttn±Grt Chl±Ab / Chl±Ab-Ep Qz-Bn-Ccp±Mo / coarse Ms Qz-Ccp-Py-Mo / fine to coarse Ms	Several roughly 100–250 m-spaced N to NE-trending Mainly 45°–65° W-dipping, minor E-dipping faults Post-mineralization

mineralization sodic-calcic alteration, particularly at depth, overprinted the earlier potassic alteration and remobilized Cu (Briskey and Bellamy, 1976; Byrne et al., 2013). Sodic-calcic alteration is characterized by north-trending quartz-epidote veins with albite–chlorite selvages (Figure 3.3A and B), pervasive epidote alteration of calcic feldspars and pervasive chlorite ± actinolite alteration of mafic minerals.

3.5.1.2. J.A.

The J.A. porphyry system was drilled extensively in the 1970s, but the drill core was not preserved so the current understanding of the system is primarily limited to historical descriptions (McMillan, 1976b; Byrne et al., 2013, and references therein). Copper mineralization at J.A. trends west-northwest with minor northeast-trending offshoots that extend from the main mineralized zone. Fracture and quartz vein-controlled potassic alteration characterized by K-feldspar ± biotite is widespread at J.A., although this alteration assemblage is not systematically well mineralized. Copper mineralization is primarily located in quartz-vein-controlled fine-grained white mica and chlorite alteration similar to the alteration present at Bethlehem. Rare quartz–sulfide veins with coarse-grained muscovite selvages, similar to the main Cu-bearing veins at Valley, are also present. Sodic-calcic veins of epidote–quartz with albite–chlorite–epidote selvages cross-cut mineralized veins at depth.

3.5.1.3. Valley

The Valley deposit forms a three-dimensional northwest-trending bell shape that is sub-vertical or dips steeply to the northeast. The Valley porphyry system is characterized by an early, central zone of intense barren quartz stockwork veins associated with strong K-feldspar alteration (Osatenko and Jones,

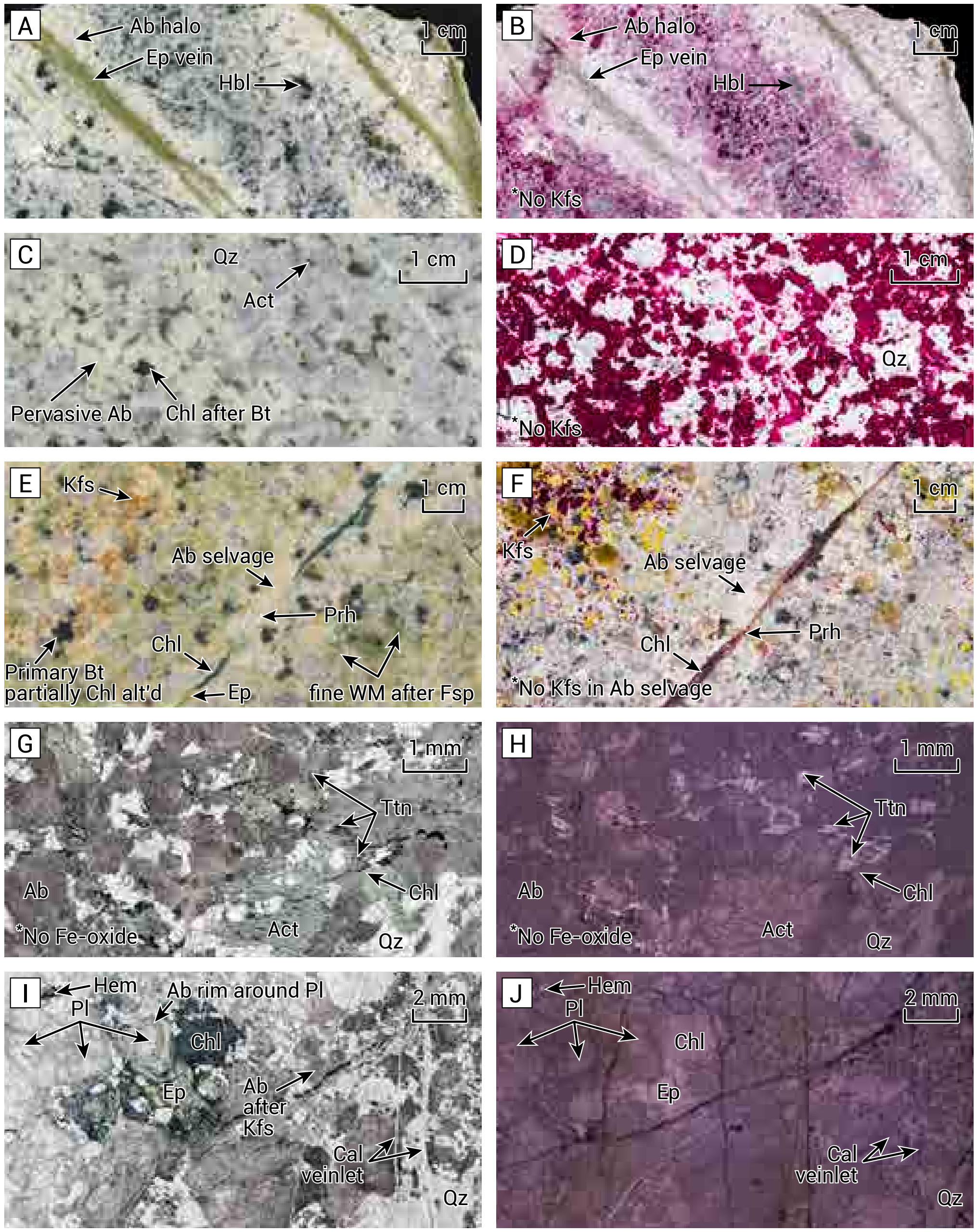

Figure 3.3. Hand sample photos and thin section photomicrographs of sodic-calcic alteration: A) and B) sample 2245244 original and stained slab showing symmetrical Ab selvages around Ep veins and complete Kfs destruction throughout the rock; C) and D) sample 2232419 original and stained slab showing strong Ab-Chl-Ep-Act pervasive alteration and complete destruction of Kfs; E) and F) sample 2232428 original and stained slab showing a Chl vein with late Prh margins, 1–2 cm wide Ab selvages, and WM-Chl overprint; G) and H) sample 2758531 under plane-polarized transmitted and reflected light showing Chl-Act-Ttn alteration of mafic sites, Ab alteration of felsic sites, and complete removal of magmatic magnetite; I) and J) sample 2758600 under plane-polarized transmitted and reflected light showing Chl-Ep alteration of mafic sites and Ab alteration of felsic sites.

1976; McMillan, 1985; Casselman et al., 1995). Away from the barren quartz veins, abundant thin (~0.5 cm) K-feldspar ± quartz ± chalcopyrite ± bornite veins (Figure 3.4D and E) transition from stockwork veins (Figure 3.4A) within the deposit to sub-parallel, evenly spaced veins (10–30 veins/m; Figure 3.4B and C) outside the deposit. Pervasive shreddy biotite alteration of magmatic hornblende is common within the deposit. K-feldspar-bearing veins are cross-cut by well-mineralized high-temperature quartz–bornite–chalcopyrite ± molybdenite veins with selvages of coarse-grained grey paragonitic muscovite, quartz and minor calcite (Figure 3.5A and C) (Osatenko and Jones, 1976; Alva Jimenez, 2011). These veins are similar to the early halo (EH) veins described at Yerington (Proffett, 2009) and the early dark micaceous (EDM) veins described at Butte (Meyer, 1965; Brimhall, 1977; Rusk et al., 2008). These veins are steeply dipping and dominantly northwest-trending, with a minor northeast-trending subset. Thick (>10 cm) banded quartz–chalcopyrite–molybdenite ± pyrite veins with extensive fine to coarse-grained grey muscovite selvages (Figure 3.5B and D) cross-cut earlier quartz–bornite–chalcopyrite veins and are typically present at the margins of the deposit. Localized pods of fracture-controlled sodic-calcic alteration characterized by albite, actinolite, chlorite, epidote and titanite have been described by Alva Jimenez (2011), however the timing of this alteration in the Valley system is not well constrained. The deposit is bound to the east by the post-mineralization, north-trending and steeply east-dipping Lornex fault (Casselman et al., 1995).

3.5.1.4. Lornex

The Lornex deposit is located at the Skeena–Bethsaida contact, and is northwest-trending and steeply northeast-dipping. A zone of barren quartz stockwork veins similar to the barren quartz veins at Valley is present (Byrne

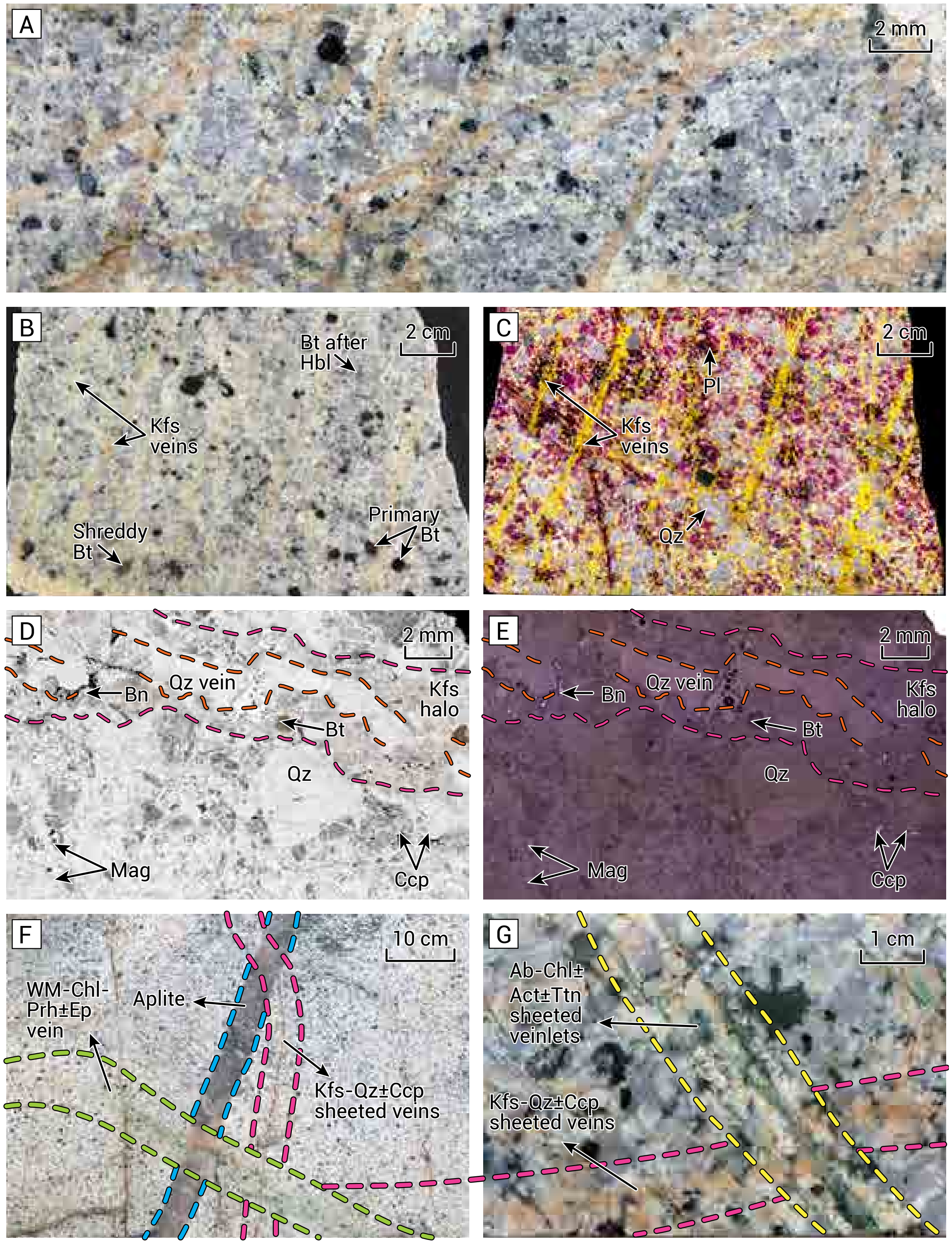

Figure 3.4. Hand sample photos and thin section photomicrographs of K-feldspar alteration: A) stockwork veins from the west wall of the Valley deposit; B) and C) sample 2232444 original and stained slab showing sheeted Kfs veins; D) and E) sample 2758518 under plane-polarized transmitted and reflected light showing thin Qz vein with symmetrical Kfs selvages and addition of Ccp and Bn; F) outcrop photo showing an early aplite dike cross-cut by sheeted Kfs-Qz veins, and both later cross-cut by a WM-Chl-Prh vein (2014GL038); and G) drill core photo showing Kfs-Qz alteration cross-cut by Ab-Chl-Act.

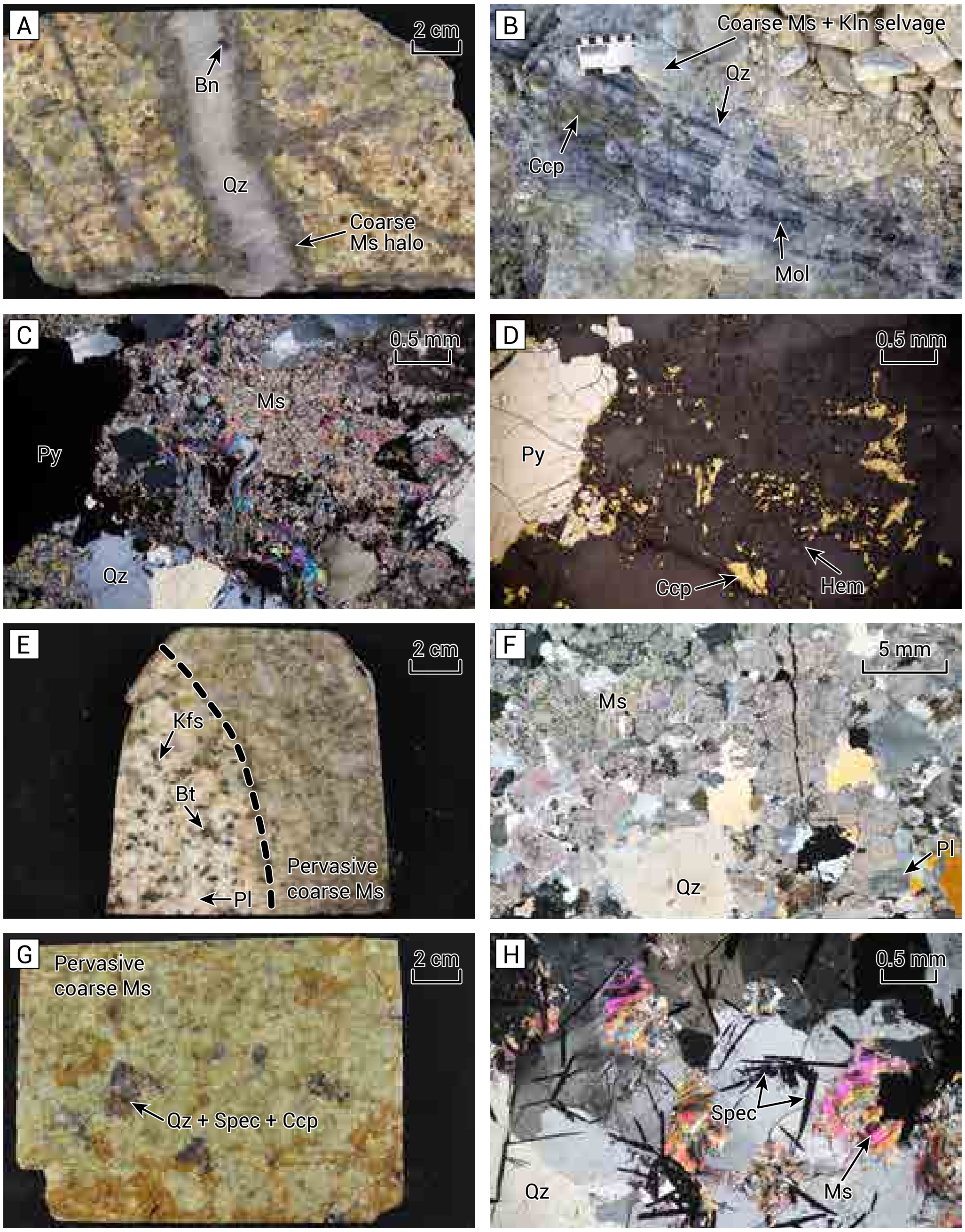

Figure 3.5. Hand sample photos and thin section photomicrographs of muscovite alteration: A) sample 2238870 slab showing symmetrical coarse-grained grey Ms selvages around Qz-Ccp-Bn veins; B) banded Qz-Mol-Ccp-Py vein from the western margin of the Valley pit; C) and D) sample 2758535 under cross-polarized transmitted and reflected light showing Ms alteration of both mafic and felsic sites and addition of Py and Ccp (A to D are from within the Valley pit); E) and F) sample 2238802 slab and under cross-polarized light showing strong pervasive greenish Ms alteration transitioning abruptly into less-altered rock (Empire Cu occurrence); G) and H) sample 2238819 slab and under cross-polarized light showing strong pervasive greenish Ms alteration associated with Qz-Spec-Ccp blebs (Alwin Cu occurrence).

et al., 2013). Potassic alteration has been described as erratically distributed (Waldner et al., 1976). Minor northwest to west-northwest-trending sub-parallel K-feldspar ± quartz ± chalcopyrite veins occur in the southern portion of the deposit. Pervasive shreddy biotite alteration of magmatic hornblende is also present in this area. K-feldspar-bearing veins were overprinted by pervasive to locally fracture-controlled sodic-calcic alteration characterized by albite–chlorite ± actinolite ± titanite ± epidote ± tourmaline (Figure 3.3C and D). Sodic-calcic alteration caused remobilization of Cu mineralization located in older K-feldspar-bearing veins, replacement of K-feldspar by albite and locally fine-grained white mica (Figure 3.3B, D, and F), and destruction of Fe-oxide minerals (Figure 3.3H and J). The bulk of the Cu mineralization was deposited after the rocks were altered to a sodic-calcic assemblage in quartz–bornite–chalcopyrite ± molybdenite veins with coarse-grained grey muscovite selvages similar to the main Cu-bearing veins at Valley. In the southern portion of the deposit, Cu-Mo-bearing veins are dominantly northwest to west-northwest-trending and steeply-dipping. Waldner et al. (1976) also reported discontinuous domains of north-northeast-trending (N022°/55°), northeast-trending (N064°/57°), and west-trending (N090°/58°) Cu-Mo-bearing veins at Lornex. Late banded quartz–chalcopyrite–molybdenite ± pyrite veins can be mapped for up to 200 m in the eastern part of the deposit (McMillan, 1985).

The Lornex deposit is truncated to the west by the 40–50 m wide, north to north-northwest-trending, ~75° west-dipping Lornex fault zone (Figure 3.6A) (Waldner et al., 1976). Horizontal slickenlines, with evidence of dextral displacement, that occur on the edges of the fault zone (Figure 3.6B) are consistent with the interpretation that the Valley and Lornex deposits were once a single porphyry system (hereafer referred to as Valley–Lornex; Allen and Richardson, 1970; Hollister et al., 1975). The Skeena–Bethsaida facies contact at Lornex is located within the deposit and is characterized by a ~20 m-wide sub-vertical fault gouge zone that also shows evidence of dextral displacement.

Alteration assemblages present on either side of the Lornex fault are significantly different. The deposit is located to the east and contains the alteration described above, whereas the rocks to the west contain rare ~0.5 cm-wide K-feldspar ± quartz veins and abundant chlorite ± epidote ± prehnite veins that have 1–3 cm-wide inner albite-chlorite-epidote selvages and outer selvages of fine-grained white mica alteration of primary plagioclase and chlorite alteration of mafic minerals locally up to 10 cm-wide (Figure 3.3E and F). Prehnite in these veins appears to have been deposited later than the chlorite and epidote after the veins were reopened. The outer fine-grained white mica-chlorite selvages are interpreted as a propylitic assemblage associated with the later fluid that deposited the prehnite and overprinted the inner sodic-calcic selvages (Figure 3.7).

Figure 3.6. Outcrop photos showing: A) the width of the major post-mineralization Lornex fault zone in the south of the Lornex pit (looking south, mineralized rocks to the left and unmineralized rocks to the right), and B) clear sub-horizontal slickenfibers on the Lornex fault indicating post-mineralization dextral strike-slip displacement.

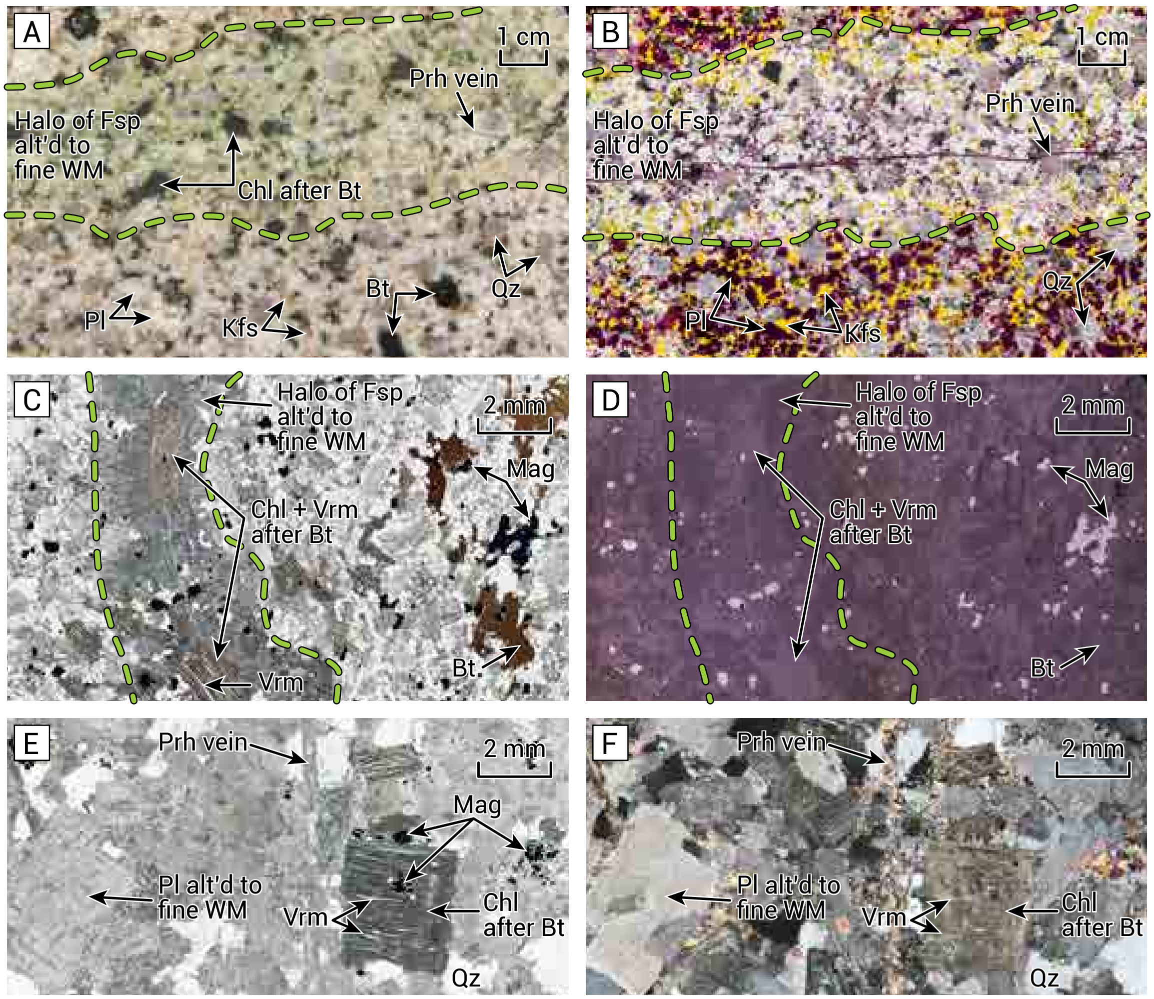

Figure 3.7. Hand sample photos and thin section photomicrographs of propylitic alteration: A) and B) sample 2758871 original and stained slab showing a prehnite vein with pale green selvages of Pl altered to fine-grained white mica and magmatic Bt altered to Chl; C) and D) sample 2758586 under plane-polarized transmitted and reflected light showing a fracture with selvages of Pl altered to fine-grained white mica and magmatic Bt altered to Chl-Vrm; in D) the magnetite crystals located within the alteration halo are more pitted than those in the least altered part of the rock, indicating that magnetite was unstable under the alteration conditions; E) and F) sample 2238749 under plane-polarized and cross-polarized transmitted light showing a prehnite vein with selvages of Pl altered to fine-grained white mica and magmatic Bt altered to Chl.

3.5.1.5. Highmont

The Highmont deposit is west-northwest-trending and is sub-parallel to the Gnawed Mountain Porphyry dike. The Highmont porphyry system is characterized by the same alteration assemblages as Valley and Lornex. Minor early ~0.5 cm-wide quartz-K-feldspar ± chalcopyrite ± bornite veins are west-northwest to northwest-trending in the southern part, and north-trending in the northern part of Highmont. Pervasive biotite alteration of magmatic hornblende is typical within the deposit. Potassic alteration was overprinted by sodic-calcic alteration (Figure 3.4G), characterized by areas of pervasive albite–actinolite–titanite ± tourmaline ± relict diopside ± relict garnet (Figure 3.3G and H) (Byrne et al., 2017), as well as actinolite-chlorite and chlorite ± epidote veins with albite–chlorite ± epidote selvages (Figure 3.3I and J) that are steeply dipping and dominantly north to north-northeast-trending. Garnet was later retrograded to chlorite ± pumpellyite. The presence of tourmaline-cemented breccias that contain clasts characterized by sodic-calcic alteration, either pervasive or forming rims on the edges of clasts, suggests that breccia emplacement was contemporaneous with sodic-calcic alteration.

Copper mineralization at Highmont post-dates the bulk of sodic-calcic alteration and is dominantly hosted in steep northeast and northwest-trending quartz–bornite–chalcopyrite ± molybdenite veins with selvages of coarse to locally fine-grained grey muscovite, quartz and minor calcite. Copper mineralization is cross-cut by post-mineralization quartz-rich quartz–feldspar-porphyritic dikes dated at 206.95 ± 0.22 Ma by D'Angelo et al. (2017), which constrains the timing of mineralization at Highmont to before ~207 Ma. However, these post-mineralization dikes are locally albitized, which indicates the occurrence of at least two periods of sodic-calcic alteration, and suggests that hydrothermal fluid flow continued for some time as the system was cooling down after the last pulse of hot metal-rich magmatic fluids.

3.5.2. Other Cu occurrences

In addition to the five HVC porphyry systems, about 160 Cu occurrences, eleven of which are past or active producers, have been documented across the GCB and in the surrounding Nicola Group rocks (McMillan et al., 2009). Public domain data (e.g., MINFILE BC, BC Assessment Report Database) from 74 of these Cu occurrences were reviewed and a number of occurrences were visited in order to characterize the style (e.g., mineralogy, texture, etc.) of mineralization and the main mineralized trend, where apparent (Figure 3.2A).

Cu occurrences throughout the GCB are dominantly characterized by vein-hosted sulfide or Cu-oxide mineralization, and are locally fault-hosted. Porphyritic dikes are also present at several Cu occurrences. Skarn mineralization characterized by high-temperature calcic alteration and Fe-metasomatism is present in two locations: north of the batholith at Brassie, and at the southern margin of the batholith at Craigmont.

Hydrothermal alteration minerals at most Cu occurrences are white mica (i.e., either coarse-grained greenish muscovite or fine-grained white mica; Figure 3.5E to H), and chlorite locally with minor carbonate, quartz, specular hematite (Figure 3.5G and H), magnetite, epidote and tourmaline. K-feldspar alteration occurs at a few Cu occurrences, but it is weakly mineralized and consistently cross-cut by vein-controlled to locally pervasive white mica alteration that is better mineralized. In general, alteration at Cu occurrences is strongly structurally controlled and forms intense, locally texturally destructive zones that extend a few tens of meters or less from the permeable structures. The coarse-grained greenish muscovite alteration is characteristic of greisen alteration in porphyry Cu systems (e.g., Shaver et al., 1991; Williams and Forrester, 1995; Seedorff et al., 2005), but the restricted footprints of the alteration zones at the Cu occurrences in the GCB suggests that they are small isolated hydrothermal systems. Two occurrences (Midway and Dansey) in the northeastern part of the batholith have banded colloform chalcedony and quartz veins with abundant K-feldspar (likely adularia) and quartz-cemented hydrothermal breccias. These textural and mineralogical features are characteristic of epithermal systems and suggest a shallower emplacement depth compared to the other occurrences. The timing of mineralization at Midway and Dansey has not been constrained, but their shallower emplacement depth compared to the other Cu occurrences in the GCB may either be attributable to the northeast tilting of the batholith or to a younger emplacement age.

Mineralized structures at the various occurrences are generally northwest-trending, particularly in the northern and southern parts of the GCB, and northeast-trending, particularly in the central and eastern parts of the batholith. Arrays of two or more similarly trending Cu occurrences occur in several places across the batholith: e.g., southeast part of the GCB, east of Highmont, east of Bethlehem, southwest of Valley (Figure 3.2A). This suggests that although we interpret the Cu occurrences across the GCB to be unrelated to each other, the controls on fluid flow in these systems are likely related to batholith-scale processes.

3.6. Batholith-scale faults and palinspastic reconstruction

The batholith-scale fault network is comprised of 25 faults that have strike lengths >4km (Figure 3.2). The strike and dip of the interpreted faults were measured on the surface in 47 locations and modeled using the airborne RTP magnetic intensity data in 81 locations (Lesage et al., 2019). The GCB is bound by two sub-parallel north-northwest-trending faults that dip steeply to the east and are sub-parallel to the Fraser fault. Faults located within the batholith are dominantly north-trending and are sub-vertical to steeply-dipping either to the west or to the east (Figure 3.2C). The Lornex fault, which is north-trending and transects the batholith in its center, has the largest dextral displacement (Allen and Richardson, 1970; Hollister et al., 1975) and several other north-trending faults have accommodated lesser, but also dextral movement. Collectively, these fault movements and offset to lithological contacts accentuate the north-northwest elongation of the batholith. A secondary fault set, which includes the Highland Valley faults that down-dropped the J.A. system, is west-northwest to northwest-trending (i.e., sub-parallel to the Cherry Creek fault) and moderately to steeply-dipping to the north.

The location of the interpreted north-trending faults in the batholith locally coincides with areas of high vein intensities, and fault orientations typically mirror proximal vein orientations. This correlation relates to two different factors: pre-existing features and hydrothermal alteration. First, a weak magmatic fabric only occurs locally amongst the mainly homogeneous and isotropic GCB granitoid rocks. In such environments, brittle faults are initiated by slip on pre-existing features (e.g., joints, veins or dikes) and grow through linkage of these features (e.g., Mazurek, 2000; Pennacchioni et al., 2006; Crider, 2015). Second, the presence of abundant white mica alteration of plagioclase within the selvage of propylitic and most sodic-calcic veins may preferentially accommodate the location of post-mineralization faults due to the soft and ductile nature of phyllosilicates.

Post-mineralization dextral displacement along the batholith-scale faults has been restored to reconstruct the original geometry of the GCB and of the alteration zones, at the current erosional surface, at the time of hydrothermal activity. The palinspastic reconstruction does not, however, restore the northeast-oriented tilting of ~12–15° interpreted from the gravity and seismic models (Ager et al., 1973; Roy and Clowes, 2000) and from Al-in-hornblende barometry (D'Angelo, 2016).

3.7. District-scale aplite and porphyritic dike distribution

Aplite dike orientations were measured in 127 locations and are highly variable across the GCB (Figure 3.8A). Although aplite dikes have intruded every facies of the batholith, their main host is the Bethsaida facies, and dike occurrence density increases towards the center of the batholith (Figure 3.9). The spatial distribution of aplite trends defines a crude radial pattern that converges on an area located ~2–3 km to the southwest of Valley and a partial radial pattern that appears to converge on the Valley system (Figure 3.9B). The east to northeast-trending and sub-vertical pole cluster in Figure 3.8A likely does not represent a batholith-scale dominant orientation, but is rather due to the fact that the majority of aplite orientations presented in this study were measured along a 3–4 km transect immediately to the west and southwest of Valley. The width of aplite dikes typically ranges from 1 to 5 cm, but can be up to 25 m.

Cross-cutting relationships between aplite dikes and other features throughout the GCB are consistent with those from Valley (Osatenko and Jones, 1976) and indicate that the emplacement of aplite dikes generally pre-dates the early K-feldspar alteration at Valley–Lornex and Highmont (Figure 3.4F). Instances where thin aplite dikes locally contain a quartz vein centerline that appears to be a transitional stage between dike and vein, and complex aplite–vein cross-

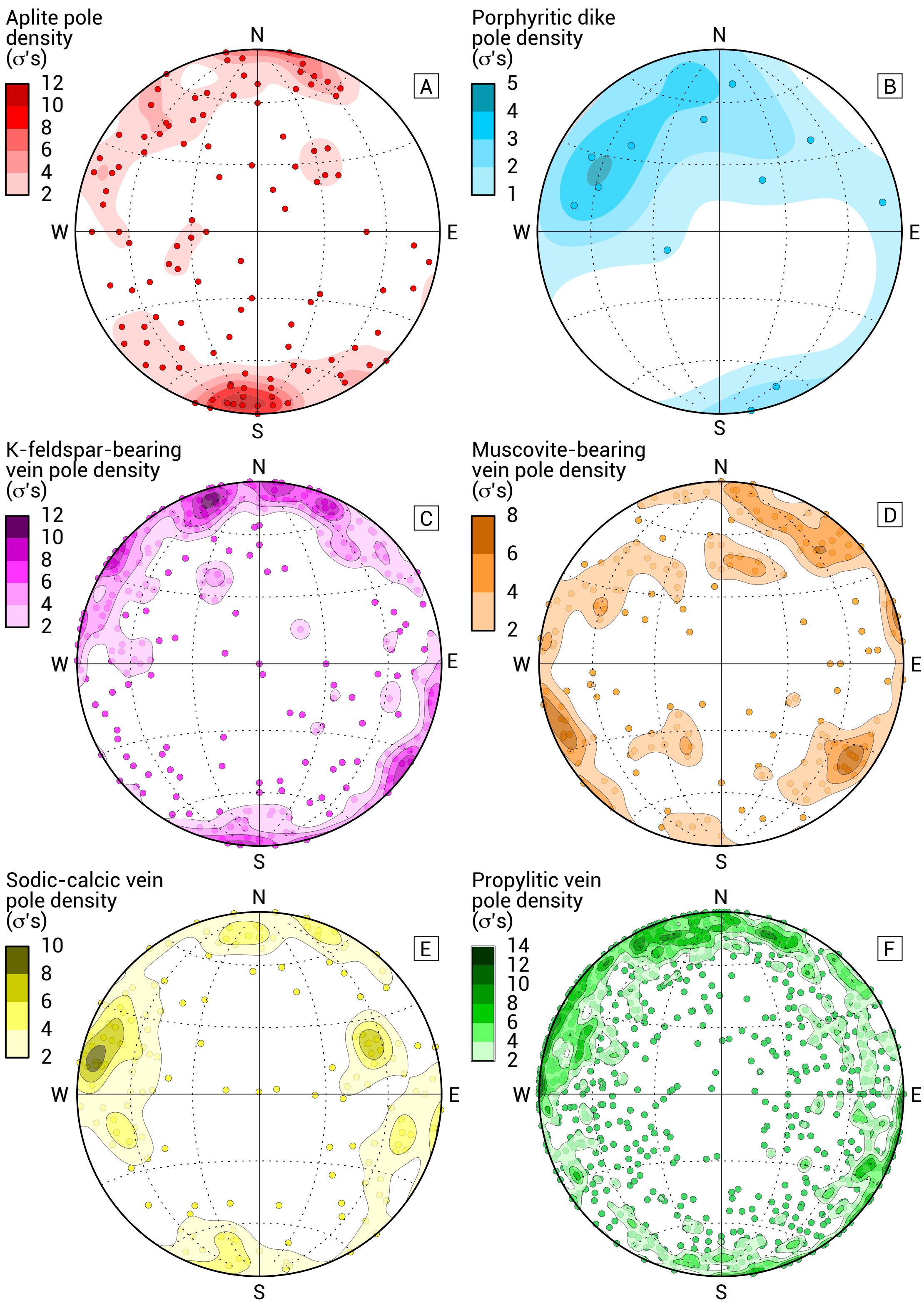

Figure 3.8. Stereonets showing the orientation of A) aplite dikes (127 poles), B) porphyritic dikes (12 poles), C) K-feldspar-bearing veins (280 poles), D) muscovite-bearing veins (194 poles), E) sodic-calcic veins (170 poles), and F) propylitic veins (1380 poles).

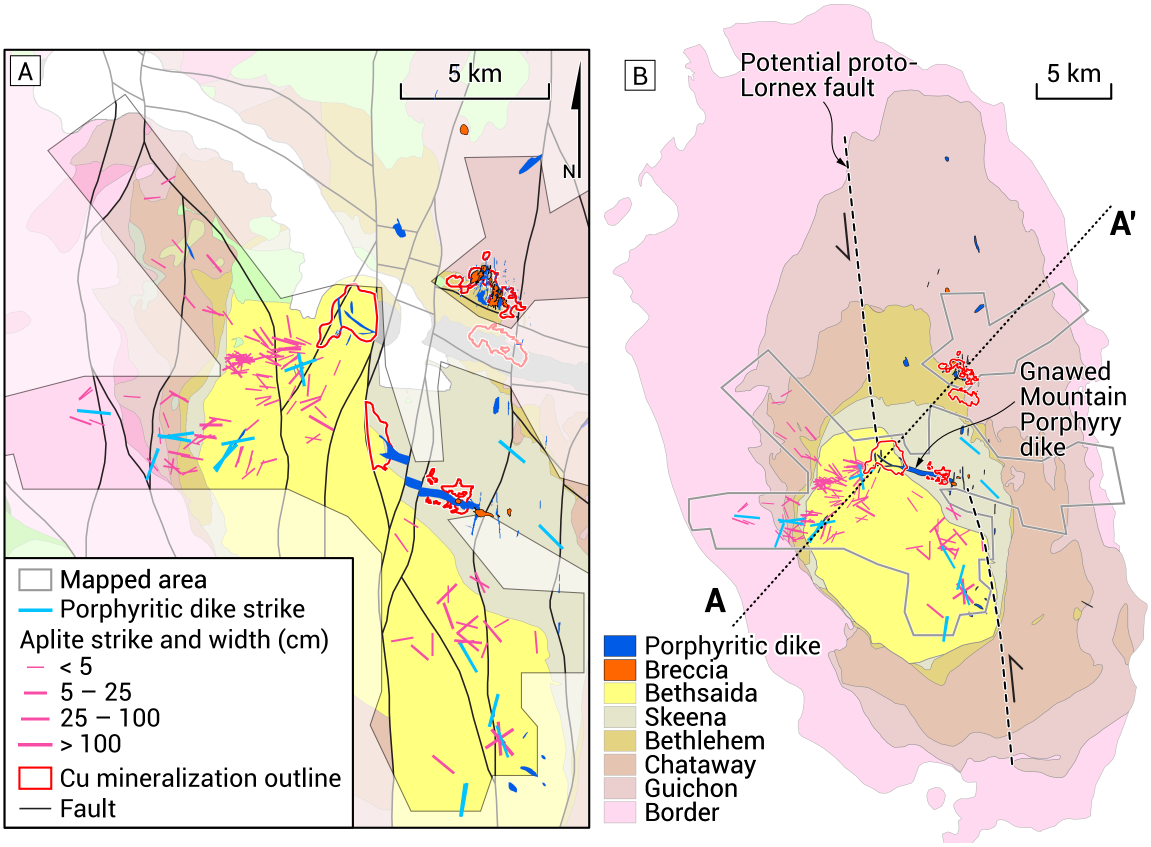

Figure 3.9. A) Map of the Guichon Creek batholith showing the location and trend of aplite and porphyritic dikes, and B) palinspastic reconstruction of the Guichon Creek batholith at ~205 Ma. The A–A' line shows the location of a schematic vertical cross-section presented in Figure 3.17.

cutting relationships in the center of the Valley deposit suggest that aplite dikes were still forming at the incipient stages of K-feldspar-bearing vein formation.

Porphyritic dikes that are mineralogically and texturally similar to syn-mineralization dikes present in the HVC porphyry systems are relatively rare across the GCB (Figure 3.9). Contrary to the typically thin width of aplite dikes, porphyritic dike width across the GCB is variable but generally >1 m, and may reach up to 60 m. Porphyritic dikes intruded in a wide range of orientations (Figure 3.8B and Figure 3.9), which suggests that a large regional horizontal differential stress was not present at the time of dike emplacement.

3.8. District-scale hydrothermal alteration

Porphyry-related hydrothermal alteration outside the HVC deposits, or "district-scale" alteration, is grouped into four categories based on vein and selvage mineralogy: K-feldspar-bearing veins; muscovite-bearing veins; sodic-calcic veins with diagnostic albite in the selvage; and propylitic veins that may contain chlorite, prehnite or epidote and have selvages of plagioclase altered to fine-grained white mica as a diagnostic feature. The HVC district-scale alteration characteristics are described below and summarized in Table 3.4, and their significance is examined in the discussion.

3.8.1. K-feldspar-bearing veins

District-scale potassic alteration is characterized by thin quartz ± chalcopyrite ± bornite ± pyrite veins or discontinuous chalcopyrite fracture coatings that have selvages of K-feldspar. Sulfide content in veins and selvages is typically <1% and decreases away from the HVC porphyry systems: chalcopyrite and pyrite are generally present within <2 km and <3 km of the deposits, respectively. Bornite is abundant in the deposits, but was only recognized in 11 veins outside the deposits and its distribution is not systematic. K-feldspar-bearing veins are sub-parallel and relatively evenly spaced at the outcrop scale. Veins are typically <0.5 cm wide, and total vein and selvage width is <2–3 cm although it locally ranges up to 6–8 cm for veins located within 2 km of the porphyry systems. Larger veins are rare and tend to occur as single veins, whereas thinner veins typically occur as clusters of sub-parallel veins. Vein intensities range from <1 cm/m to >25 cm/m, with a mean of 5 cm/m. Vein intensities are greatest along, and systematically decrease away from, an east-northeast-elongated area that

Table 3.4. Summary of district-scale alteration at HVC. Selvage width is measured on one side of veins from vein margin to edge of alteration. Upper boundary of vein width and intensity range is two standard deviations above the mean.

Characteristic mineral or assemblage	Style	Minerals	Vein width (cm)	Selvage width (cm)	Vein intensity (cm/m)	Vein orientation	District spatial distribution
K-feldspar	Proximal stockwork to distal sheeted veins; Sulfides less abundant to absent in distal veins	Vein: Qz±Ccp±Bn, Selvage: Kfs±Bt±Ccp±Bn	Range: <0.1–3.3 Mean: 0.5 Locally up to 18	Range: 0.1–2.5 Mean: 0.8 Locally up to 8	Range: <1–25 Mean: 5	Dominantly ENE-trending, subvertical to steeply-dipping; Moderately-developed radial pattern around Valley–Lornex–Highmont	Main zone E–W elongated (~12 x 2 km) and centered around Valley–Lornex and Highmont; Several small zones across the district
Muscovite	Strongly fracture-controlled alteration; Greisen-like alteration locally at district Cu occurrences	Veins: Qz±Ccp±Bn±Mol±Py±Spec Selvage: coarse Ms±Qz±Cal Destroys Mag	Range: <0.1–11 Mean: 2 Locally up to 30	Range: 0.1–7 Mean: 1.6 Locally up to 20	Range: <1–30 Mean: 5	Two orthogonal sets: Main set NW-trending and subvertical to steeply-dipping; Secondary set NE-trending, steep to moderate dip to NW	Restricted to orebodies; Largest zone is at Valley–Lornex–Highmont and is WNW-elongated (~6 x 1–2 km); Zones outside porphyry orebodies across the district are ~10s of m wide
Sodic-calcic	Pervasive higher temperature proximally; Fracture-controlled lower temperature distally; Selvages typically zoned with inner sodic-calcic and outer propylitic overprint	Pervasive: Ab±Act±Chl±Di±Grt±Tur±Ttn±Ep Vein: Chl±Ep±Act±Tur Selvage: Ab after Fsp, Chl-Ep after mafics Destroys Kfs, Mag and sulfides	Range: <0.1–1.3 Mean: 0.3 Locally up to 5	Range: 0.2–18 Mean: 4 Locally >100	Range: <1–73 Mean: 17	Dominantly N to NNE-trending, subvertical to steeply E-dipping; Variable across the district; Steep to moderate dip to the SW	Pervasive zone centered on Valley–Lornex and Highmont; Narrow NNE-elongated zones to the NE; Wider zones to the SW; Total extent ~21 km (NE-SW) x 19 km (NW-SE)
Propylitic	Fracture-controlled alteration; Occurs on its own or overprinting sodic-calcic alteration	Veins: Chl-Prh±Pmp±Ep±Cal Selvages: fine WM±Cal after Pl, Chl±Vrm±Ep after mafics Kfs stable (except where alteration is very strong), Mag slightly oxidized to Hem	Range: <0.1–2.2 Mean: 0.3 Locally up to 15	Range: 0.1–9 Mean: 2 Locally up to 50	Range: <1–33 Mean: 6	Highly variable trend with no preferred orientation; majority of veins trend from N to NE to E; dip dominantly steep to subvertical	Widespread alteration throughout the entire Guichon Creek batholith; Zone of higher vein intensity (>5 cm/m) has roughly circular shape (~10–12 km across) and is centered around the HVC porphyry systems

extends from Valley towards the southwest, which is also the area of greatest aplite dike abundance.

A total of 314 K-feldspar-bearing vein orientations and intensities were measured (Figure 3.10A): 280 poles are plotted on the stereonet in Figure 3.8C; 34 vein orientations were excluded due to poor dip confidence. The dominant vein orientation is east-northeast-trending and vertical to steeply south-dipping (Figure 3.8C), but vein orientation across the district varies considerably and forms a crude radial pattern that is centered on Valley–Lornex and Highmont (Figure 3.10B). K-feldspar-bearing vein distribution and orientations are similar to the aplite dikes within Valley (Byrne et al., 2013) and at the district scale (Figure 3.9 and Figure 3.10).

Reconstruction of the batholith geometry indicates that the largest potassic alteration zone was westerly-trending and roughly 12 x 2 km (Figure 3.10B), and was coincident with the west-northwest-trending Gnawed Mountain Porphyry dike and the Cu mineralization at Valley–Lornex and Highmont deposits. Although vein orientations are highly variable across the HVC district, the west-northwest to westerly-trending orientation of the largest potassic zone, the Gnawed Mountain Porphyry dike and the HVC deposits suggest that fractures in this orientation preferentially focused magma and hydrothermal fluid flow.

The potassic zone at Bethlehem is much smaller than at Valley–Lornex and is limited to within 1 km from the deposits. Several small K-feldspar-bearing zones (<3 km long axis) are also present in the district, typically near intrusive facies contacts, which are inferred to have acted as preferential fluid pathways. These smaller zones are characterized by low vein intensities (<1 cm/m, locally up to 2 cm/m) and typically contain no sulfide minerals or locally traces of pyrite.

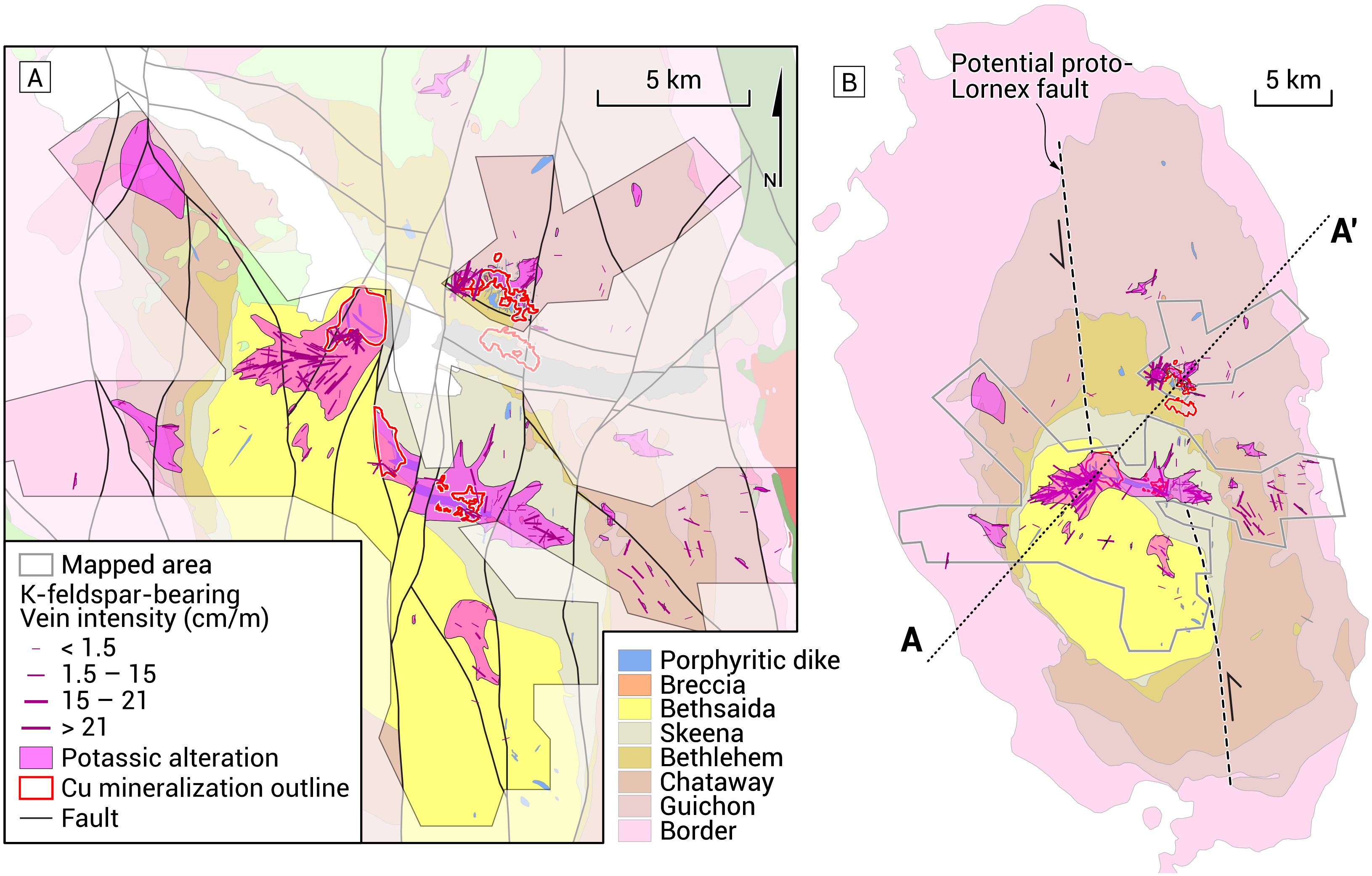

Figure 3.10. A) Map of K-feldspar alteration showing vein trend and intensity, and B) palinspastic reconstruction of the Guichon Creek batholith at ~205 Ma. The A–A' line shows the location of a schematic vertical cross-section presented in Figure 3.17.

3.8.2. Muscovite-bearing veins

Copper dominantly occurs with fine to locally medium-grained white mica alteration at Bethlehem and J.A.; coarse-grained grey white mica-bearing veins at Valley–Lornex and Highmont; and coarse-grained greenish white mica-bearing veins at the smaller Cu occurrences. For simplicity, these have been grouped and are hereafter referred to muscovite-bearing veins, without inference as to mineral chemistry (e.g., muscovitic versus paragonitic). Other minerals associated with muscovite include quartz, calcite, specular hematite, molybdenite, pyrite, and Cu-Fe-sulfide minerals such as chalcopyrite, bornite and locally chalcocite. Where present, this type of alteration is always texturally destructive. Veins are typically <10 cm-wide with an average width of ~2 cm, however some veins, particularly banded quartz–molybdenite-bearing veins, locally reach up to 30 cm. Selvage width is highly variable, with an average of <2 cm but locally up to 20 cm wide. Banded quartz–molybdenite-bearing vein selvages tend to be the widest. Vein intensity ranges between <1 and 35 cm/m within the HVC porphyry systems and within small zones located at district Cu occurrences. Elsewhere, muscovite-bearing veins are either absent of vein intensity is <1 cm/m.

Coarse-grained muscovite-bearing vein orientation and intensity were measured at 194 locations across the GCB (Figure 3.11A). Vein orientations form two main pole clusters that are northwest-trending and sub-vertical to steeply-dipping, and northeast-trending and steeply northwest-dipping (Figure 3.8E). These clusters are dominated by measurements from within the deposits, whereas the spatial distribution of vein orientations (Figure 3.11) does not indicate a preferred orientation for muscovite-bearing veins throughout GCB.

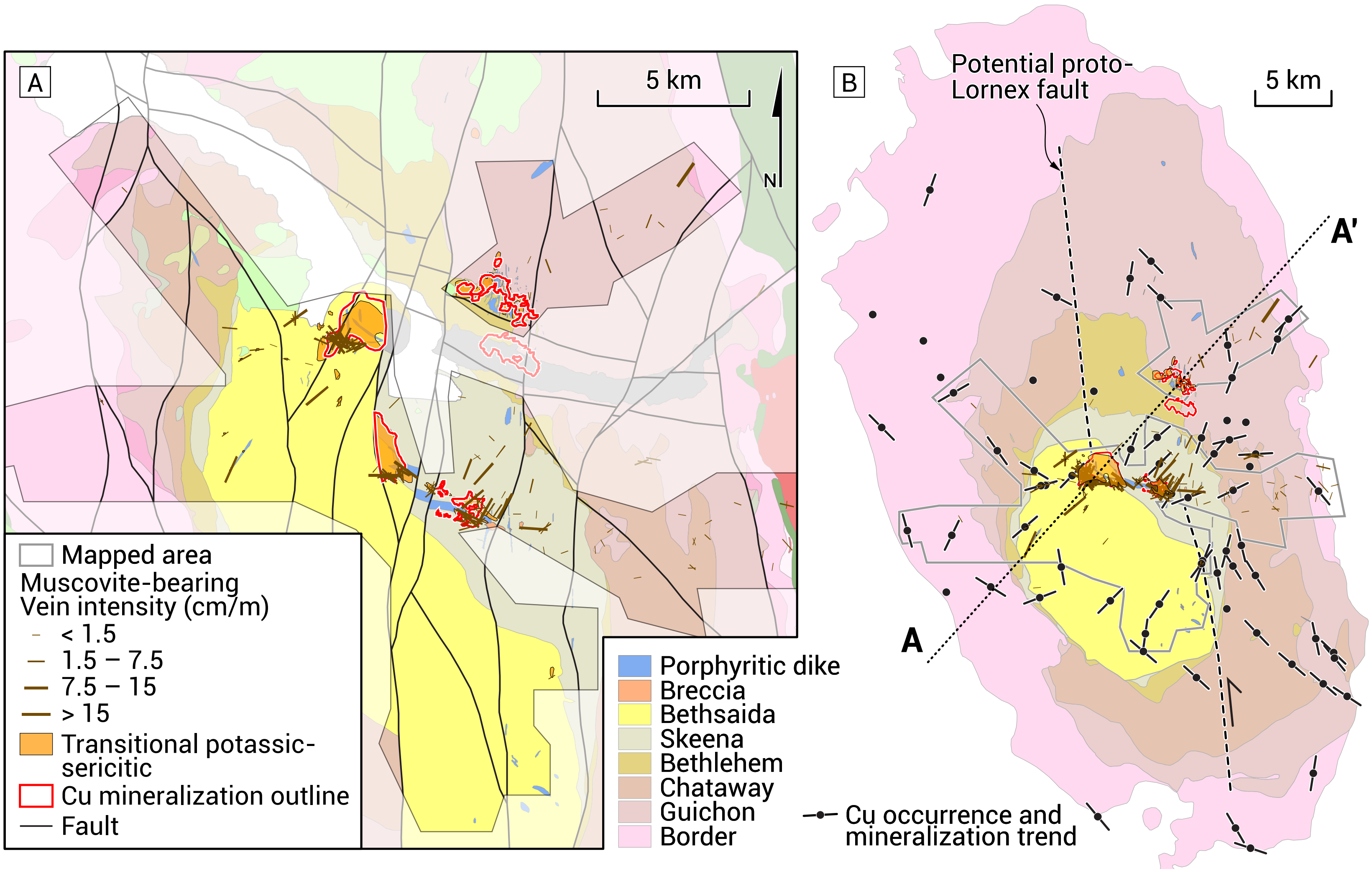

Figure 3.11. A) Map of muscovite alteration showing vein trend and intensity, and B) palinspastic reconstruction of the Guichon Creek batholith at ~205 Ma. The A–A' line shows the location of a schematic vertical cross-section presented in Figure 3.17.

Instead, most veins that are located outside the porphyry deposits broadly strike towards center of the batholith.

Coarse-grained muscovite alteration is preferentially spatially-associated with Cu mineralization, and extends up to hundreds of meters beyond the limit of the HVC deposits. In contrast, around the other district occurrences, it only forms restricted (<10s of meters) mappable zones.

3.8.3. Sodic-calcic veins

A proximal sodic-calcic assemblage generally occurs within the HVC deposits and primarily consists of albite, actinolite, chlorite and titanite. This proximal assemblage has only been observed at a few distal locations outside the deposits. Distal sodic-calcic-altered rocks typically contain chlorite ± epidote veins with selvages characterized by a K-feldspar-destructive zone of albite-altered feldspars and chlorite ± epidote-altered mafic sites. This is similar to the alteration exposed on the west side of the Lornex fault in the Lornex open pit. Sodic-calcic vein selvages commonly have an outer zone of moderate to strong fine-grained pale green white mica alteration of plagioclase and chlorite alteration of mafic sites, which is interpreted to be a lower temperature propylitic overprint. Sodic-calcic vein average width is 0.3 cm, but veins can locally be as wide as 5 cm, and K-feldspar-destructive selvage width is typically <3 cm. Vein intensity in the sodic-calcic-altered zones averages approximately 22 cm/m; however, it ranges from <1 cm/m to up to 100 cm/m in rare pervasively altered outcrops located near the porphyry deposits. The greatest vein intensities are recorded at Lornex and Highmont and in the altered zones adjacent to the deposits.

The orientation and intensity of sodic-calcic veins was measured at 170 locations (Figure 3.12A). Some alteration zones on the map in the western half of the GCB do not have orientation and intensity data because sodic-calcic minerals were only recognized in hand samples in the lab after the field work was completed. Measured vein orientations are dominantly north-northeast-trending and steeply east-dipping or sub-vertical (Figure 3.8D). This is particularly true in the northeast portion of the batholith. Throughout the district, however, the distribution of vein orientations is variable (Figure 3.12).

In the central batholith, within the Bethsaida facies to the south of Valley–Lornex and Highmont deposits, sodic-calcic alteration forms zones up to 3 km across, whereas in the northeast part of the batholith sodic-calcic alteration occurs in narrow ~0.5–1.5 km-wide north-northeast-elongated zones that are up to ~10 km-long. Elsewhere in the batholith sodic-calcic alteration is spotty and only forms relatively small zones. Apart from small isolated zones located near intrusive facies contacts, sodic-calcic alteration forms a crude inverted funnel shape that points toward the northeast and that is ~17 x 11 km at its base and <1 km-wide at its narrow end (Figure 3.12B). As indicated above, sodic-calcic alteration throughout the batholith formed from several hydrothermal fluid pulses, and the pulse that caused alteration in the Bethsaida facies may be unrelated to the pulse that caused alteration to the northeast in the Guichon facies.

3.8.4. Propylitic veins

The most extensive district-scale alteration zone at HVC is characterized by a propylitic mineral assemblage comprised of chlorite ± prehnite ± pumpellyite ± epidote veins with selvages of plagioclase that are altered to fine-grained

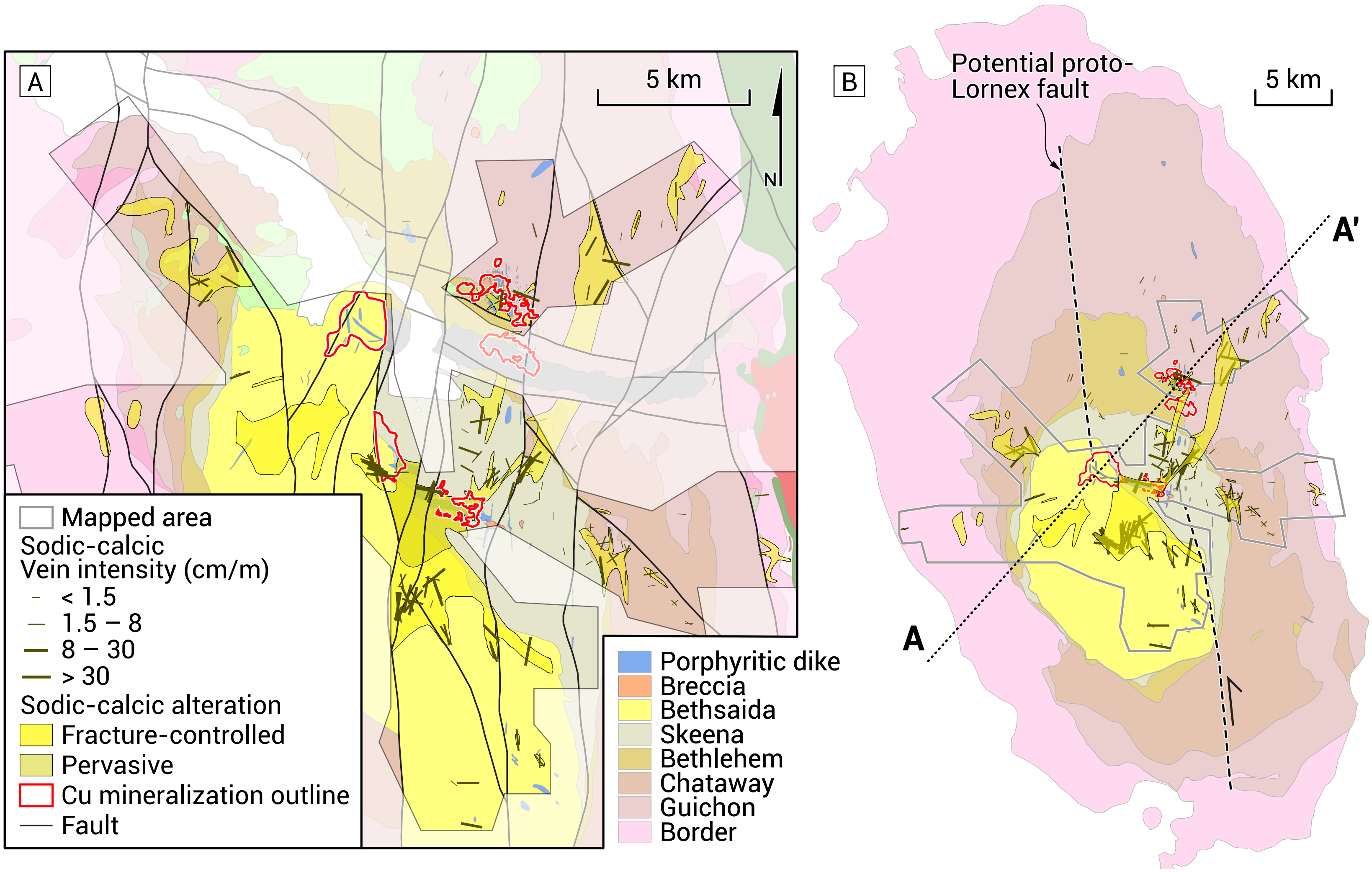

Figure 3.12. A) Map of sodic-calcic alteration showing vein trend and intensity, and B) palinspastic reconstruction of the Guichon Creek batholith at ~205 Ma. The A–A' line shows the location of a schematic vertical cross-section presented in Figure 3.17.

pale green white mica and minor calcite, and primary mafic minerals altered to a mixture of chlorite, vermiculite, or epidote (Figure 3.7). Epidote is a minor constituent of this alteration assemblage in the Bethsaida facies, but it is more abundant in the more mafic older facies of the batholith. Potassium feldspars are largely unaltered in vein selvages (Figure 3.7B), which suggests that altered rocks have only been weakly metasomatized. Magnetite is partially altered to hematite along the outer edge of the grains and along grain fractures.

Propylitic vein orientation and intensity were measured in 1380 locations across the GCB (Figure 3.13A). Vein orientation varies significantly depending on location in the batholith. Pole clusters in Figure 3.8F show that veins are dominantly north to northeast to east-southeast-trending, and sub-vertical to steeply south to southeast-dipping. Several outcrops contain two cross-cutting orientations of propylitic veins that are near orthogonal (Figure 3.14), however the orientation of the veins is not consistent from one location to another. The lack of a preferred vein orientation suggests that the district-scale fracture permeability at the time of hydrothermal activity did not form from a large regional differential stress.

Propylitic veins are widespread across the GCB. Veins are typically <0.1 to ~2 cm-wide, with an average width of ~0.3 cm, but are locally up to 15 cm. Selvage widths are typically <9 cm, average 2 cm, and are locally up to 50 cm. Average vein intensity across the batholith is 6 cm/m, but locally >35 cm/m. Figure 3.13 shows the extent of the propylitic alteration zones as defined by vein intensity >5 cm/m. The largest zone is in the central part of the batholith in the Skeena and Bethsaida facies where it forms a crude 10 km diameter circular shape that is centered on the Valley–Lornex and Highmont deposits. However, vein intensity within this zone does not systematically increase toward the porphyry

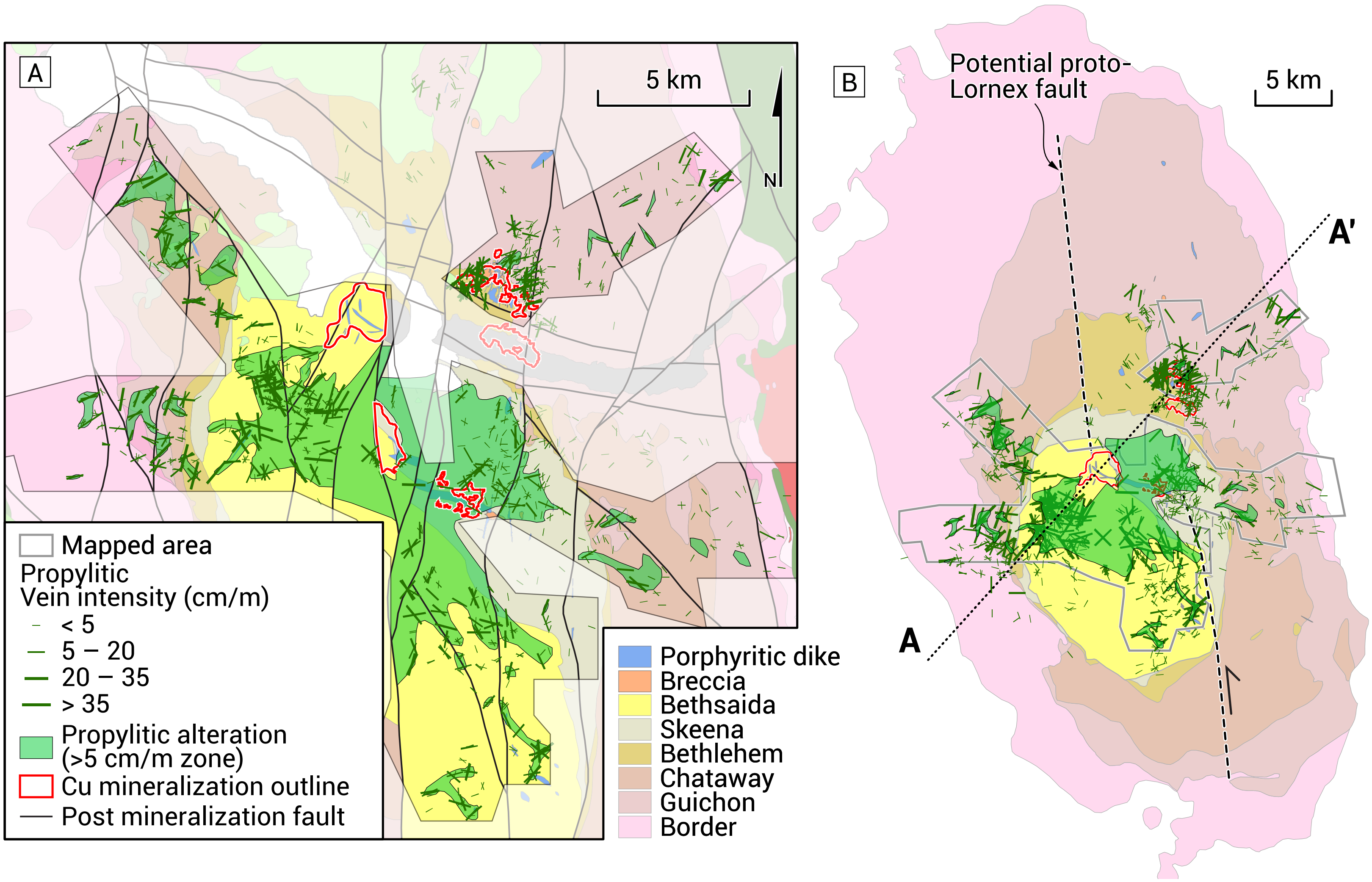

Figure 3.13. A) Map of propylitic alteration showing vein trend and intensity, and B) palinspastic reconstruction of the Guichon Creek batholith at ~205 Ma. The A–A' line shows the location of a schematic vertical cross-section presented in Figure 3.17.

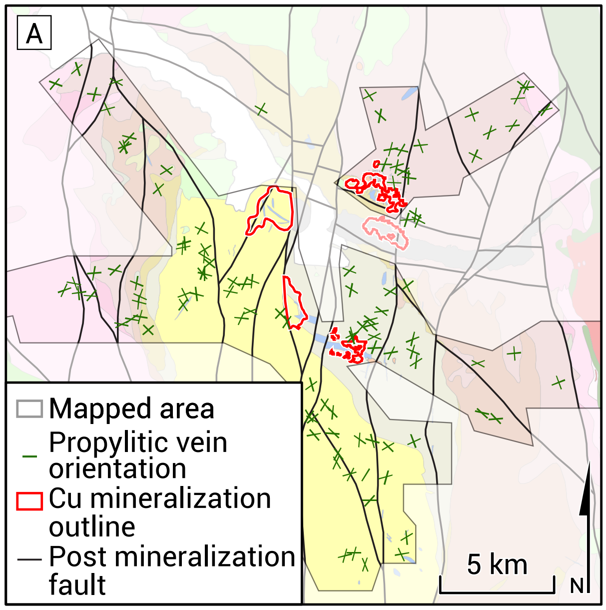

Figure 3.14. Map showing the location and trend of cross-cutting propylitic veins.

systems. Several smaller, relatively narrow zones of vein intensity >5 cm/m with a <3 km long axis are also present outside the largest propylitic zone, typically near intrusive facies contacts.

3.8.5. Vein opening

Macroscopic evidence of shearing was not observed in veins at HVC, and most veins lack offset of crystal boundaries even at the microscopic scale, which suggests that their opening mode was tensile. The generally sharp contacts between the vein-filling material and the host rocks, and the absence of stretched-crystal growth in the veins are also consistent with tensile veins. Additionally, except for the few rare veins that locally swell up to widths of more than 10 cm, the thin widths (<1 cm) of most veins indicates that only a small amount of strain was accommodated by their opening.

The total amount of pre to syn-porphyry mineralization strain accommodated by the opening of veins in the GCB was estimated by calculating the total amount of vein-filling material across the batholith. The amount of vein-filling material per meter of rock (i.e., cm/m, or %) was calculated by multiplying vein thickness by vein density per meter. The results were gridded for the north-trending veins to estimate the amount of strain accommodated along the west-southwest-oriented minor axis of the GCB (Figure 3.15A and C), and for west-trending veins to estimate the amount of strain accommodated along its north-northwest-oriented major axis (Figure 3.15B and D). K-feldspar and coarse muscovite vein-filling material is most abundant at the HVC porphyry systems (up to ~9%; Figure 3.15A and B). West-trending vein-filling material is slightly more abundant in the porphyry systems than north-trending vein-filling material. The amount of K-feldspar and coarse muscovite vein filling material outside of the porphyry systems, however, drops rapidly to <1% or zero. The zone of high vein percentage (10%) in the grid near the Bethsaida–Skeena facies contact to the southwest of the Valley porphyry system (Figure 3.15A) is caused by the presence of one anomalously veined outcrop, but is not representative of the overall area.

The spatial association between high sodic-calcic and propylitic vein percentage and the porphyry systems is not as strong as for the K-feldspar and muscovite-bearing veins (Figure 3.15C and D). Sodic-calcic and propylitic vein percentage is in general more abundant (up to ~8%) in and adjacent to the porphyry systems, as well as near the GCB intrusive contacts, which likely acted as preferential pathways that focused the flow of hydrothermal fluids. The total amount of sodic-calcic and propylitic vein-filling material across the GCB was estimated by multiplying the middle value of each grid bin by its total length in meters along the dashed lines in Figure 3.15. We estimate that the approximate amount of sodic-calcic and propylitic vein-filling material deposited along the GCB minor and major axes is respectively 420 m over a distance of ~25 km

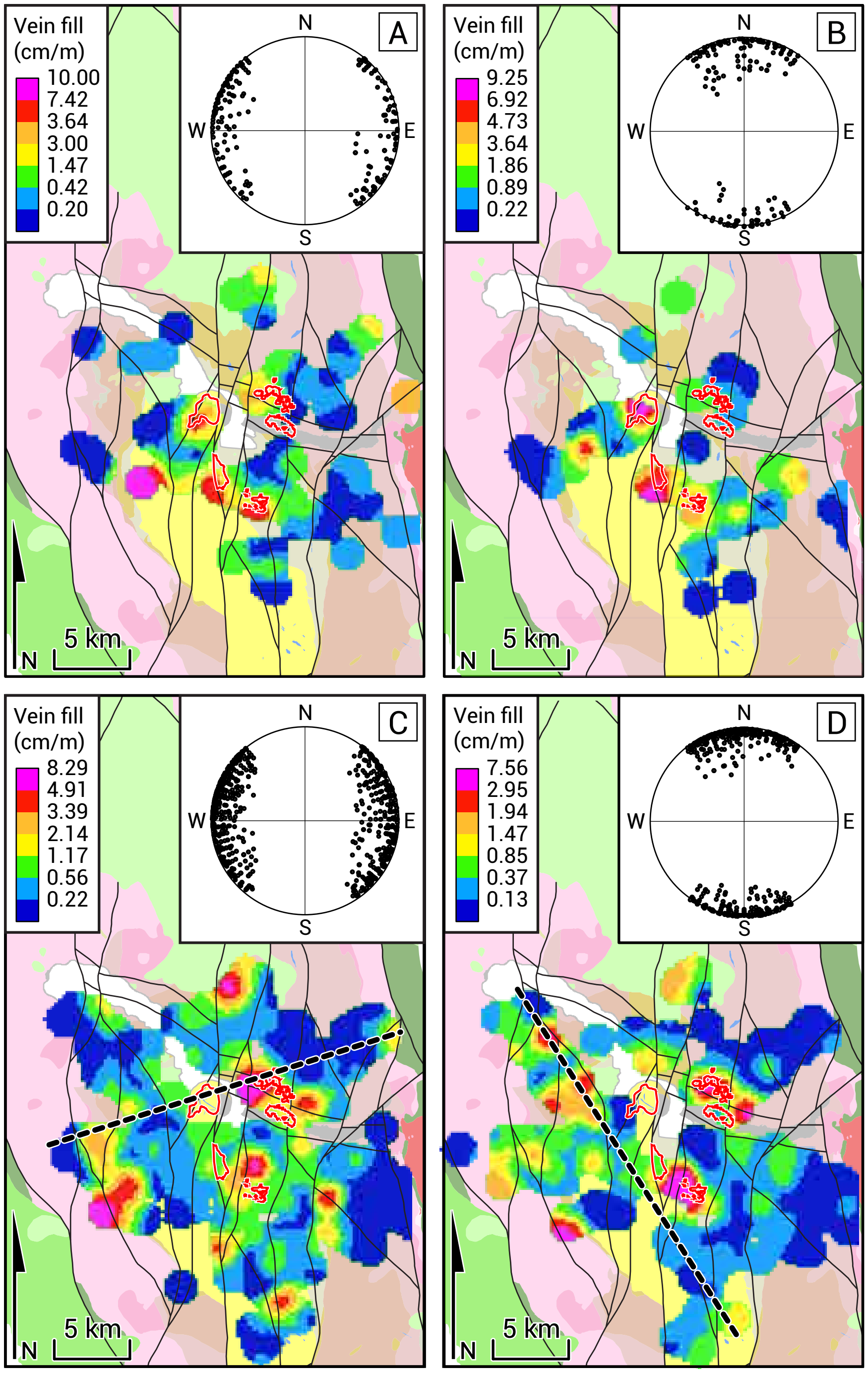

Figure 3.15. Map showing the amount of vein-filling material per meter of rock (cm/m) across the Guichon Creek batholith for A) north-trending K-feldspar and muscovite-bearing veins (241 poles), B) west-trending K-feldspar and muscovite-bearing veins (203 poles), C) north-trending sodic-calcic and propylitic veins (908 poles), and D) west-trending sodic-calcic and propylitic veins (566 poles). The total amount of sodic-calcic and propylitic vein-filling material perpendicular to the GCB axes is estimated along the dashed lines in C) at ~420 m over a distance of ~25 km (1.7%) along the minor axis, and in D) at ~265 m over a distance of ~27 km (1.0%) along the major axis.

(1.7%) for north-trending veins, and 265 m over a distance of ~27 km (1.0%) for west-trending veins.

3.9. Discussion

3.9.1. HVC district paragenesis and fluid evolution

Granodiorite porphyritic dikes generally intrude at approximately 700°C (e.g., Burnham, 1979; Dilles, 1987; Dilles et al., 2015; Lee et al., 2017). Magmatic fluids that are responsible for porphyry mineralization exsolve from porphyritic magmas in the 700–675°C range (e.g., Dilles, 1987; Mercer and Reed, 2013; Dilles et al., 2015), and mineralization is deposited at temperatures <500°C because of the decreasing copper solubility in hydrothermal fluids (e.g., Hemley et al., 1992; Hack and Mavrogenes, 2006).

Based on the various minerals present in each hydrothermal alteration assemblage, a hydrothermal fluid source and alteration temperature ranges can be assessed. Previous work at other porphyry systems indicates that K-feldspar and slightly cooler muscovite-bearing veins form from magmatic fluids at temperatures in the 700–360°C range (e.g., Brimhall, 1977; Seedorff et al., 2005; Rusk et al., 2008; Proffett, 2009), whereas sodic-calcic alteration forms from hypersaline sedimentary brines at temperatures up to 450°C (e.g., Dilles and Einaudi, 1992; Dilles et al., 1992; Dilles et al., 2000). Propylitic alteration forms at temperatures <300°C from fluids that are dominantly external (i.e., meteoric fluids or sedimentary brines) but may include a fraction of cooled magmatic fluids (e.g., Sheppard et al., 1969; Sheppard and Taylor, 1974; Zhang, 2000; Seedorff et al., 2005; Dilles et al., 2009).

Cross-cutting relationships and dating of magmatic zircons from the various facies of the GCB and molybdenite from Valley, Lornex and Highmont indicate that the HVC porphyry systems are intimately associated with the intrusion of porphyritic dikes. Furthermore, the deposits formed in two main episodes (i.e., Bethlehem–J.A. and Valley–Lornex–Highmont) over a period of ~2 m.y. that started roughly 2 m.y. after the onset of magmatism in the GCB (Figure 3.16) (Ash et al., 2006; Byrne et al., 2013; D'Angelo et al., 2017).

Individual pulses of hydrothermal fluids in other porphyry systems have been shown to persist for much shorter periods (<100 k.y.; e.g., Garwin, 2002; von Quadt et al., 2011; Spencer et al., 2015; Li et al., 2017). Therefore, the HVC

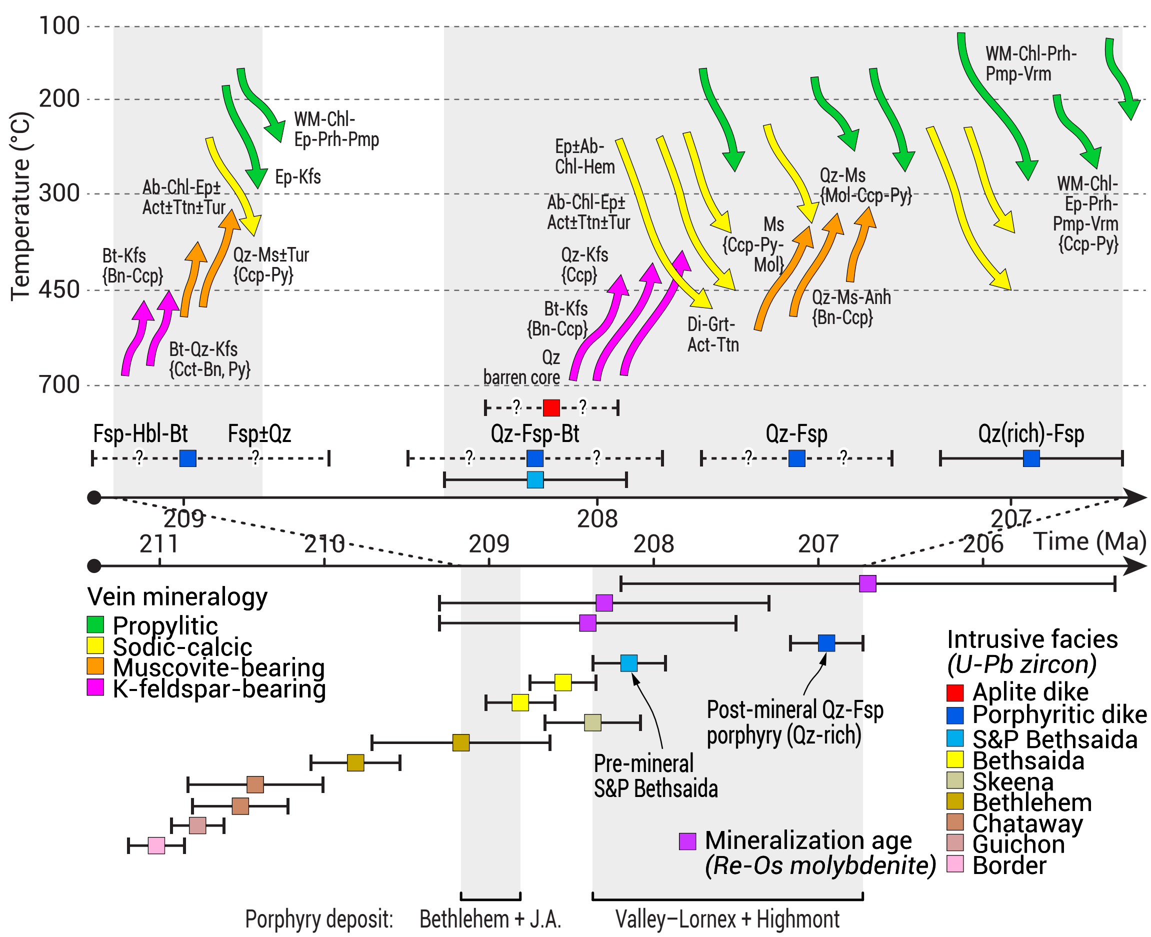

Figure 3.16. Timeline of intrusive rock emplacement (data from Ash et al., 2006; D'Angelo et al., 2017), and schematic hydrothermal fluid evolution showing the alteration paragenesis (modified from Byrne et al., 2017).

porphyry systems likely formed through multiple hydrothermal episodes, and in detail the paragenetic sequence is likely more complex than what is shown in Figure 3.16. More detailed alteration mapping could potentially resolve the distribution and timing of the different hydrothermal episodes.

The overprinting relationships between early potassic and later sodic-calcic alteration at HVC are consistent with similar observations from the Yerington district where porphyritic dikes intruded, were potassically altered, and then subsequently underwent sodic-calcic alteration (Carten, 1986; Dilles and Einaudi, 1992; Dilles et al., 1992; Dilles et al., 2000). The sequence of alternating K-feldspar–sodic-calcic–muscovite–sodic-calcic alteration present at Valley–Lornex and Highmont is consistent with the episodic nature of porphyry systems predicted by numerical models of fluid flow and rock permeability (e.g., Weis, 2014, 2015). Cross-cutting relationships indicate that sodic-calcic alteration at Bethlehem is likely older than that at Valley–Lornex and Highmont and was formed shortly after the Bethlehem deposits were formed at ~209 Ma. Episodic sodic-calcic alteration at Valley–Lornex and Highmont formed over period of at least ~1.5 m.y., as indicated by the presence of sodic-calcic alteration prior to muscovite alteration and Cu mineralization dated at 208.4 ± 0.9 Ma and within post-mineralization porphyritic dikes dated at 206.95 ± 0.22 Ma (D'Angelo et al., 2017).

From a district-scale perspective, the current understanding of the HVC porphyry system's paragenetic sequence is as follows:

1) The Border, Guichon, Chataway and Bethlehem facies of the GCB intruded the Nicola group prior to 209 Ma.

2) Intrusion of porphyritic dikes, formation of breccia bodies and deposition of Cu mineralization occurred at Bethlehem and J.A. at ~209 Ma. Hot magmatic fluids caused K-feldspar and muscovite alteration within 1 km of the deposits, and advecting heated external fluids caused sodic-calcic and propylitic alteration.

3) The Skeena, Bethsaida and "Salt and Pepper" Bethsaida facies of the GCB were emplaced between 209 and 208 Ma.

4) Intrusion of aplite dikes occurred throughout the district, but mainly in the Bethsaida facies, and porphyritic dike intrusion started at Valley–Lornex and Highmont.

5) Magmatic fluids caused the formation of the barren core of intense quartz stockwork and associated K-feldspar alteration at Valley–Lornex, and of the extensive zone of district-scale K-feldspar-bearing veins in the Bethsaida and Skeena facies. Deposition of Cu and Mo mineralization started at Valley–Lornex and Highmont at ~208 Ma.

6) As the magmatic fluid pressure waned, external fluids, including marine brines, were entrained into the hydrothermal system and heated to cause district-scale sodic-calcic alteration. Higher-temperature proximal pervasive alteration occurred at Lornex and Highmont and lower-temperature fracture-controlled alteration occurred distally.

7) Intrusion of porphyritic dikes continued at Valley–Lornex and Highmont. Breccias formed in the Highmont area. A new pulse of magmatic fluids related to main-stage Cu and Mo mineralization formed high-temperature, texturally-destructive coarse-grained

muscovite alteration at Valley–Lornex and Highmont. District-scale sodic-calcic alteration was likely ongoing.

8) Post-mineralization quartz-rich porphyritic dikes intruded at ~207 Ma and renewed sodic-calcic alteration took place at Lornex and Highmont.

9) Advection of heated external fluids caused district-scale low-temperature propylitic alteration as the magmatic-hydrothermal system waned. Temperatures returned to a range characteristic of a geothermal gradient that was slightly elevated following the intrusion of a large batholith (e.g., <200 °C at a depth of ~5 km). According to numerical modeling, a point at 5 km depth in an intrusion such as the GCB emplaced at ~800 °C may take up to 4 m.y. to cool to 200 °C by conduction alone, but will cool within <100 k.y. by convection if rock permeability is high (i.e., >1 md; Cathles, 1977; Cathles, 1981).

10) Dextral displacement along post-mineralization faults cut and displaced the GCB, the HVC deposits and the district-scale hydrothermal alteration zones.

3.9.2. Spatial distribution of porphyry-related alteration and mineralization

Lateral flow of magmatic fluids at typical depths of porphyry formation (<4–6 km; e.g., Seedorff et al., 2005) is minimal due to the high buoyancy of the hot fluids, which causes them to flow vertically (e.g., Weis et al., 2012; Weis, 2014, 2015). Where these fluids are trapped at the top of the magma chamber, increasing pressure from accumulating fluids leads to rock hydrofracturing, upward release of the fluids and intense vein formation (Burnham and Ohmoto, 1980). The small distal potassic alteration zones across the GCB are therefore interpreted to be unrelated to the large potassic zone at Valley–Lornex and Highmont, and are instead thought to be associated with separate, smaller hydrothermal systems of unknown age and mineralization potential.

The spatial correlation between aplite dikes and K-feldspar-bearing veins, and the large size of the potassic alteration zone at Valley–Lornex and Highmont (12 x 2 km) suggests that there is another significant intrusive facies at depth from which aplitic magmas and magmatic fluids were derived. We interpret this facies to be related to the “Salt and Pepper” Bethsaida facies, which does not crop out in the district but is exposed in the Valley open pit. The high vein intensity in the barren quartz vein stockwork at Valley–Lornex indicates high fluid pressures and intense fluid flow, which suggests that the apical part, or cupola, of the “Salt and Pepper” Bethsaida facies is located below this porphyry system.

A schematic northeast-oriented vertical cross-section is drawn along line A–A′ in Figure 3.9 to Figure 3.13 to illustrate the current level exposed at the surface (line A–A′ in Figure 3.17). The cross-section reflects the fact that batholiths emplaced in the upper crust generally have flat tops and bottoms, and tend to be much larger laterally than vertically (Hamilton and Myers, 1967; Dilles, 1987; McCaffrey and Petford, 1997). The depth scale in Figure 3.17 is based on hornblende crystallization depth estimates from four samples that are located near the A–A′ line (D’Angelo, 2016). These data suggest that Valley–Lornex formed primarily in the Bethsaida facies at a depth of ~5 km and that Highmont formed slightly higher in the overlying Skeena facies, whereas Bethlehem and J.A. formed the shallowest at depths of 3–4 km.

The presence of wider zones of sodic-calcic alteration to the southwest is consistent with a northeast-oriented tilting of the GCB, because it suggest a deeper level of erosion than to the northeast where alteration zones are narrow

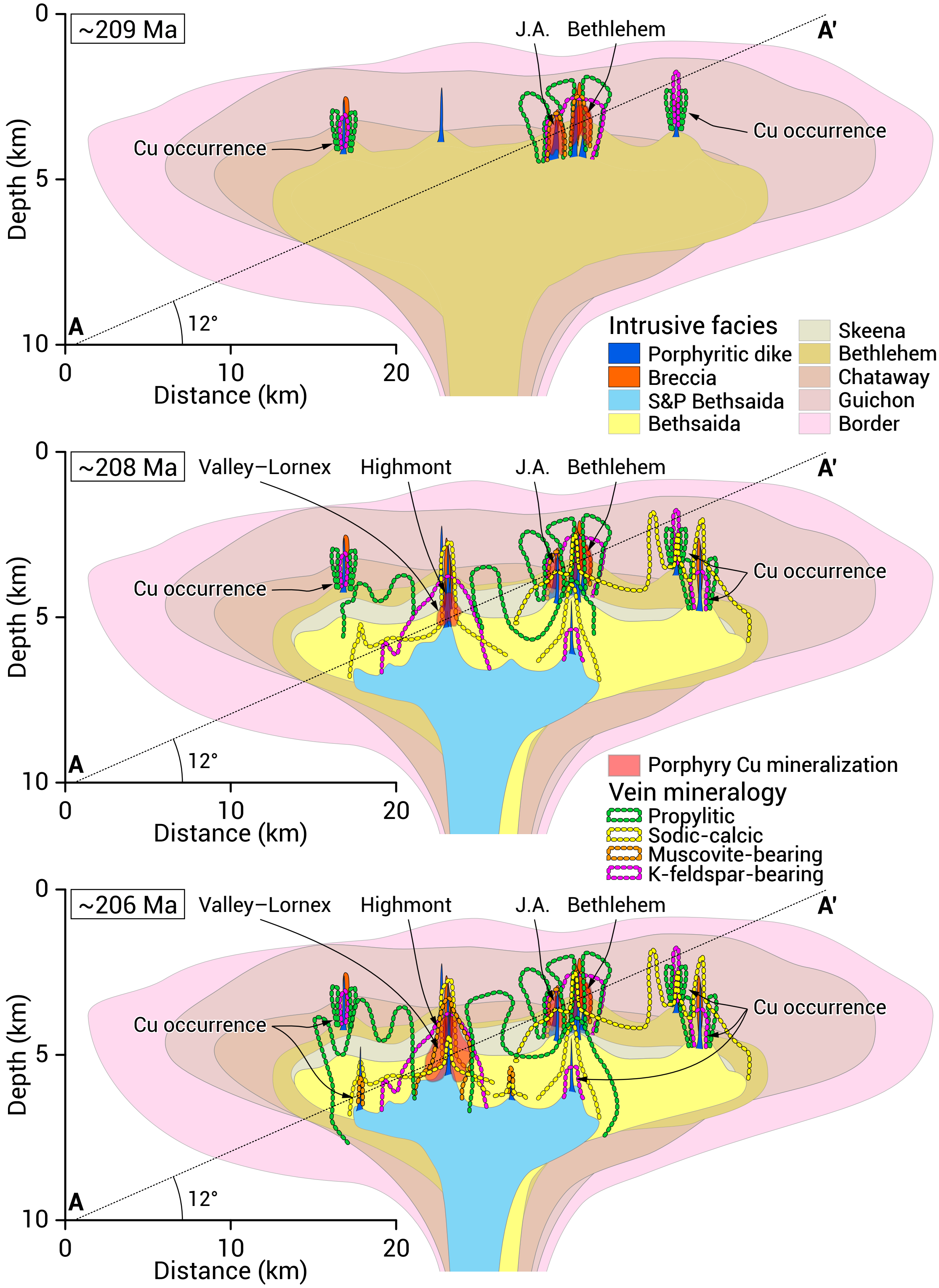

Figure 3.17. Schematic northeast-oriented cross-section of the Guichon Creek batholith at three stages of the formation of the HVC porphyry systems, but prior to tilting and post-mineralization dextral dismemberment of the batholith. The depth scale is set at 2x vertical exaggeration for visual purposes. The A–A′ line is the present day surface exposure.

and appear more structurally-controlled (Carten, 1986; Dilles et al., 2000; Seedorff et al., 2008; Halley et al., 2015).

The abundance of tourmaline-cemented breccia bodies in the HVC district, which increases from Valley–Lornex, where they are absent, to Highmont and then Bethlehem, where they are most abundant (Figure 3.9) is also consistent with the northeast-oriented tilting of the GCB. As argued by Zweng and Clark (1995) based on fluid inclusion data, porphyry systems that contain abundant tourmaline-cemented breccias formed at shallower depths (<3 km) than porphyry systems where breccias are rare. Magmatic fluids exsolved at shallow depths undergo phase separation into vapour and brine (Burnham and Ohmoto, 1980; Burnham, 1985; Fournier, 1999), which causes a significant volume increase and leads to the formation of intense hydrofracturing and abundant breccias. The strong hydrofracturing and brecciation at shallower depth likely lead to a rapid change from lithostatic to near-hydrostatic pressures, a decompression that accelerates the fluid phase separation and rock hydrofracturing. On the other hand, fluids exsolved at depth >5 km (i.e., >140 MPa) tend to stay in the single-phase domain (e.g., Rusk et al., 2008), which leads to far less volume increase and is sufficient to cause rock hydrofracturing and generate permeability, but not to form significant breccia bodies.

A shallower emplacement depth for the Bethlehem porphyry system compared to the Valley–Lornex system may explain its smaller potassic alteration zone (<1 km from the deposits). At shallower depth, the stronger hydrofracturing and brecciation likely enhanced the vertical flow of the high buoyancy fluid, and in turn caused the alteration zone to be less laterally extensive. Alternatively, the smaller potassic zone at Bethlehem may be due to its older age. Because of the earlier timing of the Bethlehem system, the magma chamber at depth had less time to undergo melting–assimilation–storage–homogenization (MASH) processes (Hildreth and Moorbath, 1988). Evolution in the MASH zone increases the oxidized sulfur, metal and water content of magmas (e.g., Richards, 2003, and references therein). The magmas that caused the formation of the Bethlehem porphyry system therefore may have contained less magmatic water than those that formed the Valley–Lornex system, which in turn lead to the smaller potassic alteration zone.

The abundant propylitic alteration at HVC, particularly in the Skeena and Bethsaida facies, may be attributed to two different factors. Firstly, the large size of the older facies of the batholith and the long period of active magmatism, which lasted for >3 m.y., likely contributed to thermal isolation of the batholith center and elevated the ambient temperature enough to cause widespread propylitic alteration. Secondly, large intrusive bodies are typically overlain by polygenic volcanoes (Takada, 1994), and the presence of a large fluid-saturated volcano above the GCB may have contributed to the broad extent of propylitic alteration at HVC, as shown by the numerical model of Weis (2015). The convection of heated external fluids would have been affected by the downward and outward pressure exerted by the down-flowing cold fluids from a topographic high, which would result in steeper alteration fronts above the porphyry systems and wider alteration zones at depth because of the enhanced lateral fluid flow.

The slight bottleneck shape of the propylitic alteration zone (Figure 3.13B), which is coincident with the Skeena–Bethsaida contact and with the location of the Valley–Lornex and Highmont porphyry systems, may be related to two causes. Firstly, a drop in fracture frequency between the Skeena and Bethsaida facies may have led to a more focused fluid flow at the facies contact in the area where abundant porphyritic dike intrusions (i.e., Gnawed Mountain Porphyry dike) and breccia formation had increased permeability. Second, retrograde quartz solubility in external fluids heated above ~370°C under hydrostatic pressure conditions (Fournier, 1999) may have inhibited the flow of external fluids within the porphyry systems by depositing quartz, effectively sealing fractures and reducing permeability.

Many studies have shown that propylitic veins can develop in intrusions that lack porphyry mineralization (e.g., Gerla, 1988; Bergbauer and Martel, 1999). At HVC, propylitic alteration is present throughout the GCB, and vein intensity does not define a clear gradient toward the porphyry systems. Further work on the whole rock lithogeochemistry, spectral characteristics (cf., Greenlaw, 2014; Halley et al., 2015) and/or mineral chemistry (cf., epidote, Cooke et al., 2014; chorite, Wilkinson et al., 2015) of propylitically altered rocks at HVC is required to determine whether the propylitic veins formed from cooling of the GCB or as part of the HVC porphyry systems. If the latter is the cause then the propylitic assemblage may be helpful in the identification of higher prospectivity zones.

3.9.3. Controls on paleopermeability

Intrusive rocks typically have very low primary porosity and intergranular permeability. Hydrothermal fluid flow in and through these rocks is therefore most effectively focused along zones of fracture permeability, which is typically high in the shallow part of the brittle crust (Ingebritsen and Manning, 2010; Ingebritsen, 2012; Weis et al., 2012). In the plutonic and porphyry-forming environment, permeability is the result of fractures generated during the interplay between regional tectonic stresses (e.g., Tosdal and Richards, 2001; Houston and Dilles, 2013) and local stresses induced by magma and fluid overpressure (e.g., Burnham and Ohmoto, 1980; Burnham, 1985; Fournier, 1999; Tosdal and Richards, 2001; Ingebritsen, 2012), or by thermal contraction during the crystallization and cooling of the magma chamber (e.g., Gerla, 1988; Bergbauer and Martel, 1999) (Figure 3.18). Fractures caused by lateral expansion during rapid uplift may also strongly influence permeability in some porphyry systems that exhibit evidence of telescoping (e.g., Collahuasi; Masterman et al., 2005), but the absence of such evidence at HVC suggests that rapid uplift did not occur at the time of porphyry mineralization.

3.9.3.1. Regional stresses

Regional tectonic stresses and crustal-scale fault systems play an important role in controlling intrusion shapes and sizes, and focusing the location of magmatism (e.g., Hutton, 1988; Petford and Atherton, 1992; Richards, 2001). In arc settings, intrusions and porphyry systems form arc-parallel linear arrays, such as the Late Triassic magmatic and porphyry system belts of the Quesnel

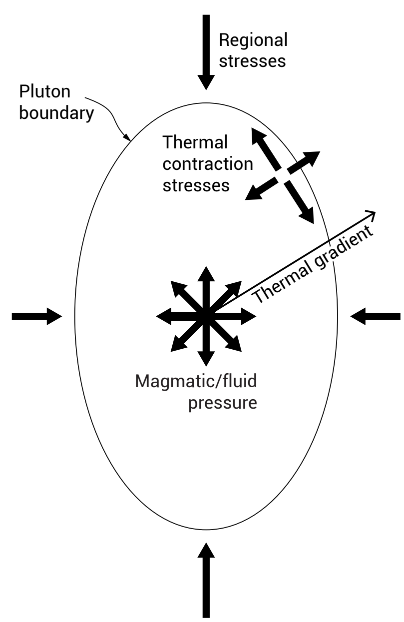

Figure 3.18. Schematic plan view of a slightly elongated intrusive body showing the various stresses that can influence fracture permeability (modified from Gerla, 1988).

and Stikine terranes (Logan and Mihalynuk, 2014; Schiarizza, 2014). The GCB likely intruded along a proto-Lornex fault that was part of a major arc-parallel fault system, along which other Late Triassic intrusions such as the Granite Mountain batholith (Schiarizza, 2014, 2015) were emplaced (Figure 3.1).

Granitoid magmas ascend through the crust as dikes or by other mechanisms such as stoping, doming or diapirism (Hutton, 1997, and references therein), but require development of a significant amount of space to form large intrusions. Crustal-scale fault systems act as preferential pathways for these magmas, regardless of the regional tectonic regime (i.e., compressional, extensional, strike-slip), because of the high fracture permeability in fault damage zones (e.g., Wallace and Morris, 1979; Cox and Scholz, 1988) and of the space created in local tensional or dilational sites such as jogs or step-overs (Hutton, 1988, 1997). We interpret the rectilinear character and north-northwest orientation of the ~5 km-long Chataway–Bethlehem contact north of the Valley–Lornex porphyry system, and of the ~7 km-long Skeena–Bethsaida contact south-southeast of Highmont to be the result of magma intrusion along strands of the proto-Lornex fault (Figure 3.9B). The southern extension of the northern proto-Lornex fault strands coincides with the location of the Valley–Lornex system, whereas the southern proto-Lornex fault strands extend to the north to a location within 1–2 km east of the Highmont system. In both cases, the proto-Lornex fault orientation matches that of several north to north-northwest-trending porphyritic dikes located on either sides of the west-northwest-trending Gnawed Mountain Porphyry dike (Figure 3.9B). We interpret the Gnawed Mountain Porphyry dike, the largest porphyritic dike complex in the GCB, to have intruded between the two proto-Lornex fault strands in a west-northwest-trending extensional linking structure that accommodated limited sinistral displacement (<500 m). The size and shape of the GCB batholith indicate however that although the regional stress regime was sinistral transpression (Nelson and Colpron, 2007), the differential stress was likely minimal at the time of its emplacement.

Environments with large regional differential stresses yield intrusions with long axes at high angles to the orientation of the minimum regional compressive stress, whereas intrusions emplaced during periods of negligible regional differential stress tend to be circular (e.g., Arndt et al., 1997; Tosdal and Richards, 2001). The reconstructed GCB has a slightly north-northwest-elongated shape (Figure 3.9B), but its nearly circular shape suggests that the regional differential stress was low. The slight elongation of the batholith may in part reflect the orientation of the regional compressive stresses at the time of emplacement and in part result from post-emplacement tilting, because northeast tilting of a relatively flat-topped circular body would result in a northwest-elongated ellipse at the erosional surface in plan view.

Takada (1994) proposed that an intrusion size is influenced by the regional stresses: a large regional differential stress inhibits the coalescence of magma-filled fractures, leading to the formation of several monogenic volcanoes with small underlying plutons, whereas a low regional differential stress promotes the formation of polygenic volcanoes with large plutonic roots. The large size of the GCB therefore suggest that although crustal-scale structures likely influenced the location of the batholith (i.e., the proto-Lornex fault), it was likely emplaced under low regional differential stress conditions. The fact that other Late Triassic (e.g., ~10 x 20 km Granite Mountain batholith) to Early Jurassic intrusive bodies (e.g., ~40 x 50 km Takomkane, ~30 x 60 km Thuya and ~30 x 55 km Pennask batholiths) in the Quesnel terrane (Figure 3.1) are also very large and have erratically orientated major axis is consistent with this interpretation.

A large regional differential stress typically controls the orientation of fracture permeability, and causes veins in hydrothermal systems to form along a preferred orientation (e.g., Chuquicamata, Lindsay et al., 1995; Cadia East, Wilson et al., 2007). Several past studies of hydrothermal systems emplaced at deep levels in the crust (i.e., >5 km) such as porphyry systems (e.g., Heidrick and Titley, 1982; Titley et al., 1986; Tosdal and Richards, 2001; Houston and Dilles, 2013) or reduced intrusion-related gold systems (e.g., Hart, 2007) have shown that dike and vein orientations tend to form simple patterns with a dominant orientation. It is not the case at HVC, where the wide range of porphyritic dike and hydrothermal vein orientations throughout the district (Figure 3.8) is consistent with a low differential stress in the GCB, under which conditions the orientation of the minimum compressive stress was not fixed (e.g., Tosdal and Richards, 2001). The location of the HVC porphyry systems in the center of the GCB, a large relatively homogeneous granitoid body, and the interpreted presence of a large partially molten viscous intrusive facies at depth under the porphyry systems (i.e., the “Salt and Pepper” Bethsaida facies; Figure 3.17), likely shielded them from the regional stresses by providing a large isotropic carapace around the porphyry systems and accommodating strain at depth in a ductile rather than brittle manner.

However, although there is not a unique vein or dike orientation at HVC, the dominant aplite dike and K-feldspar-bearing vein orientation (Figure 3.8) is west to west-northwest-trending, similar to the elongation of the deposits at all the HVC porphyry systems. Figure 3.15 also shows that vein-filling material is slightly more abundant in west-trending veins compared to north-trending veins, particularly between Valley–Lornex and Highmont. Preferential extension along west to west-northwest-trending fractures is consistent with our interpretation that the Gnawed Mountain Porphyry dike complex intruded into an extensional linking structure between two north-northwest-trending proto-Lornex fault strands. This interpretation would also explain the location of the Valley–Lornex and Highmont porphyry systems, situated at the western and eastern ends, respectively, of the extensional linking structure (Figure 3.9B).

3.9.3.2. Magma and fluid overpressure

Magma and fluid overpressure is an important mechanism that generates fracture permeability in porphyry systems (e.g., Burnham, 1979; Fournier, 1999; Tosdal and Richards, 2001). In cupolas at the top of a magma chamber, the high strain rate induced by buoyantly rising volatile-rich magmas and exsolved fluids causes rocks that may otherwise deform plastically to fail in a brittle way. The increasing pressure of fluids that are exsolved as magma crystallizes lowers the effective stress required to cause tensile fractures in rocks. Rock hydrofracturing is triggered once the fluid pressure exceeds the combined minimum compressive stress and tensile strength of the rock. The upward and outward pressure applied to the chamber roof leads to a characteristic radial and concentric vertical fracture pattern that may be subsequently filled by magma, breccia or vein material (e.g., El Salvador, Cornejo et al., 1997; Bajo de la Alumbrera, Proffett, 2003; Ridgeway, Garcia-Cuison, 2010).

A crude radial pattern defined by aplite dikes that converges on an area near the southwest margin of Valley–Lornex is interpreted to have formed because of magma overpressure (Figure 3.9B). Additionally, Cathles and Shannon (2007) proposed that zones of early barren quartz stockwork veins associated with potassic alteration, similar to the barren zone at Valley–Lornex, are formed by the nearly explosive expulsion of vast quantities of magmatic fluids at high temperature (≥600 °C) prior to the deposition of Cu mineralization in porphyry systems. In the HVC district, explosive expulsion of magmatic fluids led to the formation of the large radial patterns of fractures filled with K-feldspar-bearing veins that surround Valley–Lornex and Highmont (Figure 3.10B). The mapped radial patterns in Figure 3.10B do not completely encircle the porphyry systems, likely because mapping was done along transects rather across the entire HVC district, and because the Quaternary and anthropogenic cover prevented direct vein observations in the field north of Valley, Lornex and Highmont, and within 1–2 km to the south of Lornex and Highmont. Another possible explanation for the incomplete radial pattern is that the weakly extensional setting along the proto-Lornex fault linkage zone between Valley–Lornex and Highmont focused vein formation along an east-northeast trend (i.e., parallel to the Gnawed Mountain Porphyry dike) in that area. The multi-kilometer scale of these radial patterns is consistent with the presence at depth of large cupolas above a significant partially molten magma chamber, which we interpret to be the "Salt and Pepper" Bethsaida facies.

We interpret that magmatic fluid overpressure should also have caused K-feldspar-bearing veins to radiate around Bethlehem. However, Quaternary and anthropogenic cover around Bethlehem prevented direct observations of K-feldspar-bearing vein orientations on several sides of the porphyry system.

3.9.3.3. Thermal contraction

Heated external fluids involved in porphyry systems flow convectively under hydrostatic pressure conditions (Cathles, 1977; Norton and Knight, 1977; Cathles et al., 1997), and contrary to the magmatic fluids, lack the ability to generate fracture permeability, and therefore flow through pre-existing fractures. The most abundant fractures in the upper crust are joints, which are tensile fractures with thin openings of <1 mm and rarely up to 1 cm (Segall and Pollard, 1983; Pollard and Aydin, 1988). A common joint type in extrusive rocks (e.g., Reiter et al., 1987; Aydin and DeGraff, 1988) and intrusive rocks (e.g., Knapp and Norton, 1981; Bergbauer and Martel, 1999) are cooling joints, which form by local tensile stresses induced by thermal contraction of the rock mass during cooling. These local stresses are isotropic, and their orientation is dependent on intrusion geometry (Bergbauer et al., 1998; Bergbauer and Martel, 1999). In the absence of a large regional differential stress, cooling joints form roughly orthogonal sets: one set oriented parallel and one set oriented at high angle to the intrusion contacts. In the ideal case of a cylindrical intrusion, cooling joints form sets that are concentric with and that radiate from the center of the intrusion (e.g., Diamond Joe pluton; Gerla, 1988). The tensile opening mode and small width (<1 cm) of propylitic and sodic-calcic veins at HVC, as well as the wide range of vein orientations indicate that they were likely deposited by externally-derived hydrothermal fluids flowing through cooling joints. This interpretation is consistent with an isotope study by Byrne (2019), which concluded that sodic-calcic alteration was caused by the inflow and heating of seawater-derived fluids at a low water/rock ratio. Additionally, although the orientation of sodic-calcic and propylitic veins in the HVC district is highly variable, the majority of them are either perpendicular or parallel to the GCB facies contacts (Figure 3.12 and Figure 3.13 respectively), which is consistent with the expected orientation of cooling joints. Intersecting veins on outcrops with two propylitic vein orientations (Figure 3.14) are also generally nearly orthogonal, as is expected from joints generated by isotropic thermal contraction stresses.

Magmatic fluids in small mineralized systems across the GCB also flowed through joints, as shown by the crude batholith-scale radial pattern formed by the mineralization trend at the various Cu occurrences, which converge toward the center of the batholith (Figure 3.11B). This suggests that the flow of magmatic fluids that formed the district Cu occurrences, although locally controlled by fluid overpressure-generated hydrofractured permeability, was dominantly controlled by fluid pathways generated by cooling joints.

Additionally, except for the limited west-northwest-oriented extension at the HVC porphyry systems and at the Gnawed Mountain Porphyry dike caused by the sinistral regional stress regime, the amount of space occupied by propylitic and sodic-calcic vein-filling material in the GCB can be accounted for entirely by thermal contraction. At constant pressure conditions, the amount of thermal contraction that occurs in rocks during cooling depends on the thermal expansion coefficient of the constituent minerals (Fei, 1995). Thermal contraction resulting from a temperature decrease from 700 °C to 200 °C causes a three-dimensional volume decrease of 2.6% to 4.3% (average of 3.7%) in granodioritic rocks (Arndt et al., 1997), with the most significant volume change occurring at 573 °C because of the transition from β to α quartz. Thermal contraction therefore results in a one-dimensional length decrease of 0.88–1.42% (average of 1.24%), which is similar to the amount of vein-filling material estimated in the GCB for north-trending veins along its minor axis (1.7%; Figure 3.15A) and for west-trending veins along its major axis (1.0%; Figure 3.15B).

3.10. Conclusion

The district-scale alteration footprint of the HVC porphyry systems is characterized by large alteration zones formed both by early upward-flowing overpressured magmatic fluids (i.e., K-feldspar-bearing and muscovite-bearing veins) and by later external fluids convecting under hydrostatic pressure (i.e., sodic-calcic and propylitic veins). Hydrothermal alteration assemblages associated with both HVC porphyry mineralization events (Bethlehem–J.A. and Valley–Lornex–Highmont) are characterized by a general decrease in temperature over time and away from the porphyry systems from early K-feldspar to muscovite alteration, to sodic-calcic and propylitic alteration.

A palinspastic reconstruction of the GCB suggests that Valley–Lornex likely formed at depth of ~5 km, and that Bethlehem and J.A. likely formed at depths between 3 and 4 km. The reconstruction shows that the largest potassic alteration zone is a westerly-elongated, ~12 x 2 km area that overlaps Valley–Lornex and Highmont. Sodic-calcic alteration forms discontinuous zones that outline a crude northeast-oriented inverted funnel shape that is ~17 x 11 km in the southwest and <1 km-wide to the northeast. We interpret that at the current erosional level, the wide sodic-calcic zones to the southwest and narrow zones to the northeast are due to the tilting of the batholith, which exposes deeper areas to the southwest. Propylitic alteration is widespread across the GCB with a 10 km diameter circular zone of higher vein intensity (>5 cm/m) in the center of the batholith. Propylitic vein intensity variations do not define a gradient towards the porphyry systems.

We interpret the regional stress regime under which the GCB was emplaced to be sinistral, although the nearly circular shape and significant size of the batholith, combined with the large range of dike and vein orientations, indicate that the regional differential stress was low and that the orientation of the minimum compressive stress was not fixed.

Permeability within the GCB is dominantly the result of local stresses induced by magmatic or magmatic fluid overpressure, and more broadly by thermal contraction during cooling. The regional sinistral stress regime only locally contributed to the batholith-scale permeability along favourably-oriented west to west-northwest-trending structures within the HVC porphyry systems.

Overpressure pushes the country rock upward and outward from the magmatic source. This generates tensile fractures that radiate above and around the locus of buoyantly rising volatile-rich magmas and magmatic hydrothermal fluids, in which porphyritic or aplite dikes may intrude and high-temperature potassic alteration can form. We observe this at HVC where aplite dikes define a crude radial pattern and where K-feldspar-bearing veins radiate from the Valley–Lornex and Highmont porphyry systems.

Contraction during cooling generated orthogonal joint sets that are perpendicular and parallel to the GCB intrusive contacts. Cooling resulted in a crude concentric and radial pattern of joints that converges towards the center of the batholith because of the circular to slightly elongated shape of the GCB. Cooling joints provided pathways to focus flow of external fluids under hydrostatic pressure conditions, which caused sodic-calcic and propylitic alteration, as well as for earlier magmatic fluids that formed the smaller Cu occurrences throughout the batholith.

The implications of this study for mineral exploration are twofold. First, although the presence of extensive sodic-calcic and propylitic alteration in a large batholith is positive because it implies significant heat and fluid flow in the district, mapping the vein intensity and orientation may not always be an effective way to identify prospective areas, particularly in the case of porphyry deposits hosted in large intrusive bodies. Second, mapping the district-scale orientation of aplite dikes and K-feldspar-bearing veins can be an effective tool to identify the location of a magmatic cupola and potential porphyry Cu mineralization at depth (i.e., where the dikes and veins converge). K-feldspar-bearing veins, however, may be relatively subtle features that are difficult to recognize without feldspar staining.

Finally, the time of emplacement of aplite dikes in the HVC district has been reasonably well determined from cross-cutting relationships but no age is available for them, so further study is recommended in order to better resolve their exact timing. Individual pulses of hydrothermal fluids typically last <100 k.y., but it was shown that the HVC porphyry systems were formed by several hydrothermal pulses over a ~2 m.y. period (Ash et al., 2006; Byrne et al., 2013; D'Angelo et al., 2017), so more detailed alteration mapping could potentially better resolve the different pulses. Further research focused on the whole rock or mineral chemistry of propylitically altered rocks at HVC (cf., epidote, Cooke et al., 2014; chorite, Wilkinson et al., 2015) is also recommended in order to identify gradients in the propylitic alteration zone that indicate areas of higher prospectivity.

Chapter 4. Infrared spectra and chemistry of hydrothermal white mica in the Highland Valley Copper district, British Columbia: Implications for vectoring toward porphyry mineralization

4.1. Introduction

Porphyry-type mineral deposits account for approximately 69% of Cu and 95% of Mo worldwide production, and are important sources of other metals such as Au, Ag, W, Pt and Pd (Sinclair, 2007; Singer, 2017). Porphyry systems typically form deposits at depths between 4 and 6 km (e.g., Seedorff et al., 2005) and involve high-temperature magmatic fluids exsolved from crystallizing magmas, as well as heated external fluids that flow convectively around the magmatic heat source (e.g., Cathles, 1977; Weis, 2015). This flow of vast quantities of hot magmatic and external fluids generally results in large volumes of altered but barren rock, which form alteration zones that are centered on the economically-mineralized part of porphyry systems, or ore deposits. The relatively small size these ore deposits (typically < 1 km across; e.g., Sillitoe, 2010) relative to the large areas of associated alteration however, make them difficult targets to find, especially if they are not exposed at surface. In mature mining districts, porphyry deposits that crop out have typically been found as a result of years of mineral exploration, which has lead to a declining exploration success rate in recent years (McCuaig et al., 2009).

In the hopes of finding additional porphyry deposits, mineral explorers are increasingly exploring for deeper deposits in mature districts or in covered areas with little or no outcrop (Witherly, 2012). To explore in areas with little outcrop, the maximum amount of knowledge must be obtained from sparse data in order to focus on the most prospective areas. Effective vectoring tools can be developed on the basis of zonation patterns that form predictable alteration footprints around ore deposits. Over the last two decades, significant advances have been made in the use of short-wave infrared (SWIR) spectroscopy to recognize mineral chemistry variations as vectoring tools in volcanogenic massive sulfide (e.g., Jones et al., 2005; van Ruitenbeek et al., 2012; Laakso et al., 2015), orogenic gold (e.g., Arne et al., 2016; Simpson et al., 2016; Wang et al., 2017), iron oxide Cu-Au (e.g., Laukamp et al., 2011), base metal (e.g., Herrmann et al., 2001; Sun et al., 2001), epithermal (e.g., Bierwirth et al., 2002; Bedini et al., 2009), and porphyry deposits (e.g., Thompson et al., 1999; Cooke et al., 2014; Greenlaw, 2014; Halley et al., 2015; Wilkinson et al., 2015; Guo et al., 2017; Neal et al., 2018).

White mica minerals, which include muscovite, illite, phengite and paragonite, form in high and low-temperature porphyry-related hydrothermal alteration assemblages (e.g., Seedorff et al., 2005). Understanding the distribution of white mica compositions in the various alteration assemblages across porphyry systems can be a powerful tool to vector towards the hotter, central part of the porphyry system that may host an economic deposit. The variations in the chemical composition of white mica minerals are related to the pressure, temperature, and fluid pH at which they crystallize, but are also influenced by the chemical composition of the protolith material, and of the fluid from which they crystallize (Guidotti, 1984; Parry et al., 1984). Variations of white mica reflectance spectra as a function of composition have been investigated in porphyry deposits. These studies focused primarily on airborne mapping of hydrothermal systems (Graham et al., 2018), or on the distribution of minerals in or near porphyry deposits in alteration assemblages such as transitional potassic-sericitic to sericitic (Alva Jimenez, 2011; Benavides, 2018), sericitic or phyllic (Harraden et al., 2013; Uribe-Mogollon and Maher, 2018), or sericitic to intermediate argillic (Cohen, 2011; Graham et al., 2018) as classified by the nomenclature of Seedorff et al. (2005). To date, studies that focused on white mica as part of the propylitic or sodic-calcic alteration assemblages at the district scale are lacking.

The compositional variations of white mica minerals at Highland Valley Copper (HVC) (Alva Jimenez, 2011) and Yerington (Cohen, 2011) were determined up to 3.5 km away from porphyry deposits using SWIR spectroscopy to map variations in the Al-OH absorption feature wavelength of white mica, hereafter referred to as Al-OH wavelength. Results show that shorter wavelength paragonite is present within the porphyry deposits and that longer wavelength phengite is peripheral to the deposits. Both of these studies used the ASD TerraSpec® portable mineral analyzer, which provides spectral data from light reflected off a rock surface through a ~2.5 cm field-of-view. A limitation of these previous efforts is the relatively large field-of-view of the instrument compared to the size of the minerals present in the samples analyzed, which means that spectral data collected from one measurement most likely contain a combination of features from several minerals, or are over-represented by the most highly reflective minerals that are present in the field-of-view.

The HVC district in southern British Columbia contains five porphyry Cu-Mo systems: Bethlehem, Valley, Lornex, Highmont, and J.A. that are hosted in the Late Triassic calc-alkaline Guichon Creek batholith (GCB). In this study we examine the compositional and SWIR spectra variations in white mica from all alteration assemblages associated with these porphyry systems to distances up to 10–14 km from the deposits. We present electron microprobe compositional data from white mica minerals, as well as SWIR data and high-resolution hyperspectral imagery (~0.5 mm pixel size) from a suite of samples from across the GCB to characterize the Al-OH wavelength of the various alteration assemblages across the district. SWIR spectra from TerraSpec® and hyperspectral imagery data are compared to determine the applicability and effectiveness of both methods to recognize district-scale vectors toward mineralization.

4.2. White mica compositions

Muscovite, the most common white mica, is abundant in metamorphic rocks such as phyllites, schists and gneisses, in Si-rich intrusive rocks and in K-rich hydrothermal alteration (Kerr, 1959; Bailey, 1984; Deer et al., 1992, 2003). Muscovite is a dioctahedral phyllosilicate characterized by a crystal structure composed of one octahedral layer between two tetrahedral layers (t-o-t), separated by interlayer cations, 50% or more of which must be monovalent (e.g., K^+). The ideal formula for muscovite (in atoms per formula unit, apfu) is as follows (Rieder et al., 1998):

$K{}^{VI}Al_2\square Al^{IV}Si_3O_{10}(OH)_2$ where ${}^{IV}Si = 3.0–3.1$

${}^{VI}Al = 1.9–2.0$

$K = 0.7–1.0$, ($I \geq 0.85$)

${}^{VI}R^{2+} / ({}^{VI}R^{2+} + {}^{VI}R^{3+}) < 0.25$ (R = octahedral layer cation or ${}^{VI}Al$ site)

${}^{VI}Al / ({}^{VI}Al + {}^{VI}Fe^{3+}) = 0.5\text{-}1.0$

$Al^{IV}Si_3$= tetrahedral layer cation

□ is a vacancy

Substitutions of major and trace elements are common in all cation sites (i.e., octahedral layer, tetrahedral layer and interlayer cations), and may result in changes of the white mica species. If the interlayer cation, which is K in muscovite, is substituted by Na to approximately 1 apfu, the white mica species is paragonite [$NaAl_2\square AlSi_3O_{10}(OH)_2$], whereas if it is substituted by a vacancy, so that the K content is ~0.65 instead of 1, the white mica species is illite [$K_{0.65}Al_2\square Al_{0.65}Si_{3.35}O_{10}(OH)_2$]. If the octahedral layer cation is substituted by Mg^{2+} or Fe^{2+} and the Al in the tetrahedral layer cation is substituted by Si^{4+} [Tschermak substitution; $(Al^{3+})^{VI}+(Al^{3+})^{IV}$ <-> $(Fe^{2+}$ or $Mg^{2+})^{VI}+(Si^{4+})^{IV}$], the white mica species in phengite [$K(Al,Fe^{3+})Al_{1-x}(Mg,Fe^{2+})_x(Al_{1-x}Si_{3+x}O_{10})(OH)_2$, where x = 1–3].

For hydrothermal white mica, the magnitude of the Tschermak substitution is primarily dependent on the Fe^{2+} and K^+ composition of the fluid as well as the fluid temperature and pH, i.e., phengitic composition is favoured over muscovitic composition under low-temperature neutral conditions (e.g., Bird and Norton, 1981; Halley et al., 2015). The paragonitic substitution is dominantly controlled by the Na^+ and K^+ composition as well as the temperature of the fluid and favours the presence of paragonite–K-feldspar over muscovite–Na-plagioclase under high temperature (Brimhall, 1977; Munoz, 1984).

4.3. Regional geology

The GCB is part of the exotic Quesnel terrane, an island arc that formed off the western coast of Ancestral North America (Monger et al., 1972; Monger and Price, 2002; Nelson et al., 2013). The Quesnel terrane was accreted onto the North American continent's western margin during the Middle Jurassic (Nixon et al., 1993) following the closure of the intervening Cache Creek ocean (Mihalynuk et al., 1994).

The Late Triassic voluminous arc magmatism of Quesnel, and the contemporaneous Stikine terrane, formed large batholitic intrusions that generated many of the large porphyry Cu systems in the Canadian Cordillera (Logan and Mihalynuk, 2014). In the southern Quesnel terrane, three sub-parallel belts of porphyry systems formed between ~210 and ~195 Ma, with metal assemblages that range from Cu-Mo±Au in the west to Cu-Au in the east (Preto, 1979; Logan and Mihalynuk, 2014; Schiarizza, 2014). The GCB (Mortimer et al., 1990; McMillan et al., 1995; D'Angelo et al., 2017) is part of the oldest and westernmost of the three porphyry belts (Figure 4.1) that intrude the Nicola Group (Preto, 1979; Beatty et al., 2006; Schiarizza, 2017). The Nicola Group is composed of volcanic and sedimentary rocks that formed in a submarine environment above an east-dipping subduction zone (Mortimer, 1987; Ghosh, 1995).

Following the Quesnel terrane accretion, the tectonic regime transitioned from sinistral transpression and crustal thickening (Mihalynuk et al., 1999; Nelson and Colpron, 2007) to dextral transpression during the mid-Cretaceous to Eocene. In the area surrounding the GCB, this dextral regime is expressed primarily as north to northwest-trending faults such as the Fraser and Cherry Creek faults (Figure 4.1).

4.4. Guichon Creek batholith geology

The GCB is a large 30 x 65 km north-northwest-elongated irregularly shaped Late Triassic composite calc-alkaline batholith hosted in the coeval Nicola Group. The GCB is unconformably overlain by volcanic and sedimentary rocks of the mid-Cretaceous Spences Bridge Group to the southwest of the batholith, the Eocene Kingsvale Group to the south, and the Jurassic Ashcroft Formation and Eocene Kamloops Group to the north (McMillan et al., 2009).

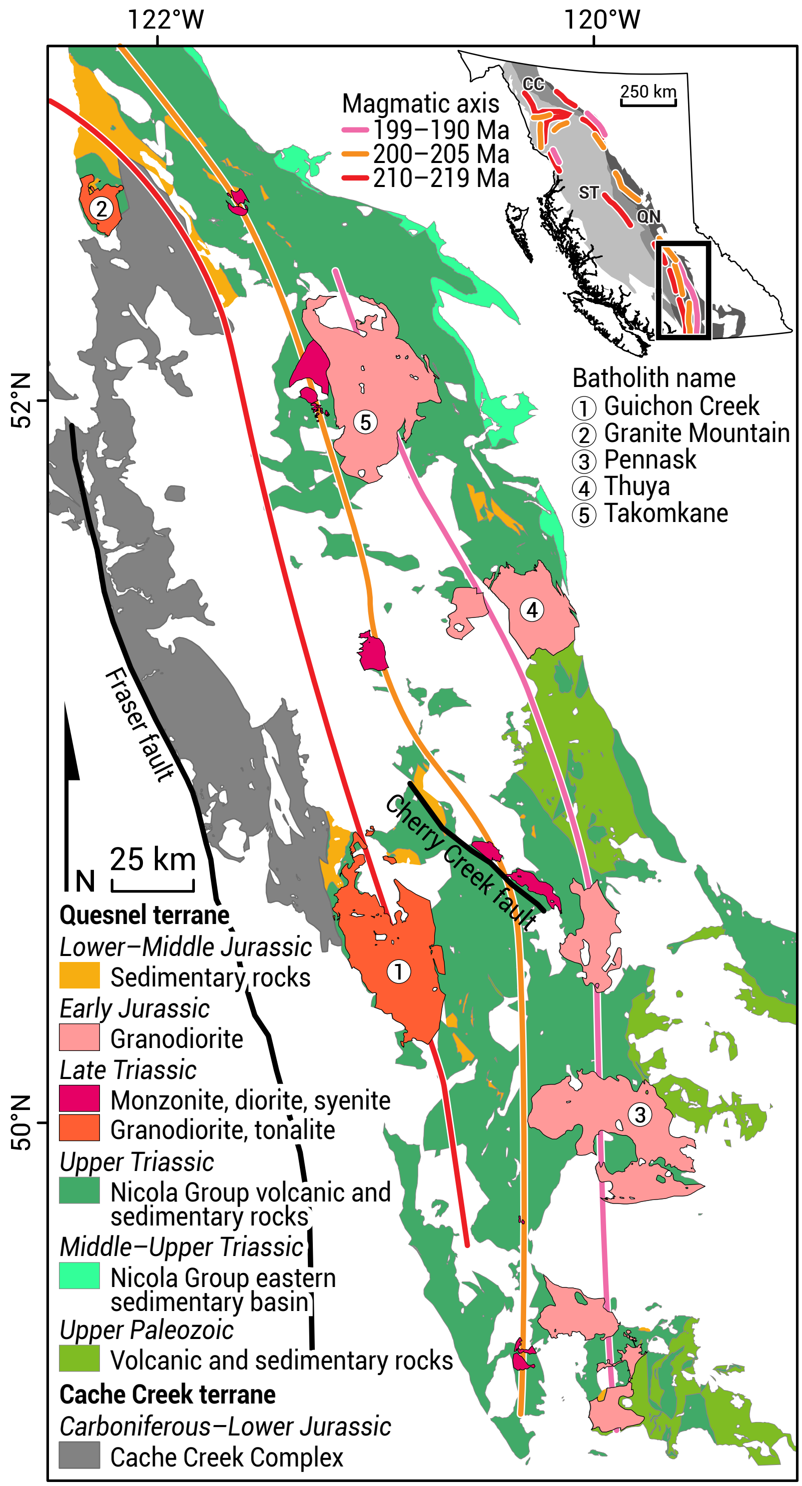

Figure 4.1. Simplified map of southern British Columbia showing rocks from the Cache Creek and Quesnel terranes, and the linear traces of Late Triassic to Early Jurassic arc intrusions (modified from Logan and Mihalynuk, 2014; Schiarizza, 2014; Cui et al., 2017). Terrane abbreviations: CC = Cache Creek, QN = Quesnel, ST = Stikine. Coordinates are in WGS1984.

Gravity and seismic models of the batholith indicate that it forms a flattened funnel-shaped body with a steeply-plunging feeder zone located below the more centrally located porphyry systems (Ager et al., 1973; Roy and Clowes, 2000). Aluminium-in-hornblende barometry (D'Angelo, 2016) indicates post-emplacement tilting to the northeast of ~12–15° , which is consistent with the gravity and seismic data (Ager et al., 1973; Roy and Clowes, 2000), as well as with the stratigraphic thickness estimates of 3–6 km for the Nicola Group rocks in the Quesnel terrane (Preto, 1979).

The GCB formed from two distinct episodes of magmatism and is compositionally zoned from mafic older marginal facies to felsic younger central

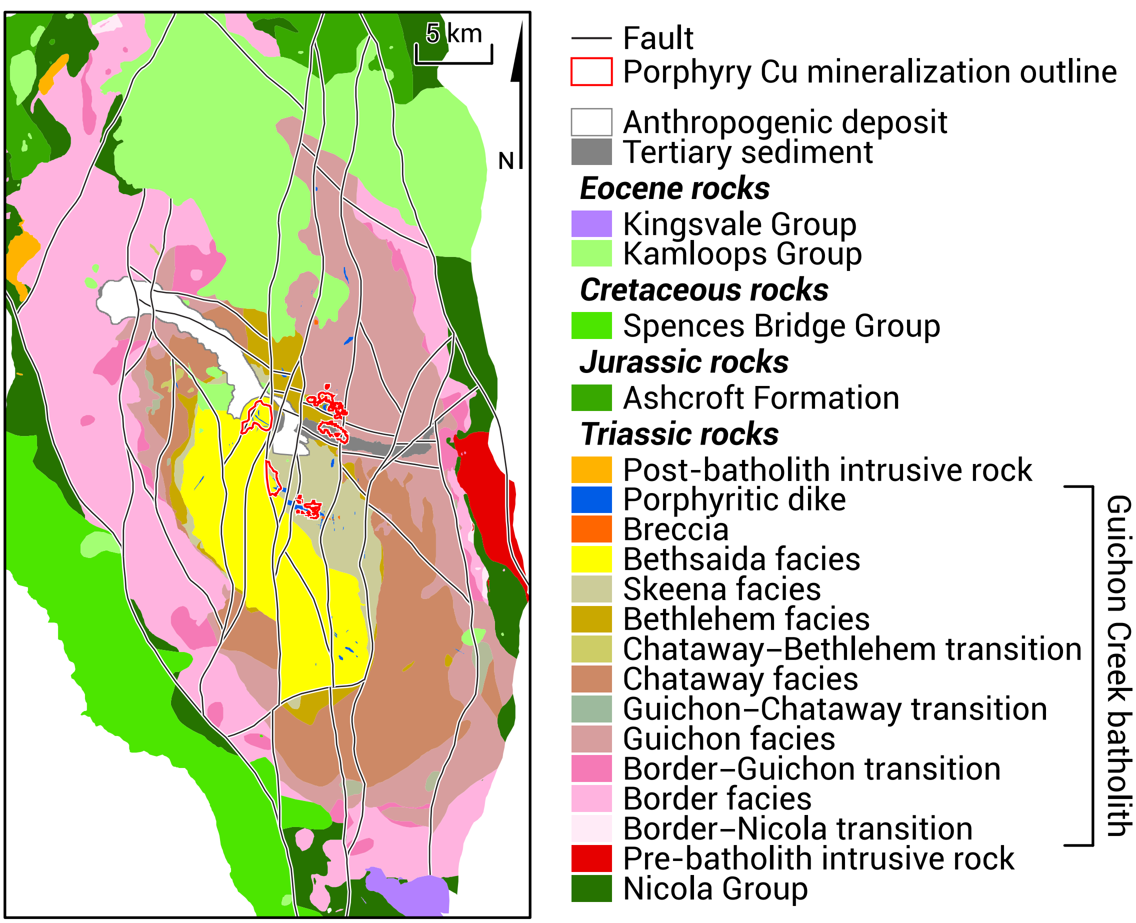

Figure 4.2. Geological map of the Guichon Creek batholith showing the location of the HVC porphyry systems (modified from McMillan et al., 2009).

facies (Figure 4.2) (Carr, 1966; Northcote, 1969; McMillan, 1976b, 1985; Byrne et al., 2013; D'Angelo et al., 2017). The first magmatic episode intruded between 211.0 ± 0.2 Ma and 210.4 ± 0.4 Ma and formed the Border facies and Highland Valley facies (Guichon and Chataway subfacies), which respectively consist of quartz-diorite and granodiorite (D'Angelo et al., 2017). The second magmatic episode intruded between 209.8 ± 0.3 Ma and 208.6 ± 0.2 Ma and formed the Bethlehem, Skeena and Bethsaida facies, which consist of granodiorite and locally monzogranite (D'Angelo et al., 2017). Abundant dikes and stocks characterized by porphyritic textures were emplaced at the porphyry centers (Byrne et al., 2013) during the second or a potential third magmatic episode. The latest of these intrusions was dated at 207 ± 0.2 Ma (D'Angelo et al., 2017).

The HVC porphyry Cu systems were emplaced during at least two main hydrothermal episodes (Byrne et al., 2013). The first hydrothermal episode formed the Bethlehem porphyry deposit at ~209 Ma immediately after the emplacement of the Bethlehem facies but before the Skeena and Bethsaida facies. Based on their similar characteristics and hosted positions in and near the contact between the Guichon and Bethlehem intrusive facies, the Bethlehem and J.A. porphyry deposits are likely coeval (Byrne et al., 2013). The Valley, Lornex and Highmont porphyry deposits were subsequently emplaced circa 208 Ma (Lornex and Highmont systems; D'Angelo et al., 2017) and 207 Ma (Valley system: Ash et al., 2006), as indicated by Re-Os ages from molybdenite. Host rocks at Valley, Lornex and Highmont are respectively Bethsaida, Skeena and Bethsaida, and Skeena facies.

Mid-Cretaceous to Eocene dextral displacements along north-trending faults caused lithological contact offsets and dismembered some of the porphyry deposits. The Valley and Lornex deposits, which are now separated by ~3.5 km across the Lornex fault (Hollister et al., 1975), are interpreted to have formed as a single porphyry system (Allen and Richardson, 1970; Hollister et al., 1975). Normal fault displacements in the Paleocene–Eocene resulted in west-northwest to northwest-trending faults such as the Highland Valley fault. The structural block that contains the J.A. system was down-thrown along such a structure and subsequently covered by up to 300 m of pre-glacial and glacial sediments (McMillan, 1976a; Bobrowsky et al., 1993).

4.5. Methodology

4.5.1. Mapping and sample collection

Geological mapping at 1:10,000 scale was focused along five transects across the GCB from 2014 to 2016. Each transect is approximately 10–14 km in length and 2.5–3.5 km wide starting at one of the porphyry deposits and ending near the outer margin of the batholith. The total area mapped is approximately 225 km^2. The area located within 3–4 km southwest of Valley was mapped at 1:5,000 scale. A total of 739 rock samples that contain fracture-controlled hydrothermal alteration were collected in a grid pattern approximately every 500 m where the mapping scale was 1:10,000 and every 250 m where the mapping scale was 1:5,000. Distance from the deposits was estimated for each sample by calculating the distance between the sample location and the closest outline of known Cu mineralization after restoration of 3.5 km dextral displacement along the Lornex fault. Slabs of each sample were cut perpendicular to the vein orientation. Sample coordinates and descriptions are presented in Appendix B.

4.5.2. Feldspar staining

Each sample slab was stained to highlight the effect of hydrothermal alteration on feldspar mineralogy. Feldspar staining was done at The University of British Columbia in Vancouver, Canada. The slabs were first etched in a bath of hydrofluoric (HF) acid for one minute, and then dipped into an amaranth solution for five seconds and into a sodium cobaltinitrate solution for 30 seconds. The slabs were rinsed and dried between each step. Sodium cobaltinitrate stains K-feldspar crystals yellow, whereas amaranth stains calcic feldspar crystals red (Gabriel and Cox, 1929; Bailey and Stevens, 1960; Laniz et al., 1964; Lyons, 1971; Norman, 1974). Other calcic minerals, such as calcite or prehnite, may also be stained by the amaranth (Norman, 1974).

4.5.3. Short-wave infrared (SWIR)

The reflectance of minerals, or the percentage of incident radiation such as light that is reflected off of them, is dependent on their crystallographic structure, which is a unique characteristic of each mineral species. Molecular bonds have specific vibrations that absorb radiation at certain wavelengths (Clark, 1999), and prevent it from being reflected (i.e., absorption feature). Minerals can therefore be identified by characterizing the position and shape of their absorption features using a plot of their reflectance as a function of wavelength (i.e., reflectance spectrum). Radiation in the SWIR wavelengths (i.e. 1100–3000 nm), are particularly sensitive to the absorption features caused by hydroxyl radicals (~1400 nm), water molecules (~1900 nm), and by cation-OH bonds such as Al-OH (~2200 nm), Fe-OH (~2250 nm) or Mg-OH (~2350 nm) present in clays and in phyllosilicates (Pontual et al., 1997; Thompson et al., 1999).

Variations in white mica composition resulting from elemental substitution can be detected using shifts in the wavelength of the Al-OH absorption feature in the 2180–2220 nm range (e.g., Duke, 1994). The Al-OH feature wavelength shifts can be used to map gradients in hydrothermal fluid composition, temperature and pH (e.g., Alva Jimenez, 2011; Cohen, 2011; Harraden et al., 2013; Halley et al., 2015). The typical Al-OH wavelength is >2195 nm for paragonite, ~2197–2208 nm for muscovite and >2208 nm for phengite (Post and Noble, 1993; Herrmann et al., 2001; Clark et al., 2007; GMEX, 2008). Other phyllosilicates that have an Al-OH absorption feature include illite (2206–2210 nm), kaolinite (2206–2208 nm), montmorillonite (2200–2213 nm), and beidellite (2181–2199 nm). This property is of particular interest in the porphyry environment because of the wide spread of phyllosilicate minerals in the various alteration assemblages (e.g., Seedorff et al., 2005).

4.5.3.1. Hyperspectral scanning

Infrared reflectance spectra were collected using a Specim SisuROCK™ hyperspectral scanner at the University of Alberta in Edmonton, Canada. A detailed description of the methodology employed was presented by Lypaczewski and Rivard (2018). Line-scan imaging was performed by a 256 spectral by 320 spatial pixel mercury-cadmium-telluride (MCT) detector array. A total of 654 samples were scanned. Spectral data were measured over the 1000–2500 nm range with a spectral resolution of 6.3 nm and a variable spatial resolution of 0.2–1.0 mm/pixel. The raw data contain signal from the sample, the light source and the electric current generated by the spectrometer in the absence of external light (i.e., dark current). A Spectralon™ white reference standard, composed of material that has a 99% reflectance, was used to calibrate the instrument against the light source illumination. The white reference and the dark current were measured for each spectral measurement. The dark current data were subtracted from the raw data and the resulting spectra were normalized using the white reference data.

Given the ~6 nm resolution of the SisuROCK™ scanner, for each spectrum (i.e., for each pixel) the measured data were interpolated in order to generate a smooth Gaussian curve joining reflectance values at every 1 nm increments. The wavelength of the reflectance minima associated with the Al-OH absorption feature was then retrieved from each of the interpolated spectra by identifying the maxima of the derivative of the spectra, and a wavelength map was generated for each sample slab. In these maps, each 1 nm wavelength interval between 2190 nm and 2215 is assigned a specific set of RGB values. The wavelength maps were then processed in the ImageJ™ software, an open-source Java-based image processing software, in order to calculate the percentage of pixels of each wavelength per sample. Percentages were calculated by normalizing the amount of pixels of each wavelength to the sum of all pixels that contain an Al-OH absorption feature in the sample. The sample population was then subdivided based on the alteration assemblage present and summary statistics, such as the pixel percentage median and interquartile range (IQR), were calculated for each wavelength interval.

4.5.3.2. Terraspec®

Infrared reflectance spectra were also collected at The University of British Columbia on a total 682 samples using an ASD TerraSpec® portable mineral analyzer for comparison purposes with results from the Specim SisuROCK™ hyperspectral scanner. The TerraSpec® instrument acquired spectral data using two scanning spectrometers that have a spectral resolution of 2 nm, and respectively span the 1000–1800 nm and the 1800–2500 nm ranges. The reflectance data were collected through a ~2.5 cm field-of-view for approximately 60 s. A Spectralon™ white reference standard was measured every 30 minutes during data collection. The dark current data was measured on every scan by blocking external light (i.e., light collected through the instrument field-of-view), and its value was automatically subtracted from the raw data. For each sample slab measurement, the instrument field-of-view was placed directly over veins or altered fracture selvages in the sample (Figure 4.3). Measurements taken from sample that do not contain hydrothermal alteration were classified as background measurements.

The resulting spectra were imported in The Spectral Geologist™ (TSG™) software, a tool for mineralogical analysis of reflectance spectra, for mineral identification using the inbuilt reference library of common minerals and for extraction of the numeric parameters relevant for white mica minerals: wavelength, width and depth of the Al-OH absorption feature. Given the 2 nm resolution of the TerraSpec® instrument, for each spectrum the TSG™

Figure 4.3. Example of ASD TerraSpec® portable mineral analyzer measurement location on altered sample slab.

software interpolates the data to generate a smooth curve joining points at every wavelength. To determine the depth of absorption features, a hull quotient spectrum was first calculated for each measurement by drawing a line between all the high points of the spectrum (i.e., a hull line), and normalizing the spectrum so that the hull line has a value of 1 at each wavelength. The depth of the measured spectrum at each wavelength relative to the normalized hull line, or hull quotient depth (hqd), was then calculated.

4.5.4. Rietveld refinement

Rietveld refinement analyses were conducted at The University of British Columbia on four clay-bearing samples to characterize and quantify their mineralogy. Samples were reduced to the optimum grain-size range for quantitative X-ray analysis (<10 μm) by grinding under ethanol in a vibratory McCrone Micronizing Mill for 10 minutes. Continuous-scan X-ray powder-diffraction data were collected over a range 3-80°2θ with Co$K\alpha$ radiation on a Bruker D8 Advance Bragg-Brentano diffractometer equipped with an Fe monochromator foil, 0.6 mm (0.3°) divergence slit, incident and diffracted-beam Soller slits and a LynxEye-XE detector. The long fine-focus Co X-ray tube was operated at 35 kV and 40 mA, using a take-off angle of 6°.

The X-ray diffractograms (Appendix D) were analyzed using the International Centre for Diffraction Database PDF-4 and Search-Match software by Bruker. The X-ray powder-diffraction data of the samples were refined with the Rietveld program Topas 4.2 (Bruker AXS) to obtain modal mineral abundances. These amounts represent the relative amounts of crystalline phases normalized to 100%.

4.5.5. Electron microprobe analyses (EPMA)

Electron microprobe analyses (EPMA) were performed using a CAMECA SX-50 instrument at The University of British Columbia. The analyses were conducted on polished thin sections from 13 samples to determine the major and minor element composition of white mica alteration minerals. Each samples was assigned to a specific alteration assemblage based on a visual assessment of the mineralogy present in the hand sample and thin section. The white mica composition was determined by wavelength-dispersive spectrometry in spot mode at an accelerating voltage of 15 kV, a beam current of 10 nA and a beam diameter of 10 μm. The peak count time was 20 s (40 s for F and Cl) and the background count time was 10 s (20 s for F and Cl). Raw data were corrected to determine the elemental concentration using the PAP method (Pouchou and Pichoir, 1984). For the elements considered, the following standards, X-ray lines and crystals were used: synthetic phlogopite, F$K\alpha$, TAP; albite, Na$K\alpha$, TAP; kyanite, Al$K\alpha$, TAP; synthetic phlogopite, Mg$K\alpha$, TAP; synthetic phlogopite, Si$K\alpha$, TAP; scapolite, Cl$K\alpha$, PET; synthetic phlogopite, K$K\alpha$, PET; diopside, Ca$K\alpha$, PET; rutile, Ti$K\alpha$, PET; synthetic magnesiochromite, Cr$K\alpha$, LIF; synthetic rhodonite, Mn$K\alpha$, LIF; synthetic fayalite, Fe$K\alpha$, LIF. Detection limits are presented in Table 4.1.

The white mica minerals were classified as occurring in feldspar sites, mafic sites, or as interstitial in cases where the host could not be identified due to the texturally destructive nature of alteration or if the white mica occurred as vein material. Where the mineral size was sufficiently large, multiple spot analyses were made per white mica crystal for better characterization. In these cases, the composition of the white mica mineral was calculated as the average of all the analyses. The Fe reported in the EPMA data is Fe^{2+}. The EPMA data, expressed

Table 4.1.EPMA analysis detection limits.

Element	Detection limit (wt.%)
Al	0.05
Ca	0.05
Cl	0.04
Cr	0.10
F	0.60
Fe	0.10
K	0.06
Mg	0.04
Mn	0.11
Na	0.08
Si	0.06
Ti	0.06

as weight percent element-oxide, were exported to Microsoft Excel to calculate the white mica chemical formula for each spot analysis on the basis of 11 anhydrous oxygens. The white mica lithium composition was estimated using the method from Monier and Robert (1986), whereas and the OH composition was estimated using the method of Tindle and Webb (1990).

4.6. Results

The characteristics of the various district-scale alteration assemblages associated with the HVC porphyry deposits are summarized below (Table 4.2), as well as the mineral chemistry and SWIR absorption features of white micas present in fresh and altered rocks of the GCB. Results of hyperspectral scan image analysis are in Table 4.3 for select representative samples, and in Appendix E for all samples. Results of TerraSpec® analyses are presented in Appendix F.

Table 4.2.Summary of hydrothermal alteration in the Guichon Creek batholith[1].

Alteration assemblage[2]		Vein minerals	Selvage minerals	Description	Paragenesis	Assemblage spatial distribution	Inferred temperature range (°C)[3]	Interpreted fluid source[4]	White mica Al-OH absorption feature wavelength (nm)[5]	Spatial distribution of white mica compositions[6]
Potassic		Qz, Ccp, Bn	Kfs, Bt, Ccp, Bn, fine-grained white mica	Discontinuous Qz±Ccp±Bn veins (<0.1–1.8 cm, average 0.5 cm) with Kfs±Bt±white mica-bearing selvages (0.1–2.5 cm, average 0.8 cm); Bt after Hbl; primary Bt stable; rare fine-grained white mica after felsic sites	Early; cut by mineralized Ms–Qz veins and sodic-calcic veins	Bt-dominant veins abundant at Bethlehem and J.A.; Kfs-dominant vein abundant at Valley, Lornex and Highmont and minor at J.A.; Kfs-dominant veins extend 3–5 km away from porphyry deposits	350–700[d,e]	Magmatic[h]	2193–2201 (mainly 2194–2198)	Muscovitic white mica alteration <2 km from deposits (strongest alteration <100s m from deposits)
Muscovite-bearing	Transitional potassic-sericitic, early-halo veins (EH)[a]; early micaceous (EDM)[b,c]	Qz, Bn, Ccp, Mol, Anh	Coarse-grained Ms (grey in porphyry systems, greenish in district Cu occurrences), Qz, Cal, Ccp, Bn, Hem	Qz–Bn–Ccp±Mol veins (<0.1–5 cm) with coarse-grained muscovite selvages (0.1–7 cm); Kfs locally present in selvages; primary Bt generally stable	Cross-cuts Kfs-bearing veins; both cross-cuts and is cross-cut by sodic-calcic veins	Associated with main Cu mineralization at Valley, Lornex and Highmont; only extends up to hundreds of meters away from the deposits; common at district Cu occurrences	550–360[d]	Magmatic[h]	2193–2202 in selvages around Qz veins (mainly 2195–2198)	Strong muscovitic white mica alteration <100s m from deposits and at smaller district Cu occurrences;
	Sericitic; phyllic	Qz, Ccp, Py, Mol, Cal, Tur	Fine to locally coarse-grained grey to pale green Ms, Chl, Cal, Ccp, Py, Hem	Fracture-controlled to pervasive fine to locally coarse-grained white mica in feldspar sites; Chl in mafic sites; thick banded Qz–Ccp–Py–Mol veins (up to 30 cm) common near syn-mineralization structures	Cross-cuts Qz–Bn–Ccp–coarse Ms veins; cross-cuts sodic-calcic veins; pre-dates intermediate argillic alteration	Associated with Cu mineralization at Bethlehem and J.A.; typically peripheral to Qz–Bn–Ccp–coarse Ms veins at Valley, Lornex and Highmont; only extends up to hundreds of meters away from the deposits; common at district Cu occurrences	550–300[d]	Magmatic[h]	2193–2202; locally 2205–2210 in mafic sites; 2205–2020 in selvages around hairline fractures or thin veins	Strong phengitic white mica alteration only within deposits, weak at smaller district Cu occurrences
Intermediate argillic[7]		---	Kln, Mnt, Chl, fine-grained white mica, Cb	Typically strong pervasive alteration; white mica–Mnt after Bt; white mica–Kln–Mnt after Pl[j].	Overprints all other alteration assemblages in porphyry deposits	Absent from Bethlehem; only present in the mineralized parts of Valley, Lornex and Highmont; stronger in and around structures	100–200[d]	---	2202–2207 (Kln interference)	White mica signal overwhelmed by Kln interference; only within deposits
Sodic-calcic		Ab, Act, Di, Tur, Chl, Ep	Ab, Grt, Ttn, Chl, Ep, fine-grained white mica	Pervasive Ab–Act±Di±Grt alteration; Ep–Chl veins (<0.1–5 cm, average 3.2 cm) with Ab–Chl–Ep–white mica-bearing Kfs-destructive selvages (0.1–18 cm); Chl and Ep after mafic sites; Ab and fine-grained white mica in feldspar sites	Post-mineralization at Bethlehem; pre to post-mineralization at Valley, Lornex and Highmont; cross-cuts Kfs-bearing veins; both cross-cuts and is cross-cut by Qz– Bn–Ccp–coarse Ms veins	Pervasive alteration near porphyry deposits, best developed at Bethlehem and Highmont; veins extend up to 7 km away from deposits	300–450[d]	External[h]	2190–2202 (mainly 2192–2198)	Paragonitic white mica alteration only in strong pervasive sodic-calcic alteration within deposits; Muscovitic white mica alteration <3 km from deposits (strongest alteration <2 km from deposits / alteration intensity increases toward Cu mineralization);
Propylitic		Chl, Prh, Pmp, Ep, Cal	Fine-grained white mica, Cal, Chl, Vrm, Ep, rare Hem, rare Kfs	Ep–Chl–Prh–Pmp–Cal veins (<0.1–2.2 cm) with Chl–Ep–Vrm–white mica±Hem-bearing Pl-destructive selvages (0.1–9 cm); rare Ep-Kfs veins; Chl, Vrm and Ep after mafic sites and white mica after Pl; primary Kfs generally stable	Late; cross-cuts all other vein types	Present throughout the Guichon Creek batholith; higher vein intensity in the center of the batholith, coincident with the HVC porphyry deposits	200–350[d,f,g]	External[h,i]	2193–2220 (mainly 2195–2200); longer wavelengths (>2207) in selvages typically nearest vein	Phengitic white mica alteration <5 km from deposits (strongest alteration between 2 to 3 km from deposits)

[1]Based on descriptions from McMillan (1985), Byrne et al. (2013), Lesage et al. (2016), Byrne et al. (2017), Byrne (2019), Lesage et al. (2019) and this study. [2]Alteration assemblage names from Seedorff et al. (2005), [a]Proffett (2009), [b]Alva Jimenez (2011), and [c]Rusk et al. (2008). [3]Temperature range estimates based on mineral stabilities presented in [d]Seedorff et al. (2005), [e]Brimhall (1977), [f]Bird and Spieler (2004), and [g]Digel and Gordon (1995). [4]Interpreted fluid source from [h]Lesage et al. (2019) and [i]Byrne (2019). [5]Determined using image analysis of hyperspectral scans. [6]Determined using hyperspectral and TerraSpec® SWIR data. [7]Description of intermediate argillic alteration at HVC from [j]Jambor and Delabio (1978) and this study.

Table 4.3.Percentage of pixels calculated from image analysis of hyperspectral scans that contain an Al-OH absorption feature of specified wavelength. Samples presented in this table are the samples shown in Figure 4.4, Figure 4.8, and Figure 4.11 to Figure 4.14. Data for all samples are available in Appendix E.

Alteration assemblage	Sample ID	Percentage (%) of pixels from sample slabs that contain an Al-OH absorption feature of specified wavelength (nm)																							
		2190–2191	2191–2192	2192–2193	2193–2194	2194–2195	2195–2197	2197–2198	2198–2199	2199–2200	2200–2201	2201–2202	2202–2203	2203–2204	2204–2205	2205–2206	2206–2207	2207–2208	2208–2209	2209–2210	2210–2211	2211–2212	2212–2213	2213–2214	2214–2220
Least altered	2238829	34.6	19.5	6.2	4.5	2.4	2.0	14.4	8.1	4.3	2.1	0.9	0.5	0.2				0.2							
	2238895	68.1	10.6	1.0	0.7	0.4	0.2	10.0	5.1	2.3	0.9	0.4	0.2					0.1							
	2238939	50.2	29.8	6.2	2.4	0.4		5.8	2.7	1.2	0.5	0.2	0.2					0.3							
	2758861	28.3	37.6	12.6	11.2	3.4	0.6	3.7	1.5	0.7	0.3	0.1	0.1												
Potassic	2238703	7.0	11.8	6.8	12.0	12.5	10.1	17.3	11.6	6.4	2.9	1.1	0.3	0.1											
	2238934	67.4	15.8	3.1	1.4	0.4	0.1	5.4	3.1	1.5	0.8	0.4	0.2	0.1				0.3							
	2245374	70.2	4.4	0.7	0.3	0.1		9.4	6.5	3.9	1.6	0.8	0.6	0.2	0.1	0.1	0.1	1.0							
	2247923	3.0	5.0	5.8	14.8	22.6	25.7	11.8	6.0	2.7	1.3	0.6	0.4	0.2	0.1	0.1									
Muscovite-bearing	2232432	0.1					0.2	0.6	1.0	2.0	5.3	12.8	23.1	25.0	13.3	6.4	3.7	0.6	0.5	0.3	0.1	0.4	1.2	0.3	2.9
	2232435	0.5	1.4	2.3	10.7	10.7	25.9	13.7	11.6	8.4	5.7	3.5	1.9	1.2	0.8	0.6	0.4	0.2					0.1		0.3
	2238870	1.4	1.6	1.1	2.4	3.0	8.2	7.1	6.6	6.5	6.4	6.8	7.4	8.2	10.3	9.4	6.3	1.7	0.4	0.2	0.1	0.2	1.2	0.2	3.3
	2238960	0.4	0.2	0.2	0.2	0.2	1.2	4.9	9.7	14.6	17.5	15.9	9.9	5.1	3.7	4.4	3.9	2.4	1.2	0.5	0.2	0.4	0.8	0.2	2.4
	2758869	0.7	2.3	2.4	6.9	6.7	18.1	15.7	16.9	13.8	8.9	4.4	1.8	0.7	0.2	0.1	0.1	0.2							
Intermediate argillic	BC14278V	0.7	0.1				0.1	0.6	1.0	2.1	2.8	4.1	6.2	8.4	37.8	31.0	2.8	1.5	0.1	0.1			0.1		0.4
	BC14281B	2.5	0.7	0.8	2.0	1.1	2.7	2.7	3.3	3.9	4.4	4.7	11.2	28.0	27.1	3.8	0.4	0.3							
	BC14294A	0.6	0.5	0.8	3.5	4.5	8.9	4.9	4.2	4.1	4.4	4.5	5.3	7.8	11.9	20.7	10.2	0.2					0.5	0.1	2.1
	BC14295A	0.5											0.3	2.1	48.1	48.2	0.8								
Sodic-calcic	2232426	0.7	0.7	0.7	1.4	3.1	16.0	17.4	18.0	15.6	10.8	6.5	3.8	2.6	1.4	0.7	0.3	0.4							
	2245302	12.8	9.0	5.0	4.3	2.7	4.6	22.2	17.7	11.0	5.8	2.7	1.2	0.5	0.2	0.1	0.1	0.2							
	2245409	16.1	11.1	6.9	9.0	8.8	13.3	18.2	9.3	4.2	1.7	0.7	0.3	0.1	0.1	0.1		0.2							
	2245474	6.2	3.8	2.3	3.3	7.1	36.0	20.7	11.6	5.3	2.2	0.9	0.4	0.2											
Propylitic	2238783	3.6	4.0	3.1	16.2	20.5	18.0	6.5	5.3	4.2	3.2	2.6	2.0	1.4	0.9	1.0	0.8	1.0	0.5	0.3	0.2	0.4	0.8	0.3	3.5
	2245418	45.3	23.8	6.3	5.4	2.5	1.0	4.0	2.2	1.5	1.3	1.2	1.1	1.1	1.0	1.0	0.7	0.3	0.1				0.1		0.1
	2245441	38.9	21.3	4.0	2.8	1.6	0.8	5.4	2.6	2.1	1.0	1.0	1.0	0.4	0.7	1.4	0.9	9.1	1.7	0.5	0.2	0.6	0.5	0.3	1.2
	2247945	17.8	24.0	12.8	31.4	7.6	1.2	1.3	0.8	0.5	0.4	0.3	0.3	0.3	0.2	0.2	0.2	0.2	0.1				0.1		0.1
	2758885	21.1	21.6	9.6	17.2	12.7	6.1	3.2	1.6	0.9	0.5	0.5	0.4	0.1	0.2	0.3	0.2	0.8	0.3	0.1	0.1	0.2	0.2	0.2	2.1
	2758890	5.5	9.1	6.4	19.6	12.7	9.1	7.8	6.3	4.7	3.8	3.0	2.4	1.9	1.5	1.3	1.2	1.1	0.3	0.2	0.1	0.1	0.4	0.1	1.2

4.6.1. Least altered GCB rocks

4.6.1.1. Short-wave infrared spectroscopy

GCB rocks that lack visible porphyry-related hydrothermal alteration are termed "least-altered" rocks. The unstained and feldspar-stained surfaces of the least-altered rocks (Figure 4.4 top and middle row) show that primary feldspars are unaltered and that no veins are present. Hyperspectral scans of these rocks (Figure 4.4 bottom row), however, show that they contain at least two populations of spectrally-active minerals (Table 4.3, Figure 4.5). Image analysis of the hyperspectral scans indicates that the main Al-OH wavelength population is characterized by short wavelengths that are typically <2192 nm: the pixel percentage median of wavelengths <2192 nm in least-altered samples is 70.4% and the interquartile range (IQR) is 54.1–79.6%. The secondary population is characterized by wavelengths between 2197 and 2199 nm, for which the pixel percentage median is 10.8% and the IQR is 6.5–15.1%. The pixel percentage of each wavelength generally decreases with increasing wavelength (Figure 4.5).

TerraSpec® measurements on least-altered rocks also consistently produce spectrally-active minerals with an Al-OH absorption feature. The median Al-OH wavelength is 2198.3 nm and the IQR is 2197.2–2199.5 nm (Figure 4.6A). Hyperspectral scans of least-altered rocks generally contain between 6% and 15% of pixels characterized by 2197–2199 nm wavelengths (Figure 4.5). The mineral responsible for these Al-OH wavelengths in hyperspectral scans is likely the same mineral detected in the TerraSpec® reflectance spectra. The Al-OH absorption feature in the TerraSpec® reflectance spectra is generally shallow (hqd IQR is 0.08–0.15, Figure 4.6B) and relatively narrow (width IQR is 26.6–29.3 nm, Figure 4.6C) compared to the Al-OH absorption feature of altered samples.

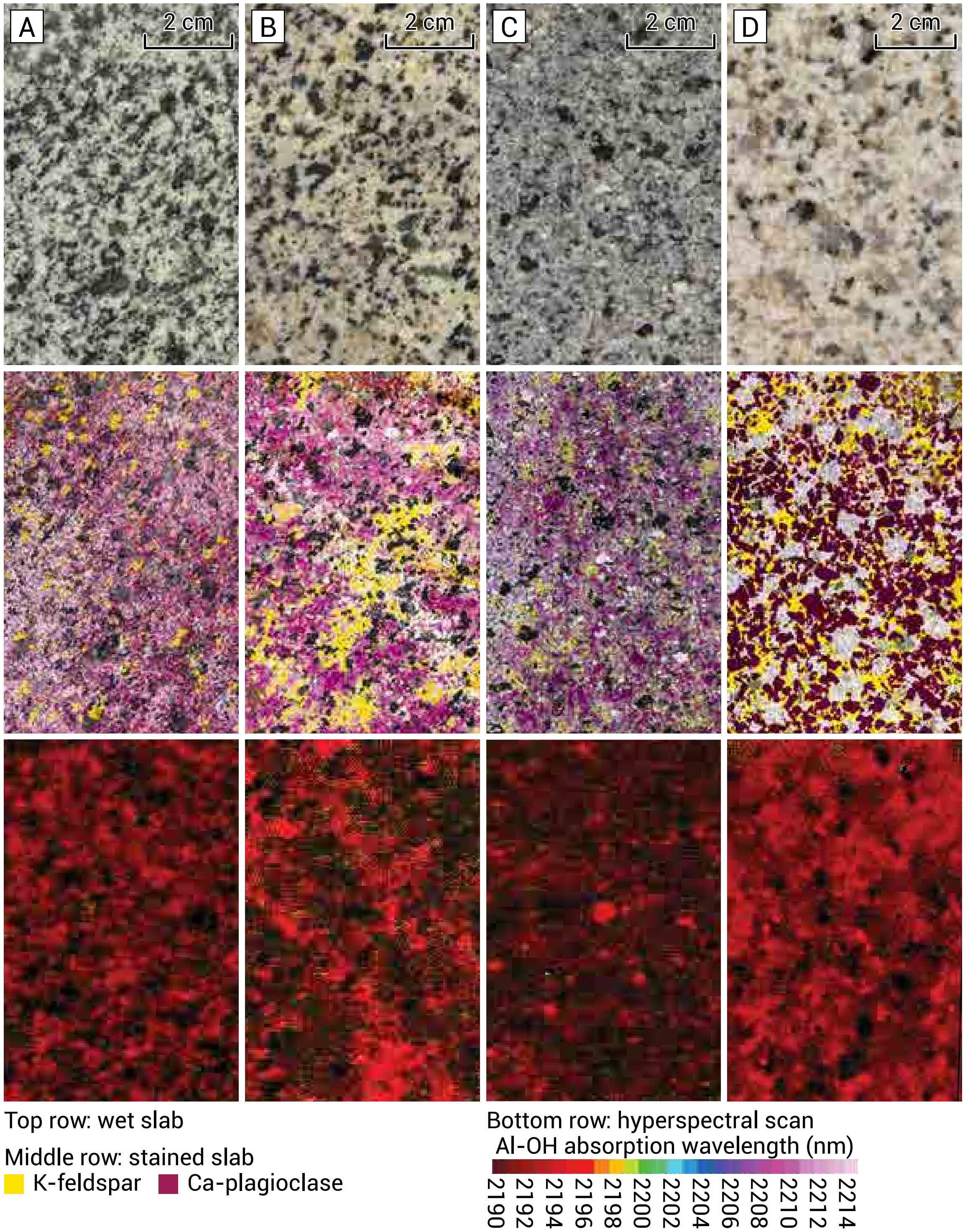

Figure 4.4. Least altered samples. Unstained slab photo (upper row), stained slab photo (middle row) and hyperspectral scan showing the Al-OH wavelength (bottom row): A) Guichon facies (sample 2238939), B) Chataway facies (sample 2238829), C) Bethlehem facies (sample 2238895), and C) Bethsaida facies (sample 2758861).

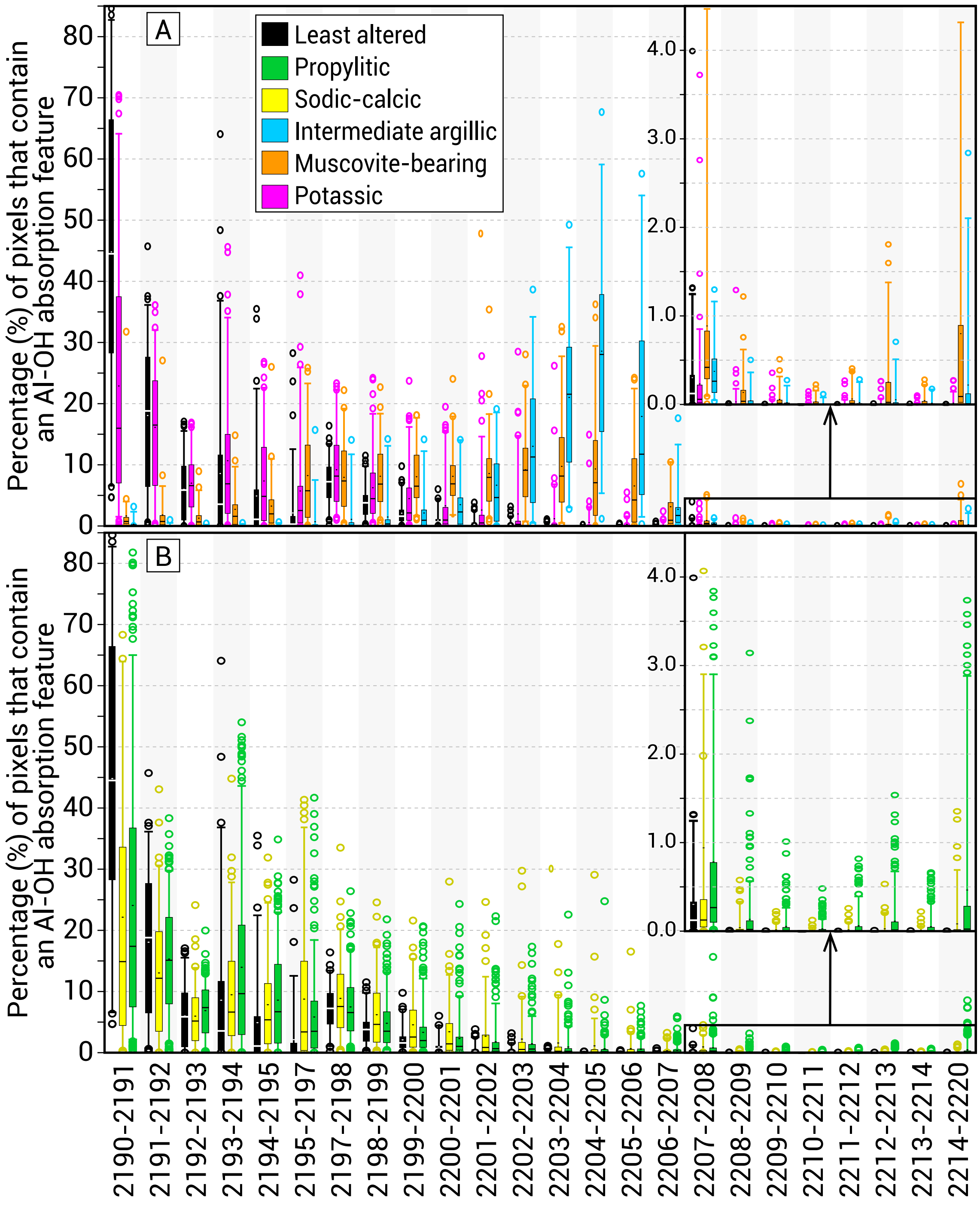

Figure 4.5. Percentage of pixels calculated from image analysis of hyperspectral scans that contain an Al-OH absorption feature of specified wavelength for each main alteration assemblage: A) least altered (105 samples), potassic alteration (92 samples), muscovite-bearing alteration (51 samples), and intermediate argillic alteration (31 samples), and B) least altered, sodic-calcic alteration (91 samples), and propylitic alteration (279 samples). For each wavelength interval, boxes show the interquartile range (IQR) and whisker are defined as 1.5 times the length of the IQR.

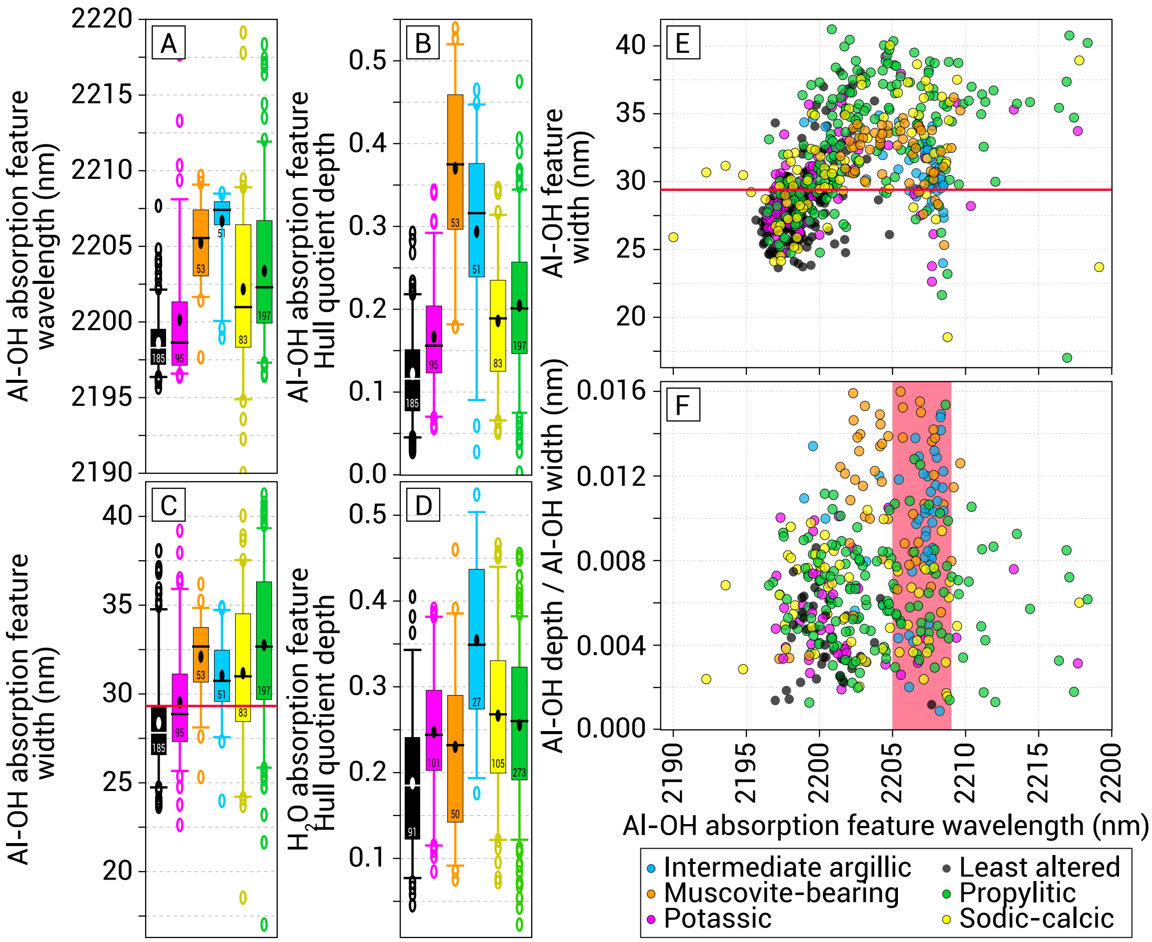

Figure 4.6. Summary statistics of white mica spectral features measured by Terraspec®: A) Al-OH wavelengths (nm), B) Al-OH feature hull quotient depth, C) Al-OH feature width (nm), and D) water absorption feature (~1900 nm) hull quotient depth. Scatterplots showing E) the Al-OH feature width (nm) and F) the Al-OH feature depth plotted against the Al-OH feature wavelength (nm). Measurements were made on least altered (190 readings), potassic alteration (107 readings), muscovite-bearing alteration (53 readings), intermediate argillic alteration (51 readings), sodic-calcic alteration (119 readings), and propylitic alteration (304 readings). The number in each box in A) to D) represents the number of measurements in which the feature is present. For each alteration assemblage, boxes show the interquartile range (IQR) and whisker are defined as 1.5 times the length of the IQR. The red line in C) and E) represents the upper limit of the least altered Al-OH absorption feature width IQR (29.3 nm). Only Al-OH absorption features with a width >29.3 nm are plotted in F), and wavelengths between 2205 nm and 2209 nm, which may reflect kaolinite interference, are highlighted in red.

This suggests that the mineral responsible for these absorption features is not as well developed as the mineral present in the GCB altered samples. The water absorption feature at ~1900 nm is also shallowest in least-altered samples (hqd IQR is 0.12–0.24) and only present in 91 of the 190 measurements (Figure 4.6D), which indicates that for least-altered rocks the TerraSpec® field-of-view contains the least amount of minerals that contain water within their crystal structure.

The spatial distribution of spectrally-active minerals in the hyperspectral scans in Figure 4.4 indicates that these minerals are hosted in plagioclase crystals. Thin section petrography shows that plagioclase crystals in least-altered GCB rocks are generally characterized by a light dusting of a very fine-grained elongate mineral. Spectral and textural evidence suggest that the mineral may be beidellite [$(Ca_{0.5},Na)_{0.33}Al_2(Si_{3.67}Al_{0.33})O_{10}(OH)_2$], a dioctahedral phyllosilicate end-member of the montmorillonite–beidellite series (Larsen and Wherry, 1925; Weir and Greene-Kelly, 1962). Beidellite has an Al-OH wavelength in the 2181–2199 nm range (Post and Noble, 1993), which is consistent with the observed wavelength range in least-altered rocks. The composition of this mineral was not determined by EPMA analyses during this study, however, so additional work is required to confirm this interpretation.

4.6.2. Potassic alteration

Two main fracture-controlled potassic alteration assemblages are present at HVC: a biotite-dominant assemblage at the Bethlehem and J.A. deposits (Table 4.2) (McMillan, 1976a; Briskey, 1980; Alva Jimenez, 2011); and a K-feldspar-dominant assemblage at Valley, Lornex and Highmont (Osatenko and Jones, 1976; McMillan, 1985; Casselman et al., 1995; Byrne et al., 2013). Biotite-dominant alteration is present up to 1 km away from Cu mineralization at the Bethlehem deposit. Potassium-feldspar-dominant alteration forms large zones that are coincident with the Valley, Lornex and Highmont deposits and that are present up to 5 km away from Cu mineralization (Figure 4.7) (Lesage et al., 2019). Outside of the porphyry deposits, the K-feldspar-dominant potassic assemblage is characterized by K-feldspar selvages around thin quartz veins (Figure 4.8) that contain minor amounts (<1%) to traces of chalcopyrite and pyrite, with trace bornite locally. Veins are typically <0.5 cm and selvages <1 cm wide, but veins and selvages may locally be ~2–3 cm wide, particularly within <2 km of the deposits. Chalcopyrite and pyrite are typically present within <2 km and <3 km of the deposits, respectively. Other smaller zones of K-feldspar-

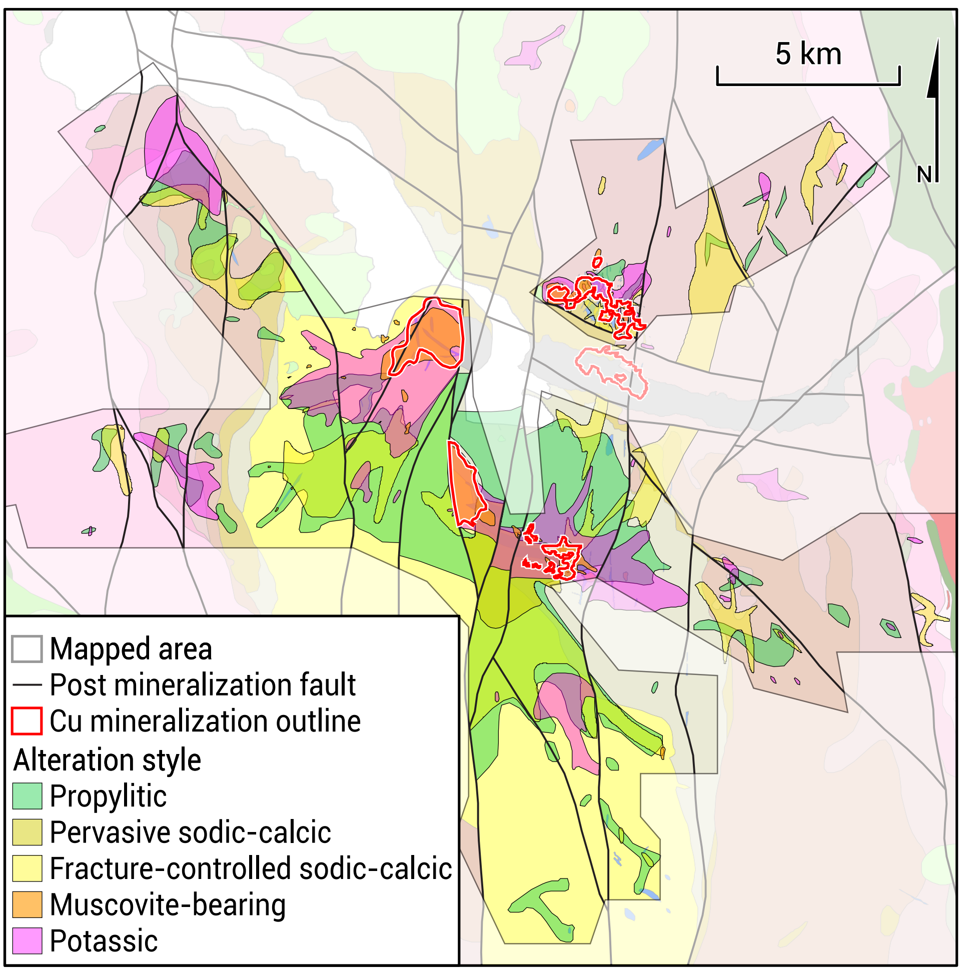

Figure 4.7. Hydrothermal alteration in the Guichon Creek batholith and location of the HVC porphyry systems (modified from Lesage et al., 2019).

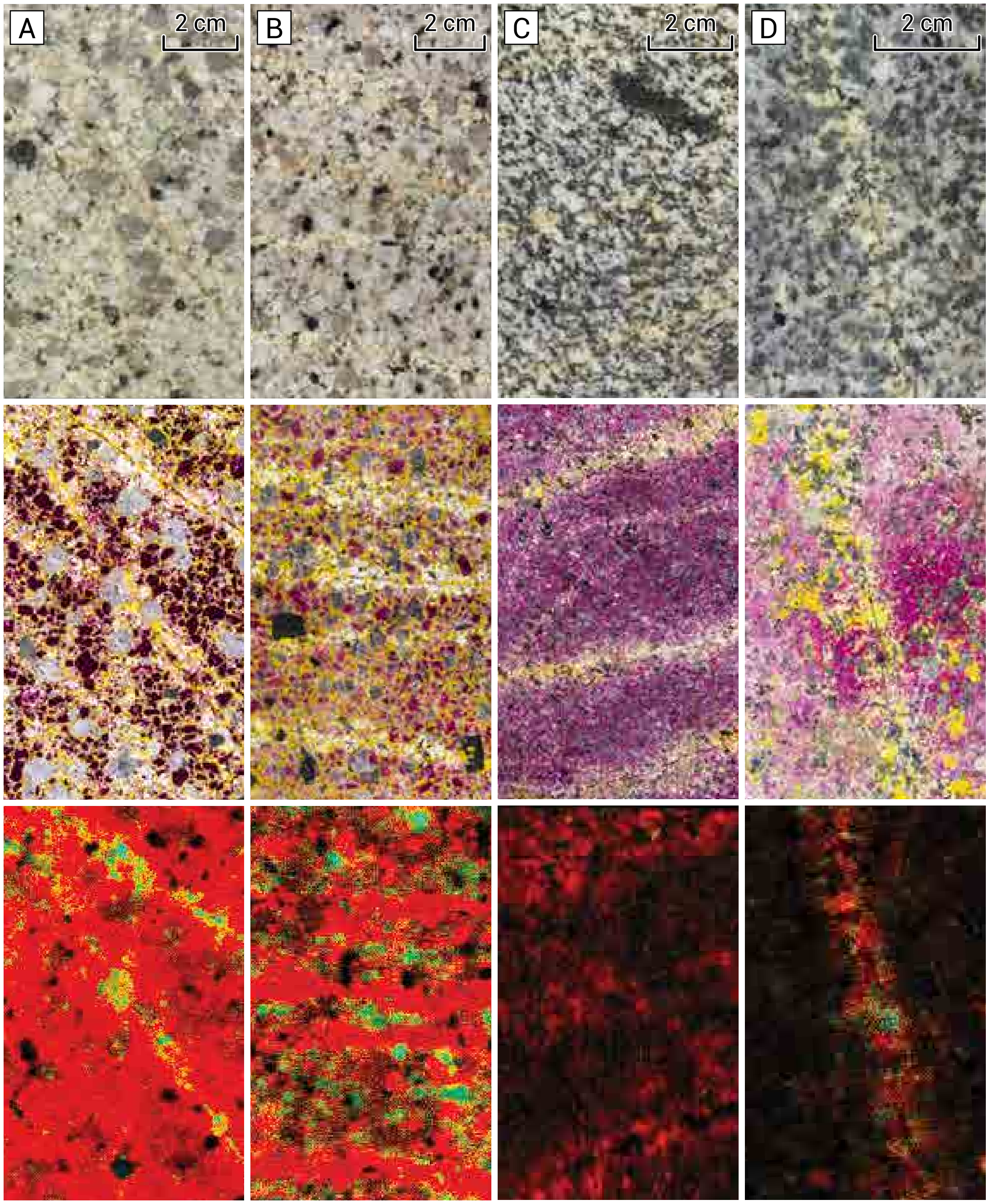

Sample ID: 2247923	**Sample ID:** 2238703	**Sample ID:** 2238934	**Sample ID:** 2245374
Lithology: Bethsaida	**Lithology:** Bethsaida	**Lithology:** Guichon	**Lithology:** Border
Alteration: Potassic	**Alteration:** Potassic	**Alteration:** Potassic	**Alteration:** Potassic
Distance to deposit: 318 m (Valley)	**Distance to deposit:** 1706 m (Valley)	**Distance to deposit:** 8506 m (Valley)	**Distance to deposit:** 9728 m (Highmont)

Figure 4.8. Potassic-altered samples. Unstained slab photo (upper row), stained slab photo (middle row) and hyperspectral scan showing the Al-OH wavelength (bottom row). Distance to the closest deposit increases from left to right. The legend for stain and hyperspectral scan colors is provided in Figure 4.4.

bearing veins (<3 km across) are also present in the GCB (Figure 4.7), but lack associations with known porphyry Cu mineralization. Combined vein and selvage width in these zones is typically <1 cm, and veins at most have trace amounts of pyrite. Lithogeochemical analyses indicate that potassic alteration in the HVC district caused minor CaO and MgO depletion, and minor K_2O and SiO_2 enrichment to the protolith (Byrne, 2019).

4.6.2.1. Short-wave infrared spectroscopy

Minor to trace amounts of fine-grained white mica alteration are in plagioclase as part of K-feldspar-bearing vein selvages. Feldspar staining highlights the white mica in plagioclase because altered plagioclase crystals do not take the red amaranth stain and thus remain white (Figure 4.8 middle row). Hyperspectral scans of samples with potassic alteration reveal that this white mica has Al-OH wavelengths in the 2193–2201 nm range (Table 4.3, Figure 4.5A), with the most abundant wavelengths along veins between 2194 and 2198 nm.

The TerraSpec® reflectance spectra of rocks that contain potassic alteration are characterized by slightly longer Al-OH wavelengths than least-altered GCB rocks. The median wavelength is 2198.6 nm and the IQR is 2197.1–2201.3 nm (Figure 4.6A), which is consistent with the hyperspectral scanning results. The Al-OH absorption feature depth (hqd IQR is 0.12–0.20, Figure 4.6B) and width (width IQR is 27.3–31.1 nm, Figure 4.6C) in these spectra are each larger than for least-altered rocks. This increase in the size of the absorption feature indicates that the causative mineral is better developed in potassic veins and selvages than in least-altered rocks.

4.6.2.2. White mica chemistry

All white mica minerals from the potassic assemblage analyzed by EPMA were fine-grained and hosted in feldspar sites, except one that partially replaced biotite (EPMA spot locations are shown in Figure 4.9A, B and C). The measured compositional range is $(K_{0.86-0.97},Na_{0.00-0.06})(Fe_{0.12-0.27},Mg_{0.10-0.35},{}^{VI}Al_{1.45-1.79})({}^{IV}Al_{0.47-0.83}Si_{3.18-3.53})O_{10}(OH)_2$, the interlayer cation site (K+Na+2Ca) occupancy is 0.93–1.04 apfu, and the octahedral site ($Fe+Mg+{}^{VI}Al$) occupancy is 1.99–2.06 apfu (Table 4.4). Calcium content is <0.01 apfu, except for one crystal that has a Ca content of 0.04 apfu. The full occupancy of the interlayer cation site indicates that the white micas are muscovite and that no illite is present (Figure 4.10A). White micas from the potassic assemblage generally have higher Fe+Mg+Mn content (0.22–0.59 apfu; i.e., more phengitic) than white micas from other alteration assemblages (Figure 4.10C and D). Additionally, within the potassic assemblage white micas located closer to a deposit (i.e., ~500 m from Valley; Figure 4.9A) are less phengitic than those located farther (i.e., ~1700 m from Valley and ~2260 m from Bethlehem; Figure 4.9B and C).

4.6.3. Muscovite-bearing alteration

For the purposes of this study, muscovite-bearing alteration refers to two different mineral assemblages: transitional potassic-sericitic, and sericitic alteration (Table 4.2). Lithogeochemical analyses show that these alteration assemblages are associated with protolith enrichments in SiO_2, calcite, H_2O, and K_2O, as well as depletions in CaO and Na_2O (Byrne, 2019).

The first muscovite-bearing assemblage consists of coarse-grained grey paragonitic muscovite (Alva Jimenez, 2011), quartz and minor calcite selvages around quartz–bornite–chalcopyrite ± molybdenite veins (Figure 4.11A top and

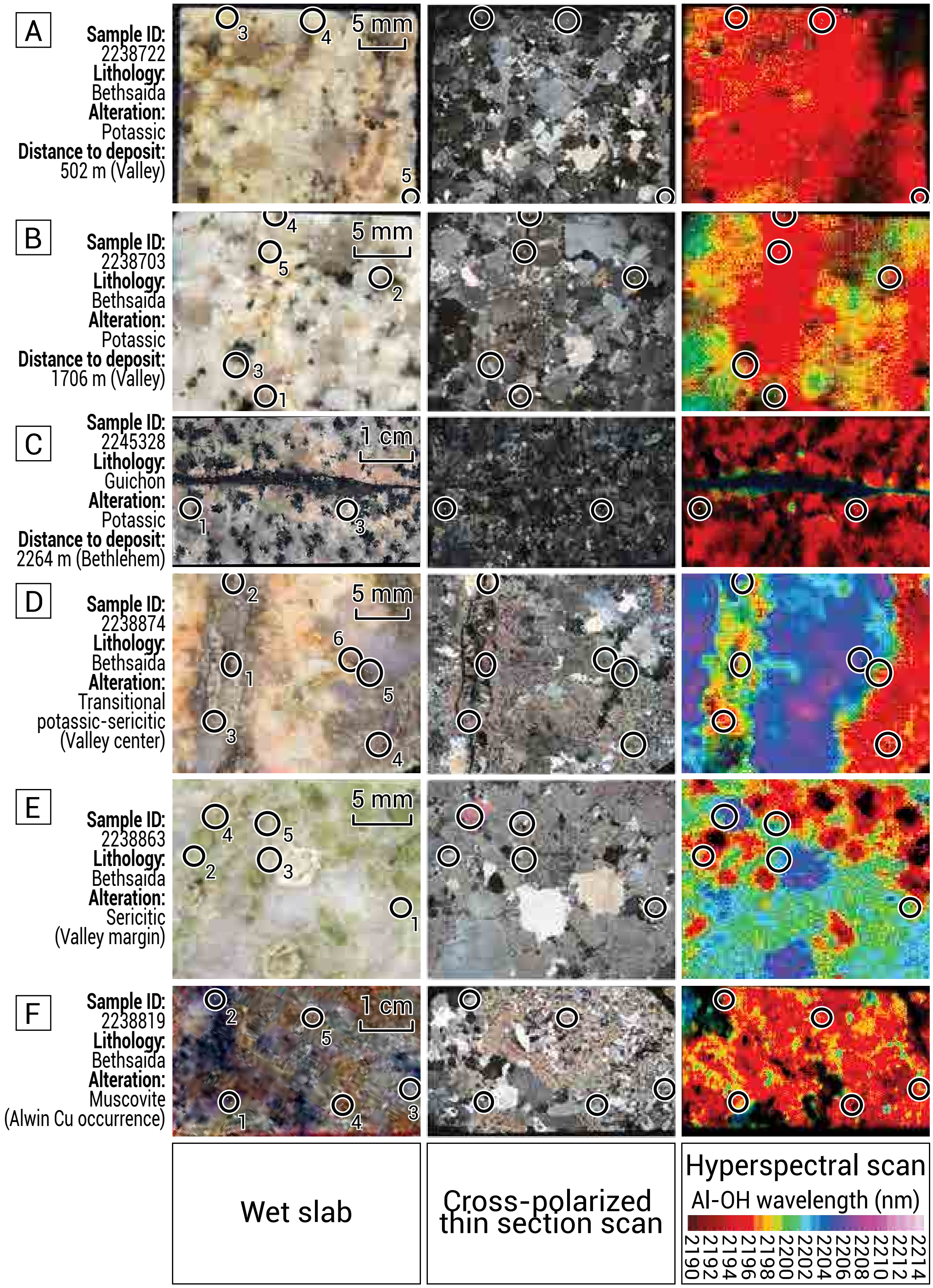

Figure 4.9. Hand sample photo, cross-polarized thin section photomicrograph and hyperspectral scan (Al-OH wavelength) showing the location of electron microprobe analyses of white mica. Numbered circles refer to the EPMA spot analysis ID (see Table 4.4).

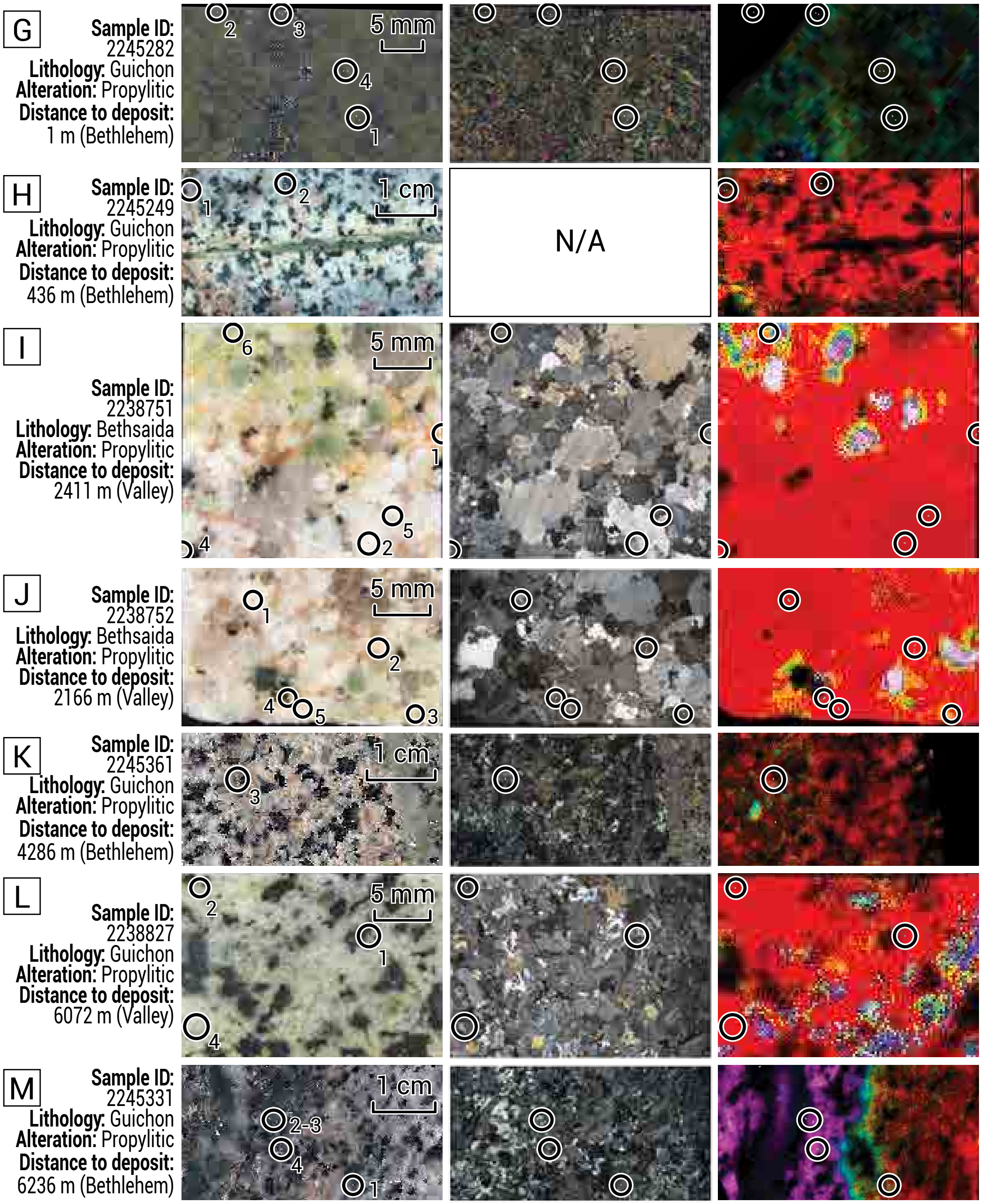

Figure 4.9. Hand sample photo, cross-polarized thin section photomicrograph and hyperspectral scan (Al-OH wavelength) showing the location of electron microprobe analyses of white mica. Numbered circles refer to the EPMA spot analysis ID (see Table 4.4). Cont'd

Table 4.4.White mica composition by EPMA analyses. Li and H_2O calculations from Monier and Robert (1986) and Tindle and Webb (1990).

Alteration style	Potassic	Potassic	Potassic	Potassic	Potassic	Potassic	Potassic	Potassic	Potassic	Potassic
White mica host	Mafic site	Feldspar site	Feldspar site	Feldspar site	Feldspar site	Feldspar site	Feldspar site	Feldspar site	Feldspar site	Feldspar site
Batholith facies	Bethsaida	Bethsaida	Bethsaida	Bethsaida	Bethsaida	Bethsaida	Bethsaida	Bethsaida	Guichon	Guichon
Al-OH wavelength (nm)	2205	2199	2199	2194	2196	2197	2195	2195	2192	2195
Sample ID	2238703	2238703	2238703	2238703	2238703	2238722	2238722	2238722	2245328	2245328
Sample-spot ID	BC14140A-1	BC14140A-2	BC14140A-3	BC14140A-4	BC14140A-5	BC14157B-3	BC14157B-4	BC14157B-5	2015KB030-1	2015KB030-3
# of analyses	3	2	2	2	2	2	3	3	3	3
Element-oxide composition determined by EPMA (wt.%)										
SiO_2	49.13	52.49	52.22	49.53	49.45	46.38	46.59	48.27	47.27	49.81
TiO_2	0.02	0.02	0.03	0.01	0.01	0.52	0.26	0.06	0.02	0.04
Al_2O_3	27.38	24.22	25.59	28.15	28.49	29.86	30.76	32.56	33.04	28.23
FeO	4.71	4.19	3.83	3.63	4.41	4.65	4.18	2.05	2.16	3.22
MnO	0.02	0.10	0.03	0.04	0.04	0.05	0.02	0.04	0.03	0.03
MgO	2.11	3.49	2.83	2.01	1.62	2.01	1.76	1.09	1.00	1.96
CaO	0.01	0.04	0.54	0.05	0.05	0.00	0.03	0.02	0.02	0.09
Na_2O	0.08	0.09	0.09	0.02	0.12	0.21	0.26	0.10	0.14	0.43
K_2O	11.09	10.64	10.06	10.60	10.76	10.96	10.97	10.94	11.33	11.23
F	0.07	0.24	0.11	0.04	0.05	0.11	0.09	0.14	0.15	0.17
Cl	0.00	0.02	0.01	0.02	0.02	0.01	0.01	0.01	0.01	0.01
Cr_2O_3	0.03	0.04	0.02	0.00	0.02	0.00	0.03	0.00	0.01	0.00
Li_2O	0.00	0.02	0.00	0.00	0.00	0.00	0.00	0.00	0.01	0.00
H_2O	4.36	4.34	4.43	4.38	4.40	4.32	4.35	4.42	4.39	4.36
Total	99.00	99.95	99.79	98.48	99.45	99.09	99.32	99.71	99.59	99.58
Element concentration in white mica structural formula (apfu, based on 11 O equivalent)										
Si	3.357	3.529	3.496	3.369	3.348	3.179	3.175	3.225	3.176	3.362
^{iv}Al	0.643	0.471	0.504	0.631	0.652	0.821	0.825	0.775	0.824	0.638
^{vi}Al	1.562	1.447	1.516	1.625	1.621	1.592	1.646	1.786	1.792	1.610
Ti	0.001	0.001	0.002	0.000	0.000	0.027	0.013	0.003	0.001	0.002
Cr	0.001	0.002	0.001	0.000	0.001	0.000	0.002	0.000	0.001	0.000
Fe	0.269	0.236	0.215	0.207	0.250	0.267	0.238	0.116	0.121	0.182
Mn	0.001	0.006	0.002	0.002	0.003	0.003	0.001	0.002	0.002	0.002
Mg	0.215	0.350	0.283	0.203	0.164	0.206	0.179	0.109	0.100	0.197
Li	0.000	0.004	0.000	0.000	0.000	0.000	0.000	0.000	0.003	0.000
Ca	0.001	0.003	0.039	0.004	0.003	0.000	0.003	0.002	0.001	0.007
Na	0.011	0.011	0.011	0.002	0.016	0.028	0.034	0.013	0.019	0.056
K	0.967	0.913	0.860	0.920	0.930	0.959	0.953	0.933	0.971	0.968
OH	1.985	1.948	1.977	1.989	1.987	1.974	1.979	1.970	1.966	1.962
F	0.015	0.050	0.022	0.009	0.011	0.024	0.020	0.029	0.033	0.036
Cl	0.000	0.002	0.001	0.002	0.002	0.001	0.001	0.002	0.001	0.001
Total	9.028	8.974	8.927	8.964	8.987	9.081	9.069	8.964	9.011	9.024

Table 4.4. White mica composition by EPMA analyses. Li and H_2O calculations from Monier and Robert (1986) and Tindle and Webb (1990). Cont'd

Alteration style	Ms-bearing	Ms-bearing	Ms-bearing	Ms-bearing	Ms-bearing	Ms-bearing	Ms-bearing	Ms-bearing	Ms-bearing
White mica host	Qz interstitial	Qz interstitial	Qz interstitial	Qz interstitial	Qz interstitial	Feldspar site	Feldspar site	Feldspar site	Mafic site
Batholith facies	Bethsaida	Bethsaida	Bethsaida	Bethsaida	Bethsaida	Bethsaida	Bethsaida	Bethsaida	Bethsaida
Al-OH wavelength (nm)	2198	2192	2198	2197	2194	2201	2196	2202	2207
Sample ID	2238819	2238819	2238819	2238819	2238819	2238863	2238863	2238863	2238863
Sample-spot ID	2238819-1	2238819-2	2238819-3	2238819-4	2238819-5	BC14284A-1	BC14284A-2	BC14284A-3	BC14284A-4
# of analyses	3	2	3	2	2	2	2	2	2
Element-oxide composition determined by EPMA (wt.%)									
SiO_2	46.63	46.17	46.58	46.87	46.41	47.57	48.32	48.28	47.90
TiO_2	0.28	0.05	0.12	0.04	0.24	0.06	0.01	0.09	1.13
Al_2O_3	33.30	31.87	31.79	32.29	32.98	32.24	33.03	32.93	30.21
FeO	2.98	4.37	4.38	4.56	3.51	2.24	1.99	2.06	3.33
MnO	0.05	0.08	0.04	0.06	0.05	0.08	0.06	0.10	0.08
MgO	0.44	0.50	0.56	0.54	0.47	1.16	0.97	0.93	1.39
CaO	0.01	0.00	0.03	0.01	0.01	0.00	0.01	0.06	0.02
Na_2O	0.23	0.18	0.24	0.21	0.35	0.12	0.09	0.13	0.16
K_2O	11.20	11.03	10.99	10.87	10.99	11.19	11.06	10.95	10.97
F	0.11	0.02	0.10	0.16	0.14	0.33	0.18	0.27	0.08
Cl	0.01	0.01	0.01	0.02	0.02	0.00	0.03	0.01	0.04
Cr_2O_3	0.02	0.00	0.00	0.00	0.00	0.00	0.00	0.01	0.01
Li_2O	0.00	0.00	0.00	0.01	0.01	0.03	0.01	0.02	0.00
H_2O	4.39	4.36	4.35	4.35	4.36	4.29	4.42	4.38	4.40
Total	99.64	98.63	99.18	99.99	99.54	99.31	100.16	100.21	99.72
Element concentration in white mica structural formula (apfu, based on 11 O equivalent)									
Si	3.144	3.166	3.176	3.168	3.141	3.206	3.214	3.212	3.232
^{iv}Al	0.856	0.834	0.824	0.832	0.859	0.794	0.786	0.788	0.768
^{vi}Al	1.790	1.741	1.730	1.741	1.771	1.767	1.804	1.795	1.634
Ti	0.014	0.002	0.006	0.002	0.012	0.003	0.000	0.004	0.057
Cr	0.001	0.000	0.000	0.000	0.000	0.000	0.000	0.001	0.000
Fe	0.168	0.251	0.250	0.258	0.199	0.126	0.111	0.114	0.188
Mn	0.003	0.005	0.002	0.003	0.003	0.005	0.004	0.005	0.005
Mg	0.044	0.051	0.057	0.054	0.047	0.116	0.096	0.093	0.140
Li	0.000	0.000	0.000	0.004	0.002	0.008	0.002	0.005	0.000
Ca	0.001	0.000	0.002	0.001	0.001	0.000	0.000	0.004	0.001
Na	0.030	0.023	0.032	0.028	0.046	0.016	0.011	0.017	0.022
K	0.963	0.965	0.956	0.937	0.949	0.962	0.938	0.929	0.944
OH	1.975	1.995	1.977	1.963	1.968	1.930	1.959	1.943	1.979
F	0.024	0.004	0.021	0.035	0.030	0.070	0.037	0.056	0.017
Cl	0.001	0.001	0.001	0.002	0.002	0.000	0.004	0.001	0.004
Total	9.014	9.039	9.035	9.027	9.030	9.003	8.967	8.967	8.992

Table 4.4. White mica composition by EPMA analyses. Li and H_2O calculations from Monier and Robert (1986) and Tindle and Webb (1990). Cont'd

Alteration style	Ms-bearing	Ms-bearing	Ms-bearing	Ms-bearing	Ms-bearing	Ms-bearing	Ms-bearing
White mica host	Mafic site	Qz interstitial	Qz interstitial	Qz interstitial	Qz interstitial	Qz interstitial	Mafic site
Batholith facies	Bethsaida	Bethsaida	Bethsaida	Bethsaida	Bethsaida	Bethsaida	Bethsaida
Al-OH wavelength (nm)	2202	2199	2202	2197	2195	2197	2206
Sample ID	2238863	2238874	2238874	2238874	2238874	2238874	2238874
Sample-spot ID	BC14284A-5	BC14294A-1	BC14294A-2	BC14294A-3	BC14294A-4	BC14294A-5	BC14294A-6
# of analyses	2	3	3	3	3	3	2
Element-oxide composition determined by EPMA (wt.%)							
SiO_2	49.04	45.99	45.53	45.79	45.63	45.28	47.46
TiO_2	0.44	0.42	0.31	0.43	0.21	0.48	0.62
Al_2O_3	31.10	32.93	32.98	32.95	33.19	33.00	30.55
FeO	2.43	4.07	4.09	3.99	3.73	3.92	4.06
MnO	0.08	0.03	0.05	0.02	0.04	0.06	0.06
MgO	1.47	0.87	0.84	0.85	0.80	0.92	1.32
CaO	0.02	0.00	0.00	0.00	0.00	0.00	0.01
Na_2O	0.16	0.50	0.49	0.56	0.40	0.54	0.27
K_2O	10.80	10.89	10.97	10.90	11.08	10.72	10.73
F	0.14	0.16	0.05	0.27	0.33	0.23	0.30
Cl	0.01	0.00	0.00	0.00	0.01	0.00	0.01
Cr_2O_3	0.01	0.01	0.02	0.01	0.01	0.02	0.00
Li_2O	0.00	0.03	0.00	0.01	0.03	0.01	0.05
H_2O	4.43	4.37	4.39	4.31	4.26	4.30	4.29
Total	100.12	100.26	99.74	100.08	99.72	99.48	99.72
Element concentration in white mica structural formula (apfu, based on 11 O equivalent)							
Si	3.268	3.103	3.090	3.097	3.096	3.079	3.212
^{iv}Al	0.732	0.897	0.910	0.903	0.904	0.921	0.788
^{vi}Al	1.710	1.721	1.729	1.724	1.750	1.725	1.650
Ti	0.022	0.021	0.016	0.022	0.011	0.025	0.032
Cr	0.001	0.001	0.001	0.001	0.001	0.001	0.000
Fe	0.135	0.230	0.232	0.226	0.211	0.223	0.230
Mn	0.004	0.002	0.003	0.001	0.002	0.003	0.003
Mg	0.146	0.087	0.085	0.086	0.081	0.093	0.133
Li	0.000	0.007	0.000	0.002	0.008	0.002	0.014
Ca	0.001	0.000	0.000	0.000	0.000	0.000	0.001
Na	0.021	0.065	0.065	0.073	0.053	0.072	0.036
K	0.918	0.938	0.950	0.940	0.959	0.930	0.927
OH	1.969	1.965	1.989	1.942	1.929	1.951	1.935
F	0.030	0.034	0.011	0.057	0.070	0.049	0.064
Cl	0.001	0.000	0.000	0.001	0.001	0.000	0.001
Total	8.958	9.071	9.082	9.075	9.076	9.074	9.026

Table 4.4. White mica composition by EPMA analyses. Li and H_2O calculations from Monier and Robert (1986) and Tindle and Webb (1990). Cont'd

Alteration style	Propylitic	Propylitic	Propylitic	Propylitic	Propylitic	Propylitic	Propylitic	Propylitic	Propylitic
White mica host	Feldspar site	Interstitial	Feldspar site	Interstitial	Feldspar site	Feldspar site	Feldspar site	Feldspar site	Feldspar site
Batholith facies	Bethsaida	Bethsaida	Bethsaida	Bethsaida	Bethsaida	Bethsaida	Bethsaida	Bethsaida	Bethsaida
Al-OH wavelength (nm)	2196	2195	2195	2195	2200	2195	2197	2198	2197
Sample ID	2238751	2238751	2238751	2238751	2238751	2238752	2238752	2238752	2238752
Sample-spot ID	BC14184H-1	BC14184H-2	BC14184H-4	BC14184H-5	BC14184H-6	BC14185H-1	BC14185H-2	BC14185H-3	BC14185H-4
# of analyses	3	2	3	2	2	5	4	2	4
Element-oxide composition determined by EPMA (wt.%)									
SiO_2	49.17	46.19	47.38	45.67	49.63	46.41	49.23	47.58	46.87
TiO_2	0.05	0.03	0.01	0.02	0.02	0.06	0.03	0.02	0.08
Al_2O_3	32.84	34.75	30.24	34.34	29.70	33.83	31.84	32.05	34.32
FeO	0.86	2.33	3.69	2.36	2.34	3.32	1.41	1.70	1.87
MnO	0.05	0.11	0.12	0.01	0.01	0.02	0.05	0.00	0.04
MgO	1.14	0.20	1.62	0.13	1.77	0.27	1.44	1.17	0.56
CaO	0.05	0.03	0.08	0.04	0.07	0.04	0.04	0.07	0.03
Na_2O	0.35	0.20	0.14	0.16	0.22	0.22	0.28	0.11	0.21
K_2O	10.76	10.85	11.24	11.03	10.63	10.92	10.63	10.12	11.22
F	0.13	0.21	0.06	0.12	0.33	0.03	0.09	0.12	0.10
Cl	0.02	0.01	0.01	0.02	0.05	0.02	0.02	0.02	0.02
Cr_2O_3	0.01	0.01	0.02	0.01	0.00	0.01	0.04	0.00	0.00
Li_2O	0.00	0.00	0.00	0.00	0.05	0.00	0.01	0.00	0.01
H_2O	4.46	4.35	4.36	4.34	4.29	4.43	4.46	4.34	4.43
Total	99.89	99.26	98.99	98.26	99.11	99.56	99.56	97.31	99.76
Element concentration in white mica structural formula (apfu, based on 11 O equivalent)									
Si	3.255	3.111	3.232	3.111	3.338	3.129	3.276	3.238	3.136
^{iv}Al	0.745	0.889	0.768	0.889	0.662	0.871	0.724	0.762	0.864
^{vi}Al	1.816	1.869	1.663	1.867	1.692	1.818	1.773	1.808	1.843
Ti	0.002	0.001	0.001	0.001	0.001	0.003	0.001	0.001	0.004
Cr	0.000	0.000	0.001	0.001	0.000	0.000	0.002	0.000	0.000
Fe	0.048	0.131	0.211	0.135	0.132	0.188	0.078	0.097	0.105
Mn	0.003	0.006	0.007	0.001	0.001	0.001	0.003	0.000	0.002
Mg	0.112	0.020	0.165	0.013	0.177	0.027	0.143	0.118	0.056
Li	0.000	0.000	0.000	0.000	0.014	0.000	0.003	0.000	0.002
Ca	0.004	0.002	0.006	0.003	0.005	0.003	0.003	0.005	0.002
Na	0.045	0.026	0.019	0.022	0.028	0.029	0.035	0.015	0.027
K	0.909	0.932	0.978	0.958	0.912	0.940	0.902	0.879	0.958
OH	1.971	1.954	1.985	1.971	1.923	1.992	1.979	1.971	1.976
F	0.027	0.045	0.014	0.026	0.071	0.006	0.020	0.027	0.022
Cl	0.002	0.001	0.002	0.003	0.006	0.002	0.002	0.002	0.003
Total	8.939	8.988	9.050	9.000	8.961	9.008	8.944	8.923	9.000

Table 4.4. White mica composition by EPMA analyses. Li and H_2O calculations from Monier and Robert (1986) and Tindle and Webb (1990). Cont'd

Alteration style	Propylitic	Propylitic	Propylitic	Propylitic	Propylitic	Propylitic	Propylitic	Propylitic
White mica host	Feldspar site	Feldspar site	Feldspar site	Feldspar site	Feldspar site	Feldspar site	Ep interstitial	Ep interstitial
Batholith facies	Bethsaida	Guichon	Guichon	Guichon	Guichon	Guichon	Guichon	Guichon
Al-OH wavelength (nm)	2195	2195	2195	2195	2198	2196	2202	2202
Sample ID	2238752	2238827	2238827	2238827	2245249	2245249	2245282	2245282
Sample-spot ID	BC14185H-5	BC14252A-1	BC14252A-2	BC14252A-4	2015KB005-1	2015KB005-2	2015KB043A-1	2015KB043A-2
# of analyses	3	1	2	1	2	2	3	2
Element-oxide composition determined by EPMA (wt.%)								
SiO_2	48.59	47.34	45.97	46.74	46.60	48.07	46.18	47.14
TiO_2	0.03	0.06	0.03	0.06	0.03	0.03	0.16	0.21
Al_2O_3	34.12	35.04	36.25	35.76	36.03	32.21	30.17	29.87
FeO	0.90	0.97	0.62	1.06	0.63	2.16	5.28	5.32
MnO	0.07	0.00	0.07	0.00	0.05	0.00	0.00	0.04
MgO	0.92	0.46	0.13	0.12	0.28	1.34	1.18	1.21
CaO	0.06	0.01	0.06	0.05	0.03	0.03	0.05	0.08
Na_2O	0.16	0.17	0.15	0.16	0.13	0.21	0.25	0.26
K_2O	10.81	11.22	10.88	11.20	11.60	11.41	10.96	10.22
F	0.20	0.32	0.04	0.02	0.10	0.10	0.07	0.13
Cl	0.02	0.00	0.00	0.03	0.01	0.00	0.02	0.03
Cr_2O_3	0.03	0.00	0.01	0.00	0.02	0.05	0.00	0.01
Li_2O	0.02	0.02	0.00	0.00	0.00	0.00	0.00	0.00
H_2O	4.45	4.36	4.45	4.49	4.46	4.44	4.31	4.31
Total	100.38	99.98	98.65	99.68	99.98	100.06	98.63	98.84
Element concentration in white mica structural formula (apfu, based on 11 O equivalent)								
Si	3.202	3.145	3.084	3.112	3.097	3.214	3.187	3.229
^{iv}Al	0.798	0.855	0.916	0.888	0.903	0.786	0.813	0.771
^{vi}Al	1.852	1.888	1.949	1.918	1.919	1.752	1.640	1.641
Ti	0.002	0.003	0.001	0.003	0.001	0.002	0.008	0.011
Cr	0.001	0.000	0.001	0.000	0.001	0.003	0.000	0.001
Fe	0.050	0.054	0.035	0.059	0.035	0.121	0.305	0.305
Mn	0.004	0.000	0.004	0.000	0.003	0.000	0.000	0.002
Mg	0.090	0.046	0.013	0.012	0.028	0.134	0.121	0.124
Li	0.005	0.006	0.000	0.000	0.000	0.000	0.000	0.000
Ca	0.004	0.001	0.004	0.004	0.002	0.002	0.003	0.006
Na	0.020	0.021	0.020	0.020	0.017	0.028	0.034	0.034
K	0.909	0.951	0.931	0.952	0.984	0.973	0.964	0.894
OH	1.957	1.932	1.992	1.993	1.978	1.979	1.982	1.969
F	0.041	0.068	0.008	0.004	0.021	0.021	0.015	0.028
Cl	0.003	0.000	0.000	0.003	0.001	0.000	0.003	0.003
Total	8.938	8.970	8.957	8.968	8.990	9.014	9.077	9.018

Table 4.4. White mica composition by EPMA analyses. Li and H_2O calculations from Monier and Robert (1986) and Tindle and Webb (1990). Cont'd

Alteration style	Propylitic	Propylitic	Propylitic	Propylitic	Propylitic	Propylitic	Propylitic
White mica host	Ep interstitial	Ep interstitial	Feldspar site	Qz interstitial	Feldspar site	Feldspar site	Feldspar site
Batholith facies	Guichon	Guichon	Guichon	Guichon	Guichon	Guichon	Guichon
Al-OH wavelength (nm)	2202	2202	2200	2210	2210	2210	2198
Sample ID	2245282	2245282	2245331	2245331	2245331	2245331	2245361
Sample-spot ID	2015KB043A-3	2015KB043A-4	2015KB085-1	2015KB085-2	2015KB085-3	2015KB085-4	2015KB111-3
# of analyses	2	2	1	2	2	2	2
Element-oxide composition determined by EPMA (wt.%)							
SiO_2	46.43	45.74	48.03	50.02	48.31	48.49	50.78
TiO_2	0.08	0.18	0.10	0.04	0.04	0.09	0.02
Al_2O_3	29.93	29.72	33.25	28.48	29.79	28.58	30.98
FeO	5.79	5.28	1.36	4.04	3.83	4.85	1.30
MnO	0.01	0.01	0.33	0.02	0.08	0.03	0.02
MgO	1.22	1.30	0.87	1.09	1.14	0.88	1.87
CaO	0.01	0.01	0.02	0.01	0.02	0.06	0.06
Na_2O	0.18	0.22	0.12	0.17	0.16	0.14	0.10
K_2O	11.02	10.75	11.43	11.19	10.43	10.27	10.58
F	0.00	0.00	0.13	0.15	0.06	0.07	0.23
Cl	0.01	0.01	0.02	0.02	0.02	0.02	0.02
Cr_2O_3	0.00	0.00	0.00	0.01	0.04	0.00	0.01
Li_2O	0.00	0.00	0.00	0.01	0.00	0.00	0.03
H_2O	4.35	4.30	4.44	4.36	4.36	4.32	4.44
Total	99.03	97.51	100.08	99.61	98.27	97.79	100.44
Element concentration in white mica structural formula (apfu, based on 11 O equivalent)							
Si	3.197	3.190	3.200	3.379	3.297	3.338	3.341
^{iv}Al	0.803	0.810	0.800	0.621	0.703	0.662	0.659
^{vi}Al	1.626	1.633	1.810	1.648	1.693	1.657	1.742
Ti	0.004	0.009	0.005	0.002	0.002	0.005	0.001
Cr	0.000	0.000	0.000	0.000	0.002	0.000	0.000
Fe	0.333	0.308	0.076	0.228	0.218	0.279	0.072
Mn	0.001	0.000	0.019	0.001	0.005	0.002	0.001
Mg	0.125	0.135	0.086	0.110	0.116	0.090	0.184
Li	0.000	0.000	0.000	0.002	0.000	0.000	0.008
Ca	0.001	0.001	0.001	0.001	0.001	0.004	0.005
Na	0.023	0.029	0.015	0.023	0.022	0.019	0.013
K	0.968	0.956	0.971	0.964	0.908	0.901	0.887
OH	1.998	1.999	1.972	1.965	1.985	1.983	1.949
F	0.000	0.000	0.026	0.032	0.013	0.015	0.048
Cl	0.002	0.001	0.002	0.003	0.002	0.002	0.002
Total	9.081	9.072	8.983	8.979	8.967	8.958	8.912

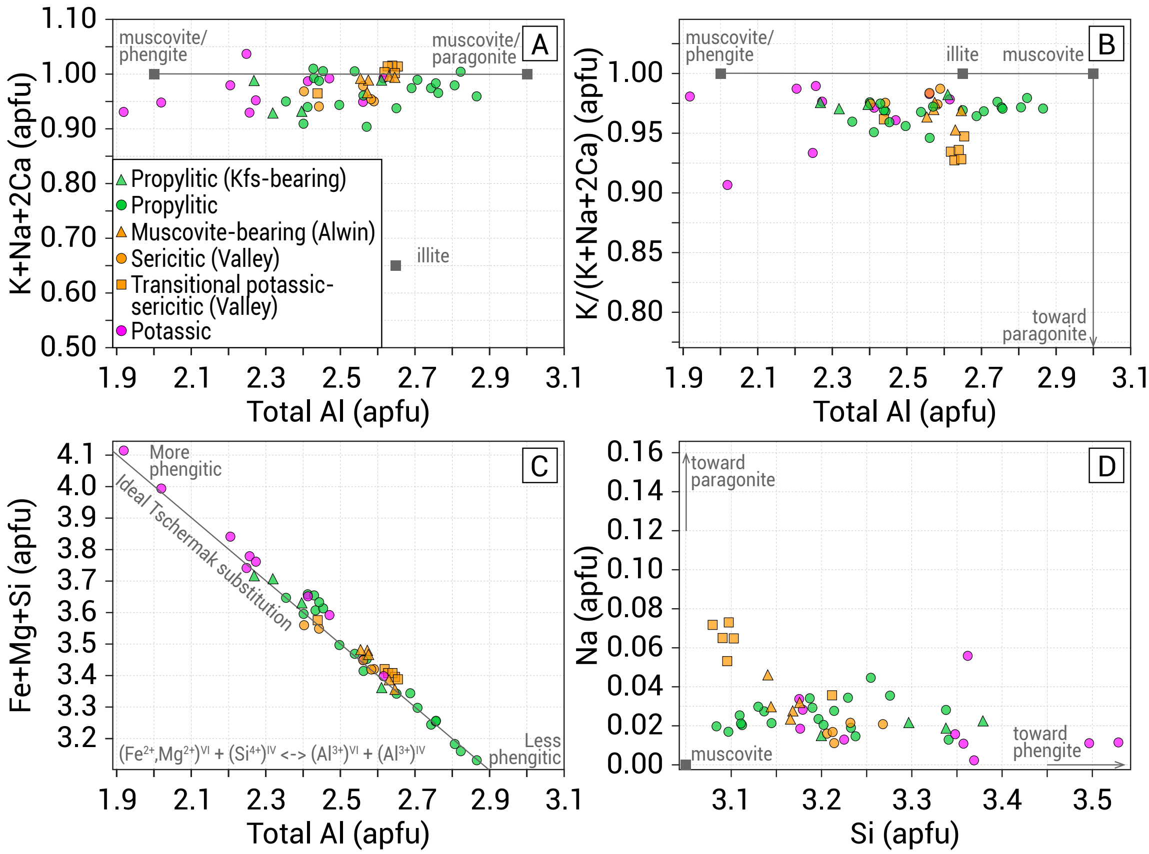

Figure 4.10. Major element variations of white mica composition in atoms per formula unit (apfu): A) K+Na+2Ca versus total Al, B) K/(K+Na+2Ca) versus total Al, C) Fe+Mg+Si versus total Al, and D) Na versus Si. Symbols are coloured according to the alteration assemblage present.

middle row), which are directly related to the main Cu mineralization at Valley, Lornex and Highmont (Osatenko and Jones, 1976; Reed and Jambor, 1976; Waldner et al., 1976; McMillan, 1985; Alva Jimenez, 2011; Byrne et al., 2013). Veins and selvages are generally <5 and <7 cm wide, respectively. These veins are equivalent to the transitional potassic-sericitic assemblage of Seedorff et al. (2005), or to the early halo (EH; Proffett, 2009) or early dark micaceous (EDM; Meyer, 1965; Brimhall, 1977; Rusk et al., 2008) veins documented at the Yerington and Butte deposits, respectively.

The second muscovite-bearing mineral assemblage consists of fracture-controlled to pervasive fine to locally coarse-grained grey to pale green white

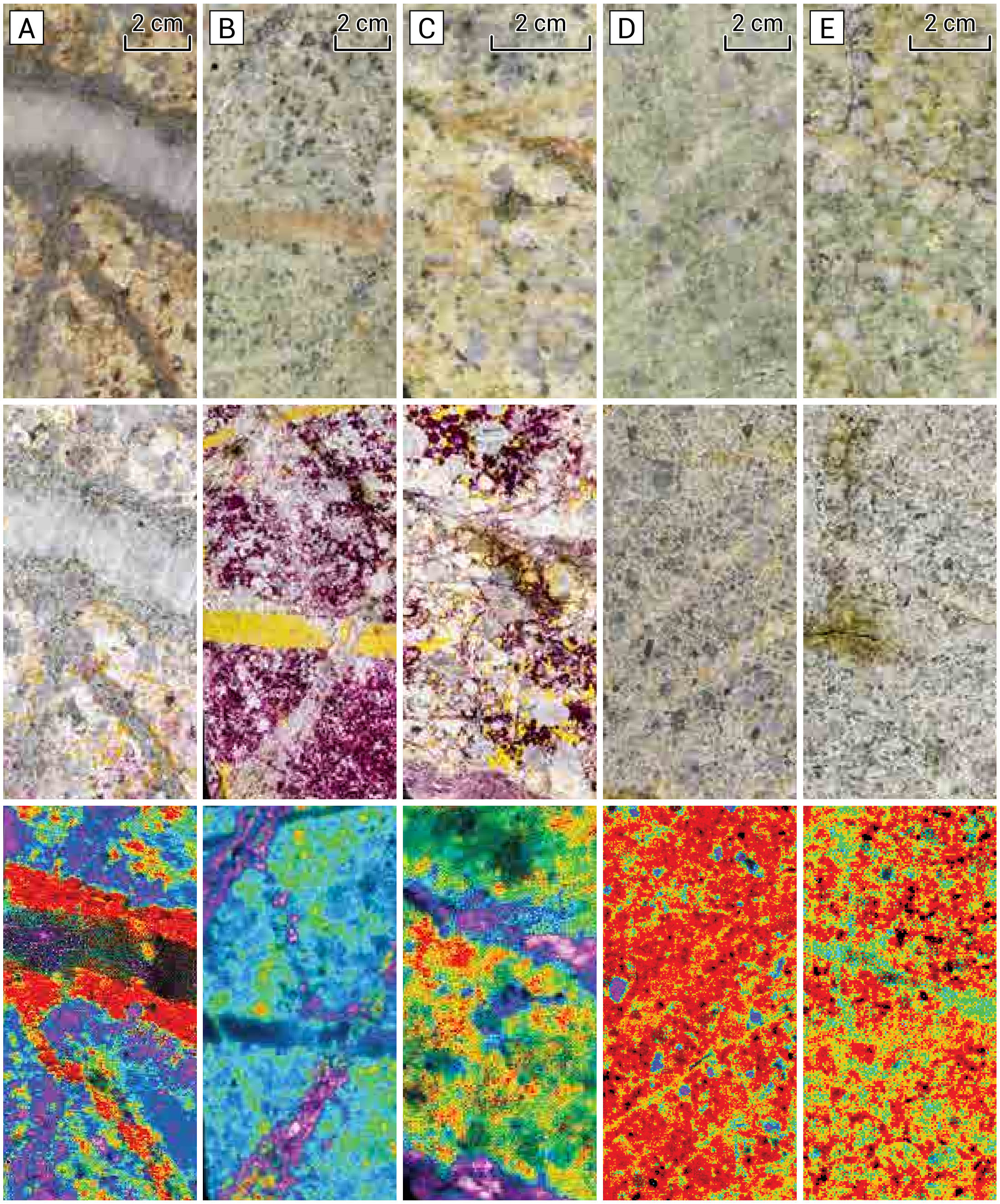

Sample ID: 2238870	**Sample ID:** 2232432	**Sample ID:** 2238960	**Sample ID:** 2232435	**Sample ID:** 2758869
Lithology: Bethsaida	**Lithology:** Bethsaida	**Lithology:** QFP	**Lithology:** Bethsaida	**Lithology:** Bethsaida
Alteration: Muscovite	**Alteration:** Muscovite	**Alteration:** Muscovite	**Alteration:** Muscovite	**Alteration:** Muscovite
Deposit: Valley	**Deposit:** Lornex	**Deposit:** Valley	**Deposit:** Valley	**Distance to deposit:** 5440 m (Highmont) Yubet Cu occurrence

Figure 4.11. Muscovite-altered samples. Unstained slab photo (upper row), stained slab photo (middle row) and hyperspectral scan showing the Al-OH wavelength (bottom row). Distance to the closest deposit increases from left to right. The legend for stain and hyperspectral scan colors is provided in Figure 4.4.

mica with minor chlorite in mafic sites (Figure 4.11B, C and D), typically associated with syn-mineralization structures and thick (>10 cm) banded quartz–chalcopyrite–molybdenite ± pyrite veins. This alteration is equivalent to a sericitic or phyllic assemblage (Seedorff et al., 2005). Sericitic alteration is located peripheral to and overprints the earlier transitional potassic-sericitic coarse-grained muscovite at Valley, Lornex and Highmont. Fracture-controlled to pervasive fine to coarse-grained pale green white mica and chlorite alteration also typically occurs at the smaller district Cu occurrences. Accessory alteration minerals at these occurrences include carbonate, quartz, specular hematite, magnetite, epidote and tourmaline.

Muscovite-bearing alteration forms up to several hundred meters away from the HVC porphyry deposits, and locally forms small alteration zones (<10s of meters) at some of the district Cu occurrences (Figure 4.7, Figure 4.11E) (Lesage et al., 2019).

4.6.3.1. Short-wave infrared spectroscopy

The Al-OH absorption feature of the coarse-grained, grey white mica present in quartz–bornite–chalcopyrite vein selvages (i.e., transitional potassic-sericitic alteration, or EH/EDM vein equivalent) is characterized by a wavelength range between 2193 and 2202 nm (Figure 4.5A) in hyperspectral data, with the most abundant wavelengths between 2195 and 2198 nm (Figure 4.11A). Fine to locally medium or coarse-grained white mica selvages around hairline fractures or thin (<0.5 cm) quartz–chalcopyrite–molybdenite ± pyrite veins (sericitic alteration; Figure 4.11A, B and C) have a different spectral signature, characterized by Al-OH wavelength >2207 nm (Table 4.3, Figure 4.5A). The timing relationship between the two types of white mica is not well constrained, however longer wavelength white mica hairline fracture selvages appear to cross-cut the shorter wavelength white mica vein selvages. Long wavelength white mica along hairline fractures typically occurs in samples that are also characterized by 2202–2207 nm Al-OH wavelengths in the groundmass (i.e., pale to dark blue colors in the hyperspectral scans in Figure 4.11A and B). This is likely related to kaolinite as a pervasive intermediate argillic overprint; kaolinite interference is discussed in the next section.

The pervasive fine to locally coarse-grained grey to pale green white mica alteration (i.e., the sericitic or phyllic equivalent) has a Al-OH wavelength range of 2193–2202 nm (Figure 4.11D), comparable to the signature of coarse-grained white mica in quartz–bornite–chalcopyrite vein selvages. Wherever white mica replaces biotite, the Al-OH wavelength is longer at 2205–2210 nm (blue–purple blebs in the bottom row of Figure 4.11D), which indicates that the white mica in mafic sites is phengitic rather that muscovitic. This is related to the presence of more Fe in primary biotite than in felsic sites, which was incorporated into the white mica alteration minerals.

White mica alteration in muscovite-bearing alteration at the district Cu occurrences has an Al-OH wavelength signature similar to that of the HVC porphyry deposits, with a wavelength range between 2193 and 2202 nm. The longer wavelengths (2198–2202 nm) within the wider range, however, are typically more abundant at the Cu occurrences than within the porphyry deposits (Figure 4.11D vs. E).

The TerraSpec® reflectance spectra of muscovite-bearing rocks contain Al-OH wavelengths that are characterized by a median of 2205.6 nm and an IQR of 2203.0–2207.4 nm (Figure 4.6A). The depth of the Al-OH absorption feature is the greatest in muscovite-bearing alteration, with a hqd IQR between 0.30 and

0.46 (Figure 4.6B). As mentioned above, this wavelength range and absorption depth are interpreted to be related to interference caused by the presence of kaolinite in the TerraSpec® field-of-view and will be discussed in the next section. The relatively shallow water absorption feature (IQR of 0.14–0.29, Figure 4.6D) in the TerraSpec® field-of-view is consistent with the presence of highly crystalline white mica and kaolinite, because neither of these minerals contain water in their crystal structure.

4.6.3.2. White mica chemistry

Electron microprobe analyses were conducted to establish compositions of white mica minerals from the transitional potassic-sericitic assemblage (Figure 4.9D) and the sericitic assemblage (Figure 4.9E), as defined in Table 4.2. White micas from the transitional potassic-sericitic assemblage are medium to coarse-grained and occur as vein material or texturally-destructive selvage alteration alongside quartz. White micas from the sericitic assemblage are fine-grained and occur as strong pervasive alteration in which relict plagioclase outlines remain recognizable. White micas from texturally-destructive pervasive coarse-muscovite alteration at the Alwin Cu occurrence were also analyzed (Figure 4.9F).

The measured compositional range is $(K_{0.92\text{-}0.97},Na_{0.01\text{-}0.07})(Fe_{0.11\text{-}0.26},Mg_{0.04\text{-}0.15},{}^{VI}Al_{1.63\text{-}1.80})({}^{IV}Al_{0.73\text{-}0.92}Si_{3.08\text{-}3.27})O_{10}(OH)_2$, the interlayer cation site (K+Na+2Ca) occupancy is 0.94–1.02 apfu, and the octahedral site (Fe+Mg+^{VI}Al) occupancy is 1.96–2.05 apfu (Table 4.4). Calcium content is negligible in all the analyzed white micas. Sodium content is highest in white micas from the transitional potassic-sericitic assemblage and lowest in white micas from the sericitic assemblage, whereas Si content is lowest in transitional potassic-sericitic white micas and highest in sericitic white micas (Figure 4.10D). This indicates more paragonitic compositions and suggests higher temperatures of formation (Guidotti and Sassi, 1976; Guidotti, 1984) for the transitional potassic-sericitic assemblage, which is consistent with observations from (Alva Jimenez, 2011). White micas from the Alwin Cu occurrence are characterized by Na contents that are intermediate between the transitional potassic-sericitic and sericitic white micas. The Fe+Mg+Mn content ranges between 0.21 and 0.37 apfu. White mica minerals with the highest Fe+Mg+Mn content (0.29–0.37 apfu) replace primary biotite (Figure 4.15B), which emphasizes the compositional control exerted by the protolith. Aside from the white micas that are hosted in mafic sites, the most phengitic white micas from the muscovite-bearing alteration assemblages are from the Alwin Cu occurrence (Figure 4.10C).

4.6.4. Intermediate argillic

Intermediate argillic alteration in the HVC district occurs as pervasive alteration, typically more intense near structures, and is characterized by kaolinite, montmorillonite, white mica and minor chlorite (Table 4.2) (Jambor and Delabio, 1978). Modal mineral percentages determined by Rietveld refinement XRD for four strongly-altered samples (Table 4.5) indicate abundant white mica, kaolinite and carbonate minerals, but montmorillonite was not detected. Intermediate argillic alteration is only present within the porphyry deposits and overprints all other alteration assemblages. It is abundant in the Valley, Lornex and Highmont deposits, but is rare at Bethlehem.

4.6.4.1. Short-wave infrared spectroscopy

Hyperspectral scans of samples that contain intermediate argillic alteration are strongly influenced by the modal percentage of kaolinite in the sample. The reflectance spectra of kaolinite is characterized by a strong Al-OH absorption feature at ~2206 nm (GMEX, 2008). Because of its very high reflectance, even at very low abundances the kaolinite Al-OH absorption feature interferes with that of white mica. An increase in kaolinite modal percentage results in a progressive increase in the 2202–2207 nm Al-OH wavelength pixel percentage and a decrease in the pixel percentage of other wavelengths in hyperspectral scan images (Figure 4.5A, Figure 4.12). For example the hyperspectral scan of sample BC14294A, composed of 2.6% kaolinite and 32.6% white mica (Figure 4.12A), contains 56% of pixels characterized by a 2202–2207 nm wavelength (Table 4.3), whereas the scan of sample BC14295A, composed of 10.6% kaolinite and 13.3% white mica (Figure 4.12D), contains 99% of pixels in the 2202–2207 nm range and 96% between 2204 and 2206 nm (Table 4.3).

The TerraSpec® reflectance spectra of samples with intermediate argillic alteration are also characterized by Al-OH wavelengths that reflect the presence of kaolinite, with a median of 2207.4 nm and an IQR of 2206.4–2208.0 nm (Figure 4.6A). The Al-OH absorption feature depth is high compared to the other alteration assemblages (except for muscovite-bearing alteration), with a hqd IQR of 0.24–0.38 (Figure 4.6B). The water absorption feature is very different than the other alteration assemblages, however, with an absence of absorption feature in 47% of the samples that is consistent with the presence of kaolinite, and a deep absorption feature in the remaining 27 samples (hqd IQR of 0.27–0.44, Figure 4.6D). The deep water absorption feature is likely caused by the presence of montmorillonite in the TerraSpec® field-of-view, which was documented in the intermediate argillic assemblage in the Valley deposit by Jambor and Delabio (1978).

Table 4.5.Modal mineral abundances determined using Rietveld Refinement (X-ray diffraction).

Sample ID	Quartz (%)	Plagioclase (%)	Illite + Muscovite (%)	K-feldspar (%)	Kaolinite (%)	Clinozoisite (%)	Gypsum (%)	Calcite (%)	Dolomite (%)	Ankerite (%)	Siderite (%)	Pyrite (%)	Hematite (%)
BC14278V	37.3	22.0	24.1		7.5			6.8				2.3	
BC14281B	46.4	14.6	22.8		4.1			10.7	0.7			0.7	
BC14294A	40.8	9.5	32.6	4.2	2.6		5.1	2.6		2.5			
BC14295A	42.8	24.1	13.3		10.6	0.7		6.9		0.8	0.3	0.2	0.2

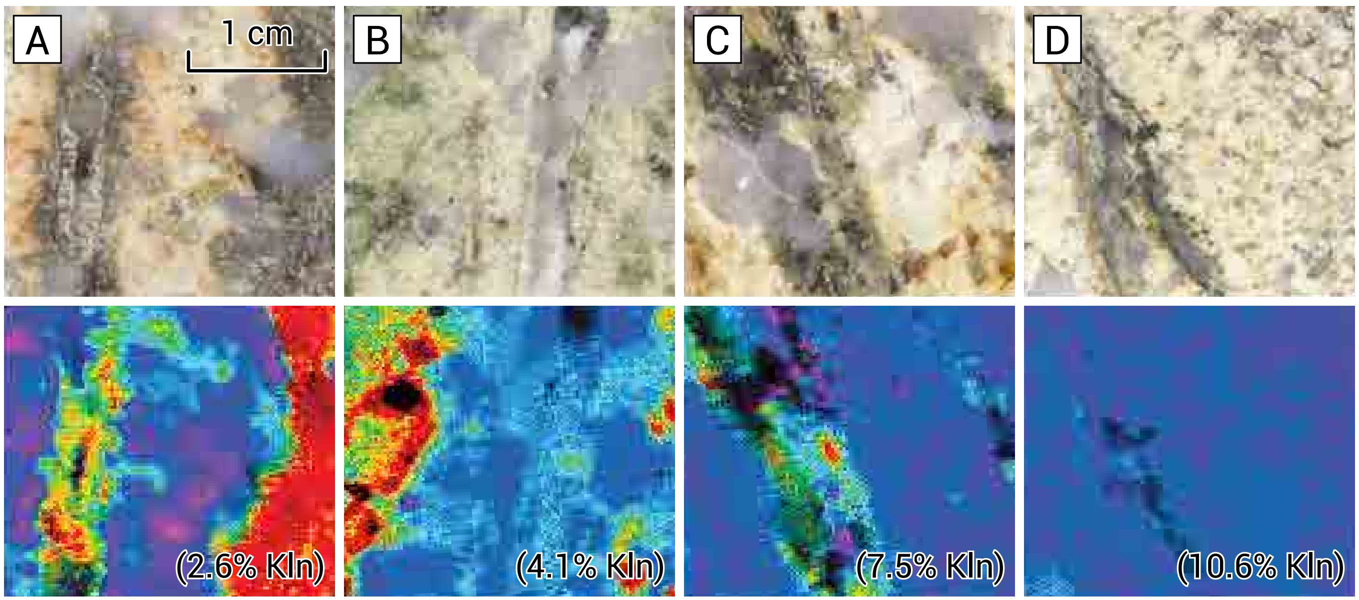

Figure 4.12. Intermediate argillic-altered samples. Unstained slab photo (upper row) and hyperspectral scan showing the Al-OH wavelength (bottom row): A) sample BC14294A, B) sample BC14281B, C) sample BC14278V, and D) sample BC14295A. Modal mineral abundances for these samples are presented in Table 4.5. Scale is the same for each sample. The legend for hyperspectral scan colors is provided in Figure 4.4.

4.6.5. Sodic-calcic alteration

Sodic-calcic alteration (Table 4.2) within 1 km of the HVC porphyry deposits is characterized by areas of pervasive albite–actinolite–titanite ± tourmaline ± diopside ± garnet alteration (Figure 4.13A). It is best developed at Bethlehem and Highmont. Diopside and garnet are rare and are generally retrograded to pumpellyite and chlorite (Byrne et al., 2017). District-scale sodic-calcic alteration is characterized by chlorite ± epidote veins with K-feldspar-destructive selvages of albite ± white mica-altered feldspars and chlorite ± epidote-altered mafic sites (Figure 4.13B, C and D) that extend up to 7 km beyond the deposits (Figure 4.7) (Byrne et al., 2017; Byrne, 2019; Lesage et al., 2019). Veins are typically <3 cm wide but are locally up to 5 cm wide, whereas selvages are typically <3 cm wide and locally up to 18 cm wide. Albite alteration tends to be restricted to the inner part of vein selvages. Selvages commonly have an outer zone of moderate to strong fine-grained pale green white mica alteration of plagioclase and chlorite alteration of mafic sites, which is interpreted to be a lower temperature propylitic overprint. Those sodic-calcic-altered samples that also have a propylitic overprint were classified as having propylitic alteration. Rocks with sodic-calcic alteration are enriched in H_2O, calcite, and Na_2O, as well as strongly to moderately depleted in K_2O and Fe_2O_3, and weakly depleted in MgO and CaO (Byrne, 2019).

4.6.5.1. Short-wave infrared spectroscopy

Hyperspectral scans show that the Al-OH wavelength of the white micas that formed as part of the sodic-calcic alteration assemblage ranges primarily between 2190 and 2202 nm (Table 4.3), but the most abundant wavelengths are in the 2192–2198 nm range (Figure 4.5B, Figure 4.13 bottom row). Scans

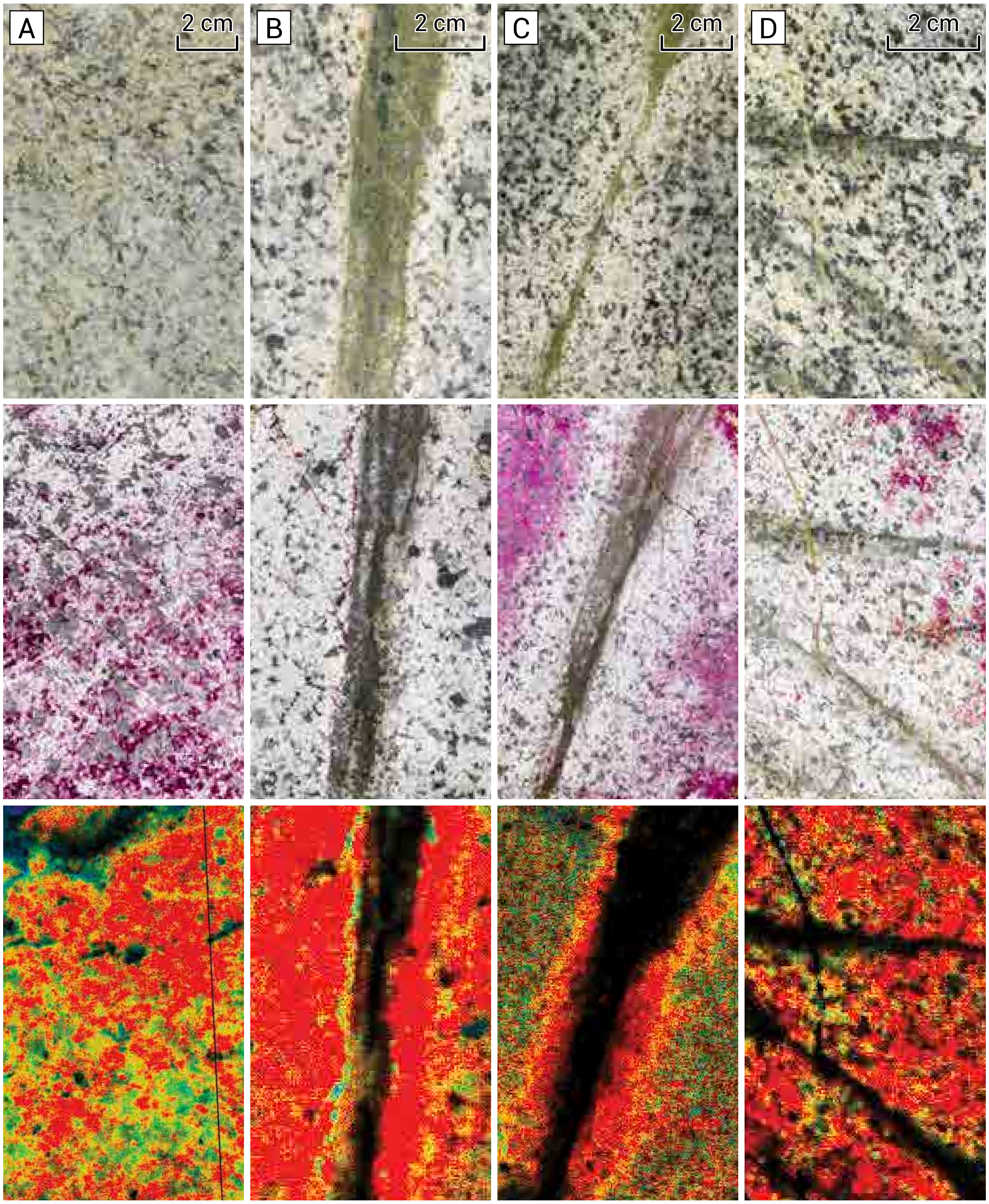

Sample ID: 2232426	**Sample ID:** 2245474	**Sample ID:** 2245302	**Sample ID:** 2245409
Lithology: Skeena	**Lithology:** Skeena	**Lithology:** Guichon	**Lithology:** Chataway
Alteration: Sodic-calcic	**Alteration:** Sodic-calcic	**Alteration:** Sodic-calcic	**Alteration:** Sodic-calcic
Distance to deposit: 0 m (Lornex)	**Distance to deposit:** 1651 m (Highmont)	**Distance to deposit:** 3055 m (Bethlehem)	**Distance to deposit:** 5918 m (Highmont)

Figure 4.13. Sodic-calcic-altered samples. Unstained slab photo (upper row), stained slab photo (middle row) and hyperspectral scan showing the Al-OH wavelength (bottom row). Distance to the closest deposit increases from left to right. The legend for stain and hyperspectral scan colors is provided in Figure 4.4.

also show that samples with fracture-controlled alteration are generally characterized by more abundant longer Al-OH wavelengths (>2202 nm) than samples with stronger pervasive alteration.

TerraSpec® reflectance spectra measured on sodic-calcic-altered samples contain Al-OH absorption features characterized by a median wavelength of 2201.0 nm and an IQR of 2198.3–2206.4 nm (Figure 4.6A). Sodic-calcic alteration yielded the TerraSpec® reflectance spectra that contain the lowest Al-OH wavelengths: six samples with intense pervasive alteration yielded wavelengths between 2190 and 2196 nm (Figure 4.6E and F). A shorter white mica Al-OH wavelength indicates that the composition of these micas is paragonitic (e.g., Herrmann et al., 2001), which is consistent with pervasive alteration that formed at high temperatures (>400°C; Dilles and Einaudi, 1992; Seedorff et al., 2005) from Na-rich seawater-derived fluids (Byrne, 2019). The addition of short wavelength paragonitic white mica in pervasive sodic-calcic alteration is not apparent in the hyperspectral data because of the abundance of equally short wavelength minerals in least-altered rocks, which overwhelms the alteration signal.

4.6.6. Propylitic alteration

Fracture-controlled propylitic alteration is ubiquitous in the GCB (Lesage et al., 2019). A domain of propylitic alteration that is >5% altered (Figure 4.7) covers an area ~50 km^2 in the center of the batholith, although weaker alteration also occurs outside this domain. Propylitic alteration is characterized by chlorite ± prehnite ± pumpellyite ± epidote veins and selvages in which plagioclase is altered to fine-grained, pale green white mica and minor calcite, and primary mafic minerals are altered to chlorite, vermiculite or epidote (Table 4.2). Primary

K-feldspar is largely stable in vein selvages (Figure 4.14 top and middle row). Propylitic alteration in the more mafic facies of the GCB (i.e., the Border, Guichon and Chataway facies) generally contains more abundant epidote, as well as rare epidote-bearing veins with selvages in which K-feldspar is the main alteration mineral. Propylitic veins are typically <2 cm wide, but locally to 15 cm, whereas vein selvages mostly range from <1 to 9 cm, but can be up to 50 cm wide. Lithogeochemical analyses show that except for local weak addition of H_2O and calcite, propylitic-altered rocks are indistinguishable from least-altered rocks (Byrne, 2019). This indicates that propylitic alteration minerals formed mainly through local redistribution of elements within the rocks, and not through metasomatism.

4.6.6.1. Short-wave infrared spectroscopy

The Al-OH wavelength signature of white micas in propylitic veins and selvages varies between 2193 nm and 2220 nm, however the most dominant wavelengths are in the 2195–2200 nm range (Figure 4.5B). Propylitic alteration is the only alteration assemblage in the HVC district that yields long Al-OH wavelengths (>2207 nm) outside the porphyry deposits (Table 4.3). Samples with sodic-calcic alteration also locally yield long wavelength white mica (Figure 4.5B), but textural evidence in the hyperspectral scans suggests that this is due to a propylitic overprint. Scans also show that the long wavelengths generally result from alteration near the vein, where the fluid–rock ratio was highest and the alteration is strongest (Figure 4.14 bottom row).

The median TerraSpec® reflectance spectra Al-OH wavelength is 2202.3 nm and the IQR ranges between 2199.9 nm and 2206.7 nm (Figure 4.6A). Consistent with the hyperspectral data, propylitic alteration yields the greatest number of

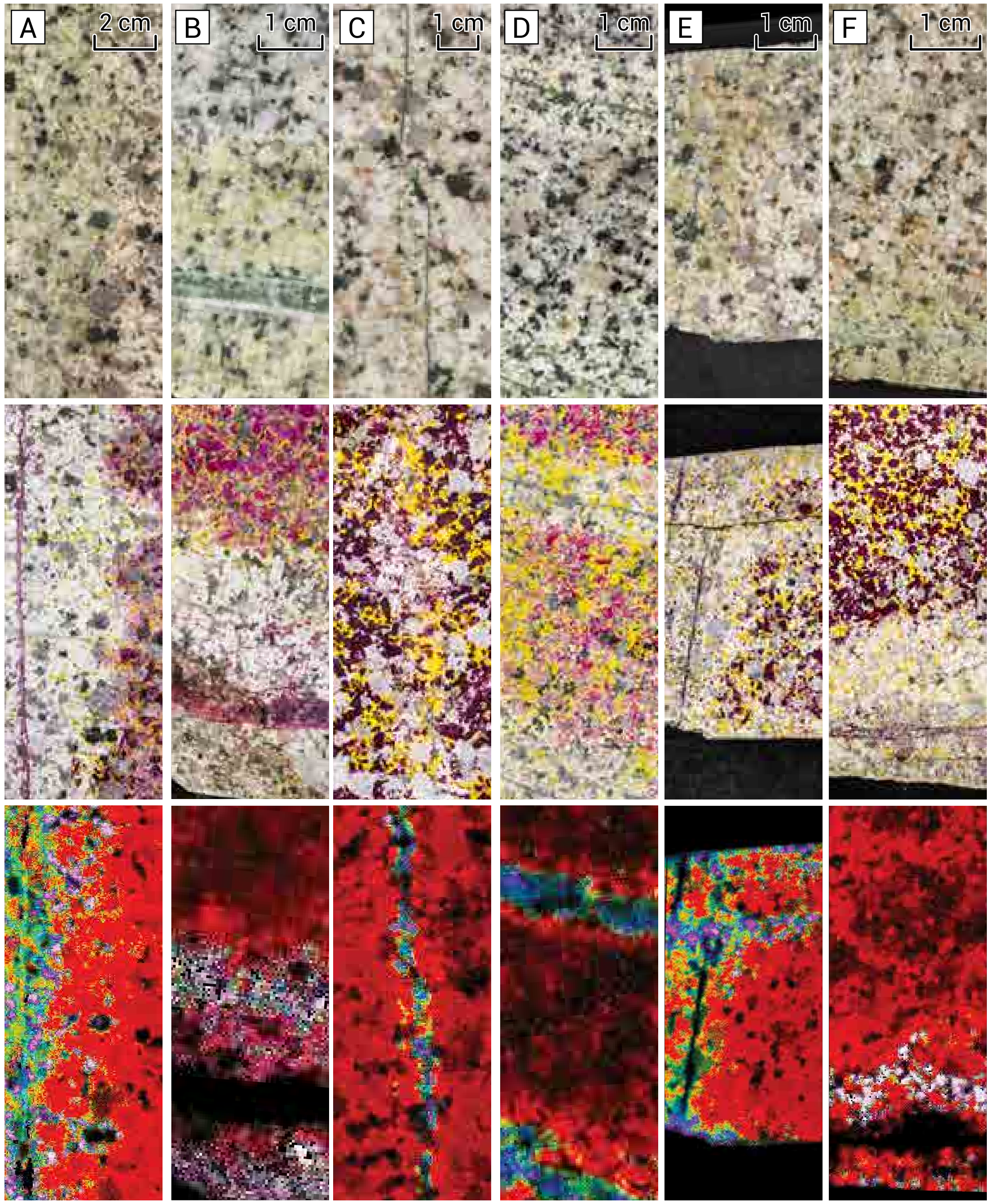

Sample ID: 2238783	**Sample ID:** 2245441	**Sample ID:** 2247945	**Sample ID:** 2245418	**Sample ID:** 2758890	**Sample ID:** 2758885
Lithology: Bethsaida	**Lithology:** Skeena	**Lithology:** Bethsaida	**Lithology:** Guichon-Chataway	**Lithology:** Bethsaida	**Lithology:** Bethsaida
Alteration: Propylitic	**Alteration:** Propylitic	**Alteration:** Propylitic	**Alteration:** Propylitic	**Alteration:** Propylitic	**Alteration:** Propylitic
Distance to deposit: 2339 m (Valley)	**Distance to deposit:** 3878 m (Highmont)	**Distance to deposit:** 4486 m (Highmont)	**Distance to deposit:** 7335 m (Highmont)	**Distance to deposit:** 7748 m (Highmont)	**Distance to deposit:** 8527 m (Highmont)

Figure 4.14. Propylitic-altered samples. Unstained slab photo (upper row), stained slab photo (middle row) and hyperspectral scan showing the Al-OH wavelength (bottom row). Distance to the closest deposit increases from left to right. The legend for stain and hyperspectral scan colors is provided in Figure 4.4.

measurements that are >2210 nm (Figure 4.6). In addition to muscovite-bearing and intermediate argillic alteration, which are restricted to within hundreds of meters of the porphyry deposits, propylitic white mica yields the deepest (IQR of 0.15–0.26, Figure 4.6B) and widest (IQR of 29.7–36.3 nm Figure 4.6C) Al-OH absorption features. The lesser 'sharpness' of the Al-OH absorption feature in samples with propylitic alteration suggests that the white mica minerals are less crystalline than those in the other alteration assemblages, which is also consistent with a lower temperature of formation (Digel and Gordon, 1995; Bird and Spieler, 2004; Seedorff et al., 2005).

4.6.6.2. White mica chemistry

Major and minor element compositions were determined by EPMA for fine-grained propylitic white mica minerals that occur in veins with epidote (Figure 4.9G), as well as for fine-grained white micas in propylitic vein selvages with K-feldspar (Figure 4.9M) or without it (Figure 4.9H to L). The measured compositional range is $(K_{0.88\text{-}0.98},Na_{0.01\text{-}0.05})(Fe_{0.04\text{-}0.33},Mg_{0.01\text{-}0.18},{}^{VI}Al_{1.63\text{-}1.95})({}^{IV}Al_{0.62\text{-}0.92}Si_{3.08\text{-}3.38})O_{10}(OH)_2$, the interlayer cation site (K+Na+2Ca) occupancy is 0.90–1.01 apfu, and the octahedral site ($Fe+Mg+{}^{VI}Al$) occupancy is 1.97–2.08 apfu (Table 4.4). Calcium content is <0.02 apfu in all propylitic white micas. The full occupancy of the interlayer cation site indicates that the analyzed white mica minerals are not illite (Figure 4.10A), whereas the high K content and low Na content indicate that they are muscovitic in composition. Tschermak substitution is an important process in propylitic white micas, as shown by the highly-variable Fe+Mg+Mn content (0.05–0.45 apfu), as well as Si and Al content (Figure 4.10C and D). Figure 4.10C shows that propylitic white mica composition includes the least phengitic white mica of all minerals analyzed, and overlaps with white micas from the muscovite-bearing alteration and some white micas from potassic alteration. Amongst all of the propylitic white mica minerals analyzed, those that occur in vein selvages with K-feldspar–epidote (Figure 4.9M) and those that occur in veins with epidote (i.e., interstitial, Figure 4.9G) are consistently more phengitic (Figure 4.10 and Figure 4.15C, respectively).

4.7. Discussion

4.7.1. White mica composition

Major and minor element compositions of white micas at HVC vary depending on their alteration assemblage and host mineral, but EPMA analyses show that all have muscovitic compositions. Based on vein distribution and orientations, and on the presence of Cu-Fe-sulfide minerals in the potassic and muscovite-bearing alteration assemblages, Lesage et al. (2019) interpreted these assemblages to have formed from magmatic fluids. Propylitic and sodic-calcic assemblages are interpreted to have formed from external fluids based on the minerals present, vein style and orientation (Lesage et al., 2019), as well as on their stable and radiogenic isotope signature (Byrne, 2019).

The composition of white micas from the potassic and muscovite-bearing assemblages provide information about the pH and temperature of the HVC magmatic fluids. Results presented in this study (Figure 4.10) are consistent with, and expand upon results from Alva Jimenez (2011).

Coarse-grained white micas that are part of the transitional potassic-sericitic assemblage from the center of the Valley deposit (sample 2238874; Figure 4.9D) are more paragonitic and less phengitic than later fine-grained white micas from the margin of the deposit, which are part of the sericitic assemblage (sample

2238863; Figure 4.9E). This compositional difference is likely due to a lower temperature of formation for the sericitic assemblage as well as its location further away from the source of the magmatic fluids. Fluids that caused sericitic alteration were likely more rock-buffered and therefore had a higher pH, and/or were more Fe-rich. White micas from the Alwin Cu occurrence (sample 2238819; Figure 4.9F) are more phengitic than those from the sericitic assemblage. This suggests that the location of the fluid source at the Alwin occurrence was likely at depth and was located farther than the distance between sample 2238863 and the source of the fluid at Valley. White micas hosted in biotite are the most phengitic of the muscovite-bearing assemblage because of the availability of Fe and Mg in the host mineral, and are therefore less directly representative of the hydrothermal fluid conditions than the other white micas that were analyzed. The most phengitic of all of the white micas analyzed are from samples that contain potassic alteration and are located further from Valley than the samples that are characterized by muscovite-bearing alteration. Lesage et al. (2019) interpreted the source of the fluids that formed the main potassic alteration zone in the HVC district to be located at depth below the Valley–Lornex and Highmont porphyry deposits based on the radial pattern of K-feldspar-bearing vein orientations that surrounds the deposits. The more phengitic results for the more distal white micas that are part of the potassic assemblage, which suggest that they formed from more rock-buffered fluids, are consistent with this interpretation.

Based on the EPMA results for white micas that are part of the popylitic alteration assemblage, no obvious trend occurs between the intensity of Tschermak substitution and distance to the closest deposit. The most phengitic propylitic white micas are those that formed in veins with epidote (Figure 4.9G), or that formed near the vein in a selvage with epidote and K-feldspar (Figure

4.9M). The composition of white micas measured from different parts of the alteration selvages varies significantly. These data suggest that the composition of white mica in veins best reflects the composition of the hydrothermal fluid, and that the composition of white mica in selvages is influenced primarily by the host mineral composition. This interpretation is consistent with the work of Byrne (2019), which showed that propylitic alteration was formed through redistribution of elements within the rocks with little to no metasomatism.

4.7.2. White mica composition vs. Al-OH wavelength

The Al-OH wavelength of the white mica minerals analyzed by EPMA was estimated based on the results of the hyperspectral scans of the thin section offcuts (Figure 4.9). The Al-OH feature wavelength of white micas from the potassic assemblage ranges between 2192 nm and 2205 nm (Table 4.4). Figure 4.15A shows a weak trend of increasing wavelength with increasing phengitic composition. For similar Fe+Mg+Si and Al compositions, however, white micas from the potassic assemblage yields shorter Al-OH wavelengths compared to muscovite-bearing or propylitic alteration (Figure 4.15B and C). The estimated Al-OH wavelength ranges between 2192 nm and 2207 nm for white micas from the muscovite-bearing alteration assemblage (Figure 4.9D, E and F), whereas it ranges between 2195 nm to 2210 nm for propylitic white micas (Figure 4.9G to M). As expected based on previous studies (e.g., Jones et al., 2005; Alva Jimenez, 2011; Cohen, 2011; Uribe-Mogollon and Maher, 2018), Figure 4.15 shows a strong correlation between the Al-OH wavelength and the intensity of the Tschermak substitution for these alteration assemblages, with the most phengitic white mica minerals characterized by the longest wavelengths.

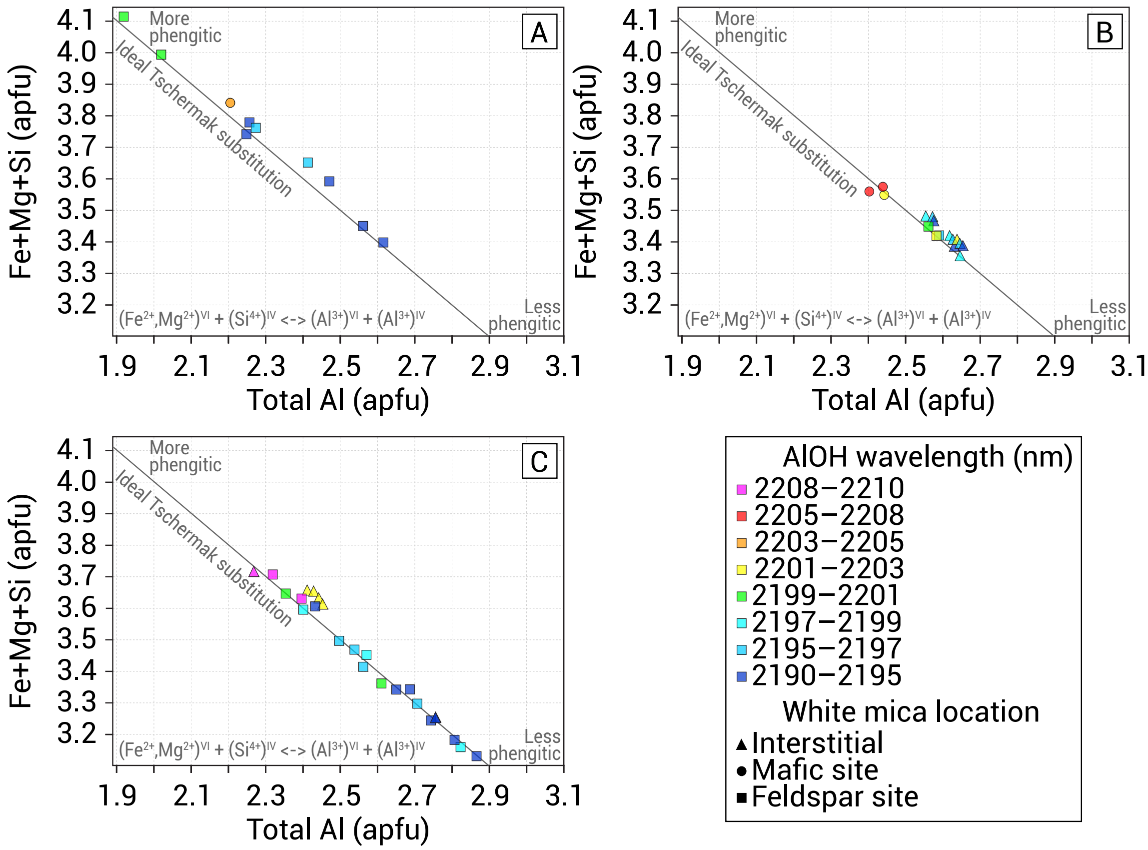

Figure 4.15. Major element variations of white mica composition in atoms per formula unit (apfu) displayed on a plot of Fe+Mg+Si versus total Al for white mica that is part of A) potassic alteration, B) muscovite-bearing alteration, and C) propylitic alteration. Colors represent the Al-OH wavelength (nm) and symbol shapes indicate the white mica mineral location.

According to the phengitic composition of white micas that formed as part of the potassic assemblage, the expected Al-OH wavelength should be longer than what is observed in hyperspectral scans. Only minor amounts of white micas were formed during potassic alteration, so the discrepancy between the mineral chemistry and the SWIR spectra may be due to interference from another mineral, such as the beidellite that is likely present in least-altered rocks. The similarities between the Al-OH wavelength (Figure 4.6A), depth (Figure 4.6B), and width (Figure 4.6C) from least-altered rocks and potassic alteration in TerraSpec® data are consistent with this hypothesis, but further work is required to confirm it.

4.7.3. Al-OH wavelength spatial distribution in hyperspectral data

As a proxy for white mica composition (e.g., Duke, 1994; Thompson et al., 1999; Halley et al., 2015), the Al-OH wavelengths across the HVC district provides information about the intensity of alteration and about the hydrothermal fluid composition, pH and temperature through time and space. The following assumptions regarding the Al-OH wavelengths in hyperspectral scans are made based on the results presented above: 1) wavelengths <2195 nm represent the background signature of least-altered samples and are likely related to the presence of beidellite formed through deuteric alteration of the batholith during late-stage cooling, 2) wavelengths between 2197 nm and 2201 nm represent muscovitic white mica alteration, 3) wavelengths between 2201 nm and 2209 may be influenced by kaolinite interference even at very low kaolinite modal percentages, and 4) wavelengths >2209 nm represent phengitic white mica alteration. The pixel percentages of muscovitic (2197–2201 nm) and phengitic (2209–2220 nm) white mica wavelengths are divided by the percentage of background wavelengths (2190–2195 nm) in order to quantify the intensity of white mica addition by hydrothermal alteration in each sample. In accordance with the SWIR observations detailed above, Figure 4.16 shows that:

1) Least-altered samples are characterized by low values for both ratios because the dominant Al-OH wavelengths in these samples are <2195 nm.

2) Samples with muscovite-bearing alteration are characterized by the highest values for both ratios because of the addition of both muscovitic and phengitic white mica combined with the destruction of primary plagioclase crystals, which contain the minerals responsible for the majority of wavelengths <2195 nm.

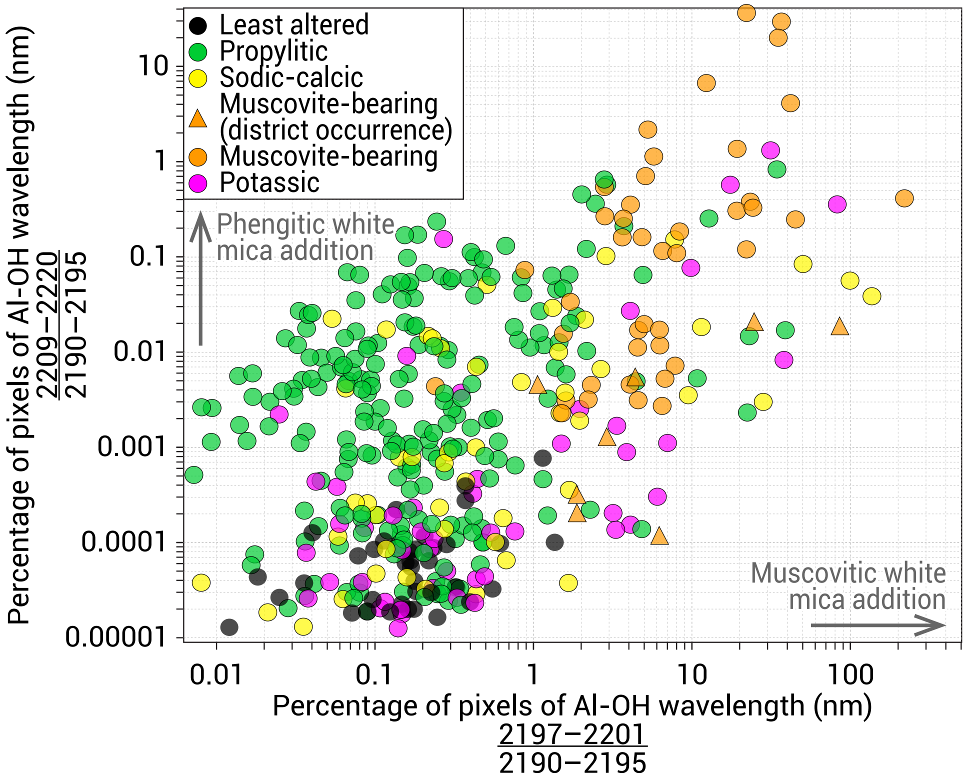

Figure 4.16. Scatterplot showing pixel percentage ratios calculated from image analysis of hyperspectral scans of the Al-OH wavelength. The X axis is the total of pixels in the 2197−2201 nm range divided by those in the 2190−2195 nm range, plotted against the total of pixels in the 2209−2220 nm range divided by those in the 2190−2195 nm range.

3) Samples with potassic alteration are mainly characterized by Al-OH wavelengths that indicate muscovitic white mica addition, and to a lesser extent phengitic white mica addition.

4) Samples with propylitic alteration are mainly characterized by phengitic white mica addition.

5) Samples with sodic-calcic alteration are characterized addition of both muscovitic and phengitic white mica, the latter is interpreted to be due to the common propylitic overprint in these samples.

Potassic and muscovite-bearing alteration are displayed together on the maps in Figure 4.17A and B because they are both interpreted to have formed from magmatic fluids (Lesage et al., 2019), whereas sodic-calcic and propylitic alteration are displayed together (Figure 4.17C and D) because both of these alteration assemblages are interpreted to have formed from external fluids (Byrne, 2019; Lesage et al., 2019) and because many sodic-calcic-altered samples also display a propylitic overprint. The white mica Al-OH wavelength ranges and the spatial distribution of white mica compositions determined using SWIR data are summarized in Table 4.2 for each alteration assemblage.

4.7.3.1. Potassic and muscovite-bearing alteration

In alteration assemblages formed from magmatic fluids, the intensity of both muscovitic and phengitic white mica alteration at the district scale consistently increases toward the porphyry deposits. Hyperspectral data image analysis shows that the ratio of muscovitic white mica pixel percentage (2197–2201 nm) to background signal pixel percentage (2190–2195 nm) is mainly <1.89 throughout the district. All samples with a pixel percentage ratio >6.24 (i.e., above the 80th percentile of the sample population) are located within 2 km of the porphyry deposits and locally at smaller Cu occurrences (Figure 4.17A). High pixel percentage ratios indicate strong muscovitic white mica addition combined with destruction of primary plagioclase. The most significant muscovitic white mica alteration (i.e., above the 90th percentile of the population) occurs within hundreds of meters of Cu mineralization at the Valley–Lornex and Highmont deposits.

Hyperspectral data also indicates that phengitic white mica alteration occurs primarily in samples with muscovite-bearing alteration, and to a lesser extent in samples with potassic alteration. The ratio of phengitic white mica pixel percentage (2209–2220 nm) to background signal pixel percentage (2190–2195

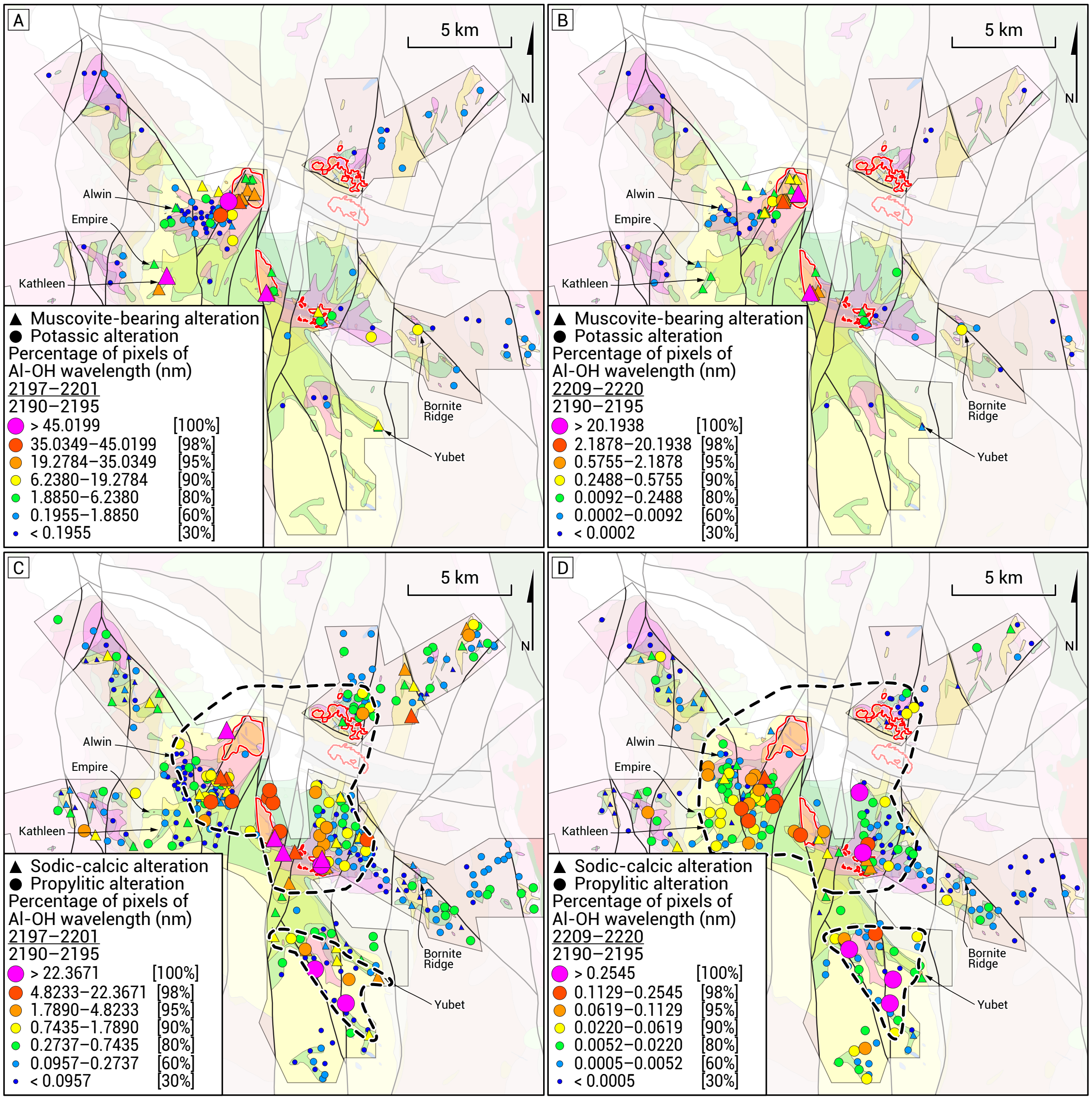

Figure 4.17. Maps showing the distribution of pixel percentage ratios calculated from image analysis of hyperspectral scans of the Al-OH wavelength. A) and C) pixels in the 2197–2201 nm range divided by pixels in the 2190–2195 nm range, B) and D) pixels in the 2209–2220 nm range divided by pixels in the 2190–2195 nm range. A) and B) show samples characterized by potassic (93 measurements) and muscovite-bearing alteration (51 measurements), whereas C) and D) show samples characterized by propylitic (279 measurements) and sodic-calcic alteration (91 measurements). Names on the maps refer to district Cu occurrences that were sampled. The dashed lines in C) and D) respectively outline zones of anomalous muscovitic and phengitic white mica addition by hydrothermal alteration.

nm) is mainly <0.01 throughout the district. All samples with a pixel percentage ratio >0.25 (i.e., above the 80th percentile of the sample population) are either located at a district Cu occurrence (i.e., Bornite Ridge) or within the Valley–Lornex deposit (Figure 4.17B). The ratio is locally up to 20 in samples from within the Valley–Lornex deposit, which suggests strong phengitic white mica addition and destruction of primary plagioclase.

Muscovitic and phengitic white mica alteration as part of the muscovite-bearing alteration assemblages both occur within the deposits, however textural evidence and mineral associations suggest that muscovitic white micas formed prior to phengitic white micas. Muscovitic white micas formed early in transitional potassic-sericitic vein selvages (i.e., EH or EDM vein equivalent; Meyer, 1965; Brimhall, 1977; Proffett, 2009), whereas phengitic white micas formed later as part of the sericitic assemblage as the hydrothermal system cooled down. The more phengitic composition of the latter is consistent with the EPMA results presented above and suggests that the hydrothermal fluids from which the sericitic alteration formed may have been less acidic and/or more Fe-rich than the fluids that caused the transitional potassic-sericitic alteration.

4.7.3.2. Sodic-calcic and propylitic alteration

In sodic-calcic and propylitic alteration, the intensity of muscovitic white mica alteration within the vein selvages consistently increases toward the porphyry deposits. Hyperspectral data shows that the 2197–2201/2190–2195 nm pixel percentage ratio is generally <0.74 throughout the HVC district. Samples with a muscovitic white mica alteration pixel percentage ratio >0.74 (i.e., above the 80th percentile of the sample population) form a coherent zone that encompasses all porphyry deposits and extends up to ~3 km away from Cu mineralization

(Figure 4.17C). Within this zone, samples with a pixel percentage ratio >4.82 (i.e., above the 95th percentile of the population) all occur within 2 km of the deposits, and the ratio consistently increases towards Cu mineralization. The size of this anomalous zone is much larger than the anomaly associated with alteration formed from magmatic fluids. Another zone of strong muscovitic white mica addition is located to the south of Highmont, is ~4 km across and is coincident with a zone of potassic alteration. These same two zones are also characterized by significant phengitic white mica addition (Figure 4.17D). Samples with a phengitic white mica alteration pixel percentage ratio >0.02 (i.e., above the 80th percentile of the population) form a zone that extends up to 2 km farther from the deposits than muscovitic white mica alteration, or ~5 km away from Cu mineralization. Samples with a pixel percentage ratio >0.11 (i.e., above the 95th percentile of the population) generally occur at distances between 2 to 3 km away from Cu mineralization.

The trend of distal phengitic to proximal muscovitic white mica alteration is best expressed to the southwest of the Valley deposit where the only host rock is the Bethsaida facies. Hyperspectral data suggest that porphyry-related white mica alteration is detectable up to 5 km away from porphyry Cu mineralization, that external fluids are dominantly neutral at distances >3 km from the porphyry deposits, and that within 3 km of the deposits the fluids become progressively more acidic with decreasing distance to Cu mineralization. A larger fraction of magmatic fluids in external fluids due to greater mixing near the deposits would likely lower the fluid pH and explain the greater abundance of muscovitic white mica at distances <3 km from the deposits.

The same trend of distal phengitic to proximal muscovitic white mica alteration occurs in the more felsic Skeena and Bethsaida facies beyond the Valley, Lornex and Highmont deposits as well as in the mafic Guichon facies beyond the Bethlehem deposit (Figure 4.17C and D). This indicates that the availability of Fe and Mg from mafic minerals in the host rock is not a major control on the composition of white mica alteration minerals hosted in feldspar sites, and that the hydrothermal fluid composition likely has a bigger influence. This interpretation is supported by the presence of more abundant phengitic white micas in propylitic alteration within 5 km of the porphyry deposits (Figure 4.17D) and the more abundant phengitic white micas in selvages near the veins, where the fluid–rock ratio was highest (Figure 4.14). We interpret the higher Fe and Mg concentrations in external fluids within 5 km of the porphyry deposits to be caused by small amounts of mixing between magmatic and external hydrothermal fluids.

4.7.4. Al-OH wavelength spatial distribution in TerraSpec® data

Short-wave infrared data collected using the TerraSpec® instrument only provide one spectra for an area ~5 cm^2. To minimize issues related to the short wavelength Al-OH absorption feature present in least-altered rocks and the absorption feature related to kaolinite interference, features of width <29.3 nm and of wavelengths between 2205 nm and 2209 nm (Figure 4.6F) are omitted from the maps in Figure 4.18.

Phengitic white micas (>2209 nm) in potassic and muscovite-bearing alteration (Figure 4.18A) occur within the porphyry deposits and at Cu occurrences, which is consistent with the hyperspectral data. Phengitic white micas in propylitic and sodic-calcic alteration are more abundant at distances <5 km from the porphyry deposits. The spatial distribution of phengitic white micas in alteration caused by external fluids, as identified from the TerraSpec® data, is spatially coincident with the anomalous zone of phengitic white mica alteration identified from the image analysis of hyperspectral scans (Figure 4.18C). Within this zone the distribution of TerraSpec® Al-OH wavelengths in propylitic and sodic-calcic alteration, however, is fairly erratic and does not define a clear trend away from porphyry Cu mineralization.

The only short wavelength white micas (<2195 nm) detected by the TerraSpec® are from samples characterized by pervasive sodic-calcic assemblage that are located within hundreds of meters from the deposits (Figure 4.18C). These data are consistent with the presence of high-Na paragonitic white mica within strong sodic-calcic alteration at the Bethlehem deposit (Alva Jimenez, 2011; Byrne et al., 2013; Byrne et al., 2017) formed from seawater-derived fluids (Byrne, 2019). Except for these shorter Al-OH wavelengths (<2195 nm) white mica present in pervasive sodic-calcic alteration within or near the porphyry deposits, samples with fracture-controlled sodic-calcic alteration show similar white mica spectral characteristics to samples with propylitic alteration (Figure 4.6). This suggests that moderate to weak district-scale sodic-calcic and propylitic alteration formed under relatively similar conditions.

For each TerraSpec® spectra, the depth of the Al-OH absorption feature was divided by its width to assess the white mica crystallinity. Crystallinity increases towards the Valley deposit in potassic and muscovite-bearing alteration, however low crystallinity white micas are also present near the deposits (Figure 4.18B). White mica crystallinity is generally lower in propylitic and sodic-calcic alteration than in potassic and muscovite-bearing alteration. Additionally, except for the deep water absorption feature in the TerraSpec® reflectance spectra of some of the samples with intermediate argillic alteration, propylitic and sodic-calcic alteration yield the deepest water absorption features of all

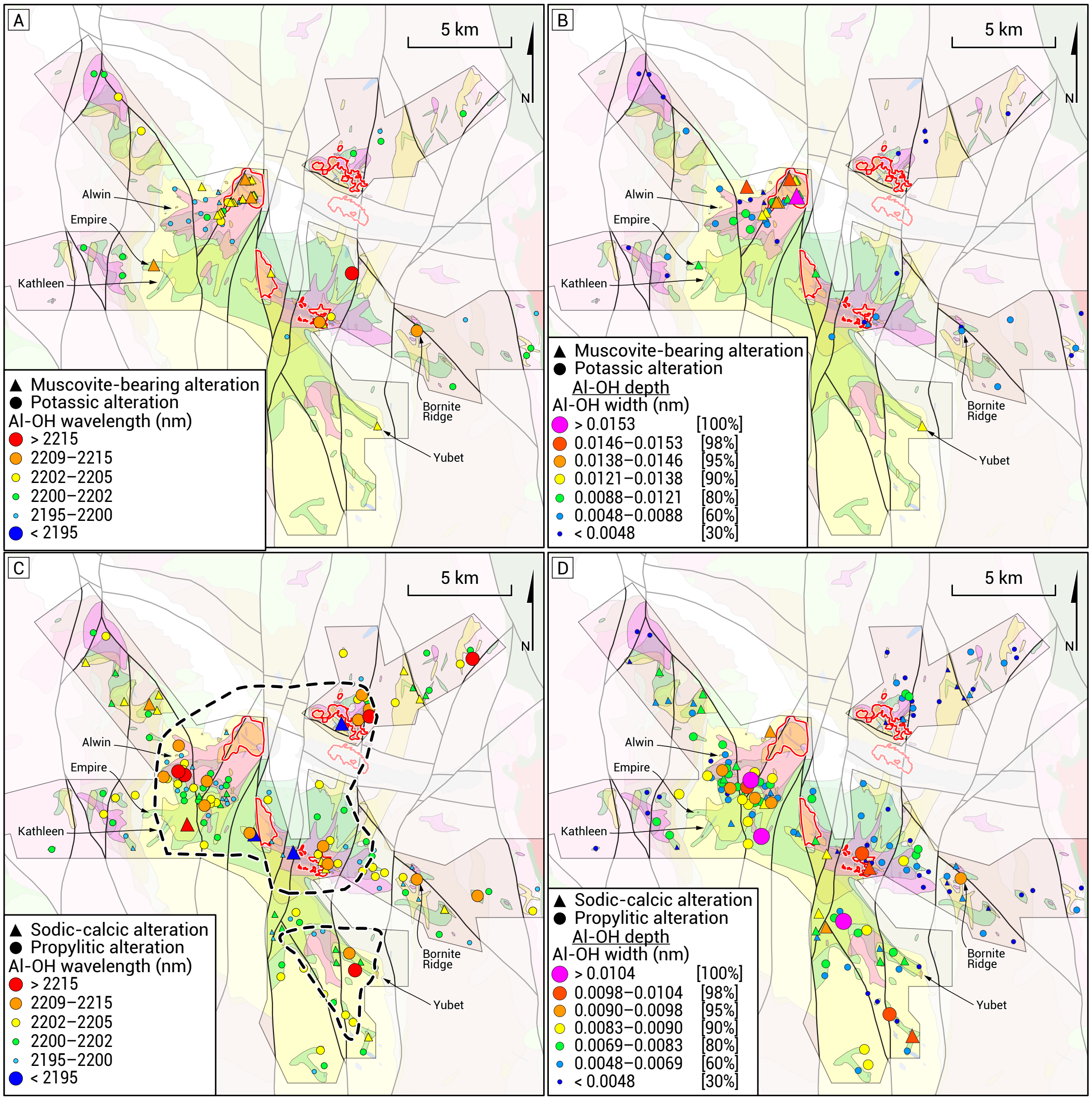

Figure 4.18. A) and B) show maps of the distribution of Al-OH wavelengths (nm) and white mica crystallinity for samples characterized by potassic (39 measurements) and muscovite-bearing alteration (30 measurements). C) and D) show maps of the distribution of Al-OH wavelengths (nm) and white mica crystallinity for samples characterized by propylitic (119 measurements) and sodic-calcic alteration (43 measurements). The white mica crystallinity was calculated by dividing the hqd of the Al-OH absorption feature by its width. Only Al-OH absorption features of width >29.3 nm are displayed. Al-OH wavelengths between 2205 nm and 2209 nm are omitted in order to minimize issues related to kaolinite interference. The dashed line in C) is the anomalous zones of phengitic white mica addition outlined in Figure 14.17C.

the assemblages (Figure 4.6D), which is another indication of lower crystallinity (GMEX, 2008). Lower white mica crystallinity is consistent with a lower temperature of formation for the district-scale sodic-calcic and propylitic alteration compared to the potassic and muscovite-bearing alteration. Propylitic and sodic-calcic white mica crystallinity is relatively high in the Valley and Highmont deposits (Figure 4.18D). The TerraSpec® data however, do not define a clear trend of increasing crystallinity towards the porphyry deposits, which may be due to interference caused by the presence of several spectrally-active minerals in the field-of-view of the instrument.

4.8. Conclusions

White mica minerals are widespread in the GCB and occur as part of every alteration assemblage associated with the HVC porphyry Cu systems. White mica compositions are strongly influenced by the composition of the host mineral (e.g., biotite vs. feldspar). Within the porphyry Cu deposits, Na-rich muscovitic white micas (2193–2202 nm) form as part of the transitional potassic-sericitic alteration (EH/EDM vein equivalent), whereas more phengitic white micas (>2205 nm) form as part of later sericitic alteration. Muscovite-bearing alteration at smaller district Cu occurrences is slightly more phengitic than transitional potassic-sericitic white mica from the porphyry deposits, however the Al-OH wavelengths (2193–2202 nm) still suggest a dominantly muscovitic composition. Minor muscovitic and phengitic white micas form as part of the district-scale potassic alteration. Short Al-OH wavelength paragonitic white micas formed in strong pervasive sodic-calcic alteration, but are spatially restricted to within the porphyry deposits. At the district scale, the Al-OH wavelength of white micas in moderate to weak fracture-controlled sodic-calcic and propylitic alteration is fairly similar, which suggests that the alteration assemblages formed under relatively similar conditions. Propylitic white mica compositions range from muscovitic to phengitic. Long Al-OH wavelength white micas (>2207 nm) outside the deposits are almost exclusively formed by propylitic alteration, with some exceptions in sodic-calcic alteration, and occur where the fluid-rock ratio is highest and the alteration is strongest.

The Al-OH wavelength of white micas is affected by elemental substitutions, and can be used as a proxy for mineral composition to help vector toward porphyry Cu mineralization at the district scale provided that the alteration assemblage to which the white micas belong is well documented. However, the presence of other minerals that contain Al-OH bonds, such as beidellite (<2199 nm) or kaolinite (2206–2208 nm), even at low modal percentages, can cause interference that complicates the interpretation of SWIR spectral data. Because of this, the higher spatial resolution of hyperspectral data makes it more effective as a vectoring tool than spectral data collected using the TerraSpec® instrument.

Hyperspectral data provide Al-OH wavelength maps for each sample that can be used to quantify the intensity of alteration. Image analysis of the Al-OH wavelength maps from samples characterized by propylitic and sodic-calcic alteration shows that at the district scale muscovitic white micas form a footprint that is detectable within 3 km of the HVC porphyry Cu deposits, and their abundance consistently increases toward the deposits. The footprint of increased phengitic white micas in these alteration assemblages is detectable to distances up to ~5 km from the HVC deposits, and phengitic white mica alteration is at a maximum at distances between 2 and 3 km from the deposits.

Chapter 5. Conclusions

5.1. Summary of the research findings

The main objective of this study was to improve upon the current understanding of the porphyry deposit footprint at the district scale. To do this, four main research questions were outlined in Chapter 1. Answers to these questions are summarized below.

5.1.1. What is the present-day GCB structural framework?

Brittle faulting processes in the GCB were shown to cause the destruction of magnetite in country rocks. A methodology was developed to interpret regional 3D fault networks from integrated geological, geophysical and topographical data sets, using a reduced-to-pole (RTP) magnetic intensity grid as base layer. Multi-layer 2D lineament mapping (e.g., Sánchez et al., 2014) was first used to identify the surface expression of faults, or fault traces. A total of 25 faults with along-strike continuity >4 km were interpreted in the GCB with this method. Fault dips were modeled along 2D magnetic intensity profiles extracted from the RTP grid perpendicular to each interpreted fault. Using synthetic magnetic susceptibility data, the modeled dips were shown to consistently be within <5° of the actual fault dip at dips >60°. A 3D structural model of the GCB was finally built using the interpreted fault traces, the modelled dips, and dips measured in the field where available.

5.1.2. What is the mineralogy and district-scale spatial extent of each alteration assemblage formed as a result of porphyry-related hydrothermal fluid flow?

Using the hydrothermal alteration nomenclature of Seedorff et al. (2005), the study of the GCB showed that the HVC porphyry systems are characterized by district-scale alteration zones formed by early high-temperature magmatic fluids (i.e., potassic, transitional potassic-sericitic and seriticic alteration), and by later heated seawater-derived external fluids (Byrne, 2019) convecting through the brittle crust (i.e., sodic-calcic and propylitic alteration). Minerals present in the alteration assemblages suggest a general decrease in temperature over time and away from the deposits: from transitional potassic-sericitic and sericitic alteration within hundreds of meters of the deposits, to potassic alteration within ~4.5 km of the deposits, to sodic-calcic and propylitic alteration up to ~7 km away from the deposits. In addition, the highest-temperature minerals that are part of the sodic-calcic assemblage (e.g., garnet, diopside and actinolite) are only present within the deposits.

A palinspastic reconstruction of the batholith shows that the largest potassic alteration zone in the HVC district is a westerly-elongated ~12 x 2 km area centered on Valley–Lornex and Highmont, and that sodic-calcic alteration forms discontinuous zones that outline a crude northeast-oriented inverted funnel shape that is ~17 x 11 km in the southwest and <1 km-wide in the northeast. Propylitic alteration is widespread across the GCB, but vein intensities > 5 cm/m form a circular zone that extends up to 5 km from the porphyry deposits located in the center of the batholith. Propylitic vein intensities, however, do not systematically increase towards the deposits.

The batholith reconstruction, however, does not account for the northeast-oriented tilting of ~12–15° interpreted from the gravity and seismic models

(Ager et al., 1973; Roy and Clowes, 2000) and from Al-in-hornblende barometry (D'Angelo, 2016). We interpret that the wider sodic-calcic zones to the southwest and narrower zones to the northeast are a consequence of the current erosional level which exposes deeper areas to the southwest.

5.1.3. What are the structural controls on fracture permeability and hydrothermal fluid flow during porphyry mineralization in a batholithic environment?

Crustal-scale faults play an important role in focusing granitoid magma ascent and in pluton emplacement (e.g., Hutton, 1988; Petford and Atherton, 1992; Richards, 2001) due to the high fracture permeability in their damage zones (e.g., Wallace and Morris, 1979; Cox and Scholz, 1988). Arc-parallel north-trending faults that were part of a proto-Lornex fault system therefore likely acted as preferential pathways for the GCB magmas during emplacement of the batholith. The west-northwest-trending zone where the Gnawed Mountain Porphyry dike complex intruded likely represented a dilational linkage zone between two north-trending proto-Lornex fault strands, which is consistent with a sinistral regional stress regime in the area during the Late Triassic (Nelson and Colpron, 2007). However, based on previous work that studied the shape and size of intrusions in relation to the regional stress field (e.g., Takada, 1994; Arndt et al., 1997; Tosdal and Richards, 2001), the large size and the nearly circular reconstructed shape of the GCB suggest that the regional stress regime under which the batholith was emplaced was characterized by a low regional differential stress. The large range of dike and vein orientations across the GCB is also consistent with a low differential stress.

Radial patterns of aplite dikes and K-feldspar-bearing veins around the Valley–Lornex and Highmont deposits, which extend up to ~4.5 km away from the deposits, imply that the fracture-controlled permeability in which the aplitic magmas and magmatic fluids flowed is the result of local stresses induced by overpressure. Radial tensile fractures around a point source form in response to an upward and outward push of the country rock above the source of the overpressure (e.g., Burnham, 1979; Fournier, 1999; Tosdal and Richards, 2001). Radial patterns also imply that vein intensity systematically decreases away from the source of the overpressure, i.e., from the porphyry deposits.

The orientations of veins that contains sodic-calcic and propylitic assemblages are highly variable. However, veins are typically broadly parallel or perpendicular to igneous facies boundaries, and wherever two vein orientations are present on a single outcrop the veins are typically nearly orthogonal. Sodic-calcic and propylitic vein intensity is generally greater in the center of the batholith but does not, however, form a clear gradient toward the porphyry deposits. We interpret that thermal contraction during cooling of the GCB magmas generated orthogonal joint sets in which the external fluids that cause sodic-calcic and propylitic alteration flowed under hydrostatic pressure conditions.

5.1.4. What are, for each alteration assemblage, the district-scale variations in white mica composition that characterize the porphyry Cu deposit footprint?

White mica minerals are a common alteration product in all alteration assemblages associated with the HVC porphyry Cu systems. White mica composition is strongly affected by the chemistry of its host mineral: in rocks showing only one alteration assemblage, white micas hosted in biotite are consistently more phengitic than white micas hosted in feldspars due to the greater availability of Fe and Mg.

The white micas that characterize the transitional potassic-sericitic alteration (EH/EDM vein equivalent) within the porphyry deposits are muscovites, as shown by their Al-OH absorption feature wavelengths between 2193 and 2202 nm, however the Na content in these muscovites as measured by EPMA generally decreases away from the center of the deposits. These data are consistent with observations by Alva Jimenez (2011), and suggest a higher temperature of formation for the Na-rich muscovite. Additionally, the use of hyperspectral imagery revealed the presence of phengitic muscovite (>2205 nm) as part of later sericitic alteration within the porphyry deposits. Away from the porphyry deposits, coarse-grained muscovite-bearing alteration at smaller district Cu occurrences shows similar but locally slightly more phengitic compositions than the transitional potassic-sericitic alteration present inside the deposits.

Only minor white micas form as part of the potassic alteration in the HVC district. Electron microprobe analyses indicate that they are phengitic muscovites and are more phengitic than all other white micas formed from magmatic fluids. Additionally, the white micas become more phengitic with increasing distance from the deposits, which is consistent with a lower fluid flux and a more neutral environment of formation away from the deposits, as predicted by Halley et al. (2015). Because of their very low abundance, however, the phengitic muscovites were not detected by SWIR methods (i.e., TerraSpec® analyses and hyperspectral scanning), which only detected short wavelength Al-OH absorption features (2193–2201 nm) in samples with potassic alteration. We interpret these short wavelengths absorption features to be caused by the presence of beidellite, a ubiquitous product of deuteric alteration formed during late-stage cooling of the GCB.

Short-wave infrared analyses show that strong pervasive sodic-calcic alteration within the porphyry deposits is characterized by paragonitic muscovite alteration (Al-OH wavelength <2195 nm). The paragonitic muscovites likely formed at high temperature from a saline seawater-derived hydrothermal fluid. This interpretation is consistent with stable isotope work by Byrne et al. (2019), which showed that sodic-calcic and propylitic alteration in the HVC district formed from dominantly seawater-derived fluids, locally mixed with magmatic fluids. At the district scale, SWIR analyses indicate that moderate to weak fracture-controlled sodic-calcic and propylitic alteration formed under comparable conditions: the analyses yielded Al-OH absorption feature wavelength ranges of 2190–2202 nm for sodic-calcic and dominantly 2193–2200 nm for propylitic alteration, which suggests similar muscovitic white mica compositions for both mineral assemblages. In addition to muscovite, however, district-scale propylitic alteration is also locally characterized by minor amounts of phengitic muscovite, as denoted by long Al-OH wavelengths (>2207 nm), in the inner part of alteration selvages where the fluid-rock ratio is highest and the alteration is strongest.

Image analysis of the Al-OH wavelength maps produced from the hyperspectral data for samples characterized by propylitic and sodic-calcic alteration shows that muscovitic white mica and phengitic white mica alteration respectively form a footprint that is detectable up to 3 km and 5 km away from the HVC porphyry Cu deposits. The abundance of muscovitic white micas consistently increases toward the deposits, whereas the abundance of phengitic white micas is highest between 2 and 3 km from the deposits.

5.2. Scientific significance of the research and application in mineral exploration

The methodology presented in Chapter 2 provides a new tool that uses remote sensing data sets (i.e., magnetic intensity and topography data) to enhance the 3D structural understanding in areas where geological data are lacking or where there is a paucity of outcrop exposure. In previous magnetic intensity data inverse modeling studies the 3D modeling attempted to identify lithological variations (e.g., Spicer et al., 2011; Mahmoodi et al., 2017), and although other work showed that magnetic intensity data contain information about brittle faults (e.g., Henkel and Guzman, 1977; Betts et al., 2015) no studies had previously attempted to model the 3D geometry of faults using these data. The methodology proposed in this study uses data that can be collected rapidly by airborne surveys over large areas and at relatively low cost (e.g., Nabighian et al., 2005), and yields strike and dip information that can be used to generate a 3D structural model. The methodology can be used as a predictive tool to help target areas to visit during surface mapping campaigns. The methodology, however, is most effective in relatively simple geological environments where faults are brittle and dominantly steeply dipping. Application of the methodology in complex geological environments where rocks may have pre-existing magnetic anisotropies or heterogeneities may be problematic. This new methodology was successfully applied to the GCB area and produced a new structural framework for the batholith, which was not previously available. This new GCB structural framework represents a significant step forward in the structural understanding of the batholith, and was the first step in order to restore the batholith to its Late Triassic geometry, i.e., when the HVC porphyry deposits were formed.

The study presented in Chapter 3 represents a significant advancement of the understanding of the district-scale hydrothermal alteration that surrounds porphyry deposits. It was shown, mainly through the use of feldspar staining and petrography, that potassic and sodic-calcic alteration assemblages can form extensive alteration zones that may be >10 km across in porphyry districts.

It is well documented that the flow of hydrothermal fluids in the brittle crust is dominantly controlled by fracture permeability (Ingebritsen and Manning, 2010; Ingebritsen, 2012; Weis et al., 2012). Regional tectonic stresses (e.g., Tosdal and Richards, 2001; Houston and Dilles, 2013) and local stresses (e.g., Burnham and Ohmoto, 1980; Bergbauer and Martel, 1999; Fournier, 1999) may both influence the orientation of fracture-controlled permeability. This study improved the understanding of the mechanisms that generate fracture permeability at the district scale around porphyry deposits hosted in large batholiths. In such environments, local stresses caused by magma or fluid overpressure or caused by thermal contraction respectively generate permeability for magmatic fluids and for external fluids (e.g., seawater-derived or meteoric). Regional stresses and crustal scale faults play an important role in the initial emplacement of the host batholith, but have little influence on the distribution and orientation of hydrothermal veins. The large size of batholiths, their relatively homogeneous granitoid body, and the likely presence of a partially molten viscous intrusive facies at depth during porphyry deposit formation shields the deposits from much of the regional stresses by providing a carapace around them and accommodating strain at depth in a ductile manner.

The study showed that the presence of large sodic-calcic and propylitic alteration zones in a batholith is positive from a mineral exploration stand point because it implies significant heat and fluid flow. However, the local stresses induced by thermal contraction, which generate permeability for external fluids, are not related to the porphyry mineralization processes and therefore sodic-calcic and propylitic vein intensity and orientation may not always be an effective way to identify prospective areas. On the other hand, the local stresses induced by magma or fluid overpressure are directly related to porphyry mineralization and form radial fracture arrays in which magmas or magmatic fluids may flow, as demonstrated in this study and in others (e.g., El Salvador, Cornejo et al., 1997; Bajo de la Alumbrera, Proffett, 2003; Ridgeway, Garcia-Cuison, 2010). Mapping the district-scale orientation of aplite dikes and K-feldspar-bearing veins can therefore be an effective tool to identify the location of a magmatic cupola and of potential porphyry Cu mineralization at depth (i.e., where the dikes and veins converge).

The minerals that commonly occur in propylitic alteration may also form in intrusions that lack porphyry deposits (e.g., Gerla, 1988; Bergbauer and Martel, 1999). This study showed that the use of SWIR data is an effective tool to identify propylitic alteration that formed in response to porphyry Cu mineralization. The Al-OH absorption feature wavelength of white micas is affected by elemental substitutions (e.g., Duke, 1994). Wavelength shifts can be used to map gradients in hydrothermal fluid composition, temperature and pH (e.g., Alva Jimenez, 2011; Cohen, 2011; Harraden et al., 2013; Halley et al., 2015). This study demonstrated that the Al-OH wavelength of white micas can be used as a proxy for mineral composition to identify propylitic alteration that forms as part of porphyry Cu systems, and to help vector toward the porphyry deposits.

The study also showed, however, that the presence of other minerals that contain Al-OH bonds, such as beidellite (<2199 nm) or kaolinite (2206–2208 nm), even at low modal percentages, can complicate the interpretation of SWIR spectral data. The higher spatial resolution of hyperspectral data therefore makes this scanning technique more effective as a vectoring tool than spectral data collected using the TerraSpec® instrument.

5.3. Future research directions

The structural interpretation methodology developed in Chapter 2 was shown to successfully model the dip of steep (>60°) linear magnetic low anomalies in synthetic data, however the method was only applied on real data in the GCB area. Additional field mapping in the GCB to ground truth the faults that were interpreted outside of the area visited while mapping for this study would provide more confidence in the interpreted GCB fault network. Application of the method in other areas, more geologically complex than the GCB, followed by field-testing of the interpreted faults may also provide better confidence in the accuracy of the method.

The interpretation of the regional and local stresses active during the Late Triassic in the GCB was based primarily on the location and orientation of veins and dikes at the batholith scale. Additional structural mapping in the open pits at the various HVC porphyry deposits may identify more kinematic indicators in mineralized veins and help better constrain the structural regime in the deposits during hydrothermal fluid flow.

Further research focused on the mineral chemistry of white micas in rocks with moderate to weak sodic-calcic and propylitic alteration would likely help refine the gradients identified in this study, and likely identify new ones. New advances in hyperspectral scanning technology will undoubtedly increase both the spatial and spectral resolution of the instruments while making analyses more affordable. The Specim SisuROCK™ instrument used for this study had a spectral resolution of ~6 nm, whereas the instrument currently used by Corescan, a hyperspectral scanning service provider, has a spectral resolution of ~4 nm. Future SWIR studies should therefore be able to improve upon the findings detailed in this study.

The use of laser ablation inductively coupled plasma mass spectrometry (LA-ICP-MS) successfully identified spatial gradients in trace element composition around porphyry deposits in alteration assemblages formed by magmatic fluids (e.g., HVC district, Alva Jimenez, 2011; Yerington district, Cohen, 2011). Application of this technique in alteration assemblages formed from external fluids (i.e., sodic-calcic and propylitic alteration) may reveal trace element compositional gradients that would highlight areas of higher prospectivity.

Bibliography

Ager, C. A., Ulrych, T. J. and McMillan, W. J., 1973, A gravity model for the Guichon Creek batholith, south-central British Columbia: Canadian Journal of Earth Sciences, v. 10, p. 920–935.

Airo, M.-L., 2002, Aeromagnetic and aeroradiometric response to hydrothermal alteration: Surveys in Geophysics, v. 23, p. 273–302.

Airo, M.-L. and Mertanen, S., 2008, Magnetic signatures related to orogenic gold mineralization, Central Lapland Greenstone Belt, Finland: Journal of Applied Geophysics, v. 64, p. 14–24.

Allen, J. M. and Richardson, J., 1970, The geological setting of the Valley Copper orebody: Canadian Institute of Mining and Metallurgy Annual General Meeting, 1970, Toronto, Ontario, 16 p.

Alva Jimenez, T., 2011, Variation in hydrothermal muscovite and chlorite composition in the Highland Valley porphyry Cu-Mo district, British Columbia, Canada: unpublished M.Sc. thesis, University of British Columbia, Vancouver, B.C., 233 p.

Arndt, J., Bartel, T., Scheuber, E. and Schilling, F., 1997, Thermal and rheological properties of granodioritic rocks from the Central Andes, North Chile: Tectonophysics, v. 271, p. 75–88.

Arne, D., House, E., Pontual, S. and Huntington, J., 2016, Hyperspectral interpretation of selected drill cores from orogenic gold deposits in central Victoria, Australia: Australian Journal of Earth Sciences, v. 63, p. 1003–1025.

Ash, C. H., Reynolds, P. H., Creaser, R. A. and Mihalynuk, M. G., 2006, $^{40}Ar/^{39}Ar$ and Re-O Isotopic Ages for Hydrothermal Alteration and Related Mineralization at the Highland Valley Cu-Mo Deposit (NTS 092I), Southwestern British Columbia: British Columbia Geological Survey, Paper 2007-1, p. 19–24.

Audétat, A., Pettke, T., Heinrich, C. A. and Bodnar, R. J., 2008, Special paper: The composition of magmatic-hydrothermal fluids in barren and mineralized intrusions: Economic Geology, v. 103, p. 877–908.

Audétat, A., Simon, A. C., Hedenquist, J. W., Harris, M. and Camus, F., 2012, Magmatic controls on porphyry copper genesis: Society of Economic Geologists Special Publication, v. 16, p. 553–572.

Aydin, A. and DeGraff, J. M., 1988, Evoluton of polygonal fracture patterns in lava flows: Science, v. 239, p. 471–476.

Bailey, E. H. and Stevens, R. E., 1960, Selective staining of K-feldspar and plagioclase on rock slabs and thin sections: American Mineralogist, v. 45, p. 1020–1025.

Bailey, S. W., 1984, Micas: Reviews in Mineralogy, Mineralogical Society of America, Washington, D.C., 584 p.

Baranov, V. and Naudy, H., 1964, Numerical calculation of the formula of reduction to the magnetic pole: Geophysics, v. 29, p. 67–79.

Beatty, T. W., Orchard, M. J., Mustard, P. S., Colpron, M. and Nelson, J., 2006, Geology and tectonic history of the Quesnel terrane in the area of Kamloops, British Columbia, *in* Colpron, M., and Nelson, J. L., eds., Paleozoic evolution and metallogeny of pericratonic terranes at the ancient Pacific margin of North America, Canadian and Alaskan Cordillera: Geological Association of Canada Special Paper, v. 45, p. 483–504.

Bedini, E., Van Der Meer, F. and Van Ruitenbeek, F., 2009, Use of HyMap imaging spectrometer data to map mineralogy in the Rodalquilar caldera, southeast Spain: International Journal of Remote Sensing, v. 30, p. 327–348.

Benavides, S., Characterisation of sericitic alteration at the Taca Taca Bajo porphyry Cu deposit, Argentina: SEG Conference Poster, 2018, Society of Economic Geologists, Keystone, 1 p.

Bergbauer, S. and Martel, S. J., 1999, Formation of joints in cooling plutons: Journal of Structural Geology, v. 21, p. 821–835.

Bergbauer, S., Martel, S. J. and Hieronymus, C. F., 1998, Thermal stress evolution in cooling pluton environments of different geometries: Geophysical Research Letters, v. 25, p. 707–710.

Bergey, W. R., Carr, J. M. and Reed, A. J., 1971, The Highmont Copper-Molybdenum Deposits, Highland Valley, British Columbia: Canadian Mining and Metallurgical Bulletin, v. 64, p. 68–76.

Bierwirth, P., Huston, D. and Blewett, R., 2002, Hyperspectral mapping of mineral assemblages associated with gold mineralization in the Central Pilbara, Western Australia: Economic Geology, v. 97, p. 819–826.

Betts, P., Ailleres, L., Armit, R., Blaikie, T., Jessell, M. W., 2015, Structural geophysics: Extended Abstracts of 14th SAGA Biennial Technical Meeting and Exhibition, p. 1–5.

Bird, D. K. and Norton, D. L., 1981, Theoretical prediction of phase relations among aqueous solutions and minerals: Salton Sea geothermal system: Geochimica et Cosmochimica Acta, v. 45, p. 1479–1494.

Bird, D. K. and Spieler, A. R., 2004, Epidote in geothermal systems: Reviews in Mineralogy and Geochemistry, v. 56, p. 235–300.

Blakely, R. J., Simpson, R. W., 1986, Approximating edges of source bodies from magnetic or gravity anomalies: Geophysics, v. 51, p. 1494–1498.

Bobrowsky, P. T., Kerr, D. E., Sibbick, S. J. and Newman, K., 1993, Drift exploration studies, Valley Copper pit, Highland Valley Copper mine, British Columbia: stratigraphy and sedimentology (92I/6, 7, 10, and 11): British Columbia Geological Survey, Paper 1993-1, p. 427–437.

Brethes, A., Guarnieri, P., Rasmussen, T. M. and Bauer, T. E., 2018, Interpretation of aeromagnetic data in the Jameson Land Basin, central East Greenland: Structures and related mineralized systems: Tectonophysics, v. 724-725, p. 116–136.

Brimhall, G. H., 1977, Early fracture-controlled disseminated mineralization at Butte, Montana: Economic Geology, v. 72, p. 37–59.

Brimhall, G. H., Agee, C. and Stoffregen, R., 1985, The hydrothermal conversion of hornblende to biotite: Canadian Mineralogist, v. 23, p. 369–379.

Briskey, J. A., 1980, Geology, petrology, and geochemistry of the Jersey, East Jersey, Huestis, and Iona porphyry copper-molybdenum deposits, Highland Valley, British Columbia: unpublished Ph.D. thesis, Oregon State University, Corvallis, Oregon, 425 p.

Briskey, J. A. and Bellamy, J. R., 1976, Bethlehem Copper's Jersey, East Jersey, Huestis and Iona deposits, *in* Sutherland Brown, A., ed., Porphyry deposits of the Canadian Cordillera, Canadian Institute of Mining and Metallurgy, Special Volume 15, p. 105–119.

Briskey, J. A., Field, C. W. and Bellamy, J. R., 1981, Geology, petrology, and geochemistry of the Jersey, East Jersey, Heustis, and Iona porphyry copper-molybdenum deposits, Highland Valley, British Columbia: Geological Society of America, Cordilleran Section Meeting, 1981, Open-File Report - U. S. Geological Survey, Corvallis, Oregon, p. 106–126.

Burnham, C. W., 1979, Magmas and hydrothermal fluids, *in* Barnes, H. L., ed., Geochemistry of Hydrothermal Ore Deposits, 2nd Edition, John Wiley and Sons Inc., New York, p. 71–136.

Burnham, C. W., 1981, Physicochemical constraints on porphyry mineralization, *in* Dickinson, W. R. and Payne, W. D., eds., Relations of tectonics to ore deposits in the southern cordillera, Geological Society of Arizona Digest, v. 14, p. 71–77.

Burnham, C. W., 1985, Energy release in subvolcanic environments: Implications for breccia formation: Economic Geology, v. 80, p. 1515–1522.

Burnham, C. W. and Ohmoto, H., 1980, Late-stage processes of felsic magmatism: Kozan Chishitsu = Mining Geology, p. 1–11.

Byrne, K., 2019, Diagnostic Features of the Rocks and Minerals Peripheral to the Highland Valley Copper District, British Columbia, Canada: Implications for the genesis of porphyry Cu systems and their footprints: unpublished Ph.D. thesis, University of Alberta, Edmonton, 232 p.

Byrne, K., Lesage, G., Gleeson, S. and Lee, R., 2017, Large-Scale Sodic-Calcific Alteration Around Porphyry Copper Systems: Examples from the Highland Valley Copper District, Guichon Batholith, South-Central British Columbia: Geoscience BC Summary of Activities 2016, Report 2017-1, p. 213–222.

Byrne, K., Lesage, G., Morris, W. A., Enkin, R. J., Gleeson, S. A. and Lee, R. G., 2019, Variability of outcrop susceptibility and its relationship to the porphyry Cu centers in the Highland Valley Copper district: Ore Geology Reviews, v. 107, p. 201–217.

Byrne, K., Stock, E., Ryan, J., Johnson, C., Nisenson, J., Alva Jimenez, T., Lapointe, M., Stewart, H., Grubisa, G. and Sykora, S., 2013, Porphyry Cu-(Mo) deposits in the Highland Valley district, south-central British Columbia, *in* Logan, J. and Schroeter, T. G., eds., Society of Economic Geologists Field Trip Guidebook, Society of Economic Geologists, v. 44, p. 99–116.

Candela, P. A., 1992, Controls on ore metal ratios in granite-related ore systems: an experimental and computational approach: Transactions of the Royal Society of Edinburgh: Earth Sciences, v. 83, p. 317–326.

Candela, P. A. and Holland, H. D., 1986, A mass transfer model for copper and molybdenum in magmatic hydrothermal systems: the origin of porphyry-type ore deposits: Economic Geology, v. 81, p. 1–19.

Candela, P. A. and Piccoli, P. M., 2005, Magmatic processes in the development of porphyry-type ore systems, *in* Hedenquist, J. W., Thompson, J. F. H., Goldfarb, R. J. and Richards, J. P., eds., Economic Geology One Hundredth Anniversary Volume: Society of Economic Geologists, Littleton, CO, United States, p. 25–37.

Carr, J. M., 1966, Geology of the Bethlehem and Craigmont copper deposits, *in* Tectonic history and mineral deposits of the Western Cordillera, Canadian Institute of Mining and Metallurgy, Special Volume 8, p. 321–328.

Carten, R. B., 1986, Sodium-calcium metasomatism; chemical, temporal, and spatial relationships at the Yerington, Nevada, porphyry copper deposit: Economic Geology, v. 81, p. 1495–1519.

Carten, R. B., Geraghty, E. P., Walker, B. M. and Shannon, J. R., 1988, Cyclic development of igneous features and their relationship to high-temperature hydrothermal features in the Henderson porphyry molybdenum deposit, Colorado: Economic Geology, v. 83, p. 266–296.

Casselman, M. J., McMillan, W. J. and Newman, K. M., 1995, Highland Valley porphyry copper deposits near Kamloops, British Columbia; a review and update with emphasis on the Valley deposit, *in* Schroeter, T. G., ed., Porphyry deposits of the Northwestern Cordillera of North America: Canadian Institute of Mining and Metallurgy, Special Volume 46, p. 161–191.

Cathles, L. M., 1977, An analysis of the cooling of intrusives by ground-water convection which includes boiling: Economic Geology, v. 72, p. 804–826.

Cathles, L. M., 1981, Fluid flow and genesis of hydrothermal ore deposits, *in* Skinner, B. J., ed., Economic Geology 75th Anniversary Volume: Society of Economic Geologists, New Haven, CT, United States, p. 424–457.

Cathles, L. M. and Shannon, R., 2007, How potassium silicate alteration suggests the formation of porphyry ore deposits begins with the nearly explosive but barren expulsion of large volumes of magmatic water: Earth and Planetary Science Letters, v. 262, p. 92–108.

Cathles, L. M., Erendi, A. H. J. and Barrie, T., 1997, How long can a hydrothermal system be sustained by a single intrusive event?: Economic Geology, v. 92, p. 766–771.

Chambefort, I., Dilles, J. H. and Kent, A. J. R., 2008, Anhydrite-bearing andesite and dacite as a source for sulfur in magmatic-hydrothermal mineral deposits: Geology, v. 36, p. 719–722.

Chevrier, V., Mathé, P.-E., Rochette, P. and Gunnlaugsson, H. P., 2006, Magnetic study of an Antarctic weathering profile on basalt: implications for recent weathering on Mars: Earth and Planetary Science Letters, v. 244, p. 501–514.

Childs, C., Walsh, J. J., Watterson, J., 1997, Complexity in fault zone structure and implications for fault seal prediction, *in* Moller-Pederson, P., Koestler, A.G., eds., Hydrocarbon Seals: Importance for Exploration and Production: Norwegian Petroleum Society Special Publications, v. 7., p. 61–72.

Clark, D. A., 1997, Magnetic petrophysics and magnetic petrology: aids to geological interpretation of magnetic surveys: AGSO Journal of Australian Geology and Geophysics, v. 17, p. 83–104.

Clark, D. A., 1999a, Magnetic petrology of igneous intrusions: implications for exploration and magnetic interpretation: Exploration Geophysics, v. 30, p. 5–26.

Clark, R. N., 1999b, Chapter 1: Spectroscopy of rocks and minerals, and principles of spectroscopy, *in* Rencz, A. N., ed., Manual of remote sensing, Volume 3, Remote sensing for the earth sciences: John Wiley and Sons, New York, p. 3–58.

Clark, R. N., Swayze, G. A., Wise, R., Livo, K. E., Hoefen, T., Kokaly, R. F. and Sutley, S. J., 2007, USGS digital spectral library splib06a: United States geological survey, digital data series 231, http://speclab.cr.usgs.gov/spectral.lib06.

Cline, J. S. and Bodnar, R. J., 1991, Can economic porphyry copper mineralization be generated by a typical calc-alkaline melt?: Journal of Geophysical Research, v. 96, p. 8113–8126.

Cloos, M., 2001, Bubbling magma chambers, cupolas, and porphyry copper deposits: International Geology Review, v. 43, p. 285–311.

Cohen, J., 2011, Compositional variations in hydrothermal white mica and chlorite from wall-rock alteration at the Ann-Mason porphyry copper deposit, Nevada: unpublished M.Sc. thesis, Oregon State University, Corvallis, Oregon, 601 p.

Colpron, M. and Nelson, J. L., 2011, A Digital Atlas of Terranes for the Northern Cordillera: BC Geofile, v. 2011-11.

Cooke, D. R., Hollings, P., Wilkinson, J. J. and Tosdal, R. M., 2014a, Geochemistry of porphyry deposits, *in* Holland, H. D. and Turekian, K. K., eds., Treatise on Geochemistry, Second Edition, Elsevier, Oxford, v. 13, p. 357–381.

Cooke, D. R., Baker, M., Hollings, P., Sweet, G., Chang, Z., Danyushevsky, L., Gilbert, S., Zhou, T., White, N. C., Gemmell, J. B. and Inglis, S., 2014b, New advances in detecting the distal geochemical footprints of porphyry systems; epidote mineral chemistry as a tool for vectoring and fertility assessments: Economic Geology, Special Publication 18, p. 127–152.

Cornejo, P., Tosdal, R. M., Mpodozis, C., Tomlinson, A. J., Rivera, O. and Fanning, C. M., 1997, El Salvador, Chile porphyry copper deposit revisited: geologic and geochronologic framework: International Geology Review, v. 39, p. 22–54.

Cox, D. P. and Singer, D. A., 1986, Mineral deposit models: US Government Printing Office Washington, D.C., United States, 380 p.

Cox, S. J. D. and Scholz, C. H., 1988, On the formation and growth of faults: an experimental study: Journal of Structural Geology, v. 10, p. 413–430.

Crider, J. G., 2015, The initiation of brittle faults in crystalline rock: Journal of Structural Geology, v. 77, p. 159–174.

Cui, Y., Miller, D., Schiarizza, P. and Diakow, L. J., 2017, British Columbia digital geology: British Columbia Ministry of Energy and Mines, British Columbia Geological Survey Paper 2017-8, p. 9.

D'Angelo, M. D., 2016, Geochemistry, petrography and mineral chemistry of the Guichon Creek and Nicola batholiths, southcentral British Columbia: unpublished M.Sc. thesis, Lakehead University, Thunder Bay, Ontario, 435 p.

D'Angelo, M. D., Alfaro, M., Hollings, P., Byrne, K., Piercey, S. J. and Creaser, R. A., 2017, Petrogenesis and magmatic evolution of the Guichon Creek Batholith: Highland Valley porphyry Cu ± (Mo) district, South-Central British Columbia: Economic Geology, v. 112, p. 1857–1888.

Deer, W. A., Howie, R. A. and Zussman, J., 1992, An introduction to The Rock-Forming Minerals, 2nd edition: New York, NY: Longman Scientific & Technical, 696 p.

Deer, W. A., Howie, R. A. and Zussman, J., 2003, Rock-Forming Minerals, Sheet silicates: Micas, v. 3A, 2nd edition: The Geological Society of London, 758 p.

Digel, S. G. and Gordon, T. M., 1995, Phase relations in metabasites and pressure-temperature conditions at the prehnite-pumpellyite to greenschist facies transition, Flin Flon, Manitoba, Canada: Geological Society of America Special Paper, v. 296, p. 67–80.

Dilles, J. H., 1987, Petrology of the Yerington Batholith, Nevada; evidence for evolution of porphyry copper ore fluids: Economic Geology, v. 82, p. 1750–1789.

Dilles, J. H. and Einaudi, M. T., 1992, Wall-rock alteration and hydrothermal flow paths about the Ann-Mason porphyry copper deposit, Nevada: A 6-km vertical reconstruction: Economic Geology, v. 87, p. 1963–2001.

Dilles, J. H., Barton, M. D. and Seedorff, E., Wall-rock alteration in porphyry copper deposits: Prediction of hydrothermal fluid compositions, fluid paths, and sulfide ore deposition: 2009 Portland GSA Annual Meeting, 2009, 1 p.

Dilles, J. H., Solomon, G. C., Taylor, H. P. and Einaudi, M. T., 1992, Oxygen and hydrogen isotope characteristics of hydrothermal alteration at the Ann-Mason porphyry copper deposit, Yerington, Nevada: Economic Geology, v. 87, p. 44–63.

Dilles, J. H., Einaudi, M. T., Proffett, J. M. and Barton, M. D., 2000, Overview of the Yerington porphyry copper district: Magmatic to nonmagmatic sources of hydrothermal fluids: Their flow paths, alteration effects on rocks and Cu-Mo-Fe-Au ores, *in* Thompson, T. B., ed., Economic Geology Guidebook 32: Society of Economic Geologists, p. 55–66.

Dilles, J. H., Kent, A. J., Wooden, J. L., Tosdal, R. M., Koleszar, A., Lee, R. G. and Farmer, L. P., 2015, Zircon compositional evidence for sulfur-degassing from ore-forming arc magmas: Economic Geology, v. 110, p. 241–251.

Duke, E. F., 1994, Near infrared spectra of muscovite, Tschermak substitution, and metamorphic reaction progress: Implications for remote sensing: Geology, v. 22, p. 621–624.

Einaudi, M. T., Hedenquist, J. W. and Inan, E. E., 2003, Sulfidation state of fluids in active and extinct hydrothermal systems: transitions from porphyry to epithermal environments, *in* Simmons, S. F. and Graham, I., eds., Volcanic, geothermal and ore-forming fluids: Rulers and witnesses of processes within the earth: Society of Economic Geologists Special Publication, v. 10, p. 285-314.

Ewing, T. E., 1981, Geology and tectonic setting of the Kamloops group, South-central British Columbia: unpublished PhD thesis, University of British Columbia, 238 p.

Fei, Y., 1995, Thermal Expansion, *in* Ahrens, T. J., ed., Mineral Physics & Crystallography: A Handbook of Physical Constants: American Geophysical Union, Washington, D.C., p. 29–44.

Ferbey, T., Plouffe, A. and Bustard, A. L., 2016, Geochemical, mineralogical, and textural data from tills in the Highland Valley Copper mine area, south-central British Columbia: British Columbia Geological Survey GeoFile 2016–11, Geological Survey of Canada Open File 8119, 20 p.

Ferrill, D. A., Morris, A. P. and McGinnis, R. N., 2009, Crossing conjugate normal faults in field exposures and seismic data: AAPG bulletin, v. 93, p. 1471–1488.

Ferrill, D. A., Morris, A. P., Stamatakos, J. A. and Sims, D. W., 2000, Crossing conjugate normal faults: AAPG bulletin, v. 84, p. 1543–1559.

Field, C. W., Zhang, L., Dilles, J. H., Rye, R. O. and Reed, M. H., 2005, Sulfur and oxygen isotopic record in sulfate and sulfide minerals of early, deep, pre-Main Stage porphyry Cu-Mo and late Main Stage base-metal mineral deposits, Butte district, Montana: Chemical Geology, v. 215, p. 61–93.

Fournier, R. O., 1999, Hydrothermal processes related to movement of fluid from plastic into brittle rock in the magmatic-epithermal environment: Economic Geology, v. 94, p. 1193–1211.

Gabriel, A. and Cox, E. P., 1929, A staining method for the quantitative determination of certain rock minerals: American Mineralogist, v. 14, p. 290–292.

Gabrielse, H., Murphy, D. C. and Mortensen, J. K., 2006, Cretaceous and Cenozoic dextral orogen-parallel displacements, magmatism, and paleogeography, north-central Canadian Cordillera: Paleogeography of the North American cordillera: Evidence for and against large-scale displacements: Geological Association of Canada Special Paper, v. 46, p. 255–276.

Garcia-Cuison, A. L., 2010, Geology and genesis of the Ridgeway porphyry Au-Cu deposit, NSW: unpublished Ph.D. Thesis, University of Tasmania, Hobart, 305 p.

Garwin, S., 2002, The geological setting of intrusion-related hydrothermal systems near the Batu Hijau porphyry copper-gold deposit, Sumbawa, Indonesia: Society of Economic Geologists Special Publication, v. 9, p. 333–366.

Gerla, P. J., 1988, Stress and fracture evolution in a cooling pluton: An example from the Diamond Joe stock, western Arizona, USA: Journal of Volcanology and Geothermal Research, v. 34, p. 267–282.

Ghosh, D. K., 1995, Nd-Sr isotopic constraints on the interactions of the Intermontane Superterrane with the western edge of North America in the southern Canadian Cordillera: Canadian Journal of Earth Sciences, v. 32, p. 1740–1758.

GMEX, 2008, Spectral interpretation field manual, 3rd edition: AusSpec International Ltd., 202 p.

Goodfellow, W. D., 2007, Mineral deposits of canada: A synthesis of major deposit-types, district metallogeny, the evolution of geological provinces, and exploration methods: Geological Association of Canada, Mineral Deposits Division, Special Publication No. 5, St. John's, NL, Canada, 1068 p.

Graden, R., 2012, NI 43-101 Technical Report: Teck Highland Valley Copper: Teck Resources Limited, 232 p.

Graham, G. E., Kokaly, R. F., Kelley, K. D., Hoefen, T. M., Johnson, M. R. and

Hubbard, B. E., 2018, Application of Imaging Spectroscopy for Mineral Exploration in Alaska: A Study over Porphyry Cu Deposits in the Eastern Alaska Range: Economic Geology, v. 113, p. 489–510.

Grant, F. S., 1985, Aeromagnetics, geology and ore environments, I. Magnetite in igneous, sedimentary and metamorphic rocks: An overview: Geoexploration, v. 23, p. 303–333.

Grauch, V. and Campbell, D. L., 1984, Does draping aeromagnetic data reduce terrain-induced effects?: Geophysics, v. 49, p. 75–80.

Greenlaw, L., 2014, Surface lithogeochemistry of the Relincho porphyry copper-molybdenum deposit, Atacama region, Chile: unpublished M.Sc. thesis, University of British Columbia, Vancouver, B.C., 135 p.

Gruen, G., Heinrich, C. A. and Schroeder, K., 2010, The Bingham Canyon porphyry Cu-Mo-Au deposit. II. Vein geometry and ore shell formation by pressure-driven rock extension: Economic Geology, v. 105, p. 69–90.

Guidotti, C. and Sassi, F., 1976, Muscovite as a petrogenetic indicator mineral in pelitic schists: Neues Jahrbuch fur Mineralogie Abhandlungen, v. 153, p. 97–142.

Guidotti, C. V., 1984, Micas in metamorphic rocks, *in* Bailey, S. W., ed., Reviews in Mineralogy: Mineralogical Society of America, v. 13, p. 357–467.

Gunn, P. J., Maidment, D. and Milligan, P. R., 1997, Interpreting aeromagnetic data in areas of limited outcrop: AGSO Journal of Australian Geology and Geophysics, v. 17, p. 175–186.

Guo, N., Thomas, C., Tang, J. and Tong, Q., 2019, Mapping white mica alteration associated with the Jiama porphyry-skarn Cu deposit, central Tibet using field SWIR spectrometry: Ore Geology Reviews, v. 108, p. 147–157.

Gustafson, L. B. and Hunt, J. P., 1975, The porphyry copper deposit at El Salvador, Chile: Economic Geology, v. 70, p. 857–912.

Hack, A. C. and Mavrogenes, J. A., 2006, A synthetic fluid inclusion study of copper solubility in hydrothermal brines from 525 to 725 $^\circ$C and 0.3 to 1.7 GPa: Geochimica et Cosmochimica Acta, v. 70, p. 3970–3985.

Halley, S., Dilles, J. H. and Tosdal, R. M., 2015, Footprints: Hydrothermal alteration and geochemical dispersion around porphyry copper deposits: SEG Newsletter, v. 100, p. 1–17.

Halter, W. E., Heinrich, C. A. and Pettke, T., 2005, Magma evolution and the formation of porphyry Cu-Au ore fluids: Evidence from silicate and sulfide melt inclusions: Mineralium Deposita, v. 39, p. 845–863.

Hamilton, W. B. and Myers, W. B., 1967, The nature of batholiths: U.S. Geological Survey Professional Paper 554-C, p. C1–C30.

Harraden, C. L., Mcnulty, B. A., Gregory, M. J. and Lang, J. R., 2013, Shortwave infrared spectral analysis of hydrothermal alteration associated with the Pebble porphyry copper-gold-molybdenum deposit, Iliamna, Alaska: Economic Geology, v. 108, p. 483–494.

Hart, C. J. R., 2007, Reduced intrusion-related gold systems, *in* Goodfellow, W. D., ed., Mineral deposits of canada: A synthesis of major deposit-types, district metallogeny, the evolution of geological provinces, and exploration methods: Geological Association of Canada, Mineral Deposits Division, Special Publication No. 5, p. 95–112.

Hattori, K. and Keith, J., 2001, Contribution of mafic melt to porphyry copper mineralization: evidence from Mount Pinatubo, Philippines, and Bingham Canyon, Utah, USA: Mineralium Deposita, v. 36, p. 799-806.

Heidrick, T. L. and Titley, S. R., 1982, Fracture and dike patterns in Laramide plutons and their structural and tectonic implications, *in* Titley, S. R., ed., Advanced in geology of the porphyry copper deposits: University of Arizona Press, Tucson, p. 73–91.

Heinrich, C. A., 2005, The physical and chemical evolution of low-salinity magmatic fluids at the porphyry to epithermal transition: A thermodynamic study: Mineralium Deposita, v. 39, p. 864–889.

Heinrich, C. A., Gunther, D., Audetat, A., Ulrich, T. and Frischknecht, R., 1999, Metal fractionation between magmatic brine and vapor, determined by microanalysis of fluid inclusions: Geology, v. 27, p. 755–758.

Hemley, J. J., Cygan, G. L., Fein, J. B., Robinson, G. R. and D'Angelo, W. M., 1992, Hydrothermal ore-forming processes in the light of studies in rock-buffered systems: I. Iron-copper-zinc-lead sulfide solubility relations: Economic Geology, v. 87, p. 1–22.

Henkel, H. and Guzman, M., 1977, Magnetic features of fracture zones: Geoexploration, v. 15, p. 173–181.

Herrmann, W., Blake, M., Doyle, M., Huston, D., Kamprad, J., Merry, N. and Pontual, S., 2001, Short wavelength infrared (SWIR) spectral analysis of hydrothermal alteration zones associated with base metal sulfide deposits at Rosebery and Western Tharsis, Tasmania, and Highway-Reward, Queensland: Economic Geology, v. 96, p. 939–955.

Hildreth, W. and Moorbath, S., 1988, Crustal contributions to arc magmatism in the Andes of Central Chile: Contributions to Mineralogy and Petrology, v. 98, p. 455-489.

Hinze, W. J., von Frese, R. R. B. and Saad, A. H., 2013, Gravity and Magnetic Exploration: Principles, Practices, and Applications: Cambridge University Press, Cambridge, 512 p.

Hobbs, W. H., 1904, Lineaments of the Atlantic border region: Geological Society of America Bulletin, v. 15, p. 483–506.

Holland, H. D., 1965, Some applications of thermochemical data to problems of ore deposits II: Mineral assemblages and the composition of ore forming fluids: Economic Geology, v. 60, p. 1101–1166.

Hollister, V. F., Allen, J. M., Anzalone, S. A. and Seraphim, R. H., 1975, Structural evolution of porphyry mineralization at Highland Valley, British Columbia: Canadian Journal of Earth Sciences, v. 12, p. 807–820.

Horsfield, W., 1980, Contemporaneous movement along crossing conjugate normal faults: Journal of Structural Geology, v. 2, p. 305–310.

Houston, R. A. and Dilles, J. H., 2013, Structural geologic evolution of the Butte district, Montana: Economic Geology, v. 108, p. 1397–1424.

Hutton, D. H., 1988, Granite emplacement mechanisms and tectonic controls: inferences from deformation studies: Earth and Environmental Science Transactions of the Royal Society of Edinburgh, v. 79, p. 245–255.

Hutton, D. H., 1997, Syntectonic granites and the principle of effective stress: A general solution to the space problem?, *in* Bouchez, J. L., Hutton,

D. H. and Stephens, W. E., eds., Granite: from segregation of melt to emplacement fabrics: Kluwer Academic Publishers, The Netherlands, p. 189–197.

Hyndman, R. J., Koehler, A. B., 2006, Another look at measures of forecast accuracy: International Journal of Forecasting, v. 22, p. 679–688.

Ingebritsen, S. and Manning, C., 2010, Permeability of the continental crust: dynamic variations inferred from seismicity and metamorphism: Geofluids, v. 10, p. 193–205.

Ingebritsen, S. E., 2012, Modeling the formation of porphyry-copper ores: Science, v. 338, p. 1551–1552.

Jambor, J. L. and Delabio, R. N., 1978, Distribution of hydrothermal clay minerals in the Valley copper porphyry deposit, Highland Valley, British Columbia: Geological Survey of Canada, Paper 77-9, p. 1–21.

Jessell, M.W., 2001, Three-dimensional geological modelling of potential-field data: Computers and Geosciences, v. 27, p. 455–465

Jessell, M. W., 2002, An atlas of structural geophysics II: Journal of the Virtual Explorer, Australian Crustal Research Centre, Monash University, Clayton, Victoria, Australia, 90 p.

Jessell, M. W., Valenta, R. K., 1996, Structural geophysics: integrated structural and geophysical modelling: Computer Methods in the Geosciences, v. 15, p. 303–324.

John, D. A., Ayuso, R. A., Barton, M. D., Blakely, R. J., Bodnar, R. J., Dilles, J. H., Gray, F., Graybeal, F. T., Mars, J. C., McPhee, D. K., Seal, R. R., Taylor, R.

D. and Vikre, P. G., 2010, Porphyry copper deposit model, *in* chap. B *of* Mineral deposit models for resource assessment, U.S. Geological Survey Scientific Investigations Report 2010–5070–B, 169 p.

Jones, S., Herrmann, W. and Gemmell, J. B., 2005, Short wavelength infrared spectral characteristics of the HW horizon: Implications for exploration in the Myra Falls volcanic-hosted massive sulfide camp, Vancouver Island, British Columbia, Canada: Economic Geology, v. 100, p. 273–294.

Keith, J. D., Whitney, J. A., Hattori, K., Ballantyne, G. H., Christiansen, E. H., Barr, D. L., Cannan, T. M. and Hook, C. J., 1997, The role of magmatic sulfides and mafic alkaline magmas in the Bingham and Tintic mining districts, Utah: Journal of Petrology, v. 38, p. 1679–1690.

Kerr, P. F., 1959, Sheet structures and Mineraloids: Optical Mineralogy, 3rd edition, chapter 16: McGraw-Hill Book Company, 383–424 p.

Knapp, R. and Norton, D., 1981, Preliminary numerical analysis of processes related to magma crystallization and stress evolution in cooling pluton environments: American Journal of Science, v. 281, p. 35–68.

Laakso, K., Rivard, B., Peter, J., White, H., Maloley, M., Harris, J. and Rogge, D., 2015, Application of airborne, laboratory, and field hyperspectral methods to mineral exploration in the Canadian Arctic: recognition and characterization of volcanogenic massive sulfide-associated hydrothermal alteration in the Izok Lake deposit area, Nunavut, Canada: Economic Geology, v. 110, p. 925–941.

Lang, J. R., Gregory, M. J., Rebagliati, C. M., Payne, J. G., Oliver, J. L. and Roberts, K., 2013, Geology and magmatic-hydrothermal evolution of the giant

Pebble porphyry copper-gold-molybdenum deposit, southwest Alaska: Economic Geology, v. 108, p. 437–462.

Langton, J. M., Williams, S. A. and Titley, S. R., 1982, Structural, petrological and mineralogical controls for the Dos Pobres orebody, Lone Star mining district, Graham County, Arizona, *in* Titley, S. R., ed., Advances in geology of porphyry copper deposits; southwestern North America: Tucson, University of Arizona Press, p. 335–352.

Laniz, R. E., Stevens, R. V. and Norman, M. B., 1964, Staining of plagioclase feldspar and other minerals with FD, and C. red no. 2: Geological Survey research, p. B152–B153.

Lapointe, P., Morris, W. A. and Harding, K., 1986, Interpretation of magnetic susceptibility: A new approach to geophysical evaluation of the degree of rock alteration: Canadian Journal of Earth Sciences, v. 23, p. 393–401.

Lapointe, P., Chomyn, B. A., Morris, W. A. and Coles, R. L., 1984, Significance of magnetic susceptibility measurements from the Lac Du Bonnet Batholith, Manitoba, Canada: Geoexploration, v. 22, p. 217–229.

Larsen, E. S. and Wherry, E. T., 1925, Beidellite, a new mineral name: Journal of the Washington Academy of Sciences, v. 15, p. 465–466.

Latham, A., Harding, K., Lapointe, P., Morris, W. and Balch, S., 1989, On the lognormal distribution of oxides in igneous rocks, using magnetic susceptibility as a proxy for oxide mineral concentration: Geophysical Journal International, v. 96, p. 179–184.

Lattman, L. H., 1958, Technique of mapping geologic fracture traces and lineaments on aerial photographs: Photogrammetric Engineering, v. 24,

p. 568–576.

Laukamp, C., Cudahy, T., Thomas, M., Jones, M., Cleverley, J. and Oliver, N., 2011, Hydrothermal mineral alteration patterns in the Mount Isa Inlier revealed by airborne hyperspectral data: Australian Journal of Earth Sciences, v. 58, p. 917–936.

Lee, M. D., Morris, W. A., Harris, J., Leblanc, G. E., 2012, An automatic network-extraction algorithm applied to magnetic survey data for the identification and extraction of geologic lineaments: Leading Edge, v. 31, p. 26–31.

Lee, R. G., Dilles, J. H., Tosdal, R. M., Wooden, J. L. and Mazdab, F. K., 2017, Magmatic evolution of granodiorite intrusions at the El Salvador porphyry copper deposit, Chile, based on trace element composition and U/Pb age of zircons: Economic Geology, v. 112, p. 245–273.

Lesage, G., Byrne, K., Lee, R. G. and Hart, C. J. R., 2019a, District-scale extent of hydrothermal alteration and vein orientations in the Highland Valley Copper district, British Columbia: Implications for permeability controls in porphyry Cu-Mo systems: Chapter 3 of this thesis.

Lesage, G., Byrne, K., Lypaczewski, P., Lee, R. G. and Hart, C. J. R., 2016, Characterizing the district-scale alteration surrounding a large porphyry Cu system: The footprint of Highland Valley Copper, British Columbia: Geological Society of Canana / Mineralogical Association of Canada Joint Annual Meeting Poster, Whitehorse, Yukon, 1 p.

Lesage, G., Byrne, K., Morris, W. A., Enkin, R. J., Lee, R. G., Mir, R. and Hart, C. J. R., 2019b, Interpreting regional 3D fault networks from integrated geological and geophysical data sets: An example from the Guichon Creek batholith, British Columbia: Journal of Structural Geology, v. 119, p. 93–106.

Lesher, M., Hannington, M. D., Galley, A. G., Ansdell, K., Astic, T., Banerjee, N., Beauchamp, S., Beaudoin, G., Bertelli, M., Bérubé, C., Beyer, S., Blacklock, N., Byrne, K., Cheng, L.-Z., Chouinard, R., Chouteau, M., Clark, J., D'Angelo, M. D., Darijani, M., Devine, M. C., Dupuis, C., El Goumi, N., Enkin, R. J., Farquharson, C., Fayol, N., Feltrin, L., Feng, J., Gaillard, N., Gleeson, S. A., Gouiza, M., Grenon, C., Guffey, S., Guilmette, C., Guo, K., Hart, C. J. R., Hattori, K., Hollings, P., Joyce, N., Kamal, D., King, J., Kyser, K., Layton-Matthews, D., Lee, R. G., Lesage, G., Leybourne, M., Linnen, R., Lypaczewski, P., McGaughey, J., Mitchinson, D., Milkereit, B., Mir, R., Morris, W. A., Oldenburg, D., Olivo, G., Perrouty, S., Piercey, S. J., Piette-Lauzière, N., Raskevicius, T., Reman, A., Rivard, B., Ross, M., Samson, I., Scott, S., Shamsipour, P., Shi, D., Smith, R., Sundaralingam, N., Taves, R., Taylor, C., Valentino, M., Vallée, M. A., Wasyliuk, K., Williams-Jones, A. E. and Winterburn, P., 2017, Integrated Multi-Parameter Exploration Footprints of the Canadian Malartic Disseminated Au, McArthur River-Millennium Unconformity U, and Highland Valley Porphyry Cu Deposits: Preliminary Results from the NSERC-CMIC Mineral Exploration Footprints Research Network: Proceedings of Exploration 17: Sixth Decennial International Conference on Mineral Exploration, Toronto, p. 325–347.

Li, Y., Selby, D., Condon, D. and Tapster, S., 2017, Cyclic Magmatic-Hydrothermal Evolution in Porphyry Systems: High-Precision U-Pb and Re-Os Geochronology Constraints on the Tibetan Qulong Porphyry Cu-Mo

Deposit: Economic Geology, v. 112, p. 1419–1440.

Lindsay, D. D., Zentilli, M. and Rivera, J. R. D. L., 1995, Evolution of an active ductile to brittle shear system controlling mineralization at the Chuquicamata porphyry copper deposit, northern Chile: International Geology Review, v. 37, p. 945–958.

Logan, J. M. and Mihalynuk, M. G., 2014, Tectonic controls on early mesozoic paired alkaline porphyry deposit belts (Cu-Au Ag-Pt-Pd-Mo) within the Canadian Cordillera: Economic Geology, v. 109, p. 827–858.

Lowell, J. D. and Guilbert, J. M., 1970, Lateral and vertical alteration-mineralization zoning in porphyry ore deposits: Economic Geology, v. 65, p. 373–408.

Luyendyk, A., 1997, Processing of airborne magnetic data: AGSO Journal of Australian Geology and Geophysics, v. 17, p. 31–38.

Lyons, P. C., 1971, Staining of feldspars on rock-slab surfaces for modal analysis: Mineralogical Magazine, v. 38, p. 518–519.

Lypaczewski, P. and Rivard, B., 2018, Estimating the Mg# and Al^{VI} content of biotite and chlorite from shortwave infrared reflectance spectroscopy: Predictive equations and recommendations for their use: International Journal of Applied Earth Observation and Geoinformation, v. 68, p. 116–126.

Mahmoodi, O., Smith, R. S. and Spicer, B., 2017, Using constrained inversion of gravity and magnetic field to produce a 3D litho-prediction model: Geophysical Prospecting, p. 1–18.

Maidment, D. W., Gibson, G. M. and Giddings, J. W., 2000, Regional structure and distribution of magnetite: implications for the interpretation of aeromagnetic data in the Broken Hill region, New South Wales: Exploration Geophysics, v. 31, p. 8–16.

Marshall, M. and Cox, A., 1972, Magnetic changes in pillow basalt due to sea floor weathering: Journal of Geophysical Research, v. 77, p. 6459–6469.

Masterman, G. J., Cooke, D. R., Berry, R. F., Walshe, J. L., Lee, A. W. and Clark, A. H., 2005, Fluid chemistry, structural setting, and emplacement history of the Rosario Cu-Mo porphyry and Cu-Ag-Au epithermal veins, Collahuasi district, northern Chile: Economic Geology, v. 100, p. 835–862.

Maughan, D. T., Keith, J. D., Christiansen, E. H., Pulsipher, T., Hattori, K. and Evans, N. J., 2002, Contributions from mafic alkaline magmas to the Bingham porphyry Cu-Au-Mo deposit, Utah, USA: Mineralium Deposita, v. 37, p. 14–37.

Mazurek, M., 2000, Geological and hydraulic properties of water-conducting features in crystalline rocks, *in* Stober, I., and Bucher, K., eds., Hydrogeology of crystalline rocks: Springer, p. 3–26.

McCaffrey, K. and Petford, N., 1997, Are granitic intrusions scale invariant?: Journal of the Geological Society, v. 154, p. 1–4.

McCuaig, T. C., Guj, P., Hronsky, J. M. A. and Schodde, R., 2009, Exploration targeting in a business context: 7th Fennoscandian Exploration and Mining Conference, Helsinki, Finland, 1 p.

McMillan, W. J., 1976a, Geology and genesis of the Highland Valley ore deposits and the Guichon Creek batholith, *in* Sutherland Brown, A., ed., Porphyry deposits of the Canadian Cordillera: Canadian Institute of Mining and Metallurgy, Special Volume 15, p. 85–104.

McMillan, W. J., 1976b, J. A., *in* Sutherland Brown, A., ed., Porphyry deposits of the Canadian Cordillera: Canadian Institute of Mining and Metallurgy, Special Volume 15, p. 144–162.

McMillan, W. J., 1985, Geology and ore deposits of the Highland Valley camp, *in* Sinclair, A. J., ed., Mineral Deposits Division field guide and reference manual series: Geological Association of Canada, v. 1, 121 p.

McMillan, W. J., Thompson, J. F. H., Hart, C. J. R. and Johnston, S. T., 1995, Regional geological and tectonic setting of porphyry deposits in British Columbia and Yukon Territory, *in* Schroeter, T. G., ed., Porphyry deposits of the Northwestern Cordillera of North America: Canadian Institute of Mining and Metallurgy, Special Volume 46, p. 40–57.

McMillan, W. J., Anderson, R. G., Chan, R. and Chow, W., 2009, Geology and mineral occurences (MINFILE), the Guichon Creek batholith and Highland Valley porphyry copper district, British Columbia: Geological Survey of Canada, Open File 6079, 6072 sheets, scale 1:100,000.

Mercer, C. N. and Reed, M. H., 2013, Porphyry Cu-Mo stockwork formation by dynamic, transient hydrothermal pulses: Mineralogic insights from the deposit at Butte, Montana: Economic Geology, v. 108, p. 1347–1377.

Meyer, C., 1965, An early potassic type of wall-rock alteration at Butte, Montana: American Mineralogist, v. 50, p. 1717–1722.

Meyer, C. and Hemley, J. J., 1967, Wall rock alteration, *in* Barnes, H. L., ed., Geochemistry of hydrothermal ore deposits: New York, Holt, Rinehart and Winston, p. 166–235.

Mihalynuk, M. G., Nelson, J. A. and Diakow, L. J., 1994, Cache Creek terrane entrapment: oroclinal paradox within the Canadian Cordillera: Tectonics, v. 13, p. 575–595.

Mihalynuk, M. G., Mountjoy, K., Smith, M., Currie, L., Gabites, J., Tipper, H., Orchard, M., Poulton, T. and Cordey, F., 1999, Geology and mineral resources of the Tagish Lake area (NTS 104M/8, 9, 10E, 15 and 104N/12W), northwestern British Columbia: British Columbia Ministry of Energy, Mines and Petroleum Resources, Bulletin 105, 217 p.

Mitchinson, D. E., Enkin, R. J. and Hart, C. J. R., 2013, Linking porphyry deposit geology to geophysics via physical properties: Adding value to Geoscience BC geophysical data: Geoscience BC Report, v. 14, 116 p.

Monger, J. W. H. and Price, R., 2002, The Canadian Cordillera: Geology and tectonic evolution: CSEG Recorder, v. 27, p. 17–36.

Monger, J. W. H., Souther, J. G. and Gabrielse, H., 1972, Evolution of the Canadian Cordillera; a plate-tectonic model: American Journal of Science, v. 272, p. 577–602.

Monier, G. and Robert, J.-L., 1986, Evolution of the miscibility gap between muscovite and biotite solid solutions with increasing lithium content: an experimental study in the system K_2O-Li_2O-MgO-FeO-Al_2O_3-SiO_2-H_2O-HF at 600 ° C, 2 kbar P H_2O: comparison with natural lithium micas: Mineralogical Magazine, v. 50, p. 641–651.

Morris, W. A., Ugalde, H., Markham, K. J., 2009, Remote predictive mapping of Cretaceous sediments in the Cypress Hills area, Alberta, using terrain data acquired from aeromagnetic surveys: Canadian Journal of Remote Sensing, v. 35, p. S142–S153.

Mortimer, N., 1987, The Nicola Group; Late Triassic and Early Jurassic subduction-related volcanism in British Columbia: Canadian Journal of Earth Sciences, v. 24, p. 2521–2536.

Mortimer, N., Van der Heyden, P., Armstrong, R. L. and Harakal, J., 1990, U-Pb and K-Ar dates related to the timing of magmatism and deformation in the Cache Creek Terrane and Quesnellia, southern British Columbia: Canadian Journal of Earth Sciences, v. 27, p. 117–123.

Mudd, G. M., Weng, Z. and Jowitt, S. M., 2013, A detailed assessment of global Cu resource trends and endowments: Economic Geology, v. 108, p. 1163–1183.

Munoz, J. L., 1984, F-OH and Cl-OH exchange in micas with applications to hydrothermal ore deposits, *in* Bailey, S. W., ed., Micas: Reviews in Mineralogy, v. 13, p. 469–494.

Nabighian, M. N., 1984, Toward a three-dimensional automatic interpretation of potential field data via generalized Hilbert transforms: Fundamental relations: Geophysics, v. 49, p. 780–786.

Nabighian, M. N., Grauch, V., Hansen, R., LaFehr, T., Li, Y., Peirce, J., Phillips, J. and Ruder, M., 2005, The historical development of the magnetic method in exploration: Geophysics, v. 70, p. 33–61.

Neal, L. C., Wilkinson, J. J., Mason, P. J. and Chang, Z., 2018, Spectral characteristics of propylitic alteration minerals as a vectoring tool for porphyry copper deposits: Journal of Geochemical Exploration, v. 184, p.

179–198.

Nelson, J. and Colpron, M., 2007, Tectonics and metallogeny of the British Columbia, Yukon and Alaskan Cordillera, 1.8 Ga to the present, *in* Goodfellow, W. D., ed., Mineral deposits of canada: A synthesis of major deposit-types, district metallogeny, the evolution of geological provinces, and exploration methods: Geological Association of Canada, Mineral Deposits Division, Special Publication No. 5, p. 755–791.

Nelson, J., Colpron, M. and Israel, S., 2013, The Cordillera of British Columbia, Yukon, and Alaska: Tectonics and metallogeny, *in* Colpron, M., Bissig, T., Rusk, B. G., and Thompson, J. F. H., eds., Tectonics, Metallogeny, and Discovery: The North American Cordillera and Similar Accretionary Settings: Society of Economic Geologists Special Publication, v. 17, p. 53–109.

Nixon, G., Archibald, D. and Heaman, L., 1993, ^{40}Ar-^{39}Ar and U-Pb geochronometry of the Polaris Alaskan-type complex, British Columbia: Precise timing of Quesnellia–North America interaction: Geological Association of Canada - Mineral Association of Canada Annual Meeting Abstract, p. A-76.

Norman, D. K., Parry, W. T. and Bowman, J. R., 1991, Petrology and geochemistry of propylitic alteration at Southwest Tintic, Utah: Economic Geology, v. 86, p. 13–28.

Norman, M. B., 1974, Improved techniques for selective staining of feldspar and other minerals using amaranth: United States Geological Survey Journal of Research, v. 2, p. 73–79.

Northcote, K. E., 1969, Geology and geochronology of the Guichon Creek batholith: British Columbia Department Mines and Petroleum Resources, Bulletin 56, p. 1–73.

Norton, D. and Knight, J. E., 1977, Transport phenomena in hydrothermal systems; cooling plutons: American Journal of Science, v. 277, p. 937–981.

Odonne, F. and Massonnat, G., 1992, Volume loss and deformation around conjugate fractures: comparison between a natural example and analogue experiments: Journal of Structural Geology, v. 14, p. 963–972.

Ohmoto, H. and Rye, R. O., 1979, Isotopes of sulfur and carbon, *in* Barnes, H. L., ed., Geochemistry of hydrothermal ore deposits, 2nd edition: John Wiley, New York, p. 509–567.

Osatenko, M. J. and Jones, M. B., 1976, Valley Copper, *in* Sutherland Brown, A., ed., Porphyry deposits of the Canadian Cordillera: Canadian Institute of Mining and Metallurgy, Special Volume 15, p. 130–143.

Parry, W. T., Ballantyne, J. M. and Jacobs, D. C., 1984, Geochemistry of hydrothermal sericite from Roosevelt Hot Springs and the Tintic and Santa Rita porphyry copper systems: Economic Geology, v. 79, p. 72–86.

Pennacchioni, G., Di Toro, G., Brack, P., Menegon, L. and Villa, I. M., 2006, Brittle–ductile–brittle deformation during cooling of tonalite (Adamello, Southern Italian Alps): Tectonophysics, v. 427, p. 171–197.

Petford, N. and Atherton, M. P., 1992, Granitoid emplacement and deformation along a major crustal lineament: the Cordillera Blanca, Peru: Tectonophysics, v. 205, p. 171–185.

Plouffe, A. and Ferbey, T., 2015, Surficial geology, Gnawed Mountain area, British Columbia, parts of NTS 921/6, I/7, I/10 and I/11: scale 1:50 000.

Pokrovski, G. S., Roux, J. and Harrichoury, J.-C., 2005, Fluid density control on vapor-liquid partitioning of metals in hydrothermal systems: Geology, v. 33, p. 657–660.

Pokrovski, G. S., Borisova, A. Y. and Harrichoury, J.-C., 2008, The effect of sulfur on vapor-liquid fractionation of metals in hydrothermal systems: Earth and Planetary Science Letters, v. 266, p. 345–362.

Pollard, D. D. and Aydin, A., 1988, Progress in understanding jointing over the past century: Geological Society of America Bulletin, v. 100, p. 1181–1204.

Pontual, S., Merry, N. and Gamson, P., 1997, Spectral Interpretation Field Manual: AusSpec International Pty Ltd: Spectral Analysis Guide for Mineral Exploration, G-Mex Vol 1, p. 169.

Post, J. L. and Noble, P. N., 1993, The near-infrared combination band frequencies of dioctahedral smectites, micas, and illites: Clays and Clay Minerals, v. 41, p. 639–639.

Pouchou, J. and Pichoir, F., 1984, A new model for quantitative x-ray microanalysis: Application to the analysis of homogeneous samples: Research in Aerospace, v. 3, p. 167–192.

Preto, V. A., 1979, Geology of the Nicola Group between Merritt and Princeton: British Columbia Ministry of Energy and Mines, Bulletin 69, 85 p.

Proffett, J. M., 2003, Geology of the Bajo de la Alumbrera porphyry copper-gold deposit, Argentina: Economic Geology, v. 98, p. 1535–1574.

Proffett, J. M., 2009, High Cu grades in porphyry Cu deposits and their relationship to emplacement depth of magmatic sources: Geology, v. 37, p. 675–678.

Pudack, C., Halter, W. E., Heinrich, C. A. and Pettke, T., 2009, Evolution of magmatic vapor to gold-rich epithermal liquid: The porphyry to epithermal transition at Nevados de Famatina, Northwest Argentina: Economic Geology, v. 104, p. 449–477.

Purucker, M. E. and Clark, D. A., 2011, Mapping and interpretation of the lithospheric magnetic field, *in* Mandea, M. and Korte, M., eds., Geomagnetic observations and models: IAGA Special Sopron Book Series, Springer, Netherlands, p. 311–337.

Reed, A. J. and Jambor, J. L., 1976, Highmont: Linearly zoned copper-molybdenum porphyry deposits and their significance in the genesis of the Highland Valley ores, *in* Sutherland Brown, A., ed., Porphyry deposits of the Canadian Cordillera: Canadian Institute of Mining and Metallurgy, Special Volume 15, p. 163–181.

Reford, M. S. and Sumner, J. S., 1964, Aeromagnetics: Geophysics, v. 29, p. 482–516.

Reid, R. P., 1985, The facies and evolution of an Upper Triassic reef complex in northern Canada: unpublished Ph.D. thesis, University of Miami, Miami, 437 p.

Reiter, M., Barroll, M. W., Minier, J. and Clarkson, G., 1987, Thermo-mechanical model for incremental fracturing in cooling lava flows: Tectonophysics,

v. 142, p. 241–260.

Reynolds, R. L., Rosenbaum, J. G., Hudson, M., Fishman, N., 1990, Rock magnetism, the distribution of magnetic minerals in the Earth's crust, and aeromagnetic anomalies: United States Geological Survey, Bulletin 1924, p. 24–45.

Richards, J. P., 2001, Discussion of "Is there a close spatial relationship between faults and plutons?" by S.R. Paterson and K.L. Schmidt: Journal of Structural Geology, v. 23, p. 2025–2027.

Richards, J. P., 2003, Tectono-magmatic precursors for porphyry Cu-(Mo-Au) deposit formation: Economic Geology, v. 98, p. 1515–1533.

Richards, J. P., 2005, Cumulative factors in the generation of giant calc-alkaline porphyry Cu deposits, *in* Porter, T. M., ed., Super porphyry copper and gold deposits: A global perspective, v. 1: Adelaide, PGC Publishing, p. 7–25.

Richards, J. P., 2009, Postsubduction porphyry Cu-Au and epithermal Au deposits: Products of remelting of subduction-modified lithosphere: Geology, v. 37, p. 247–250.

Richards, J. P., 2011, Magmatic to hydrothermal metal fluxes in convergent and collided margins: Ore Geology Reviews, v. 40, p. 1–26.

Rieder, M., Cavazzini, G., D'Yakonov, Y., Frank-Kamenetskii, V. A., Gottardi, G., Guggenheim, S., Koval, P. V., Muller, G., Neiva, A. R., Radoslovich, E. W., Robert, J.-L., Sassi, F. P., Takeda, H., Weiss, Z. and Wones, D. R., 1998, Nomenclature of the Micas: Canadian Mineralogist, v. 36, p. 905–912.

Roy, B. and Clowes, R. M., 2000, Seismic and potential-field imaging of the Guichon Creek batholith, British Columbia, Canada, to delineate structures hosting porphyry copper deposits: Geophysics, v. 65, p. 1418–1434.

Rusk, B. G., Reed, M. H. and Dilles, J. H., 2008, Fluid inclusion evidence for magmatic-hydrothermal fluid evolution in the porphyry copper-molybdenum deposit at Butte, Montana: Economic Geology, v. 103, p. 307–334.

Rusk, B. G., Reed, M. H., Dilles, J. H., Klemm, L. M. and Heinrich, C. A., 2004, Compositions of magmatic hydrothermal fluids determined by LA-ICP-MS of fluid inclusions from the porphyry copper-molybdenum deposit at Butte, MT: Chemical Geology, v. 210, p. 173–199.

Sánchez, M. G., Allan, M. M., Hart, C. J. R. and Mortensen, J. K., 2014, Extracting ore-deposit-controlling structures from aeromagnetic, gravimetric, topographic, and regional geologic data in western Yukon and eastern Alaska: Interpretation, v. 2, p. SJ75–SJ102.

Schiarizza, P., 2014, Geological setting of the Granite Mountain batholith, host to the Gibraltar porphyry Cu-Mo deposit, south-central British Columbia: Geological Fieldwork 2013, British Columbia Ministry of Energy and Mines, British Columbia Geological Survey Paper 2014-1, p. 95–110.

Schiarizza, P., 2015, Geological setting of the Granite Mountain batholith, south-central British Columbia: Geological Fieldwork 2014, British Columbia Ministry of Energy and Mines, British Columbia Geological Survey Paper 2015-1, p. 19–39.

Schiarizza, P., 2017, Ongoing stratigraphic studies in the Nicola Group: Stump Lake – Salmon River area, south-central British Columbia: Geological Fieldwork 2016, British Columbia Ministry of Energy and Mines, British Columbia Geological Survey Paper 2017-1, p. 17–33.

Schiarizza, P., Gaba, R., Glover, J., Garver, J. and Umhoefer, P., 1996, Geology and mineral occurrences of the Taseko-Bridge River area: British Columbia Ministry of Energy, Mines and Petroleum Geology, Bulletin 100, 292 p.

Seedorff, E., Barton, M. D., Stavast, W. J. and Maher, D. J., 2008, Root zones of porphyry systems: Extending the porphyry model to depth: Economic Geology, v. 103, p. 939–956.

Seedorff, E., Dilles, J. H., Proffett, J. M. J., Einaudi, M. T., Zurcher, L., Stavast, W. J. A., Johnson, D. A. and Barton, M. D., 2005, Porphyry deposits: characteristics and origin of hypogene features, *in* Hedenquist, J. W., Thompson, J. F. H., Goldfarb, R. J. and Richards, J. P., eds., Economic Geology One Hundredth Anniversary Volume: Society of Economic Geologists, Littleton, CO, United States, p. 251–298.

Segall, P. and Pollard, D. D., 1983, Joint formation in granitic rock of the Sierra Nevada: Geological Society of America Bulletin, v. 94, p. 563–575.

Shaver, S., Raines, G., Lisle, R., Schafer, R. and Wilkinson, W., 1991, Geology, alteration, mineralization and trace element geochemistry of the Hall (Nevada Moly) deposit, Nye County, Nevada: Geology and ore deposits of the Great Basin, Geological Society of Nevada Symposium, Reno/ Sparks, Proceedings, p. 303–332.

Sheppard, S. M. and Taylor, H., 1974, Hydrogen and oxygen isotope evidence for the origins of water in the Boulder batholith and the Butte ore deposits, Montana: Economic Geology, v. 69, p. 926–946.

Sheppard, S. M. F., Nielsen, R. L. and Taylor, H. P., 1969, Oxygen and hydrogen isotope ratios of clay minerals from porphyry copper deposits: Economic Geology, v. 64, p. 755–777.

Shinohara, H. and Hedenquist, J. W., 1997, Constraints on Magma Degassing beneath the Far Southeast Porphyry Cu-Au Deposit, Philippines: Journal of Petrology, v. 38, p. 1741-1752.

Sillitoe, R. H., 1972, A plate tectonic model for the origin of porphyry copper deposits: Economic Geology, v. 67, p. 184–197.

Sillitoe, R. H., 1993, Epithermal models: Genetic types, geometrical controls and shallow features: Geological Association of Canada Special Paper, v. 40, p. 403–417.

Sillitoe, R. H., 2000, Gold-rich porphyry deposits: Descriptive and genetic models and their role in exploration and discovery: Reviews in Economic Geology, v. 13, p. 315–345.

Sillitoe, R. H., 2010, Porphyry copper systems: Economic Geology, v. 105, p. 3–41.

Sillitoe, R. H. and Perelló, J., 2005, Andean copper province: tectonomagmatic settings, deposit types, metallogeny, exploration, and discovery, *in* Hedenquist, J. W., Thompson, J. F. H., Goldfarb, R. J. and Richards, J. P., eds., Economic Geology One Hundredth Anniversary Volume: Society of Economic Geologists, Littleton, CO, United States, p. 845–890.

Simon, A. C., Pettke, T., Candela, P. A., Piccoli, P. M. and Heinrich, C. A., 2007, The partitioning behavior of As and Au in S-free and S-bearing magmatic assemblages: Geochimica et Cosmochimica Acta, v. 71, p. 1764–1782.

Simpson, M., MacKenzie, D., Craw, D. and Doyle, S., 2016, Short-wave Infrared (SWIR) reflectance spectrometry studies of alteration at Frasers underground, Macraes gold mine, Otago, New Zealand: AusIMM New Zealand Branch Annual Conference, Wellington, p. 385–396.

Sinclair, W. D., 2007, Porphyry Deposits, *in* Goodfellow, W. D., ed., Mineral deposits of canada: A synthesis of major deposit-types, district metallogeny, the evolution of geological provinces, and exploration methods: Geological Association of Canada, Mineral Deposits Division, Special Publication No. 5, p. 223–243.

Singer, D. A., 2017, Future copper resources: Ore Geology Reviews, v. 86, p. 271–279.

Spencer, E. T., Wilkinson, J. J., Creaser, R. A. and Seguel, J., 2015, The distribution and timing of molybdenite mineralization at the El Teniente Cu-Mo porphyry deposit, Chile: Economic Geology, v. 110, p. 387–421.

Spicer, B., Morris, W. A. and Ugalde, H., 2011, Structure of the Rambler Rhyolite, Baie Verte Peninsula, Newfoundland: Inversions using UBC-GIF Grav3D and Mag3D: Journal of Applied Geophysics, v. 75, p. 9–18.

Stanley, G. D., Jr. and Senowbari-Daryan, B., 1999, Upper Triassic reef fauna from the Quesnel Terrane, central British Columbia, Canada: Journal of Paleontology, v. 73, p. 787–802.

Sun, Y., Seccombe, P. K. and Yang, K., 2001, Application of short-wave infrared spectroscopy to define alteration zones associated with the Elura zinc–lead–silver deposit, NSW, Australia: Journal of Geochemical Exploration, v. 73, p. 11–26.

Takada, A., 1994, The influence of regional stress and magmatic input on styles of monogenetic and polygenetic volcanism: Journal of Geophysical Research: Solid Earth, v. 99, p. 13563–13573.

Teck Resources Limited, 2018, 2017 Annual Information Form: 2017 Annual Information Form, 124 p.

Teck Resources Limited, 2019, 2018 Annual Information Form: 2018 Annual Information Form, 134 p.

Thompson, A. J. B., Hauff, P. L. and Robitaille, J. A., 1999, Alteration mapping in exploration; application of short-wave infrared (SWIR) spectroscopy: SEG Newsletter, v. 39, p. 1, 16–27.

Tindle, A. G. and Webb, P. C., 1990, Estimation of lithium contents in trioctahedral micas using microprobe data: application to micas from granitic rocks: European Journal of Mineralogy, v. 2, p. 595–610.

Titley, S. R., 1982, The style and progress of mineralization and alteration in porphyry copper systems: American southwest, *in* Titley, S. R., ed., Advances in geology of the porphyry copper deposit, southwestern North America, University of Arizona Press, Tucson, AZ, p. 139–184.

Titley, S. R., Thompson, R., Haynes, F., Manske, S., Robison, L. and White, J., 1986, Evolution of fractures and alteration in the Sierrita-Esperanza hydrothermal system, Pima County, Arizona: Economic Geology, v. 81, p. 343–370.

Tosdal, R. M. and Richards, J. P., 2001, Magmatic and Structural Controls on the Development of Porphyry Cu±Mo±Au Deposits: Reviews in Economic Geology, v. 14, p. 157–181.

Ugalde, H. and Morris, W. A., 2008, An assessment of topographic effects on airborne and ground magnetic data: The Leading Edge, v. 27, p. 76–79.

Uribe-Mogollon, C. and Maher, K., 2018, White Mica Geochemistry of the Copper Cliff Porphyry Cu Deposit: Insights from a Vectoring Tool Applied to Exploration: Economic Geology, v. 113, p. 1269–1295.

Vallée, M. A., Byrne, K., Lee, R. G., Lesage, G., King, J., Farquharson, C., Chouteau, M. and Enkin, R. J., 2017, Porphyry copper alteration imaging with aeromagnetic data at Highland Valley Copper, British Columbia, Canada: SEG International Exposition and 87th Annual Meeting, Society of Exploration Geophysicists, Houston, United States, p. 2445–2449.

van Ruitenbeek, F. J., Cudahy, T. J., van der Meer, F. D. and Hale, M., 2012, Characterization of the hydrothermal systems associated with Archean VMS-mineralization at Panorama, Western Australia, using hyperspectral, geochemical and geothermometric data: Ore Geology Reviews, v. 45, p. 33–46.

Vollmer, F. W., 1995, C program for automatic contouring of spherical orientation data using a modified Kamb method: Computers & Geosciences, v. 21, p. 31–49.

von Quadt, A., Erni, M., Martinek, K., Moll, M., Peytcheva, I. and Heinrich, C. A., 2011, Zircon crystallization and the lifetimes of ore-forming magmatic-hydrothermal systems: Geology, v. 39, p. 731–734.

Waldner, M. W., Smith, G. D. and Willis, R. D., 1976, Lornex, *in* Sutherland Brown, A., ed., Porphyry deposits of the Canadian Cordillera: Canadian Institute of Mining and Metallurgy, Special Volume 15, p. 120–129.

Wallace, R. E. and Morris, H. T., 1979, Characteristics of faults and shear zones as seen in mines at depths as much as 2.5 km below the surface: United States Geological Survey Open-File Report, v. 79, p. 79–100.

Wang, R., Cudahy, T., Laukamp, C., Walshe, J. L., Bath, A., Mei, Y., Young, C., Roache, T. J., Jenkins, A. and Roberts, M., 2017, White mica as a hyperspectral tool in exploration for the Sunrise Dam and Kanowna Belle gold deposits, Western Australia: Economic Geology, v. 112, p. 1153–1176.

Weir, A. and Greene-Kelly, R., 1962, Beidellite: American Mineralogist, v. 47, p. 137–146.

Weis, P., 2014, The physical hydrology of ore-forming magmatic-hydrothermal systems: Society of Economic Geologists Special Publication, v. 18, p. 59–75.

Weis, P., 2015, The dynamic interplay between saline fluid flow and rock permeability in magmatic-hydrothermal systems: Geofluids, v. 15, p. 350–371.

Weis, P., Driesner, T. and Heinrich, C., 2012, Porphyry-copper ore shells form at stable pressure-temperature fronts within dynamic fluid plumes: Science, v. 338, p. 1613–1616.

Whitney, D. L. and Evans, B. W., 2010, Abbreviations for names of rock-forming minerals: American Mineralogist, v. 95, p. 185–187.

Wilkinson, J. J., Chang, Z., Cooke, D. R., Baker, M. J., Wilkinson, C. C., Inglis, S., Chen, H. and Gemmell, J. B., 2015, The chlorite proximitor: A new tool for detecting porphyry ore deposits: Journal of Geochemical Exploration, v. 152, p. 10–26.

Williams, S. and Forrester, J., 1995, Characteristics of porphyry copper deposits, *in* Pierce, F. W., and Bolm, J. G., eds., Porphyry Copper Deposits of the American Cordillera: Arizona Geological Society Digest, v. 20, p. 20–34.

Williams-Jones, A. E. and Heinrich, C. A., 2005, Vapor transport of metals and the formation of magmatic-hydrothermal ore deposits, *in* Hedenquist, J. W., Thompson, J. F. H., Goldfarb, R. J. and Richards, J. P., eds., Economic Geology One Hundredth Anniversary Volume: Society of Economic Geologists, Littleton, CO, United States, p. 1287–1312.

Wilson, A. J., Cooke, D. R., Harper, B. J. and Deyell, C. L., 2007, Sulfur isotopic zonation in the Cadia district, southeastern Australia: exploration significance and implications for the genesis of alkalic porphyry gold–copper deposits: Mineralium Deposita, v. 42, p. 465–487.

Witherly, K., 2012, The evolution of minerals exploration over 60 years and the imperative to explore undercover: The Leading Edge, v. 31, p. 292–295.

Wyld, S. J., Umhoefer, P. J. and Wright, J. E., 2006, Reconstructing northern Cordilleran terranes along known Cretaceous and Cenozoic strike-slip faults: Implications for the Baja British Columbia hypothesis and other models, *in* Haggart, J. W., Enkin, R. J. and Monger, J. W. H., eds., Paleogeography of the North American cordillera: Evidence for and against large-scale displacements: Geological Association of Canada Special Paper 46, p. 277–298.

Zajacz, Z. and Halter, W., 2009, Copper transport by high temperature, sulfur-rich magmatic vapor: Evidence from silicate melt and vapor inclusions in a basaltic andesite from the Villarrica volcano (Chile): Earth and Planetary Science Letters, v. 282, p. 115–121.

Zhang, L., 2000, Stable isotope investigation of a hydrothermal alteration system: Butte porphyry copper deposit: unpublished Ph.D. thesis, Oregon State University, Corvallis, 182 p.

Zweng, P. L. and Clark, A. H., 1995, Hypogene evolution of the Toquepala porphyry copper-molybdenum deposit, Moquegua, southeastern Peru, *in* Pierce, F. W., and Bolm, J. G., eds., Porphyry Copper Deposits of the American Cordillera: Arizona Geological Society Digest, v. 20, p. 566–612.

Appendix A. Dike locations, and measured strikes and dips. Coordinates in UTM NAD1983 Zone 10.

Station ID	Northing (m)	Easting (m)	Elev (m)	Dike type	Strike	Dip	Confidence	Thickness (mm)	Comment
2014GL003	5592986	637364	1614	Aplite	250	45	High	50	
2014GL010	5592708	638115	1566	Aplite	22	75	High	40	
2014GL017	5592117	637134	1667	Aplite	185	75	High	100	
2014GL022	5591866	637627	1639	Aplite	25	85	High	10	
2014GL025	5591638	637191	1661	Aplite	255	65	High	150	
2014GL025	5591468	637194	1669	Aplite	240	70	High	150	
2014GL029	5591220	637530	1668	Aplite	315	75	High	25	Wavy
2014GL037	5592590	636822	1696	Aplite	335	55	High	30	Wavy
2014GL037	5592641	636858	1694	Porphyritic	170	80	High	500	Plagioclase-crowded, aphanitic groundmass
2014GL038	5592444	636685	1688	Aplite	220	75	High	200	3 subparallel aplites over 10 m (3, 5, and 20 cm thick)
2014GL041	5592814	636851	1684	Porphyritic	250	80	High		Dike contact
2014GL043	5593247	636736	1670	Aplite	275	85	High	30	Wavy
2014GL044	5592921	636495	1705	Aplite	240	85	High	50	
2014GL047	5592834	635923	1681	Aplite	105	70	High	10	
2014GL048	5593086	636037	1669	Aplite	265	75	High	50	
2014GL049	5593061	636342	1678	Aplite	250	70	High	20	
2014GL050	5593326	636436	1682	Aplite	265	80	High	150	2 aplites
2014GL050	5593338	636492	1677	Aplite	270	90	High	100	2 aplites
2014GL051	5593153	635966	1658	Aplite	110	75	High	50	4 aplites
2014GL051	5593153	635966	1658	Aplite	65	70	High	30	3 aplites
2014GL056	5593611	636657	1638	Aplite	290	90	High	40	
2014GL056	5593602	636663	1638	Aplite	285	90	High	100	
2014GL058	5593593	636343	1674	Aplite	285	85	High	300	
2014GL060	5594107	636476	1565	Aplite	350	37	High	100	
2014GL064	5593406	635757	1639	Aplite	305	80	High	15	
2014GL070	5593699	635528	1659	Aplite	320	85	High	150	Porphyritic aplite, wavy
2014GL073	5593664	635211	1653	Aplite	110	80	High	5	
2014GL076	5592442	635512	1668	Aplite	280	85	High	20	
2014GL076	5592467	635642	1686	Aplite	280	85	High	20	
2014GL081	5593000	635799	1680	Aplite	120	80	High	150	2 aplites, 1 m apart, cut by Qz vein
2014GL082	5592914	634900	1668	Aplite	40	70	High	50	Cut by N115 aplite
2014GL082	5592914	634900	1668	Aplite	115	80	High	20	Cuts N040 aplite, Qz in center
2014GL082	5592896	634900	1668	Aplite	10	75	High	50	Aplite pinches and disappears
2014GL082	5592884	634925	1664	Aplite	265	85	High	150	Feldspar-Qz-phyric aplite, splits into 2 and changes strike
2014GL082	5592983	634954	1662	Aplite	270	85	High	10	6 sub-parallel aplites, wavy, locally Qz in center
2014GL082	5593006	634968	1657	Aplite	225	90	High	50	
2014GL082	5593015	634983	1653	Aplite	85	75	High	20	
2014GL083	5592829	634648	1645	Aplite	65	60	High	300	
2014GL084	5593039	634553	1625	Aplite	55	85	High	10	
2014GL084	5593089	634625	1629	Aplite	100	90	High	40	
2014GL084	5593094	634677	1635	Aplite	80	65	High	100	5 aplites over a 5 m area, 2 to 10 cm each
2014GL084	5593094	634677	1635	Aplite	105	80	High	20	5 aplites over a 5 m area, 2 to 10 cm each
2014GL085	5592980	634762	1659	Aplite	325	80	High	30	
2014GL085	5593103	634848	1654	Aplite	120	75	High	20	2 subparallel aphanitic to very fine-grained aplites, cut and locally offset by later aplite and by N070 alteration
2014GL085	5593103	634848	1654	Aplite	85	85	High		Fine-grained aplite
2014GL086	5592557	634775	1654	Aplite	265	80	High	50	
2014GL087	5592652	634589	1638	Aplite	300	75	High	20	2 aplites
2014GL087	5592676	634658	1644	Aplite	320	85	High	250	
2014GL088	5591561	635629	1637	Aplite	60	90	High	20	
2014GL089	5591683	635602	1641	Aplite	80	90	High	30	
2014GL090	5592079	635747	1633	Aplite	275	67	High	10	
2014GL091	5592193	635555	1653	Aplite	140	35	High	20	
2014GL093	5591979	635265	1628	Aplite	275	75	High	40	2 subparallel aplites, 50 cm apart
2014GL099	5591835	636611	1648	Aplite	25	73	High	10	
2014GL101	5591364	636584	1655	Aplite	35	82	High	30	2 subparallel aplites, 2 and 3 cm respectively
2014GL107	5589421	635106	1715	Aplite	200	80	High	30	Cut by N320 alteration
2014GL107	5589644	635189	1710	Aplite	15	75	High	10	
2014GL108	5589568	635761	1663	Aplite	255	55	High	20	Cut by N325 alteration
2014GL112	5589347	635484	1730	Aplite	205	65	High	5	2 aplites 25 cm apart, coarse Kfs and Qz crystals
2014GL115	5590329	633593	1709	Aplite	240	80	High	50	
2014GL115	5590397	633639	1707	Aplite	278	85	High	150	

Station ID	Northing (m)	Easting (m)	Elev (m)	Dike type	Strike	Dip	Confidence	Thickness (mm)	Comment
2014GL115	5590399	633702	1696	Aplite	265	70	High	40	Coarse-grained with Qz in center
2014GL116	5590837	633766	1682	Aplite	230	72	High	20	Cut by N224 alteration
2014GL116	5590811	633775	1685	Aplite	50	67	High	20	Qz vein in center of 2 cm aplite
2014GL116	5590816	633779	1681	Aplite	45	65	High	10	2 aplites
2014GL116	5590816	633779	1681	Aplite	70	70	High	50	Coarse-grained with Qz in center
2014GL116	5590785	633833	1686	Aplite	90	70	High	200	
2014GL116	5590785	633833	1686	Aplite	90	60	High	40	
2014GL117	5590977	634126	1676	Aplite	280	75	High	150	
2014GL119	5590804	635224	1637	Aplite	230	85	High	30	
2014GL121	5589720	634353	1720	Aplite	35	65	High	80	
2014GL121	5589717	634317	1706	Porphyritic	30	70	High		Coarse-grained Qz, medium-grained Pl, aphanitic groundmass, flow-banding texture at contact (western contact)
2014GL121	5589712	634330	1711	Porphyritic	44	57	High		Coarse-grained Qz, medium-grained Pl, aphanitic groundmass eastern contact)
2014GL122	5589763	634783	1729	Aplite	190	85	High	20	
2014GL122	5589706	634797	1726	Aplite	20	85	High	150	
2014GL123	5590245	634729	1706	Porphyritic	260	90	Low		Bethsaida facies-Porphyritic dike contact, contact shows a chilled margin and is highly irregular
2014GL124	5589825	632767	1663	Aplite	282	36	High	80	Coarse-grained aplite
2014GL125	5589373	632506	1608	Aplite	280	74	High	20	Fine-grained aplite
2014GL125	5589389	632540	1614	Aplite	10	30	High	10	Coarse-grained, discontinuous, locally up to 5 cm, 3 subparallel aplites seen 40 cm apart
2014GL126	5589223	633099	1614	Aplite	260	85	High	10	
2014GL126	5589220	633102	1611	Aplite	60	60	High	15	Coarse-grained aplite
2014GL127	5589697	633185	1671	Aplite	280	75	High	80	Medium-grained aplite
2014GL128	5590180	633168	1724	Aplite	105	85	High	50	Coarse-grained with Qz in center
2014GL128	5590204	633202	1722	Aplite	50	65	High	150	Irregular aplite
2014GL131	5589453	631874	1575	Aplite	320	35	High	30	
2014GL131	5589449	631879	1575	Porphyritic	20	60	High	2000	Minor medium-grained Pl-Qz-Bt phenocrysts in a fine-grained pink groundmass
2014GL133	5589989	632007	1617	Aplite	0	23	High		Large fine-grained aplite, although full thickness not measurable
2014GL135	5590391	632680	1698	Aplite	285	85	High	20	3 aplites 5-10 cm apart
2014GL135	5590445	632686	1706	Porphyritic	82	52	High	600	Cut by N105 alteration
2014GL136	5590415	632140	1703	Aplite	355	30	High	30	
2014GL137	5590953	632317	1693	Aplite	340	43	High	30	2 aplites 40 cm apart
2014GL141	5591744	631163	1554	Aplite	275	30	Low	40	Coarse-grained with Qz in center
2014GL149	5590840	629986	1577	Aplite	110	20	High	20	2 coarse-grained aplites 3 m apart
2014GL150	5591218	629900	1584	Porphyritic	95	70	High	70	Pl-phyric, dark aphanitic groundmass
2014GL153	5591856	629581	1523	Aplite	225	40	High	30	2 aplites (coarse-grained Qz-Kfs vein), 1 m apart
2014GL153	5591815	629617	1526	Aplite	233	40	High	15	Coarse-grained Qz-Kfs vein
2014GL155	5591624	632326	1612	Aplite	50	53	High	10	Coarse-grained aplite
2014GL158	5591742	632749	1574	Aplite	290	60	Low	50	Wavy, coarse-grained in center, 5 seen over 10 m
2014GL158	5591742	632749	1574	Aplite	300	75	High	80	Wavy, coarse-grained in center, 5 seen over 10 m
2014GL184	5594938	633128	1512	Aplite	320	62	High	20	
2014GL187	5594542	633903	1547	Aplite	105	45	High	100	Coarse-grained aplite, cut by N105 alteration
2014GL187	5594598	633919	1544	Aplite	125	45	High	20	
2014GL195	5596250	632065	1469	Aplite	303	65	High	10	Coarse-grained aplite
2014GL202	5596223	633910	1556	Aplite	140	40	High	60	Fine-grained aplite
2014GL212	5598425	631849	1493	Aplite	85	30	Medium	20	
2014GL219	5598996	632404	1441	Aplite	60	45	High	20	
2015GL010	5587439	640559	1632	Aplite	120	34	High	30	
2015GL011	5586806	640249	1648	Aplite	145	45	High	100	
2015GL014	5586118	640955	1686	Aplite	270	85	High		Porphyritic with medium grained phenocrysts
2015GL020	5584676	641205	1638	Aplite	180	50	High		
2015GL024	5585072	641865	1690	Aplite	0	80	High	30	
2015GL025	5584350	641856	1659	Aplite	340	75	High	1000	
2015GL035	5585462	642884	1652	Aplite	120	80	High	70	
2015GL035	5585479	642927	1658	Aplite	335	40	High	150	
2015GL037	5584113	643618	1637	Aplite	240	80	High	50	Contains locallized coarse myoralitic Qz in center
2015GL043	5583556	640299	1578	Aplite	260	85	High	150	
2015GL045	5583073	640885	1588	Aplite	130	50	High	80	
2015GL045	5583073	640885	1588	Aplite	130	50	High	200	
2015GL047	5583383	641330	1634	Aplite	0	65	High	40	30 cm away from sub-parallel aplite
2015GL047	5583383	641330	1634	Aplite	0	65	High	100	30 cm away from sub-parallel aplite
2015GL054	5582158	642297	1568	Aplite	300	15	Low		On angular bolders
2015GL055	5584020	642476	1645	Aplite	50	80	High	300	1 observed
2015GL055	5584020	642476	1645	Aplite	50	80	High	80	1 observed
2015GL055	5584020	642476	1645	Aplite	50	80	High	20	1 observed

Station ID	Northing (m)	Easting (m)	Elev (m)	Dike type	Strike	Dip	Confidence	Thickness (mm)	Comment
2015GL055	5584020	642476	1645	Aplite	285	50	High	250	1 observed
2015GL056	5583451	642442	1631	Aplite	80	85	High	20	
2015GL056	5583474	642510	1633	Aplite	310	55	High	600	
2015GL056	5583474	642510	1633	Aplite	275	80	High	350	
2015GL058	5583163	643082	1612	Aplite	20	85	High	10	Porphyritic, laterally transforms into ~10cm mioral-itic cavity with coarse Ep
2015GL060	5583812	643339	1611	Aplite	320	70	High	400	
2015GL079	5579337	641675	1543	Aplite	310	85	High	400	Large aplite with very coarse (10-15 cm) Qz crystals in center
2015GL081	5580198	643590	1508	Aplite	55	30	High	5000	Aplite on top and to the north, exact thickness unknown but at least 5 m
2015GL081	5580198	643590	1508	Aplite	355	60	Medium	5000	Aplite on top and to the north, exact thickness unknown but at least 5 m
2015GL081	5580071	643660	1508	Aplite	140	16	High	25000	Thick aplite all the way to the top of the outcrop, Bethsaida looks strongly sheared near contact
2015GL081	5580116	643691	1511	Porphyritic	340	25	High	1400	Porphyritic Pl - Hbl+Bt (3%) - Qz eyes (5%) dike, med-grained phenocrysts
2015GL088	5578132	642402	1495	Porphyritic	10	70	High	1500	Bethsaida xenoliths in dike near contacts
2015GLVal-ley	5593901	637711	1265	Mafic	25	80	High	500	In yellow fault
2015GLVal-ley	5594055	637753	1265	Mafic	350	75	High	3000	
2015KB208	5587348	644585	1634	Aplite	335	65	High		
2015KB210	5587005	645303	1610	Porphyritic	135	60	High	4	FQP Diklet
2015KB213	5589888	643998	1586	Porphyritic	130	30	High	30	FQP Diklet

Appendix B. Structurally-controlled hydrothermal alteration descriptions, locations, and measured strikes and dips. Coordinates in UTM NAD1983 Zone 10.

Station ID	Northing (m)	Easting (m)	Elev (m)	Vein type	Strike	Dip	Conf	Density /m	Vein width (mm)	Vein minerals	Selvage width (mm)	Selvage minerals	Alteration	Lithology
2013MA009	5600033	636842	1337		20	69		2	5	Chl		Ab	Sodic-calcic	Chataway
2013MA009	5600033	636842	1337		20	69		2	5	Qz-Chl		Ab	Sodic-calcic	Chataway
2013MA010	5597859	633753	1448		312	85		4	1	Chl		Kfs	K-feldspar	Other
2013MA020	5597437	632146	1491		20	54		4	2	Ep-CuOx			Propylitic	Chataway
2013MA020	5597437	632146	1491		20	54		4	2	Ep-Chl		Ab	Sodic-calcic	Chataway
2013MA031	5594595	633922	1546		30	87		3	1	Chl			Propylitic	Bethlehem
2013MA031	5594595	633922	1546		30	87		3	1	Ep		Ab	Sodic-calcic	Bethlehem
2013MA033	5594353	634294	1594		275	75		0.2	150	Qz		Ser	Propylitic	Bethsaida
2013MA033	5594354	634290	1592		275	75		0.2	150	Qz		Ser	Propylitic	Bethsaida
2013MA034	5588344	637221	1662		330	77		3	1	Chl		Cly	Propylitic	Bethsaida
2013MA037	5587477	637759	1627		30	85		3	1	Ep			Propylitic	Bethsaida
2013MA038	5588155	646739	1508		110	80		0.2	2	Chl		Kfs	K-feldspar	Chataway
2013MA040	5587706	646483	1540		220	68		5	3	Ep			Propylitic	Bethlehem
2013MA047	5586768	646075	1584		350	65		5	1	Ep			Propylitic	Skeena
2013MA052	5585422	642370	1668		205	77		0.5	2	Ep		Cly	Propylitic	Skeena
2013MA053	5583892	643279	1620		65	87		3	1	Ep			Propylitic	Bethsaida
2013MA054	5585463	642877	1652		130	87		0.3	1	Chl			Propylitic	Skeena
2013MA056	5584847	643066	1634		335	65		4	5	Ep-Qz		Hem	Propylitic	Skeena
2013MA056	5584847	643066	1634		335	65		4	5	Ep-Qz		Hem	Propylitic	Skeena
2013MA057	5585206	643433	1695		350	70		3	2	Ep			Propylitic	Skeena
2013MA069	5585751	644412	1622		190	54		3	2	Ep			Propylitic	Skeena
2013MA071	5586049	644050	1658		150	67		0.2	3	Ep-Qz			Propylitic	Skeena
2013MA073	5585696	643847	1697		125	70		0.3	3	Ep-Qz		Cly	Propylitic	Skeena
2013MA076	5586437	646059	1572		145	30		4	1	Chl-Ep			Propylitic	Skeena
2013MA077	5586132	645224	1603		130	87		0.2	2	Ep			Propylitic	Skeena
2013MA090	5598488	635370	1335		65	74		1.5	2	Chl-Ep		Cly	Propylitic	Other
2013MA091	5598326	635625	1335		25	78		0.2	15	Ep-Chl		Kfs	K-feldspar	Chataway
2013MA091	5598326	635625	1335		25	78		0.2	15	Kfs-Bn			K-feldspar	Chataway
2013MA093	5598095	634717	1425		130	85		3	1	Chl-Ep			Propylitic	Other
2013MA095	5600015	636658	1286		200	70		0.2	3	Chl-Hem		Kfs	K-feldspar	Chataway
2013MA095	5600015	636658	1286		200	70		0.2	3	Ep		Ab	Sodic-calcic	Chataway
2013MA096	5600036	636648	1284		10	80		1	1	Ep		Kfs	K-feldspar	Other
2013MA099	5599087	640154	1600		145	87		0.2	10	Ep-Chl			Propylitic	Bethlehem
2013MA100	5597870	640076	1495		87	57		3	2	Chl-Ep		Ab	Sodic-calcic	Bethlehem
2013MA102	5588989	640890	1591		70	70		20	1	Chl-Ep			Propylitic	Skeena
2013MA103	5589037	640872	1581		45	70		0.1	20	Qz-Mol			Muscovite	Skeena
2013MA104	5589129	640855	1592		220	77		8	1	Qz-Mol			Muscovite	Skeena
2013MA105	5589195	640954	1582		55	70		0.1	20	Qz-Mol			Muscovite	Skeena
2013MA106	5589205	641002	1576		40	75		0.3	20	Qz-Mol		Hem	Muscovite	Skeena
2013MA111	5588812	641362	1582		280	62		7	10	Chl			Propylitic	Skeena
2013MA111	5588812	641362	1582		280	62		7	10	Qz-Chl			Propylitic	Skeena
2013MA112	5587770	642052	1674		255	77		9	5	Qz-Mol			Muscovite	Skeena
2013MA116	5587890	641990	1672		95	85		3	3	Bt			K-feldspar	Skeena
2013MA116	5587890	641990	1672		95	85		3	3	Qz-Ccp		Ser	Muscovite	Skeena
2013MA118	5587984	641989	1673		100	84		1.5	15	Qz-Ccp		Ser	Muscovite	Skeena

Station ID	Northing (m)	Easting (m)	Elev (m)	Vein type	Strike	Dip	Conf	Density /m	Vein width (mm)	Vein minerals	Selvage width (mm)	Selvage minerals	Alteration	Lithology
2013MA118	5587984	641989	1673		100	84		1.5	15	Qz-Mol			Muscovite	Skeena
2013MA120	5588258	642578	1728		315	57		4	2	Qz-Py		Ser	Muscovite	Bethsaida
2013MA122	5587995	642485	1726		55	55		1	20	Qz-CuOx		Ser	Propylitic	Skeena
2013MA123	5588660	642532	1589		355	85		7	2	Chl			Propylitic	Skeena
2013MA123	5588660	642532	1589		355	85		7	2	Qz-Bn		Ep	Propylitic	Skeena
2013MA124	5588683	642450	1589		167	68		5	5	Qz-Bn		Ser	Muscovite	Skeena
2013MA124	5588683	642450	1589		167	68		5	5	Qz-Mol		Kfs	K-feldspar	Skeena
2013MD051	5596284	643504	1554		67	88		0.5	1	Ep-Kfs		Ab	K-feldspar	Guichon
2013MD052	5595471	643259	1460		40	88		0.5	1	Kfs-Cal			K-feldspar	Bethlehem
2013MD052	5595471	643259	1460		40	88		0.5	1	Chl-CuOx		Ep	Propylitic	Bethlehem
2013MD053	5594729	644010	1492		31	70		5	4	Ep			Propylitic	Bethlehem
2013MD058	5595569	651747	1124		214	71		2	15	Bt-CuOx		Ser	K-feldspar	Guichon
2013MD058	5595569	651747	1124		214	71		2	15	Bt-CuOx		Ser	K-feldspar	Guichon
2013MD059	5597622	640343	1476		136	85		3	4	Chl-Qz			Propylitic	Bethlehem
2013MD062	5587710	646480	1540		220	68		5	30	Ep-Chl			Propylitic	Bethlehem
2013SB003	5582268	636837	1667		142	55		0.2	2	Ep			Propylitic	Chataway
2013SB045	5590454	631648	1637		84	80		0.1	1	CuOx-Ep-CuOx		Kfs	K-feldspar	Guichon
2013SB051	5590766	634309	1662		202	70		1	1	Chl			Propylitic	Bethsaida
2013SB052	5590898	634106	1675		55	60		1	3	Qz		Ser	Propylitic	Bethsaida
2013SB054	5590813	633809	1681		55	60		3	5	Kfs-Qz			K-feldspar	Bethsaida
2013SB054	5590813	633809	1681		55	60		3	5	Kfs-Qz			K-feldspar	Bethsaida
2013SB063	5603014	642011	1664		85	87		4	2	Ep-Chl		Ser	Propylitic	Guichon
2013SB064	5602886	642087	1661		195	63		8	2	CuOx-Qz		Kfs	K-feldspar	Guichon
2013SB064	5602886	642087	1661		195	63		8	2	Qz-Chl		Kfs	K-feldspar	Guichon
2013SB064A	5602876	642083	1662		195	63		8	2	CuOx-Qz		Kfs	K-feldspar	Guichon
2013SB064A	5602876	642083	1662		195	63		8	2	Qz-Chl		Kfs	K-feldspar	Guichon
2013SB079	5602618	641256	1792		190	63		3	2	Ep			Propylitic	Guichon
2013SB079A	5602618	641256	1792		190	63		3	2	Ep			Propylitic	Guichon
2013SB090	5593652	635158	1647		85	84		3	25	Qz		Ser	Propylitic	Bethsaida
2013SB094	5592696	635517	1675		70	80		4	1	Kfs			K-feldspar	Bethsaida
2013SB098	5592048	635689	1626		326	72		2	10	Qz-Chl		Cly	Propylitic	Bethsaida
2013SB099	5592304	635514	1668		115	82		0.3	1	Chl		Cly	Propylitic	Bethsaida
2013SB107	5590866	636208	1648		65	70		1.5	1	Chl		Cly	Propylitic	Bethsaida
2013SB115	5589093	637606	1636		280	70		2	2	Chl		Cly	Propylitic	Bethsaida
2013SB117	5587551	636930	1644		280	80		0.5	1	Qz		Chl	Propylitic	Bethsaida
2013SB125	5586454	633455	1633		270	67		1.2	35	Ep			Propylitic	Border
2013SB126	5586616	633414	1659		55	67		0.1	50	CuOx-Qz-CuOx		Ep	Propylitic	Border
2013SB130	5586887	633584	1684		157	72		2	7	Ep-Chl		Chl	Propylitic	Other
2013SB135	5586684	634315	1617		350	63		0.2	1	Chl		Ep	Propylitic	Skeena
2013SB139	5586859	634771	1631		85	60		0.1	5	Qz-CuOx		Ser	Propylitic	Bethsaida
2013SB143	5587515	635487	1676		260	85		0.1	1	Chl			Propylitic	Bethsaida
2013SB150	5602327	641210	1791		140	24		5	3	Ep		Kfs	K-feldspar	Guichon
2013SB150	5602327	641210	1791		140	24		5	3	Ep		Kfs	K-feldspar	Guichon
2013SB150A	5602333	641216	1791		140	24		5	3	Ep		Kfs	K-feldspar	Guichon
2013SB150A	5602333	641216	1791		140	24		5	3	Ep		Kfs	K-feldspar	Guichon

Station ID	Northing (m)	Easting (m)	Elev (m)	Vein type	Strike	Dip	Conf	Density /m	Vein width (mm)	Vein minerals	Selvage width (mm)	Selvage minerals	Alteration	Lithology
2013SB153	5601908	641419	1730		230	40		1	15	Ep-Kfs			K-feldspar	Guichon
2013SB153	5601908	641419	1730		230	40		1	15	Tur-Kfs			K-feldspar	Guichon
2013SB165	5600763	638718	1614		330	50		2	3	Ep			Propylitic	Bethlehem
2013SB172	5599966	638126	1525		20	73		4	3	Ep			Propylitic	Bethlehem
2013SB172	5599966	638126	1525		20	73		4	3	Ep			Propylitic	Bethlehem
2013SB177	5589485	639910	1591		335	81		0.5	40	Qz-Mol		Cly	Muscovite	Skeena
2013SB177	5589485	639910	1591		335	81		0.5	40	Qz-Mol		Cly	Muscovite	Skeena
2013SB179	5589718	638907	1592		20	60		0.5	2	Cal		Chl	Propylitic	Bethsaida
2013SB183	5589230	639205	1629		335	76		1.5	1	Chl-Cal		Chl	Propylitic	Bethsaida
2013SB183	5589230	639205	1629		335	76		1.5	1	Chl-Cly		Chl	Propylitic	Bethsaida
2013SB188	5584930	642737	1657		17	79		0.5	2	Ep		Qz	Propylitic	Skeena
2013SB188	5584930	642737	1657		17	79		0.5	2	Ep		Kfs	K-feldspar	Skeena
2013SB199	5581908	642345	1572		109	90		0.1	5	Kfs-Qz			K-feldspar	Bethsaida
2013SM003	5587156	631945	1642		0	90		1	7	Ep			Propylitic	Diorite to Quartz Diorite
2013SM004	5587131	631867	1631		0	90		2	30	Ep			Propylitic	Border
2013SM014	5598973	637868	1386		291	82		0.1	7	Ep			Propylitic	Bethlehem
2013SM016	5598922	638272	1465		70	62		1	10	Kfs			K-feldspar	Bethlehem
2013SM044	5590676	634035	1712		56	64		0.1	0	Ep			Propylitic	Bethsaida
2014GL001	5593254	637883	1539	Vein	88	64	High	3	10	Qz	20	Kfs-Ccp	K-feldspar	Bethsaida
2014GL001	5593254	637883	1539	Fracture halo	115	68	High	0.1			15	Kfs	K-feldspar	Bethsaida
2014GL002	5593125	637625	1575	Vein	85	50	High	0.1	30	Qz-Py	10	Kfs	K-feldspar	Bethsaida
2014GL003	5592986	637364	1614	Fracture halo	261	71	High	20	0.1	Mlc	5	Kfs	K-feldspar	Bethsaida
2014GL004	5593090	637127	1639	Fracture halo	265	90	High	20		Ccp-Py	3	Kfs-Ilt	K-feldspar	Bethsaida
2014GL009	5592960	637752	1594	Vein	222	85	High	13	5	Qz	2	Kfs	K-feldspar	Bethsaida
2014GL010	5592747	637854	1600	Fracture halo	215	57	High	10	0.1	Ms-Ccp			Muscovite	Bethsaida
2014GL010	5592708	638115	1566	Vein	215	80	High	3	5	Qz	3	Kfs-Ilt	K-feldspar	Bethsaida
2014GL012	5592488	637598	1634	Vein	230	60	High	2			4	Kfs-Ilt	K-feldspar	Bethsaida
2014GL013	5592584	637318	1627	Vein	225	65	High	8	2	Qz-Mlc	2	Kfs-Ccp	K-feldspar	Bethsaida
2014GL013	5592584	637318	1627	Fracture halo	164	70	High	0.1			30	Chl-Ep-Ilt	Propylitic	Bethsaida
2014GL013	5592584	637318	1627	Fracture halo	158	76	High	0.1			30	Chl-Ep-Ilt	Propylitic	Bethsaida
2014GL015	5592365	637280	1630	Fracture halo	220	80	High	8	0.1	Py-Ccp	2	Kfs-Ilt	K-feldspar	Bethsaida
2014GL016	5592270	637073	1659	Fracture halo	226	65	High	15	0.1	Py-Ccp-Mlc	30	Chl-Ser	Muscovite	Bethsaida
2014GL016	5592349	637119	1652	Fracture halo	225	70	High	15	0.1	Py-Ccp-Mlc	2	Chl-Ser	Muscovite	Bethsaida
2014GL017	5592120	637140	1665	Fracture halo	230	75	High	10	0.1	Py-Ccp-Ms	15	Ep-Chl-Ilt	Muscovite	Bethsaida
2014GL019	5592231	637623	1604	Fracture halo	220	75	High	5	0.1	Ccp-Bn	2	Kfs	K-feldspar	Bethsaida
2014GL020	5592016	637907	1613	Fracture halo	185	65	High	2.5			3	Kfs-Ilt	K-feldspar	Bethsaida
2014GL020	5592016	637907	1613	Fracture halo	225	65	High	0.1	0.1	Ms-Py-Ccp-Mlc	2	Ilt-Chl	Muscovite	Bethsaida
2014GL021	5591851	637880	1622	Vein	210	80	High	20	0.5	Ep-Qz	5	Chl-Ilt	Propylitic	Bethsaida
2014GL021	5591851	637880	1622	Fracture halo	215	77	High	0.1	0.1	Ms-Py	5	Chl-Ilt	Muscovite	Bethsaida
2014GL021	5591856	637882	1638	Fault breccia	210	75	High		150			Ilt	Propylitic	Bethsaida
2014GL021	5591872	637898	1633	Fault breccia	205	77	High		150			Ilt	Propylitic	Bethsaida
2014GL022	5591866	637627	1655	Vein	195	85	High	20	1	Ep-Qz	5	Chl-Ep-Hem-Ilt	Propylitic	Bethsaida
2014GL023	5592368	637825	1602	Vein	225	40	High	15	1	Qz	10	Kfs	K-feldspar	Bethsaida
2014GL024	5591328	637076	1688	Fracture zone	104	75	High		1000			Ilt	Propylitic	Bethsaida
2014GL024	5591366	637085	1682	Fracture halo	80	65	High	5			10	Chl-Ep-Ilt	Propylitic	Bethsaida

Station ID	Northing (m)	Easting (m)	Elev (m)	Vein type	Strike	Dip	Conf	Density /m	Vein width (mm)	Vein minerals	Selvage width (mm)	Selvage minerals	Alteration	Lithology
2014GL024	5591366	637085	1682	Fracture halo	102	75	High	1.25			50	Ep-Chl-Hem-Ilt	Propylitic	Bethsaida
2014GL024	5591366	637085	1682	Fracture halo	97	70	High	1.25			50	Ep-Chl-Hem-Ilt	Propylitic	Bethsaida
2014GL024	5591361	637110	1683	Vein	97	70	High	2	4	Qz-Ep	50	Ep-Chl-Hem-Ilt	Propylitic	Bethsaida
2014GL025	5591638	637191	1661	Fracture halo	25	70	High	2	0.1		10	Chl-Ep-Hem-Ilt	Propylitic	Bethsaida
2014GL025	5591638	637191	1661	Fracture halo	205	90	High	2	0.1		10	Chl-Ep-Hem-Ilt	Propylitic	Bethsaida
2014GL025	5591468	637194	1669	Fracture halo	25	75	High	0.1			20	Ep-Chl	Propylitic	Bethsaida
2014GL026	5591934	637058	1679	Vein	130	75	High	0.1	1	Qz-Ep	50	Ep-Chl-Ilt	Propylitic	Bethsaida
2014GL027	5591629	637420	1650	Fracture halo	135	80	High	0.1				Chl-Ep-Ilt	Propylitic	Bethsaida
2014GL027	5591671	637536	1653	Vein	25	75	High	5	1	Ep-Py	10	Chl-Ep-Ilt	Propylitic	Bethsaida
2014GL027	5591671	637536	1653	Fracture halo	245	60	High	0.1			20	Chl-Ep-Ilt	Propylitic	Bethsaida
2014GL028	5591603	637637	1643	Vein	350	80	High	3	2	Ep-Qz			Propylitic	Bethsaida
2014GL028	5591606	637637	1637	Fracture halo	30	65	High	3	0.1	Py-Ccp	10	Kfs	K-feldspar	Bethsaida
2014GL029	5591253	637323	1673	Fault breccia	270	75	High		50		250	Chl-Ep-Ilt	Propylitic	Bethsaida
2014GL029	5591336	637326	1663	Fracture halo	109	80	High	1			35	Chl-Ep	Propylitic	Bethsaida
2014GL029	5591256	637339	1668	Fracture halo	270	70	High	2			50	Chl-Ep-Ilt	Propylitic	Bethsaida
2014GL029	5591256	637339	1668	Vein	23	74	High	0.1	0.5	Chl-Ep-Mlc	20	Chl-Ep-Ilt	Propylitic	Bethsaida
2014GL029	5591226	637483	1652	Vein	15	70	High	4	1	Qz-Ep-Chl-Py	10	Chl-Ilt	Propylitic	Bethsaida
2014GL029	5591263	637489	1647	Fracture halo	20	66	High	6			25	Chl-Ep-Hem-Ilt	Propylitic	Bethsaida
2014GL030	5591356	637672	1666	Vein	5	80	High	3	1	Qz-Ep	30	Ep-Hem-Chl-Ilt	Propylitic	Bethsaida
2014GL030	5591356	637672	1666	Fracture halo	110	65	High	0.1			40	Chl-Ep-Ilt	Propylitic	Bethsaida
2014GL030	5591355	637810	1658	Fracture halo	85	85	High	3			50	Chl-Ep-Ilt	Propylitic	Bethsaida
2014GL030	5591379	637850	1652	Fracture halo	115	67	High	0.1			50	Chl-Ep-Hem-Ilt	Propylitic	Bethsaida
2014GL031	5591381	637878	1650	Fracture zone	110	75	High		1000			Chl-Ep-Py-Ccp	Propylitic	Bethsaida
2014GL031	5591362	637892	1646	Fracture zone	315	82	High		1000			Chl-Ep-Py-Ccp	Propylitic	Bethsaida
2014GL033	5591137	637699	1677	Fracture zone	85	70	High		500			Ep-Chl	Propylitic	Bethsaida
2014GL033	5591135	637705	1669	Fracture halo	85	75	High	2			50	Chl-Ep-Ilt	Propylitic	Bethsaida
2014GL034	5590839	637562	1650	Fracture halo	105	80	Med	0.1			50	Chl-Ep	Propylitic	Bethsaida
2014GL035	5591580	637973	1603	Vein	210	85	High	20	0.5	Ep-Py-Ccp-Bn	10	Ep-Chl-Hem-Ilt	Propylitic	Bethsaida
2014GL037	5592633	636843	1699	Fracture zone	210	90	High		300			Chl-Ilt	Propylitic	QFP
2014GL037	5592637	636847	1693	Fracture halo	55	90	High	1			10	Kfs	K-feldspar	QFP
2014GL038	5592444	636685	1688	Vein	330	90	High	2	2	Ep-Qz-Chl	40	Ep-Chl-Kfs-Ilt	K-feldspar	Bethsaida
2014GL038	5592444	636685	1688	Fracture halo	295	80	High	2			10	Ep-Chl-Kfs-Ilt	K-feldspar	Bethsaida
2014GL038	5592453	636724	1684	Vein	215	80	High	3	2	Qz-Kfs	10	Kfs-Ilt	K-feldspar	Bethsaida
2014GL038	5592453	636724	1684	Vein	270	55	High	1	2	Qz-Kfs	5	Kfs	K-feldspar	Bethsaida
2014GL039	5592316	636022	1665	Fracture halo	305	35	High	0.1			5	Chl-Ep-Ilt	Propylitic	Bethsaida
2014GL039	5592359	636091	1665	Vein	235	80	High	2.5	2	Qz-Mlc-Kfs	5	Ep-Chl-Kfs-Ilt	K-feldspar	Bethsaida
2014GL039	5592359	636091	1665	Fracture halo	330	35	High	0.1			5	Chl-Ep-Ilt	Propylitic	Bethsaida
2014GL040	5592660	635883	1681	Vein	150	75	High	2	0.5	Chl-Py-Mlc-Ccp	50	Ep-Chl-Hem-Ilt	Propylitic	Bethsaida
2014GL040	5592660	635883	1681	Fracture halo	185	55	High	0.1			2	Kfs	K-feldspar	Bethsaida
2014GL041	5592689	636507	1695	Fracture halo	155	70	High	0.1				Chl-Ep-Ilt	Propylitic	Bethsaida
2014GL041	5592979	636936	1661	Fracture halo	255	90	High	20			5	Chl-Ep-Kfs-Ilt	K-feldspar	Bethsaida
2014GL042	5593143	636896	1645	Fracture halo	70	57	High	5	0.1	Py	15	Chl-Ep-Ilt	Propylitic	Bethsaida
2014GL042	5593143	636896	1645	Vein	285	80	High	0.1	0.1	Py	5	Ser	Muscovite	Bethsaida
2014GL042	5593235	636903	1659	Vein	80	85	High	5	0.1	Py-Ccp	15	Chl-Ep-Ilt	Propylitic	Bethsaida
2014GL043	5593192	636682	1674	Fracture halo	95	80	High	5	0.1	Py-Ccp-Hem-Mlc	10	Kfs-Chl-Ilt	K-feldspar	Bethsaida

Station ID	Northing (m)	Easting (m)	Elev (m)	Vein type	Strike	Dip	Conf	Density /m	Vein width (mm)	Vein minerals	Selvage width (mm)	Selvage min-erals	Alteration	Lithology
2014GL043	5593241	636717	1671	Fracture halo	105	85	High	20	0.1	Py-Ccp-Hem-Mlc	10	Kfs-Chl-Ilt	K-feldspar	Bethsaida
2014GL043	5593241	636717	1671	Fracture halo	97	90	High	20	0.1	Py-Ccp-Hem-Mlc	10	Kfs-Chl-Ilt	K-feldspar	Bethsaida
2014GL043	5593247	636736	1670	Vein	102	80	High	0.1	5	Qz	2	Kfs-Ilt	K-feldspar	Bethsaida
2014GL046	5592836	636147	1686	Fracture halo	250	90	High	0.1	0.1	Chl-Ep-Py-Mlc	5	Chl	Propylitic	Bethsaida
2014GL046	5592790	636166	1686	Fracture halo	3	55	High	0.1	0.1	Chl-Ep-Py-Mlc	5	Chl	Propylitic	Bethsaida
2014GL047	5592834	635923	1681	Fracture halo	60	70	High	1		Chl-Hem-Mlc	15	Kfs-Chl-Ep-Ilt	K-feldspar	Bethsaida
2014GL047	5592834	635923	1681	Fracture halo	180	90	High	0.1	0.1	Chl			Propylitic	Bethsaida
2014GL048	5593004	636005	1675	Fracture halo	245	80	High	20			5	Chl-Ep-Kfs	K-feldspar	Bethsaida
2014GL048	5593086	636037	1669	Fracture halo	260	80	High	0.1			1	Chl-Ilt	Propylitic	Bethsaida
2014GL048	5593093	636114	1672	Fracture halo	80	85	High	10			5	Chl-Kfs-Ilt	K-feldspar	Bethsaida
2014GL049	5593113	636406	1674	Vein	250	70	High	0.1	5	Qz	5	Chl-Kfs-Ilt	K-feldspar	Bethsaida
2014GL050	5593366	636391	1683	Vein	225	90	High	0.1	5	Qz	1	Kfs	K-feldspar	Bethsaida
2014GL050	5593326	636436	1682	Vein	265	70	High	0.1	5	Qz	5	Kfs-Ilt	K-feldspar	Bethsaida
2014GL050	5593338	636489	1678	Fracture halo	280	90	High	35	0.1	Py-Ccp	5	Chl-Kfs-Ilt	K-feldspar	Bethsaida
2014GL051	5593153	635966	1658	Fracture halo	20	85	High	0.1	0.1	Chl-Py-Ccp	10	Chl-Ilt	Propylitic	Bethsaida
2014GL052	5593336	636129	1662	Fault	100	90	High		50			Ms-Ccp-Py	Muscovite	Bethsaida
2014GL053	5593384	636606	1658	Fracture halo	110	85	High	25	0.1	Py-Ccp-Chl	4	Chl-Ilt	Propylitic	Bethsaida
2014GL055	5593572	636979	1625	Fracture halo	115	77	High	10	0.1	Py-Ccp	1	Kfs-Chl-Ilt	K-feldspar	Bethsaida
2014GL056	5593602	636663	1638	Fracture halo	110	77	High	15	0.1	Py-Ccp-Chl		Kfs	K-feldspar	Bethsaida
2014GL058	5593593	636343	1674	Vein	290	85	High	0.1	60		10	Kfs	K-feldspar	Bethsaida
2014GL059	5593585	636112	1636	Fracture zone	90	80	High		30			Chl	Propylitic	Bethsaida
2014GL060	5594107	636476	1565	Fault	5	65	High		10000			Ilt	Propylitic	Bethsaida
2014GL060	5594106	636489	1566	Fault	0	65	High		10000			Ilt	Propylitic	Bethsaida
2014GL060	5594041	636632	1565	Fault	205	45	High		50			Ilt	Propylitic	Bethsaida
2014GL061	5593905	636900	1535	Fracture halo	115	85	High	10	0.1	Chl-Py-Ccp			Propylitic	Bethsaida
2014GL063	5593879	635926	1612	Fracture halo	130	85	High	10	0.1	Py	1	Kfs-Ilt	K-feldspar	Bethsaida
2014GL064	5593406	635757	1639	Vein	280	90	High	0.1	5	Qz	15	Chl-Ep-Kfs-Ilt	K-feldspar	Bethsaida
2014GL065	5593925	636102	1590	Fracture halo	125	85	High	10	0.5	Py-Ccp	1	Kfs-Chl	K-feldspar	Bethsaida
2014GL066	5593453	635435	1668	Fracture halo	275	80	High	12	0.1	Ep-Chl	2	Chl-Ilt-Mlc-Kfs	K-feldspar	Bethsaida
2014GL067	5593279	635584	1675	Vein	280	80	High	12	1	Qz	2	Chl-Ilt-Kfs	K-feldspar	Bethsaida
2014GL067	5593279	635584	1675	Vein	185	75	High	2.5	1	Ep	20	Chl-Ilt-Hem	Propylitic	Bethsaida
2014GL068	5593775	635715	1634	Vein	270	70	High	0.1	8	Qz	100	Chl-Hem	Propylitic	Bethsaida
2014GL068	5593771	635730	1632	Fracture halo	290	75	High	0.1	0.1	Py-Ccp-Mol	0.5	Chl-Ep	Muscovite	Bethsaida
2014GL069	5594157	635323	1610	Fracture halo	265	77	High	12	0.1	Chl-Mlc-Ep	10	Chl-Ep-Ilt	Propylitic	Bethsaida
2014GL070	5593626	635443	1672	Fracture halo	295	90	High	0.1			2	Chl-Ep-Hem-Ilt	Propylitic	Bethsaida
2014GL070	5593676	635451	1669	Fracture halo	30	60	High	0.1			10	Chl-Ilt	Propylitic	Bethsaida
2014GL072	5594135	634961	1608	Vein	55	80	High	5	1	Chl-Ep	5	Chl-Ep-Hem	Propylitic	Bethsaida
2014GL072	5594135	634961	1608	Vein	15	80	High	0.1	1	Chl-Ep	3	Chl-Ep-Hem	Propylitic	Bethsaida
2014GL073	5593653	635205	1650	Fracture halo	20	70	High	0.1			25	Chl-Ilt	Propylitic	Bethsaida
2014GL073	5593653	635205	1650	Fracture halo	5	80	High	0.1			25	Chl-Ilt	Propylitic	Bethsaida
2014GL074	5593326	634638	1600	Fracture halo	200	90	High	0.1			30	Ilt	Propylitic	Bethsaida
2014GL074	5593326	634638	1600	Fracture halo	180	80	High	0.1			30	Ilt	Propylitic	Bethsaida
2014GL074	5593362	634754	1578	Fracture halo	60	80	High	0.1			100	Ser	Propylitic	Bethsaida
2014GL074	5593357	634764	1599	Fault	45	55	High		5000	Ilt-Mlc		Ilt	Propylitic	Bethsaida
2014GL075	5592700	635521	1676	Fracture halo	65	70	High	16			5	Chl-Ep-Hem	Propylitic	Bethsaida

Station ID	Northing (m)	Easting (m)	Elev (m)	Vein type	Strike	Dip	Conf	Density /m	Vein width (mm)	Vein minerals	Selvage width (mm)	Selvage minerals	Alteration	Lithology
2014GL075	5592700	635521	1676	Vein	0	85	High	2.5	0.5	Chl	15	Chl-Ep-Hem-Ilt	Propylitic	Bethsaida
2014GL075	5592735	635598	1681	Fracture halo	60	82	High	16			5	Chl-Ep-Hem	Propylitic	Bethsaida
2014GL075	5592782	635601	1676	Vein	65	72	High	3	0.5	Qz	5	Chl-Ep-Hem-Ilt	Propylitic	Bethsaida
2014GL075	5592743	635605	1680	Vein	330	83	High	2.5	1	Chl	30	Chl-Ep-Hem-Ilt	Propylitic	Bethsaida
2014GL076	5592447	635521	1668	Fracture halo	65	90	High	20			2	Chl-Ep-Hem-Ilt	Propylitic	Bethsaida
2014GL076	5592447	635521	1668	Vein	355	85	High	2	1	Chl-Ep	30	Chl-Ep-Hem-Ilt	Propylitic	Bethsaida
2014GL076	5592464	635580	1677	Vein	300	80	High	0.75	1	Chl	35	Chl-Ep-Hem-Ilt	Propylitic	Bethsaida
2014GL076	5592464	635580	1677	Vein	5	80	High	2.5	2	Chl-Ep-Qz	35	Chl-Ep-Hem-Ilt	Propylitic	Bethsaida
2014GL076	5592423	635648	1685	Fracture halo	210	75	High	10	0.1	Mlc-Py	10	Hem-Chl-Ep-Ilt	Propylitic	Bethsaida
2014GL077	5592457	635186	1657	Vein	80	80	High	5	1	Chl-Ep	25	Chl-Ep-Ilt	Propylitic	Bethsaida
2014GL077	5592334	635246	1662	Fracture halo	72	85	High	0.1	0.1	Chl-Ep-Mlc	10	Chl-Ep-Ilt	Propylitic	Bethsaida
2014GL077	5592334	635246	1662	Fracture halo	125	70	High	0.1	0.1		30	Chl-Ep-Ilt-Hem	Propylitic	Bethsaida
2014GL077	5592336	635259	1662	Fracture halo	70	80	High	0.1			15	Chl-Ep-Ilt	Propylitic	Bethsaida
2014GL077	5592310	635280	1667	Fault	10	62	High		0.5	Ep			Propylitic	Bethsaida
2014GL078	5592918	635304	1674	Fracture halo	75	85	High	7			3	Kfs-Chl-Ep-Ilt	K-feldspar	Bethsaida
2014GL078	5592918	635304	1674	Vein	355	70	High	2	1	Chl-Ep	35	Ep-Chl-Ilt	Propylitic	Bethsaida
2014GL078	5592756	635405	1668	Vein	40	75	High	2	0.5	Chl	25	Chl-Ep-Kfs	K-feldspar	Bethsaida
2014GL079	5592524	635363	1669	Fracture halo	65	90	High	0.1	0.1	Chl-Ep-Mlc	2	Kfs-Chl-Ep	K-feldspar	Bethsaida
2014GL079	5592436	635421	1677	Fracture halo	60	85	High	0.1	0.1	Mlc-Ep	15	Chl-Ep-Ilt-Kfs	K-feldspar	Bethsaida
2014GL079	5592447	635441	1675	Vein	60	80	High	2	0.5	Chl-Ep	55	Chl-Ep-Ilt	Propylitic	Bethsaida
2014GL079	5592430	635442	1673	Vein	105	85	High	2	0.5	Chl-Ep	15	Chl-Ep-Ilt	Propylitic	Bethsaida
2014GL079	5592430	635442	1673	Fracture halo	65	90	High	0.1	0.1	Mlc-Ep	5	Chl-Ep-Ilt-Kfs	K-feldspar	Bethsaida
2014GL080	5593018	635515	1666	Fracture halo	65	70	High	7			5	Kfs-Chl-Ilt-Ep	K-feldspar	Bethsaida
2014GL080	5593018	635515	1666	Fracture halo	20	70	High	2	0.1	Chl	25	Chl-Ep-Ilt	Propylitic	Bethsaida
2014GL080	5593020	635528	1669	Fracture halo	75	80	High	7			5	Kfs-Chl-Ilt-Ep	K-feldspar	Bethsaida
2014GL080	5593014	635529	1668	Fracture halo	10	75	High	2	0.1	Chl	25	Chl-Ep-Ilt	Propylitic	Bethsaida
2014GL081	5593000	635799	1680	Vein	60	80	High	0.1	5	Qz	15	Kfs-Chl-Ilt	K-feldspar	Bethsaida
2014GL081	5593003	635811	1679	Vein	75	75	High	20	0.5	Qz-Mlc-Py-Hem	10	Kfs-Chl-Ep-Ilt	K-feldspar	Bethsaida
2014GL082	5592914	634900	1668	Fracture halo	75	85	High	8			3	Kfs-Chl-Ep-Ilt	K-feldspar	Bethsaida
2014GL082	5592884	634925	1664	Fracture halo	70	77	High	3			10	Kfs-Chl-Ep-Ilt	K-feldspar	Bethsaida
2014GL082	5592983	634954	1662	Fracture halo	70	75	High	0.1			5	Kfs-Ilt	K-feldspar	Bethsaida
2014GL082	5592983	634954	1662	Fracture halo	105	80	High	0.1			15	Ep	Propylitic	Bethsaida
2014GL082	5592975	634963	1659	Fracture halo	190	85	High	0.1			25	Chl-Ep-Kfs-Ilt	K-feldspar	Bethsaida
2014GL082	5593006	634968	1657	Fracture halo	95	85	High	20			0.1	Kfs-Chl-Ilt	K-feldspar	Bethsaida
2014GL082	5592870	634976	1660	Fracture halo	40	85	High	0.1			20	Chl-Ep-Kfs-Ilt	K-feldspar	Bethsaida
2014GL082	5592870	634976	1660	Fracture halo	70	70	High	0.1			5	Kfs-Ilt	K-feldspar	Bethsaida
2014GL082	5592919	634986	1656	Fracture halo	80	75	High	3	0.1	Chl	15	Chl-Ep-Kfs-Ilt	K-feldspar	Bethsaida
2014GL083	5592802	634612	1640	Fracture halo	70	90	High	15			4	Ab-Chl-Ep-Ilt	Sodic-calcic	Bethsaida
2014GL083	5592820	634617	1637	Vein	80	85	High	0.1	5	Qz	2	Kfs-Chl-Ep-Ilt	K-feldspar	Bethsaida
2014GL083	5592832	634638	1638	Fracture halo	5	65	High	0.1			10	Chl-Ep-Ilt	Propylitic	Bethsaida
2014GL083	5592832	634638	1638	Fracture halo	80	75	High	0.1			3	Chl-Ep-Ilt	Propylitic	Bethsaida
2014GL083	5592788	634645	1648	Fracture halo	65	80	High	1			10	Kfs-Ilt	K-feldspar	Bethsaida
2014GL084	5593039	634553	1625	Fracture halo	30	70	High	0.1			15	Chl-Ep-Ilt	Propylitic	Bethsaida
2014GL084	5593037	634602	1630	Fracture halo	258	80	High	2.5	0.1	Mlc	10	Chl-Ep-Ilt-Hem	Propylitic	Bethsaida
2014GL084	5593037	634602	1630	Vein	53	70	High	0.1	0.5	Ep	35	Ep-Chl-Hem-Ilt	Propylitic	Bethsaida

Station ID	Northing (m)	Easting (m)	Elev (m)	Vein type	Strike	Dip	Conf	Density /m	Vein width (mm)	Vein minerals	Selvage width (mm)	Selvage minerals	Alteration	Lithology
2014GL084	5593027	634684	1644	Fracture halo	75	85	High	0.1			2	Chl-Ep-Ilt	Propylitic	Bethsaida
2014GL084	5593027	634684	1644	Vein	175	70	High	0.1	0.5	Chl-Ep	15	Ep-Ilt-Chl	Propylitic	Bethsaida
2014GL085	5593103	634845	1654	Vein	5	65	High	0.1	1	Ep-Chl	50	Chl-Ep-Ilt-Kfs	K-feldspar	Bethsaida
2014GL085	5593103	634848	1654	Fracture halo	70	75	High	2.5	0.1	Mlc	15	Chl-Ep-Kfs-Ilt	K-feldspar	Bethsaida
2014GL086	5592556	634774	1655	Fracture halo	65	80	High	3			20	Chl-Ep-Hem-Ilt	Propylitic	Bethsaida
2014GL086	5592557	634775	1654	Vein	85	90	High	0.1	5	Qz	2	Chl-Ep-Hem-Ilt	Propylitic	Bethsaida
2014GL086	5592576	634837	1660	Fracture halo	70	85	High	2			10	Chl-Ep-Hem-Ilt	Propylitic	Bethsaida
2014GL086	5592596	634849	1657	Vein	75	82	High	25	5	Qz-Kfs			K-feldspar	Bethsaida
2014GL087	5592652	634589	1638	Fracture halo	75	80	High	3			3	Ep-Chl-Hem-Ilt	Propylitic	Bethsaida
2014GL087	5592676	634658	1644	Vein	85	83	High	0.1	5		5	Hem-Chl-Ep-Ilt	Propylitic	Bethsaida
2014GL088	5591525	635583	1622	Vein	55	85	High	0.1	10	Qz-Ep	100	Ep-Chl-Ilt-Hem	Propylitic	Bethsaida
2014GL088	5591481	635589	1614	Fracture halo	50	85	High	0.1			35	Ep-Chl-Ilt	Propylitic	Bethsaida
2014GL089	5591703	635509	1621	Vein	20	50	High	0.1	1	Ep			Propylitic	Bethsaida
2014GL089	5591703	635509	1621	Vein	320	65	High	1	0.5	Chl	15	Ep-Chl-Ilt	Propylitic	Bethsaida
2014GL089	5591651	635576	1635	Vein	320	65	High	0.5	0.5	Chl	15	Ep-Chl-Ilt	Propylitic	Bethsaida
2014GL089	5591684	635601	1638	Fracture halo	0	80	High	0.1			20	Ep-Chl-Ilt	Propylitic	Bethsaida
2014GL089	5591683	635602	1641	Vein	285	65	High	3	0.5	Chl-Qz	50	Ep-Chl-Ilt	Propylitic	Bethsaida
2014GL090	5592047	635685	1626	Vein	320	71	High	6	5	Chl-Qz-Ep	50	Ep-Chl-Ilt	Propylitic	Bethsaida
2014GL090	5592040	635690	1624	Vein	325	84	High	5	5	Chl-Qz-Ep	50	Ep-Chl-Ilt	Propylitic	Bethsaida
2014GL090	5592079	635747	1633	Vein	0	80	High	4	0.5	Ep	30	Chl-Ep-Ilt	Propylitic	Bethsaida
2014GL090	5592079	635747	1633	Fracture halo	70	80	High	2			40	Chl-Ep-Ilt	Propylitic	Bethsaida
2014GL090	5592049	635766	1634	Vein	80	80	High	2	2	Chl-Qz-Ep	50	Ep-Chl-Ilt	Propylitic	Bethsaida
2014GL090	5592118	635786	1639	Vein	50	85	High	1.5	1	Qz-Ep	15	Ilt-Chl-Ep	Propylitic	Bethsaida
2014GL090	5592118	635786	1639	Vein	130	85	High	0.7	0.5	Chl	10	Ep-Ilt-Chl	Propylitic	Bethsaida
2014GL091	5592195	635551	1653	Vein	185	85	High	1	0.5	Ep	10	Chl-Ilt-Ep	Propylitic	Bethsaida
2014GL091	5592193	635555	1653	Vein	75	80	High	10	1	Qz-Chl-Ep	20	Chl-Ilt-Ep	Propylitic	Bethsaida
2014GL092	5592110	635103	1627	Fracture halo	165	45	High	3			5	Ilt-Ep-Chl	Propylitic	Bethsaida
2014GL092	5592110	635103	1627	Vein	65	85	High	5	0.5	Qz	3	Chl-Ilt-Ep	Propylitic	Bethsaida
2014GL092	5592156	635106	1628	Vein	165	85	High	4	0.5	Chl	20	Ep-Chl-Ilt	Propylitic	Bethsaida
2014GL092	5592156	635106	1628	Fracture halo	195	74	High	0.1			10	Ilt-Chl-Ep	Propylitic	Bethsaida
2014GL092	5592124	635122	1628	Vein	165	63	High	0.1	2	Chl	40	Ep-Chl-Ilt	Propylitic	Bethsaida
2014GL093	5591999	635265	1630	Vein	165	85	High	5	1	Chl-Qz-Ep	35	Ep-Ilt-Chl	Propylitic	Bethsaida
2014GL094	5592117	636044	1635	Vein	155	75	High	0.1	1	Ep-Chl	30	Chl-Ilt-Ep	Propylitic	Bethsaida
2014GL095	5592124	636488	1671	Vein	35	70	High	2.5	2	Qz-Chl-Ep	15	Ilt-Chl-Ep	Propylitic	Bethsaida
2014GL095	5592161	636616	1670	Vein	115	80	High	5	0.5	Chl	20	Ilt-Chl-Ep	Propylitic	Bethsaida
2014GL096	5591793	636895	1672	Vein	35	80	High	6	1	Qz-Ep	7	Ilt-Chl-Ep	Propylitic	Bethsaida
2014GL096	5591793	636895	1672	Vein	110	90	High	2	0.5	Qz-Chl	50	Chl-Ep-Ilt	Propylitic	Bethsaida
2014GL096	5591793	636895	1672	Vein	165	80	High	1.5	0.5	Qz-Chl	50	Chl-Ep-Ilt	Propylitic	Bethsaida
2014GL097	5591357	636827	1688	Vein	35	60	High	0.1	1	Qz	30	Chl-Ep-Hem	Propylitic	Bethsaida
2014GL097	5591357	636827	1688	Vein	60	75	High	0.1	2	Ep	35	Ilt-Chl-Ep	Propylitic	Bethsaida
2014GL097	5591305	636854	1684	Vein	35	75	High	0.1	1	Ep	15	Ep-Chl-Ilt	Propylitic	Bethsaida
2014GL097	5591305	636854	1684	Fracture halo	120	80	High	0.1	0.1	Chl	90	Chl-Ep-Ilt	Propylitic	Bethsaida
2014GL098	5591573	636883	1655	Fracture halo	115	75	High	0.1			50	Ep-Chl-Ilt	Propylitic	Bethsaida
2014GL098	5591573	636883	1655	Fracture halo	85	75	High	10			2	Chl-Ep-Ilt	Propylitic	Bethsaida
2014GL098	5591573	636883	1655	Vein	25	85	High	0.1	0.5	Ep-Chl	20	Ep-Ilt-Chl	Propylitic	Bethsaida

Station ID	Northing (m)	Easting (m)	Elev (m)	Vein type	Strike	Dip	Conf	Density /m	Vein width (mm)	Vein minerals	Selvage width (mm)	Selvage minerals	Alteration	Lithology
2014GL099	5591835	636611	1648	Vein	45	80	High	0.1	2	Qz	10	Ilt-Ep-Chl	Propylitic	Bethsaida
2014GL101	5591256	636577	1660	Fracture halo	125	70	High	1.25	0.5	Qz-Ep	60	Ilt-Ep-Chl	Propylitic	Bethsaida
2014GL101	5591256	636577	1660	Fracture halo	145	75	High	0.1			30	Ilt-Ep-Chl	Propylitic	Bethsaida
2014GL101	5591319	636582	1660	Vein	25	65	High	0.1	0.5	Ep	5	Chl-Ep-Ilt	Propylitic	Bethsaida
2014GL102	5591512	636299	1642	Fracture halo	295	76	High	1			40	Ep-Chl-Ilt	Propylitic	Bethsaida
2014GL102	5591512	636299	1642	Fracture halo	340	80	High	2			15	Ep-Chl-Ilt	Propylitic	Bethsaida
2014GL102	5591512	636299	1642	Vein	45	75	High	0.1	5	Qz-Kfs	3	Ep-Chl-Ilt	K-feldspar	Bethsaida
2014GL103	5591785	636281	1650	Vein	170	75	High	3	0.5	Ep	5	Chl-Ep-Ilt	Propylitic	Bethsaida
2014GL103	5591781	636292	1654	Vein	35	85	High	2	5	Qz-Ep	10	Ep-Chl-Ilt	Propylitic	Bethsaida
2014GL103	5591781	636304	1654	Fracture halo	65	60	High	0.1			10	Ep-Chl-Ilt	Propylitic	Bethsaida
2014GL104	5591566	635871	1694	Vein	330	80	High	10	0.5	Chl	30	Ep-Ilt-Chl	Propylitic	Bethsaida
2014GL104	5591557	635914	1702	Vein	295	75	High	0.1	0.5	Chl	10	Ilt-Ep-Chl	Propylitic	Bethsaida
2014GL105	5591437	635803	1647	Vein	260	85	Low	6	1	Chl-Qz	15	Ilt-Ep-Chl	Propylitic	Bethsaida
2014GL105	5591445	635807	1647	Vein	290	50	High	10	0.5	Chl	10	Chl-Ilt-Ep	Propylitic	Bethsaida
2014GL105	5591445	635807	1647	Vein	35	85	High	0.1	1	Ep	10	Ilt-Chl	Propylitic	Bethsaida
2014GL106	5590336	635183	1690	Vein	145	82	High	2	2	Chl	45	Ep-Chl-Ilt	Propylitic	Bethsaida
2014GL106	5590298	635199	1693	Fracture halo	185	85	High	0.1			5	Chl-Ilt	Propylitic	Bethsaida
2014GL106	5590310	635200	1693	Vein	165	90	High	2	2	Chl	45	Ep-Chl-Ilt	Propylitic	Bethsaida
2014GL107	5589421	635106	1715	Vein	320	80	High	1	2	Chl	20	Ilt-Chl-Ep	Propylitic	Bethsaida
2014GL108	5589562	635758	1669	Fracture halo	325	88	High	3			30	Ep-Chl-Ilt	Propylitic	Bethsaida
2014GL109	5589328	633831	1615	Fracture halo	220	70	High	9			20	Ep-Chl-Ilt	Propylitic	Bethsaida
2014GL110	5589122	635109	1718	Vein	355	72	High	0.1	0.5	Chl	50	Ep-Ilt-Chl	Propylitic	Bethsaida
2014GL111	5589223	634981	1703	Fracture halo	205	80	High	4			10	Ilt-Chl-Ep	Propylitic	Bethsaida
2014GL112	5589308	635433	1727	Vein	325	75	High	2	0.5	Chl	20	Ep-Chl-Ilt	Propylitic	Bethsaida
2014GL112	5589313	635434	1732	Vein	174	68	High	1.5	0.5	Ep-Chl	25	Ilt-Ep-Chl	Propylitic	Bethsaida
2014GL112	5589313	635434	1732	Vein	25	85	High	1.5	0.5	Ep-Chl	25	Ilt-Ep-Chl	Propylitic	Bethsaida
2014GL112	5589274	635438	1729	Fracture halo	78	75	High	4			6	Chl-Ep-Ilt	Propylitic	Bethsaida
2014GL113	5590429	635661	1625	Fracture halo	110	83	High	5			30	Ilt-Chl-Ep	Propylitic	Bethsaida
2014GL113	5590379	635721	1617	Fracture halo	100	80	High	0.1			20	Chl-Ep-Ilt	Propylitic	Bethsaida
2014GL116	5590810	633803	1685	Fracture halo	65	75	High	5			10	Ep-Ilt-Chl	Propylitic	Bethsaida
2014GL117	5590977	634126	1676	Fracture halo	180	67	High	2	0.1	Ep	5	Ilt	Propylitic	Bethsaida
2014GL117	5590852	634146	1678	Fracture halo	1	75	High	0.1			10	Ep-Chl-Ilt	Propylitic	Bethsaida
2014GL118	5590840	634679	1641	Vein	158	78	High	20	1	Chl	30	Ilt-Chl-Ep	Propylitic	Bethsaida
2014GL118	5590782	634683	1646	Vein	357	90	High	1	0.5	Chl-Ep	35	Ep-Ilt-Chl	Propylitic	Bethsaida
2014GL118	5590771	634695	1647	Fracture halo	70	80	High	0.1			350	Ep-Chl-Ilt	Propylitic	Bethsaida
2014GL118	5590757	634698	1647	Vein	152	61	High	0.1	10	Ep-Qz	150	Ep-Ilt-Chl	Propylitic	Bethsaida
2014GL118	5590757	634698	1647	Vein	152	61	High	1	1	Chl	30	Ep-Ilt-Chl	Propylitic	Bethsaida
2014GL119	5590804	635224	1637	Vein	354	85	High	10	0.5	Chl	30	Ep-Ilt-Chl	Propylitic	Bethsaida
2014GL119	5590804	635224	1637	Vein	285	83	High	20	1	Chl	30	Ep-Ilt-Chl	Propylitic	Bethsaida
2014GL120	5590362	634201	1718	Fracture halo	105	80	High	0.1			25	Ep-Ilt-Chl	Propylitic	Bethsaida
2014GL121	5589718	634309	1706	Vein	25	65	High	1	100	Qz-Py-Ccp-Mlc	2500	Ms	Muscovite	QFP
2014GL121	5589718	634309	1706	Fault breccia	25	65	High		500			Ms	Muscovite	QFP
2014GL121	5589674	634342	1713	Fracture halo	80	90	High	3			20	Ilt-Ep-Chl	Propylitic	QFP
2014GL121	5589685	634347	1713	Fracture halo	90	90	High	3			20	Ilt-Ep-Chl	Propylitic	QFP
2014GL122	5589742	634753	1731	Vein	340	85	High	0.1	0.5	Chl	25	Ep-Ilt-Chl	Propylitic	Bethsaida

Station ID	Northing (m)	Easting (m)	Elev (m)	Vein type	Strike	Dip	Conf	Density /m	Vein width (mm)	Vein minerals	Selvage width (mm)	Selvage minerals	Alteration	Lithology
2014GL122	5589722	634783	1728	Vein	205	85	High	0.1	10	Qz-Py-Cal	20	Chl	Propylitic	Bethsaida
2014GL122	5589754	634799	1727	Fracture halo	95	80	High	0.1			10	Ep-Ilt-Chl	Propylitic	Bethsaida
2014GL122	5589754	634799	1727	Vein	30	85	High	0.1	1	Qz-Chl	15	Ilt-Ep-Chl	Propylitic	Bethsaida
2014GL123	5590318	634638	1699	Vein	145	85	High	5	0.5	Chl	35	Ep-Chl-Ilt	Propylitic	QFP
2014GL123	5590335	634653	1701	Vein	40	85	Med	5	1	Ep-Qz	50	Ep-Chl-Ilt	Propylitic	QFP
2014GL123	5590234	634717	1708	Fracture halo	140	80	High	0.1			5	Chl-Ep-Ilt	Propylitic	QFP
2014GL124	5589786	632762	1662	Vein	15	64	High	7	2	Ep-Chl	25	Ep-Ilt	Propylitic	Bethlehem
2014GL124	5589786	632762	1662	Fracture halo	98	85	High	0.1	0.1	Chl	2	Ep-Chl	Propylitic	Bethlehem
2014GL124	5589807	632777	1658	Fracture halo	76	74	High	2.75	0.5	Ep-Chl	3	Chl-Ep-Hem	Propylitic	Bethlehem
2014GL124	5589835	632823	1684	Vein	55	90	High	3	2	Ep-Chl	25	Ep-Chl-Hem	Propylitic	Bethlehem
2014GL124	5589835	632823	1684	Vein	72	78	High	3	2	Ep-Chl	25	Ep-Chl-Hem	Propylitic	Bethlehem
2014GL125	5589388	632525	1607	Fracture halo	270	75	High	0.1			10	Chl-Ilt	Propylitic	Chataway
2014GL125	5589389	632540	1614	Vein	50	65	High	1.5	2	Ep-Chl-Hem	45	Ep-Chl-Hem	Propylitic	Chataway
2014GL125	5589401	632542	1618	Vein	282	85	Med	2	2	Ep	5	Chl-Hem-Ilt	Propylitic	Chataway
2014GL126	5589223	633099	1614	Vein	15	88	High	20	3	Ep-Chl	10	Ep-Chl-Ilt	Propylitic	Bethlehem
2014GL126	5589220	633102	1611	Vein	50	40	High	3	1	Ep	10	Chl-Ep	Propylitic	Bethlehem
2014GL126	5589224	633102	1614	Fracture halo	315	75	High	10			10	Ep-Ilt-Chl	Propylitic	Bethlehem
2014GL127	5589677	633130	1681	Fracture halo	280	80	High	0.1			5	Ep-Chl	Propylitic	Bethlehem
2014GL127	5589705	633136	1681	Vein	60	57	High	2.5	1	Ep	5	Ep	Propylitic	Bethlehem
2014GL130	5589805	631210	1555	Vein	175	80	High	0.1	5	Ep	20	Ep-Chl	Propylitic	Border
2014GL130	5589774	631276	1558	Vein	245	85	High	2	1	Ep	30	Ep-Chl	Propylitic	Border
2014GL130	5589774	631276	1558	Vein	186	65	High	0.1	1	Ep	20	Ep-Chl	Propylitic	Border
2014GL130	5589774	631276	1558	Vein	290	55	High	2	0.5	Chl	2	Chl-Ep	Propylitic	Border
2014GL131	5589468	631867	1573	Vein	203	78	High	2	0.5	Ep	10	Ep-Chl	Propylitic	Transitional Border-Guichon
2014GL131	5589455	631870	1575	Vein	236	83	High	2	2	Ep-Qz	30	Ep-Chl	Propylitic	Transitional Border-Guichon
2014GL131	5589503	631921	1584	Vein	282	82	High	1.25	2	Qz-Ep	30	Ep-Chl	Propylitic	Transitional Border-Guichon
2014GL131	5589503	631921	1584	Vein	242	80	High	1.5	1	Ep	15	Ilt-Chl	Propylitic	Transitional Border-Guichon
2014GL132	5589676	632320	1622	Vein	302	75	High	0.1	25	Qz-Kfs			K-feldspar	Guichon
2014GL132	5589704	632325	1628	Vein	70	72	High	0.1	2	Ep	7	Chl-Ep	Propylitic	Guichon
2014GL132	5589669	632329	1626	Vein	175	75	Med	0.1	2	Ep	100	Chl-Ep	Propylitic	Guichon
2014GL132	5589684	632365	1630	Vein	112	85	High	0.1	20	Qz-Kfs			K-feldspar	Guichon
2014GL132	5589707	632396	1638	Vein	280	85	High	0.75	10	Qz-Ep-Chl	5	Chl	Propylitic	Guichon
2014GL132	5589707	632396	1638	Vein	55	85	High	2	5	Ep-Qz	5	Chl	Propylitic	Guichon
2014GL133	5590048	631999	1616	Vein	284	65	High	0.1	2	Ep	3	Ep	Propylitic	Guichon
2014GL133	5589966	632000	1615	Vein	225	90	High	20	5	Ep	50	Chl-Ep-Ilt	Propylitic	Guichon
2014GL134	5590334	631614	1625	Vein	300	72	High	0.75	10	Ep-Qz	50	Ep	Propylitic	Guichon
2014GL134	5590366	631665	1635	Vein	290	85	High	3	10	Ep-Chl	20	Ep	Propylitic	Guichon
2014GL135	5590358	632604	1706	Vein	290	80	High	0.75	5	Ep-Chl-Py-Mlc	5	Chl-Ilt	Propylitic	Chataway
2014GL135	5590432	632682	1703	Vein	280	80	High	0.75	10	Ep-Chl	20	Chl-Ep-Ilt	Propylitic	Chataway
2014GL135	5590445	632686	1706	Fracture halo	105	85	High	0.1			10	Ep-Ilt-Chl	Propylitic	Chataway
2014GL135	5590445	632686	1706	Vein	5	80	High	0.1	5	Ep-Chl	10	Chl-Ep-Ilt	Propylitic	Chataway
2014GL136	5590415	632140	1703	Vein	30	65	High	3	2	Ep	20	Ep-Chl	Propylitic	Guichon
2014GL136	5590415	632146	1705	Vein	350	90	High	0.1	2	Ep	15	Ep-Chl	Propylitic	Guichon
2014GL136	5590426	632150	1712	Vein	262	65	High	1.67	10	Ep-Qz-Chl	30	Chl-Ep-Ilt	Propylitic	Guichon
2014GL137	5590879	632261	1692	Vein	282	88	High	0.1	25	Qz-Kfs-Ep			K-feldspar	Chataway

Station ID	Northing (m)	Easting (m)	Elev (m)	Vein type	Strike	Dip	Conf	Density /m	Vein width (mm)	Vein minerals	Selvage width (mm)	Selvage minerals	Alteration	Lithology
2014GL137	5590936	632331	1696	Vein	270	85	High	1.1	0.5	Ep-Mlc	10	Chl-Ep-Kfs	K-feldspar	Chataway
2014GL138	5590716	632710	1679	Vein	285	85	High	4	1	Ep-Mlc			Propylitic	Chataway
2014GL138	5590723	632755	1672	Vein	20	65	High	0.1	1	Ep-Chl			Propylitic	Chataway
2014GL138	5590723	632755	1672	Vein	295	90	High	0.1	1	Ep	10	Chl	Propylitic	Chataway
2014GL139	5590840	631662	1640	Vein	310	65	High	0.1	2	Chl-Ep-Qz	30	Chl-Ep-Kfs	K-feldspar	Guichon
2014GL139	5590828	631692	1636	Vein	300	75	High	5	1	Chl-Ep	10	Chl-Ilt	Propylitic	Guichon
2014GL139	5590817	631693	1636	Vein	70	75	High	0.1	1	Chl-Cal-Ep	10	Chl	Propylitic	Guichon
2014GL139	5590817	631693	1636	Vein	285	75	High	0.1	0.5	Ep-Chl	15	Chl-Ilt	Propylitic	Guichon
2014GL139	5590845	631704	1630	Vein	140	30	High	0.1	2	Ep-Chl	10	Chl-Ep	Propylitic	Guichon
2014GL140	5591849	631666	1535	Vein	45	85	High	1.5	5	Ep	80	Chl-Ilt-Ep	Propylitic	Guichon
2014GL140	5591849	631666	1535	Vein	285	90	High	0.1	5	Ep	80	Chl-Ilt-Ep	Propylitic	Guichon
2014GL140	5591957	631680	1531	Vein	45	85	High	0.83	5	Ep-Qz-Chl	30	Ep-Chl-Ilt	Propylitic	Guichon
2014GL140	5591918	631686	1533	Vein	325	70	High	0.1	20	Ep	40	Ep-Chl	Propylitic	Guichon
2014GL141	5591707	631154	1556	Vein	35	85	High	0.1	5	Qz-Ep-Chl	30	Chl-Ep	Propylitic	Guichon
2014GL141	5591748	631188	1551	Vein	20	85	High	4	30	Ep-Qz-Chl		Chl-Ilt	Propylitic	Guichon
2014GL142	5591242	631152	1553	Vein	70	65	High	1.75	20	Ep	30	Chl-Ep-Ilt	Propylitic	Transitional Border-Guichon
2014GL142	5591242	631152	1553	Vein	50	65	High	1.75	20	Ep	30	Chl-Ep-Ilt	Propylitic	Transitional Border-Guichon
2014GL143	5590239	630195	1554	Fracture halo	100	68	High	10	0.1	Chl-Ep			Propylitic	Border
2014GL143	5590234	630202	1553	Vein	90	80	High	0.1	2	Qz-Chl			Propylitic	Border
2014GL143	5590235	630204	1553	Fracture halo	285	50	High	0.1	0.5	Chl			Propylitic	Border
2014GL143	5590235	630204	1553	Fracture halo	110	87	High	0.1	0.5	Chl			Propylitic	Border
2014GL143	5590235	630204	1553	Fracture halo	92	75	High	0.1	0.5	Chl			Propylitic	Border
2014GL144	5589173	629167	1500	Vein	267	85	High	0.1	150	Ep-Qz-Spec	200	Ep-Chl-Ilt	Propylitic	Border
2014GL144	5589145	629187	1497	Vein	255	72	High	2.5	7	Qz-Ep	20	Ep-Chl-Ilt	Propylitic	Border
2014GL144	5589145	629187	1497	Fracture halo	190	85	High	1.5			10	Ep-Chl-Kfs	K-feldspar	Border
2014GL145	5590948	629435	1536	Vein	70	68	High	0.1	0.5	Ep	40	Ep-Chl	Propylitic	Border
2014GL145	5590948	629435	1536	Vein	25	70	High	0.1	1	Ep	10	Ep-Chl-Ilt	Propylitic	Border
2014GL145	5590926	629476	1538	Fracture halo	25	55	High	1			5	Chl-Ep-Ilt	Propylitic	Border
2014GL145	5590933	629507	1541	Vein	55	85	High	2.5	5	Ep-Chl	20	Chl-Ep-Ilt	Propylitic	Border
2014GL146	5589955	630753	1546	Vein	305	75	High	0.1	0.5	Ep	3	Ep	Propylitic	Border
2014GL147	5590457	630968	1580	Vein	20	50	High	4	2	Ep	10	Ep-Ilt	Propylitic	Transitional Border-Guichon
2014GL148	5590736	630595	1579	Vein	275	75	High	3	5	Ep	10	Ep-Chl	Propylitic	Border
2014GL148	5590736	630595	1579	Vein	220	85	High	0.1	2	Ep-Qz	20	Chl-Ep-Ilt	Propylitic	Border
2014GL149	5590823	629985	1574	Vein	50	85	High	0.1	3	Ep-Qz	5	Chl	Propylitic	Border
2014GL149	5590844	630041	1582	Vein	73	55	High	1.5	3	Ep-Qz	5	Chl-Ilt	Propylitic	Border
2014GL149	5590844	630067	1586	Fracture halo	82	76	High	1.5	0.1	Chl-Ep	3	Chl-Ep-Ilt	Propylitic	Border
2014GL149	5590844	630067	1586	Vein	355	26	High	0.1	0.1	Ep			Propylitic	Border
2014GL150	5591259	629860	1575	Vein	100	85	Low	0.1	0.1	Chl-Ep-Py-Mlc			Propylitic	Border
2014GL150	5591263	629868	1582	Fracture halo	160	62	High	0.1			10	Chl-Ilt	Propylitic	Border
2014GL150	5591164	629884	1586	Vein	55	90	High	2	10	Qz-Chl	10	Ep	Propylitic	Border
2014GL150	5591218	629900	1584	Vein	85	68	High	5	0.1	Chl			Propylitic	Border
2014GL150	5591218	629900	1584	Vein	75	75	High	5	0.1	Chl			Propylitic	Border
2014GL151	5591728	630721	1512	Vein	75	80	High	0.1	1	Ep	10	Ep-Ilt-Chl-Kfs	K-feldspar	Guichon
2014GL151	5591728	630721	1512	Vein	50	75	High	0.1	1	Ep	10	Ep-Ilt-Chl-Kfs	K-feldspar	Guichon
2014GL151	5591716	630725	1512	Vein	10	70	High	2.5	10	Ep-Qz	40	Ep-Chl	Propylitic	Guichon

Station ID	Northing (m)	Easting (m)	Elev (m)	Vein type	Strike	Dip	Conf	Density /m	Vein width (mm)	Vein minerals	Selvage width (mm)	Selvage minerals	Alteration	Lithology
2014GL151	5591716	630725	1512	Vein	85	80	High	0.75	0.5	Ep-Chl	10	Ep-Chl-Ilt	Propylitic	Guichon
2014GL151	5591712	630731	1502	Vein	290	50	High	0.1	5	Ep-Chl-Qz	10	Kfs-Chl-Ilt	K-feldspar	Guichon
2014GL152	5591955	630043	1509	Fracture halo	330	85	High	0.1	0.1	Ms			Muscovite	Border
2014GL152	5591959	630058	1510	Vein	340	45	High	0.1	2	Ep	10	Chl-Ep-Ilt	Propylitic	Border
2014GL152	5591959	630058	1510	Fracture halo	300	85	High	0.1			10	Ep-Chl-Ilt	Propylitic	Border
2014GL153	5591865	629575	1523	Vein	115	75	High	0.1	6	Qz-Ep	25	Ep-Chl	Propylitic	Border
2014GL153	5591797	629637	1527	Vein	65	85	High	3	5	Ep-Qz-Chl	40	Ep-Chl-Ilt	Propylitic	Border
2014GL153	5591804	629650	1525	Vein	80	90	High	2.5			15	Ep-Chl-Ilt	Propylitic	Border
2014GL155	5591635	632264	1600	Fracture halo	30	45	High	0.1			10	Ep-Chl	Propylitic	Chataway
2014GL155	5591619	632267	1609	Fracture halo	285	60	High	0.1	0.1	Chl	50	Ep-Chl	Propylitic	Chataway
2014GL155	5591619	632267	1609	Vein	200	90	High	15	2	Ep	15	Chl-Ep	Propylitic	Chataway
2014GL155	5591654	632269	1607	Fracture halo	270	79	High	3	0.1	Chl	5	Ep-Chl	Propylitic	Chataway
2014GL156	5591273	632613	1636	Fracture halo	292	80	High	10			5	Ep-Chl-Hem-Ilt	Propylitic	Chataway
2014GL156	5591273	632613	1636	Fracture halo	10	20	High	2			2	Ep-Chl-Ilt	Propylitic	Chataway
2014GL157	5591764	633215	1550	Fracture halo	60	85	High	0.1			5	Chl-Ep-Ilt	Propylitic	Skeena
2014GL158	5591728	632740	1577	Fracture halo	205	85	High	0.1			2	Chl	Propylitic	Chataway
2014GL158	5591734	632741	1577	Fracture halo	95	77	High	0.1			10	Chl-Ep	Propylitic	Chataway
2014GL158	5591719	632750	1576	Vein	275	85	High	5	2	Chl-Ep-Qz	20	Ep-Hem-Chl	Propylitic	Chataway
2014GL158	5591719	632750	1576	Vein	10	45	High	2	1	Ep	30	Hem-Ep	Propylitic	Chataway
2014GL158	5591733	632762	1576	Fracture halo	104	86	High	0.1	0.1	Ep-Chl	2	Chl	Propylitic	Chataway
2014GL158	5591733	632762	1576	Vein	35	72	High	6.5	1	Ep	10	Ep-Chl	Propylitic	Chataway
2014GL182	5591270	626338	1146	Vein	72	83	High	0.1	5	Ep	20	Ep-Chl-Ab-Ilt	Sodic-calcic	Border
2014GL182	5591248	626346	1152	Fracture halo	76	70	High	3.25	0.1	Chl		Ilt	Propylitic	Border
2014GL182	5591248	626346	1152	Fracture halo	80	82	High	0.1			30	Ep-Chl-Ab-Ilt	Sodic-calcic	Border
2014GL184	5594966	633076	1508	Vein	80	73	High	3	10	Ep-Qz	50	Ep-Hem-Ilt	Propylitic	Chataway
2014GL184	5594972	633077	1506	Fracture halo	65	57	High	2			30	Ep	Propylitic	Chataway
2014GL184	5594939	633127	1512	Vein	95	55	High	2	1	Ep	35	Ep-Ilt	Propylitic	Chataway
2014GL184	5594938	633128	1512	Fracture halo	107	80	High	7.5			15	Ep-Chl-Ilt	Propylitic	Chataway
2014GL185	5595906	633240	1525	Fracture halo	305	75	High	0.1	0.1	Chl	5	Chl-Ep	Propylitic	Bethlehem
2014GL185	5595880	633254	1521	Vein	70	70	High	2.5	1	Ep	20	Ep-Chl-Ab	Sodic-calcic	Bethlehem
2014GL185	5595880	633254	1521	Vein	353	60	High	1	2	Ep-Chl	40	Ep-Chl	Propylitic	Bethlehem
2014GL185	5595875	633258	1521	Vein	10	77	High	0.1	5	Ep-Qz	50	Chl-Ep-Ab	Sodic-calcic	Bethlehem
2014GL185	5595877	633259	1521	Vein	300	65	High	3.25	5	Ep-Qz	40	Chl-Ep-Ab	Sodic-calcic	Bethlehem
2014GL185	5595877	633259	1521	Vein	355	75	High	0.1	5	Ep-Qz	50	Chl-Ep-Ab	Sodic-calcic	Bethlehem
2014GL186	5595350	633480	1525	Vein	220	75	High	6.5	1	Ep-Qz	20	Ep-Ab-Chl	Sodic-calcic	Bethlehem
2014GL186	5595401	633544	1531	Vein	47	85	High	0.1	3	Ep-Qz	30	Ep	Propylitic	Bethlehem
2014GL186	5595398	633547	1531	Fracture halo	335	60	High	0.1	0.1	Ep-Chl	5	Ep-Chl-Ilt	Propylitic	Bethlehem
2014GL187	5594542	633903	1547	Fracture halo	105	80	High	4			20	Ep-Chl-Ilt	Propylitic	Bethlehem
2014GL187	5594542	633903	1540	Vein	5	77	High	10	1	Ep-Chl	20	Ep-Chl-Ilt	Propylitic	Bethlehem
2014GL187	5594558	633911	1547	Vein	20	85	High	10	2	Ep-Qz-Chl	15	Ep-Chl-Ilt	Propylitic	Bethlehem
2014GL187	5594548	633919	1550	Fracture halo	80	85	Low	4			15	Chl-Ep-Ilt	Propylitic	Bethlehem
2014GL189	5594391	634435	1616	Vein	275	78	High	2.5	5	Ep-Chl-Qz	30	Ep-Chl-Ilt	Propylitic	Bethsaida
2014GL189	5594389	634445	1615	Fracture halo	255	85	High	3			15	Ep-Chl-Ilt	Propylitic	Bethsaida
2014GL193	5595945	634185	1567	Vein	300	75	High	6.5	2	Chl-Ep	20	Chl-Ep	Propylitic	Bethlehem
2014GL193	5595890	634267	1556	Fracture halo	115	65	High	1			5	Ep-Chl	Propylitic	Bethlehem

Station ID	Northing (m)	Easting (m)	Elev (m)	Vein type	Strike	Dip	Conf	Density /m	Vein width (mm)	Vein minerals	Selvage width (mm)	Selvage minerals	Alteration	Lithology
2014GL193	5595882	634282	1553	Vein	300	80	High	0.1	10	Ep-Qz	5	Ep	Propylitic	Bethlehem
2014GL193	5595886	634284	1553	Vein	300	75	High	3.25	10	Chl-Ep-Qz	25	Ep-Chl-Ab-Ilt	Sodic-calcic	Bethlehem
2014GL194	5596287	632694	1536	Vein	320	50	High	3.25	1	Chl	15	Chl-Ep	Propylitic	Transitional Chataway-Bethlehem
2014GL194	5596273	632706	1541	Vein	70	85	Med	0.1	0.5	Ep-Chl	20	Ep-Ilt	Propylitic	Transitional Chataway-Bethlehem
2014GL194	5596267	632717	1541	Vein	330	45	High	1.67	1	Chl	15	Chl-Ep	Propylitic	Transitional Chataway-Bethlehem
2014GL194	5596299	632718	1538	Fracture halo	70	85	Med	4	0.1	Chl-Ep	30	Ep-Chl-Hem-Ilt	Propylitic	Transitional Chataway-Bethlehem
2014GL195	5596233	632038	1466	Vein	95	70	High	0.1	2	Chl-Ep	5	Ep-Chl	Propylitic	Chataway
2014GL195	5596251	632619	1533	Fracture halo	215	85	High	2	0.1	Ep-Chl	10	Ep-Chl	Propylitic	Chataway
2014GL196	5596777	632165	1522	Vein	175	67	High	3.25	0.5	Chl	25	Ep-Ilt	Propylitic	Chataway
2014GL196	5596778	632167	1522	Fracture halo	195	90	High	6.5			20	Chl-Ep-Ilt	Propylitic	Chataway
2014GL196	5596815	632203	1523	Vein	175	68	High	0.1	1	Chl-Qz	20	Ep-Chl-Ilt	Propylitic	Chataway
2014GL196	5596728	632217	1518	Vein	215	75	High	0.1	1	Chl-Ep	20	Ep-Chl	Propylitic	Chataway
2014GL196	5596760	632219	1522	Vein	20	70	High	5	1	Chl-Ep	20	Ep	Propylitic	Chataway
2014GL196	5596721	632228	1519	Vein	315	35	High	0.1	1	Ep-Qz			Propylitic	Chataway
2014GL197	5597251	631997	1493	Fracture halo	225	62	High	3.25	0.1	Chl	15	Ep-Chl-Ilt	Propylitic	Chataway
2014GL197	5597244	632017	1496	Fracture halo	220	85	Med	3.25	0.1	Chl	15	Ep-Chl-Ilt	Propylitic	Chataway
2014GL197	5597246	632023	1496	Fracture halo	325	52	High	0.1	0.1	Ep			Propylitic	Chataway
2014GL197	5597244	632070	1497	Fracture halo	350	59	High	0.1	0.1	Ep	5	Ep-Chl	Propylitic	Chataway
2014GL197	5597244	632070	1497	Vein	105	80	High	5	1	Chl	20	Chl-Ep	Propylitic	Chataway
2014GL197	5597255	632093	1501	Fracture halo	345	54	High	2.5	0.1	Chl	5	Ep	Propylitic	Chataway
2014GL197	5597255	632093	1501	Fracture halo	70	90	Low	3.25			15	Ep	Propylitic	Chataway
2014GL198	5597447	632686	1548	Vein	148	67	High	0.1	0.1	Chl-Ep		Ilt	Propylitic	Chataway
2014GL198	5597443	632703	1550	Fracture halo	76	61	High	0.1	0.1	Ep-Chl		Ilt	Propylitic	Chataway
2014GL199	5596800	632675	1544	Vein	40	80	High	2	2	Ep-Chl	30	Ep-Ilt	Propylitic	Transitional Chataway-Bethlehem
2014GL199	5596818	632689	1549	Vein	300	56	High	0.1	3	Ep-Qz-Chl	10	Ep-Chl	Propylitic	Transitional Chataway-Bethlehem
2014GL199	5596805	632694	1551	Fracture halo	60	80	High	4	0.1	Chl-Ep	5	Ep-Chl-Ilt	Propylitic	Transitional Chataway-Bethlehem
2014GL199	5596805	632694	1551	Vein	290	60	High	0.1	2	Chl-Ep	20	Hem-Ep-Chl	Propylitic	Transitional Chataway-Bethlehem
2014GL199	5596806	632707	1546	Fracture halo	245	90	Low	6.5			10	Ep-Ilt	Propylitic	Transitional Chataway-Bethlehem
2014GL201	5596248	633201	1527	Fracture halo	65	83	High	0.1			40	Chl-Ep-Ilt	Propylitic	Chataway
2014GL202	5596195	633898	1556	Fracture halo	130	52	High	0.1			15	Ep-Chl	Propylitic	Transitional Chataway-Bethlehem
2014GL202	5596191	633898	1557	Vein	60	85	High	1	5	Ep-Chl	45	Ep-Chl	Propylitic	Transitional Chataway-Bethlehem
2014GL202	5596191	633898	1557	Fracture halo	355	85	High	0.1	0.1	Ep-Chl	10	Ep-Chl-Ilt	Propylitic	Transitional Chataway-Bethlehem
2014GL203	5596660	634315	1477	Vein	315	75	High	3	2	Ep-Qz	5	Ep-Ilt	Propylitic	Chataway
2014GL203	5596626	634352	1478	Vein	155	56	High	10	1	Ab	50	Ep-Chl-Ilt	Sodic-calcic	Chataway
2014GL203	5596626	634352	1478	Fracture halo	340	58	High	2			20	Ep-Ab-Ilt	Sodic-calcic	Chataway
2014GL203	5596626	634352	1478	Fracture halo	330	60	High	2			20	Ep-Ab-Ilt	Sodic-calcic	Chataway
2014GL205	5597701	632252	1496	Fracture halo	95	85	Med	2			15	Ep-Chl	Propylitic	Chataway
2014GL205	5597701	632252	1496	Vein	310	70	High	2	1	Ep	15	Ep-Chl-Ilt	Propylitic	Chataway

Station ID	Northing (m)	Easting (m)	Elev (m)	Vein type	Strike	Dip	Conf	Density /m	Vein width (mm)	Vein minerals	Selvage width (mm)	Selvage minerals	Alteration	Lithology
2014GL205	5597651	632255	1492	Vein	44	78	High	5.5	1	Ep-Chl	15	Ep-Chl-Ilt	Propylitic	Chataway
2014GL205	5597651	632255	1492	Fracture halo	95	65	Low	2			10	Chl-Ep	Propylitic	Chataway
2014GL205	5597651	632255	1492	Fracture halo	105	45	High	2			10	Chl-Ep-Ilt	Propylitic	Chataway
2014GL206	5597909	632627	1570	Vein	80	70	Med	2.5	5	Chl-Ep	45	Ep-Chl	Propylitic	Chataway
2014GL206	5597874	632628	1579	Vein	204	90	Low	0.1	1	Ep-Chl	20	Ilt-Ep-Chl	Propylitic	Chataway
2014GL208	5597383	633491	1517	Vein	165	50	High	0.1	0.5	Chl	5	Chl-Ilt	Propylitic	Transitional Chataway-Bethlehem
2014GL209	5597164	633165	1574	Vein	80	45	Low	0.1	0.5	Chl	2	Chl-Ilt	Propylitic	Transitional Chataway-Bethlehem
2014GL210	5598266	630810	1434	Vein	35	85	High	0.1	1	Ep	5	Ep	Propylitic	Guichon
2014GL210	5598205	630817	1437	Vein	70	60	High	10	1	Ep-Chl	15	Chl-Ep-Ilt	Propylitic	Guichon
2014GL210	5598212	630823	1437	Vein	45	67	High	0.1	2	Ep	20	Ep-Chl	Propylitic	Guichon
2014GL210	5598212	630823	1437	Fracture halo	300	85	Low	0.1				Ep-Chl	Propylitic	Guichon
2014GL211	5598291	631319	1473	Vein	120	75	High	0.63	5	Qz-Chl	25	Ep-Chl-Ilt	Propylitic	Chataway
2014GL212	5598425	631858	1494	Fracture halo	350	90	Med	0.1			5	Chl-Ep-Ilt	Propylitic	Guichon
2014GL213	5598380	632289	1507	Vein	305	38	High	0.1	5	Ep-Chl	30	Ep-Chl	Propylitic	Chataway
2014GL213	5598350	632291	1514	Fracture halo	210	78	High	0.1	0.1	Mlc	60	Ep-Chl	Propylitic	Chataway
2014GL213	5598350	632291	1514	Vein	25	62	High	0.1	0.5	Ep	15	Ep-Chl	Propylitic	Chataway
2014GL213	5598350	632291	1514	Vein	238	78	High	0.1	0.5	Ep	15	Ep-Chl	Propylitic	Chataway
2014GL214	5598396	632902	1480	Vein	345	36	Med	0.1	1	Chl-Ep	50	Chl-Ep-Ilt	Propylitic	Chataway
2014GL215	5597785	633787	1453	Vein	180	75	High	0.1	5	Qz-Ep-Chl			Propylitic	Chataway
2014GL215	5597782	633797	1451	Vein	30	57	High	2	0.5	Ep	20	Ep-Ilt	Propylitic	Chataway
2014GL216	5598893	630805	1426	Fracture halo	315	80	High	20	0.1	Mol-Py-Ccp-Mlc			Muscovite	Border
2014GL217	5598976	631287	1467	Vein	320	65	High	0.1	5	Chl-Ep		Chl	Propylitic	Chataway
2014GL217	5598909	631327	1465	Vein	255	85	High	4	1	Ep	50	Ep-Chl-Ilt	Propylitic	Chataway
2014GL217	5598909	631327	1465	Fracture halo	335	85	High	0.1	0.1	Chl			Propylitic	Chataway
2014GL218	5598919	631808	1475	Vein	255	85	High	0.1	1	Chl-Qz	50	Chl-Ep-Ilt	Propylitic	Guichon
2014GL218	5598923	631811	1476	Vein	240	90	High	25	2	Chl-Qz	20	Chl-Ep-Ilt	Propylitic	Guichon
2014GL219	5598922	632403	1444	Vein	315	57	High	2.22	0.5	Ep	5	Ep-Ilt	Propylitic	Guichon
2014GL220	5599451	631801	1443	Vein	345	64	High	2.5	2	Ep-Chl	15	Ep-Chl-Ilt	Propylitic	Border
2014GL220	5599451	631801	1443	Vein	230	60	High	4	4	Ep			Propylitic	Border
2014GL220	5599445	631810	1443	Vein	340	65	Low	0.1	0.5	Chl-Qz	15	Chl-Ep-Ilt	Propylitic	Border
2014GL222	5599605	632198	1409	Vein	190	20	High	0.1	5	Qz-Ep	20	Ep-Chl-Ilt	Propylitic	Guichon
2014GL223	5599553	630727	1463	Fracture halo	275	65	High	10			2	Chl	Propylitic	Transitional Border-Guichon
2014GL223	5599553	630727	1463	Fracture halo	195	75	High	0.1			5	Ep-Chl	Propylitic	Transitional Border-Guichon
2014GL224	5600092	630762	1437	Vein	177	60	High	0.1	1	Ep	5	Ilt	Propylitic	Guichon
2014GL225	5600116	631224	1433	Vein	315	53	High	0.1	0.1	Ep			Propylitic	Guichon
2014GL225	5600154	631239	1427	Vein	300	55	High	0.1	0.1	Ep			Propylitic	Guichon
2014GL226	5600084	631711	1396	Vein	120	60	Med	0.1	2	Ep-Chl	4	Ep-Chl	Propylitic	Guichon
2014GL226	5600084	631711	1396	Vein	70	72	High	0.1	4	Ep	20	Ep-Chl-Ilt	Propylitic	Guichon
2014GL227	5600538	631194	1370	Vein	190	68	High	5	3	Ep	10	Ep	Propylitic	Guichon
2014GL227	5600707	631209	1349	Fracture halo	200	88	High	0.1			0.75	Ilt-Chl-Kfs	K-feldspar	Guichon
2014GL228	5600940	630996	1331	Vein	270	80	High	0.1	5	Chl	5	Ilt	Propylitic	Guichon
2014GL229	5600638	629928	1350	Vein	200	25	High	5	0.1	Ep-Tur			Propylitic	Guichon
2014GL229	5600633	629989	1353	Vein	50	85	High	1	1	Ep	10	Ep	Propylitic	Guichon
2014GL229	5600638	629998	1350	Vein	162	33	High	0.1	2	Ep	5	Ep	Propylitic	Guichon

Station ID	Northing (m)	Easting (m)	Elev (m)	Vein type	Strike	Dip	Conf	Density /m	Vein width (mm)	Vein minerals	Selvage width (mm)	Selvage minerals	Alteration	Lithology
2014GL230	5600157	629476	1314	Fracture halo	70	50	High	5	2	Ep-Cal	10	Ep-Chl-Cal-Ilt	Propylitic	Border
2014GL231	5600000	629045	1266	Vein	110	70	Med	0.67	2	Qz-Ep			Propylitic	Border
2014GL231	5600000	629045	1266	Vein	40	56	High	0.1	1	Ep	15	Ep	Propylitic	Border
2014MA001	5589896	647919	1453		280	65		4	2	Chl-Bt		Ser	K-feldspar	Chataway
2014MA001	5589896	647919	1453		280	65		4	2	Ep			Propylitic	Chataway
2014MA004	5590055	648225	1448		280	80		0.2	200	Qz-Bn		Ser	Muscovite	Guichon
2014MA005	5589558	646830	1498		45	60		2	1	Chl			Propylitic	Chataway
2014MA005	5589558	646830	1498		45	60		2	1	Qz-Chl		Cly	Propylitic	Chataway
2014MA008	5589892	646631	1466		265	85		0.5	1	Chl			Propylitic	Chataway
2014MA013	5589708	648111	1501		285	75		2	1	Chl-Ep			Propylitic	Chataway
2014MA014	5589548	648114	1503		230	75		2	1	Chl		Cly	Propylitic	Chataway
2014MA014	5589548	648114	1503		230	75		2	1	Chl-Ser			Propylitic	Chataway
2014MA017	5589476	645968	1530		215	75		2	2	Chl-Qz		Cly	Propylitic	Chataway
2014MA025	5589856	645578	1527		175	15		0.5	5	Chl			Propylitic	Chataway
2014MA025	5589856	645578	1527		175	15		0.5	5	Qz-Ep			Propylitic	Chataway
2014MA027	5590378	645555	1472		65	75		0.1	50	Chl-CuOx			Propylitic	Chataway
2014MA027	5590378	645555	1472		65	75		0.1	50	Chl-CuOx			Propylitic	Chataway
2014MA029	5590292	645086	1519		180	50		0.1	1	Qz-Chl			Propylitic	Chataway
2014MA031	5590018	645245	1545		210	55		3	10	Chl-Ep			Propylitic	Chataway
2014MA031	5590018	645245	1545		210	55		3	10	Ep			Propylitic	Chataway
2014MA032	5589803	645246	1534		220	25		2	2	Ep-Chl			Propylitic	Bethlehem
2014MA034	5590188	644741	1509		215	25		0.4	3	Chl-Cly			Propylitic	Skeena
2014MA034	5590188	644741	1509		215	25		0.4	3	Ep-Qz			Propylitic	Skeena
2014MA035	5590241	644831	1498		195	25		3	5	Ep-Qz			Propylitic	Skeena
2014MA036	5590300	644621	1504		355	85		0.1	1	Ep			Propylitic	Skeena
2014MA037	5590328	644561	1501		255	60		3	1	Ep			Propylitic	Skeena
2014MA038	5590397	644325	1483		255	70		1.5	2	Ep			Propylitic	Chataway
2014MA038	5590397	644325	1483		255	70		1.5	2	Qz-Chl		Cly	Propylitic	Chataway
2014MA039	5590418	644161	1518		205	35		0.5	1	Ep			Propylitic	Chataway
2014MA039	5590418	644161	1518		205	35		0.5	1	Qz-Chl			Propylitic	Chataway
2014MA041	5590051	644261	1547		65	70		1	1	Ep			Propylitic	Skeena
2014MA043	5589812	643691	1630		45	80		2	1	Ep			Propylitic	Skeena
2014MA044	5591205	644213	1443		170	35		1	1	Ep-Chl			Propylitic	Bethlehem
2014MA045	5591041	644086	1459		205	37		5	3	Ep-Chl		Kfs	K-feldspar	Skeena
2014MA045	5591041	644086	1459		205	37		5	3	Qz-Bn		Ser	Muscovite	Skeena
2014MA045A	5591041	644086	1459		205	37		5	3	Ep-Chl		Kfs	K-feldspar	Skeena
2014MA045A	5591041	644086	1459		205	37		5	3	Qz-Ser		Ser	Propylitic	Skeena
2014MA046	5590919	644029	1495		220	50		5	3	Chl-Ep			Propylitic	Skeena
2014MA046	5590919	644029	1495		220	50		5	3	Ep-Qz			Propylitic	Skeena
2014MA047	5590930	643760	1493		190	65		0.5	1	Ep			Propylitic	Skeena
2014MA051	5591372	643547	1419		175	80		3	1	Py-Chl		Cly	Propylitic	Skeena
2014MA051	5591372	643547	1419		175	80		3	1	Qz-Ep		Kfs	K-feldspar	Skeena
2014MA053	5591469	644451	1331		120	40		5	1	Chl			Propylitic	Bethlehem
2014MA053	5591469	644451	1331		120	40		5	1	Chl-Ep			Propylitic	Bethlehem
2014MA054	5591775	643961	1329		190	45		1.5	3	Ep-Qz			Propylitic	Skeena

Station ID	Northing (m)	Easting (m)	Elev (m)	Vein type	Strike	Dip	Conf	Density /m	Vein width (mm)	Vein minerals	Selvage width (mm)	Selvage minerals	Alteration	Lithology
2014MA055	5591840	643738	1323		165	60		3	2	Chl-Ep			Propylitic	Skeena
2014MA055	5591840	643738	1323		165	60		3	2	Py-Chl			Propylitic	Skeena
2014MA057	5590415	643863	1540		180	55		3	5	Chl-Ep			Propylitic	Skeena
2014MA057	5590415	643863	1540		180	55		3	5	Ep-Qz			Propylitic	Skeena
2014MA058	5590478	643689	1537		190	75		4	2	Chl-Ep		Cly	Propylitic	Skeena
2014MA059	5590241	643290	1545		90	80		0.3	1	Ep-Chl			Propylitic	Skeena
2014MA061	5590431	643070	1525		15	70		2	1	Chl-Qz		Cly	Propylitic	Skeena
2014MA062	5590550	642845	1504		15	60		1	1	Ep-Chl			Propylitic	Skeena
2014MA063	5591353	643126	1393		180	80		3	1	Chl-Ep			Propylitic	Skeena
2014MA063	5591353	643126	1393		180	80		3	1	Ep			Propylitic	Skeena
2014MA066	5590468	642393	1512		75	75		0.5	1	Qz-Chl		Cly	Propylitic	Skeena
2014MA067	5590100	642427	1553		240	25		3	2	Qz-Ser		Ser	Propylitic	Skeena
2014MA068	5589878	642108	1555		330	80		4	30	Ep-Qz		Cly	Propylitic	Skeena
2014MA069	5589538	642653	1607		250	50		1	2	Ep		Cly	Propylitic	Skeena
2014MA071	5590211	641896	1547		85	75		0.2	1	Chl		Cly	Propylitic	Skeena
2014MA076	5583374	645450	1591		185	55		2	1	Chl		Cly	Propylitic	Skeena
2014MA088	5588390	642865	1713		215	60		4	3	Qz		Ser	Propylitic	Skeena
2014MA089	5588359	643113	1712		215	65		10	3	Qz-Hem		Ser	Propylitic	Skeena
2014MA090	5588249	643284	1708		115	85		5	1	Bt-Chl		Kfs	K-feldspar	Skeena
2014MA090	5588249	643284	1708		115	85		5	1	Chl			Propylitic	Skeena
2014MA092	5588200	643581	1708		95	85		4	3	Chl-CuOx			Propylitic	Skeena
2014MA092	5588200	643581	1708		95	85		4	3	Qz-Bn		Kfs	K-feldspar	Skeena
2014MA093	5588209	643899	1667		90	80		0.5	5	Qz-CuOx		Kfs	K-feldspar	Skeena
2014MA094	5588544	643327	1659		200	80		0.1	300	Qz-Mol			Muscovite	Skeena
2014MA096	5588677	643282	1641		200	75		5	1	Chl-Py			Propylitic	Skeena
2014MA096	5588677	643282	1641		200	75		5	1	Qz-Ep			Propylitic	Skeena
2014MA097	5588575	643182	1664		210	55		5	1	Qz		Kfs	K-feldspar	Skeena
2014MA101	5588855	643451	1624		220	50		3	1	Chl-Py			Propylitic	Skeena
2014MA101	5588855	643451	1624		220	50		3	1	Ep			Propylitic	Skeena
2014MA102	5589009	643526	1631		60	40		2	1	Ep			Propylitic	Skeena
2014MA104	5588860	643700	1625		205	80		3	1	Chl			Propylitic	Skeena
2014MA104	5588860	643700	1625		205	80		3	1	Ep			Propylitic	Skeena
2014MA105	5589237	643839	1615		185	55		0.2	50	Ep-Qz			Propylitic	Skeena
2014MA106	5596988	645015	1487		230	80		0.2	1	Ep-Chl			Propylitic	Guichon
2014MA111	5596948	644142	1525		10	45		0.5	1	Qz-Ep			Propylitic	Guichon
2014MA111	5596948	644142	1525		10	45		0.5	1	Chl			Propylitic	Guichon
2014MA112	5602466	641451	1761		230	30		1.5	1	Ep-Chl			Propylitic	Guichon
2014MA112	5602466	641451	1761		230	30		1.5	1	Ep		Kfs	K-feldspar	Guichon
2014MA113	5602502	641291	1785		85	50		5	5	Ep			Propylitic	Guichon
2014MA114	5602613	641298	1785		60	65		2	5	Ep			Propylitic	other
2014MA114	5602613	641298	1785		60	65		2	5	Ep			Propylitic	other
2014MA115	5602711	641253	1793		215	70		3	5	Ep-Ab			Sodic-calcic	Guichon
2014MA116	5602876	641259	1776		40	65		4	5	Ep			Propylitic	Guichon
2014MA117	5602637	641491	1752		150	80		5	2	Chl			Propylitic	Guichon
2014MA117	5602637	641491	1752		150	80		5	2	Ep			Propylitic	Guichon

Station ID	Northing (m)	Easting (m)	Elev (m)	Vein type	Strike	Dip	Conf	Density /m	Vein width (mm)	Vein minerals	Selvage width (mm)	Selvage minerals	Alteration	Lithology
2014MA118	5602562	641523	1747		160	60		4	2	Ep-Chl			Propylitic	Guichon
2014MA119	5602525	641583	1729		75	75		4	2	Ep-Chl			Propylitic	Guichon
2014MA120	5602651	641884	1711		320	55		1	1	Ep			Propylitic	other
2014MA121	5602560	641964	1699		330	75		4	1	Chl-Ep			Propylitic	other
2014MA122	5602325	641731	1713		130	30		0.5	1	Ep-Chl			Propylitic	other
2014MA123	5602318	641529	1735		320	30		0.5	1	Ep			Propylitic	Guichon
2014MA124	5602061	641661	1712		340	70		2	1	Chl			Propylitic	Guichon
2014MA124	5602061	641661	1712		340	70		2	1	Chl			Propylitic	Guichon
2014MA125	5601995	641630	1711		325	30		5	3	Ep			Propylitic	Guichon
2014MA125	5601995	641630	1711		325	30		5	3	Ep			Propylitic	Guichon
2014MA127	5601583	641679	1673		65	25		0.3	1	Kfs			K-feldspar	Guichon
2014MA127	5601583	641679	1673		65	25		0.3	1	Chl			Propylitic	Guichon
2014MA128	5601640	641858	1666		190	45		0.3	1	Ep			Propylitic	Guichon
2014MA130	5601974	641849	1695		85	65		0.5	1	Ep			Propylitic	other
2014MA131	5601409	641724	1656		25	70		0.2	3	Chl			Propylitic	Guichon
2014MA132	5601436	641633	1664		220	50		8	1	Ep			Propylitic	Guichon
2014MA132	5601436	641633	1664		220	50		8	1	Chl			Propylitic	Guichon
2014MA133	5601553	641152	1745		150	50		3	1	Ep			Propylitic	Guichon
2014MA133	5601553	641152	1745		150	50		3	1	Chl			Propylitic	Guichon
2014MA134	5601511	641144	1746		190	30		5	10	Chl			Propylitic	Guichon
2014MA135	5602289	640476	1848		215	75		3	2	Ep		Kfs	K-feldspar	Guichon
2014MA136	5602324	640387	1844		230	35		3	3	Ep			Propylitic	Guichon
2014MA136	5602324	640387	1844		230	35		3	3	Ep			Propylitic	Guichon
2014MA136A	5602324	640387	1844		230	35		3	3	Ep			Propylitic	Guichon
2014MA136A	5602324	640387	1844		230	35		3	3	Ep			Propylitic	Guichon
2014MA140	5602178	640378	1859		350	30		1.5	3	Ep			Propylitic	Guichon
2014MA142	5602038	640334	1886		150	20		1	3	Chl			Propylitic	Guichon
2014MA142	5602038	640334	1886		150	20		1	3	Ep			Propylitic	Guichon
2014MA143	5601978	640748	1821		260	55		4	4	Chl-Ep			Propylitic	Guichon
2014MA143	5601978	640748	1821		260	55		4	4	Ep		Kfs	K-feldspar	Guichon
2014MA144	5601958	640597	1838		190	40		2	30	Chl			Propylitic	Guichon
2014MA144	5601958	640597	1838		190	40		2	30	Ep			Propylitic	Guichon
2014MA145	5602010	640503	1850		225	55		2	30	Ep			Propylitic	Guichon
2014MA146	5587189	636975	1639		265	65		0.2	1	Chl-Ep			Propylitic	Bethsaida
2014MA147	5587198	636872	1650		235	65		0.1	2	Chl		Cly	Propylitic	Bethsaida
2014MA148	5587196	636726	1652		295	80		0.2	3	Chl		Cly	Propylitic	Bethsaida
2014MA157	5597104	644175	1515		210	85		0.3	2	Ep			Propylitic	Guichon
2014MA158	5597319	644211	1491		200	80		0.2	1	Ep			Propylitic	Guichon
2014MA159	5597414	643615	1489		140	85		3	1	Chl			Propylitic	Guichon
2014MA159	5597414	643615	1489		140	85		3	1	Chl			Propylitic	Guichon
2014MA161	5597318	643833	1522		75	10		0.2	2	Chl-Ep			Propylitic	Guichon
2014MA162	5596498	631381	1431		315	60		0.5	2	Ep		Hem	Propylitic	Chataway
2014MA162	5596498	631381	1431		315	60		0.5	2	Ep		Cly	Propylitic	Chataway
2014MA163	5596360	631653	1437		50	65		0.5	2	Chl		Cly	Propylitic	Chataway
2014MA164	5596119	631671	1453		190	65		3	1	Ep			Propylitic	Chataway

Station ID	Northing (m)	Easting (m)	Elev (m)	Vein type	Strike	Dip	Conf	Density /m	Vein width (mm)	Vein minerals	Selvage width (mm)	Selvage minerals	Alteration	Lithology
2014MA165	5596083	631831	1449		320	40		1.5	1	Cly-Chl			Propylitic	Chataway
2014MA166	5595913	631977	1465		305	60		1.5	1	Chl-Lm			Propylitic	Chataway
2014MA167	5596175	632109	1468		285	60		1	3	Ep			Propylitic	Chataway
2014MA168	5596063	632331	1492		135	87		2	1	Chl-Ep			Propylitic	Chataway
2014MA169	5596247	632229	1497		330	40		0.3	5	Ep			Propylitic	Chataway
2014MA170	5596220	631943	1458		50	85		2	1	Ep			Propylitic	Chataway
2014MA171	5596307	632089	1475		170	65		2	10	Ep-Qz		Cly	Propylitic	Chataway
2014MA172	5596161	632406	1516		225	80		0.5	2	Ep		Cly	Propylitic	Chataway
2014MA173	5596035	632284	1483		305	55		2.5	1	Chl-Lm		Cly	Propylitic	Chataway
2014MA175	5588643	643077	1656		190	80		0.3	1	Chl-CuOx			Propylitic	Skeena
2014MA184	5597392	638848	1357		115	88		3	5	Chl-Ab		Ep	Sodic-calcic	Skeena
2014MA185	5597503	638804	1354		330	50		0.5	3	Ab-Chl		Ep	Sodic-calcic	Skeena
2014MA185	5597503	638804	1354		330	50		0.5	3	Chl-CuOx			Propylitic	Skeena
2014MA188	5597791	638524	1351		210	85		4	2	Chl-Ep			Propylitic	Bethlehem
2014MA189	5597709	638697	1353		325	45		0.2	5	Qz-Chl			Propylitic	Skeena
2014MA191	5598903	638061	1419		300	85		0.3	10	Chl		Cly	Propylitic	Chataway
2014MA191	5598903	638061	1419		300	85		0.3	10	Ep-Kfs		Chl	K-feldspar	Chataway
2014MA192	5599054	638165	1456		15	70		0.2	2	Ep		Cly	Propylitic	Chataway
2014MA192	5599054	638165	1456		15	70		0.2	2	Ep-Cly		Cly	Propylitic	Chataway
2014MA193	5599091	638053	1431		5	60		0.2	2	Ep		Cly	Propylitic	Chataway
2014MA193	5599091	638053	1431		5	60		0.2	2	Mag-Chl			Propylitic	Chataway
2014MA194	5598850	637955	1384		35	65		1.5	1	Ep		Ab	Sodic-calcic	Bethlehem
2014MA195	5598410	638158	1361		30	70		2	3	Ep		Ab	Sodic-calcic	Bethlehem
2014MA195	5598410	638158	1361		30	70		2	3	Qz		Ser	Propylitic	Bethlehem
2014OG002	5591337	644584	1333		75	75		6	2	Chl-Ep		Cly	Propylitic	Guichon
2014OG002	5591337	644584	1333		75	75		6	2	Ep		Ab	Sodic-calcic	Guichon
2014OG003	5591182	644471	1407		335	80		3	1	Chl			Propylitic	Bethlehem
2014OG004	5591179	644485	1405		50	85		3	10	Chl			Propylitic	Bethlehem
2014OG011	5590426	645576	1464		50	55		0.1	10	Chl		Ser	Propylitic	Chataway
2014OG011	5590426	645576	1464		50	55		0.1	10	Chl-Ab			Sodic-calcic	Chataway
2014OG016	5591183	645419	1340		120	80		3	1	Chl			Propylitic	Chataway
2014OG017	5591296	647097	1269		305	75		1.5	2	Ep			Propylitic	Chataway
2014OG017	5591296	647097	1269		305	75		1.5	2	Ep-Bn		Cly	Propylitic	Chataway
2014OG018	5591094	645665	1352		125	75		0.5	3	Chl-Hem			Propylitic	Chataway
2014OG021	5590745	646925	1355		320	44		2	1	Chl			Propylitic	Chataway
2014OG023	5590632	647024	1355		180	30		0.1	3	Chl-Bn		Cly	Propylitic	Chataway
2014OG023	5590632	647024	1355		180	30		0.1	3	Kfs			K-feldspar	Chataway
2014OG024	5590526	647165	1360		70	80		4	3	Chl-Bn		Kfs	K-feldspar	Guichon
2014OG026	5590638	647553	1350		260	60		3	3	Chl-Ep		Kfs	K-feldspar	Chataway
2014OG027	5590506	647753	1373		80	72		7	2	Chl-Cly		Cly	Propylitic	Guichon
2014OG027	5590506	647753	1373		80	72		7	2	Ep-Chl			Propylitic	Guichon
2014OG029	5590596	647914	1358		215	85		2	2	Chl-Ep		Kfs	K-feldspar	Chataway
2014OG029	5590596	647914	1358		215	85		2	2	Qz-Chl		Cly	Propylitic	Chataway
2014OG030	5590530	648103	1369		150	55		6	2	Qz-Chl		Cly	Propylitic	Chataway
2014OG031	5589946	647957	1452		280	80		5	10	Qz-Bn		Ser	Muscovite	Chataway

Station ID	Northing (m)	Easting (m)	Elev (m)	Vein type	Strike	Dip	Conf	Density /m	Vein width (mm)	Vein minerals	Selvage width (mm)	Selvage minerals	Alteration	Lithology
2014OG032	5590043	647993	1441		115	85		1	3	Ep-Qz			Propylitic	Chataway
2014OG033	5590222	648134	1426		295	80		0.2	1	Ep			Propylitic	Chataway
2014OG034	5589956	647872	1456		275	70		0.2	2	Ep			Propylitic	Chataway
2014OG034	5589956	647872	1456		275	70		0.2	2	Ep-CuOx		Kfs	K-feldspar	Chataway
2014OG035	5589944	647830	1464		250	55		3	5	Ep-Qz		Ser	Propylitic	Guichon
2014OG035	5589944	647830	1464		250	55		3	5	Qz		Ser	Propylitic	Guichon
2014OG037	5590077	647674	1449		235	60		0.5	1	Chl		Kfs	K-feldspar	Guichon
2014SM005	5590450	649052	1303		266	54		1	2	Ep		Cly	Propylitic	Guichon
2014SM032	5588246	649141	1432		89	71		0.1	1	Chl		Cly	Propylitic	Guichon
2014SM038	5587849	649510	1472		30	68		0.1	1	Qz-Chl		Cly	Propylitic	Guichon
2014SM050	5590029	648391	1433		170	60		2	2	Ep		Kfs	K-feldspar	Transitional Guichon-Chataway
2014SM050	5590029	648391	1433		170	60		2	2	Ep-Chl		Kfs	K-feldspar	Transitional Guichon-Chataway
2014SM058	5589793	649277	1423		44	56		0.2	1	Chl		Chl	Propylitic	Guichon
2014SM072	5590306	649986	1418		339	60		0.5	2	Chl		Cly	Propylitic	Transitional Guichon-Chataway
2014SM073	5590322	649765	1423		331	71		0.5	3	Chl		Cly	Propylitic	Transitional Guichon-Chataway
2014SM080	5590336	649199	1341		304	76		1	1	Chl		Cly	Propylitic	Transitional Guichon-Chataway
2014SM081	5592609	650227	1183		203	58		3	0.5	Ab		Ser	Sodic-calcic	Transitional Border-Guichon
2014SM081	5592609	650227	1183		203	58		3	0.5	Chl		Ab	Sodic-calcic	Transitional Border-Guichon
2014SM089	5587079	646693	1556		148	44		3	3	Ep			Propylitic	Chataway
2014SM089	5587079	646693	1556		148	44		3	3	Ep-Qz		Hem	Propylitic	Chataway
2014SM090	5587123	646597	1553		165	40		1	0.5	Ep-Qz			Propylitic	other
2014SM091	5587106	646428	1571		162	40		0.2	7	Ep-Qz		Cly	Propylitic	Guichon
2014SM095	5587216	647344	1513		145	56		1	3	Chl		Hem	Propylitic	Chataway
2014SM096	5587127	647318	1525		160	60		2	4	Chl-Ab		Ep	Sodic-calcic	Chataway
2014SM097	5587219	647196	1538		165	55		3	2	Chl-Ab		Hem	Sodic-calcic	Transitional Guichon-Chataway
2014SM100	5587712	646833	1536		234	40		0.1	70	Qz-Bn		Ser	Muscovite	Chataway
2014SM104	5587596	646150	1568		245	67		0.2	2	Ep-Cly		Chl	Propylitic	Guichon
2014SM105	5587712	646137	1555		88	80		4	6	Ep			Propylitic	Chataway
2014SM105	5587712	646137	1555		88	80		4	6	Qz-Chl			Propylitic	Chataway
2014SM106	5587797	646164	1552		161	83		0.2	1	Chl-Cly		Hem	Propylitic	Chataway
2014SM106	5587797	646164	1552		161	83		0.2	1	Chl-Cly		Hem	Propylitic	Chataway
2014SM107	5588919	644573	1602		37	50		0.1	20	Chl-Qz			Propylitic	Skeena
2014SM107	5588919	644573	1602		37	50		0.1	20	Ep-Bn			Propylitic	Skeena
2014SM120	5587045	644610	1632		351	62		1	2	Kfs-Chl-Bn		Ep	K-feldspar	Skeena
2014SM120	5587045	644610	1632		351	62		1	2	Qz		Ser	Propylitic	Skeena
2014SM122	5587247	644646	1642		189	84		0.2	5	Kfs-Ep		Chl	K-feldspar	Skeena
2014SM126	5589512	643362	1612		86	73		1	3	Ep		Cly	Propylitic	Skeena
2014SM127	5589508	643247	1607		195	69		1	4	Ep		Cly	Propylitic	Skeena
2014SM128	5589564	643154	1625		195	72		1.5	3	Ep-Chl		Cly	Propylitic	Skeena
2014SM135	5587129	644125	1659		60	49		3	2	Ep		Kfs	K-feldspar	Skeena
2014SM135	5587129	644125	1659		60	49		3	2	Tur-Chl		Kfs	K-feldspar	Skeena
2014SM137	5587341	644243	1660		92	74		1	1	Chl-Ep		Kfs	K-feldspar	Skeena
2014SM138	5587582	644233	1668		99	80		1	2	Chl		Kfs	K-feldspar	Skeena
2014SM140	5587776	644395	1649		13	78		1	2	Chl-Ep		Kfs	K-feldspar	Skeena
2014SM140	5587776	644395	1649		13	78		1	2	Ep-Chl		Kfs	K-feldspar	Skeena

Station ID	Northing (m)	Easting (m)	Elev (m)	Vein type	Strike	Dip	Conf	Density /m	Vein width (mm)	Vein minerals	Selvage width (mm)	Selvage minerals	Alteration	Lithology
2014SM141	5587892	644557	1624		190	63		0.2	2	Ep			Propylitic	Skeena
2014SM144	5587468	644616	1627		296	37		1	180	Kfs-Mag		Chl	K-feldspar	Skeena
2014SM145	5591927	641958	1383		2	49		1	2	Ep		Ab	Sodic-calcic	Skeena
2014SM159	5587442	640561	1632		178	82		1	2	Chl			Propylitic	Bethsaida
2014SM161	5584472	644735	1644		200	41		0.5	3	Ep-Chl		Cly	Propylitic	Skeena
2014SM161	5584472	644735	1644		200	41		0.5	3	Ep-Qz		Cly	Propylitic	Skeena
2014SM162	5584158	644834	1614		200	39		0.5	20	Ep-Chl		Cly	Propylitic	Skeena
2014SM163	5584216	646190	1579		110	77		1	3	Chl-Ep		Cly	Propylitic	Skeena
2014SM163	5584216	646190	1579		110	77		1	3	Qz-Ep		Cly	Propylitic	Skeena
2014SM165	5587873	644293	1652		354	50		3	5	Chl			Propylitic	Bethsaida
2014SM165	5587873	644293	1652		354	50		3	5	Kfs-Chl			K-feldspar	Bethsaida
2014SM167	5587941	644198	1660		70	85		3	6	Qz-Chl		Kfs	K-feldspar	Bethsaida
2014SM167	5587941	644198	1660		70	85		3	6	Tur		Kfs	K-feldspar	Bethsaida
2014SM173	5583372	644590	1626		220	87		0.5	3	Ep		Cly	Propylitic	Bethsaida
2014SM177	5594157	647381	1335		46	88		1	1	Chl		Kfs	K-feldspar	Guichon
2014SM178	5594149	646909	1334		13	73		2	1.5	Chl		Ser	Propylitic	Guichon
2014SM178	5594149	646909	1334		13	73		2	1.5	Chl-Ep		Ser	Propylitic	Guichon
2014SM179	5594154	646862	1323		193	85		2	1	Ep		Kfs	K-feldspar	Guichon
2014SM181	5595318	646541	1380		22	78		2	1	Chl		Ser	Propylitic	Guichon
2014SM181	5595318	646541	1380		22	78		2	1	Ep		Kfs	K-feldspar	Guichon
2014SM182	5595405	646532	1388		16	87		3	1	Ep			Propylitic	Guichon
2014SM184	5595528	646507	1394		201	88		8	1	Ep		Kfs	K-feldspar	Guichon
2014SM184	5595528	646507	1394		201	88		8	1	Chl			Propylitic	Guichon
2014SM192	5600924	642162	1629		196	35		2	1	Chl			Propylitic	Guichon
2014SM192	5600924	642162	1629		196	35		2	1	Ep		Kfs	K-feldspar	Guichon
2014SM193	5599092	640154	1600		324	88		2	1.5	Chl-Ep		Ser	Propylitic	Bethlehem
2014SM195	5598961	640208	1614		125	75		1	1	Chl		Ser	Propylitic	Bethlehem
2014SM197	5598963	640397	1635		152	80		0.5	2	Chl-Ep		Ser	Propylitic	Bethlehem
2014SM198	5599539	640297	1642		208	75		2	1	Chl		Ser	Propylitic	Bethlehem
2014SM198	5599539	640297	1642		208	75		2	1	Chl		Ser	Propylitic	Bethlehem
2014SM201	5599596	640963	1572		146	85		3	1	Chl-Ep			Propylitic	Bethlehem
2014SM203	5599167	640543	1623		136	82		3	2	Chl-Ep			Propylitic	Bethlehem
2015GL001	5589227	637069	1700	Vein	205	80	High	2.91	1	Ep	20	Ilt-Chl-Ep	Propylitic	Bethsaida
2015GL001	5589233	637072	1695	Fracture halo	310	80	Med	2.5				Ilt-Chl-Ep	Propylitic	Bethsaida
2015GL001	5589251	637098	1694	Vein	355	85	High	0.1	3	Ep	50	Chl-Ilt-Ep	Propylitic	Bethsaida
2015GL001	5589247	637104	1690	Fracture halo	155	60	Med	5			25	Ilt-Chl-Ep	Propylitic	Bethsaida
2015GL001	5589247	637104	1690	Vein	150	20	High	5	10	Qz-Chl	10	Ilt-Chl-Ep	Propylitic	Bethsaida
2015GL002	5589366	636539	1629	Vein	145	85	Med	5	2	Ep	50	Ep	Propylitic	Bethsaida
2015GL002	5589360	636551	1634	Vein	340	65	Med	1	1	Qz-Chl	50	Chl-Ilt-Ep	Propylitic	Bethsaida
2015GL003	5590038	636805	1662	Vein	35	85	High	6.67	3	Kfs-Py			K-feldspar	Bethsaida
2015GL003	5590038	636805	1662	Vein	325	85	High	1	0.5	Chl-Ep	10	Ilt-Chl	Propylitic	Bethsaida
2015GL003	5590038	636805	1662	Vein	100	70	High	1	0.5	Chl-Ep	10	Ilt-Chl	Propylitic	Bethsaida
2015GL003	5590038	636805	1662	Vein	350	65	High	0.1	0.5	Chl-Ep	10	Ilt-Chl	Propylitic	Bethsaida
2015GL004	5589729	637195	1639	Vein	95	85	High	3.33	2	Chl	60	Chl-Ilt	Propylitic	Bethsaida
2015GL004	5589729	637195	1639	Vein	25	38	High	0.1	3	Qz-Ep	40	Ilt-Chl	Propylitic	Bethsaida

Station ID	Northing (m)	Easting (m)	Elev (m)	Vein type	Strike	Dip	Conf	Density /m	Vein width (mm)	Vein minerals	Selvage width (mm)	Selvage minerals	Alteration	Lithology
2015GL005	5590725	636713	1676	Fracture halo	215	80	High	2			40	Chl-Ep-Ilt	Propylitic	Bethsaida
2015GL005	5590886	636720	1676	Vein	30	80	High	1	4	Ep	50	Ilt-Ep-Chl	Propylitic	Bethsaida
2015GL005	5590886	636720	1676	Vein	100	75	High	3.89	1	Chl	20	Ilt-Ep-Chl	Propylitic	Bethsaida
2015GL005	5590886	636720	1676	Vein	40	85	High	2	2	Kfs-Qz			K-feldspar	Bethsaida
2015GL005	5590867	636739	1678	Vein	225	85	High	0.1	2	Kfs-Qz			K-feldspar	Bethsaida
2015GL005	5590886	636741	1678	Vein	30	80	High	1	4	Ep	50	Ilt-Ep-Chl	Propylitic	Bethsaida
2015GL005	5590835	636763	1682	Fracture halo	325	80	High	0.1			2	Ilt	Propylitic	Bethsaida
2015GL006	5591009	636198	1643	Vein	40	75	High	3.33	2	Kfs-Qz			K-feldspar	Bethsaida
2015GL007	5590421	636466	1653	Fracture halo	325	70	High	0.1			10	Chl-Ep	Propylitic	Bethsaida
2015GL007	5590456	636522	1663	Vein	50	85	High	0.1	3	Kfs-Qz			K-feldspar	Bethsaida
2015GL007	5590456	636522	1663	Vein	215	85	High	2	2	Ep	70	Chl-Ep-Ilt	Propylitic	Bethsaida
2015GL007	5590437	636544	1664	Vein	85	90	High	1.75	3	Ep	30	Ep-Ilt-Chl	Propylitic	Bethsaida
2015GL007	5590437	636544	1664	Vein	125	75	High	0.1	1	Ep	30	Ep-Ilt-Chl	Propylitic	Bethsaida
2015GL008	5590314	637289	1645	Fracture halo	80	85	High	3			20	Chl-Ilt-Ep	Propylitic	Bethsaida
2015GL009	5590021	637578	1632	Fracture halo	115	80	High	1			50	Ilt-Chl-Ep	Propylitic	Bethsaida
2015GL009	5590021	637578	1632	Vein	70	90	High	1.43	1	Ep	70	Ilt-Chl-Ep	Propylitic	Bethsaida
2015GL009	5590026	637579	1632	Fracture halo	115	80	High	1			50	Ilt-Chl-Ep	Propylitic	Bethsaida
2015GL010	5587411	640555	1633	Vein	140	40	High	50	0.5	Ccp-Py		Chl	Propylitic	Bethsaida
2015GL010	5587398	640557	1633	Vein	178	60	Med	8	2	Ep-Chl	10	Ep	Propylitic	Bethsaida
2015GL010	5587442	640564	1632	Vein	170	70	High	2.5	3	Ep-Chl			Propylitic	Bethsaida
2015GL010	5587447	640610	1637	Vein	170	70	High	1.25	2	Ep			Propylitic	Bethsaida
2015GL010	5587439	640615	1643	Vein	170	70	High	1.25	1	Ep-Ilt			Propylitic	Bethsaida
2015GL011	5586805	640238	1646	Vein	215	70	High	6	0.5	Ep	20	Chl-Ilt-Ep-Hem	Propylitic	Bethsaida
2015GL011	5586806	640249	1648	Vein	215	70	High	6	0.5	Ep	20	Chl-Ilt-Ep-Hem	Propylitic	Bethsaida
2015GL011	5586819	640250	1644	Vein	235	85	High	6	0.5	Ep	20	Chl-Ilt-Ep-Hem	Propylitic	Bethsaida
2015GL011	5586819	640250	1644	Vein	165	35	High	3.33	1	Ep	10	Hem-Chl-Ep	Propylitic	Bethsaida
2015GL013	5596058	639916	1285	Fracture halo	85	90	High	0.01			500	Chl-Ilt	Propylitic	Bethsaida
2015GL013	5586038	639951	1615	Vein	350	70	High	0.5	1	Ep	35	Ab-Chl-Ep	Sodic-calcic	Bethsaida
2015GL013	5586038	639951	1615	Vein	30	60	High	0.5	1	Ep	35	Ab-Chl-Ep	Sodic-calcic	Bethsaida
2015GL013	5586034	639952	1618	Vein	350	70	High	0.5	1	Ep	35	Ab-Chl-Ep	Sodic-calcic	Bethsaida
2015GL014	5586097	640965	1688	Fracture halo	15	65	High	1			10	Chl-Ep-Ilt	Propylitic	Bethsaida
2015GL014	5586097	640965	1688	Vein	100	60	High	1.43	2	Ab-Chl	20	Ep-Chl-Ilt	Sodic-calcic	Bethsaida
2015GL014	5586123	640989	1687	Vein	230	90	High	13.33	0.5	Ep	15	Chl-Ab-Ep-Ilt	Sodic-calcic	Bethsaida
2015GL014	5586107	640990	1687	Vein	230	90	High	13.33	0.5	Ep	15	Chl-Ab-Ep-Ilt	Sodic-calcic	Bethsaida
2015GL014	5586107	641003	1687	Fracture halo	330	65	Med	0.91			10	Chl-Ep-Ilt	Propylitic	Bethsaida
2015GL015	5585950	640842	1679	Fracture halo	15	90	High	1			40	Ilt-Chl	Propylitic	Bethsaida
2015GL015	5585947	640852	1680	Vein	30	60	Med	1.33	0.5	Ep-Chl	15	Chl-Ilt	Propylitic	Bethsaida
2015GL015	5585947	640852	1680	Vein	145	65	High	0.1	0.5	Ep	5	Ep	Propylitic	Bethsaida
2015GL015	5585655	641130	1692	Vein	160	55	High	2.5	2	Ep	5	Ab-Chl	Sodic-calcic	Bethsaida
2015GL015	5585653	641133	1692	Vein	160	55	High	10	2	Ep	50	Ab-Chl	Sodic-calcic	Bethsaida
2015GL015	5585684	641134	1694	Vein	155	60	High	2.5	2	Ep	5	Ab-Chl	Sodic-calcic	Bethsaida
2015GL015	5585653	641137	1693	Vein	150	55	High	2.5	2	Ep	5	Ab-Chl	Sodic-calcic	Bethsaida
2015GL015	5585621	641161	1689	Vein	135	55	High	0.1	2	Ep	50	Chl-Ilt	Propylitic	Bethsaida
2015GL015	5585624	641165	1690	Vein	185	70	High	0.1	2	Qz-Ep	20	Chl	Propylitic	Bethsaida
2015GL015	5585624	641165	1690	Vein	135	55	High	0.1	2	Ep	50	Chl-Ilt	Propylitic	Bethsaida

Station ID	Northing (m)	Easting (m)	Elev (m)	Vein type	Strike	Dip	Conf	Density /m	Vein width (mm)	Vein minerals	Selvage width (mm)	Selvage minerals	Alteration	Lithology
2015GL016	5585798	640714	1669	Vein	20	80	High	0.25	2	Ep-Qz	30	Ilt-Chl-Hem	Propylitic	Bethsaida
2015GL016	5585798	640714	1669	Vein	145	55	High	0.1	1	Ep			Propylitic	Bethsaida
2015GL016	5585788	640718	1671	Vein	145	55	High	0.1	1	Ep			Propylitic	Bethsaida
2015GL016	5585808	640731	1672	Vein	10	80	High	6.67	3	Ep	10	Ep-Ab	Sodic-calcic	Bethsaida
2015GL016	5585827	640733	1673	Vein	10	80	High	6.67	3	Ep	10	Ep-Ab	Sodic-calcic	Bethsaida
2015GL016	5585817	640741	1672	Vein	145	55	High	0.1	2	Ep			Propylitic	Bethsaida
2015GL017	5584621	640349	1609	Vein	140	65	High	3	1	Chl	40	Ilt-Chl	Propylitic	Bethsaida
2015GL017	5584621	640349	1609	Vein	10	55	High	10	1	Qz-Kfs-Ccp-Py			K-feldspar	Bethsaida
2015GL017	5584621	640349	1609	Vein	80	85	High	3	1	Chl	40	Ilt-Chl	Propylitic	Bethsaida
2015GL017	5584619	640351	1609	Vein	10	55	High	10	1	Qz-Kfs-Ccp-Py			K-feldspar	Bethsaida
2015GL017	5584619	640351	1609	Vein	140	65	High	3	1	Chl	40	Ilt-Chl	Propylitic	Bethsaida
2015GL018	5585441	640126	1628	Vein	155	55	High	5	0.5	Ep-Chl	100	Ab-Chl-Ilt	Sodic-calcic	Bethsaida
2015GL018	5585441	640126	1628	Vein	195	70	High	5	0.5	Ep-Chl	100	Ab-Chl-Ilt	Sodic-calcic	Bethsaida
2015GL018	5585450	640128	1628	Fracture halo	160	35	High	0.1			20	Ab-Chl	Sodic-calcic	Bethsaida
2015GL018	5585458	640129	1628	Fracture halo	220	50	Low	5			30	Ilt	Propylitic	Bethsaida
2015GL018	5585458	640129	1628	Fracture halo	140	48	High	5			30	Ilt	Propylitic	Bethsaida
2015GL018	5585458	640129	1628	Fracture halo	150	48	High	5			30	Ilt	Propylitic	Bethsaida
2015GL018	5585359	640300	1637	Vein	40	80	High	10	3	Ep-Chl	50	Ab-Chl	Sodic-calcic	Bethsaida
2015GL018	5585359	640300	1637	Vein	195	75	High	10	3	Ep-Chl	50	Ab-Chl	Sodic-calcic	Bethsaida
2015GL018	5585360	640302	1637	Vein	195	75	High	10	2	Ep-Chl	50	Ab-Chl-Ilt	Sodic-calcic	Bethsaida
2015GL018	5585345	640304	1636	Fracture halo	50	50	Low	1			15	Ilt	Propylitic	Bethsaida
2015GL018	5585345	640304	1636	Vein	300	85	High	1	0.5	Chl	30	Ilt-Chl	Propylitic	Bethsaida
2015GL018	5585355	640305	1637	Vein	105	90	High	6.67	0.5	Chl-Ep	15	Ab-Chl	Sodic-calcic	Bethsaida
2015GL019	5585282	640910	1667	Fracture halo	20	80	High	0.1			25	Chl-Ab	Sodic-calcic	Bethsaida
2015GL019	5585294	640936	1670	Vein	135	55	Low	1	1	Ep	25	Ilt-Chl	Propylitic	Bethsaida
2015GL020	5584734	641163	1636	Fracture halo	310	75	High	2.22			20	Ilt-Chl	Propylitic	Bethsaida
2015GL020	5584740	641170	1636	Fracture halo	95	85	High	2.22			10	Ilt-Chl	Propylitic	Bethsaida
2015GL020	5584740	641170	1636	Fracture halo	310	75	High	2.22			20	Ilt-Chl	Propylitic	Bethsaida
2015GL022	5588902	640327	1655	Fracture halo	92	70	High	10			15	Ilt-Chl	Propylitic	Bethsaida
2015GL022	5588889	640338	1654	Vein	215	85	High	33.33	1	Qz-Kfs			K-feldspar	Bethsaida
2015GL023	5585199	642283	1696	Vein	345	70	High	2	3	Ep	20	Chl-Ep-Ilt	Propylitic	Bethsaida
2015GL023	5585199	642283	1696	Vein	20	55	High	2	3	Ep	20	Chl-Ep-Ilt	Propylitic	Bethsaida
2015GL023	5585199	642283	1696	Vein	70	70	High	0.1	40	Qz	5	Kfs	K-feldspar	Bethsaida
2015GL023	5585194	642283	1700	Vein	345	70	High	2	3	Ep	20	Chl-Ep-Ilt	Propylitic	Bethsaida
2015GL023	5585189	642327	1692	Vein	155	60	High	3.5	2	Ep-Qz	30	Chl-Ep-Ilt	Propylitic	Bethsaida
2015GL023	5585195	642352	1688	Vein	70	60	High	0.1	1	Ep	10	Chl-Ep	Propylitic	Bethsaida
2015GL024	5585066	641867	1689	Vein	120	80	High	2	1	Ep	30	Chl-Ep-Ilt	Propylitic	Bethsaida
2015GL024	5585066	641867	1689	Vein	210	85	High	0.1	0.2	Kfs			K-feldspar	Bethsaida
2015GL025	5584416	641815	1653	Vein	120	65	High	10	1	Kfs-Qz			K-feldspar	Bethsaida
2015GL025	5584418	641815	1653	Vein	120	65	High	10	1	Kfs-Qz			K-feldspar	Bethsaida
2015GL026	5584416	642372	1676	Vein	125	70	High	1	1	Ep	30	Chl-Ilt	Propylitic	Bethsaida
2015GL026	5584417	642373	1676	Vein	5	90	High	0.1	0.5	Ep	15	Ep-Chl	Propylitic	Bethsaida
2015GL026	5584417	642373	1676	Vein	120	75	High	0.1	1	Kfs	5	Chl	K-feldspar	Bethsaida
2015GL026	5584417	642373	1676	Vein	125	70	High	1	1	Ep	30	Chl-Ilt	Propylitic	Bethsaida
2015GL026	5584417	642373	1676	Vein	120	75	High	0.1	1	Kfs	5	Chl	K-feldspar	Bethsaida

Station ID	Northing (m)	Easting (m)	Elev (m)	Vein type	Strike	Dip	Conf	Density /m	Vein width (mm)	Vein minerals	Selvage width (mm)	Selvage minerals	Alteration	Lithology
2015GL028	5593233	637322	1604	Fracture halo	270	87	High	16.67			5	Ccp-Chl-Kfs	K-feldspar	Bethsaida
2015GL028	5593231	637323	1604	Fracture halo	270	87	High	16.67			5	Ccp-Chl-Kfs	K-feldspar	Bethsaida
2015GL029	5593407	637088	1642	Fracture halo	115	85	High	10		Mlc	2	Kfs-Ccp-Chl	K-feldspar	Bethsaida
2015GL029	5593384	637104	1640	Fracture halo	115	85	High	10		Mlc	2	Kfs-Ccp-Chl	K-feldspar	Bethsaida
2015GL030	5593532	637187	1598	Vein	115	85	High	14.29	2	Qz	2	Ccp-Kfs	K-feldspar	Bethsaida
2015GL030	5593582	637217	1586	Vein	90	75	High	0.1	5	Qz-Kfs	4	Ms	Muscovite	Bethsaida
2015GL030	5593577	637225	1580	Vein	115	85	High	14.29	2	Qz	2	Ccp-Kfs	K-feldspar	Bethsaida
2015GL031	5593915	637267	1531	Vein	110	75	High	3.25	3	Qz-Ms	5	Ms	Muscovite	Bethsaida
2015GL031	5593915	637269	1531	Vein	115	70	High	3.25	3	Qz-Ms	5	Ms	Muscovite	Bethsaida
2015GL031	5593915	637269	1531	Vein	110	75	High	3.25	3	Qz-Ms	5	Ms	Muscovite	Bethsaida
2015GL031	5593915	637269	1531	Fracture halo	345	60	High	1			2.5	Ms	Muscovite	Bethsaida
2015GL033	5584985	642668	1659	Vein	165	75	High	2.5	1	Ep	15	Ep-Chl	Propylitic	Bethsaida
2015GL033	5584985	642676	1659	Vein	165	75	High	2.5	1	Ep	15	Ep-Chl	Propylitic	Bethsaida
2015GL033	5584995	642681	1657	Fracture halo	305	65	Low	0.1			5	Kfs-Chl-Ep	K-feldspar	Bethsaida
2015GL033	5594946	642708	1511	Vein	205	65	High	0.1	2	Ep-Chl	10	Ilt-Ep-Chl	Propylitic	Bethsaida
2015GL033	5594946	642708	1511	Vein	185	55	High	6.67	2	Ep-Chl	10	Ilt-Ep-Chl	Propylitic	Bethsaida
2015GL033	5594946	642708	1511	Vein	155	65	High	6.67	2	Ep-Chl	10	Ilt-Ep-Chl	Propylitic	Bethsaida
2015GL035	5585462	642884	1652	Vein	145	90	High	1	1	Chl	10	Chl-Ep-Ilt	Propylitic	Skeena
2015GL035	5585464	642890	1654	Vein	145	90	High	1	1	Chl	10	Chl-Ep-Ilt	Propylitic	Skeena
2015GL036	5584503	643368	1617	Fracture halo	355	65	High	3.33			10	Chl-Ilt	Propylitic	Skeena
2015GL036	5584507	643371	1618	Fracture halo	355	65	High	3.33			10	Chl-Ilt	Propylitic	Skeena
2015GL036	5584551	643393	1624	Vein	350	42	High	3.33	2	Chl-Ilt-Ep	10	Chl-Ilt	Propylitic	Skeena
2015GL037	5584105	643573	1636	Vein	170	75	High	2	1	Ep	30	Ep-Chl-Ilt-Hem	Propylitic	Bethsaida
2015GL037	5584113	643618	1637	Vein	60	85	High	2.5	1.5	Ep	3	Ilt-Chl	Propylitic	Bethsaida
2015GL037	5584113	643618	1637	Vein	135	80	High	2	1	Ep	5	Chl-Ep	Propylitic	Bethsaida
2015GL037	5584111	643622	1638	Vein	95	70	High	0.1	20	Qz-Spec-Ep	50	Chl-Ilt	Propylitic	Bethsaida
2015GL038	5584376	642874	1653	Fracture halo	105	80	High	5.33			30	Ilt-Chl-Ep	Propylitic	Bethsaida
2015GL038	5584281	642888	1660	Vein	135	85	High	5	2	Ep	10	Chl-Ab	Sodic-calcic	Bethsaida
2015GL038	5584281	642888	1660	Fracture halo	70	80	High	2.5			10	Chl-Ep-Ilt	Propylitic	Bethsaida
2015GL038	5584339	642899	1653	Vein	135	85	High	5	2	Ep	10	Chl-Ab	Sodic-calcic	Bethsaida
2015GL038	5584348	642910	1650	Fracture halo	105	80	High	5.33			30	Ilt-Chl-Ep	Propylitic	Bethsaida
2015GL038	5584348	642910	1650	Vein	165	85	High	1.43	5	Ep-Chl	30	Ep-Chl-Ilt-Hem	Propylitic	Bethsaida
2015GL039	5584841	644679	1627	Fracture halo	200	65	High	2.5			30	Chl-Ilt-Ep	Propylitic	Skeena
2015GL039	5584869	644698	1622	Fracture halo	200	65	High	2.5			30	Chl-Ilt-Ep	Propylitic	Skeena
2015GL040	5584352	644709	1652	Fracture halo	160	80	High	0.67			35	Ep-Chl-Ilt	Propylitic	Skeena
2015GL040	5584362	644733	1663	Vein	245	80	High	0.1	7	Ep	13	Ep-Chl	Propylitic	Skeena
2015GL041	5583431	644812	1624	Vein	160	90	High	0.1	1	Chl-Ep	10	Chl-Ilt	Propylitic	Bethsaida
2015GL042	5584062	640314	1591	Fracture halo	260	75	High	1.43			10	Chl-Ilt-Ep	Propylitic	Bethsaida
2015GL042	5584035	640315	1590	Fracture halo	260	75	High	1.43			10	Chl-Ilt-Ep	Propylitic	Bethsaida
2015GL043	5583442	640264	1573	Vein	25	75	High	3.33	0.5	Chl	25	Chl-Ilt-Ep	Propylitic	Bethsaida
2015GL043	5583571	640305	1579	Vein	340	80	Low	6.67	0.5	Chl	10	Chl-Ilt	Propylitic	Bethsaida
2015GL044	5583001	640254	1553	Vein	25	80	High	5	1	Ep	20	Chl-Ilt-Ep	Propylitic	Bethsaida
2015GL044	5583001	640254	1553	Vein	15	70	High	5	1	Ep	20	Chl-Ilt-Ep	Propylitic	Bethsaida
2015GL044	5583000	640258	1555	Vein	25	80	High	5	1	Ep	20	Chl-Ilt-Ep	Propylitic	Bethsaida
2015GL045	5583079	640880	1588	Fracture halo	245	80	High	0.1			10	Ilt-Chl	Propylitic	Bethsaida

Station ID	Northing (m)	Easting (m)	Elev (m)	Vein type	Strike	Dip	Conf	Density /m	Vein width (mm)	Vein minerals	Selvage width (mm)	Selvage minerals	Alteration	Lithology
2015GL045	5583071	640894	1588	Fracture halo	255	55	High	0.1			10	Ilt-Chl	Propylitic	Bethsaida
2015GL045	5583071	640894	1588	Fracture halo	245	80	High	0.1			10	Ilt-Chl	Propylitic	Bethsaida
2015GL047	5583380	641344	1635	Vein	135	65	High	1	1	Chl	20	Ilt-Ep-Chl	Propylitic	Bethsaida
2015GL047	5583407	641356	1638	Vein	150	60	High	1	1	Chl	20	Ilt-Ep-Chl	Propylitic	Bethsaida
2015GL047	5583407	641356	1638	Fracture halo	25	70	High	0.1	0.1		10	Chl-Ilt	Propylitic	Bethsaida
2015GL047	5583409	641360	1638	Fracture halo	25	70	High	0.1	0.1		10	Chl-Ilt	Propylitic	Bethsaida
2015GL048	5583259	641870	1595	Vein	250	80	High	0.5	1	Ep-Chl	35	Chl-Ilt-Hem	Propylitic	Bethsaida
2015GL048	5583258	641876	1595	Vein	250	80	High	0.5	1	Ep-Chl	35	Chl-Ilt-Hem	Propylitic	Bethsaida
2015GL048	5583258	641876	1595	Vein	225	65	High	0.5	1	Ep-Chl	35	Chl-Ilt-Hem	Propylitic	Bethsaida
2015GL048	5583220	641882	1593	Fracture halo	30	70	High	0.1	0.1	Chl			Propylitic	Bethsaida
2015GL048	5583240	641884	1595	Vein	20	50	High	0.1	1	Ep	10	Ilt-Chl	Propylitic	Bethsaida
2015GL049	5583744	641792	1617	Fracture halo	95	80	High	1			7	Chl-Ilt-Ep	Propylitic	Bethsaida
2015GL049	5583744	641792	1617	Vein	135	55	High	0.1	1	Ep	7	Chl-Ilt-Ep	Propylitic	Bethsaida
2015GL049	5583744	641792	1617	Vein	340	80	High	1	1	Ep	7	Chl-Ilt-Ep	Propylitic	Bethsaida
2015GL049	5583806	641806	1626	Vein	55	80	High	1	1	Ep	7	Chl-Ilt-Ep	Propylitic	Bethsaida
2015GL050	5583812	641406	1601	Vein	190	80	High	2.22	1	Ep-Chl	10	Ilt-Chl-Hem	Propylitic	Bethsaida
2015GL050	5583812	641406	1601	Fracture halo	150	65	High	0.1		Chl-Hem-Mlc		Ilt-Chl-Ep	Propylitic	Bethsaida
2015GL050	5583827	641409	1601	Vein	225	80	High	0.1	1	Ep-Chl	10	Ilt-Chl-Hem	Propylitic	Bethsaida
2015GL050	5583827	641409	1601	Vein	190	80	High	2.22	1	Ep-Chl	10	Ilt-Chl-Hem	Propylitic	Bethsaida
2015GL050	5583795	641439	1602	Fracture halo	30	65	High	0.1			10	Ilt-Chl-Ep	Propylitic	Bethsaida
2015GL050	5583795	641439	1602	Fracture halo	140	65	High	0.1		Chl-Hem-Mlc		Ilt-Chl-Ep	Propylitic	Bethsaida
2015GL050	5583795	641439	1602	Fracture halo	140	65	High	0.1			10	Ilt-Chl-Ep	Propylitic	Bethsaida
2015GL051	5584225	641400	1611	Fracture halo	105	85	High	5	0.1	Chl-Ep	30	Ilt-Chl-Ep	Propylitic	Bethsaida
2015GL051	5584226	641400	1611	Fracture halo	105	85	High	5	0.1	Chl-Ep	30	Ilt-Chl-Ep	Propylitic	Bethsaida
2015GL051	5584247	641408	1612	Vein	345	60	High	0.1	2	Ep	400	Chl-Ep-Ab-Ilt	Sodic-calcic	Bethsaida
2015GL051	5584247	641408	1612	Vein	150	65	High	0.1	2	Ep	400	Chl-Ep-Ab-Ilt	Sodic-calcic	Bethsaida
2015GL051	5584247	641408	1612	Vein	150	55	High	0.1	2	Ep	400	Chl-Ep-Ab-Ilt	Sodic-calcic	Bethsaida
2015GL051	5584235	641409	1611	Vein	150	65	High	0.1	2	Ep	400	Chl-Ep-Ab-Ilt	Sodic-calcic	Bethsaida
2015GL051	5584231	641420	1611	Vein	95	80	High	1	1	Chl	10	Chl-Ilt-Ep	Propylitic	Bethsaida
2015GL052	5582755	641871	1592	Fracture halo	125	55	High	0.67	0.5	Chl	10	Ep-Chl	Propylitic	Bethsaida
2015GL052	5582740	641893	1591	Fracture halo	140	55	High	0.67	0.5	Chl	10	Ep-Chl	Propylitic	Bethsaida
2015GL052	5582916	641939	1587	Vein	205	85	High	0.1	0.5	Ep			Propylitic	Bethsaida
2015GL052	5582916	641939	1587	Fracture halo	75	80	High	2			35	Ep-Ilt-Chl	Propylitic	Bethsaida
2015GL053	5582915	642475	1608	Fracture halo	130	70	High	2			5	Kfs-Py-Bt	K-feldspar	Bethsaida
2015GL053	5582915	642475	1608	Fracture halo	130	70	High	2			5	Ep-Chl-Ilt	Propylitic	Bethsaida
2015GL053	5582915	642475	1608	Vein	205	85	High	0.1	0.5	Ep	3	Kfs	K-feldspar	Bethsaida
2015GL053	5582914	642475	1608	Fracture halo	130	70	High	2			5	Ep-Chl-Ilt	Propylitic	Bethsaida
2015GL053	5582938	642503	1610	Vein	130	72	High	0.1	1	Ep-Chl	5	Ilt-Chl-Ep	Propylitic	Bethsaida
2015GL053	5582878	642615	1612	Fracture halo	105	80	High	2			4	Ilt-Chl-Hem	Propylitic	Bethsaida
2015GL053	5582878	642615	1612	Vein	210	78	High	0.1	1	Ep	15	Chl-Ep-Ilt-Hem	Propylitic	Bethsaida
2015GL054	5582158	642297	1568	Fracture halo	135	85	High	0.1			6	Chl-Ep-Ilt	Propylitic	Bethsaida
2015GL054	5582139	642336	1569	Vein	135	85	High	0.1	2	Ep-Py	10	Chl-Ep-Ilt	Propylitic	Bethsaida
2015GL055	5584068	642454	1648	Vein	140	80	High	0.1	0.5	Ep-Py-Mlc	2	Kfs	K-feldspar	Bethsaida
2015GL055	5584066	642455	1648	Vein	140	80	High	5.33	2	Kfs-Py-Mlc-Ep			K-feldspar	Bethsaida
2015GL055	5584055	642456	1647	Vein	90	90	High	0.1	1	Chl	20	Chl-Ep-Hem-Ilt	Propylitic	Bethsaida

Station ID	Northing (m)	Easting (m)	Elev (m)	Vein type	Strike	Dip	Conf	Density /m	Vein width (mm)	Vein minerals	Selvage width (mm)	Selvage minerals	Alteration	Lithology
2015GL055	5584055	642456	1647	Vein	145	75	High	3.33	0.5	Ep-Py-Mlc	2	Kfs	K-feldspar	Bethsaida
2015GL055	5584055	642464	1647	Fracture halo	330	80	Med	2.5			25	Chl-Ep-Ilt	Propylitic	Bethsaida
2015GL055	5584055	642464	1647	Fracture halo	145	75	High	2.5			25	Chl-Ep-Ilt	Propylitic	Bethsaida
2015GL055	5584084	642482	1648	Vein	145	75	High	0.1	0.5	Ep-Py-Mlc	2	Kfs	K-feldspar	Bethsaida
2015GL055	5584049	642488	1647	Vein	90	90	High	6	1	Chl	20	Chl-Ep-Hem-Ilt	Propylitic	Bethsaida
2015GL055	5584049	642488	1647	Fracture halo	145	75	High	0.1			25	Chl-Ep-Ilt	Propylitic	Bethsaida
2015GL055	5584049	642488	1647	Vein	215	90	Med	0.1	1	Ep	20	Ep-Ilt	Propylitic	Bethsaida
2015GL056	5583485	642396	1627	Vein	160	70	Med	3.33	1	Ep	5	Chl-Ep-Hem	Propylitic	Bethsaida
2015GL057	5582603	643023	1593	Vein	130	65	High	10	0.1	Kfs		Ep-Chl	K-feldspar	Bethsaida
2015GL057	5582602	643026	1596	Vein	130	65	High	10	0.1	Kfs		Ep-Chl	K-feldspar	Bethsaida
2015GL058	5583107	643021	1612	Vein	285	85	Med	0.67	4	Chl-Ep	20	Chl-Ilt-Ep	Propylitic	Bethsaida
2015GL058	5583163	643082	1612	Fracture halo	245	55	Med	2.5			7	Chl-Ilt-Ep	Propylitic	Bethsaida
2015GL058	5583160	643118	1620	Vein	40	85	Med	0.1	0.5	Ep	10	Chl-Ep-Ilt	Propylitic	Bethsaida
2015GL058	5583158	643121	1620	Vein	40	85	Med	0.1	0.5	Ep	10	Chl-Ep-Ilt	Propylitic	Bethsaida
2015GL059	5583713	642914	1627	Vein	345	70	High	3.5	1	Ep	10	Chl-Ep-Ab	Sodic-calcic	Bethsaida
2015GL059	5583713	642914	1627	Fracture halo	90	80	High	1			20	Ep-Chl-Ilt	Propylitic	Bethsaida
2015GL059	5583710	642926	1631	Vein	340	65	High	3.75	10	Ep-Chl	15	Ep-Chl-Ab-Ilt	Sodic-calcic	Bethsaida
2015GL059	5583710	642926	1631	Fault	330	80	High		4000			Ilt-Chl	Propylitic	Bethsaida
2015GL059	5583710	642927	1631	Vein	340	65	High	3.75	10	Ep-Chl	15	Ep-Chl-Ab-Ilt	Sodic-calcic	Bethsaida
2015GL059	5583689	642947	1628	Vein	165	90	Low	1.11	2	Chl	10	Chl-Ep-Ab-Ilt	Sodic-calcic	Bethsaida
2015GL059	5583689	642947	1628	Vein	85	75	High	0.1	2	Qz-Ep	25	Chl-Ep-Ilt	Propylitic	Bethsaida
2015GL060	5583812	643339	1611	Vein	0	90	Med	2.5	0.5	Ep	10	Ilt-Chl	Propylitic	Bethsaida
2015GL060	5583873	643402	1609	Fracture halo	150	60	Low	0.1			5	Ep-Chl-Ilt	Propylitic	Bethsaida
2015GL062	5583735	644097	1617	Vein	190	68	Low	10	0.5	Ep	50	Chl-Ep-Ab-Ilt	Sodic-calcic	Bethsaida
2015GL062	5583731	644100	1617	Vein	190	68	Low	10	0.5	Ep	50	Chl-Ep-Ab-Ilt	Sodic-calcic	Bethsaida
2015GL063	5583304	643813	1583	Fracture halo	105	65	High	0.1			10	Ep-Chl-Ilt	Propylitic	Bethsaida
2015GL063	5583294	643839	1584	Fracture halo	120	65	High	0.1			10	Ep-Chl-Ilt	Propylitic	Bethsaida
2015GL063	5583310	643843	1584	Fracture halo	60	85	Low	0.1			7	Chl-Ilt-Ep	Propylitic	Bethsaida
2015GL063	5583311	643845	1584	Fracture halo	60	85	Low	0.1			7	Chl-Ilt-Ep	Propylitic	Bethsaida
2015GL064	5582780	643507	1608	Fracture halo	75	85	High	1.33			20	Ilt-Chl-Ep	Propylitic	Bethsaida
2015GL064	5582780	643507	1608	Vein	195	85	High	2.86	0.5	Cal	20	Ilt-Chl-Ep-Cal	Propylitic	Bethsaida
2015GL064	5582769	643512	1611	Vein	190	85	High	2.86	0.5	Cal	20	Ilt-Chl-Ep-Cal	Propylitic	Bethsaida
2015GL066	5582876	644891	1595	Fracture halo	240	65	High	0.1	0.1	Ms-Chl	50	Ms-Chl	Muscovite	Bethsaida
2015GL067	5583106	644552	1604	Vein	155	75	High	3.33	0.5	Chl	15	Ilt-Ep-Chl	Propylitic	Bethsaida
2015GL067	5583113	644559	1604	Vein	155	75	High	3.33	0.5	Chl	15	Ilt-Ep-Chl	Propylitic	Bethsaida
2015GL068	5582352	643459	1596	Fracture halo	205	80	High	1			10	Chl-Ep-Ilt	Propylitic	Bethsaida
2015GL069	5581647	643230	1582	Vein	5	55	Med	10	0.5	Ep	5	Chl-Ep-Ilt	Propylitic	Bethsaida
2015GL069	5581689	643247	1580	Fracture halo	105	68	High	0.1			30	Ilt-Ep-Chl	Propylitic	Bethsaida
2015GL069	5581656	643320	1570	Fracture halo	40	80	High	0.1			200	Ilt-Chl	Propylitic	Bethsaida
2015GL069	5581613	643361	1572	Fracture halo	40	80	High	0.1			200	Ilt-Chl	Propylitic	Bethsaida
2015GL070	5581748	642803	1595	Fracture halo	90	90	High	0.1			4	Ilt-Chl	Propylitic	Bethsaida
2015GL070	5581748	642803	1595	Vein	42	90	High	1.5	1	Ep-Qz	30	Ilt-Chl-Ep	Propylitic	Bethsaida
2015GL070	5581748	642803	1595	Vein	55	90	High	0.5	1	Ep-Qz	30	Ilt-Chl-Ep	Propylitic	Bethsaida
2015GL071	5580242	642160	1616	Vein	260	80	High	2	2	Ep	10	Ilt-Chl-Ep	Propylitic	Bethsaida
2015GL071	5580302	642173	1623	Fracture halo	70	75	High	0.67			7.5	Chl-Ilt	Propylitic	Bethsaida

Station ID	Northing (m)	Easting (m)	Elev (m)	Vein type	Strike	Dip	Conf	Density /m	Vein width (mm)	Vein minerals	Selvage width (mm)	Selvage minerals	Alteration	Lithology
2015GL071	5580299	642175	1621	Fracture halo	70	75	High	0.67			7.5	Chl-Ilt	Propylitic	Bethsaida
2015GL071	5580280	642180	1621	Fracture halo	260	90	High	2			10	Ep-Chl-Ilt	Propylitic	Bethsaida
2015GL073	5581133	643386	1560	Fracture halo	335	35	High	3.33			10	Chl-Ilt-Ep	Propylitic	Bethsaida
2015GL073	5581137	643386	1560	Fracture halo	335	55	High	0.1	1000			Ilt-Chl-Ep	Propylitic	Bethsaida
2015GL073	5581094	643404	1566	Fracture halo	335	55	High	0.1	1000			Ilt-Chl-Ep	Propylitic	Bethsaida
2015GL074	5580801	643744	1550	Vein	175	85	High	5	1	Chl-Ep	20	Ep-Chl-Ab-Ilt	Sodic-calcic	Bethsaida
2015GL074	5580801	643744	1550	Fracture halo	40	90	High	5			5	Chl-Ilt	Propylitic	Bethsaida
2015GL076	5578976	642590	1538	Fracture halo	340	60	High	0.67			25	Ep-Chl-Ilt	Propylitic	Bethsaida
2015GL076	5578991	642615	1536	Fracture halo	200	85	High	0.1	1			Ilt	Propylitic	Bethsaida
2015GL077	5579441	642114	1563	Vein	15	65	High	1.75	3	Ep	50	Ep-Chl-Ilt	Propylitic	Bethsaida
2015GL077	5579441	642114	1563	Vein	195	85	High	1.75	3	Ep	50	Ep-Chl-Ilt	Propylitic	Bethsaida
2015GL077	5579441	642114	1563	Fracture halo	90	80	High	2			10	Ep-Chl-Ilt	Propylitic	Bethsaida
2015GL077	5579376	642119	1563	Vein	90	80	High	1	3	Chl-Ab-Ep	40	Chl-Ep-Ilt	Sodic-calcic	Bethsaida
2015GL077	5579443	642166	1562	Fracture halo	280	85	High	0.67			35	Ep-Chl-Ilt	Propylitic	Bethsaida
2015GL077	5579443	642166	1562	Fracture halo	205	80	High	0.1			2	Ep-Chl-Ilt	Propylitic	Bethsaida
2015GL077	5579442	642171	1562	Fracture halo	90	80	High	2			10	Ep-Chl-Ilt	Propylitic	Bethsaida
2015GL078	5579818	641934	1595	Fracture halo	310	85	High	1.67			10	Ep-Chl-Ilt	Propylitic	Bethsaida
2015GL078	5579839	641949	1596	Vein	95	90	High	0.83	2	Ep	10	Ep-Chl-Ilt-Hem	Propylitic	Bethsaida
2015GL079	5579316	641643	1545	Vein	130	90	High	2	1	Qz	20	Ep-Chl-Ilt-Hem	Propylitic	Bethsaida
2015GL079	5579380	641667	1548	Vein	130	90	High	0.1	2	Ep	10	Ab-Chl-Ep	Sodic-calcic	Bethsaida
2015GL079	5579358	641698	1545	Fracture halo	255	75	High	3			20	Ep-Chl-Ilt	Propylitic	Bethsaida
2015GL079	5579369	641701	1547	Fracture halo	195	90	High	15			0.1	Ilt	Propylitic	Bethsaida
2015GL080	5580130	644448	1467	Fracture halo	355	55	High	6.67			20	Ilt-Chl	Propylitic	Bethsaida
2015GL080	5580130	644448	1467	Fracture halo	60	80	High	5			20	Ilt-Chl	Propylitic	Bethsaida
2015GL080	5580113	644474	1483	Vein	140	80	High	2.5	1	Ep-Chl	5	Ab	Sodic-calcic	Bethsaida
2015GL080	5580113	644474	1483	Vein	180	80	High	2.5	1	Ep-Chl	5	Ab	Sodic-calcic	Bethsaida
2015GL080	5580116	644476	1483	Vein	75	90	High	10	1	Ep	15	Ilt-Chl-Ep	Propylitic	Bethsaida
2015GL080	5580116	644476	1483	Vein	310	70	High	10	1	Ep	15	Ilt-Chl-Ep	Propylitic	Bethsaida
2015GL080	5580105	644560	1502	Fracture halo	50	60	High	10			20	Ilt-Chl-Ep	Propylitic	Bethsaida
2015GL080	5580105	644568	1502	Fracture halo	50	60	High	10			20	Ilt-Chl-Ep	Propylitic	Bethsaida
2015GL080	5580146	644569	1508	Vein	205	75	High	1.33	1	Ep	10	Chl-Ilt	Propylitic	Bethsaida
2015GL080	5580098	644583	1504	Fracture halo	55	75	High	0.1			10	Chl-Ilt	Propylitic	Bethsaida
2015GL080	5580098	644583	1504	Fracture halo	60	65	High	0.1			500	Chl-Ilt-Ep	Propylitic	Bethsaida
2015GL081	5580198	643590	1508	Fracture halo	305	90	High	0.1				Ilt-Chl	Propylitic	Bethsaida
2015GL081	5580186	643592	1508	Fault breccia	100	80	High		3000			Ilt	Propylitic	Bethsaida
2015GL081	5580071	643660	1508	Fracture halo	30	85	High	3			2	Ilt	Propylitic	Bethsaida
2015GL082	5579397	644228	1467	Fracture halo	335	90	High	2.5			25	Ilt-Chl-Ep	Propylitic	Bethsaida
2015GL082	5579397	644228	1467	Fracture halo	80	85	High	2			25	Ilt-Chl-Ep	Propylitic	Bethsaida
2015GL082	5579362	644242	1465	Fracture halo	35	85	High	10			15	Ilt-Chl	Propylitic	Bethsaida
2015GL082	5579351	644248	1470	Fracture halo	35	85	High	10			15	Ilt-Chl	Propylitic	Bethsaida
2015GL082	5579351	644248	1470	Fracture halo	45	50	High	10			15	Ilt-Chl	Propylitic	Bethsaida
2015GL083	5580329	644419	1489	Fracture halo	210	75	High	5			1	Ilt	Propylitic	QFP
2015GL083	5580350	644427	1486	Fracture halo	230	90	High	5	1	Ilt			Propylitic	QFP
2015GL084	5578202	640831	1416	Fracture halo	60	40	Med	1			10	Ilt-Chl-Ep	Propylitic	Bethsaida
2015GL085	5578788	640829	1455	Vein	260	80	High	1.67	1	Chl-Qz	35	Ilt-Chl-Hem-Ep	Propylitic	Bethsaida

Station ID	Northing (m)	Easting (m)	Elev (m)	Vein type	Strike	Dip	Conf	Density /m	Vein width (mm)	Vein minerals	Selvage width (mm)	Selvage minerals	Alteration	Lithology
2015GL085	5578778	640841	1453	Vein	65	75	High	2	1	Chl-Qz	35	Ilt-Chl-Hem-Ep	Propylitic	Bethsaida
2015GL085	5578681	640890	1453	Vein	75	80	High	0.1	1	Chl-Qz	35	Ilt-Chl-Hem-Ep	Propylitic	Bethsaida
2015GL085	5578769	640900	1460	Vein	75	80	High	2.5	1	Chl-Qz	20	Ilt-Chl-Hem-Ep	Propylitic	Bethsaida
2015GL086	5578794	641804	1501	Vein	355	75	High	0.1	0.5	Ep	10	Ilt-Chl-Ep	Propylitic	Bethsaida
2015GL086	5578806	641810	1501	Vein	355	90	High	0.1	0.5	Ep	10	Ilt-Chl-Ep	Propylitic	Bethsaida
2015GL087	5578417	641869	1489	Fracture halo	105	90	High	8			20	Ilt-Ep-Chl	Propylitic	Bethsaida
2015GL087	5578405	641878	1491	Fracture halo	235	90	High	0.1			1	Ilt	Propylitic	Bethsaida
2015GL087	5578408	641878	1491	Fracture halo	260	85	High	0.1			150	Ilt-Ep-Chl-Py	Propylitic	Bethsaida
2015GL087	5578465	641966	1484	Fault	140	85	High		10000			Ilt	Propylitic	Bethsaida
2015GL087	5578447	641966	1484	Fracture halo	160	70	High	10			10	Ilt	Propylitic	Bethsaida
2015GL087	5578426	641984	1483	Fault	205	85	High		350			Ilt-Chl-Ep	Propylitic	Bethsaida
2015GL088	5577997	642235	1467	Fault	85	70	High		5000			Ilt-Chl	Propylitic	Bethsaida
2015GL088	5577968	642244	1455	Vein	280	85	High	2	3	Chl-Ab	50	Chl-Ep-Ilt	Sodic-calcic	Bethsaida
2015GL088	5577983	642247	1460	Vein	280	85	High	2	3	Chl-Ab	50	Chl-Ep-Ilt	Sodic-calcic	Bethsaida
2015GL088	5578063	642255	1488	Vein	225	80	High	2.5	1	Ep	20	Chl-Ep-Ilt	Propylitic	Bethsaida
2015GL089	5578162	642350	1489	Fracture halo	50	80	High	7			10	Ilt	Propylitic	Aplite
2015GL090	5578699	642353	1524	Fracture halo	72	90	High	1.25			10	Ilt-Chl-Ep	Propylitic	Bethsaida
2015GL090	5578699	642364	1524	Fracture halo	72	90	High	1.25			10	Ilt-Chl-Ep	Propylitic	Bethsaida
2015GL091	5585188	639820	1577	Vein	185	90	High	15	2	Ep	35	Chl-Ab-Ep-Ilt	Sodic-calcic	Bethsaida
2015GL091	5585188	639820	1577	Vein	355	62	High	15	2	Ep	35	Chl-Ab-Ep-Ilt	Sodic-calcic	Bethsaida
2015GL091	5585188	639820	1577	Vein	10	90	High	10	1	Chl-Qz	50	Chl-Ab-Ep-Ilt	Sodic-calcic	Bethsaida
2015GL092	5584947	639834	1584	Vein	20	50	High	15	3	Chl-Qz		Ab-Chl-Ep	Sodic-calcic	Bethsaida
2015GL092	5584947	639834	1584	Vein	40	60	High	15	3	Chl-Qz		Ab-Chl-Ep	Sodic-calcic	Bethsaida
2015GL092	5584892	639877	1574	Vein	170	45	High	5	10	Chl-Qz		Ab-Chl-Ep	Sodic-calcic	Bethsaida
2015GL092	5584892	639877	1574	Vein	30	90	High	5	1	Ep-Chl		Ab-Chl-Ep	Sodic-calcic	Bethsaida
2015GL092	5584892	639877	1574	Vein	175	40	High	5	1	Ep-Chl		Ab-Chl-Ep	Sodic-calcic	Bethsaida
2015GL092	5584892	639877	1574	Vein	175	50	High	5	1	Ep-Chl		Ab-Chl-Ep	Sodic-calcic	Bethsaida
2015GL092	5584880	639879	1574	Vein	15	60	High	20	1	Ep		Ab-Chl-Ep	Sodic-calcic	Bethsaida
2015GL093	5594404	637327	1429	Vein	210	35	High	0.1	10	Qz-Ms			Muscovite	Bethsaida
2015GL093	5594414	637238	1429	Vein	347	90	High	3	1	Ms-Ccp-Mlc			Muscovite	Bethsaida
2015GL093	5594416	637224	1429	Vein	347	90	High	3	1	Ms-Ccp-Mlc			Muscovite	Bethsaida
2015GL094	5594689	636426	1427	Vein	155	70	High	0.1	10	Qz-Ser			Propylitic	QFP
2015GL094	5594685	636427	1427	Fracture halo	180	55	High	0.1			200	Ser	Propylitic	QFP
2015GL094	5594685	636427	1427	Fracture halo	235	70	High	20	0.5	Lm	5	Ser	Propylitic	QFP
2015GL094	5594668	636412	1427	Fault	90	90	High		3000	Hem		Ser	Propylitic	QFP
2015GL094	5594649	636396	1427	Fault	175	70	High		1000	Hem		Ser	Propylitic	QFP
2015GLLornex	5589594	639915	1438	Vein	150	90	High	4	0.5	Ccp-Py-Chl			Propylitic	
2015GLLornex	5589592	639909	1438	Vein	345	50	High	2	4	Qz-Mol			Muscovite	
2015GLLornex	5589588	639898	1438	Vein	45	65	High	0.1	20	Qz-Py			Muscovite	
2015GLLornex	5589575	639870	1438	Vein	165	90	High	5	4	Qz-Ccp-Py-Mol			Muscovite	
2015GLLornex	5589573	639866	1438	Vein	215	85	High	0.1	0.5	Mol-Ccp-Py			Muscovite	
2015GLLornex	5589551	639804	1417	Vein	165	90	High	0.1	1	Ms-Py			Muscovite	
2015GLLornex	5589553	639808	1417	Vein	125	70	Med	2	0.5	Chl			Propylitic	
2015GLLornex	5589541	639779	1417	Vein	180	90	High	10	2	Qz-Py			Muscovite	
2015GLLornex	5589534	639767	1417	Vein	170	85	High	0.1	20	Qz-Mol			Muscovite	

Station ID	Northing (m)	Easting (m)	Elev (m)	Vein type	Strike	Dip	Conf	Density /m	Vein width (mm)	Vein minerals	Selvage width (mm)	Selvage minerals	Alteration	Lithology
2015GLLornex	5589522	639731	1417	Vein	170	85	Low	0.1	0.5	Qz	2	Kfs	K-feldspar	
2015GLLornex	5589512	639679	1417	Vein	125	65	High	1	10	Qz-Mol-Py			Muscovite	
2015GLLornex	5589513	639681	1417	Fracture halo	125	70	High	0.1				Kfs	K-feldspar	
2015GLLornex	5589517	639693	1417	Vein	125	70	High	0.1	0.5	Qz-Ccp	2	Ms	Muscovite	
2015GLLornex	5589594	639915	1438	Fracture halo	90	75	High	5			2	Ab	Sodic-calcic	
2015GLLornex	5589482	639547	1417	Vein	135	65	High	7	5	Qz-Py-Ccp-Mol	5	Ms	Muscovite	
2015GLLornex	5589501	639501	1434	Vein	110	50	High	0.1	25	Qz-Py-Ccp-Mol	10	Ms	Muscovite	
2015GLLornex	5589640	640036	1438	Vein	30	50	High	0.67	10	Qz-Py			Muscovite	
2015GLLornex	5589600	639929	1438	Vein	160	90	High	10	1	Qz-Ccp-Mol			Muscovite	
2015GLLornex	5589618	639983	1438	Vein	120	85	High	10	3	Qz-Py-Ccp-Mol			Muscovite	
2015GLLornex	5589621	639987	1438	Vein	20	60	High	0.4	10	Qz-Mol			Muscovite	
2015GLLornex	5589635	640020	1438	Vein	120	75	High	5	4	Qz-Py-Ccp-Mol	5	Ms	Muscovite	
2015GLLornex	5589872	640169	1470	Vein	130	85	High	2	2	Hem-Chl			Propylitic	
2015GLLornex	5589667	640056	1438	Vein	45	55	High	4	20	Qz-Ep-Chl-Hem			Propylitic	
2015GLLornex	5589697	640080	1438	Vein	125	70	High	10	5	Qz-Ccp-Py-Mol	10	Ms	Muscovite	
2015GLLornex	5589623	639992	1438	Vein	125	85	High	3	1	Chl-Py-Ccp			Propylitic	
2015GLLornex	5589610	639956	1438	Vein	175	75	High	12	0.5	Ccp-Py	1	Ms	Muscovite	
2015GLLornex	5589912	638938	1434	Fault	245	65	High		1500	Hem-Chl			Propylitic	
2015GLLornex	5589826	638992	1434	Fault breccia	175	60	High		3000	Hem		Ilt	Propylitic	
2015GLLornex	5589796	639017	1434	Fault breccia	190	70	High		500		1000	Ilt	Propylitic	
2015GLLornex	5589745	639057	1434	Fault breccia	185	45	High		4000	Hem		Ilt	Propylitic	
2015GLLornex	5589705	639086	1434	Fault gouge	220	80	High		400	Hem		Ilt-Ms	Muscovite	
2015GLLornex	5589698	639091	1434	Fault breccia	180	45	High		5000	Hem		Ilt	Propylitic	
2015GLLornex	5589629	639128	1434	Fault breccia	195	75	High		400	Hem		Ilt	Propylitic	
2015GLLornex	5589564	639170	1434	Fault breccia	160	50	High		400	Hem		Ilt	Propylitic	
2015GLLornex	5589586	639149	1434	Fault	215	60	High		300	Hem		Ilt	Propylitic	
2015GLLornex	5589567	639167	1434	Fault	210	75	High		1000			Ilt	Propylitic	
2015GLLornex	5589644	639121	1434	Fault gouge	190	65	High		2000	Hem		Ilt	Propylitic	
2015GLLornex	5589702	639089	1434	Fault gouge	220	80	High		400	Hem		Ilt-Ms	Muscovite	
2015GLLornex	5589954	638880	1434	Vein	315	75	High	5	0.5	Chl-Ep	30	Chl-Ep-Ilt	Propylitic	
2015GLLornex	5589954	638880	1434	Fracture halo	225	88	High	10			15	Chl-Ep-Ilt	Propylitic	
2015GLLornex	5589937	638904	1434	Vein	110	85	High	1	2	Ep	70	Chl-Ab-Ilt	Sodic-calcic	
2015GLLornex	5589907	638936	1434	Fault	245	65	High		1500	Chl-Hem			Propylitic	
2015GLLornex	5589851	638975	1434	Vein	50	70	High	0.1	5	Qz-Ep	35	Ab	Sodic-calcic	
2015GLLornex	5589853	638977	1434	Vein	330	70	High	20	1	Ep	5	Ab	Sodic-calcic	
2015GLLornex	5589836	638987	1434	Vein	295	75	High	2	1	Chl	40	Ab-Chl-Ilt-Ep	Sodic-calcic	
2015GLLornex	5589828	638991	1434	Vein	340	75	High	0.1	0.5	Ep-Chl			Propylitic	
2015GLLornex	5589790	639014	1434	Fault breccia	190	70	High		500		2000	Hem-Ilt	Propylitic	
2015GLLornex	5589791	639015	1434	Vein	225	80	High	3	0.5	Chl-Ilt-Hem			Propylitic	
2015GLLornex	5589791	639015	1434	Vein	160	70	High	3	2	Ep-Chl	45	Ab-Chl-Ilt-Ep	Sodic-calcic	
2015GLLornex	5589791	639015	1434	Vein	240	90	High	0.1	0.5	Ep	45	Ab-Chl-Ilt	Sodic-calcic	
2015GLLornex	5589768	639040	1434	Vein	295	85	High	5	2	Ab-Chl	45	Ab-Chl-Ilt-Ep	Sodic-calcic	
2015GLLornex	5589737	639062	1434	Vein	125	70	High	5	1	Chl	35	Ab-Chl-Ilt-Ep	Sodic-calcic	
2015GLLornex	5589737	639062	1434	Vein	165	65	High	5	1	Chl	35	Ab-Chl-Ilt-Ep	Sodic-calcic	
2015GLLornex	5589737	639062	1434	Fault	185	45	High		4000	Hem	100	Ilt	Propylitic	

Station ID	Northing (m)	Easting (m)	Elev (m)	Vein type	Strike	Dip	Conf	Density /m	Vein width (mm)	Vein minerals	Selvage width (mm)	Selvage minerals	Alteration	Lithology
2015GLLornex	5589705	639078	1434	Vein	275	75	High	20	2	Kfs			K-feldspar	
2015GLLornex	5589643	639119	1434	Vein	140	85	High	20	0.5	Ep-Chl			Propylitic	
2015GLLornex	5589642	639121	1434	Vein	75	80	High	25	0.5	Chl			Propylitic	
2015GLLornex	5589642	639123	1434	Fracture halo	180	65	High	0.1				Ilt	Propylitic	
2015GLLornex	5589629	639125	1434	Vein	285	70	High	4	1	Chl	35	Ab-Chl-Ilt-Ep	Sodic-calcic	
2015GLLornex	5589603	639144	1434	Vein	270	75	High	0.1	0.5	Chl	15	Ab-Chl-Ilt	Sodic-calcic	
2015GLLornex	5589603	639144	1434	Fracture halo	210	85	High	5			2.5	Hem-Kfs	K-feldspar	
2015GLLornex	5589603	639144	1434	Vein	300	60	High	1	5	Chl-Ab	60	Ab-Ilt-Ep-Chl	Sodic-calcic	
2015GLLornex	5589513	639218	1434	Vein	95	75	High	5	2	Ab-Chl	40	Ab-Chl-Ep-Ilt	Sodic-calcic	
2015GLLornex	5589508	639316	1434	Vein	270	55	High	4	30	Qz-Ccp	10	Ms	Muscovite	
2015GLLornex	5589508	639316	1434	Vein	335	85	High	2	10	Qz-Mol-Ccp			Muscovite	
2015GLLornex	5589507	639354	1434	Vein	250	50	High	0.67	50	Qz-Mol			Muscovite	
2015GLLornex	5589514	639424	1434	Vein	135	65	High	2.5	20	Qz-Mol-Ccp			Muscovite	
2015GLLornex	5589514	639424	1434	Vein	135	65	High	0.1	0.5	Ccp	5	Ms	Muscovite	
2015GLLornex	5589507	639492	1434	Vein	125	50	High	0.1	40	Qz-Mol-Ccp-Tur			Muscovite	
2015GLLornex	5589507	639492	1434	Vein	110	65	High	0.1	2	Qz-Ccp-Py	3	Ms	Muscovite	
2015GLLornex	5589507	639492	1434	Vein	125	50	High	0.1	8	Qz-Mol			Muscovite	
2015GLLornex	5589502	639510	1434	Vein	140	80	High	5	2	Qz-Py-Ccp	5	Ms	Muscovite	
2015GLLornex	5589490	639531	1417	Vein	110	45	High	0.5	100	Qz-Mol-Ccp			Muscovite	
2015GLLornex	5589489	639538	1417	Vein	140	80	High	7	0.5	Py	1	Ms	Muscovite	
2015GLLornex	5589490	639544	1417	Vein	90	55	High	10	0.5	Py	1	Ms	Muscovite	
2015GLLornex	5589490	639547	1417	Vein	135	70	High	5	0.5	Qz-Py	10	Kfs	K-feldspar	
2015GLLornex	5589492	639565	1417	Vein	135	75	High	15	1	Qz-Py-Ccp	2	Ms	Muscovite	
2015GLLornex	5589492	639565	1417	Vein	170	85	High	5	3	Kfs			K-feldspar	
2015GLLornex	5589492	639573	1417	Vein	85	35	High	2	50	Qz-Mol-Ccp			Muscovite	
2015GLLornex	5589501	639642	1417	Vein	90	65	High	0.1	4	Qz	20	Kfs	K-feldspar	
2015GLLornex	5589564	639837	1438	Vein	35	60	High	0.1	40	Qz-Mol-Ccp			Muscovite	
2015GLValley	5594022	637686	1265	Vein	290	45	High	0.1	100	Qz-Mol			Muscovite	
2015GLValley	5594028	637687	1265	Vein	90	43	High	2	10	Qz-Ccp-Py	2	Ms	Muscovite	
2015GLValley	5594028	637687	1265	Vein	240	70	High	0.7	0.1	Ccp-Py	2	Ms	Muscovite	
2015GLValley	5594018	637688	1265	Fault	290	45	High		1000			Cly-Ser	Propylitic	
2015GLValley	5594018	637688	1265	Vein	290	45	High	0.1	100	Qz-Mol			Muscovite	
2015GLValley	5593965	637690	1265	Fault	295	35	High		2000			Ser-Kln	Propylitic	
2015GLValley	5593965	637690	1265	Vein	295	35	High	0.1	300	Qz-Mol-Ccp-Py			Muscovite	
2015GLValley	5593958	637694	1265	Vein	110	45	High	0.1	150	Qz-Ccp-Mol			Muscovite	
2015GLValley	5593958	637694	1265	Fault	110	45	High		100		500	Ser-Ms	Muscovite	
2015GLValley	5593958	637694	1265	Vein	110	45	High	3	5	Qz-Ccp	10	Ms	Muscovite	
2015GLValley	5593977	637696	1265	Vein	240	65	High	3	2	Qz-Ccp	5	Ms	Muscovite	
2015GLValley	5593977	637696	1265	Vein	130	65	High	3	10	Qz-Ccp-Ms	5	Kfs-Ms	Muscovite	
2015GLValley	5594042	637700	1265	Vein	325	85	High	0.1	100	Qz-Mol	30	Ms-Py	Muscovite	
2015GLValley	5593903	637706	1265	Vein	315	60	High	0.1	10	Qz-Mol	5	Ms	Muscovite	
2015GLValley	5594066	637737	1265	Fault breccia	305	45	High		1000	Mol		Ser	Muscovite	
2015GLValley	5593874	637750	1265	Vein	295	20	High	2	5	Qz-Py-Ccp	60	Ser-Ms	Muscovite	
2015GLValley	5593874	637750	1265	Vein	320	30	High	2	5	Qz-Py-Ccp	60	Ser-Ms	Muscovite	
2015GLValley	5593874	637750	1265	Fracture halo	155	85	High	15		Qz-Ccp	2	Kfs-Ms	Muscovite	

Station ID	Northing (m)	Easting (m)	Elev (m)	Vein type	Strike	Dip	Conf	Density /m	Vein width (mm)	Vein minerals	Selvage width (mm)	Selvage minerals	Alteration	Lithology
2015GLValley	5594055	637753	1265	Vein	350	75	High	0.1	100	Qz-Mol			Muscovite	
2015GLValley	5594063	637765	1265	Vein	215	75	High	2	1	Qz-Ccp-Py	2	Ms	Muscovite	
2015GLValley	5594063	637765	1265	Vein	105	70	High	3	1	Qz-Ccp-Py	2.5	Ms	Muscovite	
2015GLValley	5594063	637765	1265	Vein	290	40	High	0.5	30	Qz-Mol-Ccp	5	Ms-Ser	Muscovite	
2015GLValley	5593885	637782	1265	Vein	310	30	High	0.1	40	Qz-Mol-Py			Muscovite	
2015GLValley	5593885	637782	1265	Vein	345	80	High	0.1	80	Qz-Mol-Ccp			Muscovite	
2015GLValley	5593888	637789	1265	Vein	100	50	High	0.2	30	Qz-Mol			Muscovite	
2015GLValley	5594068	637789	1265	Fault	160	85	High		1500			Ms-Kln	Muscovite	
2015GLValley	5594068	637832	1265	Fault	340	80	High		150			Ser	Propylitic	
2015GLValley	5594069	637840	1265	Vein	125	90	High	0.1	30	Qz-Mol-Ccp			Muscovite	
2015GLValley	5594069	637840	1265	Vein	205	80	High	5	0.1	Py	15	Ser	Muscovite	
2015GLValley	5594069	637840	1265	Vein	305	35	High	0.1	10	Qz-Mol-Py-Ccp			Muscovite	
2015GLValley	5594069	637840	1265	Vein	140	90	High	8	2	Qz-Ccp-Mol	10	Ms	Muscovite	
2015GLValley	5593904	637889	1265	Fracture halo	45	60	High	20			4	Kfs	K-feldspar	
2015GLValley	5593904	637889	1265	Vein	130	80	High	10	10	Qz-Ccp-Bn	25		Muscovite	
2015GLValley	5593923	637952	1265	Vein	150	90	High	20	2	Qz-Ccp	3	Kfs-Ms	Muscovite	
2015GLValley	5593930	637985	1265	Vein	65	50	High	0.1	50	Qz-Py-Ccp	150	Ms-Ser	Muscovite	
2015GLValley	5593930	637985	1265	Vein	70	40	High	30	1	Qz-Ccp	2	Kfs	K-feldspar	
2015GLValley	5593925	637989	1265	Vein	65	45	High	10	0.1	Ccp	2	Kfs	K-feldspar	
2015GLValley	5593936	637994	1265	Fracture halo	120	85	High	10			0.5	Ms	Muscovite	
2015GLValley	5593936	638042	1265	Vein	315	45	High	0.1	20	Qz-Mol			Muscovite	
2015GLValley	5593936	638042	1265	Vein	25	60	High	5	10	Qz-Py-Ccp	30	Ms	Muscovite	
2015GLValley	5593936	638059	1265	Vein	325	52	High	0.1	5	Qz-Mol			Muscovite	
2015GLValley	5593936	638059	1265	Fracture halo	330	85	High	50			1	Ms	Muscovite	
2015GLValley	5593936	638059	1265	Vein	90	55	High	5	10	Qz	3	Kfs	K-feldspar	
2015GLValley	5593947	638098	1265	Vein	25	80	High	0.1	0.1	Ccp-Py	20	Ser	Muscovite	
2015GLValley	5593947	638102	1265	Vein	310	50	High	5	30	Qz-Mol-Ccp			Muscovite	
2015GLValley	5593947	638102	1265	Vein	65	45	High	20	10	Qz	3	Kfs	K-feldspar	
2015GLValley	5593947	638102	1265	Vein	115	80	High	1	10	Qz-Ccp-Hem			Muscovite	
2015GLValley	5593947	638103	1265	Vein	50	40	High	0.1	5	Qz	1	Kfs	K-feldspar	
2015GLValley	5593954	638110	1265	Vein	150	65	High	0.33	15	Qz-Ccp-Bn			Muscovite	
2015GLValley	5593954	638110	1265	Vein	105	45	High	0.1	0.1	Ccp	2	Kfs	K-feldspar	
2015GLValley	5593945	638137	1265	Fault	55	35	High		1000			Ser	Propylitic	
2015GLValley	5593933	638162	1265	Vein	305	65	High	0.1	5	Qz-Ccp-Bn			Muscovite	
2015GLValley	5593933	638162	1265	Vein	140	70	High	2	5	Qz-Ccp-Bn			Muscovite	
2015GLValley	5593939	638202	1250	Vein	65	40	High	5	3	Qz-Ccp-Mol	5	Kfs	Muscovite	
2015GLValley	5593939	638202	1250	Vein	160	70	High	5	2	Qz-Ccp-Bn			Muscovite	
2015GLValley	5593939	638202	1250	Vein	330	75	High	0.1	20	Qz-Ms	5		Muscovite	
2015GLValley	5593934	638208	1250	Vein	240	30	High	2	5	Qz-Bn-Ccp			Muscovite	
2015GLValley	5593934	638208	1250	Fracture halo	330	75	High	10			0.5	Ms	Muscovite	
2015GLValley	5593920	638217	1250	Vein	330	70	High	10	4	Qz-Bn-Ccp-Ms			Muscovite	
2015GLValley	5593920	638217	1250	Vein	215	25	High	0.1	20	Qz-Bn-Ccp			Muscovite	
2015GLValley	5593917	638219	1250	Vein	240	60	High	20	1	Qz-Bn-Ccp			Muscovite	
2015GLValley	5593906	638236	1250	Fault	220	85	High		200			Ser	Propylitic	
2015GLValley	5593905	638243	1250	Vein	250	60	High	2	10	Qz-Bn-Ccp			Muscovite	

Station ID	Northing (m)	Easting (m)	Elev (m)	Vein type	Strike	Dip	Conf	Density /m	Vein width (mm)	Vein minerals	Selvage width (mm)	Selvage minerals	Alteration	Lithology
2015GLValley	5593883	638268	1250	Vein	315	75	High	0.1	30	Qz-Ccp-Bn-Tur	5	Kfs	K-feldspar	
2015GLValley	5593883	638268	1250	Vein	185	35	High	0.1	5	Qz-Bn-Ccp			Muscovite	
2015GLValley	5593883	638268	1250	Fracture halo	55	45	High	2.5			5	Kfs	K-feldspar	
2015GLValley	5593883	638268	1250	Fracture halo	200	45	High	2.5			5	Kfs	K-feldspar	
2015GLValley	5593883	638268	1250	Vein	60	40	High	3	10	Qz-Ccp-Mol	4	Ms-Ser	Muscovite	
2015GLValley	5593882	638270	1250	Vein	30	40	High	0.1		Qz-Mol-Ccp			Muscovite	
2015GLValley	5593862	638281	1250	Vein	245	70	High	0.1	10	Qz-Ccp	5	Kfs	K-feldspar	
2015GLValley	5593855	638300	1250	Fracture halo	65	45	High	3			2	Kfs	K-feldspar	
2015GLValley	5593855	638300	1250	Vein	215	75	High	0.1	5	Qz-Bn-Ccp			Muscovite	
2015GLValley	5593855	638300	1250	Fracture halo	95	50	High	6			15	Ser-Ms	Muscovite	
2015GLValley	5593814	638337	1250	Vein	225	20	High	0.1	100	Qz-Bn-Ccp	20	Hem-Ccp	Muscovite	
2015GLValley	5593813	638340	1250	Vein	85	45	High	2	5	Qz-Mol			Muscovite	
2015GLValley	5593813	638340	1250	Vein	240	60	High	0.1	5	Qz-Bn-Ccp			Muscovite	
2015GLValley	5593803	638352	1250	Fracture halo	55	35	High	30			2.5	Kfs	K-feldspar	
2015GLValley	5593797	638356	1250	Vein	210	35	High	0.1	10	Qz-Bn-Ccp			Muscovite	
2015GLValley	5593789	638373	1250	Vein	55	30	High	2	10	Qz-Py-Mol-Ccp			Muscovite	
2015GLValley	5593756	638405	1250	Vein	185	90	High	0.1	5	Qz-Mol-Ccp			Muscovite	
2015GLValley	5593746	638411	1250	Vein	135	80	High	16.67	0.1	Bt-Ccp			K-feldspar	
2015GLValley	5593746	638411	1250	Fracture halo	35	60	High	30			2	Kfs	K-feldspar	
2015GLValley	5593741	638419	1250	Vein	65	65	High	3.3	40	Qz-Mol-Py-Ccp			Muscovite	
2015GLValley	5593738	638426	1250	Vein	50	85	High	0.5	15	Qz	5	Kfs	K-feldspar	
2015GLValley	5593738	638426	1250	Fracture halo	0	55	High	10		Ccp	2	Kfs	K-feldspar	
2015GLValley	5593737	638429	1250	Vein	45	60	High	0.1	10	Qz-Mol-Py			Muscovite	
2015GLValley	5593703	638456	1250	Vein	35	65	High	0.75	25	Qz	3	Kfs	K-feldspar	
2015GLValley	5593703	638456	1250	Fracture halo	5	70	High	20			4	Kfs	K-feldspar	
2015GLValley	5593703	638456	1250	Fracture halo	320	90	High	20			4	Kfs	K-feldspar	
2015GLValley	5593705	638466	1250	Vein	95	45	High	1	10	Qz-Mol-Py-Ccp			Muscovite	
2015GLValley	5593705	638466	1250	Vein	55	35	High	0.1	0.75	Qz-Py	2	Kfs	K-feldspar	
2015GLValley	5593694	638480	1250	Vein	85	55	High	0.1	100	Qz-Mol-Ccp			Muscovite	
2015GLValley	5593689	638488	1250	Vein	265	75	High	0.1	20	Qz-Bn-Ccp			Muscovite	
2015GLValley	5593689	638488	1250	Vein	45	45	High	0.5	10	Qz-Mol			Muscovite	
2015GLValley	5593681	638495	1250	Vein	65	45	High	0.1	25	Qz-Mol-Ccp			Muscovite	
2015GLValley	5593670	638501	1250	Fracture halo	245	50	High	0.1			2	Kfs	K-feldspar	
2015GLValley	5593673	638518	1250	Vein	60	50	High	0.1	70	Qz-Mol-Ccp	50	Ms-Ser	Muscovite	
2015KB001	5595250	643185	1527	Vein	10	60	High	13	1	Qz	10	Ab-Chl	Sodic-calcic	Bethlehem
2015KB001	5595250	643185	1527	Vein	60	50	High	1	3	Ep-Qz	10	Ab-Chl	Sodic-calcic	Bethlehem
2015KB002	5596333	643455	1548	Veinlet	38	85	High	15	1	Chl-Ep-CuOx	10	Ep-Chl-Ser	Propylitic	Guichon
2015KB003	5596343	643443	1550	Veinlet	62	85	High	3	1	Chl-Ep	20	Ep-Chl-Ser	Propylitic	Guichon
2015KB004	5596353	643372	1538	Veinlet	50	90	High	1.5	1	Chl-Ep	10	Chl-Ep-Ser	Propylitic	Guichon
2015KB005	5596264	643767	1568	Vein	10	85	High	1	2	Ep-Qz-Chl	10	Chl-Ser	Propylitic	Guichon
2015KB006	5596300	643752	1572	Veinlet	252	85	High	3	1	Ep-Ser	10	Chl-Ser	Propylitic	Guichon
2015KB007	5596549	643456	1559	Veinlet	70	70	High	1	2	Ep-Chl	20	Chl	Propylitic	Guichon
2015KB008	5596700	643564	1549	Fracture coating	20	80	High	0.5	0.5	Ep-Chl-Ccp-Lm	20	Chl-Ep	Propylitic	Guichon
2015KB010	5597068	643771	1531	Veinlet	108	85	High	0.5	1	Ep	20	Chl	Propylitic	Guichon
2015KB012	5597139	643722	1538	Vein	16	70	High	1	1	Ep-Chl	10	Chl-Ep	Propylitic	Guichon

Station ID	Northing (m)	Easting (m)	Elev (m)	Vein type	Strike	Dip	Conf	Density /m	Vein width (mm)	Vein minerals	Selvage width (mm)	Selvage minerals	Alteration	Lithology
2015KB012	5597139	643722	1538	Vein	82	80	High	1	1	Ep-Chl	10	Chl-Ep	Propylitic	Guichon
2015KB013	5597329	643764	1525	Veinlet	72	70	High	0.5	0.1	Ep	10	Chl-Ep	Propylitic	Guichon
2015KB014	5597266	643665	1500	Veinlet	26	80	High	0.5	0.1	Ep-Chl	10	Chl-Ep	Propylitic	Guichon
2015KB014	5597266	643665	1500	Veinlet	160	85	High	0.1	0.2	Kfs	0		K-feldspar	Guichon
2015KB015	5594187	643579	1509	Veinlet	82	91	High	0.25	1	Ep-Chl	5	Ab	Sodic-calcic	Guichon
2015KB016	5596768	644014	1533	Veinlet	222	78	Med	0.1	1	Chl-Ep	10	Chl	Propylitic	Guichon
2015KB017	5596974	644114	1529	Veinlet	82	85	High	0.2	1	Ep-Chl	5	Chl-Ser	Propylitic	Guichon
2015KB018	5597109	644176	1530	Veinlet	282	80	High	4	1	Ep-Chl	5	Chl	Propylitic	Guichon
2015KB020	5596603	644165	1510	Veinlet	192	90	High	0.1	1	Ep-Chl	5	Ep-Chl	Propylitic	Guichon
2015KB020	5596603	644165	1510	Fracture halo	205	80	Med	0.1	0		5	Ser	Propylitic	Guichon
2015KB021	5596600	644049	1551	Veinlet	205	90	High	0.05	1	Ep-Chl	5	Chl	Propylitic	Guichon
2015KB022	5596401	644002	1564	Veinlet	68	82	High	0.3	1	Ep-Chl	0		Propylitic	Guichon
2015KB022	5596401	644002	1564	Veinlet	12	80	High	0.3	1	Chl-Ep	0		Propylitic	Guichon
2015KB022	5596401	644002	1564	Veinlet	74	88	High	0.3	1	Ep-Chl	0		Propylitic	Guichon
2015KB022	5596401	644002	1564	Veinlet	18	90	High	0.3	1	Chl-Ep	0		Propylitic	Guichon
2015KB023	5596387	643968	1539	Veinlet	24	88	High	0.4	1	Ep-Chl	5	Chl	Propylitic	Guichon
2015KB024	5596645	644408	1482	Veinlet	65	84	High	0.1	2	Ep	5	Chl	Propylitic	Guichon
2015KB024	5596645	644408	1482	Veinlet	47	86	High	0.1	2	Ep	5	Chl	Propylitic	Guichon
2015KB025	5596475	644330	1510	Veinlet	146	85	High	0.05	0.5	Ep	0		Propylitic	Guichon
2015KB026	5597208	644427	1326	Fracture coating	62	80	High	2	1		5	Chl-Ser	Propylitic	Guichon
2015KB027	5597569	644312	1297	Veinlet	163	80	High	2	1	Ep	5	Ab-Chl	Sodic-calcic	Guichon
2015KB027	5597569	644312	1297	Veinlet	47	82	High	3	1	Ep	0		Propylitic	Guichon
2015KB029	5597298	645047	1301	Veinlet	85	84	High	0.75	1	Ep-Chl	5	Chl	Propylitic	Guichon
2015KB029	5597298	645047	1301	Veinlet	340	85	High	0.05	1	Ep-Chl	5	Chl	Propylitic	Guichon
2015KB031	5596851	645094	1308	Fracture coating	16	52	High	0.3	1	Ep	0		Propylitic	Guichon
2015KB033	5596261	644468	1522	Veinlet	42	88	High	0.3	1	Ser-Chl	5	Ser	Propylitic	Guichon
2015KB033	5596261	644468	1522	Veinlet	62	90	High	0.3	1	Ser-Chl	5	Ser	Propylitic	Guichon
2015KB033	5596261	644468	1522	Veinlet	48	84	High	0.2	1	Ep	0		Propylitic	Guichon
2015KB034	5595912	644521	1517	Veinlet	277	85	Med	0.2	1	Ser-Chl	5	Ser	Propylitic	Guichon
2015KB034	5595912	644521	1517	Veinlet	2	86	Med	0.1	0.5	Ep-Chl	2.5	Ser	Propylitic	Guichon
2015KB035	5595693	644496	1541	Fracture halo	92	90	High	0.1	0	Ep	0		Propylitic	Guichon
2015KB036	5595570	644540	1536	Vein	109	82	High	0.2	10	Ep-Hem	10	Ser-Chl	Propylitic	Guichon
2015KB037	5595478	644707	1508	Veinlet	145	61	Med	0.5	1	Ep-Ccp-Lm	5	Chl	Propylitic	Guichon
2015KB038	5595936	643751	1581	Vein	58	78	High	3	10	Ep-Qz-Chl	20		Propylitic	Guichon
2015KB038	5595936	643751	1581	Veinlet	62	72	High	3	2	Ep-Chl			Propylitic	Guichon
2015KB038	5595936	643751	1581	Veinlet	80	81	High	3	2	Ep-Chl			Propylitic	Guichon
2015KB038	5595936	643751	1581	Veinlet	21	82	High	4	1	Tur-Ep			Propylitic	Guichon
2015KB038	5595936	643751	1581	Veinlet	16	80	High	4	1	Tur-Ep-Ccp			Propylitic	Guichon
2015KB040	5595801	643721	1563	Veinlet	61	80	High	1	1	Ep	0		Propylitic	FPM
2015KB041	5595660	643873	1550	Fracture coating	80	61	High	0.5	2	Ep-Chl	5	Chl-Ep	Propylitic	Guichon
2015KB041	5595660	643873	1550	Fracture coating	93	84	High	0.2	10		10	Ser-Chl-Ep	Propylitic	Guichon
2015KB041	5595660	643873	1550	Fracture coating	351	82	High	0.2	10	Lm-CuOx	10	Ser-Chl-Ep	Propylitic	Guichon
2015KB042	5595659	643995	1542	Vein	4	75	High	1	10	Ep-Qz	20	Chl-Ep	Propylitic	Guichon
2015KB042	5595659	643995	1542	Vein	90	85	High	1	10	Ep-Qz	20	Ser-Chl	Propylitic	Guichon
2015KB042	5595659	643995	1542	Vein	43	74	High	0.5	20	Chl-Ser	30		Propylitic	Guichon

Station ID	Northing (m)	Easting (m)	Elev (m)	Vein type	Strike	Dip	Conf	Density /m	Vein width (mm)	Vein minerals	Selvage width (mm)	Selvage minerals	Alteration	Lithology
2015KB043A	5595408	643997	1546	Vein	44	82	High	0.5	15	Ep-Qz		Chl	Propylitic	Guichon
2015KB043A	5595408	643997	1546	Vein	74	80	High	10	200	Ep-Spec-Ccp	200	Ser-Chl	Muscovite	Guichon
2015KB043B	5595416	644029	1541	Vein	111	79	High	10	20	Ep	20	Ab-Act	Sodic-calcic	Guichon
2015KB044	5595617	644175	1531	Vein	81	56	High	2.5	10	Ep-Qz-Chl	20	Chl-Ep	Propylitic	Guichon
2015KB044	5595617	644175	1531	Vein	61	63	High	2.5	10	Ep-Qz-Chl	20	Chl-Ep	Propylitic	Guichon
2015KB045	5595878	644177	1536	Vein	39	74	High	1.5	10	Ep-Chl	25	Chl-Ser-Ep	Propylitic	Guichon
2015KB045	5595878	644177	1536	Vein	71	80	High	1.5	10	Ep-Chl	25	Chl-Ser	Propylitic	Guichon
2015KB046	5596132	644282	1536	Veinlet	59	75	Med	0.75	2	Ep-Qz	10	Chl-Ser	Propylitic	Guichon
2015KB046	5596132	644282	1536	Veinlet	110	80	Med	0.75	2	Ep-Qz	10	Chl-Ser	Propylitic	Guichon
2015KB047	5597401	643621	1490	Vein	170	62	High	6	2	Tur-Qz-Ccp	20	Chl-Ser	Muscovite	Guichon
2015KB047	5597401	643621	1490	Fracture coating	52	75	High	2	0.5	Chl-Ep	10	Ser-Chl	Propylitic	Guichon
2015KB047	5597401	643621	1490	Fracture coating	120	30	High	2	0.5	Chl-Ep	10		Propylitic	Guichon
2015KB048	5597559	644140	1469	Fracture halo	280	75	Low	0.1	5		5	Ser-Chl	Propylitic	Guichon
2015KB049	5597385	644140	1506	Veinlet	63	85	Med	0.5	1.5	Ep	5	Ep-Chl	Propylitic	Guichon
2015KB049	5597385	644140	1506	Fracture coating	29	81	Med	0.75	0.5	Ep-Chl-Py	10	Chl-Ser-Ep	Muscovite	Guichon
2015KB049	5597385	644140	1506	Fracture coating	57	70	Med	0.75	0.5	Ep-Chl-Py	10	Chl-Ser-Ep	Muscovite	Guichon
2015KB050	5598618	643276	1500	Veinlet	132	20	Med	0.75	1	Ep	0		Propylitic	Bethlehem
2015KB050	5598618	643276	1500	Veinlet	11	70	Med	0.75	1	Ep	0		Propylitic	Bethlehem
2015KB051	5599517	642804	1502	Fracture coating	351	82	Med	0.2	0.5	Ep-Chl	5	Chl	Propylitic	Guichon
2015KB051	5599517	642804	1502	Fracture coating	243	80	Med	0.2	0.5	Ep-Chl	5	Chl	Propylitic	Guichon
2015KB051	5599517	642804	1502	Veinlet	325	90	Med	3	1	Chl-Ep	10	Chl-Ep	Propylitic	Guichon
2015KB053	5599491	643245	1488	Fracture coating	108	30	High	1	0.5	Ep-Chl	5	Chl	Propylitic	Chataway
2015KB054	5599468	644583	1456	Fracture coating	357	80	Med	0.1	0.5	Ep	0		Propylitic	Chataway
2015KB055	5596504	646992	1377	Fracture coating	131	32	Med	0.2	0.5	Ep	5	Chl	Propylitic	Guichon
2015KB055	5596504	646992	1377	Fracture coating	82	90	Med	0.2	0.5	Ep	5	Chl	Propylitic	Guichon
2015KB055	5596504	646992	1377	Fracture coating	262	72	Med	0.5	0.5	Chl	10	Chl-Ser	Propylitic	Guichon
2015KB055	5596504	646992	1377	Fracture coating	22	85	Med	0.5	0.5	Chl	10	Chl-Ser	Propylitic	Guichon
2015KB055	5596504	646992	1377	Veinlet	281	65	Med	3	10	Ep	100	Ab-Chl	Sodic-calcic	Guichon
2015KB056	5596434	646965	1371	Fracture coating	260	69	Med	0.2	0.5	Ep	0		Propylitic	Guichon
2015KB056	5596434	646965	1371	Fracture halo	11	75	Med	0.2	0.5		30	Ab-Chl-Tur	Sodic-calcic	Guichon
2015KB057	5597036	646181	1414	Vein	209	49	High	4	3	Ep-Qz-Chl	20	Ab-Chl-Ep	Sodic-calcic	Guichon
2015KB058	5596960	646152	1419	Fracture coating	148	72	Med	0.5	0.5	Chl	0		Propylitic	Guichon
2015KB060	5597794	646190	1416	Veinlet	9	85	Med	0.5	2	Ep-Chl	50	Ab-Chl	Sodic-calcic	Guichon
2015KB062	5596976	646623	1399	Veinlet	13	89	Med	8	2	Ep-Chl-Qz	3	Ep-Ab-Chl	Sodic-calcic	Guichon
2015KB062	5596976	646623	1399	Fracture coating	112	81	Med	5	0.5		5	Chl-Ser	Propylitic	Guichon
2015KB063	5598843	650526	1134	Fracture coating	37	78	High	20	1	Chl-Ser	5	Chl	Propylitic	Border
2015KB063	5598843	650526	1134	Veinlet	75	32	High	4	0.5	Ep-Cal-Ccp			Propylitic	Border
2015KB064A	5598922	650482	1147	Vein	270	80	High	1	2	Ep-Qz	100		Propylitic	Border
2015KB065	5599003	650463	1140	Fracture halo	56	71	Med	1	0.5	CuOx-Lm	1200	Ser-Chl	Propylitic	Border
2015KB066	5599149	650255	1161	Fracture coating	198	32	Med	2	0.5	Lm-Chl-Lm-Ccp	0		Propylitic	Border
2015KB066	5599149	650255	1161	Fracture coating	241	83	Med	1.5	0.5	Chl-Ser	0		Propylitic	Border
2015KB067	5599841	649718	1194	Veinlet	86	82	High	0.2	0.5	Ep	30	Chl-Ep	Propylitic	Border
2015KB067	5599841	649718	1194	Fracture coating	25	70	High	0.5	0.5	Chl-Ep			Propylitic	Border
2015KB068	5599917	649514	1224	Fracture halo	128	60	High	1	0.5	Ep-Ccp-Py	20	Ep-Chl	Propylitic	Guichon
2015KB068	5599917	649514	1224	Fracture halo	211	79	High	1	0.5	Ep-Lm-Py	20	Ep-Chl	Propylitic	Guichon

Station ID	Northing (m)	Easting (m)	Elev (m)	Vein type	Strike	Dip	Conf	Density /m	Vein width (mm)	Vein minerals	Selvage width (mm)	Selvage minerals	Alteration	Lithology
2015KB069	5599013	650192	1171	Veinlet	259	88	Med	0.1	1	Ep-Chl-Qz	0		Propylitic	Border
2015KB070	5599011	649808	1246	Fracture halo	22	78	Med	2	0.5	Ep-Chl	10	Ep-Chl	Propylitic	Border
2015KB070	5599011	649808	1246	Fracture halo	199	89	Med	2	0.5	Ep-Chl	10	Ep-Chl	Propylitic	Border
2015KB070	5599011	649808	1246	Veinlet	180	40	Med	5	1	Chl-Tur	5	Chl	Propylitic	Border
2015KB071	5599748	649176	1268	Vein	22	90	High	1.5	10	Ep-Qz-Ccp-Lm	10	Ep-Chl-Ser	Muscovite	Guichon
2015KB072	5599400	649294	1279	Vein	26	85	Med	3	3	Ep-Chl	20	Ep-Chl	Propylitic	Guichon
2015KB072	5599400	649294	1279	Veinlet	265	78	Med	1	1		5	Ep-Chl	Propylitic	Guichon
2015KB072	5599400	649294	1279	Fault zone	215	79	Med	1		Lm	200	Ser	Propylitic	Guichon
2015KB073	5598766	649421	1255	Veinlet	272	80	High	0.5	0.5	Ep	5	Chl	Propylitic	Guichon
2015KB074	5598916	648959	1334	Veinlet	124	58	High	0.2	1	Ep	5	Chl	Propylitic	Guichon
2015KB074	5598916	648959	1334	Vein	1	60	High	0.5	5	Ep	50	Ab-Ep-Chl	Sodic-calcic	Guichon
2015KB075	5599396	648369	1341	Veinlet	0	90	Low	0.1	0.5	Ep	0		Propylitic	Guichon
2015KB080	5598549	648659	1357	Veinlet	346	88	Med	1.5	0.5	Ep-Chl	10	Chl-Ep	Propylitic	Guichon
2015KB082	5598188	649070	1311	Veinlet	211	86	Med	0.2	1	Ep	5	Chl	Propylitic	Guichon
2015KB082	5598188	649070	1311	Fracture coating	264	45	Med	0.2	0.5	Chl-Ep	10	Chl	Propylitic	Guichon
2015KB084	5599272	649843	1201	Fracture halo	89	88	Med	0.5		Ccp-Py	5	Ser-Chl	Muscovite	Border
2015KB085	5598354	649523	1277	Veinlet	44	90	Med	0.2	0.5	Ep-Chl	0.5		Propylitic	Guichon
2015KB087	5597775	648506	1364	Vein	191	87	Med	0.1	5	Tur	20	Ab-Act-Chl	Sodic-calcic	Guichon
2015KB087	5597775	648506	1364	Fracture coating	190	85	Med	1	0.5	Chl-Tur	10	Chl	Propylitic	Guichon
2015KB087	5597775	648506	1364	Fracture halo	132	88	Med	0.5	0		10	Ser	Propylitic	Guichon
2015KB089	5597864	648075	1355	Fracture coating	65	89	Med	1	0.5		5	Chl-Ser	Propylitic	Guichon
2015KB089	5597864	648075	1355	Fracture coating	17	90	Med	1	0.5		5	Chl-Ser	Propylitic	Guichon
2015KB089	5597864	648075	1355	Fracture halo	21	86	Med	0.5		Lm-Py	50	Ser	Muscovite	Guichon
2015KB090	5597830	647675	1373	Veinlet	19	88	High	2	2	Tur-Act-Ccp	10	Chl-Ab-Ser	Muscovite	Guichon
2015KB091	5598449	647709	1363	Fracture halo	16	90	Med	1	0.5	Tur	5	Chl-Kfs	K-feldspar	Guichon
2015KB091	5598449	647709	1363	Veinlet	61	88	Med	0.1	1	Ep	12	Chl-Ser	Propylitic	Guichon
2015KB092	5599066	647797	1385	Veinlet	347	88	Med	0.2	1	Ser	5	Ser-Chl	Propylitic	Chataway
2015KB093	5598812	647553	1392	Veinlet	358	88	Med	0.2	2	Tur-Qz-Lm	20	Chl-Kfs-Ser	K-feldspar	Chataway
2015KB094	5598631	647308	1380	Fracture halo	161	89	Med	1			15	Chl-Ser	Propylitic	Guichon
2015KB094	5598631	647308	1380	Fracture halo	69	85	Med	0.2			10	Chl-Ser	Propylitic	Guichon
2015KB095	5598456	646981	1415	Fracture halo	47	87	Low	0.1			5	Ser-Chl	Propylitic	Guichon
2015KB097	5598266	646585	1465	Veinlet	78	85	Low	0.1	1	Ser	5	Ser	Propylitic	Guichon
2015KB098	5597628	646809	1463	Veinlet	351	87	Low	0.1	1		4	Ser	Propylitic	Guichon
2015KB099	5597366	647143	1438	Veinlet	63	87	Low	0.1	1	Ser	0.2		Propylitic	Guichon
2015KB099	5597366	647143	1438	Fracture coating	11	81	Low	0.1	0.5	Tur-Act-Chl	0		Sodic-calcic	Guichon
2015KB100	5596235	645786	1451	Veinlet	19	87	High	0.25	1	Ep	10	Chl-Ser	Propylitic	Guichon
2015KB100	5596235	645786	1451	Veinlet	187	88	High	0.5	1	Chl	20	Chl-Ser-Tur	Propylitic	Guichon
2015KB101	5595931	645783	1442	Veinlet	4	86	High	0.75	1	Chl	50		Propylitic	Guichon
2015KB101	5595931	645783	1442	Fracture halo	168	58	High	1	0.05	Ep-Chl	10	Chl-Ep-Ser	Propylitic	Guichon
2015KB102	5595515	646085	1447	Fracture coating	33	87	High	0.2	0.05	Ep-Chl	5	Chl-Hem	Propylitic	Guichon
2015KB102	5595515	646085	1447	Fracture coating	262	70	High	0.2	0.05	Ep-Chl	5	Chl-Hem	Propylitic	Guichon
2015KB102	5595515	646085	1447	Vein	11	79	High	0.5	5	Ep-Qz-Lm	40	Ab-Chl	Sodic-calcic	Guichon
2015KB103A	5595539	646516	1423	Veinlet	31	76	High	10	1	Ep	20	Ab-Chl	Sodic-calcic	Chataway
2015KB104	5595420	646480	1414	Veinlet	11	89	High	0.2	0.05	Chl-Ep	2	Chl	Propylitic	Chataway
2015KB105A	5596149	646578	1392	Fracture halo	26	87	High	0.3	0.05		10	Chl-Ser	Propylitic	Guichon

Station ID	Northing (m)	Easting (m)	Elev (m)	Vein type	Strike	Dip	Conf	Density /m	Vein width (mm)	Vein minerals	Selvage width (mm)	Selvage minerals	Alteration	Lithology
2015KB105A	5596149	646578	1392	Fracture halo	335	75	High	0.1	0.05	Kfs-Ccp	0	Ser	Muscovite	Guichon
2015KB106	5596831	647425	1395	Veinlet	116	86	High	0.25	0.5	Chl-Ep	5	Chl-Hem	Propylitic	Guichon
2015KB106	5596831	647425	1395	Fracture halo	23	85	High	1	0	Py	40	Ser-Chl	Muscovite	Guichon
2015KB107	5596598	647245	1379	Fracture coating	83	75	High	0.5	0.5	Ep-Chl-Tur	5	Chl	Propylitic	Guichon
2015KB107	5596598	647245	1379	Fracture coating	15	86	High	0.5	0.5	Ep-Chl-Tur	5	Chl	Propylitic	Guichon
2015KB109	5598102	647356	1400	Fracture coating	83	66	High	0.05	0	Tur-Chl	5		Propylitic	Guichon
2015KB110	5598205	647448	1382	Fracture halo	67	81	High	1.5	0	Ser-Ep	20	Ser-Chl	Propylitic	Guichon
2015KB111	5596986	648084	1390	Veinlet	329	81	High	3	1	Ser-Qz	15	Ser-Chl-Hem	Propylitic	Guichon
2015KB112	5597224	648489	1362	Fracture coating	33	72	Med	0.2	0	Ep-Chl-Tur	0		Propylitic	Guichon
2015KB116	5587372	653387	1258	Veinlet	75	85	High	0.1	1	Ser-Qz-Tur	15	Ser-ksp	Propylitic	Gump
2015KB120	5587195	652400	1294	Veinlet	302	80	High	0.5	1	Prh	10	Chl-Ser-hem	Propylitic	Border
2015KB120	5587195	652400	1294	Veinlet	279	83	High	0.25	1	Ep	10	Chl-Ser	Propylitic	Border
2015KB121A	5586632	653129	1264	Fracture halo	19	90	High	1	2		1.5	Ser-Py	Muscovite	Border
2015KB121B	5586635	653140	1264	Fracture halo	19	90	High	1	2		1.5	Ser-Py	Muscovite	Border
2015KB122	5587255	651987	1313	Veinlet	116	80	High	1.5	3	Ep	15	Chl-Hem-Ser	Propylitic	Guichon
2015KB123	5586509	652132	1358	Veinlet	7	82	High	0.1	1	Ser	10	Ser	Propylitic	Border
2015KB123	5586509	652132	1358	Fracture halo	259	89	High	0.5	0.5	Chl-Ep	5	Chl-Ep	Propylitic	Border
2015KB124	5586172	652433	1401	Veinlet	101	80	High	0.2	10	Ep-Chl-Py-Ccp	30	Chl-Ser	Muscovite	Border
2015KB124	5586172	652433	1401	Veinlet	100	82	High	1.2	1	Ep-Chl	10	Chl	Propylitic	Border
2015KB125	5586065	651975	1394	Fracture halo	93	85	High	0.1	0.5	Ep	2.5	Chl	Propylitic	Border
2015KB128A	5586921	651813	1360	Veinlet	11	82	High	0.2	2	Prh	5	Ser-Chl	Propylitic	Border
2015KB128B	5586919	651816	1360	Veinlet	91	69	High	0.25	4	Ep-Prh-Ccp	10	Chl-Ab	Sodic-calcic	Border
2015KB129	5586861	652338	1334	Veinlet	63	74	High	0.3	1	Chl-Tur-Lm-Ccp	10	Chl-Ser-Kfs	Muscovite	Border
2015KB130	5587234	652628	1287	Fracture halo	319	90	Med	2	0		15	Ser	Propylitic	Border
2015KB132	5588538	652604	1373	Veinlet	103	75	High	1	1	Prh	10	Ser	Propylitic	Gump
2015KB132	5588538	652604	1373	Veinlet	92	85	High	0.1	1	Ep	5		Propylitic	Gump
2015KB133	5587735	651707	1332	Veinlet	331	79	High	0.1	1	Prh-Ep	15	Ser-Chl	Propylitic	Border
2015KB134	5588306	651653	1355	Veinlet	80	80	High	0.4	1	Ep	0	Chl-Ser	Propylitic	Border
2015KB135A	5588856	651790	1378	Veinlet	86	76	High	0.75	0.5	Ep	12	Chl-Ab-Ep	Sodic-calcic	Border
2015KB135A	5588856	651790	1378	Veinlet	276	90	High	2	2	Ep	8	Chl-Ser-Kfs	K-feldspar	Border
2015KB136	5586490	651134	1406	Fracture halo	131	85	High	2	2	Ep	20	Chl-Kfs-Ser	K-feldspar	Transitional Guichon-Chataway
2015KB137	5586911	651083	1412	Veinlet	69	90	High	0.25	1.5	Ep	10	Chl	Propylitic	Guichon
2015KB137	5586911	651083	1412	Veinlet	160	85	High	0.6	1	Prh-Chl	15	Ser-Chl	Propylitic	Guichon
2015KB137	5586911	651083	1412	Fracture coating	289	84	High	0.1	0.5	Ep-Chl-CuOx-Ccp	5	Chl	Propylitic	Guichon
2015KB138	5587595	650750	1375	Veinlet	221	79	Med	0.2	0.5	Ep	5	Chl	Propylitic	Guichon
2015KB140	5588096	650241	1392	Veinlet	244	82	Med	0.1	2	Ep-Hem	5	Chl	Propylitic	Transitional Guichon-Chataway
2015KB141	5587958	650025	1420	Veinlet	141	82	Med	0.2	1.5	Prh	8	Ser-Chl	Propylitic	Chataway
2015KB141	5587958	650025	1420	Fracture halo	169	78	Med					Kfs	K-feldspar	Chataway
2015KB142	5587498	650012	1432	Veinlet	274	85	Med	0.1	0.5	Ep-Chl	5	Chl	Propylitic	Chataway
2015KB143	5587111	650308	1420	Veinlet	89	90	Low	0.15	1	Prh	20	Ser-Chl	Propylitic	Transitional Guichon-Chataway
2015KB144A	5586864	650179	1425	Veinlet	147	78	Med	0.5	1	Prh		Chl-Ser	Propylitic	Transitional Guichon-Chataway
2015KB144A	5586864	650179	1425	Fracture halo	114	65	Med	0.1	0.5			Ep	Propylitic	Transitional Guichon-Chataway
2015KB145	5586489	649496	1448	Veinlet	33	84	Med	0.15	0.5	Ep-Chl	15	Chl	Propylitic	Transitional Guichon-Chataway
2015KB145	5586489	649496	1448	Fracture coating	28	80	Med	0.3	0.5	Chl-Ep			Propylitic	Transitional Guichon-Chataway
2015KB146	5588700	649895	1395	Fracture halo	106	90	Med	0.15	0.5	Ep-Chl	12	Chl-Ser	Propylitic	Chataway

Station ID	Northing (m)	Easting (m)	Elev (m)	Vein type	Strike	Dip	Conf	Density /m	Vein width (mm)	Vein minerals	Selvage width (mm)	Selvage minerals	Alteration	Lithology
2015KB146	5588700	649895	1395	Fracture halo	75	54	Med	0.1			7	Ser-Chl	Propylitic	Chataway
2015KB146	5588700	649895	1395	Vein	141	87	Med	0.5	3	Prh	25	Ser-Chl	Propylitic	Chataway
2015KB147	5587824	649496	1476	Vein	113	82	Med	1.1	3	Prh	10	Ser	Propylitic	Chataway
2015KB147	5587824	649496	1476	Veinlet	321	78	Med	0.2	1	Prh	10	Ser-Chl	Propylitic	Chataway
2015KB148	5587347	649565	1466	Veinlet	336	84	Low	0.1	1.5	Prh	10	Ser-Hem	Propylitic	Chataway
2015KB148	5587347	649565	1466	Veinlet	20	78	Low	0.1	1.5	Prh	11	Ser	Propylitic	Chataway
2015KB149A	5588230	649178	1440	Fracture halo	87	90	High	0.25			6	Kfs-Mag	K-feldspar	Transitional Guichon-Chataway
2015KB149A	5588230	649178	1440	Fracture halo	274	81	High	0.2			10	Hem-Ab	Sodic-calcic	Transitional Guichon-Chataway
2015KB149A	5588230	649178	1440	Fracture halo	235	80	High			Bn	1	Kfs	K-feldspar	Transitional Guichon-Chataway
2015KB149A	5588230	649178	1440	Fracture halo	97	73	High				10	Ser	Propylitic	Transitional Guichon-Chataway
2015KB149B	5588230	649178	1440	Veinlet	175	72	High	0.8	2	Qz-Ser-Bn	15	Ser-Hem-Chl	Muscovite	Transitional Guichon-Chataway
2015KB150	5588141	649771	1432	Veinlet	341	72	Med	0.3	1	Prh	15	Ser-Chl	Propylitic	Chataway
2015KB151	5584642	649378	1443	Fracture halo	223	70	High	0.15	0.5		10	Ser-Chl-Cly	Propylitic	
2015KB151	5584642	649378	1443	Veinlet	73	85	High	0.2	2	Prh	20	Hem-Ser-Chl	Propylitic	
2015KB151	5584642	649378	1443	Veinlet	120	82	High	0.1	1	Ep	15	Ab-Ser-Chl	Sodic-calcic	
2015KB152A	5585313	648917	1462	Veinlet	136	66	High	0.65	0.5	Ep	7	Ab-Chl-Ser	Sodic-calcic	Chataway
2015KB152A	5585313	648917	1462	Veinlet	53	90	High	0.2	1	Ep	10	Chl-Ab	Sodic-calcic	Chataway
2015KB153B	5585851	648618	1463	Veinlet	273	80	High	0.2	1	Prh	20	Chl-Ser	Propylitic	
2015KB154	5586106	648591	1477	Veinlet	143	78	Med	0.25	1	Ser	8	Ser-Chl	Propylitic	Chataway
2015KB155A	5586276	648151	1498	Vein	259	72	High	0.75	3	Ep-Ab	15	Chl-Ab	Sodic-calcic	Chataway
2015KB155A	5586276	648151	1498	Veinlet	181	25	High	0.2	1	Ep-Ab	5	Chl-Ab	Sodic-calcic	Chataway
2015KB155B	5586260	648129	1498	Veinlet	151	84	High	1.2	1.5	Prh	22	Ser-Ser-Chl	Propylitic	Chataway
2015KB156	5585853	648164	1513	Fracture coating	115	59	High	1.2	1	Ep-Ser-Qz	15	Chl-Ser	Propylitic	Chataway
2015KB156	5585853	648164	1513	Veinlet	261	85	High	0.5	2	Ep-Prh	10	Chl-Ab	Sodic-calcic	Chataway
2015KB157	5585342	648338	1538	Veinlet	266	80	Low	0.5	1	Prh-Ser-Ep	10	Ser-Chl	Propylitic	Chataway
2015KB157	5585342	648338	1538	Veinlet	136	50	Low	0.1	0.5	Ep-Chl	2	Chl-Ep	Propylitic	Chataway
2015KB158	5584954	648503	1517	Fracture coating	89	45	Low	0.1	0.5	Ep-Chl-CuOx			Propylitic	Chataway
2015KB159	5588106	651218	1335	Veinlet	266	84	Low	0.2	1.2	Ep	12	Kfs-Chl	K-feldspar	Guichon
2015KB160A	5588750	651215	1352	Veinlet	261	83	Med	0.1	1.5	Ep	12	Chl-Ser	Propylitic	Guichon
2015KB160B	5588762	651210	1352	Veinlet	339	88	Med	0.1	1	Prh	10	Chl-Ser	Propylitic	Guichon
2015KB161B	5589297	651193	1378	Veinlet	285	84	Low	0.1	1	Ep		Chl-Hem	Propylitic	Guichon
2015KB161B	5589297	651193	1378	Fracture halo	332	77	Low	0.15	0.5	Prh		Chl-Ser	Propylitic	Guichon
2015KB162	5588567	650992	1352	Fracture coating	322	77	Med		0.5	Ep			Propylitic	Transitional Guichon-Chataway
2015KB163A	5586902	649764	1445	Veinlet	346	82	High	0.75	0.5	Prh	12	Chl-Ser	Propylitic	Transitional Guichon-Chataway
2015KB163A	5586902	649764	1445	Veinlet	110	78	High	0.5	0.5	Prh	10	Chl-Ser	Propylitic	Transitional Guichon-Chataway
2015KB164	5586893	649344	1460	Veinlet	342	78	High	0.5	1	Prh	15	Ser	Propylitic	Transitional Guichon-Chataway
2015KB164	5586893	649344	1460	Fracture coating	106	89	High	0.2	0.5	Ser	0.5	Ser	Propylitic	Transitional Guichon-Chataway
2015KB165	5585002	648569	1509	Veinlet	136	84	High	0.75	1	Prh	15	Chl-Ser	Propylitic	Transitional Guichon-Chataway
2015KB165	5585002	648569	1509	Fracture halo	356	62	High	0.2	0.2	Ep-CuOx	5	Ep	Propylitic	Transitional Guichon-Chataway
2015KB166A	5585645	647716	1539	Vein	282	80	High	2	4	Prh	70	Chl-Ep-Ser	Propylitic	Chataway
2015KB166A	5585645	647716	1539	Vein	131	65	High	2	4	Prh	70	Chl-Ep-Ser	Propylitic	Chataway
2015KB166A	5585645	647716	1539	Veinlet	325	78	High	0.5	1.5	Prh	20	Chl-Prh	Propylitic	Chataway
2015KB167	5585039	647913	1532	Veinlet	263	82	High	0.4	1	Prh	10	Ser-Chl	Propylitic	Chataway
2015KB167	5585039	647913	1532	Fracture halo	159	68	High	0.1	0.5	Bn-Mol	7	Bt-Chl	K-feldspar	Chataway
2015KB167	5585039	647913	1532	Veinlet	148	80	High	1.5	1.5	Prh	13	Chl-Ser-Kfs	K-feldspar	Chataway

Station ID	Northing (m)	Easting (m)	Elev (m)	Vein type	Strike	Dip	Conf	Density /m	Vein width (mm)	Vein minerals	Selvage width (mm)	Selvage minerals	Alteration	Lithology
2015KB168	5586167	647703	1538	Vein	137	76	High	1	2	Prh	15	Ep-Ser-Hem	Propylitic	Chataway
2015KB169A	5586974	647351	1531	Veinlet	20	78	High	0.5	1.5	CuOx	20	Chl-Ser-Hem	Propylitic	Chataway
2015KB169A	5586974	647351	1531	Fracture halo	355	85	Med		0		8	Kfs	K-feldspar	Chataway
2015KB169B	5586974	647351	1531	Vein	22	58	High	0.75	2.5	Ep-Chl	10	Chl-Ab	Sodic-calcic	Chataway
2015KB170	5586114	647305	1558	Veinlet	124	79	High	2.5	1	Prh	15	Chl-Ser-Hem	Propylitic	Chataway
2015KB170	5586114	647305	1558	Vein	1	54	High	0.5	3	Ep-Qz	25	Chl-Ab	Sodic-calcic	Chataway
2015KB170	5586114	647305	1558	Vein	95	72	High	0.8	3	Ep-Qz	25		Propylitic	Chataway
2015KB171	5588317	646588	1501	Vein	106	85	Med	0.5	4	Ep-Qz	10	Chl-Ab	Sodic-calcic	Guichon
2015KB171	5588317	646588	1501	Vein	260	52	Med	0.5	4		10	Chl-Ab	Sodic-calcic	Guichon
2015KB171	5588317	646588	1501	Fracture halo	210	80	Med	0.25	0		11	Ser-Chl-Hem	Propylitic	Guichon
2015KB171	5588317	646588	1501	Fracture halo	349	71	Med	0.25	0		11	Ser-Chl-Hem	Propylitic	Guichon
2015KB172	5587799	646165	1550	Veinlet	333	84	High	0.75	1.5	Prh	17	Chl-Ser	Propylitic	Guichon
2015KB172	5587799	646165	1550	Veinlet	171	81	High	0.75	1.5	Prh	10	Chl-Ser	Propylitic	Guichon
2015KB172	5587799	646165	1550	Fracture halo	179	75	High	0.5	0	Ep	15	Ab-Chl	Sodic-calcic	Guichon
2015KB172	5587799	646165	1550	Fracture halo	81	72	High	0.5	0	Ep	15	Ab-Chl	Sodic-calcic	Guichon
2015KB173	5587573	645310	1588	Veinlet	266	72	High	0.8	1	Prh		Ser-Chl-Hem	Propylitic	Skeena
2015KB173	5587573	645310	1588	Fracture halo	278	75	High	0.25	0.5	Prh		Ser-Chl-Hem	Propylitic	Skeena
2015KB173	5587573	645310	1588	Veinlet	315	85	High	0.5	1	Prh		Ser-Chl-Hem	Propylitic	Skeena
2015KB174	5588019	645268	1582	Veinlet	303	81	High	0.75	2	Ser-Cly-Lm	30	Chl-Ser-Ep	Propylitic	Skeena
2015KB174	5588019	645268	1582	Fracture halo	168	72	High	0.2	0.5	Ser	12	Chl-Ser-Ep	Propylitic	Skeena
2015KB174	5588019	645268	1582	Fracture halo	320	65	High	0.2	0	Ser	12	Chl-Ser	Propylitic	Skeena
2015KB175	5587781	647551	1475	Veinlet	298	56	High	0.25	1	Ser	20	Ser-Chl	Propylitic	Skeena
2015KB175	5587781	647551	1475	Fracture halo	325	59	High	0.8	0.5	Ser	22	Ser-Chl-Ep	Propylitic	Skeena
2015KB175	5587781	647551	1475	Fracture halo	70	40	High	0.2	0.5	Ser	8	Ser-Chl	Propylitic	Skeena
2015KB176	5588037	647264	1507	Fracture halo	220	39	Low	0.2	0			Ser-Chl	Propylitic	Guichon
2015KB177	5587877	646808	1511	Vein	2	50	Med	0.2	4	Ep-Bn	25	Kfs-Chl	K-feldspar	Guichon
2015KB177	5587877	646808	1511	Vein	17	40	Med	0.1	3	Ep	15	Kfs-Chl	K-feldspar	Guichon
2015KB177	5587877	646808	1511	Fracture halo	259	75	Med	0.4	0		5	Ser-Chl-Hem	Propylitic	Guichon
2015KB177	5587877	646808	1511	Fracture halo	1	70	Med	0.3	0		4	Kfs	K-feldspar	Guichon
2015KB178	5586768	646900	1573	Vein	149	51	High	1	3	Ep	25	Ep-Ab-Chl	Sodic-calcic	Guichon
2015KB178	5586768	646900	1573	Vein	233	64	High	1.15	0.5	Ep	25	Ab-Chl	Sodic-calcic	Guichon
2015KB178	5586768	646900	1573	Vein	185	44	High	0.1	2	Prh	10	Ser-Chl	Propylitic	Guichon
2015KB179	5587286	646563	1550	Fracture halo	261	83	High	2	0.5	Ep	12	Ab-Chl	Sodic-calcic	Transitional Guichon-Chataway
2015KB179	5587286	646563	1550	Fracture halo	20	75	High	1	0.5	Ep	12	Ab-Chl	Sodic-calcic	Transitional Guichon-Chataway
2015KB179	5587286	646563	1550	Veinlet	153	42	High	0.2	0.5	Prh	5	Ser	Propylitic	Transitional Guichon-Chataway
2015KB180	5587062	646281	1602	Veinlet	149	50	Low	0.2	0.5	Ser	10	Ser-Chl	Propylitic	Guichon
2015KB180	5587062	646281	1602	Vein	356	60	Low	0.15	10	Qz-Lm-Bn	5	Ser	Muscovite	Guichon
2015KB181	5586606	646112	1597	Veinlet	240	60	High	2	1	Prh	20	Ser-Chl	Propylitic	Skeena
2015KB181	5586606	646112	1597	Veinlet	84	89	High	1	0.5	Prh	10	Ser-Chl	Propylitic	Skeena
2015KB181	5586606	646112	1597	Veinlet	236	70	High	0.2	0.5	Ep	7	Ab-Chl	Sodic-calcic	Skeena
2015KB182	5586377	646525	1575	Vein	172	69	High	3	15	Ep-Chl-Qz	1500	Ab-Chl-Ep	Sodic-calcic	Skeena
2015KB183	5587130	645857	1595	Fracture halo	110	82	Med	0.4	0.5	Prh	15	Ser-Chl	Propylitic	Skeena
2015KB183	5587130	645857	1595	Veinlet	315	75	Med	0.15	1	Ep	10	Ab-Chl	Sodic-calcic	Skeena
2015KB184	5587500	646156	1578	Veinlet	279	70	High	0.5	2	Ep	10	Ab-Chl	Sodic-calcic	Chataway
2015KB184	5587500	646156	1578	Fracture halo	208	41	Med	0.25	0.5		5	Ser-Chl	Propylitic	Chataway

Station ID	Northing (m)	Easting (m)	Elev (m)	Vein type	Strike	Dip	Conf	Density /m	Vein width (mm)	Vein minerals	Selvage width (mm)	Selvage minerals	Alteration	Lithology
2015KB185A	5587697	646830	1546	Vein	270	60	High	0.5	10	Qz	5	Kfs	K-feldspar	Chataway
2015KB185B	5587697	646830	1546	Vein	235	51	High	3	5	Qz-Ser-Lm	40	Ser-Chl	Propylitic	Chataway
2015KB185B	5587697	646830	1546	Veinlet	206	68	High			Ep			Propylitic	Chataway
2015KB186	5587551	647121	1542	Veinlet	168	86	High	0.4	1	Prh-Cly	7	Ser-Chl	Propylitic	Chataway
2015KB187	5587539	646814	1542	Vein	350	80	High	0.75	7	Ep-Qz-CuOx-Bn	20	Ab-Chl	Sodic-calcic	Guichon
2015KB188	5588277	644704	1627	Fracture halo	113	65	High	1.05	0.5	Ser	25	Ser-Chl-Ep	Propylitic	Skeena
2015KB188	5588277	644704	1627	Veinlet	16	55	Med	0.2			10	Ser-Chl	Propylitic	Skeena
2015KB189	5587839	644823	1630	Fracture halo	239	68	High	0.75	0.5		10	Ser-Chl	Propylitic	Skeena
2015KB189	5587839	644823	1630	Fracture halo	185	65	High	0.5	0.5	CuOx	10	Ser-Chl-Ep	Propylitic	Skeena
2015KB190	5587793	644652	1633	Fracture halo	36	58	High	0.5	0.5	Prh	15	Ser	Propylitic	Skeena
2015KB191A	5588822	644669	1596	Fracture halo	249	76	Low	0.25	0.5		10	Ser-Chl	Propylitic	Skeena
2015KB191A	5588822	644669	1596	Veinlet	194	90	Low	0.15	1	Qz-Bn	5	Chl	Propylitic	Skeena
2015KB192	5588656	644308	1646	Veinlet	59	86	Med	0.2	1	Ep	15	Ab-Chl	Sodic-calcic	Skeena
2015KB193	5588545	644069	1684	Veinlet	308	69	Med	0.2	2	Prh	15	Ser-Chl	Propylitic	Skeena
2015KB193	5588545	644069	1684	Veinlet	71	80	Med	0.1	1	Ser-Ccp	15	Ser-Chl	Muscovite	Skeena
2015KB193	5588545	644069	1684	Fracture coating	19	70	Med		0.5	Ser		Ser-Chl	Propylitic	Skeena
2015KB193	5588545	644069	1684	Veinlet	202	60	Med		2	Ser	12	Ser-Chl	Propylitic	Skeena
2015KB193	5588545	644069	1684	Veinlet	260	85	Med	0.15	1	Ep	20	Ab-Chl	Sodic-calcic	Skeena
2015KB194	5588229	644385	1662	Veinlet	186	81	Med	0.15	1.5	Ser			Propylitic	Skeena
2015KB194	5588229	644385	1662	Veinlet	262	80	Med	0.2	2.5	Qz-Bn			Muscovite	Skeena
2015KB194	5588229	644385	1662	Veinlet	174	55	Med	0.1	1	Ep			Propylitic	Skeena
2015KB195	5587766	644261	1664	Vein	94	68	High	5	120	Ser-Qz	40	Ms	Muscovite	Skeena
2015KB195	5587766	644261	1664	Vein	92	80	High	1	10	Qz	5	Kfs	K-feldspar	Skeena
2015KB196	5588099	644216	1659	Veinlet	144	75	High	3	1	Ser-Qz	9	Ser-Chl	Propylitic	Skeena
2015KB196	5588099	644216	1659	Vein	62	76	High	0.75	4	Qz-CuOx	5	Kfs	K-feldspar	Skeena
2015KB197	5588216	643738	1705	Veinlet	29	71	High	0.5	0.5	Hem	12	Kfs	K-feldspar	Skeena
2015KB197	5588216	643738	1705	Veinlet	278	85	High	2.5	1	Ser-Qz-Ccp	10	Ser-Chl	Muscovite	Skeena
2015KB197	5588216	643738	1705	Veinlet	208	68	High	2	0.5	Ser-CuOx	10	Ser-Chl	Propylitic	Skeena
2015KB197	5588216	643738	1705	Veinlet	81	40	High	2	0.5	Ser-CuOx	10	Ser-Chl	Propylitic	Skeena
2015KB197	5588216	643738	1705	Veinlet	270	84	High	0.1	10	Qz-Ser-Bn-Mol	15	Ser-Chl	Muscovite	Skeena
2015KB198A	5588253	643301	1714	Veinlet	246	81	High	0.2	1.5	Ep-Chl			Propylitic	Skeena
2015KB198A	5588253	643301	1714	Veinlet	30	85	High	3	1	Qz-Ser-Ccp-Lm	17	Ser-Chl	Muscovite	Skeena
2015KB199	5588377	642690	1707	Vein	9	85	High	3	10	Qz		Kfs	K-feldspar	Skeena
2015KB199	5588377	642690	1707	Veinlet	341	70	High	5	2	Ser-Qz-Ccp-Lm		Ser-Chl	Muscovite	Skeena
2015KB199B	5588350	642690	1721	Vein	210	53	High	6	3	Qz-Ccp-Bn	15	Ms-Chl	Muscovite	
2015KB200	5589173	644217	1622	Fracture coating	257	88	High	2	0.5	Ser-CuOx-Lm	25	Ser-Chl	Propylitic	Skeena
2015KB200	5589173	644217	1622	Vein	193	55	High	7	3	Cal-Ser-Lm			Propylitic	Skeena
2015KB201	5588975	644319	1612	Veinlet	259	84	High	3	1.5	Qz	15	Kfs	K-feldspar	QFP
2015KB201	5588975	644319	1612	Veinlet	128	85	High	2	1	Ser	17	Ser-Chl	Propylitic	QFP
2015KB202	5588825	644490	1624	Vein	183	38	Low	0.15	4	Ep	25	Chl-Ep-Ab	Sodic-calcic	Skeena
2015KB202	5588825	644490	1624	Veinlet	208	70	Low	0.1	0.5	Ser	7	Ser-Chl	Propylitic	Skeena
2015KB202	5588825	644490	1624	Veinlet	161	72	Low	0.25	0.5	Ser	10	Ser-Chl	Propylitic	Skeena
2015KB203	5589171	644560	1584	Vein	186	62	Med	0.1	3	Ep	20	Ab-Chl	Sodic-calcic	Skeena
2015KB203	5589171	644560	1584	Fracture halo	359	50	Med	0.2			15	Ser-Chl	Propylitic	Skeena
2015KB203	5589171	644560	1584	Fracture halo	235	75	Med				15	Ser-Chl	Propylitic	Skeena

Station ID	Northing (m)	Easting (m)	Elev (m)	Vein type	Strike	Dip	Conf	Density /m	Vein width (mm)	Vein minerals	Selvage width (mm)	Selvage minerals	Alteration	Lithology
2015KB204	5589107	644769	1561	Veinlet	206	82	Med	0.55	1	Ser-Qz-Lm-CuOx	8	Ser-Chl	Propylitic	Skeena
2015KB205	5589507	643936	1608	Veinlet	254	74	Low	1	1	Ser	10	Ser-Chl	Propylitic	Skeena
2015KB205	5589507	643936	1608	Vein	212	60	Low	2	3	Ep-CuOx	25	Ab-Chl	Sodic-calcic	Skeena
2015KB206	5589063	643752	1630	Veinlet	21	78	High	1.2	1.5	Ser-Cly-Qz	12	Ser-Chl	Propylitic	Skeena
2015KB206	5589063	643752	1630	Fracture halo	210	51	High	1.5	0.5		10	Ser-Chl	Propylitic	Skeena
2015KB206	5589063	643752	1630	Veinlet	83	65	High		1	Lm-CuOx	15	Ser-Chl	Propylitic	Skeena
2015KB207	5588792	643937	1663	Veinlet	332	81	Med	0.75	2	Ser	15	Ser-Chl	Propylitic	Skeena
2015KB208	5587348	644585	1634	Veinlet	9	82	High	0.1	1	Ep			Propylitic	Skeena
2015KB208	5587348	644585	1634	Veinlet	95	85	High	0.5	1	Ser	5	Kfs-Chl	K-feldspar	Skeena
2015KB208	5587348	644585	1634	Veinlet	35	60	High	1.5	1.5	Ep	12	Kfs-Chl-Ser	K-feldspar	Skeena
2015KB209	5587268	645022	1648	Veinlet	78	80	High	0.75	0.5	Ser-Lm-CuOx	11	Ser-Kfs-Chl	K-feldspar	Skeena
2015KB209	5587268	645022	1648	Veinlet	318	58	High	3	1	Py-Ccp-Lm-CuOx	8	Kfs-Chl	K-feldspar	Skeena
2015KB209	5587268	645022	1648	Fracture halo	105	78	High	1.5			12	Kfs-Bt	K-feldspar	Skeena
2015KB210	5587005	645303	1610	Veinlet	68	88	High	0.15	0.5	Ser	10		Propylitic	Skeena
2015KB210	5587005	645303	1610	Veinlet	164	8	High	0.5	1	Ep	10	Ep-Ab	Sodic-calcic	Skeena
2015KB210	5587005	645303	1610	Fracture halo	226	75	High	0.15	0.5		15	Ser-Chl	Propylitic	Skeena
2015KB211	5589613	644133	1609	Veinlet	201	75	High	0.15	1.5	Ep	5	Ser-Ab-Chl	Sodic-calcic	Skeena
2015KB211	5589613	644133	1609	Veinlet	78	76	High	0.2		Ep	20	Chl-Ab	Sodic-calcic	Skeena
2015KB212	5589524	644384	1592	Veinlet	40	75	High	0.75	1	Lm-Ser	25	Chl-Ser	Propylitic	Skeena
2015KB213	5589888	643998	1586	Veinlet	18	66	High	0.75		Ep	15	Chl	Propylitic	Skeena
2015KB213	5589888	643998	1586	Vein	220	65	High	0.15	4	Ep	400	Ab-Chl-Ser	Sodic-calcic	Skeena
2015KB214	5589681	644012	1601	Vein	25	76	High	8	4	Ep-Qz	35	Ab-Chl	Sodic-calcic	Skeena
2015KB214	5589681	644012	1601	Vein	41	35	High	8	4	Ep-Qz	35	Ab-Chl	Sodic-calcic	Skeena
2015KB215	5590167	643829	1549	Veinlet	217	40	High	5	2	Ep		Ab-Chl	Sodic-calcic	Skeena
2015KB215	5590167	643829	1549	Fracture halo	42	72	High	3	0.5	Ser-Lm-CuOx	20	Ser-Chl	Propylitic	Skeena
2015KB216	5590052	644272	1524	Veinlet	110	82	Med	3	1.5	Ep-Qz	30	Ab-Chl	Sodic-calcic	Skeena
2015KB216	5590052	644272	1524	Vein	228	50	Med	2.5	4	Ep-Qz	30	Ab-Chl	Sodic-calcic	Skeena
2015KB216	5590052	644272	1524	Veinlet	46	72	Med	2	2	Ep	30	Ab-Chl	Sodic-calcic	Skeena
2015KB217	5589680	642833	1610	Veinlet	277	80	Med	0.75	0.5	Ep-Chl	7	Chl-Ep-Ab	Sodic-calcic	Skeena
2015KB217	5589680	642833	1610	Veinlet	254	86	Med	0.25	1.5	Ep	7	Chl-Ep	Propylitic	Skeena
2015KB217	5589680	642833	1610	Fracture halo	307	71	Med	0.6			15	Ser-Chl	Propylitic	Skeena
2015KB218	5589418	642894	1625	Veinlet	75	73	Med	0.5	1.5	Ser	20	Ser-Chl	Propylitic	Skeena
2015KB218	5589418	642894	1625	Veinlet	132	80	Med	1.2	1	Ser	15	Ser-Chl	Propylitic	Skeena
2015KB218	5589418	642894	1625	Vein	230	80	Med	2.5	2.5	Ep	35	Ab-Chl	Sodic-calcic	Skeena
2015KB218	5589418	642894	1625	Vein	203	70	Med	2.5	2.5	Ep	35	Ab-Chl	Sodic-calcic	Skeena
2015KB219	5589254	642983	1635	Vein	32	79	High	0.3	10	Ep-Qz-CuOx	35	Ab-Chl	Sodic-calcic	Skeena
2015KB219	5589254	642983	1635	Veinlet	11	70	High	4	2	Ep-Qz	12	Ser-Chl	Propylitic	Skeena
2015KB220	5589439	643318	1623	Veinlet	37	81	Med	0.8	1.5	Ep	22	Chl-Ab	Sodic-calcic	Skeena
2015KB220	5589439	643318	1623	Veinlet	136	88	Med	0.5	0.5	Ser	20	Ser-Chl	Propylitic	Skeena
2015KB221	5590037	643320	1580	Veinlet	183	74	Med	0.1	2	Qz	12	Kfs-Ep	K-feldspar	Skeena
2015KB221	5590037	643320	1580	Fracture halo	128	50	Med	0.5			20	Chl-Ser	Propylitic	Skeena
2015KB221	5590037	643320	1580	Fracture coating	82	75	Med	0.4	0.5	Chl-Ser			Propylitic	Skeena
2015KB222	5588921	643028	1629	Veinlet	62	57	Low	0.5	1.5	Ep	10	Chl-Ser	Propylitic	Skeena
2015KB222	5588921	643028	1629	Veinlet	110	78	Low		2	Ser	18	Ser-Chl	Propylitic	Skeena
2015KB223	5588860	643281	1630	Vein	150	87	Med	0.5	3	Tur-Qz	60	Ser-Chl	Propylitic	Skeena

Station ID	Northing (m)	Easting (m)	Elev (m)	Vein type	Strike	Dip	Conf	Density /m	Vein width (mm)	Vein minerals	Selvage width (mm)	Selvage minerals	Alteration	Lithology
2015KB223	5588860	643281	1630	Vein	235	72	Med	0.1	5	Qz-Kfs			K-feldspar	Skeena
2015KB223	5588860	643281	1630	Veinlet	125	80	Med	2	1	Ser	15	Ser-Chl	Propylitic	Skeena
2015KB223	5588860	643281	1630	Veinlet	28	50	Med	0.2	1	Ccp-Lm-CuOx	10	Ser	Muscovite	Skeena
2015KB224	5589271	643394	1620	Vein	220	84	Med	0.15	8	Ep-Qz-Tur	35	Chl	Propylitic	Skeena
2015KB224	5589271	643394	1620	Veinlet	84	79	Med	0.75	1	Ep	12	Chl	Propylitic	Skeena
2015KB225	5588727	643115	1640	Veinlet	186	80	Med	4	0.5	Ccp-Qz-CuOx	0.5	Kfs-Bt	K-feldspar	Skeena
2015KB225	5588727	643115	1640	Fracture coating	190	68	Med	2	0.5	Hem	5	Ser-Chl	Propylitic	Skeena
2015KB225	5588727	643115	1640	Veinlet	130	84	Med	2.5	1	Ser-Ccp-Lm	15	Ser-Chl	Muscovite	Skeena
2015KB225	5588727	643115	1640	Veinlet	88	70	Med	0.2	1	Ep			Propylitic	Skeena
2015KB226	5588467	643015	1705	Vein	31	80	Low	0.15	20	Qz-Kfs			K-feldspar	Skeena
2015KB226	5588467	643015	1705	Veinlet	20	75	Low	2	0.5	Ser-Chl-Lm-CuOx			Propylitic	Skeena
2015KB226	5588467	643015	1705	Veinlet	268	80	Low	1.5	0.5	Ser-Chl-Lm-CuOx			Propylitic	Skeena
2015KB227	5588498	643345	1678	Vein	30	75	Med	2	25	Qz-Cal-Lm-Py	30	Ser-Cal	Muscovite	Skeena
2015KB227	5588498	643345	1678	Veinlet	210	80	Med	10	2	Ser-Lm	25	Ser	Propylitic	Skeena
2015KB228	5588363	643873	1657	Veinlet	221	85	Med	0.1	1	Ep	7	Kfs-Hem	K-feldspar	Skeena
2015KB228	5588363	643873	1657	Fracture halo	88	87	Med	0.5			15	Kfs	K-feldspar	Skeena
2015KB229A	5588947	643536	1634	Vein	80	74	High	0.5	30	Qz-Ep			Propylitic	Skeena
2015KB229B	5588947	643531	1634	Veinlet	16	85	High	2.4	1	Ep	30	Chl-Ep-Ab	Sodic-calcic	Skeena
2015KB230A	5589832	643445	1581	Veinlet	341	74	Med	0.25	0.5	Ep	40	Ab-Chl	Sodic-calcic	Skeena
2015KB230A	5589832	643438	1581	Veinlet	82	90	Med	0.5	0.5	Ep	5	Ep-Chl	Propylitic	Skeena
2015KB230B	5589832	643438	1581	Fracture halo	286	86	Med				12	Ser-Chl	Propylitic	Skeena
2015KB231	5589579	642639	1607	Veinlet	97	80	High	2	0.5	Ep	15	Ep-Chl-Ser	Propylitic	Skeena
2015KB231	5589579	642639	1607	Veinlet	10	75	Med	0.5	0.5	Ep			Propylitic	Skeena
2015KB231	5589579	642639	1607	Fracture halo	223	69	High	1	0.5	Ep-Ser	40	Ser-Chl	Propylitic	Skeena
2015KB231	5589579	642639	1607	Vein	222	74	High	3	2	Ep-Qz	25	Ser	Propylitic	Skeena
2015KB232	5589388	642510	1630	Veinlet	42	90	High	2.5	1	Ep-Ser	32	Chl-Ser-Ep	Propylitic	Skeena
2015KB232	5589388	642510	1630	Veinlet	314	89	High	1	1	Ep-Ser	40	Chl-Ser-Ep	Propylitic	Skeena
2015KB233A	5589299	642302	1603	Vein	165	72	High	2.5	0.75	Tur	15	Ser-Kfs	K-feldspar	Skeena
2015KB233A	5589299	642302	1603	Fracture halo	283	30	High	4		Chl-Ser-Ep			Propylitic	Skeena
2015KB233B	5589305	642302	1603	Vein	226	57	High	3	2	Ep-Cal-Lm	30	Chl-Ep-Ser	Propylitic	Skeena
2015KB233B	5589305	642302	1603	Veinlet	71	40	High	2	1.5	Ep-Ser-CuOx	25	Chl-Ser	Propylitic	Skeena
2015KB233B	5589305	642302	1603	Fracture halo	334	82	High	4		Chl-Ser-Ep			Propylitic	Skeena
2015KB233B	5589305	642302	1603	Fracture Zone	242	71	High		1	Ser-Chl-Qz-Lm			Propylitic	Skeena
2015KB234	5589722	642104	1563	Vein	21	86	High	1	3	Tur-Ep	60	Ep-Ser	Propylitic	Skeena
2015KB234	5589722	642104	1563	Veinlet	120	84	High	1.5	1	Ep	15	Chl-Ab	Sodic-calcic	Skeena
2015KB235	5590226	641899	1546	Veinlet	181	87	High	2	0.5	Ep	25	Ser-Chl-Kfs	K-feldspar	Skeena
2015KB236A	5590107	642428	1549	Vein	307	89	High	0.5		Qz-Tur-Ms	10	Ms	Muscovite	Skeena
2015KB236B	5590107	642428	1549	Veinlet	220	80	High	2		Ep	15	Ab-Chl	Sodic-calcic	Skeena
2015KB237	5590335	642165	1535	Veinlet	110	50	High	2.5	1	Ep	25	Chl-Ab-Ser	Sodic-calcic	Skeena
2015KB238	5590225	642762	1550	Veinlet	34	77	High	2	1.5	Ep-Tur-Chl	20	Chl-Hem-Kfs	K-feldspar	Skeena
2015KB238	5590225	642762	1550	Veinlet	139	81	High	0.5	0.5	Ser	12	Ser-Chl	Propylitic	Skeena
2015KB238	5590225	642762	1550	Fracture halo	20	67	High	1.2	0.5	Ep-Chl-Kfs	7	Kfs	K-feldspar	Skeena
2015KB239	5590742	642906	1491	Fracture halo	14	69	High	2	0.5	Chl-Ep-Hem	5	Kfs	K-feldspar	Skeena
2015KB239	5590742	642906	1491	Fracture halo	260	44	High	0.5	0.5	Chl-Ep-Hem			Propylitic	Skeena
2015KB239	5590742	642906	1491	Veinlet	29	80	High	0.2		Ep-Chl	25	Chl-Ser	Propylitic	Skeena

Station ID	Northing (m)	Easting (m)	Elev (m)	Vein type	Strike	Dip	Conf	Density /m	Vein width (mm)	Vein minerals	Selvage width (mm)	Selvage minerals	Alteration	Lithology
2015KB240	5590742	642906	1491	Fracture halo	38	39	High		0.5	Ep-Chl	10	Chl	Propylitic	Skeena
2015KB240	5590742	642906	1491	Fracture halo	137	85	High				15	Ep-Ser	Propylitic	Skeena
2015KB240	5590983	642002	1457	Veinlet	11	50	Med			Ep		Ser-Chl	Propylitic	Skeena
2015KB241	5590983	642002	1457	Veinlet	118	71	High	0.5	1	Ep	12	Chl-Ser-Ab	Sodic-calcic	Skeena
2015KB241	5590983	642002	1457	Veinlet	122	80	Med	0.1	0.5	Qz	25	Ser-Chl	Propylitic	Skeena
2015KB243	5591322	642548	1375	Vein	7	15	High	3	15	Ep-Qz	80	Ab-Chl	Sodic-calcic	Skeena
2015KB243	5591322	642548	1375	Veinlet	80	1	High	3.5	1	Ep	30	Ab-Chl	Sodic-calcic	Skeena
2015KB244	5591542	639633	1445	Fracture halo	155	77	High	2.5	0.5	Chl-Ep	5	Chl-Ser-Ep	Propylitic	Skeena
2015KB244	5591542	639633	1445	Veinlet	21	80	High	2		Chl-Ep	10	Chl-Ser-Ep	Propylitic	Skeena
2015KB246	5591811	641901	1399	Fracture halo	225	67	High	10	0.5	Chl-Ep	7	Chl-Ser	Propylitic	Skeena
2015KB246	5591811	641901	1399	Fracture halo	109	89	High	1	0.5	Ep-Hem			Propylitic	Skeena
2015KB246	5591811	641901	1399	Fracture halo	129	89	High	0.5	0.5	Ep-Hem			Propylitic	Skeena
2015KB246	5591811	641901	1399	Vein	10	42	High	0.1		Ep	25	Ab-Chl-Ser	Sodic-calcic	Skeena
2015KB248	5592106	641927	1359	Fracture halo	95	80	High	0.6	0.5	Ccp-Hem	7.5	Ser	Muscovite	Skeena
2015KB248	5592106	641927	1359	Veinlet	352	79	High	0.5	2	Ep-Ser	30	Ser-Chl	Propylitic	Skeena
2015KB249	5592278	642119	1314	Veinlet	132	81	High	0.5	1	Chl-Ep			Propylitic	Skeena
2015KB249	5592278	642119	1314	Fracture halo	345	60	High	0.5	0.5	Ep-Qz			Propylitic	Skeena
2015KB250A	5591903	639686	1405	Vein	190	79	High	3	4	Ep-Qz-Ccp	5	Chl	Propylitic	Skeena
2015KB250A	5591903	639686	1405	Vein	45	20	High	1	25	Qz-Cb-Py	17.5	Ser	Muscovite	Skeena
2015KB250A	5591903	639686	1405	Vein	223	81	High	4	0.5	Chl-Ser			Propylitic	Skeena
2015KB251B	5591620	643098	1346	Vein	3	81	High	0.5	2	Ep	20	Ab-Chl	Sodic-calcic	QFP
2015KB251B	5591620	643098	1346	Vein	27	50	High	0.5	2	Ep-Lm-CuOx	10	Ser-Chl	Propylitic	QFP
2015KB252	5591356	643130	1401	Vein	191	78	High	3	2	Ep-Chl	15	Ser-Chl	Propylitic	Skeena
2015KB252	5591356	643130	1401	Vein	263	77	High	1	2	Ep-Chl	15	Ser-Chl	Propylitic	Skeena
2015KB253A	5591366	643540	1414	Veinlet	11	80	High	4	0.5	Chl-Ser-Ccp			Muscovite	Skeena
2015KB253A	5591366	643540	1414	Veinlet	240	75	High	2.5	0.5	Chl-Ser-Lm			Propylitic	Skeena
2015KB254	5591038	643312	1468	Veinlet	9	80	Low	0.25	0.5	Lm-Chl			Propylitic	Skeena
2015KB254	5591038	643312	1468	Fracture halo	85	75	Low	0.5			17	Ser-Chl	Propylitic	Skeena
2015KB254	5591038	643312	1468	Fracture coating	61	79	Low	0.15	0.5	Ep-Chl-Lm	5	Ser	Propylitic	Skeena
2015KB255	5590926	643708	1478	Veinlet	296	83	High	0.75	1.5	Ser-Qz-Lm	15	Ser-Chl	Propylitic	Skeena
2015KB255	5590926	643708	1478	Veinlet	232	80	High		1.5	Ser-Qz	15	Ser-Chl	Propylitic	Skeena
2015KB256	5590318	643200	1530	Veinlet	36	82	High	2	0.5	Lm-Ccp-Py	10	Ser	Muscovite	Skeena
2015KB256	5590318	643200	1530	Vein	8	70	High	0.15	3	Ep-Lm-CuOx	15	Sp-Chl	Propylitic	Skeena
2015KB257	5590476	643695	1541	Veinlet	179	72	High	5	1.5	Ep-Qz-Chl	25	Ser-Chl	Propylitic	Skeena
2015KB257	5590476	643695	1541	Fracture coating	154	50	High	2	1	Ep-Qz-Chl	10	Ser	Propylitic	Skeena
2015KB258	5590631	643316	1539	Fracture coating	36	80	Med	0.75	0.5	Lm-Hem-Ser	5	Ser-Chl	Propylitic	Skeena
2015KB259A	5591650	643629	1374	Veinlet	4	88	Low	0.5	0.5	Lm-Ccp-Py	5	Ser	Muscovite	Skeena
2015KB259A	5591650	643629	1374	Veinlet	120	83	Low	0.5	1	Ser-Chl	15	Ser-Chl	Propylitic	Skeena
2015KB260	5589030	642037	1597	Fracture coating	242	64	High	4	0.5	Ser-Chl	5	Ser	Propylitic	Skeena
2015KB260	5589030	642037	1597	Veinlet	164	63	High	0.5	1	Ep-Chl-Tur	5	Ser	Propylitic	Skeena
2015KB260	5589030	642037	1597	Veinlet	47	65	High	4.5	1	Ser-Lm-CuOx	5	Ser-Chl	Propylitic	Skeena
2015KB261	5596081	644872	1484	Veinlet	269	78	High	0.25	0.5	Ep	5	Chl-Ser-Hem	Propylitic	Guichon
2015KB261	5596081	644872	1484	Fracture halo	276	80	High	0.25	0.5	Ep-Bn	20	Ser-Chl	Muscovite	Guichon
2015KB262	5596390	644766	1518	Veinlet	341	82	High	2	2	Ep-Ccp	12	Ser-Ccp-Hem	Muscovite	Guichon
2015KB263	5596571	645078	1478	Veinlet	274	70	High	0.5	1	Ep-Hem	7	Chl-Kfs-Hem	K-feldspar	Guichon

Station ID	Northing (m)	Easting (m)	Elev (m)	Vein type	Strike	Dip	Conf	Density /m	Vein width (mm)	Vein minerals	Selvage width (mm)	Selvage minerals	Alteration	Lithology
2015KB265	5588443	642526	1644	Vein	262	70	High	2	10	Qz-Ccp-Bn	5	Ms-Chl	Muscovite	Skeena
2015KB265	5588443	642526	1644	Fracture coating	35	75	High	0.75	0.5	Ep-Chl-Cal			Propylitic	Skeena
2015KB266A	5588280	642490	1644	Vein	310	80	High	10		Tur-Qz		Ser	Propylitic	QFP
2015KB268	5588124	642328	1643	Veinlet	120	75	High	2	3	Ser-Ccp-Qz	20	Ser-Chl	Muscovite	Skeena
2015KB268	5588128	642335	1643	Vein	356	88	High	0.1	50	Qz-Tur-Ep	15	Ab-Chl	Sodic-calcic	Skeena
2015KB269	5588054	642296	1646	Vein	110	75	High	3.5	12	Qz-Bn	5	Kfs	K-feldspar	Skeena
2015KB269	5588054	642296	1646	Vein	110	75	High	5	10	Qz-Bn-Ccp	10	Ms	Muscovite	Skeena
2015KB270	5588281	642180	1645	Vein	310	80	High	10		Tur-Qz		Ser-Chl	Propylitic	QFP
2015KB271	5588201	642152	1646	Vein	115	78	High	3	25	Qz-Ccp	15	Ms	Muscovite	Skeena
2015KB271	5588201	642152	1646	Vein	100	80	High	0.5	10	Qz		Kfs	K-feldspar	Skeena
2015KB272	5588119	642125	1650	Vein	130	70		8	10	Qz-Bn-Ccp	10	Ms	Muscovite	Skeena
2015KB272	5588119	642125	1650	Vein	230	80		1.5	10	Qz-Bn-Ccp	5	Ms	Muscovite	Skeena
2015KB272	5588119	642125	1650	Vein	128	72		2	15	Qz	10	Kfs	K-feldspar	Skeena
2015KB272A	5588122	642001	1650	Vein	130	75		0.25	10	Qz-Ccp	10	Ms	Muscovite	Skeena
2015KB272B	5588370	642025	1650	Vein	310	80		0.1	5	Qz-Ccp	10	Ms	Muscovite	Skeena
2015KB273	5588681	642506	1536	Vein	135	75		0.5	10	Qz-Bn	10	Ms	Muscovite	Skeena
2015KB273	5588681	642506	1536	Vein	220	60		0.12	50	Qz-Mol-Bn	40	Ser-Chl	Muscovite	Skeena
2015KB273	5588681	642506	1536	Vein	290	80		0.1	5	Ep	12	Ab-Chl	Sodic-calcic	Skeena
2015KB274	5588720	642263	1580	Veinlet	95	90		0.15	1	Ep	15	Ab-Chl	Sodic-calcic	Skeena
2015KB274	5588720	642263	1580	Vein	230	60		0.75	20	Qz-Mol-Ccp	200	Ser-Chl	Muscovite	Skeena
2015KB275	5588902	642059	1593	Veinlet	340	80		2	1	Ser-Chl	25	Ser-Chl	Propylitic	Skeena
2015KB275	5588902	642059	1593	Veinlet	225	70		3	1	Ser-Chl	25	Ser-Chl	Propylitic	Skeena
2015KB276	5589062	640869	1563	Veinlet	285	52		6	0.5	Act	2.5		Sodic-calcic	Skeena
2015KB276	5589062	640869	1563	Veinlet	132	80		2	0.5	Qz-Mol-Bn	10	Ser-Chl	Muscovite	Skeena
2015KB277	5589001	640888	1561	Vein	280	70		5	20	Ep	100	Ab-Act-Chl	Sodic-calcic	Skeena
2015KB277A	5589200	640965	1561	Vein	20	60		0.15	15	Qz-Mol-Bn	20	Ser-Chl	Muscovite	Skeena
2015KB277A	5589200	640965	1561	Vein	280	80		2	5	Qz	5	Kfs	K-feldspar	Skeena
2015KB278	5589025	640854	1593	Vein	285	70		3	20	Ep-Act	50	Ab	Sodic-calcic	Skeena
2015KB278	5589025	640854	1593	Veinlet	25	80		2	10	Ep-Act	50	Ab	Sodic-calcic	Skeena
2015KB279	5588954	640894	1593	Vein	20	70		4	2	Act-Chl-Ep	30	Ab	Sodic-calcic	Skeena
2015KB279	5588954	640894	1593	Vein	50	70		0.1	30	Qz-Mol-Bn	50	Ser	Muscovite	Skeena
Teck-2012-002	5596450	642937	1545	Veinlet	1	90		0.63	4	Tur-Qz	10	Ep	Propylitic	
Teck-2012-004	5596080	643498	1558	Veinlet	8	90		2	2	Tur-Qz	10	Ep	Propylitic	
Teck-2012-007	5596110	643492	1559	Veinlet	8	90		2	3	Chl-Ep-Ccp	10	Chl	Propylitic	
Teck-2012-008	5596100	643496	1559	Veinlet	5	90		2	2	Ep-Ccp	10	Chl	Propylitic	
Teck-2012-009	5596100	643474	1558	Veinlet	35	90		2	5	Chl-Ep	10	Chl	Propylitic	
Teck-2012-013	5595930	643738	1572	Veinlet	98	90		2.5	5	Ep-Qz	0		Propylitic	
Teck-2012-014	5595930	643747	1572	Veinlet	53	90		2.5	5	Ep-Qz	0		Propylitic	
Teck-2012-015	5595940	643747	1572	Veinlet	17	90		2.5	2	Tur	30	Ep	Propylitic	
Teck-2012-016	5595960	643756	1580	Veinlet	274	28		4	2	Ep	0		Propylitic	
Teck-2012-023	5597040	644058	1527	Fracture halo	35	90			0	Chl	100	Chl	Propylitic	
Teck-2012-024	5596270	643779	1565	Veinlet	14	90			2	Ep	0	Kfs	K-feldspar	
Teck-2012-025	5596340	643752	1568	Vein	34	90		0.5	10	Ep	0		Propylitic	
Teck-2012-026	5596330	643750	1568	Veinlet	24	90			3	Ep-Qz	0		Propylitic	
Teck-2012-027	5596270	643681	1560	Vein	356	90		0.5	10	Ep-Tur-Ccp	5	Chl	Propylitic	

Station ID	Northing (m)	Easting (m)	Elev (m)	Vein type	Strike	Dip	Conf	Density /m	Vein width (mm)	Vein minerals	Selvage width (mm)	Selvage minerals	Alteration	Lithology
Teck-2012-030	5596300	643534	1561	Veinlet	5	90			2	Chl-Ep	0		Propylitic	
Teck-2012-031	5596290	643531	1561	Veinlet	33	90			2	Chl-Ep	0		Propylitic	
Teck-2012-032	5596310	643535	1566	Vein	6	90			20	Chl-Ep	0	Chl	Propylitic	
Teck-2012-033	5596390	643550	1571	Veinlet	16	90			5	Ep-Qz	10	Ep	Propylitic	
Teck-2012-034	5596440	643557	1569	Veinlet	216	90			3	Ep	0		Propylitic	
Teck-2012-035	5596440	643531	1575	Veinlet	78	90			1	Chl-Ep	0	Chl	Propylitic	
Teck-2012-037	5596410	643472	1563	Veinlet	69	90		0.67	1	Ep-Tur	5	Ep	Propylitic	
Teck-2012-038	5596380	643499	1571	Veinlet	12	90		0.67	3	Ep-Qz	10	Ep	Propylitic	
Teck-2012-039	5596380	643501	1571	Vein	2	90		0.5	10	Ep-Qz-Ccp	10		Propylitic	
Teck-2012-041	5596470	643473	1560	Vein	21	90		1	10	Chl-Ep	5	Chl	Propylitic	
Teck-2012-042	5596470	643479	1564	Vein	91	90		1	10	Chl-Ep	5	Chl	Propylitic	
Teck-2012-047	5595800	643684	1548	Veinlet	6	48		1	2	Ep-Chl	0		Propylitic	
Teck-2012-053	5596780	644036	1541	Veinlet	184	64			0	Chl	0		Propylitic	
Teck-2012-058	5596400	644293	1515	Veinlet	19	75			2	Ep	0		Propylitic	
Teck-2012-061	5596440	644175	1532	Veinlet	65	90			1	Ep-Qz	0	Kfs	K-feldspar	
Teck-2012-062	5596420	644159	1534	Veinlet	65	90		5	2	Chl	3	Chl	Propylitic	
Teck-2012-066	5596420	644161	1534	Veinlet	75	90			1	Ep	0		Propylitic	
Teck-2012-068	5596370	644088	1549	Veinlet	62	76			2	Chl-Ep	4	Kfs	K-feldspar	
Teck-2012-071	5596380	644005	1555	Veinlet	75	90		0.5	3	Ep	2	Kfs	K-feldspar	
Teck-2012-072	5596440	644324	1517	Veinlet	35	90			1	Ep	0	Kfs	K-feldspar	
Teck-2012-077	5596260	644259	1519	Veinlet	58	90		0.5	2	Ep	0	Kfs	K-feldspar	
Teck-2012-078	5596250	644261	1519	Veinlet	11	90		0.5	2	Ep	10	Kfs	K-feldspar	
Teck-2012-079	5596260	644257	1515	Veinlet	2	90			1	Chl	0		Propylitic	
Teck-2012-082	5596210	644297	1529	Veinlet	248	90			1	Ep-Chl	0	Ep	Propylitic	
Teck-2012-083	5596210	644300	1529	Veinlet	11	90			1	Ep-Chl-CuOx	0	Kfs	K-feldspar	
Teck-2012-086	5596120	644295	1527	Veinlet	95	90		0.67	1	Ep	3	Kfs	K-feldspar	
Teck-2012-086	5596120	644295	1527	Veinlet	74	90		0.67	1	Ep	3	Kfs	K-feldspar	
Teck-2012-087	5596090	644237	1528	Veinlet	67	90		0.5	1	Ep-Qz	0		Propylitic	
Teck-2012-090	5596060	644177	1525	Veinlet	78	90			3	Ep	80	Kfs	K-feldspar	
Teck-2012-092	5595890	644192	1535	Veinlet	4	90			1	Ep-Chl-CuOx	0		Propylitic	
Teck-2012-093	5595960	642295	1497	Vein	134	44		2	10	Ep-Qz-Ccp-CuOx	5	Chl	Propylitic	
Teck-2012-094	5595960	642299	1497	Fracture halo	27	72			0	Ep	0.5	Chl	Propylitic	
Teck-2012-102	5595890	642310	1501	Veinlet	238	26		2	1	Ep-Chl	10	Kfs	K-feldspar	
Teck-2012-103	5595880	642309	1499	Veinlet	233	88		3.33	2	Ep-Chl	25	Kfs	K-feldspar	
Teck-2012-104	5595880	642293	1493	Veinlet	213	89		2.5	2	Ep-Qz	8	Kfs	K-feldspar	
Teck-2012-108	5595780	642406	1476	Fracture halo	186	45			1	Ep-Chl-CuOx	0.5	Chl	Propylitic	
Teck-2012-109	5595790	642425	1478	Vein	184	72		20	10	Ep-Qz-Spec	30	Chl	Propylitic	
Teck-2012-110	5595800	642431	1477	Vein	113	77		10	10	Ep-Qz-CuOx	5	Chl	Propylitic	
Teck-2012-112	5595810	642437	1477	Vein	113	77		10	10	Ep-Qz-Spec	6	Chl	Propylitic	
Teck-2012-113	5595820	642441	1484	Vein	191	72		20	10	Ep-Qz-Spec	30	Chl	Propylitic	
Teck-2012-114	5595830	642441	1484	Vein	115	77		10	10	Ep-Qz	6	Chl	Propylitic	
Teck-2012-116	5595860	644173	1533	Veinlet	115	85			1	Ep-Ser	20	Kfs	K-feldspar	
Teck-2012-119	5595790	644160	1530	Veinlet	98	25		1	2	Chl-Ep	0		Propylitic	
Teck-2012-120	5595770	644131	1528	Veinlet	33	85		2.86	1	Ep	10	Kfs	K-feldspar	
Teck-2012-121	5595760	644130	1528	Veinlet	277	58		1	2	Chl-Ep-Ccp	4	Ep	Propylitic	

Station ID	Northing (m)	Easting (m)	Elev (m)	Vein type	Strike	Dip	Conf	Density /m	Vein width (mm)	Vein minerals	Selvage width (mm)	Selvage minerals	Alteration	Lithology
Teck-2012-124	5595710	644073	1533	Vein	53	90		2	8	Ep-Qz	30	Kfs	K-feldspar	
Teck-2012-126	5595680	644032	1541	Veinlet	33	90		1	1	Ep	50	Kfs	K-feldspar	
Teck-2012-128	5595620	644019	1545	Veinlet	356	90			4	Mag	20	Ep	Propylitic	
Teck-2012-129	5595600	644010	1542	Veinlet	7	45		10	3	Ep	40	Chl	Propylitic	
Teck-2012-131	5595670	644259	1525	Veinlet	8	90			1	Ep	0		Propylitic	
Teck-2012-134	5595590	644185	1536	Veinlet	1	90		1	3	Ep-Chl	40	Chl	Propylitic	
Teck-2012-136	5595580	644170	1529	Veinlet	23	90		1	3	Ep-Tur	40		Propylitic	
Teck-2012-137	5595520	644101	1533	Veinlet	0.8	90			1	Ep-Qz	0	Chl	Propylitic	
Teck-2012-141	5595450	643992	1533	Veinlet	3	68		20	2	Chl	30	Ep	Propylitic	
Teck-2012-142	5595430	644018	1540	Vein	42	52		1	8	Ep	50	Chl	Propylitic	
Teck-2012-144	5595410	643978	1527	Veinlet	2	63		1.25	3	Ep-Chl	60	Ep	Propylitic	
Teck-2012-146	5595380	644001	1530	Vein	124	42			10	Ep-Qz	0		Propylitic	
Teck-2012-148	5595480	644175	1537	Veinlet	7	76			1	Chl	0		Propylitic	
Teck-2012-149	5595480	644178	1537	Veinlet	7	76			1	Chl	0		Propylitic	
Teck-2012-151	5595480	644207	1537	Vein	6	75			10	Ep	50	Chl	Propylitic	
Teck-2012-153	5595460	644245	1531	Fracture coating	85	90			0.5	Ep	0		Propylitic	
Teck-2012-154	5595410	644142	1526	Veinlet	344	75		2.5	4	Ep-Qz	5		Propylitic	
Teck-2012-155	5595410	644145	1526	Veinlet	7	90		2.5	4	Ep-Qz-Ccp	5		Propylitic	
Teck-2012-156	5595400	644150	1526	Fracture halo	8	90			0	Ser-Ccp	100	Ser	Muscovite	
Teck-2012-157	5595400	644147	1526	Fracture halo	173	90			0	Ser	100	Ser	Propylitic	
Teck-2012-159	5595360	644312	1526	Veinlet	6	56			1	Ep	0	Ep	Propylitic	
Teck-2012-160	5595350	644311	1526	Veinlet	344	90			1	Ep	0		Propylitic	
Teck-2012-163	5595330	644330	1523	Vein	83	78		0.5	10	Ep	15	Chl	Propylitic	
Teck-2012-169	5595180	644327	1508	Veinlet	64	68		6.25	3	Ep-Qz	2	Chl	Propylitic	
Teck-2012-174	5595290	644160	1534	Vein	92	86		1	2	Ep-Qz-Ccp	1	Chl	Propylitic	
Teck-2012-175	5595280	644154	1531	Fracture coating	5	90			0.5	Ep-Qz	0	Chl	Propylitic	
Teck-2012-180	5595120	644144	1513	Veinlet	8	83		0.83	3	Ep-Qz	0		Propylitic	
Teck-2012-182	5595130	644041	1506	Veinlet	248	64		3.33	1	Ep	5	Chl	Propylitic	
Teck-2012-183	5595140	644037	1506	Veinlet	352	65		2.22	1	Chl-Ccp	0		Propylitic	
Teck-2012-185	5595030	644041	1505	Fracture halo	29	58			0	Chl	0.5		Propylitic	
Teck-2012-189	5595040	644214	1510	Veinlet	5	74		1	3	Ep-Ccp	10	Chl	Propylitic	
Teck-2012-190	5595050	644147	1514	Vein	27	68		1	8	Ep	10	Chl	Propylitic	
Teck-2012-195	5594940	644289	1488	Veinlet	78	65		3.33	1	Chl-Ccp	10	Chl	Propylitic	
Teck-2012-196	5594890	644300	1472	Veinlet	78	65		4	1	Chl	10	Chl	Propylitic	
Teck-2012-201	5594850	644042	1504	Veinlet	8	65		0.67	2	Qz-Ep	5	Kfs	K-feldspar	
Teck-2012-202	5594810	644014	1500	Vein	4	90		3.33	3	Qz-Ccp	0	Ep	Propylitic	
Teck-2012-203	5594430	644353	1474	Vein	11	85		0.50	6	Ep-Qz-Ccp	20	Chl	Propylitic	
Teck-2012-204	5594430	644353	1478	Vein	11	85		0.5	6	Chl	20	Chl	Propylitic	
Teck-2012-205	5594510	644393	1494	Fracture halo	285	65		20	0.5	Chl	0		Propylitic	
Teck-2012-208	5594190	644280	1413	Veinlet	88	90		1	3	Ep-Chl	0		Propylitic	
Teck-2012-212	5595990	644492	1512	Veinlet	3	23			3	Ep	0		Propylitic	
Teck-2012-213	5595990	644557	1506	Veinlet	6	90			2	Ep	5	Kfs	K-feldspar	
Teck-2012-214	5595970	644566	1506	Veinlet	58	90			3	Chl-Qz	9	Chl	Propylitic	
Teck-2012-215	5595550	644638	1519	Veinlet	63	90			1	Chl-Lm	10		Propylitic	
Teck-2012-216	5595510	644556	1524	Fracture coating	117	90			0.5	Ep-Qz	1000	Chl	Propylitic	

Station ID	Northing (m)	Easting (m)	Elev (m)	Vein type	Strike	Dip	Conf	Density /m	Vein width (mm)	Vein minerals	Selvage width (mm)	Selvage minerals	Alteration	Lithology
Teck-2012-217	5595520	644577	1524	Veinlet	5	90			2	Ep-Chl	15	Ep	Propylitic	
Teck-2012-218	5595510	644570	1524	Veinlet	13	90			2	Ep-Chl	15	Ep	Propylitic	
Teck-2012-219	5595300	644499	1509	Veinlet	25	89			2	Ep-Qz	10	Ep	Propylitic	
Teck-2012-220	5595290	644491	1506	Fracture halo	1	82			0.5	Chl	0		Propylitic	
Teck-2012-221	5595260	644477	1507	Veinlet	91	24			3	Ep	20	Chl	Propylitic	
Teck-2012-225	5595000	644435	1470	Veinlet	68	82			3	Ep-Qz-Bn	5	Chl	Propylitic	
Teck-2012-226	5594020	644504	1373	Vein	35	75			10	Chl-Tur-Bn	10	Chl	Propylitic	
Teck-2012-230	5594030	644471	1369	Fracture coating	86	64			0.5	Ep-Qz	0	Chl	Propylitic	
Teck-2012-231	5594040	644450	1365	Vein	18	58		5	5	Ep-Ccp-CuOx	10		Propylitic	
Teck-2012-237	5594170	644458	1444	Vein	285	73		1	6	Ep-Qz	10	Kfs	K-feldspar	
Teck-2012-240	5594190	644532	1461	Veinlet	296	78		0.5	6	Qz	20	Chl	Propylitic	
Teck-2012-243	5594190	644573	1463	Vein	264	48			30	Ep-Qz	20	Chl	Propylitic	
Teck-2012-244	5594170	644603	1457	Veinlet	94	85		0.5	1	Ep	0		Propylitic	
Teck-2012-247	5594200	644677	1469	Veinlet	113	72		20	2	Chl-Ep	0		Propylitic	
Teck-2012-250	5594260	644829	1462	Veinlet	8	85			4	Ep-Qz	10	Chl	Propylitic	
Teck-2012-251	5594270	644817	1463	Vein	124	73		3.33	8	Ep	3	Chl	Propylitic	
Teck-2012-255	5594200	644897	1457	Veinlet	18	89		50	2	Chl	0		Propylitic	
Teck-2012-260	5594000	644935	1405	Veinlet	24	48		0.5	2	Chl	30	Ep	Propylitic	
Teck-2012-261	5594020	644927	1418	Veinlet	116	85			2	Ep-Qz	0		Propylitic	
Teck-2012-275	5596140	642510	1521	Vein	237	57			10	Ep-Qz	100	Chl	Propylitic	
Teck-2012-280	5596150	642587	1508	Veinlet	165	69		10	2	Qz-Ep-Lm	8	Chl	Propylitic	
Teck-2012-283	5596140	642576	1503	Veinlet	12	90		2.5	2	Qz	15	Ep	Propylitic	
Teck-2012-286	5596130	642566	1508	Veinlet	118	69		0.33	2	Ep-Chl	20	Chl	Propylitic	
Teck-2012-290	5596110	642535	1511	Vein	236	90		3.33	10	Ep-Qz	40	Chl	Propylitic	
Teck-2012-301	5595500	642374	1516	Vein	343	45			10	Ep-Qz-Ccp-CuOx	10	Chl	Propylitic	
Teck-2012-302	5595570	642423	1521	Veinlet	68	90		4	2	Ep-Qz-CuOx	0		Propylitic	
Teck-2012-303	5595550	642422	1529	Vein	5	22		33.33	10	Ep-Spec	3	Chl	Propylitic	
Teck-2012-307	5595530	642413	1531	Veinlet	16	90		25	3	Ep	10	Kfs	K-feldspar	
Teck-2012-310	5595530	642411	1531	Vein	2	58			15	Ep-Qz-Spec	20	Kfs	K-feldspar	
Teck-2012-313	5595540	642432	1529	Vein	148	35		5.56	7	Ep-Qz	7	Chl	Propylitic	
Teck-2012-318	5595550	642483	1532	Fracture halo	48	65		6.67	0	Chl	0.5	Ser	Propylitic	
Teck-2012-320	5595550	642488	1532	Veinlet	82	38		3.33	1	Ep	1	Chl	Propylitic	
Teck-2012-321	5595560	642500	1533	Veinlet	43	48			2	Ep-Ccp	2	Chl	Propylitic	
Teck-2012-330	5595520	642447	1538	Veinlet	67	78		33.33	3	Ep-CuOx	1	Chl	Propylitic	
Teck-2012-331	5595500	642436	1540	Fracture halo	3	38			0	Chl-Bn-CuOx	0		Propylitic	
Teck-2012-333	5595500	642480	1546	Vein	18	55		20	7	Ep-Qz-CuOx	2	Chl	Propylitic	
Teck-2012-335	5595520	642510	1542	Veinlet	61	82		2	1	Ep	0		Propylitic	
Teck-2012-336	5595510	642503	1549	Veinlet	61	82		2	1	Ep	0		Propylitic	
Teck-2012-351	5595420	642489	1557	Veinlet	138	68			0	Ep-CuOx	0	Chl	Propylitic	
Teck-2012-353	5595410	642456	1554	Vein	151	64		20	8	Ep-Qz-Bn-CuOx	1	Chl	Propylitic	
Teck-2012-354	5595400	642455	1552	Vein	16	64		20	8	Ep-Qz	1	Chl	Propylitic	
Teck-2012-356	5595930	642116	1468	Veinlet	224	86		50	2	Ep-Spec	1	Chl	Propylitic	
Teck-2012-357	5595930	642111	1462	Veinlet	11	84		33.33	2	Ep	1	Chl	Propylitic	
Teck-2012-359	5595940	642105	1462	Vein	1	90			30	Ep-Qz	20	Kfs	K-feldspar	
Teck-2012-361	5595940	642090	1458	Fracture halo	228	90			0	Chl	0	Chl	Propylitic	

Station ID	Northing (m)	Easting (m)	Elev (m)	Vein type	Strike	Dip	Conf	Density /m	Vein width (mm)	Vein minerals	Selvage width (mm)	Selvage minerals	Alteration	Lithology
Teck-2012-364	5595930	642081	1453	Veinlet	212	35		50	2	Ep-Qz-Ccp-CuOx	0		Propylitic	
Teck-2012-365	5595940	642070	1447	Veinlet	13	47		20	3	Ep-Qz	10	Kfs	K-feldspar	
Teck-2012-366	5595930	642066	1447	Veinlet	25	58		5	3	Ep-Qz-CuOx	10	Kfs	K-feldspar	
Teck-2012-367	5595950	642015	1439	Vein	17	16		10	20	Qz-Kfs-CuOx	0		K-feldspar	
Teck-2012-372	5595910	641844	1389	Veinlet	2	88		33.33	1	Qz-Ep-Ccp-CuOx	1	Chl	Propylitic	
Teck-2012-373	5595890	641833	1384	Vein	317	62		2.86	5	Ep-Chl-CuOx	10	Kfs	K-feldspar	
Teck-2012-377	5595830	641788	1386	Veinlet	19	84		10	3	Qz-Chl-Ccp-CuOx	2	Kfs	K-feldspar	
Teck-2012-379	5595550	641701	1408	Veinlet	234	64		50	2	Chl	2	Ep	Propylitic	
Teck-2012-380	5595550	641705	1408	Vein	264	72			5	Qz	3	Ep	Propylitic	
Teck-2012-382	5595540	641714	1403	Veinlet	24	90		10	2	Ep-CuOx	1	Chl	Propylitic	
Teck-2012-383	5595540	641711	1408	Veinlet	1	90		50	1	Chl-CuOx	10	Kfs	K-feldspar	
Teck-2012-385	5595530	641714	1403	Veinlet	225	88		6.67	3	Ep-Qz-CuOx	3	Chl	Propylitic	
Teck-2012-388	5595520	641720	1404	Veinlet	3	87		2.86	1	Ep-CuOx	1	Chl	Propylitic	
Teck-2012-392	5595500	641728	1398	Veinlet	35	88		6.67	3	Ep-Chl	10	Kfs	K-feldspar	
Teck-2012-395	5595480	641742	1399	Fracture halo	46	77		10	0.5	Ep-Chl-CuOx	1	Kfs	K-feldspar	
Teck-2012-397	5595470	641745	1393	Fracture halo	42	39		1.54	0.5	Ep-Chl-CuOx	3	Chl	Propylitic	
Teck-2012-399	5595460	641747	1393	Veinlet	124	62		8.33	2	Ep-CuOx	10	Kfs	K-feldspar	
Teck-2012-401	5595450	641759	1399	Veinlet	95	42		2	2	Ep-Chl-CuOx	10	Kfs	K-feldspar	
Teck-2012-403	5595440	641758	1399	Vein	28	90			15	Kfs	0		K-feldspar	
Teck-2012-406	5595440	641763	1399	Veinlet	43	90			5	Chl-CuOx	10	Kfs	K-feldspar	
Teck-2012-408	5595430	641769	1399	Vein	38	90		3.33	15	Kfs-Qz-CuOx	0		K-feldspar	
Teck-2012-412	5595410	641778	1406	Fracture halo	345	48		5	0.5	Ep-Chl-CuOx	0		Propylitic	
Teck-2012-415	5595400	641794	1409	Veinlet	174	62			3	Ep-Chl-CuOx	3	Kfs	K-feldspar	
Teck-2012-417	5595360	641895	1408	Fracture halo	355	56			0.5	Ep-Chl-CuOx	0	Ep	Propylitic	
Teck-2012-418	5595360	641888	1415	Veinlet	14	89		3.33	3	Ep-Qz-Lm	1	Chl	Propylitic	
Teck-2012-424	5595350	641872	1412	Fracture halo	138	82		20	0.5	Chl-CuOx	0		Propylitic	
Teck-2012-425	5595350	641863	1411	Veinlet	2	85		6.67	2	Ep-Qz-Lm	5	Chl	Propylitic	
Teck-2012-426	5595350	641860	1411	Fracture halo	14	82		6.67	0.5	Ep-Chl	0		Propylitic	
Teck-2012-430	5595340	641877	1412	Fracture halo	342	76		5	0.5	Chl-CuOx	0		Propylitic	
Teck-2012-431	5595330	641875	1421	Fracture halo	182	87		5	0.5	Chl	0		Propylitic	
Teck-2012-433	5595320	641869	1421	Veinlet	322	90		3.33	1	Ccp-Chl	1		Propylitic	
Teck-2012-441	5595320	641948	1436	Fracture halo	116	83		5	0.5	Chl-Lm	0		Propylitic	
Teck-2012-445	5595300	641920	1437	Veinlet	215	88		10	2	Chl	0		Propylitic	
Teck-2012-447	5595310	641984	1450	Fracture halo	198	74		20	0.5	Chl	0		Propylitic	
Teck-2012-449	5595300	641968	1447	Vein	23	52		1	8	Ep-Qz-Ccp-CuOx	15	Chl	Propylitic	
Teck-2012-452	5595280	641960	1452	Veinlet	29	87			1	Ep-Qz	30	Chl	Propylitic	
Teck-2012-453	5595280	641963	1452	Veinlet	222	71		3.33	1	Ep	10	Chl	Propylitic	
Teck-2012-454	5595280	641961	1452	Veinlet	34	77		3.33	2	Kfs	1	Chl	K-feldspar	
Teck-2012-455	5595270	641962	1452	Veinlet	4	82		3.33	1		10	Chl	Propylitic	
Teck-2012-456	5595270	641962	1451	Veinlet	38	82		6.67	3	Ep-CuOx	2	Chl	Propylitic	
Teck-2012-461	5595250	641974	1454	Veinlet	342	90		10	3	Ep-Qz	5	Chl	Propylitic	
Teck-2012-463	5595280	642009	1462	Vein	28	90		5	7	Ep-Qz-CuOx	20	Chl	Propylitic	
Teck-2012-464	5595280	642017	1465	Veinlet	38	90		6.67	4	Ep-CuOx	1	Chl	Propylitic	
Teck-2012-465	5595280	642023	1465	Veinlet	38	90		6.67	4	Ep	1	Chl	Propylitic	
Teck-2012-466	5595280	642028	1465	Veinlet	356	90		1.25	5	Ep-Qz-CuOx	3	Chl	Propylitic	

Station ID	Northing (m)	Easting (m)	Elev (m)	Vein type	Strike	Dip	Conf	Density /m	Vein width (mm)	Vein minerals	Selvage width (mm)	Selvage minerals	Alteration	Lithology
Teck-2012-467	5595270	642029	1465	Veinlet	43	90		10	1	Ep-Spec-Ccp-CuOx	1	Chl	Propylitic	
Teck-2012-469	5595270	642044	1469	Veinlet	26	54		1	2	Ep-CuOx	4	Chl	Propylitic	
Teck-2012-470	5595280	642050	1470	Veinlet	214	73		6.67	2	Ep-CuOx	3	Chl	Propylitic	
Teck-2012-471	5595280	642052	1470	Vein	24	90		0.5	10	Qz-Ep	30	Chl	Propylitic	
Teck-2012-472	5595280	642062	1473	Veinlet	211	78		10	4	Ep	10	Chl	Propylitic	
Teck-2012-474	5595290	642068	1473	Veinlet	332	90		6.67	3	Ep	17	Chl	Propylitic	
Teck-2012-479	5595280	642130	1487	Veinlet	192	76		10	2	Ep-CuOx	2	Chl	Propylitic	

Appendix C. Sample location, lithology and alteration descriptions. Coordinates in UTM NAD1983 Zone 10.

Sample ID	Station ID	Northing (m)	Easting (m)	Elev (m)	Lithology	Alteration	Alteration intensity	Distance to deposit	Nearest deposit
2232401	2015GL091	5585179	639819	1578	Bethsaida	Sodic-calcic	Strong	3297	Highmont
2232402	2015GL092	5584880	639874	1568	Bethsaida	Sodic-calcic	Strong	3553	Highmont
2232403	2015GL093	5594416	637225	1429	Bethsaida	Muscovite-bearing	Trace	418	Valley
2232404	2015GL094	5594684	636429	1427	QFP	Muscovite-bearing	Moderate	1225	Valley
2232405	2015GL095	5594550	636179	1444	Bethsaida	Intermediate argillic	Weak	1402	Valley
2232406	2015GL096	5589507	639267	1428	FZ	Intermediate argillic	Strong	0	Lornex
2232407	2015GL096	5589520	639256	1426	FZ	Intermediate argillic	Strong	0	Lornex
2232408	2015GL097	5589509	639286	1432	Bethsaida	Intermediate argillic	Strong	0	Lornex
2232409	2015GL097	5589505	639293	1435	Bethsaida	Intermediate argillic	Strong	0	Lornex
2232412	2015GL098	5589523	639719	1427	Bethsaida	Intermediate argillic	Strong	0	Lornex
2232413	2015GL099	5589526	639753	1430	FZ	Intermediate argillic	Strong	0	Lornex
2232414	2015GL100	5589538	639771	1429	Skeena	Intermediate argillic	Strong	0	Lornex
2232415	2015GL101	5589548	639791	1432	QFP	Intermediate argillic	Strong	0	Lornex
2232416	2015GL102	5589837	640157	1476	Skeena	Intermediate argillic	Strong	113	Lornex
2232417	2015GL103	5589723	640102	1469	QFP	Sodic-calcic	Strong	69	Lornex
2232418	2015GL104	5589918	640179	1482	Skeena	Propylitic	Strong	149	Lornex
2232419	2015GL105	5589696	640076	1460	Skeena	Sodic-calcic	Strong	69	Lornex
2232420	2015GL106	5589648	640036	1455	QFP	Intermediate argillic	Strong	100	Lornex
2232421	2015GL107	5589604	639935	1441	Skeena	Intermediate argillic	Strong	79	Lornex
2232423	2015GL108	5589599	639929	1442	Skeena	Intermediate argillic	Strong	75	Lornex
2232424	2015GL109	5589586	639899	1436	Skeena	Muscovite-bearing	Strong	55	Lornex
2232425	2015GL110	5589571	639869	1434	Skeena	K-feldspar-bearing	Moderate	34	Lornex
2232426	2015GL111	5589548	639799	1425	Skeena	Sodic-calcic	Strong	0	Lornex
2232427	2015GL112	5589897	638956	1434	Bethsaida	Sodic-calcic	Strong	3733	Valley
2232428	2015GL113	5589752	639055	1435	Bethsaida	Propylitic	Moderate	3876	Valley
2232429	2015GL114	5589638	639121	1437	Bethsaida	Propylitic	Strong	3990	Valley
2232430	2015GL115	5589487	639534	1433	Bethsaida	Muscovite-bearing	Weak	0	Lornex
2232431	2015GL116	5589498	639510	1434	Bethsaida	Muscovite-bearing	Strong	0	Lornex
2232432	2015GL117	5589502	639632	1426	Bethsaida	Muscovite-bearing	Strong	0	Lornex
2232435	2015GL118	5593922	637980	1262	Bethsaida	Muscovite-bearing	Strong	0	Valley
2232436	2015GL119	5593916	637893	1261	Bethsaida	K-feldspar-bearing	Moderate	0	Valley
2232437	2015GL120	5593902	637708	1272	Bethsaida	K-feldspar-bearing	Strong	0	Valley
2232438	2015GL121	5593674	638529	1251	Salt and Pepper Bethsaida	Intermediate argillic	Strong	229	Valley
2232439	2015GL122	5593695	638478	1248	QFP	Intermediate argillic	Strong	256	Valley
2232440	2015GL123	5593951	638187	1251	QFP	K-feldspar-bearing	Strong	3	Valley
2232441	2015GL124	5593944	638143	1263	QFP	Intermediate argillic	Strong	0	Valley
2232442	2015GL125	5593893	638261	1248	Bethsaida	K-feldspar-bearing	Moderate	89	Valley
2232443	2015GL126	5593803	638356	1250	Bethsaida	Intermediate argillic	Strong	196	Valley
2232444	2015GL127	5593728	638441	1243	Bethsaida	K-feldspar-bearing	Moderate	270	Valley
2232446	2015GL128	5593619	638572	1258	Salt and Pepper Bethsaida	Intermediate argillic	Strong	241	Valley
2232447	2015GL129	5593654	638512	1261	Salt and Pepper Bethsaida	Propylitic	Trace	255	Valley
2238654	2014GL001	5593253	637884	1539	Bethsaida	K-feldspar-bearing	Strong	303	Valley
2238655	2014GL002	5593134	637626	1575	Bethsaida	K-feldspar-bearing	Moderate	301	Valley
2238656	2014GL003	5592985	637365	1614	Bethsaida	K-feldspar-bearing	Weak	453	Valley
2238657	2014GL004	5593089	637128	1639	Bethsaida	K-feldspar-bearing	Weak	453	Valley
2238658	2014GL005	5592762	636954	1668	Bethsaida	K-feldspar-bearing	Weak	821	Valley
2238659	2014GL006	5592728	637244	1638	Bethsaida	Sodic-calcic	Weak	734	Valley
2238660	2014GL007	5592527	637724	1632	Bethsaida	Propylitic	Weak	916	Valley
2238662	2014GL008	5592834	637431	1618	Bethsaida	K-feldspar-bearing	Weak	591	Valley
2238663	2014GL009	5592960	637752	1594	Bethsaida	K-feldspar-bearing	Weak	504	Valley
2238664	2014GL010	5592747	637855	1602	Bethsaida	Muscovite-bearing	Weak	740	Valley
2238665	2014GL011	5592560	637806	1614	Bethsaida	Least Altered	Weak	901	Valley
2238666	2014GL012	5592488	637599	1634	Bethsaida	K-feldspar-bearing	Weak	942	Valley
2238667	2014GL012	5592488	637598	1637	Bethsaida	Sodic-calcic	Moderate	941	Valley
2238668	2014GL013	5592583	637319	1627	Bethsaida	Sodic-calcic	Weak	856	Valley
2238669	2014GL014	5592558	637061	1650	Bethsaida	Least altered	Trace	955	Valley
2238670	2014GL015	5592365	637282	1631	Bethsaida	K-feldspar-bearing	Trace	1077	Valley
2238671	2014GL016	5592348	637120	1652	Bethsaida	Propylitic	Moderate	1134	Valley
2238674	2014GL017	5592119	637141	1665	Bethsaida	Propylitic	Weak	1348	Valley
2238675	2014GL018	5592148	637381	1634	Bethsaida	Propylitic	Moderate	1279	Valley
2238676	2014GL019	5592230	637624	1604	Bethsaida	Propylitic	Weak	1200	Valley
2238677	2014GL020	5592015	637908	1613	Bethsaida	K-feldspar-bearing	Weak	1454	Valley
2238678	2014GL021	5591850	637881	1622	Bethsaida	Propylitic	Weak	1610	Valley

Sample ID	Station ID	Northing (m)	Easting (m)	Elev (m)	Lithology	Alteration	Alteration intensity	Distance to deposit	Nearest deposit
2238679	2014GL022	5591865	637628	1639	Bethsaida	Sodic-calcic	Moderate	1564	Valley
2238680	2014GL023	5592367	637826	1602	Bethsaida	Intermediate argillic	Weak	1093	Valley
2238681	2014GL024	5591412	637142	1665	Bethsaida	Propylitic	Moderate	2040	Valley
2238682	2014GL025	5591696	637119	1653	Bethsaida	Propylitic	Weak	1765	Valley
2238683	2014GL026	5591934	637059	1679	Bethsaida	Propylitic	Weak	1548	Valley
2238685	2014GL027	5591628	637421	1650	Bethsaida	Sodic-calcic	Weak	1796	Valley
2238686	2014GL028	5591606	637613	1635	Bethsaida	Sodic-calcic	Moderate	1822	Valley
2238687	2014GL028	5591603	637637	1637	Bethsaida	K-feldspar-bearing	Weak	1827	Valley
2238688	2014GL029	5591329	637327	1663	Bethsaida	Sodic-calcic	Weak	2100	Valley
2238689	2014GL030	5591355	637673	1666	Bethsaida	Propylitic	Weak	2077	Valley
2238690	2014GL031	5591376	637880	1634	Bethsaida	Propylitic	Moderate	2077	Valley
2238691	2014GL032	5591053	637983	1625	Bethsaida	Least altered	Weak	2412	Valley
2238692	2014GL033	5591134	637706	1669	Bethsaida	Propylitic	Weak	2299	Valley
2238693	2014GL034	5590838	637562	1650	Bethsaida	Least altered	Trace	2587	Valley
2238694	2014GL035	5591579	637974	1603	Bethsaida	Propylitic	Trace	1894	Valley
2238697	2014GL036	5592591	636655	1688	QFP	Propylitic	Strong	1139	Valley
2238698	2014GL036	5592595	636611	1692	Bethsaida	K-feldspar-bearing	Weak	1165	Valley
2238699	2014GL037	5592636	636848	1693	Bethsaida	Sodic-calcic	Weak	985	Valley
2238700	2014GL037	5592640	636859	1694	QFP	Propylitic	Trace	975	Valley
2238701	2014GL038	5592399	636656	1677	Bethsaida	K-feldspar-bearing	Weak	1289	Valley
2238702	2014GL038	5592443	636686	1679	Bethsaida	Propylitic	Moderate	1236	Valley
2238703	2014GL039	5592359	636092	1665	Bethsaida	K-feldspar-bearing	Moderate	1706	Valley
2238704	2014GL040	5592660	635885	1681	Bethsaida	Propylitic	Moderate	1712	Valley
2238705	2014GL041	5592813	636873	1679	QFP	Propylitic	Moderate	829	Valley
2238706	2014GL041	5592861	636822	1669	Bethsaida	K-feldspar-bearing	Moderate	827	Valley
2238708	2014GL042	5593142	636897	1645	Bethsaida	K-feldspar-bearing	Weak	593	Valley
2238709	2014GL043	5593179	636696	1669	Bethsaida	K-feldspar-bearing	Moderate	758	Valley
2238710	2014GL044	5592827	636506	1695	Bethsaida	K-feldspar-bearing	Weak	1093	Valley
2238711	2014GL045	5592927	636328	1688	Bethsaida	Least Altered	Weak	1196	Valley
2238712	2014GL046	5592836	636147	1686	Bethsaida	Least Altered	Trace	1399	Valley
2238713	2014GL047	5592834	635924	1681	Bethsaida	K-feldspar-bearing	Weak	1604	Valley
2238714	2014GL048	5593092	636115	1672	Bethsaida	K-feldspar-bearing	Weak	1338	Valley
2238715	2014GL049	5593114	636409	1672	Bethsaida	K-feldspar-bearing	Trace	1051	Valley
2238716	2014GL050	5593362	636394	1678	Bethsaida	K-feldspar-bearing	Trace	1012	Valley
2238717	2014GL051	5593153	635967	1658	Bethsaida	Sodic-calcic	Weak	1468	Valley
2238720	2014GL052	5593335	636130	1662	Bethsaida	Propylitic	Weak	1277	Valley
2238721	2014GL053	5593384	636607	1658	Bethsaida	Least altered	Trace	798	Valley
2238722	2014GL054	5593371	636908	1652	Bethsaida	K-feldspar-bearing	Weak	502	Valley
2238723	2014GL055	5593585	636951	1619	Bethsaida	K-feldspar-bearing	Weak	453	Valley
2238724	2014GL056	5593606	636657	1627	Bethsaida	Least altered	Trace	747	Valley
2238725	2014GL057	5593874	636655	1589	Bethsaida	Least altered	Trace	829	Valley
2238726	2014GL058	5593617	636360	1668	Bethsaida	Least altered	Trace	1043	Valley
2238727	2014GL058	5593592	636347	1668	Bethsaida	Intermediate argillic	Trace	1053	Valley
2238728	2014GL059	5593584	636110	1631	Bethsaida	K-feldspar-bearing	Trace	1289	Valley
2238729	2014GL060	5594033	636620	1572	Bethsaida	K-feldspar-bearing	Weak	861	Valley
2238731	2014GL061	5593875	636891	1534	Bethsaida	K-feldspar-bearing	Weak	605	Valley
2238732	2014GL062	5593843	636415	1615	Bethsaida	Propylitic	Trace	1038	Valley
2238733	2014GL063	5593879	635928	1611	Bethsaida	K-feldspar-bearing	Weak	1515	Valley
2238734	2014GL064	5593406	635757	1639	Bethsaida	K-feldspar-bearing	Weak	1642	Valley
2238735	2014GL065	5593924	636103	1590	Bethsaida	K-feldspar-bearing	Trace	1360	Valley
2238736	2014GL066	5593452	635436	1668	Bethsaida	K-feldspar-bearing	Trace	1961	Valley
2238737	2014GL067	5593289	635601	1676	Bethsaida	K-feldspar-bearing	Moderate	1808	Valley
2238738	2014GL067	5593302	635608	1671	Bethsaida	Propylitic	Moderate	1800	Valley
2238739	2014GL068	5593771	635731	1632	Bethsaida	Least Altered	Weak	1687	Valley
2238740	2014GL069	5594156	635325	1610	Bethsaida	Propylitic	Weak	2162	Valley
2238743	2014GL070	5593675	635450	1663	Bethsaida	Propylitic	Weak	1954	Valley
2238744	2014GL071	5594189	635133	1608	Bethsaida	Least altered	Trace	2356	Valley
2238745	2014GL072	5594135	634962	1607	Bethsaida	Least Altered	Trace	2515	Valley
2238746	2014GL073	5593653	635234	1648	QFP	Muscovite-bearing	Strong	2168	Valley
2238747	2014GL073	5593665	635206	1650	Bethsaida	Propylitic	Weak	2196	Valley
2238748	2014GL074	5593361	634755	1578	Bethsaida	Propylitic	Trace	2646	Valley
2238749	2014GL075	5592741	635608	1685	Bethsaida	Propylitic	Moderate	1931	Valley
2238750	2014GL076	5592466	635582	1677	Bethsaida	Propylitic	Weak	2071	Valley
2238751	2014GL077	5592310	635279	1662	Bethsaida	Propylitic	Trace	2411	Valley
2238752	2014GL078	5592915	635306	1677	Bethsaida	Propylitic	Weak	2166	Valley
2238754	2014GL079	5592524	635364	1669	Bethsaida	Sodic-calcic	Moderate	2240	Valley
2238755	2014GL080	5593020	635528	1673	Bethsaida	K-feldspar-bearing	Moderate	1925	Valley
2238756	2014GL080	5593020	635522	1673	Bethsaida	Propylitic	Moderate	1931	Valley
2238757	2014GL081	5593001	635803	1678	Bethsaida	Propylitic	Moderate	1663	Valley
2238758	2014GL081	5592998	635801	1682	Bethsaida	K-feldspar-bearing	Moderate	1666	Valley
2238759	2014GL082	5592878	634928	1664	Bethsaida	K-feldspar-bearing	Moderate	2541	Valley
2238760	2014GL083	5592818	634619	1637	Bethsaida	K-feldspar-bearing	Moderate	2856	Valley

Sample ID	Station ID	Northing (m)	Easting (m)	Elev (m)	Lithology	Alteration	Alteration intensity	Distance to deposit	Nearest deposit
2238761	2014GL083	5592802	634613	1635	Bethsaida	K-feldspar-bearing	Weak	2865	Valley
2238762	2014GL084	5593038	634603	1624	Bethsaida	Propylitic	Weak	2831	Valley
2238763	2014GL085	5593104	634844	1646	Bethsaida	Least altered	Trace	2583	Valley
2238766	2014GL085	5593099	634861	1647	Bethsaida	K-feldspar-bearing	Moderate	2567	Valley
2238767	2014GL086	5592555	634774	1655	Bethsaida	Propylitic	Weak	2778	Valley
2238768	2014GL087	5592651	634589	1640	Bethsaida	Propylitic	Weak	2927	Valley
2238769	2014GL088	5591495	635593	1615	Bethsaida	Propylitic	Moderate	2664	Valley
2238770	2014GL089	5591779	635553	1618	Bethsaida	Propylitic	Weak	2493	Valley
2238771	2014GL090	5592049	635691	1621	Bethsaida	Propylitic	Moderate	2213	Valley
2238772	2014GL091	5592191	635560	1642	Bethsaida	Propylitic	Weak	2232	Valley
2238773	2014GL092	5592150	635106	1628	Bethsaida	Propylitic	Weak	2640	Valley
2238774	2014GL093	5591980	635266	1627	Bethsaida	Propylitic	Moderate	2594	Valley
2238775	2014GL094	5592117	636045	1635	Bethsaida	Propylitic	Moderate	1903	Valley
2238777	2014GL095	5592109	636505	1677	Bethsaida	Propylitic	Weak	1613	Valley
2238778	2014GL096	5591789	636892	1665	Bethsaida	Propylitic	Moderate	1737	Valley
2238779	2014GL097	5591348	636856	1679	Bethsaida	Propylitic	Weak	2167	Valley
2238780	2014GL098	5591573	636884	1655	Bethsaida	Propylitic	Moderate	1944	Valley
2238781	2014GL099	5591854	636627	1649	Bethsaida	Least altered	Moderate	1774	Valley
2238782	2014GL100	5591582	636579	1631	Bethsaida	Least altered	Moderate	2040	Valley
2238783	2014GL101	5591263	636571	1659	Bethsaida	Propylitic	Moderate	2339	Valley
2238784	2014GL102	5591502	636276	1638	Bethsaida	Propylitic	Trace	2250	Valley
2238785	2014GL103	5591749	636299	1650	Bethsaida	Sodic-calcic	Moderate	2028	Valley
2238786	2014GL104	5591623	635950	1688	Bethsaida	Least altered	Trace	2334	Valley
2238789	2014GL105	5591437	635804	1645	Bethsaida	Propylitic	Weak	2571	Valley
2238790	2014GL106	5590336	635182	1678	Bethsaida	Propylitic	Moderate	3825	Valley
2238791	2014GL107	5589648	635160	1709	Bethsaida	Propylitic	Weak	4414	Valley
2238792	2014GL108	5589561	635761	1663	Bethsaida	Propylitic	Moderate	4221	Valley
2238793	2014GL109	5589328	633830	1612	Bethsaida	Propylitic	Moderate	5455	Valley
2238794	2014GL110	5589066	634441	1668	Bethsaida	Least Altered	No alteration	5291	Valley
2238795	2014GL111	5589217	634986	1700	Bethsaida	Propylitic	Weak	4874	Valley
2238796	2014GL112	5589307	635434	1727	Bethsaida	Propylitic	Weak	4586	Valley
2238797	2014GL113	5590379	635723	1601	Bethsaida	Sodic-calcic	Moderate	3500	Valley
2238798	2014GL114	5589987	633635	1669	Bethsaida	Least altered	No alteration	5118	Valley
2238800	2014GL115	5590408	633652	1701	Bethsaida	Least altered	Trace	4829	Valley
2238801	2014GL116	5590831	633771	1670	Bethsaida	Least altered	No alteration	4478	Valley
2238802	2014GL117	5590898	634109	1668	Bethsaida	Muscovite-bearing	Strong	4167	Valley
2238803	2014GL117	5590964	634123	1668	Bethsaida	Least altered	No alteration	4116	Valley
2238804	2014GL118	5590839	634681	1631	Bethsaida	Propylitic	Moderate	3772	Valley
2238805	2014GL119	5590804	635225	1632	Bethsaida	Propylitic	Moderate	3427	Valley
2238806	2014GL120	5590297	634204	1708	Bethsaida	Least altered	Trace	4492	Valley
2238807	2014GL121	5589720	634310	1690	Bethsaida	Muscovite-bearing	Strong	4845	Valley
2238808	2014GL121	5589714	634327	1699	QFP	Muscovite-bearing	Strong	4839	Valley
2238809	2014GL122	5589775	634741	1722	Bethsaida	Least altered	Trace	4538	Valley
2238812	2014GL123	5590314	634636	1683	Bethsaida	Propylitic	Moderate	4182	Valley
2238813	2014GL123	5590316	634729	1690	QFP	Muscovite-bearing	Strong	4120	Valley
2238814	2014GL124	5589786	632763	1650	Bethlehem	Propylitic	Weak	5912	Valley
2238815	2014GL125	5589387	632526	1607	Chataway	Propylitic	Weak	6347	Valley
2238816	2014GL126	5589227	633104	1612	Bethlehem	Sodic-calcic	Moderate	6027	Valley
2238817	2014GL127	5589695	633189	1671	Bethlehem	Least altered	No alteration	5645	Valley
2238818	2014GL128	5590175	633247	1696	Skeena	Least altered	No alteration	5292	Valley
2238819	2014GL129	5593629	635155	1641	Bethsaida	Muscovite-bearing	Strong	2245	Valley
2238820	2014GL130	5589775	631278	1552	Border	Sodic-calcic	Weak	7144	Valley
2238821	2014GL131	5589457	631869	1564	Transitional Border–Guichon	Propylitic	Moderate	6824	Valley
2238823	2014GL132	5589727	632352	1626	Guichon	Least altered	Trace	6275	Valley
2238824	2014GL133	5589973	632006	1607	Guichon	K-feldspar-bearing	Strong	6421	Valley
2238825	2014GL134	5590363	631666	1624	Guichon	Least altered	No alteration	6516	Valley
2238826	2014GL135	5590363	632600	1699	Chataway	K-feldspar-bearing	Weak	5710	Valley
2238827	2014GL136	5590436	632133	1701	Guichon	Propylitic	Moderate	6072	Valley
2238828	2014GL137	5590936	632334	1692	Chataway	K-feldspar-bearing	Moderate	5658	Valley
2238829	2014GL138	5590714	632717	1661	Chataway	Least altered	Trace	5427	Valley
2238830	2014GL139	5590849	631698	1620	Guichon	Propylitic	Moderate	6271	Valley
2238831	2014GL140	5591850	631665	1521	Guichon	Propylitic	Moderate	5958	Valley
2238832	2014GL141	5591753	631190	1543	Guichon	Sodic-calcic	Moderate	6442	Valley
2238835	2014GL142	5591238	631147	1536	Transitional Border–Guichon	Sodic-calcic	Moderate	6636	Valley
2238836	2014GL143	5590233	630216	1540	Border	Least altered	Strong	7875	Valley
2238837	2014GL144	5589147	629189	1493	Border	Propylitic	Moderate	9273	Valley
2238838	2014GL145	5590925	629479	1529	Border	Propylitic	Weak	8318	Valley
2238839	2014GL146	5589953	630752	1532	Border	Least altered	Strong	7515	Valley
2238840	2014GL147	5590474	630973	1573	Transitional Border–Guichon	Least altered	Moderate	7086	Valley
2238841	2014GL148	5590736	630595	1571	Border	Least altered	Strong	7330	Valley

Sample ID	Station ID	Northing (m)	Easting (m)	Elev (m)	Lithology	Alteration	Alteration intensity	Distance to deposit	Nearest deposit
2238842	2014GL149	5590843	630067	1577	Border	Sodic-calcic	Moderate	7786	Valley
2238843	2014GL150	5591259	629861	1575	Border	Least altered	Moderate	7855	Valley
2238844	2014GL150	5591266	629868	1571	Border	Sodic-calcic	Moderate	7847	Valley
2238846	2014GL151	5591711	630732	1502	Guichon	K-feldspar-bearing	Moderate	6895	Valley
2238847	2014GL152	5591954	630040	1496	Border	Sodic-calcic	Strong	7515	Valley
2238848	2014GL152	5591956	630056	1500	Border	Sodic-calcic	Strong	7498	Valley
2238849	2014GL153	5591817	629621	1509	Border	Sodic-calcic	Trace	7953	Valley
2238850	2014GL154	5591106	630295	1581	Border	Sodic-calcic	Trace	7486	Valley
2238851	2014GL155	5591635	632265	1600	Chataway	Propylitic	Weak	5450	Valley
2238852	2014GL156	5591273	632614	1628	Chataway	K-feldspar-bearing	Weak	5262	Valley
2238853	2014GL157	5591764	633220	1544	Skeena	Propylitic	Trace	4511	Valley
2238854	2014GL158	5591734	632765	1563	Bethlehem	Least altered	Weak	4947	Valley
2238855	2014GL159	5594843	637621	1290	Bethsaida	Intermediate argillic	Strong	311	Valley
2238858	2014GL160	5594818	637616	1288	Bethsaida	Sodic-calcic	Strong	313	Valley
2238859	2014GL161	5594306	637775	1290	Bethsaida	Muscovite-bearing	Strong	74	Valley
2238860	2014GL162	5594267	637790	1291	Bethsaida	Intermediate argillic	Strong	35	Valley
2238861	2014GL163	5593935	637887	1280	Bethsaida	Muscovite-bearing	Strong	0	Valley
2238862	2014GL164	5593931	637876	1279	Bethsaida	Muscovite-bearing	Strong	0	Valley
2238863	2014GL165	5593912	637814	1280	Bethsaida	Muscovite-bearing	Strong	0	Valley
2238864	2014GL166	5594496	638611	848	Bethsaida	K-feldspar-bearing	Strong	0	Valley
2238865	2014GL167	5594491	638612	851	Bethsaida	Muscovite-bearing	Strong	0	Valley
2238866	2014GL168	5594954	638728	844	Bethsaida	Muscovite-bearing	Strong	0	Valley
2238867	2014GL169	5595008	638847	833	Bethsaida	Muscovite-bearing	Strong	0	Valley
2238869	2014GL170	5595053	638505	870	Bethsaida	Muscovite-bearing	Strong	0	Valley
2238870	2014GL171	5595046	638525	870	Bethsaida	Muscovite-bearing	Strong	0	Valley
2238871	2014GL172	5588595	642216	1510	Skeena	Sodic-calcic	Strong	0	Highmont
2238872	2014GL173	5588603	642018	1512	Skeena	Muscovite-bearing	Strong	0	Highmont
2238873	2014GL174	5589442	639677	1481	Skeena	Intermediate argillic	Strong	0	Lornex
2238874	2014GL175	5594992	638770	835	Bethsaida	Muscovite-bearing	Strong	0	Valley
2238875	2014GL176	5589442	639681	1480	Skeena	Intermediate argillic	Strong	0	Lornex
2238876	2014GL177	5589799	638863	1497	Bethsaida	Sodic-calcic	Strong	3834	Valley
2238877	2014GL178	5589934	638752	1498	Bethsaida	Propylitic	Moderate	3691	Valley
2238878	2014GL179	5590509	639767	1295	Skeena	Muscovite-bearing	Strong	18	Lornex
2238881	2014GL180	5591227	626896	1322	Border	Least altered	Moderate	10741	Valley
2238882	2014GL181	5591296	626411	1179	Border	Propylitic	Strong	11202	Valley
2238883	2014GL181	5591282	626410	1178	Border	Sodic-calcic	Moderate	11206	Valley
2238884	2014GL182	5591269	626339	1146	Border	Sodic-calcic	Strong	11278	Valley
2238885	2014GL183	5590486	627174	1332	Border	Least altered	No alteration	10651	Valley
2238886	2014GL184	5594940	633123	1505	Chataway	Propylitic	Weak	4456	Valley
2238887	2014GL185	5595872	633255	1517	Bethlehem	Propylitic	Moderate	4607	Valley
2238888	2014GL186	5595395	633543	1522	Bethlehem	Least altered	Trace	4169	Valley
2238889	2014GL187	5594541	633905	1540	Bethlehem	Propylitic	Trace	3616	Valley
2238890	2014GL188	5594908	634137	1523	Bethlehem	Least altered	Trace	3460	Valley
2238892	2014GL189	5594400	634439	1609	Bethsaida	Propylitic	Weak	3068	Valley
2238893	2014GL190	5594552	635137	1552	Bethsaida	K-feldspar-bearing	Weak	2406	Valley
2238894	2014GL191	5594879	634624	1538	Bethsaida	Propylitic	Weak	2982	Valley
2238895	2014GL192	5595684	633858	1550	Bethlehem	Propylitic	Trace	3978	Valley
2238896	2014GL193	5595890	634271	1550	Bethlehem	Sodic-calcic	Moderate	3697	Valley
2238897	2014GL194	5596313	632682	1533	Transitional Chat-away–Bethlehem	Sodic-calcic	Trace	5308	Valley
2238898	2014GL195	5596227	632070	1464	Chataway	Sodic-calcic	Weak	5839	Valley
2238899	2014GL196	5596774	632176	1513	Chataway	Propylitic	Weak	5963	Valley
2238900	2014GL197	5597238	632068	1503	Chataway	Propylitic	Moderate	6278	Valley
2238901	2014GL198	5597417	632723	1546	Chataway	Propylitic	Moderate	5811	Valley
2238904	2014GL199	5596803	632691	1539	Transitional Chat-away–Bethlehem	Sodic-calcic	Weak	5521	Valley
2238905	2014GL200	5596622	633149	1527	FPM	Intermediate argillic	Moderate	5034	Valley
2238906	2014GL201	5596252	633202	1522	Chataway	Propylitic	Weak	4812	Valley
2238907	2014GL202	5596185	633899	1551	Transitional Chat-away–Bethlehem	Sodic-calcic	Trace	4166	Valley
2238908	2014GL203	5596626	634354	1477	Chataway	Sodic-calcic	Strong	3998	Valley
2238909	2014GL204	5596665	633617	1530	Chataway	Least altered	No alteration	4658	Valley
2238910	2014GL205	5597698	632253	1499	Chataway	Sodic-calcic	Moderate	6356	Valley
2238911	2014GL206	5597914	632622	1571	Chataway	Least altered	Trace	6129	Valley
2238912	2014GL207	5597685	633247	1488	Transitional Chat-away–Bethlehem	Propylitic	Trace	5473	Valley
2238913	2014GL208	5597352	633514	1516	Transitional Chat-away–Bethlehem	K-feldspar-bearing	Weak	5077	Valley
2238915	2014GL209	5597156	633168	1562	Transitional Chat-away–Bethlehem	Sodic-calcic	Weak	5296	Valley
2238916	2014GL210	5598203	630815	1434	Guichon	Sodic-calcic	Weak	7848	Valley
2238917	2014GL211	5598255	631342	1479	Chataway	Sodic-calcic	Weak	7420	Valley
2238918	2014GL212	5598454	631873	1489	Guichon	Sodic-calcic	Strong	7048	Valley

Sample ID	Station ID	Northing (m)	Easting (m)	Elev (m)	Lithology	Alteration	Alteration intensity	Distance to deposit	Nearest deposit
2238919	2014GL212	5598423	631858	1487	Guichon	K-feldspar-bearing	Weak	7045	Valley
2238920	2014GL213	5598373	632302	1508	Chataway	Propylitic	Strong	6637	Valley
2238921	2014GL214	5598367	632885	1472	Chataway	Sodic-calcic	Trace	6143	Valley
2238922	2014GL215	5597783	633801	1436	Chataway	Least altered	Trace	5058	Valley
2238923	2014GL216	5598884	630806	1425	Border	Propylitic	Strong	8188	Valley
2238924	2014GL217	5598907	631328	1470	Chataway	Least altered	Weak	7748	Valley
2238927	2014GL218	5598924	631809	1482	Guichon	Propylitic	Weak	7348	Valley
2238928	2014GL219	5598995	632406	1435	Guichon	K-feldspar-bearing	Weak	6897	Valley
2238929	2014GL220	5599445	631804	1440	Border	Propylitic	Moderate	7649	Valley
2238930	2014GL221	5599456	632366	1411	Guichon	Least altered	No alteration	7207	Valley
2238931	2014GL222	5599614	631197	1476	Guichon	Propylitic	Moderate	8241	Valley
2238932	2014GL223	5599567	630715	1463	Transitional Border–Guichon	Least altered	No alteration	8616	Valley
2238933	2014GL224	5600096	630756	1437	Guichon	K-feldspar-bearing	Trace	8880	Valley
2238934	2014GL225	5600111	631231	1426	Guichon	K-feldspar-bearing	Trace	8506	Valley
2238935	2014GL226	5600081	631719	1402	Guichon	K-feldspar-bearing	Weak	8103	Valley
2238936	2014GL227	5600518	631160	1375	Guichon	Least altered	Trace	8812	Valley
2238938	2014GL228	5600981	630993	1331	Guichon	Least altered	No alteration	9236	Valley
2238939	2014GL229	5600621	629978	1353	Guichon	Least altered	Weak	9818	Valley
2238940	2014GL230	5600189	629494	1303	Border	Least altered	No alteration	9981	Valley
2238941	2014GL230	5600157	629479	1303	Border	Propylitic	Moderate	9977	Valley
2238942	2014GL231	5599999	629043	1267	Border	K-feldspar-bearing	Trace	10271	Valley
2238951	2015GL-V11-06	5594160	638800	952	Bethsaida	Muscovite-bearing	Strong	0	Valley
2238952	2015GL-V11-06	5594170	638810	929	Bethsaida	Muscovite-bearing	Strong	0	Valley
2238953	2015GL-V11-06	5594200	638840	857	Bethsaida	Muscovite-bearing	Strong	0	Valley
2238954	2015GL-V11-06	5594210	638856	820	Bethsaida	Muscovite-bearing	Strong	0	Valley
2238955	2015GL-V11-06	5594230	638879	769	Bethsaida	Muscovite-bearing	Strong	0	Valley
2238956	2015GL-V11-06	5594270	638929	668	Bethsaida	Muscovite-bearing	Moderate	0	Valley
2238957	2015GL-V11-06	5594290	638949	631	Bethsaida	Muscovite-bearing	Strong	0	Valley
2238958	2015GL-V11-06	5594300	638960	611	Bethsaida	Muscovite-bearing	Strong	0	Valley
2238959	2015GL-V11-06	5594310	638978	579	Bethsaida	Muscovite-bearing	Strong	0	Valley
2238960	2015GL-V11-13	5593930	638203	1278	QFP	Muscovite-bearing	Moderate	24	Valley
2238962	2015GL-V11-13	5593960	638231	1214	QFP	Intermediate argillic	Moderate	43	Valley
2238963	2015GL-V11-13	5594000	638278	1114	QFP	Muscovite-bearing	Moderate	78	Valley
2238964	2015GL-V11-13	5594030	638314	1043	Bethsaida	Muscovite-bearing	Moderate	78	Valley
2238965	2015GL-V11-13	5594060	638355	967	Bethsaida	Muscovite-bearing	Moderate	33	Valley
2238966	2015GL-V11-13	5594080	638387	911	Bethsaida	Muscovite-bearing	Moderate	0	Valley
2238967	2015GL-V11-13	5594090	638401	887	Bethsaida	Intermediate argillic	Strong	0	Valley
2238968	2015GL-V11-13	5594090	638405	880	Bethsaida	Muscovite-bearing	Moderate	0	Valley
2238969	2015GL-V11-50	5593450	637376	1536	Bethsaida	Muscovite-bearing	Strong	28	Valley
2238970	2015GL-V11-50	5593440	637360	1503	Bethsaida	Muscovite-bearing	Strong	45	Valley
2238971	2015GL-V11-50	5593410	637333	1451	Bethsaida	Intermediate argillic	Strong	81	Valley
2238974	2015GL-V11-50	5593410	637330	1445	Bethsaida	Muscovite-bearing	Strong	84	Valley
2238975	2015GL-V11-50	5593390	637301	1393	Bethsaida	Muscovite-bearing	Strong	119	Valley
2238976	2015GL-V11-50	5593380	637286	1365	Bethsaida	Muscovite-bearing	Strong	137	Valley
2238977	2015GL-V11-50	5593350	637245	1295	Bethsaida	Muscovite-bearing	Strong	188	Valley
2238978	2015GL-V11-50	5593320	637204	1231	Bethsaida	Intermediate argillic	Strong	238	Valley
2238979	2015GL-V11-50	5593310	637183	1199	Bethsaida	Muscovite-bearing	Strong	261	Valley
2238980	2015GL-V11-50	5593290	637137	1134	Bethsaida	Muscovite-bearing	Strong	311	Valley
2238981	2015GL001	5589227	637070	1701	Bethsaida	Propylitic	Moderate	4217	Valley
2238982	2015GL002	5589360	636552	1632	Bethsaida	Propylitic	Weak	4168	Valley
2238983	2015GL003	5590041	636809	1659	Bethsaida	K-feldspar-bearing	Moderate	3448	Valley
2238985	2015GL003	5590039	636813	1660	Bethsaida	Propylitic	Moderate	3449	Valley
2238986	2015GL004	5589726	637198	1644	Bethsaida	Propylitic	Weak	3708	Valley
2238987	2015GL005	5590781	636755	1682	Bethsaida	Propylitic	Weak	2740	Valley
2238988	2015GL006	5591023	636201	1639	Bethsaida	Propylitic	Moderate	2708	Valley
2238989	2015GL007	5590436	636545	1661	Bethsaida	Propylitic	Moderate	3130	Valley
2238990	2015GL008	5590269	637288	1638	Bethsaida	Propylitic	Weak	3161	Valley
2238991	2015GL009	5590025	637580	1635	Bethsaida	Propylitic	Trace	3400	Valley
2238992	2015GL010	5587446	640611	1644	Bethsaida	Sodic-calcic	Strong	911	Highmont
2238993	2015GL010	5587411	640556	1640	Bethsaida	K-feldspar-bearing	Weak	970	Highmont
2238994	2015GL011	5586814	640262	1638	Bethsaida	Sodic-calcic	Moderate	1632	Highmont
2238997	2015GL011	5586804	640240	1640	Bethsaida	Sodic-calcic	Moderate	1652	Highmont
2238998	2015GL012	5586189	640103	1627	Bethsaida	Least altered	No alteration	2259	Highmont
2238999	2015GL013	5586034	639953	1621	Bethsaida	Sodic-calcic	Moderate	2465	Highmont
2239000	2015GL014	5586106	640991	1685	Bethsaida	Propylitic	Trace	1991	Highmont
2242901	2015KB238	5590225	642762	1550	Skeena	Propylitic	Moderate	1366	Highmont
2242902	2015KB239	5590742	642906	1491	Skeena	Propylitic	Weak	1898	Highmont
2242903	2015KB240	5590983	642002	1457	Skeena	Propylitic	Strong	1798	Highmont
2242904	2015KB241	5590721	642020	1510	Skeena	Propylitic	Strong	1565	Highmont
2242905	2015KB242	5590892	642254	1469	Skeena	Propylitic	Weak	1826	Highmont
2242906	2015KB243	5591322	642548	1375	Skeena	Propylitic	Strong	2060	J.A.

Sample ID	Station ID	Northing (m)	Easting (m)	Elev (m)	Lithology	Alteration	Alteration intensity	Distance to deposit	Nearest deposit
2242907	2015KB244	5591542	639633	1445	Skeena	Propylitic	Moderate	372	Lornex
2242908	2015KB245	5591306	639849	1478	Skeena	Propylitic	Strong	441	Lornex
2242909	2015KB246	5591811	641901	1399	Skeena	Propylitic	Strong	1857	J.A.
2242911	2015KB247	5592115	641931	1391	Skeena	Propylitic	Strong	1579	J.A.
2242912	2015KB248	5592106	641927	1359	Skeena	Propylitic	Moderate	1588	J.A.
2242913	2015KB249	5592278	642119	1314	Skeena	Propylitic	Weak	1342	J.A.
2242914	2015KB250A	5591903	639686	1405	Skeena	Propylitic	Strong	589	Lornex
2242915	2015KB251A	5591620	643098	1346	Skeena	Propylitic	Moderate	1583	J.A.
2242916	2015KB251B	5591620	643098	1346	QFP	Sodic-calcic	Moderate	1583	J.A.
2242917	2015KB252	5591356	643130	1401	Skeena	Propylitic	Moderate	1784	J.A.
2242918	2015KB254	5591038	643312	1468	Skeena	Propylitic	Weak	1987	J.A.
2242919	2015KB255	5590926	643708	1478	Skeena	Propylitic	Weak	1938	J.A.
2242921	2015KB256	5590318	643200	1530	Skeena	Propylitic	Weak	1668	Highmont
2242922	2015KB257	5590476	643695	1541	Skeena	K-feldspar-bearing	Moderate	2025	Highmont
2242923	2015KB258	5590631	643316	1539	Skeena	Propylitic	Weak	1991	Highmont
2242924	2015KB259A	5591650	643629	1374	Skeena	Propylitic	Weak	1297	J.A.
2242925	2015KB260	5589030	642037	1597	Skeena	Propylitic	Moderate	135	Highmont
2242926	2015KB261	5596081	644872	1484	Guichon	Propylitic	Trace	1101	Bethlehem
2242927	2015KB263	5596571	645077	1478	Guichon	K-feldspar-bearing	Weak	1585	Bethlehem
2242928	2015KB264	5588356	642511	1640	QFP	Propylitic	Moderate	0	Highmont
2242929	2015KB265	5588443	642526	1644	Skeena	Propylitic	Strong	0	Highmont
2242931	2015KB268	5588124	642328	1643	Skeena	Sodic-calcic	Moderate	0	Highmont
2242932	2015KB269	5588054	642296	1646	Skeena	Muscovite-bearing	Moderate	0	Highmont
2242933	2015KB270	5588281	642180	1645	QFP	Propylitic	Strong	0	Highmont
2242934	2015KB271	5588201	642152	1646	Skeena	Sodic-calcic	Moderate	79	Highmont
2242935	2015KB272	5588119	642125	1650	Skeena	K-feldspar-bearing	Moderate	0	Highmont
2242936	2015KB273	5588681	642506	1536	Skeena	Propylitic	Moderate	0	Highmont
2242937	2015KB274	5588720	642263	1580	Skeena	Sodic-calcic	Moderate	0	Highmont
2242938	2015KB275	5588902	642059	1593	Skeena	Propylitic	Strong	70	Highmont
2242939	2015KB276	5589062	640869	1563	Skeena	Sodic-calcic	Moderate	245	Highmont
2242941	2015KB277	5589001	640888	1561	Skeena	Sodic-calcic	Moderate	229	Highmont
2242942	2015KB278	5589025	640854	1593	Skeena	Sodic-calcic	Strong	260	Highmont
2242943	2015KB279	5588954	640894	1593	Skeena	Sodic-calcic	Moderate	235	Highmont
2242944	2015KB266A	5588254	642466	1648	QFP	Propylitic	Strong	4	Highmont
2242945	2015KB266B	5588280	642490	1644	Skeena	Sodic-calcic	Strong	24	Highmont
2242946	2015KB267	5588231	642403	1642	QFP	Sodic-calcic	Strong	0	Highmont
2245246	2015KB001	5595249	643187	1527	Bethlehem	Sodic-calcic	Strong	101	Bethlehem
2245247	2015KB002	5596333	643456	1548	Guichon	Propylitic	Moderate	318	Bethlehem
2245248	2015KB004	5596352	643373	1538	Guichon	Propylitic	Strong	236	Bethlehem
2245249	2015KB005	5596264	643768	1568	Guichon	K-feldspar-bearing	Weak	436	Bethlehem
2245251	2015KB007	5596549	643457	1559	Guichon	Propylitic	Trace	246	Bethlehem
2245252	2015KB008	5596700	643566	1549	Guichon	Least altered	Trace	367	Bethlehem
2245253	2015KB011	5597028	643876	1534	Guichon	Least altered	Trace	786	Bethlehem
2245254	2015KB012	5597139	643723	1538	Guichon	Propylitic	Trace	734	Bethlehem
2245255	2015KB015	5597185	643581	1512	Guichon	Least altered	Trace	675	Bethlehem
2245256	2015KB016	5596763	644028	1549	Guichon	Least altered	Trace	832	Bethlehem
2245257	2015KB017	5596970	644113	1529	Guichon	Propylitic	Weak	972	Bethlehem
2245258	2015KB019	5596888	644297	1510	Guichon	Least altered	No alteration	1122	Bethlehem
2245259	2015KB020	5596610	644172	1528	Guichon	Propylitic	Trace	959	Bethlehem
2245261	2015KB022	5596400	644003	1564	Guichon	Propylitic	Trace	695	Bethlehem
2245262	2015KB023	5596387	643969	1545	Guichon	Propylitic	Moderate	661	Bethlehem
2245263	2015KB024	5596643	644410	1489	Guichon	Least altered	Trace	1162	Bethlehem
2245264	2015KB025	5596475	644333	1519	Guichon	Propylitic	Trace	1001	Bethlehem
2245265	2015KB027	5597549	644336	1470	Guichon	Least altered	Trace	1465	Bethlehem
2245266	2015KB028	5597761	644645	1479	Guichon	Propylitic	Trace	1838	Bethlehem
2245267	2015KB031	5596851	645096	1484	Guichon	K-feldspar-bearing	Trace	1812	Bethlehem
2245268	2015KB032A	5596823	645039	1488	Bethlehem	Propylitic	Moderate	1755	Bethlehem
2245269	2015KB032B	5596823	645039	1488	Guichon	Propylitic	Weak	1755	Bethlehem
2245271	2015KB033	5596261	644468	1522	Guichon	Propylitic	Trace	972	Bethlehem
2245272	2015KB034	5595912	644521	1517	Guichon	Propylitic	Trace	725	Bethlehem
2245274	2015KB035	5595693	644496	1541	Guichon	Propylitic	Trace	571	Bethlehem
2245275	2015KB036	5595570	644540	1536	Guichon	Propylitic	Trace	561	Bethlehem
2245276	2015KB037	5595478	644707	1508	Guichon	Propylitic	Trace	667	Bethlehem
2245277	2015KB009	5596886	643729	1543	Guichon	Least altered	No alteration	587	Bethlehem
2245278	2015KB038	5595936	643751	1581	Guichon	Propylitic	Moderate	251	Bethlehem
2245279	2015KB040	5595801	643721	1563	FPM	Propylitic	Weak	243	Bethlehem
2245281	2015KB041	5595660	643873	1550	Guichon	Propylitic	Weak	249	Bethlehem
2245282	2015KB043A	5595408	643997	1546	Guichon	Propylitic	Moderate	1	Bethlehem
2245283	2015KB043B	5595416	644029	1541	Guichon	Sodic-calcic	Moderate	29	Bethlehem
2245284	2015KB044	5595617	644175	1531	Guichon	Propylitic	Strong	272	Bethlehem
2245285	2015KB045	5595878	644177	1536	Guichon	Propylitic	Moderate	498	Bethlehem
2245286	2015KB046	5596132	644282	1536	Guichon	Propylitic	Moderate	773	Bethlehem

Sample ID	Station ID	Northing (m)	Easting (m)	Elev (m)	Lithology	Alteration	Alteration intensity	Distance to deposit	Nearest deposit
2245287	2015KB047	5597401	643621	1490	Guichon	Propylitic	Moderate	880	Bethlehem
2245288	2015KB048	5597559	644140	1469	Guichon	Propylitic	Trace	1326	Bethlehem
2245289	2015KB049	5597385	644140	1506	Guichon	Propylitic	Weak	1209	Bethlehem
2245291	2015KB050	5598618	643276	1500	Bethlehem	Propylitic	Weak	1984	Bethlehem
2245292	2015KB051	5599517	642804	1502	Guichon	Least altered	Weak	2905	Bethlehem
2245293	2015KB052	5599529	642845	1504	QFP	Least altered	Moderate	2911	Bethlehem
2245294	2015KB053	5599491	643245	1488	Chataway	Propylitic	Weak	2856	Bethlehem
2245295	2015KB054	5599468	644583	1456	Chataway	Propylitic	Trace	3158	Bethlehem
2245296	2015KB055	5596504	646992	1377	Guichon	Propylitic	Moderate	3106	Bethlehem
2245297	2015KB056	5596434	646965	1371	Guichon	Sodic-calcic	Weak	3045	Bethlehem
2245298	2015KB057	5597036	646181	1414	Guichon	Sodic-calcic	Moderate	2721	Bethlehem
2245299	2015KB059	5596496	645776	1437	Guichon	Least altered	Trace	2082	Bethlehem
2245301	2015KB060	5597794	646190	1416	Guichon	Sodic-calcic	Strong	3206	Bethlehem
2245302	2015KB062	5596976	646623	1399	Guichon	Sodic-calcic	Moderate	3055	Bethlehem
2245303	2015KB063	5598843	650526	1134	Border	Propylitic	Moderate	7343	Bethlehem
2245304	2015KB064A	5598922	650482	1147	Border	Propylitic	Strong	7351	Bethlehem
2245305	2015KB064B	5598922	650490	1147	Border	Least altered	Weak	7357	Bethlehem
2245306	2015KB065	5599003	650463	1140	Border	Propylitic	Strong	7381	Bethlehem
2245307	2015KB066	5599149	650255	1161	Border	Least altered	Moderate	7288	Bethlehem
2245308	2015KB067	5599841	649718	1194	Border	Propylitic	Trace	7234	Bethlehem
2245309	2015KB068	5599917	649514	1224	Guichon	Propylitic	Trace	7118	Bethlehem
2245311	2015KB069	5599013	650192	1171	Border	Propylitic	Moderate	7164	Bethlehem
2245312	2015KB071	5599748	649176	1268	Guichon	Sodic-calcic	Weak	6740	Bethlehem
2245313	2015KB070	5599011	649808	1246	Border	Sodic-calcic	Weak	6834	Bethlehem
2245314	2015KB072	5599400	649294	1279	Guichon	Propylitic	Moderate	6630	Bethlehem
2245315	2015KB073	5598766	649421	1255	Guichon	Propylitic	Trace	6376	Bethlehem
2245316	2015KB074	5598916	648959	1334	Guichon	Sodic-calcic	Weak	6073	Bethlehem
2245317	2015KB075	5599397	648872	1313	Guichon	Least altered	Trace	6296	Bethlehem
2245318	2015KB076	5599396	648369	1341	Guichon	Least altered	Trace	5862	Bethlehem
2245319	2015KB077	5598910	648419	1369	Guichon	Least altered	Trace	5638	Bethlehem
2245321	2015KB078	5598498	648356	1350	Guichon	Least altered	Trace	5340	Bethlehem
2245322	2015KB079	5598240	648225	1346	Guichon	Propylitic	Trace	5085	Bethlehem
2245323	2015KB081	5598560	648842	1330	Guichon	Least altered	Trace	5777	Bethlehem
2245324	2015KB082	5598188	649070	1311	Guichon	K-feldspar-bearing	Trace	5774	Bethlehem
2245325	2015KB026	5597207	644429	1487	Guichon	Least altered	Trace	1356	Bethlehem
2245326	2015KB083	5599441	649685	1205	Border	Propylitic	Weak	6970	Bethlehem
2245327	2015KB029	5597338	645053	1461	Guichon	K-feldspar-bearing	No alteration	1981	Bethlehem
2245328	2015KB030	5597348	645350	1451	Guichon	K-feldspar-bearing	Trace	2264	Bethlehem
2245329	2015KB084	5599272	649843	1201	Border	K-feldspar-bearing	Weak	7004	Bethlehem
2245331	2015KB085	5598354	649523	1277	Guichon	Propylitic	Weak	6239	Bethlehem
2245332	2015KB086	5597806	648854	1350	Guichon	Least altered	Trace	5377	Bethlehem
2245333	2015KB087	5597775	648506	1364	Guichon	Sodic-calcic	Weak	5075	Bethlehem
2245334	2015KB088	5598100	648925	1324	Chataway	Propylitic	Weak	5605	Bethlehem
2245335	2015KB089	5597864	648075	1355	Guichon	Least altered	Moderate	4757	Bethlehem
2245336	2015KB090	5597830	647675	1373	Guichon	Least altered	Weak	4401	Bethlehem
2245337	2015KB091	5598449	647709	1363	Guichon	Least altered	Trace	4795	Bethlehem
2245338	2015KB092	5599066	647797	1385	Chataway	Least altered	Weak	5203	Bethlehem
2245339	2015KB093	5598812	647553	1392	Chataway	Propylitic	Weak	4869	Bethlehem
2245341	2015KB094	5598631	647308	1380	Guichon	Propylitic	Trace	4568	Bethlehem
2245342	2015KB095	5598456	646981	1415	Guichon	Least altered	No alteration	4199	Bethlehem
2245343	2015KB096	5598113	646924	1432	Guichon	Least altered	Trace	3983	Bethlehem
2245344	2015KB097	5598266	646585	1465	Guichon	Least altered	No alteration	3759	Bethlehem
2245345	2015KB098	5597628	646809	1463	Guichon	Least altered	No alteration	3580	Bethlehem
2245346	2015KB099	5597366	647143	1438	Guichon	Least altered	No alteration	3702	Bethlehem
2245347	2015KB100	5596235	645786	1451	Guichon	Propylitic	Weak	1968	Bethlehem
2245348	2015KB101	5595931	645783	1442	Guichon	Least altered	Moderate	1793	Bethlehem
2245349	2015KB102	5595515	646085	1447	Guichon	K-feldspar-bearing	Weak	1830	Bethlehem
2245351	2015KB103A	5595539	646516	1423	Chataway	Sodic-calcic	Strong	2239	Bethlehem
2245352	2015KB104	5595420	646480	1414	Chataway	Propylitic	Moderate	2166	Bethlehem
2245353	2015KB105A	5596149	646578	1392	Guichon	Propylitic	Weak	2565	Bethlehem
2245354	2015KB105A	5596149	646578	1392	Guichon	Propylitic	Weak	2565	Bethlehem
2245355	2015KB106	5596831	647425	1395	Guichon	Propylitic	Weak	3648	Bethlehem
2245356	2015KB107	5596598	647245	1379	Guichon	Sodic-calcic	Weak	3369	Bethlehem
2245357	2015KB108	5597940	646612	1455	Guichon	Least altered	No alteration	3637	Bethlehem
2245358	2015KB109	5598102	647356	1400	Guichon	K-feldspar-bearing	No alteration	4303	Bethlehem
2245359	2015KB110	5598205	647448	1382	Guichon	Propylitic	Weak	4439	Bethlehem
2245361	2015KB111	5596986	648084	1390	Guichon	Propylitic	Weak	4286	Bethlehem
2245362	2015KB112	5597224	648489	1362	Guichon	Least altered	Weak	4756	Bethlehem
2245363	2015KB113	5588851	653127	1308	Gump	Least altered	No alteration	9624	J.A.
2245364	2015KB115	5588097	653482	1296	Gump	Least altered	Trace	10279	J.A.
2245365	2015KB116	5587372	653387	1258	Gump	Propylitic	Trace	10559	J.A.
2245366	2015KB117	5586872	653419	1236	Gump	Least altered	Trace	10856	J.A.

Sample ID	Station ID	Northing (m)	Easting (m)	Elev (m)	Lithology	Alteration	Alteration intensity	Distance to deposit	Nearest deposit
2245367	2015KB118	5586267	653451	1190	Gump	Least altered	Trace	11068	Highmont
2245368	2015KB119	5586405	653068	1241	Gump	Least altered	No alteration	10664	Highmont
2245369	2015KB120	5587195	652400	1294	Border	Propylitic	Weak	9835	J.A.
2245371	2015KB121A	5586632	653129	1264	Border	Propylitic	Weak	10677	Highmont
2245372	2015KB121B	5586635	653140	1264	Border	Propylitic	Weak	10687	Highmont
2245373	2015KB122	5587255	651987	1313	Guichon	K-feldspar-bearing	Trace	9444	Highmont
2245374	2015KB123	5586509	652132	1358	Border	K-feldspar-bearing	Weak	9728	Highmont
2245375	2015KB124	5586172	652433	1401	Border	Propylitic	Weak	10101	Highmont
2245376	2015KB125	5586065	651975	1394	Border	Least altered	Trace	9686	Highmont
2245377	2015KB127	5586521	651642	1374	Guichon	Least altered	Trace	9249	Highmont
2245378	2015KB128A	5586921	651813	1360	Border	Propylitic	Weak	9330	Highmont
2245379	2015KB128B	5586919	651816	1360	Border	Propylitic	Weak	9333	Highmont
2245381	2015KB129	5586861	652338	1334	Border	K-feldspar-bearing	Weak	9857	Highmont
2245382	2015KB131	5587231	652658	1270	Border	Propylitic	Strong	10025	J.A.
2245383	2015KB132	5588538	652604	1373	Gump	K-feldspar-bearing	Weak	9297	J.A.
2245384	2015KB133	5587735	651707	1332	Border	Propylitic	Trace	8958	J.A.
2245385	2015KB134	5588306	651653	1355	Border	Least altered	Trace	8594	J.A.
2245386	2015KB135A	5588856	651790	1378	Border	Least altered	Strong	8430	J.A.
2245387	2015KB136	5586490	651134	1406	Transitional Guichon–Chataway	K-feldspar-bearing	Trace	8764	Highmont
2245388	2015KB137	5586911	651083	1412	Guichon	K-feldspar-bearing	Weak	8617	Highmont
2245389	2015KB138	5587595	650750	1375	Guichon	Least altered	Weak	8170	Highmont
2245391	2015KB139	5588508	650693	1384	Guichon	Propylitic	Weak	7683	J.A.
2245392	2015KB140	5588096	650241	1392	Transitional Guichon–Chataway	Propylitic	Weak	7572	J.A.
2245393	2015KB141	5587958	650025	1420	Chataway	Propylitic	Weak	7407	Highmont
2245394	2015KB142	5587498	650012	1432	Chataway	Least altered	Weak	7455	Highmont
2245395	2015KB143	5587111	650308	1420	Transitional Guichon–Chataway	Propylitic	Weak	7818	Highmont
2245396	2015KB144A	5586864	650179	1425	Transitional Guichon–Chataway	Propylitic	Weak	7746	Highmont
2245397	2015KB145	5586489	649496	1448	Transitional Guichon–Chataway	Propylitic	Weak	7173	Highmont
2245398	2015KB146	5588700	649895	1395	Chataway	Propylitic	Weak	6926	J.A.
2245399	2015KB147	5587824	649496	1476	Chataway	Propylitic	Weak	6896	Highmont
2245401	2015KB148	5587347	649565	1466	Chataway	Propylitic	Weak	7042	Highmont
2245402	2015KB149C	5588230	649178	1440	Transitional Guichon–Chataway	K-feldspar-bearing	Trace	6539	Highmont
2245403	2015KB149B	5588210	649185	1440	Transitional Guichon–Chataway	Propylitic	Weak	6547	Highmont
2245404	2015KB150	5588141	649771	1432	Chataway	K-feldspar-bearing	Trace	7137	Highmont
2245405	2015KB151A	5584642	649378	1443	Transitional Guichon–Chataway	Propylitic	Weak	7650	Highmont
2245406	2015KB152A	5585313	648917	1462	Chataway	Sodic-calcic	Weak	6960	Highmont
2245407	2015KB153	5585772	648700	1475	Chataway	K-feldspar-bearing	Weak	6596	Highmont
2245408	2015KB154	5586106	648591	1477	Chataway	Propylitic	Weak	6388	Highmont
2245409	2015KB155A	5586276	648151	1498	Chataway	Sodic-calcic	Weak	5918	Highmont
2245411	2015KB155B	5586260	648129	1498	Chataway	Propylitic	Weak	5902	Highmont
2245412	2015KB156	5585853	648164	1513	Chataway	Propylitic	Trace	6064	Highmont
2245413	2015KB157	5585342	648338	1538	Chataway	Propylitic	Weak	6414	Highmont
2245414	2015KB159	5588106	651218	1335	Guichon	K-feldspar-bearing	Weak	8344	J.A.
2245415	2015KB160B	5588762	651210	1352	Guichon	Propylitic	Weak	7976	J.A.
2245416	2015KB161B	5589297	651193	1378	Guichon	Propylitic	Weak	7694	J.A.
2245417	2015KB162	5588567	650992	1352	Transitional Guichon–Chataway	Propylitic	Weak	7897	J.A.
2245418	2015KB163A	5586902	649764	1445	Transitional Guichon–Chataway	Propylitic	Weak	7335	Highmont
2245419	2015KB163B	5586835	649903	1442	Transitional Guichon–Chataway	Least altered	Weak	7486	Highmont
2245421	2015KB164	5586893	649344	1460	Transitional Guichon–Chataway	Propylitic	Weak	6930	Highmont
2245422	2015KB165	5585002	648569	1509	Transitional Guichon–Chataway	K-feldspar-bearing	Trace	6765	Highmont
2245423	2015KB166A	5585645	647716	1539	Chataway	Propylitic	Moderate	5723	Highmont
2245424	2015KB167	5585039	647913	1532	Chataway	Propylitic	Weak	6162	Highmont
2245425	2015KB168	5586167	647703	1538	Chataway	Propylitic	Moderate	5524	Highmont
2245426	2015KB169A	5586974	647351	1531	Chataway	Propylitic	Trace	4975	Highmont
2245427	2015KB169B	5586974	647351	1531	Chataway	Sodic-calcic	Trace	4975	Highmont
2245428	2015KB170	5586114	647305	1558	Chataway	Propylitic	Weak	5167	Highmont
2245429	2015KB171	5588317	646588	1501	Guichon	Sodic-calcic	Weak	3950	Highmont
2245431	2015KB172	5587799	646165	1550	Guichon	Propylitic	Weak	3625	Highmont
2245432	2015KB173	5587573	645310	1588	Skeena	Propylitic	Moderate	2860	Highmont
2245433	2015KB174	5588019	645268	1582	Skeena	Propylitic	Moderate	2702	Highmont

Sample ID	Station ID	Northing (m)	Easting (m)	Elev (m)	Lithology	Alteration	Alteration intensity	Distance to deposit	Nearest deposit
2245434	2015KB175	5587781	647551	1475	Skeena	K-feldspar-bearing	Weak	4982	Highmont
2245435	2015KB176	5588037	647264	1507	Guichon	Least altered	Trace	4657	Highmont
2245436	2015KB177	5587877	646808	1511	Guichon	K-feldspar-bearing	Moderate	4235	Highmont
2245437	2015KB178	5586768	646900	1573	Guichon	Sodic-calcic	Moderate	4581	Highmont
2245438	2015KB179	5587286	646563	1550	Transitional Guichon–Chataway	Propylitic	Moderate	4142	Highmont
2245439	2015KB180	5587062	646281	1602	Guichon	Propylitic	Weak	3910	Highmont
2245441	2015KB181	5586606	646112	1597	Skeena	Propylitic	Moderate	3878	Highmont
2245442	2015KB182	5586377	646525	1575	Skeena	Sodic-calcic	Strong	4344	Highmont
2245443	2015KB183	5587130	645857	1595	Skeena	Sodic-calcic	Weak	3482	Highmont
2245444	2015KB184	5587500	646156	1578	Chataway	Sodic-calcic	Moderate	3699	Highmont
2245445	2015KB185A	5587697	646830	1546	Chataway	Propylitic	Strong	4295	Highmont
2245446	2015KB185B	5587697	646830	1546	Chataway	K-feldspar-bearing	Strong	4295	Highmont
2245447	2015KB186	5587551	647121	1542	Chataway	Propylitic	Weak	4613	Highmont
2245448	2015KB188	5588277	644704	1627	Skeena	Propylitic	Moderate	2093	Highmont
2245449	2015KB189	5587839	644823	1630	Skeena	Propylitic	Moderate	2322	Highmont
2245451	2015KB190	5587793	644652	1633	Skeena	K-feldspar-bearing	Weak	2171	Highmont
2245452	2015KB191A	5588822	644669	1596	Skeena	Propylitic	Weak	2012	Highmont
2245453	2015KB192	5588656	644308	1646	Skeena	Propylitic	Weak	1651	Highmont
2245454	2015KB193	5588545	644069	1684	Skeena	Propylitic	Weak	1422	Highmont
2245455	2015KB195	5587766	644261	1664	Skeena	Propylitic	Strong	1795	Highmont
2245456	2015KB196	5588099	644216	1659	Skeena	Propylitic	Moderate	1672	Highmont
2245457	2015KB197	5588216	643738	1705	Skeena	Propylitic	Strong	1181	Highmont
2245458	2015KB198A	5588253	643301	1714	Skeena	Propylitic	Strong	746	Highmont
2245459	2015KB199	5588377	642690	1707	Skeena	K-feldspar-bearing	Strong	125	Highmont
2245461	2015KB200	5589173	644217	1622	Skeena	Propylitic	Strong	1619	Highmont
2245462	2015KB201	5588975	644319	1612	QFP	Propylitic	Weak	1677	Highmont
2245463	2015KB202	5588825	644490	1624	Skeena	Propylitic	Weak	1834	Highmont
2245464	2015KB204	5589107	644769	1561	Skeena	Propylitic	Weak	2143	Highmont
2245465	2015KB205	5589507	643936	1608	Skeena	Sodic-calcic	Weak	1492	Highmont
2245466	2015KB206	5589063	643752	1630	Skeena	Propylitic	Moderate	1142	Highmont
2245467	2015KB207	5588792	643937	1663	Skeena	Propylitic	Weak	1280	Highmont
2245468	2015KB208	5587348	644585	1634	Skeena	K-feldspar-bearing	Weak	2195	Highmont
2245469	2015KB209	5587268	645022	1648	Skeena	Propylitic	Trace	2638	Highmont
2245471	2015KB210	5587005	645303	1610	Skeena	Propylitic	Trace	2982	Highmont
2245472	2015KB212	5589524	644384	1592	Skeena	Propylitic	Weak	1898	Highmont
2245473	2015KB213	5589888	643998	1586	Skeena	Propylitic	Moderate	1767	Highmont
2245474	2015KB214	5589681	644012	1601	Skeena	Sodic-calcic	Strong	1651	Highmont
2245475	2015KB215	5590167	643829	1549	Skeena	Propylitic	Moderate	1849	Highmont
2245476	2015KB216	5590052	644272	1524	Skeena	Sodic-calcic	Trace	2082	Highmont
2245477	2015KB217	5589680	642833	1610	Skeena	Propylitic	Weak	941	Highmont
2245478	2015KB218	5589418	642894	1625	Skeena	Sodic-calcic	Moderate	720	Highmont
2245479	2015KB219	5589254	642983	1635	Skeena	Propylitic	Weak	611	Highmont
2245481	2015KB221	5590037	643320	1580	Skeena	Propylitic	Weak	1460	Highmont
2245482	2015KB222	5588921	643028	1629	Skeena	Propylitic	Weak	414	Highmont
2245483	2015KB224	5589271	643394	1620	Skeena	Propylitic	Moderate	910	Highmont
2245484	2015KB225	5588727	643115	1640	Skeena	K-feldspar-bearing	Moderate	457	Highmont
2245485	2015KB226	5588467	643015	1705	Skeena	Propylitic	Weak	434	Highmont
2245486	2015KB227	5588498	643345	1678	Skeena	Propylitic	Weak	721	Highmont
2245487	2015KB228	5588363	643873	1657	Skeena	Least altered	Weak	1266	Highmont
2245488	2015KB229A	5588947	643531	1634	Skeena	Sodic-calcic	Strong	898	Highmont
2245489	2015KB229B	5588947	643531	1634	Skeena	Sodic-calcic	Weak	898	Highmont
2245491	2015KB230B	5589832	643438	1581	Skeena	Propylitic	Trace	1345	Highmont
2245492	2015KB231	5589579	642639	1607	Skeena	Propylitic	Moderate	741	Highmont
2245493	2015KB233A	5589299	642302	1603	Skeena	Propylitic	Moderate	335	Highmont
2245494	2015KB233B	5589305	642302	1603	Skeena	Propylitic	Moderate	341	Highmont
2245495	2015KB234	5589722	642104	1563	Skeena	Propylitic	Trace	748	Highmont
2245496	2015KB235	5590226	641899	1546	Skeena	Propylitic	Trace	1073	Highmont
2245497	2015KB236A	5590107	642428	1549	Skeena	Propylitic	Moderate	1151	Highmont
2245498	2015KB236B	5590107	642428	1549	Skeena	Propylitic	Moderate	1151	Highmont
2245499	2015KB237	5590335	642165	1535	Skeena	Propylitic	Moderate	1315	Highmont
2247901	2015GL015	5585654	641131	1690	Bethsaida	Sodic-calcic	Weak	2346	Highmont
2247902	2015GL015	5585621	641162	1686	Bethsaida	Propylitic	Weak	2367	Highmont
2247903	2015GL016	5585827	640735	1670	Bethsaida	Sodic-calcic	Moderate	2360	Highmont
2247904	2015GL016	5585787	640719	1668	Bethsaida	Propylitic	Moderate	2402	Highmont
2247905	2015GL017	5584618	640352	1606	Bethsaida	K-feldspar-bearing	Weak	3607	Highmont
2247906	2015GL017	5584618	640352	1606	Bethsaida	Sodic-calcic	Weak	3606	Highmont
2247908	2015GL018	5585360	640303	1640	Bethsaida	Sodic-calcic	Moderate	2959	Highmont
2247909	2015GL019	5585259	640944	1671	Bethsaida	Sodic-calcic	Trace	2781	Highmont
2247910	2015GL020	5584733	641164	1644	Bethsaida	Propylitic	Weak	3219	Highmont
2247911	2015GL021	5584742	640725	1648	Bethsaida	Propylitic	Trace	3343	Highmont
2247912	2015GL022	5588898	640343	1649	Bethsaida	Sodic-calcic	Strong	719	Lornex
2247913	2015GL023	5585194	642284	1700	Bethsaida	Propylitic	Moderate	2624	Highmont

Sample ID	Station ID	Northing (m)	Easting (m)	Elev (m)	Lithology	Alteration	Alteration intensity	Distance to deposit	Nearest deposit
2247914	2015GL024	5585059	641864	1696	Bethsaida	Propylitic	Weak	2788	Highmont
2247915	2015GL024	5585063	641867	1700	Bethsaida	Least altered	Trace	2784	Highmont
2247916	2015GL025	5584417	641816	1652	Bethsaida	K-feldspar-bearing	Weak	3431	Highmont
2247917	2015GL026	5584415	642373	1683	Bethsaida	Sodic-calcic	Trace	3404	Highmont
2247920	2015GL026	5584415	642373	1683	Bethsaida	K-feldspar-bearing	Trace	3404	Highmont
2247921	2015GL027	5584823	642211	1700	Bethsaida	Propylitic	Trace	2996	Highmont
2247922	2015GL028	5593232	637322	1591	Bethsaida	K-feldspar-bearing	Weak	232	Valley
2247923	2015GL029	5593406	637089	1637	Bethsaida	K-feldspar-bearing	Weak	318	Valley
2247924	2015GL030	5593577	637226	1568	Bethsaida	K-feldspar-bearing	Strong	186	Valley
2247925	2015GL031	5593915	637270	1513	Bethsaida	Muscovite-bearing	Trace	225	Valley
2247926	2015GL032	5593473	637482	1558	Bethsaida	K-feldspar-bearing	Moderate	0	Valley
2247927	2015GL033	5584984	642670	1664	Bethsaida	Propylitic	Weak	2859	Highmont
2247928	2015GL034	5585048	643219	1661	Skeena	Least altered	No alteration	2918	Highmont
2247929	2015GL035	5585464	642891	1663	Skeena	Propylitic	Weak	2429	Highmont
2247931	2015GL036	5584507	643372	1627	Skeena	Sodic-calcic	Weak	3480	Highmont
2247932	2015GL037	5584128	643566	1635	Bethsaida	Propylitic	Weak	3900	Highmont
2247933	2015GL038	5584338	642900	1656	Bethsaida	Sodic-calcic	Moderate	3533	Highmont
2247934	2015GL038	5584376	642876	1656	Bethsaida	Propylitic	Moderate	3492	Highmont
2247935	2015GL039	5584840	644680	1633	Skeena	Propylitic	Weak	3782	Highmont
2247936	2015GL040	5584352	644710	1655	Skeena	Propylitic	Trace	4199	Highmont
2247937	2015GL041	5583430	644814	1627	Bethsaida	Propylitic	Trace	5043	Highmont
2247938	2015GL042	5584034	640316	1591	Bethsaida	K-feldspar-bearing	Weak	4153	Highmont
2247939	2015GL043	5583570	640306	1579	Bethsaida	Propylitic	Weak	4587	Highmont
2247940	2015GL044	5583000	640259	1556	Bethsaida	Propylitic	Moderate	5140	Highmont
2247943	2015GL045	5583078	640881	1593	Bethsaida	Least altered	Trace	4895	Highmont
2247944	2015GL046	5583743	640977	1603	Bethsaida	Least altered	No alteration	4226	Highmont
2247945	2015GL047	5583409	641361	1633	Bethsaida	Propylitic	Weak	4486	Highmont
2247946	2015GL048	5583258	641871	1591	Bethsaida	Propylitic	Strong	4578	Highmont
2247947	2015GL049	5583793	641824	1632	Bethsaida	Propylitic	Weak	4050	Highmont
2247948	2015GL050	5583812	641407	1602	Bethsaida	Propylitic	Weak	4081	Highmont
2247949	2015GL050	5583811	641407	1602	Bethsaida	Least altered	Weak	4081	Highmont
2247950	2015GL051	5584234	641410	1627	Bethsaida	Sodic-calcic	Strong	3661	Highmont
2758851	2015GL051	5584225	641400	1629	Bethsaida	Propylitic	Strong	3672	Highmont
2758852	2015GL052	5582754	641872	1590	Bethsaida	Propylitic	Weak	5080	Highmont
2758854	2015GL053	5582913	642475	1610	Bethsaida	Least altered	Weak	4908	Highmont
2758855	2015GL054	5582138	642337	1571	Bethsaida	Propylitic	Trace	5680	Highmont
2758856	2015GL055	5584068	642455	1652	Bethsaida	K-feldspar-bearing	Moderate	3754	Highmont
2758857	2015GL056	5583564	642441	1624	Bethsaida	Propylitic	Trace	4257	Highmont
2758858	2015GL057	5582602	643025	1597	Bethsaida	Least altered	Moderate	5267	Highmont
2758859	2015GL058	5583159	643120	1617	Bethsaida	Propylitic	Weak	4732	Highmont
2758860	2015GL059	5583709	642928	1631	Bethsaida	Sodic-calcic	Strong	4158	Highmont
2758861	2015GL060	5583818	643340	1611	Bethsaida	Least altered	No alteration	4135	Highmont
2758862	2015GL061	5583811	644141	1620	Bethsaida	Least altered	No alteration	4403	Highmont
2758863	2015GL062	5583731	644100	1616	Bethsaida	Sodic-calcic	Moderate	4460	Highmont
2758866	2015GL063	5583310	643846	1584	Bethsaida	Propylitic	Trace	4764	Highmont
2758867	2015GL064	5582769	643512	1606	Bethsaida	Propylitic	Weak	5194	Highmont
2758868	2015GL065	5583128	644915	1599	Aplite dike	Muscovite-bearing	Strong	5357	Highmont
2758869	2015GL065	5583022	644891	1593	Bethsaida	Muscovite-bearing	Strong	5440	Highmont
2758870	2015GL066	5582875	644891	1591	Bethsaida	Sodic-calcic	Weak	5570	Highmont
2758871	2015GL067	5583112	644559	1599	Bethsaida	Propylitic	Weak	5212	Highmont
2758872	2015GL068	5582352	643463	1605	Bethsaida	Least altered	Trace	5590	Highmont
2758873	2015GL069	5581613	643362	1565	Bethsaida	Propylitic	Moderate	6297	Highmont
2758874	2015GL070	5581748	642800	1592	Bethsaida	Propylitic	Weak	6092	Highmont
2758875	2015GL071	5580301	642174	1618	Bethsaida	Propylitic	Weak	7517	Highmont
2758877	2015GL072	5581694	642334	1558	Bethsaida	Least altered	No alteration	6124	Highmont
2758878	2015GL073	5581150	643385	1567	QFP	Propylitic	Weak	6757	Highmont
2758879	2015GL073	5581136	643387	1565	Bethsaida	Propylitic	Strong	6771	Highmont
2758880	2015GL074	5580798	643747	1543	Bethsaida	Propylitic	Weak	7169	Highmont
2758881	2015GL075	5579702	642719	1574	Bethsaida	Propylitic	Weak	8127	Highmont
2758882	2015GL076	5578972	642595	1532	Bethsaida	Least altered	Trace	8851	Highmont
2758883	2015GL077	5579441	642172	1556	Bethsaida	Propylitic	Weak	8377	Highmont
2758884	2015GL078	5579807	641915	1576	Bethsaida	Least altered	No alteration	8020	Highmont
2758885	2015GL079	5579315	641644	1548	Bethsaida	Propylitic	Moderate	8527	Highmont
2758886	2015GL080	5580110	644477	1476	Bethsaida	Sodic-calcic	Strong	8012	Highmont
2758889	2015GL081	5580162	643649	1512	Aplite dike	Intermediate argillic	Trace	7776	Highmont
2758890	2015GL081	5580180	643590	1513	Bethsaida	Propylitic	Moderate	7748	Highmont
2758891	2015GL082	5579362	644243	1454	Bethsaida	Propylitic	Moderate	8678	Highmont
2758892	2015GL083	5580330	644424	1483	QFP	Propylitic	Moderate	7785	Highmont
2758893	2015GL084	5578203	640836	1419	Bethsaida	Least altered	Trace	9718	Highmont
2758894	2015GL085	5578769	640901	1460	Bethsaida	Propylitic	Weak	9148	Highmont
2758895	2015GL086	5578794	641804	1498	Bethsaida	Propylitic	Trace	9037	Highmont
2758896	2015GL087	5578416	641875	1501	Bethsaida	Propylitic	Weak	9411	Highmont

Sample ID	Station ID	Northing (m)	Easting (m)	Elev (m)	Lithology	Alteration	Alteration intensity	Distance to deposit	Nearest deposit
2758897	2015GL088	5577968	642245	1462	Bethsaida	Propylitic	Moderate	9850	Highmont
2758898	2015GL089	5578161	642348	1490	Aplite dike	Propylitic	Weak	9657	Highmont
2758900	2015GL090	5578699	642354	1524	Bethsaida	Propylitic	Trace	9120	Highmont

Appendix D. Rietveld refinement quantitative mineralogy: X-ray diffractograms

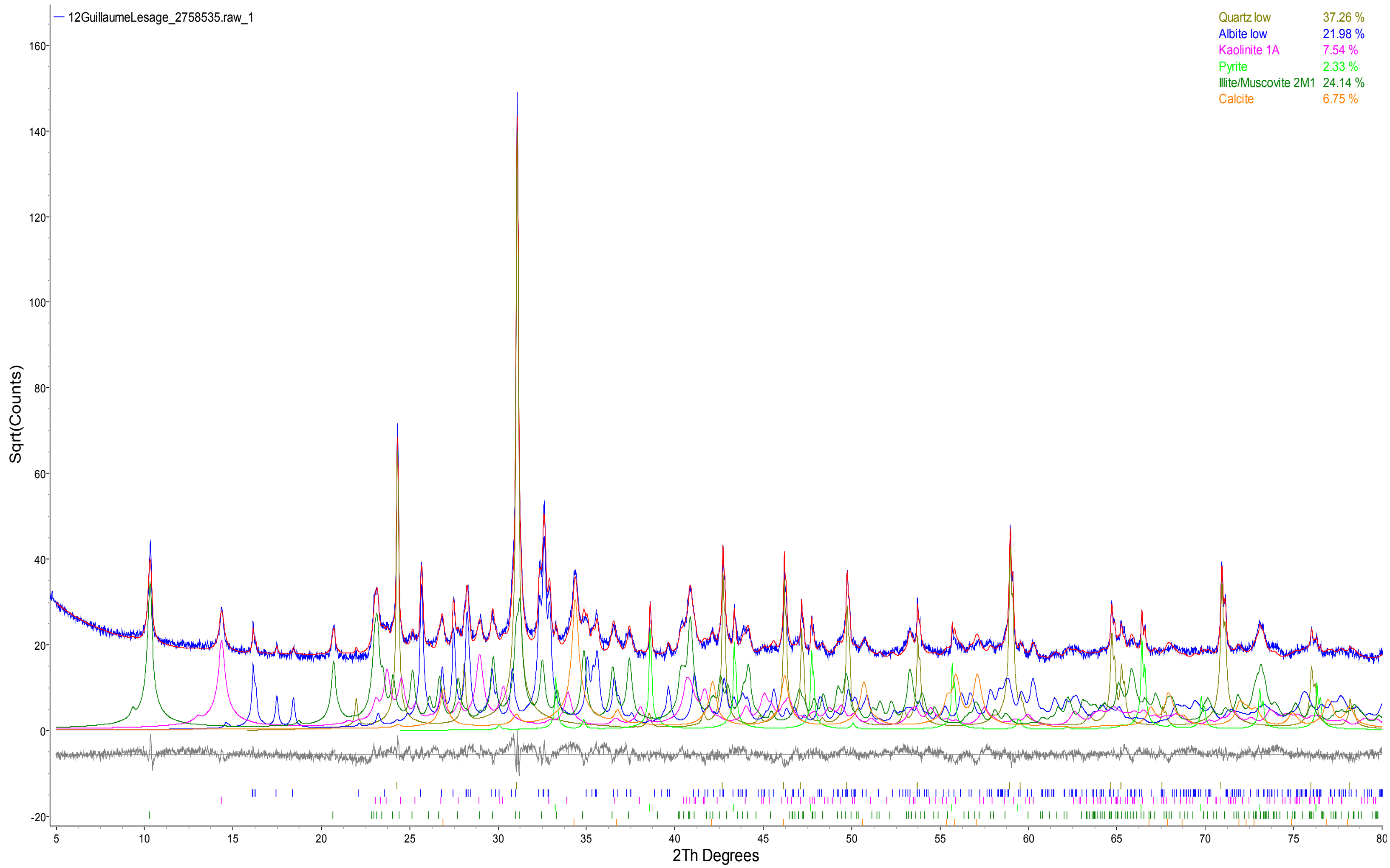

Rietveld refinement plot of sample **BC14278V** (blue line - observed intensity at each step; red line - calculated pattern; solid grey line below – difference between observed and calculated intensities; vertical bars - positions of all Bragg reflections). Coloured lines are individual diffraction patterns of all phases.

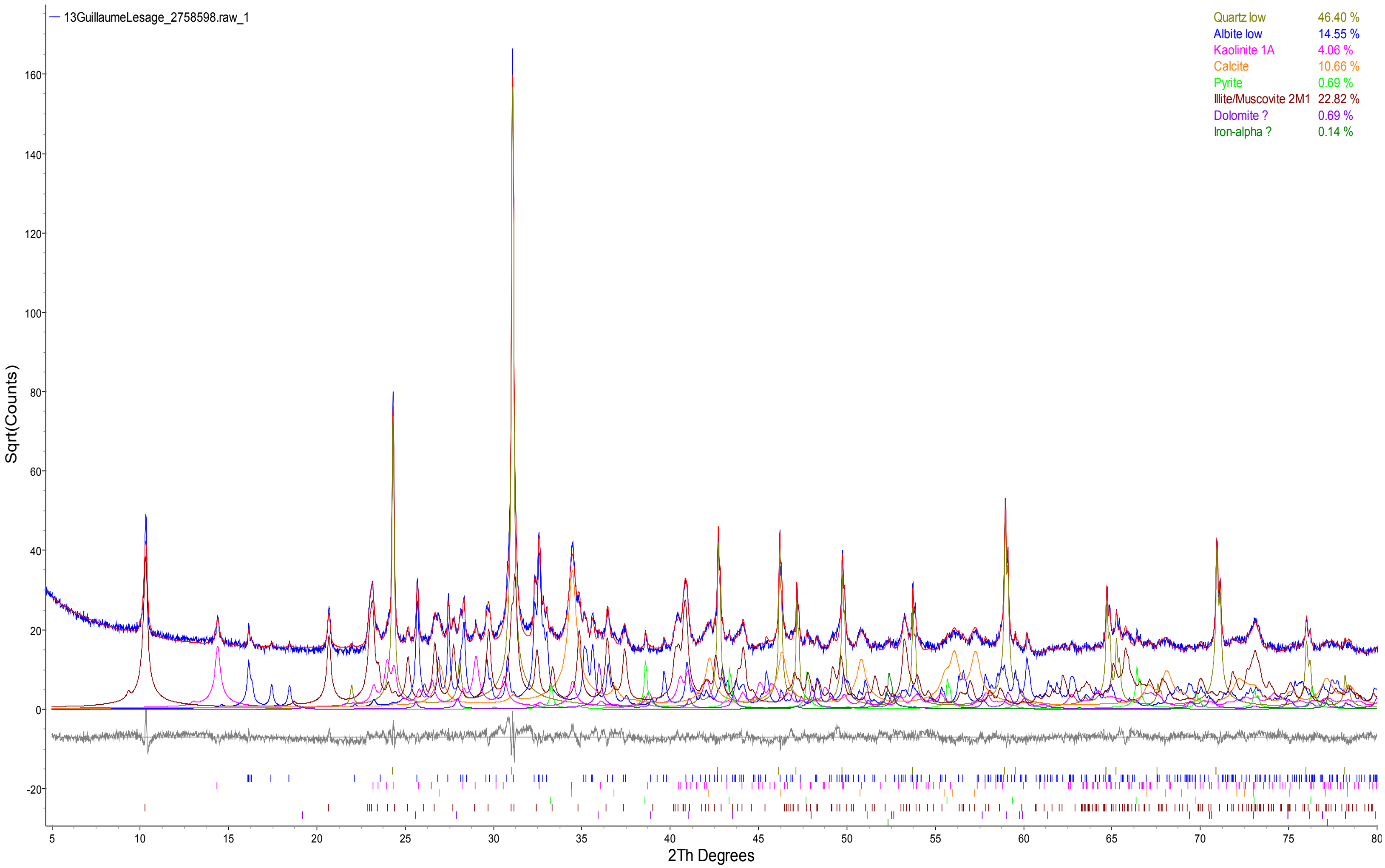

Rietveld refinement plot of sample **BC14281B** (blue line - observed intensity at each step; red line - calculated pattern; solid grey line below – difference between observed and calculated intensities; vertical bars - positions of all Bragg reflections). Coloured lines are individual diffraction patterns of all phases.

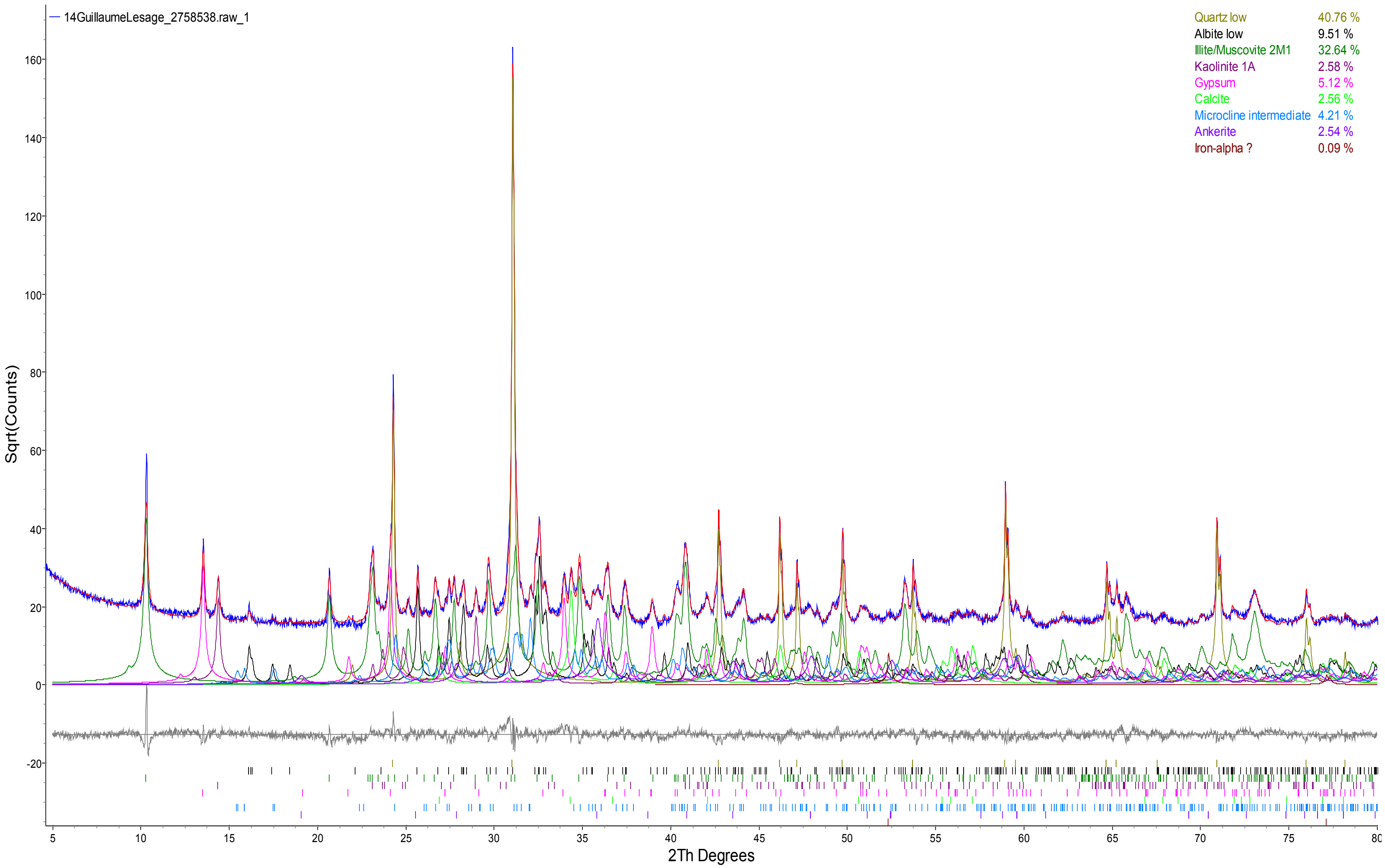

Rietveld refinement plot of sample **BC14294A** (blue line - observed intensity at each step; red line - calculated pattern; solid grey line below – difference between observed and calculated intensities; vertical bars - positions of all Bragg reflections). Coloured lines are individual diffraction patterns of all phases.

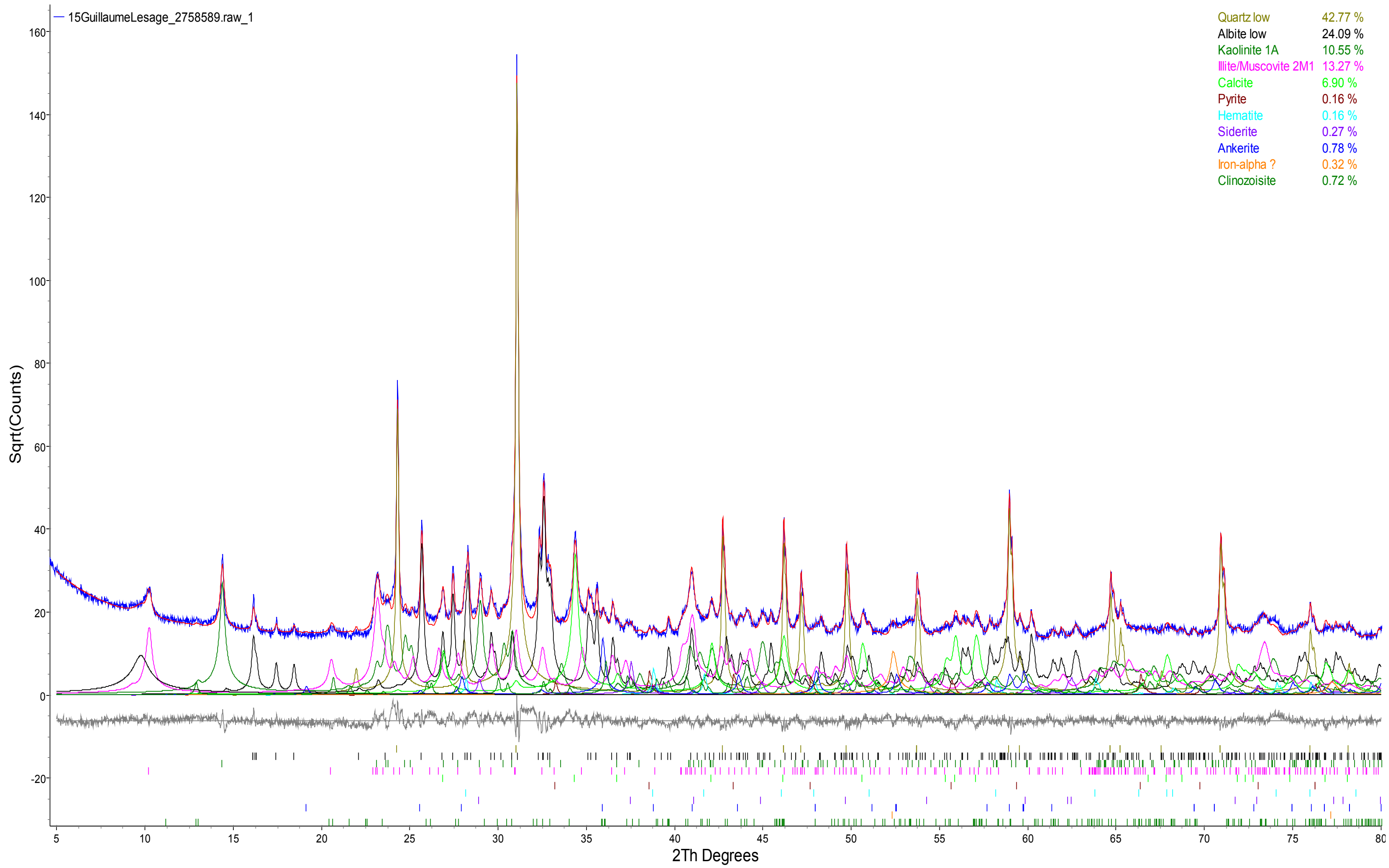

Rietveld refinement plot of sample **BC14295A** (blue line - observed intensity at each step; red line - calculated pattern; solid grey line below – difference between observed and calculated intensities; vertical bars - positions of all Bragg reflections). Coloured lines are individual diffraction patterns of all phases.

Appendix E. SWIR data: hyperspectral scan results (Al-OH absorption feature wavelength).

Sample ID	Station ID	Percentage (%) of pixels from sample slabs that contain an Al-OH absorption feature of specified wavelength (nm)																							
		2190 – 2191	2191 – 2192	2192 – 2193	2193 – 2194	2194 – 2195	2195 – 2197	2197 – 2198	2198 – 2199	2199 – 2200	2200 – 2201	2201 – 2202	2202 – 2203	2203 – 2204	2204 – 2205	2205 – 2206	2206 – 2207	2207 – 2208	2208 – 2209	2209 – 2210	2210 – 2211	2211 – 2212	2212 – 2213	2213 – 2214	2214 – 2220
2232401	2015GL091	8.21	19.71	18.55	27.21	10.21	8.55	3.95	2.09	0.91	0.35	0.16	0.04	0.02	0.00	0.01	0.01	0.02	0.00	0.00	0.00	0.00	0.00	0.00	0.00
2232402	2015GL092	1.25	3.49	4.97	17.05	13.02	18.14	8.47	7.24	6.96	7.00	5.23	3.14	1.94	1.43	0.53	0.06	0.07	0.00	0.00	0.00	0.00	0.00	0.00	0.00
2232403	2015GL093	1.03	1.68	1.70	1.96	1.11	1.22	9.87	14.00	16.80	17.89	16.10	10.60	3.71	1.05	0.59	0.33	0.29	0.01	0.00	0.00	0.01	0.00	0.00	0.03
2232404	2015GL094	0.40	0.35	0.35	1.53	2.71	13.46	9.44	8.51	8.02	7.48	7.09	6.86	7.53	10.76	14.41	0.89	0.15	0.02	0.00	0.00	0.00	0.02	0.00	0.04
2232406	2015GL096	3.16	0.99	0.41	0.50	0.30	1.57	10.14	12.35	10.95	9.17	9.38	11.28	11.66	9.74	5.38	1.72	1.30	0.00	0.00	0.00	0.00	0.00	0.00	0.00
2232407	2015GL096	0.10	0.00	0.00	0.00	0.00	0.00	0.00	0.00	0.00	0.00	0.03	0.24	2.77	36.85	57.60	2.12	0.26	0.01	0.00	0.00	0.00	0.00	0.00	0.00
2232408	2015GL097	0.37	0.09	0.05	0.10	0.18	0.79	0.82	1.02	1.46	2.29	3.83	5.71	11.40	35.52	31.09	4.48	0.54	0.05	0.02	0.01	0.02	0.02	0.01	0.12
2232409	2015GL097	0.18	0.05	0.02	0.03	0.64	15.70	14.07	14.22	14.16	14.09	12.36	8.58	4.13	1.18	0.30	0.11	0.16	0.00	0.00	0.00	0.00	0.00	0.00	0.00
2232412	2015GL098	0.05	0.00	0.00	0.00	0.00	0.18	0.55	1.50	2.87	4.96	8.30	14.58	25.23	29.00	11.74	0.95	0.09	0.00	0.00	0.00	0.00	0.00	0.00	0.01
2232413	2015GL099	0.79	0.02	0.02	0.03	0.03	0.12	0.48	1.73	4.57	10.11	18.19	24.96	22.38	11.30	3.63	0.94	0.68	0.01	0.00	0.00	0.00	0.00	0.00	0.01
2232414	2015GL100	0.03	0.00	0.00	0.00	0.00	0.01	0.15	0.89	3.61	9.54	19.12	30.74	22.99	9.68	2.81	0.31	0.10	0.00	0.00	0.00	0.00	0.00	0.00	0.00
2232415	2015GL101	0.05	0.00	0.00	0.00	0.00	0.01	0.10	0.46	1.38	3.81	9.67	18.14	29.02	28.04	8.74	0.45	0.10	0.01	0.00	0.00	0.00	0.00	0.00	0.00
2232416	2015GL102	0.07	0.00	0.00	0.00	0.00	0.00	0.00	0.02	0.04	0.32	1.52	11.40	49.24	32.60	4.21	0.41	0.16	0.00	0.00	0.00	0.00	0.00	0.00	0.00
2232417	2015GL103	0.03	0.00	0.00	0.00	0.00	0.00	0.01	0.05	0.17	0.60	1.72	7.68	31.35	41.00	15.21	2.03	0.13	0.00	0.00	0.00	0.00	0.00	0.00	0.00
2232418	2015GL104	0.88	1.90	2.05	2.15	0.91	0.64	7.20	9.15	10.58	11.80	11.92	12.12	11.01	8.64	4.64	2.36	1.09	0.44	0.15	0.04	0.09	0.11	0.03	0.09
2232419	2015GL105	38.99	29.97	7.10	6.64	3.26	1.34	6.79	3.15	1.46	0.59	0.32	0.23	0.14	0.02	0.00	0.00	0.01	0.00	0.00	0.00	0.00	0.00	0.00	0.00
2232420	2015GL106	0.05	0.00	0.00	0.01	0.04	0.30	0.67	1.42	2.62	4.20	6.82	11.02	21.54	34.46	15.39	1.23	0.21	0.00	0.00	0.00	0.00	0.00	0.00	0.00
2232421	2015GL107	0.06	0.01	0.00	0.00	0.00	0.02	0.08	0.38	1.24	4.49	14.98	29.75	30.09	15.70	2.88	0.26	0.08	0.00	0.00	0.00	0.00	0.00	0.00	0.00
2232423	2015GL108	0.04	0.00	0.00	0.00	0.00	0.00	0.01	0.02	0.09	0.10	0.27	1.06	6.71	53.39	36.40	1.76	0.14	0.00	0.00	0.00	0.00	0.00	0.00	0.00
2232424	2015GL109	0.40	0.60	0.66	1.16	1.06	1.80	3.18	4.30	6.39	8.44	11.19	13.30	13.22	12.29	9.68	6.36	1.04	0.50	0.20	0.13	0.28	1.00	0.22	2.59
2232425	2015GL110	4.89	6.51	2.56	1.85	0.86	0.58	11.68	13.85	14.34	13.14	10.43	7.73	6.04	4.04	1.12	0.23	0.12	0.00	0.00	0.00	0.00	0.00	0.00	0.00
2232426	2015GL111	0.66	0.74	0.67	1.38	3.08	15.97	17.40	17.99	15.64	10.81	6.46	3.77	2.64	1.39	0.67	0.31	0.36	0.04	0.00	0.00	0.00	0.01	0.00	0.01
2232427	2015GL112	26.61	43.06	10.80	5.53	1.30	0.31	3.09	2.34	1.98	1.44	1.06	0.87	0.58	0.45	0.29	0.16	0.10	0.01	0.01	0.00	0.00	0.00	0.00	0.00
2232428	2015GL113	5.95	7.74	5.86	24.17	14.45	10.46	4.54	2.77	2.31	1.21	1.67	1.47	0.47	0.57	1.25	1.22	3.09	0.81	0.37	0.20	0.53	0.97	0.59	7.33
2232429	2015GL114	0.03	0.00	0.00	0.00	0.00	0.00	0.01	0.03	0.11	0.54	2.62	19.53	42.25	23.07	9.32	2.25	0.21	0.00	0.00	0.00	0.00	0.00	0.00	0.02
2232430	2015GL115	0.09	0.01	0.00	0.01	0.01	0.18	0.77	2.33	5.92	17.34	35.39	28.04	8.25	1.18	0.25	0.08	0.09	0.01	0.00	0.00	0.00	0.01	0.00	0.03
2232431	2015GL116	0.08	0.01	0.01	0.01	0.00	0.03	0.18	0.42	1.06	2.38	5.95	14.77	31.82	24.55	11.00	3.83	0.45	0.16	0.08	0.05	0.13	0.85	0.10	2.08
2232432	2015GL117	0.13	0.02	0.02	0.04	0.03	0.22	0.58	1.02	2.04	5.27	12.80	23.13	25.02	13.30	6.40	3.72	0.62	0.49	0.27	0.14	0.36	1.22	0.28	2.86
2232435	2015GL118	0.46	1.36	2.32	10.70	10.72	25.88	13.72	11.60	8.43	5.73	3.47	1.94	1.24	0.79	0.57	0.43	0.21	0.02	0.01	0.01	0.02	0.10	0.00	0.26
2232436	2015GL119	2.14	2.09	0.97	0.96	0.93	1.72	6.47	8.50	11.37	16.52	21.63	14.83	6.81	3.10	1.51	0.36	0.09	0.00	0.00	0.00	0.00	0.00	0.00	0.00
2232437	2015GL120	0.13	0.04	0.02	0.03	0.03	0.41	1.38	3.27	6.56	9.71	12.60	18.69	26.19	14.93	4.37	1.12	0.39	0.03	0.02	0.00	0.02	0.01	0.01	0.03
2232438	2015GL121	0.07	0.00	0.00	0.00	0.00	0.00	0.02	0.07	0.36	1.17	4.65	23.05	43.09	21.29	5.84	0.33	0.06	0.00	0.00	0.00	0.00	0.00	0.00	0.00
2232439	2015GL122	0.15	0.03	0.07	0.14	0.10	0.08	0.82	1.85	4.30	8.43	15.28	20.78	21.20	15.43	7.60	3.01	0.51	0.05	0.02	0.01	0.02	0.03	0.01	0.09
2232440	2015GL123	0.30	0.16	0.08	0.15	0.17	0.50	2.12	4.25	7.81	12.69	17.21	18.53	15.61	10.23	5.50	2.41	0.78	0.35	0.19	0.11	0.23	0.26	0.08	0.27
2232441	2015GL124	0.05	0.00	0.00	0.00	0.00	0.32	0.63	1.01	1.99	3.98	9.31	22.12	32.05	20.56	6.31	1.34	0.26	0.02	0.00	0.00	0.00	0.01	0.00	0.02
2232442	2015GL125	7.42	3.57	1.09	1.04	0.85	1.91	9.92	13.18	15.37	15.65	13.22	9.16	4.88	1.78	0.61	0.22	0.12	0.01	0.00	0.00	0.00	0.00	0.00	0.01
2232443	2015GL126	0.04	0.00	0.00	0.00	0.00	0.02	0.10	0.36	1.39	4.60	14.49	31.21	29.24	12.74	4.36	1.17	0.10	0.00	0.00	0.00	0.00	0.00	0.00	0.15
2232444	2015GL127	26.53	22.36	7.14	5.64	2.91	1.50	10.31	8.03	6.10	4.14	2.65	1.66	0.60	0.19	0.09	0.05	0.06	0.00	0.00	0.00	0.00	0.01	0.00	0.02
2232446	2015GL128	0.16	0.01	0.00	0.00	0.00	0.02	0.04	0.06	0.07	0.14	0.33	0.71	3.20	31.08	42.76	17.62	1.01	0.27	0.17	0.05	0.23	0.29	0.18	1.61
2232447	2015GL129	15.47	31.07	12.01	14.25	7.71	3.09	5.65	3.66	2.60	1.81	1.20	0.83	0.39	0.14	0.04	0.01	0.01	0.00	0.00	0.00	0.00	0.00	0.00	0.05
2238654	2014GL001	0.87	0.42	0.32	0.74	2.91	22.67	18.70	14.87	10.53	7.66	6.16	4.56	3.41	2.31	1.67	1.01	0.65	0.14	0.06	0.02	0.04	0.08	0.02	0.18
2238655	2014GL002	4.06	5.19	5.34	9.77	12.04	17.39	17.17	11.41	8.21	6.29	2.59	0.42	0.07	0.01	0.01	0.01	0.02	0.00	0.00	0.00	0.00	0.00	0.00	0.00
2238656	2014GL003	3.82	4.92	4.01	7.59	13.90	22.55	19.56	12.40	6.26	3.05	1.45	0.39	0.07	0.00	0.01	0.01	0.01	0.00	0.00	0.00	0.00	0.00	0.00	0.00

Sample ID	Station ID	Percentage (%) of pixels from sample slabs that contain an Al-OH absorption feature of specified wavelength (nm)																							
		2190 – 2191	2191 – 2192	2192 – 2193	2193 – 2194	2194 – 2195	2195 – 2197	2197 – 2198	2198 – 2199	2199 – 2200	2200 – 2201	2201 – 2202	2202 – 2203	2203 – 2204	2204 – 2205	2205 – 2206	2206 – 2207	2207 – 2208	2208 – 2209	2209 – 2210	2210 – 2211	2211 – 2212	2212 – 2213	2213 – 2214	2214 – 2220
2238657	2014GL004	7.65	12.02	9.81	29.09	22.31	10.70	5.02	1.96	0.91	0.32	0.11	0.05	0.02	0.01	0.02	0.00	0.01	0.00	0.00	0.00	0.00	0.00	0.00	0.00
2238658	2014GL005	20.84	22.79	7.40	7.18	5.61	3.04	15.66	9.86	4.67	1.87	0.75	0.22	0.06	0.00	0.01	0.00	0.02	0.00	0.00	0.00	0.00	0.00	0.00	0.00
2238659	2014GL006	9.49	16.42	13.18	44.80	12.99	2.27	0.50	0.19	0.05	0.03	0.01	0.01	0.00	0.00	0.02	0.01	0.01	0.00	0.00	0.00	0.00	0.00	0.00	0.00
2238660	2014GL007	2.17	5.69	5.25	7.95	9.27	16.53	21.45	12.08	5.19	2.85	2.36	2.24	2.29	2.07	1.34	0.78	0.25	0.03	0.01	0.01	0.01	0.05	0.01	0.13
2238662	2014GL008	4.55	6.96	6.05	9.51	11.27	29.28	22.16	7.61	1.86	0.45	0.18	0.08	0.03	0.00	0.00	0.00	0.00	0.00	0.00	0.00	0.00	0.00	0.00	0.00
2238663	2014GL009	9.70	11.67	11.69	31.09	18.91	6.88	4.26	2.22	1.52	0.95	0.56	0.34	0.14	0.03	0.01	0.00	0.01	0.00	0.00	0.00	0.00	0.00	0.00	0.00
2238664	2014GL010	4.43	5.34	6.32	14.83	26.01	25.23	7.36	4.55	3.16	1.61	0.74	0.30	0.08	0.01	0.01	0.00	0.01	0.00	0.00	0.00	0.00	0.00	0.00	0.00
2238667	2014GL012	1.16	0.93	0.84	1.33	2.40	14.95	16.79	16.91	15.16	12.28	9.38	4.80	2.05	0.75	0.15	0.03	0.09	0.00	0.00	0.00	0.00	0.00	0.00	0.00
2238668	2014GL013	1.52	1.22	0.57	0.88	2.41	15.45	14.91	14.32	12.46	9.74	8.27	6.28	4.38	2.84	1.67	1.03	0.71	0.33	0.11	0.04	0.10	0.21	0.06	0.51
2238669	2014GL014	29.78	45.72	11.12	6.00	1.66	0.18	3.70	1.18	0.41	0.16	0.04	0.02	0.01	0.00	0.00	0.00	0.00	0.00	0.00	0.00	0.00	0.00	0.00	0.00
2238670	2014GL015	11.54	23.97	16.85	27.21	11.21	3.54	3.74	1.36	0.39	0.12	0.04	0.01	0.01	0.00	0.00	0.00	0.01	0.00	0.00	0.00	0.00	0.00	0.00	0.00
2238671	2014GL016	3.05	3.79	3.24	5.57	8.53	41.68	22.83	8.03	2.18	0.67	0.21	0.12	0.05	0.01	0.02	0.00	0.04	0.00	0.00	0.00	0.00	0.00	0.00	0.00
2238674	2014GL017	9.10	14.53	9.80	27.29	14.83	9.32	4.97	3.14	2.00	1.41	0.91	0.60	0.44	0.39	0.37	0.30	0.34	0.03	0.02	0.00	0.01	0.07	0.02	0.12
2238675	2014GL018	3.75	4.08	3.28	9.63	24.25	35.23	9.70	4.80	2.61	1.39	0.69	0.30	0.17	0.04	0.03	0.01	0.03	0.00	0.00	0.00	0.00	0.00	0.00	0.01
2238676	2014GL019	2.86	3.84	3.54	6.33	9.66	24.80	21.17	13.16	7.01	3.27	1.53	0.91	0.49	0.33	0.22	0.17	0.18	0.02	0.02	0.00	0.02	0.07	0.02	0.40
2238677	2014GL020	2.05	2.40	1.44	1.74	1.42	2.98	16.18	23.94	23.73	14.82	6.54	2.23	0.41	0.07	0.02	0.01	0.02	0.00	0.00	0.00	0.00	0.00	0.00	0.00
2238678	2014GL021	5.75	5.77	3.97	37.05	25.38	13.11	3.23	1.60	1.07	0.49	0.49	0.47	0.17	0.17	0.26	0.21	0.37	0.02	0.00	0.00	0.02	0.06	0.04	0.27
2238679	2014GL022	1.73	0.94	0.39	4.76	23.06	41.35	8.88	7.33	6.03	3.67	1.27	0.39	0.14	0.03	0.02	0.00	0.02	0.00	0.00	0.00	0.00	0.00	0.00	0.00
2238681	2014GL024	5.77	7.07	6.72	30.40	22.87	13.31	4.19	2.02	1.25	0.62	0.52	0.44	0.25	0.25	0.39	0.39	0.45	0.14	0.06	0.01	0.07	0.32	0.09	2.40
2238682	2014GL025	11.09	14.16	10.28	29.53	17.92	7.73	4.02	2.09	1.11	0.56	0.39	0.21	0.06	0.07	0.09	0.09	0.14	0.04	0.01	0.01	0.02	0.06	0.03	0.30
2238683	2014GL026	8.07	9.87	7.78	34.26	15.66	6.35	2.24	1.25	1.04	0.53	0.83	1.26	0.34	0.51	1.14	0.99	2.10	0.57	0.26	0.13	0.30	0.53	0.28	3.74
2238685	2014GL027	4.26	4.71	4.10	18.54	27.45	25.03	6.97	3.48	1.56	0.77	0.48	0.33	0.22	0.15	0.28	0.20	0.51	0.07	0.03	0.02	0.05	0.13	0.04	0.60
2238686	2014GL028	5.57	8.68	8.22	19.11	22.55	25.17	7.05	2.38	0.69	0.28	0.14	0.09	0.06	0.01	0.01	0.00	0.01	0.00	0.00	0.00	0.00	0.00	0.00	0.00
2238687	2014GL028	8.46	9.06	6.81	35.15	15.99	7.21	5.92	4.10	2.79	1.95	1.25	0.71	0.35	0.12	0.04	0.04	0.05	0.00	0.00	0.00	0.00	0.01	0.00	0.00
2238688	2014GL029	2.94	3.36	3.05	31.93	27.80	19.69	4.17	2.13	1.26	0.59	0.39	0.23	0.15	0.14	0.20	0.23	0.47	0.09	0.02	0.02	0.03	0.13	0.03	0.96
2238689	2014GL030	5.31	6.57	7.10	47.63	9.43	9.29	5.36	3.73	2.44	1.37	0.75	0.46	0.21	0.10	0.05	0.05	0.08	0.02	0.01	0.00	0.00	0.00	0.00	0.03
2238690	2014GL031	1.05	0.42	0.37	0.68	1.81	13.36	14.73	15.46	13.92	11.32	9.08	6.57	4.56	2.55	1.50	0.84	0.51	0.16	0.07	0.03	0.06	0.22	0.04	0.68
2238691	2014GL032	7.69	9.76	10.51	64.07	7.25	0.42	0.17	0.06	0.02	0.02	0.01	0.02	0.00	0.00	0.00	0.00	0.00	0.00	0.00	0.00	0.00	0.00	0.00	0.00
2238692	2014GL033	1.86	1.98	1.82	21.54	20.60	18.10	4.81	2.98	2.34	1.58	1.50	1.36	1.00	0.98	1.15	1.24	2.90	0.96	0.37	0.17	0.53	1.05	0.60	8.56
2238693	2014GL034	7.07	6.46	5.44	48.37	23.73	6.93	1.23	0.39	0.15	0.09	0.05	0.03	0.02	0.01	0.00	0.01	0.02	0.01	0.00	0.00	0.00	0.00	0.00	0.00
2238694	2014GL035	13.19	24.06	16.13	27.94	11.00	2.31	2.09	1.08	0.70	0.34	0.26	0.46	0.06	0.07	0.10	0.08	0.07	0.02	0.01	0.00	0.00	0.00	0.00	0.02
2238697	2014GL036	2.72	4.16	3.31	8.06	12.54	17.20	12.63	9.87	8.46	7.07	5.55	4.14	2.43	1.05	0.37	0.15	0.20	0.00	0.01	0.00	0.00	0.02	0.00	0.07
2238698	2014GL036	6.25	12.57	11.29	22.30	26.48	14.16	4.85	1.29	0.44	0.19	0.06	0.02	0.00	0.00	0.01	0.00	0.06	0.01	0.00	0.00	0.00	0.00	0.00	0.01
2238699	2014GL037	2.48	1.86	1.25	3.19	12.72	38.15	15.14	10.80	7.44	4.51	1.81	0.48	0.13	0.01	0.01	0.01	0.01	0.00	0.00	0.00	0.00	0.00	0.00	0.00
2238700	2014GL037	11.29	8.77	2.25	1.71	1.04	0.96	13.28	11.74	9.61	7.39	5.74	4.50	3.31	2.35	2.37	2.03	8.98	1.06	0.30	0.11	0.21	0.24	0.10	0.67
2238701	2014GL038	12.00	18.87	12.76	30.76	19.57	3.76	1.49	0.50	0.15	0.05	0.04	0.01	0.01	0.00	0.01	0.00	0.03	0.00	0.00	0.00	0.00	0.00	0.00	0.00
2238702	2014GL038	3.17	3.91	3.55	11.89	21.34	27.37	9.05	4.86	2.97	1.73	1.36	1.00	0.58	0.52	0.61	0.64	0.73	0.34	0.12	0.08	0.22	0.52	0.22	3.22
2238703	2014GL039	6.96	11.84	6.76	11.99	12.54	10.05	17.29	11.63	6.45	2.91	1.14	0.33	0.06	0.02	0.00	0.00	0.01	0.00	0.00	0.00	0.00	0.00	0.00	0.00
2238704	2014GL040	6.34	9.89	8.94	40.15	22.96	7.23	1.68	0.83	0.47	0.26	0.24	0.36	0.11	0.08	0.12	0.10	0.08	0.02	0.01	0.01	0.02	0.02	0.01	0.06
2238705	2014GL041	14.04	20.12	12.58	19.22	16.56	6.90	6.06	2.37	1.04	0.54	0.23	0.16	0.05	0.04	0.02	0.01	0.05	0.00	0.00	0.00	0.00	0.00	0.00	0.00
2238706	2014GL041	3.72	4.59	3.28	4.75	7.73	26.41	21.74	14.97	7.54	2.97	1.13	0.47	0.26	0.14	0.11	0.10	0.03	0.00	0.00	0.00	0.00	0.01	0.00	0.04
2238708	2014GL042	13.48	25.47	10.29	6.68	3.18	1.69	19.58	11.30	5.28	2.09	0.74	0.16	0.04	0.01	0.01	0.01	0.02	0.00	0.00	0.00	0.00	0.00	0.00	0.00
2238709	2014GL043	7.24	18.55	16.92	37.83	13.98	2.38	1.33	0.54	0.33	0.14	0.09	0.08	0.06	0.06	0.05	0.07	0.12	0.02	0.01	0.01	0.02	0.05	0.02	0.10

Sample ID	Station ID	Percentage (%) of pixels from sample slabs that contain an Al-OH absorption feature of specified wavelength (nm)																							
		2190 – 2191	2191 – 2192	2192 – 2193	2193 – 2194	2194 – 2195	2195 – 2197	2197 – 2198	2198 – 2199	2199 – 2200	2200 – 2201	2201 – 2202	2202 – 2203	2203 – 2204	2204 – 2205	2205 – 2206	2206 – 2207	2207 – 2208	2208 – 2209	2209 – 2210	2210 – 2211	2211 – 2212	2212 – 2213	2213 – 2214	2214 – 2220
2238710	2014GL044	7.67	11.46	9.27	44.75	19.05	4.31	2.15	0.81	0.35	0.10	0.04	0.02	0.00	0.00	0.00	0.00	0.00	0.00	0.00	0.00	0.00	0.00	0.00	0.00
2238711	2014GL045	4.07	5.34	4.98	31.99	34.86	14.10	2.02	0.99	0.68	0.56	0.29	0.08	0.03	0.00	0.00	0.00	0.01	0.00	0.00	0.00	0.00	0.00	0.00	0.00
2238713	2014GL047	3.45	4.92	4.46	8.86	16.39	40.98	13.61	4.63	1.62	0.64	0.26	0.10	0.03	0.01	0.02	0.00	0.01	0.00	0.00	0.00	0.00	0.00	0.00	0.00
2238714	2014GL048	8.35	23.23	13.76	19.74	17.75	8.02	5.40	2.40	0.84	0.31	0.10	0.05	0.01	0.01	0.00	0.00	0.01	0.00	0.00	0.00	0.00	0.00	0.00	0.00
2238715	2014GL049	11.96	25.40	15.74	23.09	15.23	4.85	2.29	0.84	0.30	0.15	0.07	0.04	0.01	0.00	0.01	0.00	0.01	0.00	0.00	0.00	0.00	0.00	0.00	0.00
2238716	2014GL050	8.68	13.36	7.97	31.21	18.21	9.03	3.94	2.74	1.87	1.26	0.84	0.53	0.24	0.06	0.02	0.01	0.02	0.00	0.00	0.00	0.00	0.00	0.00	0.00
2238717	2014GL051	6.89	16.32	9.91	13.46	15.80	16.43	8.44	3.99	2.30	1.44	1.16	0.92	0.63	0.48	0.46	0.29	0.34	0.05	0.03	0.01	0.04	0.09	0.03	0.50
2238720	2014GL052	4.23	5.55	5.07	9.95	19.23	39.03	8.74	3.27	1.76	1.01	0.62	0.47	0.25	0.18	0.18	0.12	0.29	0.01	0.00	0.00	0.00	0.01	0.00	0.03
2238721	2014GL053	4.67	8.35	8.41	15.79	21.54	23.64	11.74	4.16	1.17	0.29	0.10	0.04	0.01	0.01	0.01	0.01	0.06	0.00	0.00	0.00	0.00	0.00	0.00	0.00
2238722	2014GL054	19.14	31.82	14.92	15.02	8.92	2.63	4.34	1.56	0.92	0.49	0.15	0.05	0.01	0.00	0.00	0.01	0.01	0.00	0.00	0.00	0.00	0.00	0.00	0.00
2238723	2014GL055	10.80	23.79	14.97	24.94	16.04	5.21	2.43	0.95	0.42	0.19	0.10	0.07	0.02	0.01	0.02	0.01	0.02	0.00	0.00	0.00	0.00	0.00	0.00	0.00
2238724	2014GL056	7.12	18.43	15.21	18.76	13.25	10.19	10.95	4.31	1.30	0.34	0.09	0.03	0.01	0.00	0.00	0.00	0.01	0.00	0.00	0.00	0.00	0.00	0.00	0.00
2238725	2014GL057	19.40	35.34	16.59	20.23	5.90	0.68	0.92	0.47	0.26	0.13	0.06	0.01	0.00	0.00	0.00	0.00	0.01	0.00	0.00	0.00	0.00	0.00	0.00	0.00
2238726	2014GL058	16.29	30.54	16.29	17.45	11.87	2.80	3.17	0.98	0.39	0.13	0.04	0.02	0.01	0.00	0.00	0.00	0.00	0.00	0.00	0.00	0.00	0.00	0.00	0.00
2238728	2014GL059	10.81	23.03	16.67	33.50	12.97	1.61	1.00	0.28	0.08	0.04	0.01	0.00	0.00	0.00	0.00	0.00	0.00	0.00	0.00	0.00	0.00	0.00	0.00	0.00
2238729	2014GL060	7.79	7.23	2.36	2.36	1.42	2.73	19.30	21.56	17.97	11.12	4.50	1.34	0.20	0.04	0.02	0.02	0.05	0.00	0.00	0.00	0.00	0.00	0.00	0.00
2238731	2014GL061	20.39	36.10	12.54	9.90	6.06	1.76	7.73	3.29	1.38	0.49	0.23	0.09	0.02	0.00	0.01	0.00	0.01	0.00	0.00	0.00	0.00	0.00	0.00	0.00
2238733	2014GL063	28.00	30.78	9.91	7.63	4.39	2.71	9.55	4.37	1.70	0.55	0.22	0.10	0.03	0.01	0.01	0.01	0.03	0.00	0.00	0.00	0.00	0.00	0.00	0.00
2238734	2014GL064	7.40	11.15	8.53	32.95	26.84	6.81	2.03	1.25	0.97	0.63	0.51	0.40	0.27	0.13	0.08	0.02	0.02	0.00	0.00	0.00	0.00	0.00	0.00	0.00
2238736	2014GL066	17.92	29.90	13.50	13.36	8.78	3.87	7.71	3.15	1.14	0.38	0.15	0.06	0.02	0.01	0.01	0.01	0.03	0.00	0.00	0.00	0.00	0.00	0.00	0.00
2238737	2014GL067	16.17	23.08	12.96	21.12	17.13	4.67	3.08	1.04	0.40	0.16	0.07	0.04	0.01	0.01	0.01	0.01	0.03	0.00	0.00	0.00	0.00	0.00	0.00	0.00
2238738	2014GL067	7.77	10.85	9.42	35.34	21.99	9.80	2.11	0.88	0.48	0.27	0.17	0.14	0.09	0.06	0.08	0.07	0.09	0.04	0.03	0.01	0.03	0.04	0.03	0.23
2238740	2014GL069	8.98	12.34	7.20	7.19	4.73	7.63	20.68	13.30	6.46	3.53	2.65	2.00	1.24	0.67	0.38	0.30	0.09	0.01	0.01	0.00	0.02	0.11	0.02	0.50
2238743	2014GL070	5.18	8.19	7.48	32.81	26.35	12.75	3.57	1.79	0.87	0.39	0.28	0.16	0.07	0.02	0.03	0.02	0.02	0.01	0.00	0.00	0.00	0.00	0.00	0.01
2238744	2014GL071	6.39	17.92	15.02	31.65	21.91	5.48	1.11	0.34	0.10	0.04	0.02	0.01	0.00	0.00	0.00	0.00	0.01	0.00	0.00	0.00	0.00	0.00	0.00	0.00
2238746	2014GL073	0.97	1.71	2.68	8.63	11.37	8.30	12.26	12.25	12.07	11.21	9.65	6.16	1.78	0.41	0.14	0.12	0.27	0.01	0.00	0.00	0.00	0.00	0.00	0.01
2238747	2014GL073	6.42	15.96	13.04	19.76	23.93	13.31	4.41	1.59	0.63	0.38	0.18	0.11	0.07	0.02	0.03	0.01	0.07	0.02	0.01	0.01	0.01	0.01	0.01	0.02
2238749	2014GL075	7.37	11.20	10.25	48.69	9.92	3.34	1.20	0.72	0.67	0.32	0.50	0.52	0.15	0.22	0.45	0.31	1.40	0.39	0.13	0.08	0.19	0.32	0.20	1.45
2238750	2014GL076	9.05	15.04	12.59	46.10	8.26	2.58	1.14	0.59	0.50	0.24	0.31	0.61	0.13	0.17	0.32	0.29	0.68	0.12	0.06	0.03	0.07	0.14	0.05	0.92
2238751	2014GL077	4.66	6.46	5.82	54.01	14.92	7.53	1.81	1.03	0.64	0.45	0.41	0.55	0.20	0.14	0.19	0.21	0.17	0.03	0.02	0.01	0.02	0.11	0.03	0.56
2238752	2014GL078	4.61	8.00	6.93	32.39	16.76	14.87	5.30	3.23	2.03	1.38	1.02	0.69	0.44	0.28	0.26	0.23	0.25	0.05	0.04	0.02	0.04	0.10	0.06	1.01
2238754	2014GL079	13.97	23.08	12.19	23.19	10.79	5.84	2.17	1.14	0.77	0.38	0.56	1.16	0.22	0.37	0.73	0.54	0.82	0.21	0.10	0.03	0.12	0.21	0.15	1.26
2238755	2014GL080	3.88	5.00	3.85	6.72	10.50	23.93	23.31	13.60	5.82	2.13	0.77	0.30	0.09	0.03	0.02	0.01	0.02	0.00	0.00	0.00	0.00	0.01	0.00	0.02
2238756	2014GL080	4.78	7.07	6.11	37.43	27.67	10.79	2.14	1.05	0.57	0.36	0.31	0.44	0.16	0.10	0.15	0.11	0.21	0.04	0.02	0.00	0.05	0.05	0.03	0.36
2238757	2014GL081	4.12	8.39	6.75	11.07	16.14	28.01	16.20	5.86	1.91	0.64	0.35	0.26	0.13	0.04	0.04	0.02	0.06	0.00	0.00	0.00	0.00	0.00	0.00	0.02
2238758	2014GL081	7.41	13.03	9.35	12.93	14.20	16.55	9.55	4.92	3.10	2.27	1.79	1.48	1.14	0.86	0.61	0.35	0.19	0.04	0.02	0.01	0.01	0.04	0.01	0.12
2238759	2014GL082	3.76	7.05	3.40	3.08	1.77	4.40	23.34	24.22	17.29	8.22	2.63	0.59	0.13	0.05	0.03	0.01	0.02	0.00	0.00	0.00	0.00	0.00	0.00	0.00
2238760	2014GL083	3.99	4.68	2.41	2.67	3.89	16.38	22.28	19.22	11.66	6.05	3.12	1.99	1.17	0.34	0.06	0.02	0.05	0.00	0.00	0.00	0.00	0.00	0.00	0.03
2238761	2014GL083	15.79	29.26	13.73	13.11	10.20	5.53	8.12	2.79	0.90	0.33	0.12	0.06	0.01	0.00	0.01	0.00	0.03	0.00	0.00	0.00	0.00	0.00	0.00	0.00
2238762	2014GL084	4.35	10.78	8.32	11.72	13.79	12.80	9.18	6.30	4.48	3.23	3.28	3.04	2.14	1.29	0.90	0.72	0.25	0.05	0.02	0.01	0.05	0.37	0.04	2.88
2238763	2014GL085	6.68	6.31	5.22	36.49	35.49	8.06	0.99	0.40	0.19	0.08	0.02	0.03	0.01	0.01	0.00	0.01	0.01	0.00	0.00	0.00	0.00	0.00	0.00	0.00
2238766	2014GL085	5.11	4.59	3.63	45.63	24.27	12.19	1.86	0.86	0.51	0.30	0.23	0.19	0.13	0.08	0.14	0.10	0.13	0.01	0.00	0.00	0.00	0.01	0.01	0.02
2238767	2014GL086	6.95	8.96	7.54	44.41	25.11	5.15	0.86	0.33	0.19	0.07	0.05	0.05	0.02	0.03	0.04	0.03	0.07	0.02	0.01	0.00	0.01	0.02	0.01	0.06

Sample ID	Station ID	Percentage (%) of pixels from sample slabs that contain an Al-OH absorption feature of specified wavelength (nm)																							
		2190 – 2191	2191 – 2192	2192 – 2193	2193 – 2194	2194 – 2195	2195 – 2197	2197 – 2198	2198 – 2199	2199 – 2200	2200 – 2201	2201 – 2202	2202 – 2203	2203 – 2204	2204 – 2205	2205 – 2206	2206 – 2207	2207 – 2208	2208 – 2209	2209 – 2210	2210 – 2211	2211 – 2212	2212 – 2213	2213 – 2214	2214 – 2220
2238768	2014GL087	6.60	10.40	8.20	13.51	18.15	20.86	8.30	3.62	1.96	1.03	0.90	0.75	0.44	0.35	0.48	0.46	0.27	0.14	0.07	0.02	0.11	0.33	0.13	2.92
2238769	2014GL088	8.39	15.99	12.12	50.21	8.08	1.85	0.59	0.34	0.26	0.12	0.19	0.32	0.08	0.12	0.24	0.12	0.38	0.08	0.02	0.01	0.03	0.08	0.04	0.35
2238770	2014GL089	11.25	12.74	11.63	51.65	5.77	1.88	0.70	0.37	0.38	0.12	0.28	0.74	0.13	0.22	0.49	0.32	0.66	0.10	0.06	0.02	0.06	0.09	0.06	0.26
2238772	2014GL091	6.43	7.98	8.63	48.42	14.77	6.29	1.62	0.90	0.54	0.28	0.47	0.73	0.14	0.24	0.48	0.45	0.71	0.16	0.07	0.03	0.08	0.11	0.06	0.41
2238773	2014GL092	8.17	11.50	8.84	34.79	19.52	8.60	3.62	2.09	1.18	0.54	0.32	0.15	0.07	0.05	0.08	0.06	0.11	0.01	0.00	0.00	0.00	0.03	0.01	0.27
2238774	2014GL093	6.40	9.80	7.95	50.29	11.61	4.85	1.30	0.81	0.73	0.35	0.55	0.95	0.21	0.32	0.70	0.72	0.75	0.20	0.10	0.07	0.12	0.17	0.11	0.96
2238775	2014GL094	2.31	2.33	2.09	13.70	27.77	32.60	9.24	4.29	2.21	1.24	0.81	0.52	0.31	0.09	0.08	0.08	0.13	0.04	0.01	0.01	0.02	0.02	0.01	0.09
2238777	2014GL095	5.82	8.92	7.47	40.00	25.07	8.48	2.31	0.95	0.41	0.17	0.12	0.08	0.04	0.03	0.04	0.04	0.03	0.00	0.00	0.00	0.00	0.00	0.00	0.00
2238778	2014GL096	5.40	7.14	5.64	26.33	20.87	16.19	5.49	3.12	1.91	1.06	0.79	0.78	0.36	0.37	0.46	0.38	1.06	0.22	0.11	0.05	0.16	0.37	0.09	1.64
2238779	2014GL097	2.69	0.95	0.51	0.95	1.67	11.65	17.12	21.79	20.51	13.73	5.74	1.96	0.43	0.09	0.07	0.04	0.06	0.00	0.00	0.00	0.00	0.01	0.00	0.02
2238780	2014GL098	3.07	2.55	1.99	5.32	11.10	28.55	15.75	10.88	6.41	3.96	2.60	1.87	1.32	1.00	1.03	0.78	0.60	0.09	0.03	0.01	0.06	0.26	0.03	0.73
2238781	2014GL099	4.71	5.39	4.63	17.55	33.88	28.26	4.00	1.04	0.28	0.12	0.06	0.03	0.01	0.01	0.00	0.00	0.01	0.00	0.00	0.00	0.00	0.00	0.00	0.00
2238782	2014GL100	4.31	4.02	2.83	5.45	11.00	23.39	16.65	12.92	9.13	5.70	2.85	1.08	0.21	0.08	0.06	0.04	0.12	0.01	0.00	0.01	0.01	0.02	0.00	0.12
2238783	2014GL101	3.60	4.00	3.14	16.21	20.48	17.97	6.48	5.31	4.18	3.18	2.56	1.98	1.35	0.95	0.98	0.81	0.99	0.49	0.25	0.16	0.39	0.76	0.33	3.46
2238784	2014GL102	5.73	7.16	5.88	15.45	28.85	27.14	6.47	2.21	0.67	0.25	0.08	0.04	0.01	0.00	0.01	0.01	0.05	0.00	0.00	0.00	0.00	0.00	0.00	0.00
2238785	2014GL103	4.03	2.69	1.97	3.88	10.05	40.43	16.51	9.12	4.79	2.83	1.66	0.95	0.57	0.23	0.09	0.05	0.08	0.01	0.00	0.00	0.00	0.01	0.00	0.04
2238786	2014GL104	9.11	13.46	9.96	30.93	21.04	8.81	4.04	1.57	0.66	0.24	0.09	0.03	0.01	0.00	0.01	0.00	0.03	0.00	0.00	0.00	0.00	0.00	0.00	0.00
2238789	2014GL105	10.61	14.28	10.47	39.38	10.79	4.62	1.44	0.81	0.68	0.32	0.49	0.85	0.19	0.33	0.69	0.72	0.97	0.25	0.11	0.03	0.14	0.23	0.12	1.48
2238790	2014GL106	5.72	9.22	7.50	45.01	17.75	6.85	1.62	0.91	0.60	0.29	0.37	0.42	0.13	0.17	0.36	0.36	0.37	0.13	0.05	0.03	0.10	0.19	0.11	1.74
2238791	2014GL107	16.05	26.52	13.30	33.01	7.13	0.97	0.78	0.45	0.28	0.12	0.25	0.16	0.06	0.08	0.19	0.16	0.10	0.05	0.03	0.01	0.04	0.06	0.04	0.15
2238792	2014GL108	8.87	13.01	9.55	41.39	14.94	4.61	1.28	0.74	0.57	0.27	0.69	0.97	0.15	0.27	0.55	0.52	0.47	0.12	0.06	0.04	0.09	0.12	0.11	0.63
2238793	2014GL109	23.78	26.83	8.55	8.96	5.82	3.87	9.78	5.81	3.18	1.62	0.88	0.41	0.12	0.06	0.07	0.05	0.15	0.02	0.01	0.00	0.00	0.01	0.00	0.02
2238795	2014GL111	5.60	10.59	7.55	12.29	16.17	16.98	9.57	5.35	3.30	2.06	1.74	1.22	1.05	0.78	0.78	0.54	1.07	0.22	0.12	0.06	0.14	0.26	0.14	2.41
2238796	2014GL112	9.44	15.84	12.50	49.89	9.04	1.20	0.42	0.20	0.19	0.09	0.18	0.12	0.05	0.06	0.15	0.13	0.19	0.04	0.02	0.01	0.03	0.06	0.03	0.10
2238797	2014GL113	24.49	21.54	5.29	3.56	1.46	0.34	14.38	11.03	7.77	4.77	2.74	1.49	0.64	0.19	0.09	0.07	0.15	0.00	0.00	0.00	0.00	0.00	0.00	0.00
2238798	2014GL114	24.95	22.59	6.06	4.78	2.74	1.02	14.10	9.94	6.15	3.51	2.00	1.04	0.40	0.18	0.15	0.09	0.28	0.00	0.00	0.00	0.00	0.00	0.00	0.00
2238800	2014GL115	29.20	31.44	9.41	9.55	4.15	0.94	8.19	3.94	1.78	0.81	0.30	0.15	0.05	0.02	0.01	0.01	0.05	0.00	0.00	0.00	0.00	0.00	0.00	0.00
2238801	2014GL116	24.63	28.79	8.42	6.51	2.72	0.44	11.84	7.62	4.65	2.38	1.11	0.51	0.13	0.05	0.03	0.04	0.11	0.00	0.00	0.00	0.00	0.00	0.00	0.02
2238802	2014GL117	0.63	0.87	1.32	3.23	3.72	5.13	8.90	10.58	11.58	12.08	13.04	13.36	9.69	3.87	1.11	0.42	0.39	0.01	0.00	0.00	0.00	0.01	0.00	0.04
2238803	2014GL117	31.60	39.35	12.65	13.62	0.90	0.02	1.13	0.40	0.18	0.07	0.03	0.01	0.00	0.00	0.00	0.00	0.03	0.00	0.00	0.00	0.00	0.00	0.00	0.00
2238804	2014GL118	7.51	12.43	9.50	25.12	18.51	8.44	4.06	2.36	1.93	0.82	1.00	0.60	0.24	0.39	0.92	0.60	1.21	0.58	0.31	0.16	0.42	0.66	0.39	1.83
2238805	2014GL119	5.04	7.79	6.04	27.81	20.36	12.99	4.49	2.52	1.78	1.16	1.12	1.09	0.77	0.80	0.90	0.78	1.84	0.33	0.16	0.07	0.18	0.28	0.14	1.56
2238806	2014GL120	11.76	26.77	19.18	27.63	9.80	1.36	2.16	0.89	0.24	0.10	0.04	0.03	0.00	0.00	0.01	0.00	0.01	0.00	0.00	0.00	0.00	0.00	0.00	0.00
2238807	2014GL121	1.09	5.08	4.24	9.03	8.31	11.58	8.46	7.62	7.00	6.51	6.26	6.60	7.12	6.52	3.06	0.94	0.43	0.04	0.01	0.01	0.01	0.01	0.01	0.09
2238808	2014GL121	0.82	0.23	0.12	0.43	0.97	9.08	13.29	17.65	18.12	15.01	10.61	6.81	3.71	1.73	0.63	0.24	0.45	0.03	0.01	0.01	0.00	0.02	0.00	0.02
2238809	2014GL122	15.84	30.52	15.39	28.32	7.83	0.79	0.77	0.26	0.11	0.04	0.02	0.06	0.01	0.01	0.01	0.01	0.01	0.00	0.00	0.00	0.00	0.00	0.00	0.00
2238812	2014GL123	6.08	9.68	7.06	36.43	14.45	7.51	3.99	3.16	2.44	1.79	1.50	1.24	0.86	0.62	0.62	0.52	0.40	0.13	0.04	0.02	0.05	0.22	0.04	1.15
2238813	2014GL123	0.36	0.02	0.03	0.11	0.11	1.05	3.39	8.73	18.12	24.05	21.58	13.47	5.94	2.06	0.52	0.22	0.23	0.00	0.00	0.00	0.00	0.00	0.00	0.01
2238814	2014GL124	30.59	28.32	11.49	12.07	7.66	3.02	4.33	1.55	0.58	0.17	0.10	0.06	0.02	0.00	0.00	0.01	0.03	0.00	0.00	0.00	0.00	0.00	0.00	0.00
2238815	2014GL125	69.12	13.77	2.20	1.12	0.39	0.17	6.63	3.12	1.49	0.62	0.31	0.18	0.06	0.03	0.06	0.03	0.53	0.05	0.01	0.00	0.02	0.02	0.01	0.03
2238816	2014GL126	12.69	14.69	7.50	9.58	8.74	9.52	12.77	7.31	4.35	2.64	1.77	1.26	0.85	0.74	0.87	0.61	0.93	0.47	0.22	0.13	0.26	0.53	0.22	1.35
2238817	2014GL127	42.89	35.33	5.08	2.53	0.87	0.19	7.95	3.17	1.24	0.41	0.15	0.09	0.03	0.01	0.01	0.01	0.05	0.00	0.00	0.00	0.00	0.00	0.00	0.00
2238818	2014GL128	63.28	18.02	1.56	0.70	0.21	0.03	8.61	4.16	2.00	0.81	0.30	0.16	0.04	0.02	0.02	0.01	0.07	0.00	0.00	0.00	0.00	0.00	0.00	0.00

Sample ID	Station ID	Percentage (%) of pixels from sample slabs that contain an Al-OH absorption feature of specified wavelength (nm)																							
		2190 – 2191	2191 – 2192	2192 – 2193	2193 – 2194	2194 – 2195	2195 – 2197	2197 – 2198	2198 – 2199	2199 – 2200	2200 – 2201	2201 – 2202	2202 – 2203	2203 – 2204	2204 – 2205	2205 – 2206	2206 – 2207	2207 – 2208	2208 – 2209	2209 – 2210	2210 – 2211	2211 – 2212	2212 – 2213	2213 – 2214	2214 – 2220
2238819	2014GL129	1.18	2.29	2.67	8.33	9.69	21.43	14.44	13.52	10.80	6.89	4.05	2.21	1.16	0.59	0.31	0.19	0.27	0.00	0.00	0.00	0.00	0.00	0.00	0.00
2238820	2014GL130	38.26	1.66	0.10	0.07	0.04	0.04	9.61	10.55	9.65	8.07	6.41	5.00	2.94	0.90	1.15	1.01	4.52	0.00	0.00	0.00	0.00	0.00	0.00	0.00
2238821	2014GL131	43.15	19.09	6.27	5.42	3.15	1.74	7.63	3.64	1.87	0.84	0.43	0.91	0.41	0.70	0.83	0.12	1.78	0.56	0.25	0.11	0.23	0.31	0.18	0.38
2238823	2014GL132	66.72	14.77	2.45	1.04	0.42	0.15	7.95	3.62	1.71	0.53	0.24	0.12	0.04	0.01	0.01	0.03	0.18	0.01	0.00	0.00	0.00	0.00	0.00	0.00
2238824	2014GL133	39.60	20.74	9.20	7.07	3.92	1.94	6.18	3.56	2.06	0.99	0.64	0.67	0.32	0.21	0.19	0.11	1.48	0.40	0.11	0.07	0.10	0.18	0.10	0.18
2238825	2014GL134	55.54	23.50	4.68	3.03	1.68	0.67	5.77	2.64	1.18	0.49	0.23	0.14	0.05	0.02	0.02	0.04	0.31	0.01	0.00	0.00	0.00	0.00	0.00	0.00
2238826	2014GL135	37.86	22.04	6.24	3.98	1.65	0.76	10.55	6.63	4.06	2.41	1.49	0.97	0.52	0.16	0.17	0.15	0.38	0.00	0.00	0.00	0.00	0.00	0.00	0.00
2238827	2014GL136	24.69	25.54	12.50	12.32	8.88	5.74	3.29	1.23	0.49	0.15	0.10	1.24	0.39	0.80	1.18	0.15	0.57	0.16	0.07	0.05	0.08	0.11	0.11	0.16
2238828	2014GL137	30.36	23.61	10.54	10.94	8.81	3.95	6.36	2.81	1.25	0.54	0.23	0.23	0.09	0.04	0.06	0.02	0.11	0.01	0.00	0.00	0.00	0.01	0.00	0.01
2238829	2014GL138	34.65	19.51	6.20	4.53	2.44	1.96	14.35	8.15	4.29	2.07	0.89	0.51	0.18	0.04	0.04	0.04	0.15	0.00	0.00	0.00	0.00	0.00	0.00	0.00
2238830	2014GL139	31.38	22.07	5.93	4.47	2.68	1.82	6.62	3.46	2.53	1.04	0.83	1.27	0.61	1.39	3.03	0.80	3.84	1.72	0.62	0.36	0.71	0.95	0.66	1.24
2238831	2014GL140	16.81	21.87	12.22	11.80	6.89	5.98	11.14	4.92	2.48	1.24	0.65	0.91	0.27	0.24	0.30	0.09	1.27	0.34	0.11	0.04	0.11	0.13	0.06	0.13
2238832	2014GL141	32.58	23.05	8.98	6.64	2.72	1.26	8.59	4.62	2.43	1.34	0.67	0.97	0.31	0.40	0.44	0.16	3.21	0.58	0.19	0.07	0.19	0.21	0.10	0.28
2238835	2014GL142	26.68	24.85	11.67	9.73	3.88	1.76	11.60	4.83	2.18	1.06	0.55	0.36	0.19	0.12	0.11	0.07	0.34	0.00	0.00	0.00	0.00	0.00	0.00	0.01
2238836	2014GL143	53.98	3.26	0.34	0.11	0.03	0.01	13.19	10.54	7.66	4.17	2.43	1.67	0.71	0.20	0.22	0.22	1.22	0.02	0.00	0.00	0.00	0.00	0.00	0.00
2238837	2014GL144	77.06	2.54	0.06	0.02	0.00	0.00	7.90	4.98	3.08	1.46	0.76	0.53	0.26	0.07	0.13	0.15	0.99	0.01	0.00	0.00	0.00	0.00	0.00	0.00
2238838	2014GL145	48.92	14.48	4.09	3.42	2.02	1.81	10.89	6.25	3.26	1.54	0.89	0.61	0.22	0.06	0.13	0.17	1.23	0.01	0.00	0.00	0.00	0.00	0.00	0.01
2238839	2014GL146	19.32	0.45	0.05	0.05	0.02	0.01	7.55	10.74	13.54	13.56	11.98	9.50	5.46	1.90	1.58	1.16	3.10	0.01	0.00	0.00	0.00	0.00	0.00	0.00
2238840	2014GL147	46.89	28.42	7.56	4.61	2.02	0.80	5.80	2.37	0.96	0.31	0.12	0.07	0.02	0.00	0.00	0.01	0.03	0.00	0.00	0.00	0.00	0.00	0.00	0.00
2238841	2014GL148	62.44	18.51	2.71	1.03	0.23	0.08	7.72	3.78	1.85	0.73	0.31	0.19	0.05	0.02	0.02	0.04	0.31	0.00	0.00	0.00	0.00	0.00	0.00	0.00
2238842	2014GL149	62.55	4.47	0.44	0.21	0.05	0.01	10.43	7.34	4.86	2.73	1.67	1.23	0.60	0.24	0.32	0.38	2.39	0.02	0.00	0.00	0.00	0.01	0.00	0.01
2238843	2014GL150	61.53	12.11	1.32	0.39	0.08	0.04	10.31	6.06	3.39	1.59	0.84	0.66	0.27	0.08	0.12	0.13	1.06	0.00	0.00	0.00	0.00	0.00	0.00	0.00
2238844	2014GL150	64.41	18.81	1.38	0.16	0.01	0.00	7.03	3.65	1.97	0.83	0.49	0.33	0.15	0.04	0.04	0.04	0.66	0.00	0.00	0.00	0.00	0.00	0.00	0.00
2238846	2014GL151	41.99	36.11	6.11	2.24	0.56	0.24	7.27	3.04	1.37	0.50	0.20	0.13	0.04	0.01	0.01	0.02	0.16	0.00	0.00	0.00	0.00	0.00	0.00	0.00
2238847	2014GL152	47.28	30.41	7.48	3.82	0.98	0.15	5.18	2.49	1.04	0.42	0.19	0.11	0.05	0.01	0.02	0.03	0.30	0.00	0.00	0.00	0.00	0.00	0.00	0.00
2238848	2014GL152	99.53	0.00	0.00	0.00	0.00	0.00	0.17	0.10	0.05	0.03	0.02	0.02	0.00	0.02	0.01	0.01	0.02	0.00	0.00	0.00	0.00	0.00	0.00	0.00
2238849	2014GL153	7.29	10.22	7.99	18.51	31.90	16.88	4.14	1.61	0.76	0.30	0.15	0.10	0.03	0.00	0.01	0.01	0.06	0.01	0.00	0.00	0.00	0.00	0.00	0.01
2238850	2014GL154	96.15	0.05	0.00	0.00	0.00	0.01	0.73	0.66	0.47	0.20	0.11	0.22	0.08	0.05	0.13	0.12	1.04	0.00	0.00	0.00	0.00	0.00	0.00	0.00
2238851	2014GL155	42.42	27.40	7.81	5.11	2.83	1.80	7.09	2.84	1.30	0.53	0.25	0.11	0.06	0.01	0.03	0.05	0.36	0.01	0.00	0.00	0.00	0.00	0.00	0.00
2238852	2014GL156	29.69	25.06	9.04	7.14	4.78	4.48	10.92	4.86	2.21	0.99	0.42	0.20	0.07	0.02	0.02	0.02	0.09	0.00	0.00	0.00	0.00	0.00	0.00	0.00
2238853	2014GL157	6.07	10.74	7.89	9.65	7.09	9.70	26.40	13.96	5.39	1.84	0.67	0.30	0.10	0.05	0.04	0.02	0.05	0.00	0.00	0.00	0.00	0.01	0.00	0.01
2238854	2014GL158	47.23	24.67	6.79	7.08	4.50	1.28	4.58	2.05	1.02	0.42	0.17	0.10	0.02	0.01	0.02	0.01	0.04	0.00	0.00	0.00	0.00	0.00	0.00	0.00
2238855	2014GL159	0.51	0.17	0.08	0.16	0.12	0.17	0.53	0.83	1.57	2.85	4.44	7.63	13.44	37.85	26.53	2.40	0.52	0.04	0.01	0.01	0.01	0.03	0.01	0.08
2238858	2014GL160	0.40	0.04	0.09	0.33	0.84	4.17	7.55	10.89	13.61	16.14	17.10	14.32	9.45	4.30	0.57	0.10	0.06	0.00	0.00	0.00	0.00	0.00	0.00	0.00
2238859	2014GL161	1.06	2.97	3.26	8.86	8.48	16.86	12.01	11.67	10.29	8.13	5.54	3.65	2.29	1.51	1.14	0.82	0.58	0.06	0.02	0.01	0.01	0.18	0.02	0.59
2238860	2014GL162	1.77	0.08	0.05	0.24	0.37	2.05	3.51	5.55	9.22	13.99	17.49	16.57	12.86	8.13	5.13	1.58	1.07	0.06	0.02	0.01	0.01	0.06	0.01	0.16
2238861	2014GL163	0.24	0.06	0.03	0.05	0.10	1.41	2.30	3.82	6.11	9.37	15.07	22.80	21.96	11.40	4.25	0.69	0.22	0.01	0.01	0.00	0.00	0.02	0.00	0.09
2238863	2014GL165	1.55	1.50	1.19	2.59	3.35	18.08	16.81	13.55	9.54	6.90	5.71	5.39	6.27	5.48	1.13	0.36	0.42	0.04	0.02	0.01	0.02	0.02	0.01	0.09
2238865	2014GL167	0.23	0.07	0.06	0.14	0.47	4.46	4.20	4.76	5.60	6.61	8.20	10.97	16.07	20.85	14.58	2.50	0.12	0.01	0.00	0.00	0.01	0.01	0.01	0.08
2238866	2014GL168	3.72	1.28	0.61	2.36	4.31	21.73	19.35	15.62	12.45	8.34	3.73	1.82	0.96	0.59	0.48	0.41	2.02	0.08	0.02	0.01	0.03	0.03	0.02	0.03
2238867	2014GL169	0.84	1.14	1.01	1.43	1.42	3.15	5.73	5.92	5.78	6.50	8.14	10.00	12.11	14.03	12.41	5.04	2.87	0.39	0.15	0.07	0.16	0.39	0.09	1.21
2238869	2014GL170	2.42	2.86	2.21	4.06	5.36	17.66	16.24	11.74	6.90	4.33	3.26	3.29	4.32	8.04	6.06	0.59	0.53	0.03	0.00	0.01	0.01	0.01	0.01	0.03
2238870	2014GL171	1.41	1.62	1.13	2.37	2.99	8.18	7.10	6.61	6.54	6.43	6.79	7.38	8.19	10.25	9.44	6.30	1.70	0.37	0.20	0.08	0.22	1.23	0.16	3.29

Sample ID	Station ID	Percentage (%) of pixels from sample slabs that contain an Al-OH absorption feature of specified wavelength (nm)																							
		2190 – 2191	2191 – 2192	2192 – 2193	2193 – 2194	2194 – 2195	2195 – 2197	2197 – 2198	2198 – 2199	2199 – 2200	2200 – 2201	2201 – 2202	2202 – 2203	2203 – 2204	2204 – 2205	2205 – 2206	2206 – 2207	2207 – 2208	2208 – 2209	2209 – 2210	2210 – 2211	2211 – 2212	2212 – 2213	2213 – 2214	2214 – 2220
2238871	2014GL172	0.35	0.03	0.01	0.00	0.01	0.01	0.37	1.36	4.93	13.39	24.63	27.19	17.76	7.06	2.04	0.61	0.21	0.01	0.00	0.00	0.00	0.00	0.00	0.03
2238872	2014GL173	0.46	0.11	0.13	0.56	0.96	3.19	3.20	3.80	3.73	3.78	4.26	6.71	14.47	34.08	17.88	1.81	0.54	0.07	0.04	0.01	0.03	0.06	0.01	0.10
2238873	2014GL174	0.31	0.00	0.00	0.00	0.00	0.00	0.02	0.08	0.33	2.36	17.23	38.65	28.33	10.27	2.28	0.11	0.03	0.00	0.00	0.00	0.00	0.00	0.00	0.00
2238874	2014GL175	3.37	8.29	5.51	7.46	5.94	8.15	10.46	7.60	5.09	3.81	3.39	3.42	4.07	5.47	7.17	3.88	4.34	0.36	0.13	0.06	0.11	0.53	0.08	1.33
2238875	2014GL176	0.23	0.01	0.00	0.00	0.00	0.00	0.02	0.04	0.06	0.12	0.35	0.68	9.41	67.67	20.71	0.60	0.10	0.00	0.00	0.00	0.00	0.00	0.00	0.00
2238876	2014GL177	32.58	8.82	0.81	0.34	0.03	0.00	1.44	0.68	0.53	0.61	0.29	0.54	0.24	0.35	1.83	2.40	48.53	0.00	0.00	0.00	0.00	0.00	0.00	0.00
2238877	2014GL178	1.35	1.82	1.89	6.16	11.37	20.33	9.95	7.69	6.27	5.63	5.96	6.55	5.96	3.30	1.67	0.98	1.29	0.38	0.14	0.08	0.13	0.30	0.16	0.64
2238878	2014GL179	0.54	0.23	0.21	0.98	1.43	4.87	3.80	3.99	4.14	4.99	8.35	14.02	19.51	21.53	9.83	1.17	0.31	0.03	0.02	0.00	0.01	0.01	0.00	0.03
2238881	2014GL180	76.24	9.66	0.60	0.15	0.04	0.01	6.20	3.34	1.74	0.74	0.33	0.19	0.07	0.02	0.04	0.06	0.56	0.00	0.00	0.00	0.00	0.00	0.00	0.00
2238885	2014GL183	65.90	13.15	2.75	2.13	1.09	0.37	7.56	3.83	1.83	0.68	0.30	0.17	0.05	0.01	0.04	0.02	0.11	0.00	0.00	0.00	0.00	0.00	0.00	0.00
2238886	2014GL184	30.75	28.96	8.62	5.89	3.16	2.25	11.30	4.87	2.13	0.84	0.35	0.28	0.09	0.05	0.06	0.04	0.27	0.03	0.00	0.00	0.01	0.02	0.01	0.02
2238887	2014GL185	10.16	16.17	11.47	18.04	20.73	11.40	4.98	2.42	1.44	0.87	0.64	0.65	0.31	0.19	0.19	0.08	0.14	0.03	0.01	0.00	0.01	0.01	0.01	0.04
2238888	2014GL186	70.08	0.95	0.08	0.04	0.02	0.01	11.41	7.90	5.07	2.09	1.11	0.61	0.13	0.07	0.05	0.03	0.31	0.01	0.01	0.00	0.00	0.01	0.00	0.01
2238889	2014GL187	39.56	20.71	3.05	1.68	0.84	0.58	16.39	9.27	4.58	1.87	0.79	0.39	0.10	0.02	0.03	0.04	0.11	0.00	0.00	0.00	0.00	0.00	0.00	0.00
2238890	2014GL188	11.37	16.49	11.06	14.67	18.51	18.10	6.55	2.00	0.72	0.29	0.14	0.04	0.02	0.00	0.01	0.00	0.02	0.00	0.00	0.00	0.00	0.00	0.00	0.00
2238893	2014GL190	3.91	5.38	4.29	6.69	8.64	37.88	22.81	7.44	2.03	0.60	0.19	0.07	0.03	0.01	0.01	0.00	0.02	0.00	0.00	0.00	0.00	0.00	0.00	0.00
2238895	2014GL192	68.08	10.55	1.05	0.67	0.41	0.22	9.97	5.09	2.32	0.92	0.36	0.18	0.03	0.01	0.02	0.02	0.10	0.00	0.00	0.00	0.00	0.00	0.00	0.00
2238896	2014GL193	32.61	24.42	6.19	6.11	5.37	2.45	10.54	5.54	2.81	1.60	0.98	0.58	0.30	0.14	0.08	0.07	0.17	0.01	0.00	0.00	0.00	0.00	0.00	0.00
2238897	2014GL194	27.61	30.90	12.21	11.42	7.56	3.07	4.43	1.59	0.56	0.17	0.11	0.13	0.03	0.03	0.06	0.02	0.07	0.01	0.00	0.00	0.00	0.00	0.00	0.01
2238898	2014GL195	24.20	18.01	7.78	11.69	8.34	4.37	10.35	6.28	3.74	2.05	1.28	0.90	0.45	0.15	0.07	0.07	0.26	0.00	0.00	0.00	0.00	0.00	0.00	0.00
2238899	2014GL196	39.77	25.83	9.47	10.93	5.60	1.69	3.20	1.33	0.73	0.25	0.15	0.49	0.08	0.06	0.06	0.03	0.29	0.01	0.00	0.00	0.00	0.00	0.00	0.00
2238900	2014GL197	30.95	21.03	10.26	14.09	9.32	4.71	2.10	0.79	0.38	0.12	0.08	2.62	0.58	0.73	0.88	0.17	0.60	0.12	0.05	0.03	0.06	0.11	0.06	0.13
2238901	2014GL198	22.25	26.69	12.51	17.76	12.99	4.02	2.07	0.77	0.35	0.15	0.07	0.25	0.03	0.03	0.02	0.01	0.02	0.00	0.00	0.00	0.00	0.00	0.00	0.00
2238904	2014GL199	41.98	29.78	6.39	3.62	1.37	0.37	8.33	3.61	1.60	0.70	0.39	0.41	0.28	0.31	0.28	0.23	0.24	0.05	0.01	0.00	0.02	0.01	0.01	0.01
2238906	2014GL201	14.15	16.54	10.86	18.16	22.37	10.70	2.85	1.39	0.81	0.52	0.31	0.65	0.16	0.13	0.15	0.05	0.13	0.02	0.00	0.00	0.01	0.01	0.00	0.02
2238907	2014GL202	41.80	4.62	0.60	0.37	0.17	0.10	13.61	11.05	8.93	6.31	4.80	3.27	1.58	0.63	0.55	0.38	0.88	0.12	0.05	0.01	0.03	0.04	0.02	0.07
2238908	2014GL203	28.66	29.56	8.69	4.75	1.30	0.25	7.41	5.37	4.57	3.91	2.90	1.68	0.59	0.13	0.08	0.01	0.06	0.02	0.01	0.01	0.01	0.01	0.01	0.02
2238909	2014GL204	50.75	0.62	0.08	0.02	0.00	0.00	12.35	11.51	9.78	6.02	3.84	2.56	0.94	0.18	0.24	0.27	0.83	0.00	0.00	0.00	0.00	0.00	0.00	0.00
2238910	2014GL205	34.62	19.40	7.40	10.68	9.32	3.52	7.70	3.73	1.93	0.85	0.38	0.25	0.07	0.01	0.02	0.02	0.09	0.00	0.00	0.00	0.00	0.00	0.00	0.00
2238911	2014GL206	38.92	31.46	10.79	9.72	4.43	0.52	2.47	0.97	0.42	0.14	0.06	0.04	0.01	0.01	0.01	0.00	0.03	0.00	0.00	0.00	0.00	0.00	0.00	0.00
2238912	2014GL207	36.74	20.03	6.68	7.45	5.93	2.80	8.54	4.58	2.76	1.61	1.05	0.74	0.39	0.19	0.14	0.08	0.27	0.01	0.00	0.00	0.00	0.00	0.00	0.01
2238913	2014GL208	10.08	16.74	10.59	19.11	22.68	10.24	4.39	2.33	1.37	1.07	0.64	0.42	0.22	0.05	0.02	0.01	0.03	0.00	0.00	0.00	0.00	0.00	0.00	0.00
2238915	2014GL209	63.63	15.40	4.07	7.03	1.66	0.24	4.38	2.04	0.92	0.32	0.13	0.07	0.02	0.01	0.01	0.01	0.06	0.00	0.00	0.00	0.00	0.00	0.00	0.00
2238916	2014GL210	23.77	19.79	11.40	21.42	15.67	4.26	2.01	0.77	0.40	0.13	0.08	0.07	0.02	0.01	0.02	0.02	0.17	0.00	0.00	0.00	0.00	0.00	0.00	0.00
2238917	2014GL211	20.63	20.19	11.56	22.83	11.30	3.39	2.99	1.46	0.92	0.29	0.21	1.41	0.33	0.47	0.89	0.32	0.37	0.08	0.05	0.02	0.05	0.07	0.04	0.12
2238918	2014GL212	14.59	5.65	2.34	2.78	2.16	2.12	10.62	10.84	9.83	8.39	7.53	9.09	5.73	3.29	2.59	1.14	0.93	0.11	0.04	0.01	0.05	0.05	0.05	0.07
2238919	2014GL212	51.45	22.60	6.10	4.13	1.75	0.39	6.39	3.41	1.89	0.83	0.48	0.25	0.09	0.02	0.03	0.03	0.18	0.00	0.00	0.00	0.00	0.00	0.00	0.00
2238920	2014GL213	16.89	11.94	6.15	7.34	6.79	6.68	9.77	7.34	5.67	3.74	3.04	3.83	1.99	1.58	2.18	1.21	0.54	0.28	0.12	0.05	0.15	0.75	0.13	1.83
2238921	2014GL214	32.73	31.92	12.55	12.25	6.18	0.79	2.10	0.78	0.37	0.13	0.06	0.07	0.01	0.01	0.01	0.01	0.05	0.00	0.00	0.00	0.00	0.00	0.00	0.00
2238922	2014GL215	27.98	26.24	11.35	19.80	10.63	1.38	1.46	0.57	0.28	0.09	0.05	0.07	0.02	0.01	0.01	0.01	0.05	0.00	0.00	0.00	0.00	0.00	0.00	0.00
2238923	2014GL216	56.46	19.91	3.01	1.43	0.37	0.19	8.75	4.44	2.29	1.04	0.58	0.36	0.19	0.05	0.08	0.09	0.74	0.02	0.00	0.00	0.00	0.00	0.00	0.00
2238924	2014GL217	29.87	20.85	8.69	14.25	13.56	4.88	4.48	1.90	0.91	0.32	0.12	0.07	0.01	0.00	0.00	0.01	0.06	0.00	0.00	0.00	0.00	0.00	0.00	0.00
2238927	2014GL218	30.05	22.73	10.96	14.85	9.74	2.75	3.95	1.93	0.99	0.40	0.23	0.79	0.14	0.16	0.10	0.05	0.17	0.00	0.00	0.00	0.00	0.01	0.00	0.00

Sample ID	Station ID	Percentage (%) of pixels from sample slabs that contain an Al-OH absorption feature of specified wavelength (nm)																							
		2190 – 2191	2191 – 2192	2192 – 2193	2193 – 2194	2194 – 2195	2195 – 2197	2197 – 2198	2198 – 2199	2199 – 2200	2200 – 2201	2201 – 2202	2202 – 2203	2203 – 2204	2204 – 2205	2205 – 2206	2206 – 2207	2207 – 2208	2208 – 2209	2209 – 2210	2210 – 2211	2211 – 2212	2212 – 2213	2213 – 2214	2214 – 2220
2238928	2014GL219	26.38	28.53	14.52	16.00	6.93	1.51	3.09	1.47	0.68	0.29	0.15	0.19	0.04	0.02	0.02	0.01	0.15	0.01	0.00	0.00	0.00	0.00	0.00	0.01
2238929	2014GL220	63.92	7.27	0.39	0.09	0.02	0.00	11.47	7.38	4.14	2.00	1.12	0.61	0.24	0.04	0.09	0.12	1.09	0.00	0.00	0.00	0.00	0.00	0.00	0.00
2238930	2014GL221	35.38	28.75	11.14	8.92	5.23	1.65	5.09	2.17	0.86	0.34	0.16	0.11	0.02	0.01	0.02	0.02	0.13	0.00	0.00	0.00	0.00	0.00	0.00	0.00
2238931	2014GL222	79.67	5.11	0.54	0.21	0.07	0.01	5.89	3.44	2.02	0.80	0.46	0.34	0.11	0.03	0.07	0.12	1.12	0.00	0.00	0.00	0.00	0.00	0.00	0.00
2238932	2014GL223	74.09	9.80	1.56	0.88	0.26	0.14	6.41	3.45	1.68	0.66	0.34	0.21	0.09	0.02	0.03	0.03	0.33	0.00	0.00	0.00	0.00	0.00	0.00	0.00
2238933	2014GL224	61.93	24.95	5.18	3.30	0.83	0.09	2.21	0.84	0.37	0.12	0.04	0.03	0.01	0.01	0.01	0.01	0.05	0.00	0.00	0.00	0.00	0.00	0.00	0.00
2238934	2014GL225	67.43	15.75	3.07	1.41	0.45	0.10	5.37	3.06	1.54	0.75	0.40	0.24	0.10	0.01	0.02	0.04	0.25	0.00	0.00	0.00	0.00	0.00	0.00	0.00
2238935	2014GL226	45.80	17.32	3.63	1.87	0.65	0.28	13.99	7.92	4.19	1.89	0.94	0.57	0.23	0.04	0.07	0.10	0.51	0.00	0.00	0.00	0.00	0.00	0.00	0.00
2238936	2014GL227	63.64	20.95	4.16	2.54	0.86	0.18	4.03	1.89	0.95	0.34	0.15	0.09	0.02	0.00	0.02	0.02	0.14	0.00	0.00	0.00	0.00	0.00	0.00	0.00
2238938	2014GL228	44.04	36.42	7.60	3.72	0.95	0.07	3.96	1.63	0.75	0.29	0.15	0.12	0.06	0.01	0.04	0.02	0.15	0.00	0.00	0.00	0.00	0.00	0.00	0.00
2238939	2014GL229	50.21	29.82	6.19	2.37	0.39	0.04	5.79	2.65	1.18	0.53	0.24	0.16	0.05	0.02	0.04	0.03	0.28	0.00	0.00	0.00	0.00	0.00	0.00	0.00
2238940	2014GL230	74.90	6.38	0.97	0.55	0.16	0.03	7.15	4.38	2.66	1.04	0.52	0.44	0.17	0.04	0.07	0.08	0.46	0.00	0.00	0.00	0.00	0.00	0.00	0.00
2238941	2014GL230	27.26	19.67	7.48	6.05	3.35	2.07	12.72	8.25	5.33	3.15	2.14	1.42	0.63	0.14	0.12	0.06	0.14	0.00	0.00	0.00	0.00	0.00	0.00	0.00
2238942	2014GL231	55.08	25.32	5.49	3.19	1.38	0.57	4.82	2.15	1.02	0.43	0.16	0.10	0.03	0.01	0.02	0.02	0.19	0.00	0.00	0.00	0.00	0.00	0.00	0.00
2238951	2015GL-V11-06	2.96	3.14	2.25	3.47	4.48	12.67	9.49	6.61	5.24	4.80	5.08	5.74	7.45	9.17	8.22	4.07	5.07	0.06	0.01	0.01	0.01	0.01	0.00	0.01
2238952	2015GL-V11-06	0.36	0.41	0.33	0.93	0.86	2.13	2.32	3.19	4.24	5.53	7.20	9.67	13.17	15.28	15.25	10.46	1.78	0.53	0.25	0.12	0.33	1.60	0.21	3.84
2238953	2015GL-V11-06	0.71	0.47	0.43	1.80	3.69	12.06	8.44	7.97	8.05	9.87	11.02	11.55	9.46	6.28	3.91	2.27	0.71	0.16	0.05	0.02	0.06	0.22	0.03	0.76
2238954	2015GL-V11-06	0.49	0.34	0.44	1.91	2.14	5.23	5.21	5.59	4.61	3.92	3.74	4.93	9.58	21.46	23.92	5.29	0.30	0.03	0.02	0.01	0.03	0.12	0.02	0.66
2238955	2015GL-V11-06	0.55	0.22	0.07	0.27	0.50	2.41	2.02	2.08	1.91	2.15	3.05	6.59	17.70	36.24	19.53	3.28	0.26	0.05	0.03	0.02	0.04	0.25	0.01	0.79
2238956	2015GL-V11-06	1.53	1.39	1.10	2.62	3.53	8.99	8.02	6.85	6.71	7.14	8.26	9.95	12.46	10.57	5.59	2.15	0.33	0.08	0.08	0.08	0.14	0.77	0.19	1.48
2238957	2015GL-V11-06	0.14	0.05	0.01	0.01	0.00	0.12	0.48	0.99	1.36	1.84	2.30	3.11	3.90	6.33	21.50	47.81	1.91	0.35	0.13	0.06	0.12	0.43	0.15	6.88
2238958	2015GL-V11-06	0.40	0.14	0.20	0.20	0.24	1.21	2.32	3.22	3.87	5.16	7.61	10.82	15.31	16.92	12.84	9.83	0.99	0.76	0.39	0.18	0.37	1.81	0.18	5.03
2238959	2015GL-V11-06	0.43	0.73	0.66	1.58	2.51	7.49	5.03	4.66	5.39	6.76	8.68	11.05	12.74	13.98	11.04	4.92	0.73	0.12	0.05	0.03	0.04	0.21	0.03	1.13
2238960	2015GL-V11-13	0.37	0.17	0.17	0.20	0.20	1.23	4.91	9.69	14.59	17.47	15.87	9.87	5.06	3.69	4.36	3.89	2.42	1.22	0.51	0.22	0.41	0.85	0.23	2.39
2238962	2015GL-V11-13	0.35	0.03	0.00	0.00	0.00	0.06	0.33	0.60	1.64	3.66	10.16	22.21	33.10	23.17	3.55	0.59	0.51	0.02	0.02	0.00	0.00	0.01	0.00	0.00
2238963	2015GL-V11-13	0.44	0.16	0.10	0.10	0.11	0.47	1.34	2.07	4.63	9.70	14.48	18.07	19.42	15.52	8.09	3.45	0.49	0.07	0.05	0.02	0.04	0.23	0.03	0.89
2238964	2015GL-V11-13	3.26	4.08	1.52	2.02	2.91	15.41	19.06	19.43	15.53	9.10	3.98	1.83	0.85	0.34	0.17	0.08	0.33	0.05	0.01	0.00	0.00	0.01	0.01	0.01
2238965	2015GL-V11-13	0.72	0.34	0.24	0.36	0.77	5.76	8.18	13.03	17.42	17.93	14.55	10.17	5.38	2.27	0.99	0.63	0.32	0.02	0.00	0.01	0.00	0.32	0.00	0.59
2238966	2015GL-V11-13	1.04	0.42	0.28	0.40	0.78	5.15	5.06	5.86	6.51	6.99	7.95	9.11	11.28	11.33	12.11	10.45	4.67	0.07	0.02	0.01	0.02	0.03	0.02	0.44
2238967	2015GL-V11-13	0.06	0.03	0.00	0.01	0.01	0.11	0.30	0.34	0.39	0.36	0.68	1.94	9.28	45.99	33.01	5.41	0.42	0.04	0.02	0.01	0.03	0.38	0.03	1.16
2238968	2015GL-V11-13	1.47	2.06	1.14	1.13	0.85	1.61	5.09	5.67	6.45	9.91	14.92	20.58	19.05	7.21	1.78	0.55	0.49	0.01	0.00	0.00	0.01	0.01	0.00	0.02
2238969	2015GL-V11-50	1.20	1.21	1.09	2.18	2.70	8.18	12.29	13.93	13.86	12.18	10.03	7.42	5.73	4.86	2.15	0.44	0.40	0.00	0.00	0.00	0.00	0.04	0.01	0.09
2238970	2015GL-V11-50	1.06	0.83	0.92	3.48	3.33	8.46	5.78	5.51	5.34	4.68	4.53	5.02	5.85	19.21	24.24	1.35	0.37	0.01	0.00	0.00	0.00	0.01	0.00	0.02
2238971	2015GL-V11-50	0.06	0.00	0.00	0.00	0.00	0.00	0.01	0.02	0.02	0.13	0.36	0.75	3.63	42.61	48.84	2.79	0.50	0.04	0.02	0.00	0.02	0.05	0.02	0.12
2238974	2015GL-V11-50	0.25	0.12	0.13	0.21	0.23	1.11	2.65	3.78	4.99	6.56	9.88	22.85	32.57	9.30	3.36	1.36	0.34	0.02	0.01	0.01	0.01	0.01	0.02	0.24
2238975	2015GL-V11-50	0.53	0.28	0.14	0.20	0.46	6.49	8.56	10.05	10.55	10.09	10.85	12.97	14.47	7.08	4.40	1.87	0.40	0.06	0.04	0.01	0.04	0.14	0.03	0.28
2238976	2015GL-V11-50	0.89	1.29	0.73	1.27	2.27	13.22	13.58	12.21	9.23	8.57	9.63	9.50	8.16	6.21	2.33	0.52	0.36	0.01	0.00	0.00	0.00	0.01	0.00	0.03
2238977	2015GL-V11-50	1.98	1.06	0.77	1.81	1.97	4.85	7.15	10.79	14.50	16.77	14.36	10.43	6.61	3.83	1.62	0.68	0.79	0.01	0.00	0.00	0.01	0.00	0.00	0.00
2238978	2015GL-V11-50	0.05	0.00	0.00	0.00	0.00	0.00	0.01	0.02	0.09	0.44	1.65	3.83	10.44	24.45	51.66	6.54	0.42	0.10	0.05	0.02	0.02	0.02	0.01	0.18
2238979	2015GL-V11-50	1.76	2.83	2.37	5.58	7.17	22.02	13.71	8.33	4.74	3.04	3.16	4.79	8.90	9.00	1.92	0.28	0.36	0.02	0.01	0.00	0.00	0.01	0.00	0.02
2238980	2015GL-V11-50	0.46	0.24	0.12	0.39	0.54	1.34	1.51	2.45	3.86	6.18	8.89	12.72	20.00	26.34	10.73	2.99	0.83	0.22	0.03	0.02	0.03	0.02	0.01	0.08
2238981	2015GL001	11.66	19.67	13.46	43.61	7.97	1.04	0.23	0.25	0.26	0.04	0.16	0.34	0.10	0.22	0.39	0.14	0.16	0.07	0.03	0.01	0.04	0.05	0.04	0.08
2238982	2015GL002	7.48	11.46	8.80	34.10	15.11	5.71	2.50	1.62	1.47	0.57	1.13	0.84	0.23	0.33	0.83	0.65	1.61	0.55	0.26	0.13	0.42	0.67	0.40	3.12

Sample ID	Station ID	Percentage (%) of pixels from sample slabs that contain an Al-OH absorption feature of specified wavelength (nm)																							
		2190 – 2191	2191 – 2192	2192 – 2193	2193 – 2194	2194 – 2195	2195 – 2197	2197 – 2198	2198 – 2199	2199 – 2200	2200 – 2201	2201 – 2202	2202 – 2203	2203 – 2204	2204 – 2205	2205 – 2206	2206 – 2207	2207 – 2208	2208 – 2209	2209 – 2210	2210 – 2211	2211 – 2212	2212 – 2213	2213 – 2214	2214 – 2220
2238983	2015GL003	18.05	32.44	16.15	22.28	8.00	0.77	1.32	0.54	0.17	0.10	0.04	0.04	0.01	0.01	0.01	0.01	0.04	0.00	0.00	0.00	0.00	0.00	0.00	0.00
2238985	2015GL003	9.23	13.41	9.75	20.37	17.19	8.47	5.20	3.03	2.14	1.25	1.01	0.74	0.40	0.41	0.61	0.55	1.91	0.52	0.24	0.13	0.30	0.42	0.27	2.46
2238986	2015GL004	9.32	12.99	9.61	32.45	15.93	9.04	3.54	1.80	1.22	0.74	0.64	0.47	0.28	0.19	0.25	0.22	0.32	0.05	0.03	0.02	0.03	0.11	0.05	0.69
2238987	2015GL005	8.72	12.95	12.18	48.91	14.06	2.07	0.39	0.18	0.09	0.04	0.03	0.10	0.03	0.04	0.08	0.02	0.05	0.02	0.01	0.00	0.01	0.01	0.01	0.01
2238988	2015GL006	6.70	7.83	6.40	25.95	13.41	8.32	3.80	2.39	1.98	1.12	1.77	1.82	0.51	0.68	1.40	1.18	3.43	1.07	0.47	0.26	0.56	1.00	0.54	7.42
2238989	2015GL007	0.99	0.56	0.50	2.89	12.34	36.93	14.88	10.30	7.36	4.72	2.81	1.50	0.79	0.45	0.39	0.31	0.15	0.02	0.01	0.00	0.02	0.23	0.02	1.82
2238990	2015GL008	7.26	9.45	8.28	51.09	17.24	4.82	0.74	0.34	0.15	0.07	0.08	0.09	0.02	0.03	0.06	0.05	0.05	0.02	0.01	0.00	0.02	0.03	0.02	0.08
2238991	2015GL009	10.04	15.85	10.82	31.45	15.20	6.39	3.05	1.64	1.05	0.58	0.48	0.38	0.18	0.21	0.27	0.20	0.64	0.19	0.12	0.07	0.15	0.20	0.13	0.72
2238992	2015GL010	13.78	13.58	1.90	0.60	0.06	0.01	13.48	16.06	17.19	14.15	7.08	1.78	0.27	0.03	0.02	0.00	0.01	0.00	0.00	0.00	0.00	0.00	0.00	0.00
2238993	2015GL010	7.85	14.38	6.72	5.69	3.83	3.60	16.99	14.57	12.10	8.84	3.94	1.07	0.25	0.07	0.04	0.03	0.02	0.00	0.00	0.00	0.00	0.00	0.00	0.00
2238994	2015GL011	6.92	11.31	7.14	14.95	14.19	13.94	9.80	6.57	4.51	2.89	2.04	1.44	0.99	0.72	0.67	0.50	0.89	0.14	0.04	0.02	0.04	0.08	0.03	0.17
2238997	2015GL011	8.85	18.32	11.56	24.47	15.30	11.35	4.72	2.50	1.35	0.65	0.41	0.22	0.11	0.05	0.03	0.03	0.05	0.01	0.00	0.00	0.00	0.00	0.00	0.01
2238998	2015GL012	7.28	14.24	13.18	37.61	19.44	6.75	1.11	0.28	0.08	0.02	0.01	0.01	0.00	0.00	0.00	0.00	0.00	0.00	0.00	0.00	0.00	0.00	0.00	0.00
2238999	2015GL013	3.01	2.32	1.82	9.82	21.24	39.23	12.39	6.13	2.56	0.88	0.34	0.12	0.06	0.02	0.01	0.01	0.02	0.00	0.00	0.00	0.00	0.00	0.00	0.00
2239000	2015GL014	13.66	28.11	11.54	11.09	6.98	8.30	8.47	4.56	2.43	1.38	0.93	0.65	0.40	0.18	0.17	0.12	0.15	0.06	0.04	0.01	0.05	0.08	0.06	0.58
2242901	2015KB238	37.60	30.10	8.35	7.17	3.89	1.32	6.00	2.71	1.24	0.49	0.25	0.23	0.07	0.07	0.08	0.06	0.16	0.08	0.01	0.01	0.03	0.03	0.01	0.04
2242902	2015KB239	47.83	32.22	6.58	5.19	2.86	0.71	2.76	1.07	0.44	0.15	0.08	0.04	0.01	0.00	0.00	0.01	0.05	0.00	0.00	0.00	0.00	0.00	0.00	0.00
2242903	2015KB240	29.04	22.11	6.17	6.60	5.43	2.70	12.59	7.49	4.13	2.01	0.90	0.43	0.15	0.06	0.04	0.04	0.12	0.00	0.00	0.00	0.00	0.00	0.00	0.00
2242904	2015KB241	12.67	20.16	11.06	12.67	10.11	9.06	6.67	4.55	3.39	2.55	2.07	1.79	0.91	0.61	0.42	0.24	0.23	0.07	0.04	0.01	0.03	0.09	0.04	0.58
2242905	2015KB242	11.42	14.88	10.05	20.56	22.77	15.26	3.19	1.07	0.35	0.15	0.07	0.12	0.01	0.01	0.02	0.01	0.05	0.00	0.00	0.00	0.00	0.00	0.00	0.00
2242906	2015KB243	11.99	10.03	5.54	6.39	5.94	8.37	10.65	7.85	6.31	5.32	4.73	4.24	3.45	3.01	2.44	1.64	1.21	0.16	0.05	0.02	0.06	0.19	0.04	0.38
2242907	2015KB244	2.18	1.52	0.72	1.02	0.99	2.12	12.23	17.87	20.67	19.54	13.62	5.56	1.36	0.35	0.12	0.05	0.07	0.01	0.00	0.00	0.00	0.00	0.00	0.00
2242908	2015KB245	0.59	0.62	0.38	0.43	0.32	0.64	5.47	10.49	15.51	20.56	21.52	14.53	6.30	1.89	0.57	0.12	0.07	0.01	0.00	0.00	0.00	0.00	0.00	0.00
2242909	2015KB246	6.72	2.56	0.75	0.74	0.43	0.84	7.11	7.00	6.78	6.66	6.30	5.97	4.87	4.97	5.74	5.63	19.71	3.14	0.88	0.30	0.70	0.71	0.25	1.24
2242911	2015KB247	6.58	10.71	6.21	7.48	7.89	13.19	11.84	7.46	5.65	4.86	4.43	4.50	4.25	2.82	1.44	0.45	0.19	0.01	0.00	0.00	0.01	0.01	0.00	0.01
2242912	2015KB248	47.95	25.06	5.46	4.28	1.53	0.21	5.94	3.27	2.13	1.27	0.92	0.67	0.43	0.28	0.20	0.14	0.25	0.00	0.00	0.00	0.00	0.00	0.00	0.00
2242913	2015KB249	15.13	28.40	14.69	18.41	14.08	5.99	2.21	0.78	0.23	0.05	0.01	0.00	0.00	0.00	0.00	0.00	0.00	0.00	0.00	0.00	0.00	0.00	0.00	0.00
2242914	2015KB250A	2.83	2.00	0.96	1.42	1.35	3.72	12.57	16.15	18.02	17.23	13.72	6.74	2.20	0.68	0.20	0.09	0.11	0.00	0.00	0.00	0.00	0.00	0.00	0.00
2242915	2015KB251A	17.39	22.09	11.25	14.25	12.60	7.69	7.41	3.51	1.75	0.88	0.54	0.32	0.14	0.06	0.04	0.03	0.05	0.00	0.00	0.00	0.00	0.00	0.00	0.00
2242916	2015KB251B	14.88	11.75	4.64	4.26	2.12	1.73	15.37	13.67	12.08	8.80	5.62	2.99	1.29	0.47	0.14	0.03	0.15	0.00	0.00	0.00	0.00	0.00	0.00	0.00
2242917	2015KB252	18.65	21.16	8.60	9.17	6.10	4.32	7.91	4.83	3.47	2.52	1.71	1.46	0.96	0.90	0.94	0.79	1.86	1.11	0.55	0.28	0.61	0.74	0.37	0.99
2242918	2015KB254	38.14	23.73	4.98	4.50	3.82	2.17	10.50	6.10	3.06	1.51	0.74	0.38	0.15	0.05	0.04	0.02	0.10	0.00	0.00	0.00	0.00	0.00	0.00	0.00
2242919	2015KB255	29.47	32.27	10.64	12.17	6.44	2.43	3.90	1.57	0.62	0.28	0.11	0.05	0.02	0.01	0.01	0.01	0.03	0.00	0.00	0.00	0.00	0.00	0.00	0.00
2242921	2015KB256	24.61	26.30	7.37	5.00	2.45	1.46	12.92	7.61	4.45	2.62	1.78	1.18	0.82	0.47	0.39	0.20	0.35	0.02	0.00	0.01	0.00	0.00	0.00	0.00
2242922	2015KB257	8.67	12.64	7.29	9.76	11.00	8.89	6.37	3.37	2.12	1.52	1.20	1.29	1.44	1.49	2.26	2.70	7.81	2.55	0.99	0.47	0.99	1.82	0.62	2.75
2242923	2015KB258	30.36	31.91	8.89	8.24	4.18	1.71	7.58	3.55	1.64	0.70	0.37	0.33	0.16	0.17	0.11	0.05	0.04	0.00	0.00	0.00	0.00	0.01	0.00	0.01
2242924	2015KB259A	29.65	35.74	11.32	8.52	4.21	1.50	5.14	2.07	0.98	0.47	0.17	0.11	0.03	0.01	0.01	0.01	0.06	0.00	0.00	0.00	0.00	0.00	0.00	0.00
2242925	2015KB260	18.25	18.91	7.66	6.22	3.17	2.42	17.37	11.36	6.99	3.74	2.11	1.03	0.46	0.15	0.06	0.03	0.07	0.00	0.00	0.00	0.00	0.00	0.00	0.00
2242926	2015KB261	81.77	4.46	0.22	0.03	0.00	0.00	6.64	3.58	1.83	0.49	0.23	0.15	0.04	0.01	0.04	0.05	0.44	0.01	0.00	0.00	0.00	0.00	0.00	0.01
2242927	2015KB263	56.79	15.53	4.62	3.39	1.61	0.39	8.36	4.57	2.31	0.94	0.41	0.24	0.09	0.01	0.03	0.06	0.64	0.00	0.00	0.00	0.00	0.00	0.00	0.00
2242928	2015KB264	0.05	0.03	0.01	0.00	0.00	0.01	0.10	0.33	0.94	2.29	5.21	12.08	24.66	33.70	17.17	2.96	0.36	0.02	0.00	0.00	0.00	0.01	0.00	0.07
2242929	2015KB265	5.70	9.02	6.89	7.49	3.62	2.06	16.92	13.99	9.92	6.64	4.62	3.05	2.21	1.60	1.57	1.17	2.68	0.44	0.08	0.02	0.05	0.06	0.04	0.17
2242931	2015KB268	3.47	4.93	4.07	6.32	6.59	8.50	11.65	8.49	7.28	6.16	5.40	5.49	5.35	4.64	3.89	2.53	4.07	0.46	0.12	0.07	0.11	0.18	0.04	0.21

Sample ID	Station ID	Percentage (%) of pixels from sample slabs that contain an Al-OH absorption feature of specified wavelength (nm)																							
		2190 – 2191	2191 – 2192	2192 – 2193	2193 – 2194	2194 – 2195	2195 – 2197	2197 – 2198	2198 – 2199	2199 – 2200	2200 – 2201	2201 – 2202	2202 – 2203	2203 – 2204	2204 – 2205	2205 – 2206	2206 – 2207	2207 – 2208	2208 – 2209	2209 – 2210	2210 – 2211	2211 – 2212	2212 – 2213	2213 – 2214	2214 – 2220
2242932	2015KB269	31.76	27.06	8.95	5.17	1.98	0.45	8.44	4.85	2.98	1.76	1.16	1.05	0.73	0.40	0.61	0.41	1.70	0.21	0.03	0.03	0.04	0.06	0.05	0.13
2242933	2015KB270	0.14	0.09	0.02	0.08	0.07	0.13	0.79	2.29	4.83	7.78	11.23	16.28	22.57	24.76	7.68	1.00	0.25	0.00	0.00	0.00	0.00	0.00	0.00	0.00
2242934	2015KB271	36.58	12.06	4.01	4.14	3.05	1.55	11.02	6.99	4.76	3.12	2.54	2.65	2.16	1.49	1.29	0.94	1.55	0.03	0.01	0.00	0.02	0.01	0.01	0.01
2242935	2015KB272	6.39	3.65	1.06	0.89	0.42	0.45	9.97	12.67	14.13	13.88	11.79	9.18	6.23	3.08	1.82	1.04	2.76	0.24	0.05	0.03	0.07	0.06	0.02	0.11
2242936	2015KB273	0.10	0.01	0.00	0.00	0.00	0.00	0.10	0.76	2.69	5.36	7.83	9.75	12.49	21.18	32.98	5.73	0.54	0.08	0.03	0.01	0.04	0.06	0.01	0.24
2242937	2015KB274	49.08	13.96	3.02	1.48	0.53	0.24	12.83	8.27	4.95	2.55	1.41	0.92	0.33	0.08	0.10	0.08	0.19	0.00	0.00	0.00	0.00	0.00	0.00	0.00
2242938	2015KB275	4.56	3.85	1.85	1.97	1.61	3.72	10.94	11.23	9.77	8.26	6.97	5.67	4.27	3.02	2.96	2.86	6.09	2.38	1.01	0.48	0.82	1.54	0.56	3.58
2242939	2015KB276	47.22	18.23	6.90	15.27	5.27	0.28	3.80	1.67	0.80	0.30	0.10	0.08	0.02	0.01	0.01	0.00	0.06	0.00	0.00	0.00	0.00	0.00	0.00	0.00
2242941	2015KB277	61.91	13.41	5.17	7.44	4.69	1.03	2.97	1.45	0.67	0.33	0.17	0.10	0.03	0.02	0.08	0.14	0.34	0.02	0.00	0.00	0.00	0.00	0.00	0.00
2242942	2015KB278	49.91	13.62	2.31	1.35	0.21	0.03	6.80	3.77	4.16	3.32	4.31	5.66	2.54	1.29	0.57	0.09	0.06	0.00	0.00	0.00	0.00	0.00	0.00	0.00
2242943	2015KB279	0.16	0.04	0.04	0.53	0.85	4.87	3.86	4.42	4.65	5.70	6.42	7.06	13.14	29.08	16.53	2.30	0.32	0.00	0.00	0.00	0.00	0.00	0.00	0.03
2242944	2015KB266A	0.03	0.00	0.00	0.00	0.00	0.00	0.00	0.00	0.02	0.06	0.50	3.57	22.35	49.11	20.63	3.45	0.14	0.00	0.01	0.00	0.00	0.00	0.00	0.10
2242945	2015KB266B	0.12	0.00	0.00	0.00	0.00	0.00	0.01	0.05	0.21	0.88	4.49	18.14	39.50	27.82	7.18	1.32	0.29	0.00	0.00	0.00	0.00	0.00	0.00	0.00
2242946	2015KB267	1.00	2.69	2.13	3.59	3.08	3.31	7.27	8.97	9.84	9.74	9.09	8.79	9.39	9.06	7.02	3.24	0.40	0.11	0.07	0.01	0.04	0.27	0.05	0.83
2245246	2015KB001	23.50	26.07	6.97	5.51	2.49	1.47	10.18	7.86	5.91	4.02	2.64	1.67	0.93	0.47	0.24	0.07	0.01	0.00	0.00	0.00	0.00	0.00	0.00	0.00
2245247	2015KB002	75.27	9.38	1.11	0.59	0.18	0.04	7.79	3.43	1.38	0.46	0.18	0.08	0.03	0.01	0.01	0.01	0.06	0.00	0.00	0.00	0.00	0.00	0.00	0.00
2245248	2015KB004	51.70	24.68	2.49	0.87	0.25	0.08	11.59	5.20	1.93	0.65	0.23	0.14	0.04	0.01	0.03	0.04	0.07	0.00	0.00	0.00	0.00	0.00	0.00	0.00
2245249	2015KB005	69.78	16.67	1.18	0.29	0.04	0.01	7.50	2.82	1.12	0.33	0.10	0.06	0.02	0.00	0.01	0.01	0.06	0.00	0.00	0.00	0.00	0.00	0.00	0.00
2245251	2015KB007	60.50	8.31	1.00	0.32	0.05	0.01	15.36	9.11	4.01	1.05	0.21	0.06	0.01	0.01	0.00	0.00	0.00	0.00	0.00	0.00	0.00	0.00	0.00	0.00
2245252	2015KB008	69.14	17.01	3.28	2.08	0.82	0.09	4.77	1.77	0.60	0.20	0.10	0.04	0.01	0.01	0.01	0.01	0.05	0.00	0.00	0.00	0.00	0.00	0.00	0.00
2245253	2015KB011	86.31	0.75	0.06	0.01	0.00	0.00	6.19	3.50	1.68	0.51	0.24	0.20	0.05	0.02	0.02	0.08	0.38	0.00	0.00	0.00	0.00	0.01	0.01	0.00
2245254	2015KB012	64.05	13.01	3.05	1.56	0.52	0.12	8.06	4.55	2.58	1.01	0.45	0.34	0.09	0.02	0.06	0.04	0.49	0.00	0.00	0.00	0.00	0.00	0.00	0.00
2245255	2015KB015	77.48	2.04	0.04	0.00	0.00	0.00	10.14	5.71	2.72	1.06	0.37	0.19	0.04	0.01	0.02	0.02	0.16	0.00	0.00	0.00	0.00	0.00	0.00	0.00
2245256	2015KB016	52.78	20.11	4.41	2.09	0.44	0.11	10.45	5.15	2.37	0.99	0.47	0.29	0.08	0.01	0.03	0.03	0.19	0.00	0.00	0.00	0.00	0.00	0.00	0.00
2245257	2015KB017	43.59	26.68	7.72	4.01	0.81	0.18	10.09	3.96	1.59	0.77	0.28	0.12	0.04	0.01	0.03	0.02	0.12	0.00	0.00	0.00	0.00	0.00	0.00	0.00
2245258	2015KB019	67.17	18.81	1.27	0.28	0.04	0.01	7.35	3.02	1.29	0.40	0.17	0.08	0.02	0.01	0.01	0.00	0.06	0.00	0.00	0.00	0.00	0.00	0.00	0.00
2245259	2015KB020	26.09	7.29	2.12	1.40	0.54	0.61	16.22	12.79	8.67	5.98	4.67	3.48	2.63	1.95	1.58	1.22	2.15	0.17	0.04	0.02	0.06	0.09	0.03	0.20
2245261	2015KB022	48.65	28.13	6.80	3.97	1.73	0.74	5.98	2.37	0.96	0.34	0.09	0.08	0.03	0.00	0.01	0.01	0.10	0.00	0.00	0.00	0.00	0.00	0.00	0.00
2245262	2015KB023	53.21	1.70	0.05	0.01	0.00	0.00	11.04	9.55	7.46	4.92	3.37	2.77	1.75	1.14	1.07	0.71	1.19	0.03	0.00	0.01	0.01	0.00	0.00	0.03
2245263	2015KB024	65.83	13.19	3.24	2.02	0.78	0.12	7.54	3.82	1.96	0.65	0.32	0.19	0.05	0.01	0.02	0.01	0.23	0.00	0.00	0.00	0.00	0.00	0.00	0.00
2245264	2015KB025	35.07	11.27	3.70	3.16	1.55	1.22	17.25	12.49	7.27	3.70	1.60	0.85	0.43	0.08	0.09	0.09	0.19	0.00	0.00	0.00	0.00	0.00	0.00	0.00
2245265	2015KB027	71.31	11.78	1.21	0.44	0.10	0.02	7.86	3.93	1.87	0.65	0.31	0.19	0.04	0.01	0.01	0.04	0.23	0.00	0.00	0.00	0.00	0.00	0.00	0.00
2245266	2015KB028	65.00	13.21	0.86	0.16	0.02	0.01	10.98	5.69	2.51	0.83	0.33	0.17	0.05	0.01	0.02	0.02	0.13	0.00	0.00	0.00	0.00	0.00	0.00	0.00
2245267	2015KB031	53.14	19.34	4.09	2.20	0.68	0.27	9.38	5.06	2.75	1.26	0.66	0.42	0.15	0.04	0.07	0.07	0.42	0.00	0.00	0.00	0.00	0.00	0.00	0.00
2245268	2015KB032A	46.09	15.37	0.80	0.23	0.04	0.00	14.82	9.14	5.26	2.92	1.58	0.87	0.54	0.21	0.23	0.18	1.49	0.12	0.01	0.01	0.01	0.01	0.00	0.08
2245269	2015KB032B	49.76	16.78	2.97	1.39	0.33	0.12	11.62	6.44	3.55	1.82	1.21	0.93	0.76	0.54	0.58	0.45	0.54	0.08	0.01	0.01	0.02	0.04	0.02	0.06
2245271	2015KB033	40.29	33.78	9.44	4.21	1.02	0.23	6.45	2.66	1.06	0.43	0.16	0.09	0.05	0.01	0.01	0.02	0.09	0.00	0.00	0.00	0.00	0.00	0.00	0.00
2245272	2015KB034	35.41	3.28	0.34	0.10	0.00	0.00	10.49	9.14	7.46	5.65	4.35	4.09	3.43	3.33	3.99	3.95	2.09	0.51	0.23	0.14	0.29	0.63	0.13	0.98
2245274	2015KB035	54.96	15.19	3.30	1.65	0.37	0.05	11.57	6.43	3.41	1.40	0.69	0.39	0.17	0.04	0.03	0.05	0.32	0.00	0.00	0.00	0.00	0.00	0.00	0.00
2245275	2015KB036	1.74	0.00	0.00	0.00	0.00	0.00	0.14	0.26	0.51	0.94	1.93	4.40	8.25	14.03	20.46	20.67	19.19	3.17	0.99	0.40	0.75	0.86	0.31	1.00
2245276	2015KB037	40.20	10.24	2.96	2.01	0.72	0.49	17.33	11.70	7.15	3.59	1.67	0.93	0.35	0.07	0.08	0.09	0.43	0.00	0.00	0.00	0.00	0.00	0.00	0.00
2245277	2015KB009	70.75	17.68	1.85	0.44	0.06	0.01	5.93	2.17	0.70	0.18	0.08	0.05	0.02	0.01	0.00	0.02	0.06	0.00	0.00	0.00	0.00	0.00	0.00	0.00
2245278	2015KB038	30.09	28.37	8.46	4.45	1.14	0.27	11.43	6.29	3.73	2.13	1.28	0.91	0.53	0.16	0.31	0.23	0.22	0.00	0.00	0.00	0.00	0.00	0.00	0.00

Sample ID	Station ID	Percentage (%) of pixels from sample slabs that contain an Al-OH absorption feature of specified wavelength (nm)																							
		2190 – 2191	2191 – 2192	2192 – 2193	2193 – 2194	2194 – 2195	2195 – 2197	2197 – 2198	2198 – 2199	2199 – 2200	2200 – 2201	2201 – 2202	2202 – 2203	2203 – 2204	2204 – 2205	2205 – 2206	2206 – 2207	2207 – 2208	2208 – 2209	2209 – 2210	2210 – 2211	2211 – 2212	2212 – 2213	2213 – 2214	2214 – 2220
2245279	2015KB040	58.89	9.73	0.38	0.12	0.02	0.01	15.32	8.89	4.08	1.64	0.55	0.26	0.06	0.01	0.01	0.01	0.02	0.00	0.00	0.00	0.00	0.00	0.00	0.00
2245281	2015KB041	38.80	26.61	11.68	9.37	4.02	1.06	4.99	2.00	0.79	0.31	0.11	0.13	0.02	0.00	0.01	0.01	0.08	0.00	0.00	0.00	0.00	0.00	0.00	0.00
2245282	2015KB043A	26.35	0.00	0.00	0.00	0.00	0.00	1.47	2.96	5.81	7.58	11.37	17.34	13.08	4.50	5.03	2.79	1.73	0.00	0.00	0.00	0.00	0.00	0.00	0.00
2245283	2015KB043B	24.77	37.62	17.39	9.73	2.11	0.37	4.61	1.72	0.80	0.38	0.24	0.11	0.07	0.03	0.01	0.01	0.02	0.00	0.00	0.00	0.00	0.00	0.00	0.00
2245284	2015KB044	15.33	6.33	2.49	2.13	1.18	0.85	15.01	14.59	12.57	9.26	6.97	5.48	3.66	1.50	0.99	0.47	0.31	0.22	0.09	0.06	0.09	0.12	0.03	0.28
2245285	2015KB045	22.31	15.11	9.26	11.82	8.78	8.98	15.23	5.53	1.73	0.60	0.30	0.20	0.03	0.01	0.02	0.00	0.07	0.00	0.00	0.00	0.00	0.00	0.00	0.00
2245286	2015KB046	50.78	21.75	3.94	1.68	0.47	0.21	10.95	5.58	2.63	1.06	0.47	0.22	0.06	0.03	0.03	0.02	0.13	0.00	0.00	0.00	0.00	0.00	0.00	0.00
2245287	2015KB047	63.33	11.45	2.27	1.35	0.45	0.23	10.96	5.46	2.50	0.95	0.44	0.33	0.10	0.02	0.03	0.02	0.13	0.00	0.00	0.00	0.00	0.00	0.00	0.00
2245289	2015KB049	50.18	30.02	6.53	2.97	0.79	0.11	5.98	2.10	0.84	0.21	0.10	0.11	0.02	0.00	0.00	0.01	0.04	0.00	0.00	0.00	0.00	0.00	0.00	0.00
2245291	2015KB050	73.38	2.24	0.00	0.00	0.00	0.00	11.26	6.69	3.64	1.45	0.70	0.39	0.09	0.01	0.03	0.03	0.10	0.00	0.00	0.00	0.00	0.00	0.00	0.00
2245292	2015KB051	58.65	22.00	4.84	2.40	0.58	0.07	6.51	2.89	1.19	0.35	0.17	0.12	0.04	0.01	0.02	0.02	0.14	0.00	0.00	0.00	0.00	0.00	0.00	0.00
2245293	2015KB052	36.50	17.07	3.11	1.72	0.50	0.08	13.28	10.14	7.06	4.42	2.74	1.53	0.69	0.20	0.21	0.20	0.55	0.00	0.00	0.00	0.00	0.00	0.00	0.00
2245294	2015KB053	60.35	15.78	1.36	0.50	0.10	0.01	9.27	5.47	3.05	1.57	0.94	0.58	0.28	0.09	0.13	0.11	0.39	0.00	0.00	0.00	0.00	0.00	0.00	0.00
2245295	2015KB054	72.26	7.79	0.38	0.12	0.02	0.00	9.93	5.24	2.40	1.00	0.36	0.23	0.06	0.01	0.02	0.01	0.17	0.00	0.00	0.00	0.00	0.00	0.00	0.00
2245296	2015KB055	8.04	13.06	13.46	34.68	25.61	4.20	0.61	0.22	0.09	0.02	0.01	0.00	0.00	0.00	0.00	0.00	0.00	0.00	0.00	0.00	0.00	0.00	0.00	0.00
2245297	2015KB056	61.81	8.13	4.35	9.20	4.73	0.51	5.40	2.81	1.48	0.55	0.22	0.24	0.06	0.00	0.06	0.08	0.36	0.00	0.00	0.00	0.00	0.00	0.00	0.00
2245298	2015KB057	33.60	14.58	6.86	8.05	7.48	8.32	11.87	5.47	2.50	0.78	0.32	0.09	0.04	0.01	0.00	0.01	0.01	0.00	0.00	0.00	0.00	0.00	0.00	0.00
2245299	2015KB059	44.84	27.39	3.71	0.78	0.06	0.02	10.69	6.01	3.18	1.45	0.74	0.45	0.18	0.07	0.06	0.06	0.31	0.00	0.00	0.00	0.00	0.00	0.00	0.00
2245301	2015KB060	9.32	6.18	2.29	1.94	0.93	1.10	24.73	24.57	15.70	7.39	3.40	1.45	0.65	0.12	0.11	0.04	0.08	0.00	0.00	0.00	0.00	0.00	0.00	0.00
2245302	2015KB062	12.77	8.98	5.00	4.28	2.65	4.61	22.18	17.69	10.97	5.81	2.68	1.22	0.55	0.24	0.10	0.08	0.17	0.01	0.00	0.00	0.00	0.00	0.00	0.00
2245303	2015KB063	80.13	0.00	0.00	0.00	0.00	0.00	6.06	4.45	3.47	1.07	0.77	0.74	0.23	0.05	0.14	0.29	2.60	0.00	0.00	0.00	0.00	0.00	0.00	0.00
2245304	2015KB064A	79.83	0.03	0.00	0.00	0.00	0.00	4.90	4.60	3.56	1.28	0.80	0.62	0.60	0.51	1.05	1.26	0.95	0.00	0.00	0.00	0.00	0.00	0.00	0.00
2245305	2015KB064B	75.74	0.11	0.00	0.00	0.00	0.00	7.85	5.79	4.21	1.95	1.23	1.07	0.37	0.07	0.13	0.17	1.31	0.00	0.00	0.00	0.00	0.00	0.00	0.00
2245307	2015KB066	82.39	0.37	0.01	0.00	0.00	0.00	6.35	4.36	2.64	1.09	0.64	0.55	0.17	0.01	0.07	0.14	1.22	0.00	0.00	0.00	0.00	0.00	0.00	0.00
2245308	2015KB067	62.27	4.72	0.18	0.06	0.02	0.01	10.76	8.09	5.68	3.11	1.81	1.35	0.62	0.15	0.17	0.16	0.85	0.00	0.00	0.00	0.00	0.00	0.00	0.00
2245309	2015KB068	34.66	2.57	0.31	0.15	0.05	0.03	11.73	13.35	12.12	9.10	6.31	4.29	2.17	0.90	0.69	0.51	1.04	0.01	0.00	0.00	0.00	0.00	0.00	0.00
2245311	2015KB069	69.65	1.56	0.11	0.02	0.00	0.00	6.96	6.65	5.40	3.90	2.63	1.51	0.68	0.29	0.17	0.20	0.22	0.05	0.01	0.00	0.00	0.00	0.00	0.00
2245312	2015KB071	17.90	0.92	0.20	0.10	0.05	0.02	6.64	9.73	11.91	12.00	10.71	9.27	6.82	4.37	3.50	2.40	2.70	0.34	0.09	0.03	0.07	0.07	0.05	0.10
2245313	2015KB070	51.54	14.44	4.51	4.59	2.08	0.35	10.08	5.86	3.43	1.37	0.73	0.48	0.12	0.03	0.05	0.05	0.30	0.00	0.00	0.00	0.00	0.00	0.00	0.00
2245314	2015KB072	7.72	4.67	0.79	0.24	0.03	0.00	8.90	11.69	13.56	13.76	13.21	11.77	8.03	3.33	1.47	0.51	0.31	0.01	0.00	0.00	0.00	0.00	0.00	0.00
2245315	2015KB073	71.45	6.91	0.26	0.03	0.00	0.00	10.58	5.55	2.96	1.12	0.47	0.28	0.08	0.02	0.03	0.02	0.24	0.00	0.00	0.00	0.00	0.00	0.00	0.00
2245316	2015KB074	15.81	17.20	9.36	9.33	4.53	3.98	19.39	11.15	5.27	2.11	0.85	0.53	0.25	0.08	0.03	0.01	0.12	0.00	0.00	0.00	0.00	0.00	0.00	0.00
2245317	2015KB075	28.23	25.74	11.19	11.21	7.66	2.84	6.95	3.16	1.52	0.61	0.35	0.20	0.06	0.01	0.05	0.04	0.15	0.00	0.00	0.00	0.00	0.00	0.00	0.00
2245318	2015KB076	76.44	7.80	0.48	0.10	0.03	0.00	7.27	3.98	2.17	0.77	0.33	0.16	0.08	0.01	0.04	0.04	0.30	0.00	0.01	0.00	0.00	0.00	0.00	0.00
2245319	2015KB077	71.17	10.89	2.03	0.91	0.44	0.13	7.41	3.59	1.71	0.63	0.28	0.22	0.06	0.01	0.07	0.06	0.39	0.01	0.01	0.00	0.00	0.00	0.00	0.00
2245321	2015KB078	65.83	14.42	2.15	1.05	0.45	0.24	8.86	3.95	1.74	0.59	0.25	0.17	0.05	0.01	0.04	0.07	0.12	0.00	0.00	0.00	0.00	0.00	0.00	0.00
2245322	2015KB079	62.97	13.70	3.82	3.44	1.95	1.00	7.18	3.17	1.54	0.50	0.28	0.17	0.07	0.03	0.03	0.03	0.12	0.00	0.00	0.00	0.00	0.00	0.00	0.00
2245323	2015KB081	49.21	28.98	4.35	1.24	0.18	0.04	9.25	4.12	1.57	0.54	0.21	0.11	0.03	0.01	0.01	0.02	0.14	0.00	0.00	0.00	0.00	0.00	0.00	0.00
2245324	2015KB082	34.77	27.87	5.49	2.08	0.52	0.36	13.22	7.68	4.08	2.01	1.01	0.47	0.16	0.05	0.04	0.04	0.15	0.00	0.00	0.00	0.00	0.00	0.00	0.00
2245325	2015KB026	62.87	17.25	3.84	2.28	0.67	0.08	6.63	3.25	1.68	0.60	0.25	0.21	0.08	0.01	0.02	0.04	0.24	0.00	0.00	0.00	0.00	0.00	0.00	0.00
2245326	2015KB083	87.85	1.58	0.07	0.00	0.00	0.00	5.30	2.92	1.38	0.42	0.19	0.10	0.02	0.01	0.01	0.02	0.13	0.00	0.00	0.00	0.00	0.00	0.00	0.00
2245327	2015KB029	27.55	28.32	9.38	6.44	2.92	2.43	13.26	5.83	2.38	0.83	0.36	0.16	0.07	0.01	0.01	0.01	0.04	0.00	0.00	0.00	0.00	0.00	0.00	0.00
2245328	2015KB030	70.46	12.34	2.05	0.64	0.11	0.04	6.61	3.57	1.72	0.67	0.35	0.27	0.17	0.14	0.29	0.25	0.32	0.00	0.00	0.00	0.00	0.00	0.00	0.00

Sample ID	Station ID	Percentage (%) of pixels from sample slabs that contain an Al-OH absorption feature of specified wavelength (nm)																							
		2190 – 2191	2191 – 2192	2192 – 2193	2193 – 2194	2194 – 2195	2195 – 2197	2197 – 2198	2198 – 2199	2199 – 2200	2200 – 2201	2201 – 2202	2202 – 2203	2203 – 2204	2204 – 2205	2205 – 2206	2206 – 2207	2207 – 2208	2208 – 2209	2209 – 2210	2210 – 2211	2211 – 2212	2212 – 2213	2213 – 2214	2214 – 2220
2245329	2015KB084	48.07	18.00	1.55	0.40	0.07	0.03	14.40	8.72	4.44	2.09	0.91	0.49	0.22	0.08	0.09	0.09	0.34	0.00	0.00	0.00	0.00	0.00	0.00	0.00
2245331	2015KB085	37.01	20.32	2.32	0.40	0.04	0.00	9.17	5.03	2.75	1.45	0.87	0.76	0.71	0.53	1.03	1.49	15.66	0.32	0.04	0.01	0.03	0.03	0.00	0.04
2245332	2015KB086	44.60	29.72	6.35	2.91	0.67	0.26	9.24	3.76	1.51	0.57	0.22	0.08	0.03	0.02	0.01	0.00	0.06	0.00	0.00	0.00	0.00	0.00	0.00	0.00
2245333	2015KB087	68.32	13.55	1.76	0.70	0.14	0.00	4.09	2.11	0.94	0.49	0.37	0.41	0.57	0.41	1.82	2.49	1.82	0.00	0.00	0.00	0.00	0.00	0.00	0.00
2245335	2015KB089	35.58	37.06	8.88	3.56	0.65	0.13	8.64	3.28	1.33	0.46	0.20	0.12	0.03	0.01	0.01	0.01	0.05	0.00	0.00	0.00	0.00	0.00	0.00	0.00
2245336	2015KB090	72.41	9.18	0.95	0.23	0.05	0.00	8.23	4.25	2.29	0.87	0.41	0.36	0.15	0.07	0.11	0.11	0.33	0.00	0.00	0.00	0.00	0.00	0.00	0.00
2245337	2015KB091	55.51	18.97	3.38	1.53	0.48	0.14	10.09	5.10	2.50	0.97	0.52	0.35	0.11	0.03	0.05	0.03	0.24	0.00	0.00	0.00	0.00	0.00	0.00	0.00
2245338	2015KB092	49.17	27.66	4.58	2.04	0.50	0.10	8.79	3.95	1.77	0.76	0.33	0.16	0.08	0.01	0.02	0.03	0.06	0.00	0.00	0.00	0.00	0.00	0.00	0.00
2245339	2015KB093	26.66	21.92	4.41	1.92	0.42	0.14	11.79	6.40	4.10	2.82	2.67	2.63	2.88	2.80	3.20	2.61	1.99	0.25	0.11	0.05	0.05	0.09	0.02	0.09
2245341	2015KB094	54.89	7.52	1.54	0.95	0.34	0.25	14.52	9.54	5.12	2.19	1.09	0.75	0.33	0.10	0.11	0.12	0.64	0.00	0.00	0.00	0.00	0.00	0.00	0.00
2245342	2015KB095	77.37	1.33	0.02	0.01	0.00	0.00	8.96	5.49	3.59	1.25	0.61	0.45	0.14	0.04	0.05	0.10	0.59	0.00	0.00	0.00	0.00	0.00	0.00	0.00
2245343	2015KB096	80.92	2.91	0.10	0.02	0.00	0.00	7.65	4.42	2.04	0.78	0.36	0.25	0.06	0.02	0.04	0.06	0.36	0.00	0.00	0.00	0.00	0.00	0.00	0.00
2245344	2015KB097	83.55	1.66	0.20	0.05	0.01	0.00	6.54	3.82	2.37	0.68	0.32	0.26	0.05	0.01	0.03	0.06	0.40	0.00	0.00	0.00	0.00	0.00	0.00	0.00
2245345	2015KB098	84.64	3.31	0.13	0.01	0.02	0.00	5.81	3.18	1.53	0.44	0.23	0.19	0.03	0.01	0.03	0.05	0.36	0.01	0.00	0.00	0.00	0.00	0.00	0.00
2245346	2015KB099	44.50	26.11	6.48	3.24	0.89	0.22	10.17	4.74	2.12	0.74	0.36	0.18	0.06	0.02	0.03	0.04	0.12	0.00	0.00	0.00	0.00	0.00	0.00	0.00
2245347	2015KB100	32.44	18.50	6.19	4.54	2.19	1.03	16.72	10.43	4.88	1.77	0.72	0.29	0.10	0.03	0.01	0.02	0.14	0.00	0.00	0.00	0.00	0.00	0.00	0.00
2245348	2015KB101	31.25	28.12	9.51	6.38	1.76	0.41	12.52	5.61	2.59	0.94	0.44	0.22	0.07	0.03	0.02	0.02	0.10	0.00	0.00	0.00	0.00	0.00	0.00	0.00
2245349	2015KB102	27.13	1.94	0.23	0.15	0.05	0.01	9.46	9.73	9.72	9.71	10.47	10.01	6.82	2.58	1.16	0.36	0.48	0.00	0.00	0.00	0.00	0.00	0.00	0.00
2245351	2015KB103A	4.80	1.40	1.06	1.52	1.53	17.19	33.52	22.23	9.29	4.30	1.89	0.70	0.24	0.10	0.07	0.07	0.08	0.00	0.00	0.00	0.00	0.00	0.00	0.00
2245353	2015KB105A	71.16	12.18	2.69	1.20	0.30	0.06	6.56	3.32	1.47	0.54	0.16	0.12	0.03	0.01	0.02	0.01	0.16	0.00	0.00	0.00	0.00	0.00	0.00	0.00
2245355	2015KB106	56.60	14.92	0.94	0.25	0.04	0.01	13.34	7.36	3.57	1.44	0.68	0.37	0.12	0.06	0.05	0.04	0.19	0.00	0.00	0.00	0.00	0.00	0.00	0.00
2245356	2015KB107	7.49	18.98	24.13	28.78	10.72	2.82	5.62	1.10	0.23	0.04	0.02	0.03	0.01	0.00	0.00	0.00	0.03	0.00	0.00	0.00	0.00	0.00	0.00	0.00
2245357	2015KB108	79.13	1.70	0.04	0.00	0.00	0.00	7.35	4.91	3.16	1.20	0.64	0.50	0.21	0.02	0.07	0.12	0.94	0.00	0.00	0.00	0.00	0.00	0.00	0.00
2245358	2015KB109	61.94	13.80	2.43	0.97	0.20	0.07	10.84	5.41	2.37	0.94	0.43	0.27	0.12	0.04	0.05	0.03	0.08	0.00	0.00	0.00	0.00	0.00	0.00	0.00
2245359	2015KB110	43.29	25.82	7.71	4.05	1.04	0.19	10.35	4.27	1.74	0.69	0.32	0.16	0.08	0.02	0.04	0.02	0.23	0.00	0.00	0.00	0.00	0.00	0.00	0.00
2245361	2015KB111	67.65	11.20	0.95	0.24	0.02	0.00	10.16	5.13	2.49	0.97	0.41	0.25	0.07	0.01	0.03	0.03	0.38	0.00	0.00	0.00	0.00	0.00	0.00	0.00
2245362	2015KB112	47.04	24.30	4.50	2.02	0.38	0.08	11.63	5.50	2.51	1.06	0.43	0.24	0.09	0.02	0.03	0.02	0.16	0.00	0.00	0.00	0.00	0.00	0.00	0.00
2245363	2015KB113	27.10	3.12	0.72	0.58	0.32	0.34	11.27	11.75	11.28	9.10	7.24	6.79	4.26	1.10	1.42	1.16	2.45	0.00	0.00	0.00	0.00	0.00	0.00	0.00
2245364	2015KB115	54.35	2.65	0.34	0.25	0.04	0.02	13.38	10.71	7.52	4.51	2.41	1.73	0.64	0.09	0.16	0.18	1.01	0.00	0.00	0.00	0.00	0.00	0.00	0.00
2245365	2015KB116	42.48	9.27	1.47	0.58	0.18	0.16	13.50	10.57	7.63	4.88	3.05	2.31	1.33	0.49	0.70	0.59	0.81	0.00	0.00	0.00	0.00	0.00	0.00	0.00
2245366	2015KB117	57.81	0.75	0.11	0.07	0.02	0.00	8.83	8.21	7.10	4.44	3.07	3.19	1.11	0.13	0.42	0.74	3.99	0.00	0.00	0.00	0.00	0.00	0.00	0.00
2245367	2015KB118	50.69	19.58	5.87	4.55	2.18	0.79	8.37	4.19	2.15	0.82	0.33	0.21	0.06	0.01	0.04	0.02	0.14	0.00	0.00	0.00	0.00	0.00	0.00	0.00
2245368	2015KB119	31.43	4.27	1.39	1.35	1.72	7.93	17.12	14.14	9.43	5.29	2.67	1.66	0.58	0.10	0.15	0.14	0.61	0.00	0.00	0.00	0.00	0.00	0.00	0.02
2245369	2015KB120	39.41	21.67	4.06	1.00	0.18	0.06	16.99	9.22	4.06	1.59	0.79	0.40	0.14	0.03	0.05	0.04	0.32	0.00	0.00	0.00	0.00	0.00	0.00	0.01
2245373	2015KB122	30.48	16.32	7.40	7.49	4.85	2.93	13.01	7.79	4.47	2.28	1.27	0.75	0.36	0.17	0.14	0.10	0.17	0.01	0.00	0.00	0.00	0.00	0.00	0.01
2245374	2015KB123	70.19	4.42	0.69	0.29	0.06	0.03	9.41	6.52	3.94	1.61	0.78	0.58	0.24	0.06	0.06	0.12	0.99	0.01	0.00	0.00	0.00	0.00	0.00	0.00
2245375	2015KB124	29.43	26.24	6.25	2.71	0.83	0.52	16.45	9.87	4.72	1.81	0.73	0.23	0.10	0.02	0.03	0.02	0.05	0.00	0.00	0.00	0.00	0.00	0.00	0.00
2245376	2015KB125	39.47	26.61	7.87	4.63	1.46	0.29	9.67	4.92	2.61	1.23	0.54	0.26	0.12	0.04	0.09	0.06	0.14	0.00	0.00	0.00	0.00	0.00	0.00	0.00
2245377	2015KB127	36.69	33.68	7.87	4.03	1.34	0.44	9.71	3.84	1.41	0.53	0.20	0.09	0.04	0.02	0.03	0.01	0.05	0.00	0.00	0.00	0.00	0.00	0.00	0.00
2245378	2015KB128A	51.87	25.87	7.30	4.56	2.16	0.64	4.73	1.71	0.69	0.21	0.10	0.06	0.01	0.01	0.00	0.01	0.07	0.00	0.00	0.00	0.00	0.00	0.00	0.00
2245379	2015KB128B	44.61	1.59	0.53	0.39	0.11	0.25	7.74	6.71	6.60	5.46	5.55	5.02	4.28	2.87	2.76	2.16	3.23	0.05	0.01	0.00	0.00	0.03	0.02	0.03
2245381	2015KB129	16.73	14.38	9.68	12.22	8.89	14.75	13.14	5.12	2.40	1.10	0.69	0.47	0.19	0.04	0.04	0.05	0.11	0.00	0.00	0.00	0.00	0.00	0.00	0.00
2245383	2015KB132	50.06	18.36	6.46	6.09	3.99	1.90	7.11	3.29	1.41	0.55	0.27	0.15	0.05	0.01	0.05	0.04	0.21	0.00	0.00	0.00	0.00	0.00	0.00	0.00

Sample ID	Station ID	Percentage (%) of pixels from sample slabs that contain an Al-OH absorption feature of specified wavelength (nm)																							
		2190 – 2191	2191 – 2192	2192 – 2193	2193 – 2194	2194 – 2195	2195 – 2197	2197 – 2198	2198 – 2199	2199 – 2200	2200 – 2201	2201 – 2202	2202 – 2203	2203 – 2204	2204 – 2205	2205 – 2206	2206 – 2207	2207 – 2208	2208 – 2209	2209 – 2210	2210 – 2211	2211 – 2212	2212 – 2213	2213 – 2214	2214 – 2220
2245384	2015KB133	35.39	23.01	9.77	9.77	6.55	3.71	6.91	2.73	1.07	0.44	0.16	0.13	0.03	0.01	0.03	0.03	0.22	0.00	0.00	0.00	0.00	0.00	0.00	0.00
2245385	2015KB134	49.75	22.06	6.46	4.73	2.36	0.67	7.24	3.44	1.59	0.67	0.34	0.25	0.07	0.00	0.03	0.03	0.31	0.00	0.00	0.00	0.00	0.00	0.00	0.00
2245386	2015KB135A	67.02	5.81	0.41	0.13	0.02	0.00	10.82	7.15	4.03	1.70	0.81	0.67	0.17	0.07	0.11	0.13	0.96	0.00	0.00	0.00	0.00	0.00	0.00	0.00
2245387	2015KB136	24.13	7.04	2.24	1.28	0.30	0.07	14.89	14.15	12.76	9.68	6.32	3.61	1.75	0.53	0.36	0.26	0.62	0.00	0.00	0.00	0.00	0.00	0.00	0.00
2245388	2015KB137	39.91	25.54	7.98	6.24	2.65	0.87	9.20	4.26	1.76	0.78	0.39	0.18	0.05	0.01	0.02	0.01	0.13	0.00	0.00	0.00	0.00	0.00	0.00	0.00
2245389	2015KB138	37.79	23.54	6.84	5.45	3.48	1.14	10.32	5.43	2.96	1.38	0.77	0.46	0.21	0.07	0.06	0.04	0.07	0.00	0.00	0.00	0.00	0.00	0.00	0.00
2245391	2015KB139	31.55	19.20	8.74	10.17	6.48	2.00	7.54	4.11	2.39	1.39	0.92	0.69	0.33	0.42	0.63	0.60	2.74	0.05	0.00	0.02	0.00	0.00	0.00	0.02
2245392	2015KB140	23.41	24.14	11.55	14.49	10.75	4.29	5.79	2.70	1.41	0.66	0.31	0.19	0.08	0.02	0.04	0.04	0.12	0.00	0.00	0.00	0.00	0.00	0.00	0.00
2245393	2015KB141	18.65	22.92	13.13	16.27	10.37	4.67	5.87	3.12	1.84	1.08	0.59	0.46	0.31	0.14	0.13	0.11	0.33	0.00	0.00	0.00	0.00	0.00	0.00	0.00
2245394	2015KB142	38.15	22.81	9.98	12.06	7.08	1.54	4.19	2.06	1.02	0.48	0.23	0.16	0.05	0.02	0.02	0.02	0.12	0.00	0.00	0.00	0.00	0.00	0.00	0.00
2245395	2015KB143	28.47	21.35	8.47	8.46	5.71	2.77	9.96	5.68	3.44	2.02	1.25	0.94	0.57	0.21	0.20	0.17	0.32	0.00	0.00	0.00	0.00	0.00	0.00	0.00
2245396	2015KB144A	32.44	21.82	5.60	3.82	1.70	0.63	8.18	5.88	5.16	4.22	3.74	3.03	1.93	0.74	0.50	0.24	0.35	0.01	0.00	0.00	0.00	0.00	0.00	0.00
2245397	2015KB145	39.09	31.70	10.64	9.40	4.28	0.71	2.64	0.81	0.35	0.13	0.07	0.04	0.01	0.01	0.02	0.01	0.09	0.00	0.00	0.00	0.00	0.00	0.00	0.00
2245398	2015KB146	54.44	22.27	4.18	2.38	0.78	0.26	7.68	3.66	1.71	0.95	0.54	0.41	0.21	0.06	0.08	0.09	0.28	0.02	0.00	0.00	0.01	0.01	0.00	0.01
2245399	2015KB147	57.18	27.10	4.21	1.22	0.25	0.07	6.05	2.41	0.90	0.29	0.15	0.08	0.02	0.00	0.01	0.00	0.04	0.00	0.00	0.00	0.00	0.00	0.00	0.00
2245401	2015KB148	48.44	24.91	7.78	5.44	2.06	0.37	5.59	2.65	1.41	0.56	0.27	0.16	0.08	0.01	0.04	0.03	0.17	0.00	0.00	0.00	0.00	0.00	0.00	0.00
2245402	2015KB149C	36.37	28.21	9.94	12.61	8.18	2.06	1.71	0.57	0.24	0.04	0.04	0.01	0.00	0.00	0.00	0.00	0.01	0.00	0.00	0.00	0.00	0.00	0.00	0.00
2245403	2015KB149B	39.65	27.06	9.26	10.47	5.91	1.21	3.65	1.50	0.69	0.28	0.11	0.07	0.03	0.01	0.02	0.01	0.07	0.00	0.00	0.00	0.00	0.00	0.00	0.00
2245404	2015KB150	46.91	27.67	8.35	5.53	2.20	0.50	5.23	2.03	0.92	0.32	0.13	0.08	0.01	0.01	0.02	0.01	0.08	0.00	0.00	0.00	0.00	0.00	0.00	0.00
2245405	2015KB151A	46.98	14.52	2.48	1.00	0.26	0.07	13.80	9.08	5.21	2.65	1.40	0.85	0.38	0.14	0.19	0.17	0.81	0.00	0.00	0.00	0.00	0.00	0.00	0.00
2245406	2015KB152A	39.14	24.46	9.27	14.39	5.38	0.94	3.06	1.57	0.84	0.42	0.20	0.15	0.04	0.01	0.02	0.03	0.11	0.00	0.00	0.00	0.00	0.00	0.00	0.00
2245407	2015KB153	62.34	13.86	2.43	0.98	0.21	0.02	8.31	4.98	2.86	1.59	0.82	0.61	0.19	0.06	0.09	0.07	0.58	0.00	0.00	0.00	0.00	0.00	0.00	0.00
2245408	2015KB154	37.63	19.15	4.47	2.53	1.15	0.53	11.35	7.18	4.71	2.97	1.98	1.56	0.81	0.45	0.66	0.58	2.17	0.05	0.03	0.01	0.00	0.01	0.01	0.04
2245409	2015KB155A	16.07	11.07	6.88	9.05	8.76	13.34	18.19	9.27	4.15	1.72	0.73	0.31	0.14	0.06	0.05	0.04	0.15	0.01	0.00	0.00	0.00	0.00	0.00	0.00
2245411	2015KB155B	27.56	19.35	8.58	8.43	5.69	3.31	10.04	5.41	3.15	1.59	1.17	1.45	0.38	0.40	0.63	0.31	1.55	0.27	0.10	0.06	0.12	0.14	0.10	0.22
2245412	2015KB156	28.18	15.86	7.68	9.97	8.03	4.97	9.41	5.84	3.56	1.96	1.21	1.26	0.37	0.29	0.31	0.18	0.79	0.06	0.01	0.01	0.01	0.01	0.00	0.02
2245413	2015KB157	30.62	14.80	6.64	8.92	8.20	5.67	8.85	5.21	3.08	1.74	1.13	2.27	0.40	0.38	0.32	0.23	1.22	0.12	0.04	0.02	0.03	0.04	0.01	0.08
2245414	2015KB159	58.52	15.35	3.24	2.05	0.73	0.11	10.11	5.08	2.60	1.07	0.45	0.27	0.08	0.02	0.04	0.04	0.24	0.00	0.00	0.00	0.00	0.00	0.00	0.00
2245415	2015KB160B	42.11	20.81	6.63	4.55	1.77	0.56	10.47	5.65	3.04	1.49	0.95	0.69	0.35	0.13	0.15	0.14	0.51	0.00	0.00	0.00	0.00	0.00	0.00	0.00
2245416	2015KB161B	39.43	22.31	8.82	8.26	5.66	2.23	6.53	3.13	1.50	0.75	0.35	0.26	0.12	0.04	0.06	0.07	0.49	0.00	0.00	0.00	0.00	0.00	0.00	0.00
2245417	2015KB162	38.41	30.03	9.54	6.23	2.38	0.98	6.97	3.00	1.35	0.55	0.26	0.14	0.05	0.01	0.03	0.01	0.07	0.00	0.00	0.00	0.00	0.00	0.00	0.00
2245418	2015KB163A	45.35	23.83	6.32	5.38	2.51	0.99	3.96	2.24	1.54	1.28	1.17	1.10	1.11	0.97	1.02	0.69	0.26	0.07	0.03	0.02	0.04	0.05	0.02	0.06
2245419	2015KB163B	36.02	27.06	9.69	11.63	9.19	2.29	2.79	0.87	0.30	0.09	0.02	0.02	0.00	0.00	0.00	0.00	0.02	0.00	0.00	0.00	0.00	0.00	0.00	0.00
2245421	2015KB164	59.11	12.79	2.50	1.33	0.39	0.11	8.92	5.89	3.67	1.83	1.07	0.90	0.31	0.06	0.10	0.15	0.87	0.00	0.00	0.00	0.00	0.00	0.00	0.00
2245422	2015KB165	42.42	15.16	4.13	2.77	1.11	0.47	12.62	8.28	5.20	3.00	1.80	1.31	0.62	0.13	0.18	0.15	0.66	0.00	0.00	0.00	0.00	0.00	0.00	0.00
2245423	2015KB166A	42.43	16.69	7.39	7.97	4.69	2.39	6.26	3.38	2.16	1.06	0.70	1.11	0.28	0.25	0.30	0.13	2.03	0.31	0.09	0.03	0.09	0.10	0.03	0.12
2245424	2015KB167	35.45	16.89	7.95	8.68	6.27	4.10	9.43	4.96	2.44	1.31	0.71	0.62	0.22	0.09	0.15	0.10	0.62	0.01	0.00	0.00	0.00	0.00	0.00	0.00
2245425	2015KB168	43.59	20.63	8.03	6.97	3.41	1.56	7.42	3.67	1.70	0.79	0.37	0.58	0.15	0.08	0.05	0.06	0.78	0.07	0.02	0.01	0.01	0.02	0.01	0.03
2245426	2015KB169A	56.26	16.74	5.94	4.71	2.30	0.88	6.06	2.89	1.48	0.64	0.35	0.49	0.09	0.08	0.15	0.07	0.71	0.06	0.01	0.01	0.03	0.01	0.02	0.02
2245427	2015KB169B	7.12	8.34	6.54	15.45	24.05	22.52	6.64	3.15	1.86	1.17	0.99	0.92	0.68	0.24	0.12	0.06	0.13	0.00	0.00	0.00	0.00	0.00	0.00	0.00
2245428	2015KB170	33.39	21.53	10.29	13.19	9.63	4.39	3.64	1.39	0.57	0.21	0.16	0.71	0.07	0.12	0.08	0.04	0.41	0.07	0.02	0.01	0.02	0.01	0.01	0.04
2245429	2015KB171	43.86	22.65	8.63	7.01	3.02	0.50	7.74	3.54	1.64	0.68	0.28	0.20	0.06	0.01	0.02	0.02	0.13	0.00	0.00	0.00	0.00	0.00	0.00	0.00
2245431	2015KB172	16.95	18.02	11.21	20.37	18.53	7.69	4.19	1.64	0.66	0.25	0.14	0.17	0.03	0.02	0.01	0.01	0.09	0.00	0.00	0.00	0.00	0.00	0.00	0.00

Sample ID	Station ID	Percentage (%) of pixels from sample slabs that contain an Al-OH absorption feature of specified wavelength (nm)																							
		2190 – 2191	2191 – 2192	2192 – 2193	2193 – 2194	2194 – 2195	2195 – 2197	2197 – 2198	2198 – 2199	2199 – 2200	2200 – 2201	2201 – 2202	2202 – 2203	2203 – 2204	2204 – 2205	2205 – 2206	2206 – 2207	2207 – 2208	2208 – 2209	2209 – 2210	2210 – 2211	2211 – 2212	2212 – 2213	2213 – 2214	2214 – 2220
2245432	2015KB173	14.40	16.59	10.32	19.80	18.19	9.36	4.54	1.98	0.92	0.49	0.32	1.43	0.19	0.34	0.32	0.12	0.47	0.08	0.02	0.02	0.02	0.04	0.01	0.04
2245433	2015KB174	21.14	26.07	12.91	21.99	11.04	2.63	1.22	0.49	0.22	0.09	0.07	0.56	0.08	0.15	0.26	0.15	0.55	0.09	0.04	0.01	0.04	0.06	0.05	0.08
2245434	2015KB175	40.58	22.62	9.37	11.50	7.78	2.07	3.16	1.25	0.63	0.25	0.13	0.19	0.04	0.03	0.03	0.02	0.29	0.03	0.01	0.00	0.00	0.00	0.00	0.01
2245435	2015KB176	65.43	4.61	0.63	0.40	0.15	0.10	9.63	6.63	4.70	2.25	1.59	1.24	0.45	0.18	0.32	0.37	1.32	0.00	0.00	0.00	0.00	0.00	0.00	0.00
2245436	2015KB177	43.28	18.66	7.17	7.39	5.42	2.90	8.19	3.69	1.79	0.63	0.30	0.16	0.08	0.00	0.03	0.06	0.22	0.00	0.00	0.00	0.00	0.01	0.00	0.01
2245437	2015KB178	19.31	24.17	14.07	29.72	10.50	1.19	0.65	0.21	0.09	0.03	0.00	0.04	0.00	0.00	0.01	0.00	0.01	0.00	0.00	0.00	0.00	0.00	0.00	0.00
2245438	2015KB179	35.98	22.94	6.42	5.03	3.06	2.33	11.29	5.55	2.75	1.34	0.67	0.45	0.14	0.11	0.29	0.14	1.29	0.07	0.02	0.02	0.01	0.02	0.02	0.05
2245439	2015KB180	16.22	20.58	13.86	25.56	18.20	3.84	1.09	0.35	0.15	0.05	0.03	0.01	0.01	0.00	0.01	0.00	0.02	0.00	0.00	0.00	0.00	0.00	0.00	0.01
2245441	2015KB181	38.90	21.26	4.01	2.84	1.56	0.76	5.40	2.58	2.08	1.02	1.04	1.03	0.44	0.65	1.35	0.88	9.06	1.73	0.53	0.22	0.58	0.53	0.33	1.20
2245442	2015KB182	4.44	12.13	13.13	21.52	25.12	13.20	6.46	2.37	0.98	0.39	0.15	0.08	0.03	0.00	0.00	0.00	0.00	0.00	0.00	0.00	0.00	0.00	0.00	0.00
2245443	2015KB183	41.30	22.90	8.25	11.42	8.23	1.81	3.73	1.36	0.52	0.18	0.07	0.09	0.03	0.02	0.02	0.01	0.05	0.01	0.00	0.00	0.00	0.00	0.00	0.00
2245444	2015KB184	20.24	29.22	12.58	17.09	11.33	2.04	4.03	1.62	0.79	0.43	0.26	0.20	0.10	0.03	0.01	0.01	0.02	0.00	0.00	0.00	0.00	0.00	0.00	0.00
2245445	2015KB185A	0.13	0.00	0.00	0.00	0.00	0.00	0.04	0.02	0.04	0.04	0.14	0.21	0.27	0.64	2.42	7.64	15.86	6.85	3.08	1.81	4.46	13.31	4.07	38.96
2245446	2015KB185B	1.87	0.49	0.07	0.03	0.00	0.00	3.10	7.00	13.30	19.49	20.51	14.68	7.84	2.77	1.43	1.01	3.72	1.29	0.36	0.15	0.27	0.26	0.10	0.27
2245447	2015KB186	29.30	22.70	10.95	9.40	4.88	1.87	8.97	4.60	2.51	1.39	0.82	1.00	0.33	0.17	0.18	0.13	0.68	0.06	0.01	0.01	0.02	0.00	0.01	0.02
2245448	2015KB188	14.48	16.50	10.85	32.98	15.25	4.37	1.67	0.76	0.45	0.25	0.22	0.40	0.10	0.09	0.18	0.07	0.76	0.17	0.06	0.04	0.09	0.07	0.07	0.14
2245449	2015KB189	13.01	21.35	13.57	18.43	16.05	8.83	4.88	1.89	0.76	0.36	0.19	0.23	0.06	0.07	0.07	0.03	0.15	0.01	0.01	0.01	0.02	0.02	0.01	0.02
2245451	2015KB190	26.83	26.90	10.40	15.70	13.73	3.84	1.58	0.57	0.31	0.07	0.03	0.01	0.01	0.00	0.00	0.00	0.01	0.00	0.00	0.00	0.00	0.00	0.00	0.00
2245452	2015KB191A	9.46	14.06	9.35	24.97	22.78	11.06	4.29	1.85	1.03	0.54	0.32	0.13	0.06	0.04	0.02	0.01	0.04	0.00	0.00	0.00	0.00	0.00	0.00	0.00
2245453	2015KB192	10.62	17.70	12.91	22.32	18.86	6.61	3.99	2.26	1.33	1.01	0.69	0.54	0.40	0.26	0.16	0.15	0.18	0.01	0.00	0.00	0.00	0.01	0.00	0.00
2245454	2015KB193	23.81	27.41	10.96	20.11	12.13	2.74	1.71	0.58	0.25	0.12	0.06	0.05	0.02	0.00	0.01	0.01	0.03	0.00	0.00	0.00	0.00	0.00	0.00	0.00
2245455	2015KB195	0.08	0.02	0.04	0.02	0.03	0.02	0.22	0.51	1.27	2.70	5.46	11.12	19.14	23.65	19.49	10.44	0.90	0.50	0.27	0.12	0.28	0.71	0.16	2.84
2245456	2015KB196	10.24	16.22	10.33	16.73	14.87	7.23	5.67	3.72	3.01	2.62	2.16	1.92	1.56	1.19	0.92	0.67	0.80	0.08	0.04	0.00	0.01	0.01	0.00	0.01
2245457	2015KB197	11.45	18.21	12.03	18.86	15.95	8.77	6.09	3.18	1.78	1.12	0.66	0.45	0.33	0.23	0.20	0.17	0.45	0.03	0.01	0.01	0.01	0.01	0.00	0.01
2245458	2015KB198A	3.43	5.82	4.46	7.08	6.88	9.57	13.46	10.64	8.38	6.31	5.36	4.90	4.12	2.95	2.14	1.30	1.50	0.45	0.25	0.11	0.21	0.27	0.14	0.28
2245459	2015KB199	7.69	4.35	1.35	1.19	0.63	0.80	13.05	16.49	17.56	15.19	10.81	6.29	2.86	0.90	0.38	0.17	0.28	0.00	0.00	0.00	0.00	0.00	0.00	0.00
2245461	2015KB200	0.01	0.00	0.00	0.00	0.00	0.00	0.00	0.00	0.04	0.17	0.78	3.83	15.88	44.62	30.25	4.04	0.31	0.02	0.00	0.00	0.01	0.01	0.00	0.04
2245462	2015KB201	22.71	14.44	3.48	2.79	2.22	2.70	17.39	12.89	8.29	4.83	2.77	1.68	0.90	0.48	0.37	0.39	1.01	0.17	0.08	0.02	0.05	0.10	0.06	0.20
2245463	2015KB202	17.92	22.99	11.53	15.13	12.58	7.11	4.59	2.06	1.25	0.44	0.47	0.75	0.13	0.21	0.46	0.21	0.88	0.27	0.14	0.09	0.17	0.19	0.11	0.29
2245464	2015KB204	14.53	15.44	9.03	30.21	23.14	5.85	1.03	0.36	0.10	0.05	0.03	0.15	0.02	0.01	0.01	0.01	0.05	0.00	0.00	0.00	0.00	0.00	0.00	0.00
2245465	2015KB205	10.70	17.80	11.16	16.61	19.21	15.81	5.74	1.79	0.65	0.26	0.12	0.06	0.02	0.01	0.01	0.00	0.05	0.00	0.00	0.00	0.00	0.00	0.00	0.00
2245466	2015KB206	20.52	22.77	11.68	11.68	7.62	3.67	7.00	3.73	2.10	1.26	0.99	1.30	0.67	0.63	0.88	0.45	1.76	0.40	0.12	0.09	0.15	0.17	0.09	0.27
2245467	2015KB207	23.46	24.95	10.82	20.01	13.69	4.50	1.57	0.58	0.24	0.07	0.04	0.03	0.01	0.00	0.01	0.00	0.02	0.00	0.00	0.00	0.00	0.00	0.00	0.00
2245468	2015KB208	1.99	1.74	1.32	1.93	2.11	8.68	17.45	17.86	15.59	12.84	8.75	5.61	2.88	0.85	0.25	0.07	0.06	0.00	0.00	0.00	0.00	0.00	0.00	0.00
2245469	2015KB209	16.79	23.32	12.51	22.00	17.02	5.67	1.77	0.56	0.20	0.06	0.04	0.01	0.00	0.00	0.01	0.01	0.02	0.00	0.00	0.00	0.00	0.00	0.00	0.00
2245471	2015KB210	9.40	19.92	12.76	20.19	21.19	9.00	4.42	1.65	0.75	0.36	0.14	0.12	0.03	0.01	0.00	0.01	0.03	0.00	0.00	0.00	0.00	0.00	0.00	0.00
2245472	2015KB212	1.60	1.72	1.28	2.24	1.93	4.29	15.04	19.26	19.65	15.95	10.06	4.35	1.54	0.70	0.24	0.07	0.07	0.00	0.00	0.00	0.00	0.00	0.00	0.00
2245473	2015KB213	11.44	15.11	8.63	13.18	17.00	16.15	10.01	4.32	1.86	0.95	0.45	0.30	0.18	0.08	0.11	0.07	0.17	0.00	0.00	0.00	0.00	0.00	0.00	0.00
2245474	2015KB214	6.19	3.75	2.33	3.31	7.14	35.95	20.68	11.63	5.25	2.17	0.92	0.38	0.17	0.05	0.01	0.02	0.04	0.00	0.00	0.00	0.00	0.00	0.00	0.00
2245475	2015KB215	19.14	16.79	6.80	6.76	5.07	3.50	13.27	9.31	6.10	4.07	2.68	2.15	1.59	1.09	0.78	0.43	0.39	0.02	0.02	0.01	0.01	0.02	0.00	0.01
2245476	2015KB216	10.10	12.17	8.25	22.05	22.06	13.41	5.91	2.66	1.34	0.71	0.44	0.30	0.18	0.07	0.08	0.07	0.14	0.02	0.00	0.00	0.00	0.01	0.01	0.03
2245477	2015KB217	32.62	19.07	9.22	14.30	11.66	4.53	3.24	1.43	0.78	0.47	0.35	0.26	0.12	0.13	0.17	0.13	1.00	0.08	0.05	0.01	0.05	0.08	0.03	0.21
2245478	2015KB218	22.88	5.82	3.06	3.81	4.74	26.39	17.15	7.57	3.93	2.20	1.13	0.55	0.26	0.12	0.10	0.08	0.22	0.00	0.00	0.00	0.00	0.00	0.00	0.00

Sample ID	Station ID	Percentage (%) of pixels from sample slabs that contain an Al-OH absorption feature of specified wavelength (nm)																							
		2190 – 2191	2191 – 2192	2192 – 2193	2193 – 2194	2194 – 2195	2195 – 2197	2197 – 2198	2198 – 2199	2199 – 2200	2200 – 2201	2201 – 2202	2202 – 2203	2203 – 2204	2204 – 2205	2205 – 2206	2206 – 2207	2207 – 2208	2208 – 2209	2209 – 2210	2210 – 2211	2211 – 2212	2212 – 2213	2213 – 2214	2214 – 2220
2245479	2015KB219	45.21	29.20	4.44	2.23	0.84	0.53	9.99	4.41	1.81	0.67	0.31	0.16	0.05	0.03	0.03	0.01	0.07	0.00	0.00	0.00	0.00	0.00	0.00	0.00
2245481	2015KB221	35.18	29.75	8.54	11.33	6.69	1.79	3.32	1.51	0.79	0.36	0.24	0.24	0.07	0.05	0.06	0.01	0.08	0.00	0.00	0.00	0.00	0.00	0.00	0.00
2245482	2015KB222	20.11	16.46	8.62	14.25	17.06	10.86	5.48	2.65	1.54	0.97	0.57	0.61	0.32	0.10	0.14	0.05	0.16	0.01	0.00	0.00	0.00	0.01	0.02	0.01
2245483	2015KB224	9.55	14.20	9.11	12.14	12.23	13.10	15.32	7.19	3.34	1.54	0.82	0.70	0.44	0.13	0.06	0.05	0.09	0.00	0.00	0.00	0.00	0.00	0.00	0.00
2245484	2015KB225	20.55	19.16	12.02	18.61	15.95	5.55	4.28	1.74	0.78	0.37	0.24	0.25	0.08	0.06	0.05	0.05	0.26	0.00	0.00	0.00	0.00	0.00	0.00	0.00
2245485	2015KB226	32.09	31.21	11.18	5.05	1.14	0.35	8.85	4.07	2.20	1.11	0.85	0.63	0.27	0.17	0.29	0.09	0.28	0.05	0.02	0.00	0.03	0.03	0.01	0.03
2245486	2015KB227	0.02	0.00	0.00	0.00	0.00	0.00	0.01	0.02	0.09	0.13	0.22	0.51	1.10	3.81	46.82	41.92	1.09	0.17	0.05	0.03	0.05	0.36	0.08	3.52
2245487	2015KB228	38.78	35.74	8.98	5.86	2.38	0.49	4.92	1.72	0.65	0.25	0.11	0.06	0.04	0.00	0.00	0.00	0.03	0.00	0.00	0.00	0.00	0.00	0.00	0.00
2245488	2015KB229A	13.63	22.53	13.73	22.79	19.38	5.86	1.27	0.44	0.15	0.08	0.04	0.02	0.01	0.00	0.01	0.01	0.04	0.00	0.00	0.00	0.00	0.00	0.00	0.00
2245489	2015KB229B	21.63	23.89	11.07	23.36	13.61	4.08	1.36	0.55	0.28	0.10	0.04	0.02	0.00	0.00	0.00	0.00	0.00	0.00	0.00	0.00	0.00	0.00	0.00	0.00
2245491	2015KB230B	14.33	12.19	4.50	5.15	4.43	2.49	10.05	9.05	8.54	7.68	6.49	5.71	4.30	2.45	1.32	0.69	0.63	0.01	0.00	0.00	0.00	0.00	0.00	0.00
2245492	2015KB231	13.88	20.74	10.39	13.38	15.19	11.86	8.46	3.39	1.42	0.58	0.29	0.16	0.08	0.03	0.03	0.02	0.07	0.01	0.00	0.00	0.00	0.00	0.00	0.01
2245493	2015KB233A	4.33	1.32	0.73	1.16	1.67	6.32	8.73	8.07	9.02	8.45	8.05	8.20	7.67	6.14	6.72	5.93	5.32	0.24	0.11	0.04	0.12	0.58	0.06	1.03
2245494	2015KB233B	22.62	14.12	1.57	0.64	0.17	0.00	16.87	12.36	8.01	5.66	4.12	3.00	2.66	2.35	2.01	1.78	0.80	0.21	0.11	0.02	0.10	0.22	0.10	0.51
2245495	2015KB234	3.90	5.78	3.57	4.67	4.98	10.32	16.15	14.55	11.06	7.93	5.51	3.89	2.81	1.87	1.48	0.89	0.37	0.03	0.01	0.00	0.01	0.06	0.01	0.15
2245496	2015KB235	19.61	25.00	14.27	19.34	13.93	4.41	2.18	0.72	0.31	0.11	0.05	0.04	0.01	0.01	0.01	0.01	0.01	0.00	0.00	0.00	0.00	0.00	0.00	0.00
2245497	2015KB236A	1.03	2.71	3.00	3.78	1.73	0.61	8.81	13.32	16.51	15.84	13.30	9.12	5.45	2.57	1.00	0.51	0.62	0.02	0.01	0.01	0.01	0.01	0.00	0.02
2245498	2015KB236B	1.75	2.46	1.92	3.16	3.09	10.57	19.37	17.43	13.45	9.48	6.91	4.67	3.09	1.84	0.58	0.14	0.10	0.00	0.00	0.00	0.00	0.00	0.00	0.00
2245499	2015KB237	8.77	7.85	4.90	9.02	10.79	18.42	14.83	9.49	5.56	3.41	2.43	1.56	0.76	0.38	0.39	0.21	0.54	0.12	0.04	0.01	0.04	0.13	0.04	0.29
2247910	2015GL020	27.38	16.94	2.60	1.65	1.03	1.63	7.32	6.42	5.51	4.76	4.36	3.82	3.31	2.66	2.43	1.86	1.29	0.33	0.20	0.10	0.32	0.79	0.28	3.00
2247911	2015GL021	3.99	8.38	8.29	11.22	9.87	11.93	16.40	9.54	5.85	4.05	2.80	1.93	1.37	0.87	0.69	0.55	0.43	0.09	0.04	0.02	0.06	0.25	0.06	1.32
2247912	2015GL022	0.32	0.06	0.03	0.04	0.05	1.93	5.63	12.31	21.60	27.96	19.23	7.53	2.46	0.57	0.16	0.07	0.04	0.01	0.00	0.00	0.00	0.00	0.00	0.01
2247913	2015GL023	31.70	28.08	9.30	12.93	6.55	2.34	4.02	1.98	1.05	0.56	0.34	0.23	0.13	0.09	0.11	0.08	0.25	0.06	0.04	0.02	0.03	0.05	0.02	0.06
2247914	2015GL024	43.83	7.77	2.33	3.01	2.59	4.12	10.71	8.28	6.14	4.22	3.04	1.96	0.90	0.41	0.19	0.15	0.27	0.02	0.00	0.01	0.01	0.01	0.01	0.02
2247915	2015GL024	50.20	16.55	2.00	0.81	0.19	0.03	12.61	8.06	4.68	2.39	1.19	0.72	0.23	0.08	0.05	0.05	0.16	0.00	0.00	0.00	0.00	0.00	0.00	0.00
2247916	2015GL025	31.95	34.95	10.03	11.92	5.17	1.35	2.95	1.00	0.41	0.15	0.05	0.03	0.01	0.00	0.00	0.00	0.03	0.00	0.00	0.00	0.00	0.00	0.00	0.00
2247917	2015GL026	17.73	18.82	7.82	12.41	10.23	10.70	8.21	4.91	3.18	2.04	1.38	0.97	0.62	0.37	0.27	0.16	0.13	0.01	0.01	0.00	0.00	0.01	0.00	0.02
2247920	2015GL026	30.95	27.57	9.74	14.21	4.84	0.96	5.06	2.86	1.64	0.90	0.42	0.29	0.13	0.08	0.10	0.07	0.17	0.00	0.00	0.00	0.00	0.00	0.00	0.00
2247921	2015GL027	26.35	22.12	7.35	9.71	6.41	3.03	10.50	6.12	3.65	2.02	1.11	0.69	0.33	0.14	0.11	0.07	0.20	0.02	0.01	0.01	0.01	0.02	0.01	0.02
2247922	2015GL028	0.63	0.10	0.05	0.08	0.06	0.59	2.83	5.94	10.34	16.08	27.77	28.50	6.24	0.59	0.10	0.03	0.04	0.00	0.00	0.00	0.00	0.00	0.00	0.00
2247923	2015GL029	2.99	4.96	5.81	14.84	22.57	25.66	11.75	6.00	2.74	1.33	0.61	0.37	0.20	0.06	0.06	0.02	0.02	0.00	0.00	0.00	0.00	0.00	0.00	0.00
2247924	2015GL030	12.14	19.96	7.83	6.68	4.87	3.26	17.07	12.08	8.06	4.52	2.09	0.90	0.31	0.10	0.07	0.01	0.04	0.00	0.00	0.00	0.00	0.00	0.00	0.00
2247927	2015GL033	5.47	8.37	5.83	10.57	10.94	10.61	10.71	7.63	5.31	3.87	2.93	2.40	1.86	1.56	1.58	1.40	2.60	0.95	0.46	0.20	0.55	1.01	0.45	2.73
2247928	2015GL034	61.42	13.12	1.93	1.48	0.63	0.10	9.16	5.60	3.20	1.49	0.79	0.49	0.17	0.04	0.05	0.06	0.28	0.00	0.00	0.00	0.00	0.00	0.00	0.00
2247929	2015GL035	36.70	28.17	9.48	12.96	5.40	1.78	1.61	0.67	0.40	0.16	0.12	0.58	0.13	0.22	0.37	0.13	0.60	0.13	0.06	0.03	0.05	0.07	0.05	0.13
2247931	2015GL036	9.77	13.11	9.24	22.83	24.10	14.87	3.42	1.27	0.50	0.35	0.23	0.19	0.08	0.03	0.00	0.00	0.01	0.00	0.00	0.00	0.00	0.00	0.00	0.00
2247932	2015GL037	17.62	20.72	10.55	28.83	8.87	4.43	2.16	1.24	0.90	0.60	0.53	0.58	0.42	0.37	0.37	0.24	0.68	0.11	0.05	0.02	0.06	0.16	0.06	0.44
2247933	2015GL038	3.32	3.71	2.57	4.74	9.45	34.74	19.82	11.73	5.66	2.32	0.96	0.49	0.22	0.11	0.06	0.04	0.06	0.00	0.00	0.00	0.00	0.00	0.00	0.00
2247934	2015GL038	19.24	24.64	10.38	21.23	12.86	4.50	3.23	1.47	0.68	0.42	0.24	0.16	0.09	0.09	0.10	0.08	0.12	0.06	0.04	0.02	0.05	0.08	0.04	0.17
2247935	2015GL039	6.10	6.59	4.44	21.78	16.92	13.78	6.56	4.59	3.38	2.59	2.14	1.88	1.19	0.94	1.05	0.89	1.52	0.32	0.17	0.08	0.22	0.38	0.20	2.31
2247936	2015GL040	7.65	12.84	7.92	17.68	10.61	7.23	6.20	5.82	5.67	5.48	4.56	3.65	2.13	1.05	0.57	0.29	0.33	0.06	0.03	0.01	0.03	0.06	0.03	0.09
2247937	2015GL041	26.41	24.03	9.43	14.99	6.51	3.51	5.40	3.10	1.88	1.18	0.80	0.61	0.47	0.41	0.37	0.29	0.17	0.02	0.01	0.00	0.01	0.14	0.01	0.25
2247938	2015GL042	11.63	23.41	16.11	24.29	15.63	5.19	2.23	0.72	0.34	0.15	0.08	0.10	0.04	0.03	0.01	0.00	0.02	0.00	0.00	0.00	0.00	0.00	0.00	0.00

Sample ID	Station ID	Percentage (%) of pixels from sample slabs that contain an Al-OH absorption feature of specified wavelength (nm)																							
		2190 – 2191	2191 – 2192	2192 – 2193	2193 – 2194	2194 – 2195	2195 – 2197	2197 – 2198	2198 – 2199	2199 – 2200	2200 – 2201	2201 – 2202	2202 – 2203	2203 – 2204	2204 – 2205	2205 – 2206	2206 – 2207	2207 – 2208	2208 – 2209	2209 – 2210	2210 – 2211	2211 – 2212	2212 – 2213	2213 – 2214	2214 – 2220
2247939	2015GL043	11.97	20.98	10.26	14.35	10.73	6.91	8.70	4.99	3.08	1.93	1.47	1.21	0.97	0.76	0.61	0.44	0.37	0.05	0.01	0.01	0.01	0.06	0.02	0.14
2247940	2015GL044	14.42	23.27	12.58	21.68	11.38	5.64	3.84	2.05	1.16	0.86	0.68	0.55	0.41	0.33	0.31	0.27	0.18	0.02	0.01	0.01	0.01	0.12	0.01	0.21
2247943	2015GL045	13.58	23.27	12.54	25.32	10.29	3.08	5.16	2.95	1.60	0.88	0.48	0.35	0.17	0.09	0.09	0.03	0.13	0.00	0.00	0.00	0.00	0.00	0.00	0.00
2247944	2015GL046	27.49	32.24	10.59	11.41	4.99	1.64	6.36	2.94	1.30	0.52	0.24	0.12	0.06	0.02	0.01	0.01	0.04	0.00	0.00	0.00	0.00	0.00	0.00	0.00
2247945	2015GL047	17.85	24.04	12.82	31.36	7.61	1.22	1.27	0.76	0.47	0.40	0.33	0.32	0.26	0.25	0.24	0.21	0.23	0.06	0.03	0.01	0.03	0.09	0.02	0.14
2247946	2015GL048	1.13	0.48	0.29	0.33	0.31	1.20	5.70	10.85	17.50	24.31	22.30	10.42	3.28	1.01	0.50	0.19	0.16	0.01	0.00	0.00	0.00	0.01	0.00	0.02
2247947	2015GL049	19.90	24.15	12.37	30.04	7.67	2.08	1.27	0.64	0.36	0.17	0.16	0.21	0.06	0.08	0.11	0.07	0.20	0.09	0.03	0.02	0.04	0.07	0.05	0.17
2247948	2015GL050	33.99	29.64	10.10	15.51	5.11	1.16	2.44	1.05	0.48	0.19	0.14	0.09	0.02	0.00	0.01	0.02	0.06	0.00	0.00	0.00	0.00	0.00	0.00	0.00
2247949	2015GL050	42.00	32.39	7.38	6.02	2.19	0.68	5.02	2.23	1.04	0.41	0.19	0.15	0.09	0.05	0.05	0.03	0.09	0.00	0.00	0.00	0.00	0.00	0.00	0.00
2247950	2015GL051	2.70	2.81	2.28	5.96	8.28	19.03	13.74	11.77	9.84	7.80	6.09	4.08	2.52	1.48	0.79	0.40	0.36	0.02	0.00	0.00	0.01	0.01	0.01	0.02
2758851	2015GL051	2.25	2.33	2.02	3.52	6.48	17.41	12.08	9.27	6.96	5.16	4.40	3.85	3.38	2.85	3.06	2.92	3.77	0.72	0.33	0.19	0.57	1.32	0.48	4.67
2758852	2015GL052	6.33	7.95	5.82	32.49	24.75	14.57	2.98	1.44	0.74	0.42	0.34	0.59	0.15	0.13	0.17	0.16	0.40	0.11	0.03	0.03	0.06	0.09	0.04	0.24
2758854	2015GL053	50.93	25.39	4.47	3.20	0.84	0.11	6.97	3.87	2.01	0.95	0.47	0.26	0.17	0.13	0.10	0.03	0.09	0.00	0.00	0.00	0.00	0.00	0.00	0.00
2758855	2015GL054	19.32	20.84	11.82	24.00	7.98	6.73	3.21	1.81	1.18	0.76	0.49	0.39	0.24	0.24	0.20	0.18	0.22	0.05	0.03	0.01	0.01	0.09	0.02	0.18
2758856	2015GL055	28.12	18.60	4.53	7.65	4.85	1.74	12.69	9.28	6.09	3.30	1.67	0.79	0.32	0.10	0.07	0.05	0.13	0.00	0.00	0.00	0.00	0.00	0.00	0.00
2758857	2015GL056	17.09	22.46	12.09	36.94	9.39	1.17	0.51	0.18	0.07	0.03	0.02	0.02	0.00	0.00	0.00	0.00	0.02	0.00	0.00	0.00	0.00	0.00	0.00	0.00
2758858	2015GL057	31.57	27.79	7.32	7.13	4.25	1.61	10.10	5.32	2.66	1.24	0.54	0.26	0.09	0.03	0.02	0.03	0.04	0.00	0.00	0.00	0.00	0.00	0.00	0.00
2758859	2015GL058	27.58	24.74	10.74	26.73	5.37	1.03	1.83	0.87	0.50	0.20	0.13	0.08	0.03	0.03	0.03	0.02	0.05	0.01	0.00	0.00	0.00	0.00	0.00	0.01
2758860	2015GL059	2.68	3.04	2.33	8.26	9.86	23.96	17.35	14.69	9.96	4.82	2.03	0.66	0.21	0.05	0.03	0.02	0.05	0.00	0.00	0.00	0.00	0.00	0.00	0.00
2758861	2015GL060	28.28	37.59	12.61	11.23	3.35	0.58	3.67	1.53	0.66	0.27	0.11	0.05	0.02	0.01	0.00	0.00	0.03	0.00	0.00	0.00	0.00	0.00	0.00	0.00
2758862	2015GL061	27.57	29.74	10.18	13.88	5.96	1.37	5.66	2.76	1.34	0.66	0.36	0.22	0.13	0.04	0.03	0.03	0.07	0.00	0.00	0.00	0.00	0.00	0.00	0.00
2758863	2015GL062	5.14	7.14	5.87	9.85	16.21	28.50	14.61	7.51	3.32	1.25	0.41	0.12	0.03	0.01	0.00	0.01	0.01	0.00	0.00	0.00	0.00	0.00	0.00	0.00
2758866	2015GL063	7.63	13.53	10.26	27.04	22.79	13.16	3.56	1.09	0.42	0.19	0.10	0.08	0.02	0.02	0.02	0.02	0.04	0.01	0.01	0.00	0.00	0.01	0.00	0.00
2758867	2015GL064	1.15	1.58	1.20	2.96	5.49	14.34	11.27	9.51	7.62	6.22	6.32	5.78	4.85	3.51	2.95	2.24	3.60	1.33	0.62	0.31	0.74	1.23	0.65	4.54
2758868	2015GL065	0.76	0.67	0.88	3.89	4.28	21.85	22.21	22.71	14.65	5.98	1.49	0.26	0.13	0.05	0.04	0.05	0.10	0.00	0.00	0.00	0.00	0.00	0.00	0.00
2758869	2015GL065	0.75	2.29	2.35	6.86	6.74	18.07	15.69	16.91	13.79	8.93	4.41	1.81	0.73	0.23	0.12	0.07	0.21	0.02	0.00	0.00	0.00	0.00	0.00	0.01
2758870	2015GL066	4.16	3.93	2.49	4.51	5.52	8.73	13.41	14.86	14.59	12.02	7.82	4.18	1.95	0.76	0.40	0.20	0.29	0.03	0.01	0.00	0.02	0.02	0.01	0.07
2758871	2015GL067	14.96	20.94	11.13	19.82	13.58	6.90	4.19	2.08	1.29	0.54	0.53	0.90	0.21	0.33	0.65	0.39	0.78	0.18	0.08	0.04	0.09	0.10	0.07	0.22
2758872	2015GL068	20.83	18.15	6.85	8.70	5.68	2.11	13.51	9.62	6.44	3.66	2.14	1.18	0.61	0.15	0.12	0.07	0.17	0.00	0.00	0.00	0.00	0.00	0.00	0.00
2758873	2015GL069	0.53	0.20	0.11	0.18	0.36	7.53	9.81	12.08	13.18	13.06	12.64	10.90	8.35	4.92	2.68	1.52	0.53	0.23	0.12	0.06	0.11	0.27	0.07	0.54
2758874	2015GL070	24.85	25.79	10.52	24.47	7.24	2.63	1.75	0.77	0.41	0.19	0.21	0.41	0.06	0.08	0.17	0.15	0.14	0.05	0.01	0.01	0.01	0.02	0.02	0.02
2758875	2015GL071	20.57	28.68	10.79	20.86	5.76	2.69	2.50	1.86	1.24	0.90	0.83	0.61	0.45	0.34	0.33	0.31	0.43	0.12	0.05	0.03	0.08	0.14	0.06	0.38
2758877	2015GL072	15.57	25.51	14.36	33.55	7.83	0.79	1.29	0.56	0.25	0.14	0.08	0.03	0.01	0.00	0.00	0.00	0.02	0.00	0.00	0.00	0.00	0.00	0.00	0.00
2758878	2015GL073	16.09	38.34	19.97	20.34	3.49	0.27	0.53	0.21	0.12	0.05	0.04	0.07	0.03	0.06	0.09	0.02	0.11	0.05	0.02	0.01	0.01	0.02	0.02	0.04
2758879	2015GL073	8.32	11.28	8.05	29.80	21.78	11.89	3.42	1.67	1.06	0.61	0.54	0.38	0.26	0.19	0.22	0.14	0.18	0.04	0.01	0.01	0.01	0.03	0.01	0.07
2758880	2015GL074	9.13	9.43	6.42	42.93	16.18	6.58	2.67	1.37	0.91	0.46	0.39	0.54	0.18	0.15	0.31	0.24	0.76	0.15	0.05	0.04	0.07	0.13	0.06	0.83
2758881	2015GL075	14.49	19.91	11.38	35.05	12.78	3.42	1.15	0.48	0.26	0.12	0.07	0.26	0.06	0.07	0.13	0.08	0.12	0.01	0.01	0.00	0.02	0.02	0.01	0.10
2758882	2015GL076	18.24	24.06	11.90	26.54	11.69	3.58	2.24	0.93	0.40	0.16	0.07	0.07	0.02	0.01	0.02	0.01	0.04	0.00	0.00	0.00	0.00	0.00	0.00	0.01
2758883	2015GL077	6.87	9.44	6.05	23.39	20.34	11.22	4.74	2.79	1.96	1.10	1.18	1.00	0.42	0.37	0.77	0.70	0.80	0.38	0.20	0.12	0.34	0.57	0.33	4.91
2758884	2015GL078	39.89	27.58	8.67	11.71	3.96	0.54	3.35	1.82	0.94	0.48	0.27	0.23	0.08	0.03	0.06	0.07	0.31	0.00	0.00	0.00	0.00	0.00	0.00	0.00
2758885	2015GL079	21.10	21.59	9.56	17.15	12.66	6.13	3.23	1.58	0.93	0.47	0.47	0.37	0.14	0.16	0.31	0.21	0.78	0.27	0.14	0.07	0.17	0.24	0.16	2.10
2758886	2015GL080	2.71	3.01	2.72	6.75	10.82	22.29	15.06	11.74	8.50	5.89	3.90	2.60	1.69	1.00	0.55	0.31	0.34	0.04	0.02	0.00	0.01	0.02	0.00	0.05
2758890	2015GL081	5.50	9.05	6.44	19.62	12.68	9.13	7.85	6.27	4.75	3.81	3.04	2.42	1.87	1.50	1.33	1.22	1.14	0.27	0.15	0.08	0.14	0.43	0.11	1.19

Sample ID	Station ID	Percentage (%) of pixels from sample slabs that contain an Al-OH absorption feature of specified wavelength (nm)																							
		2190–2191	2191–2192	2192–2193	2193–2194	2194–2195	2195–2197	2197–2198	2198–2199	2199–2200	2200–2201	2201–2202	2202–2203	2203–2204	2204–2205	2205–2206	2206–2207	2207–2208	2208–2209	2209–2210	2210–2211	2211–2212	2212–2213	2213–2214	2214–2220
2758891	2015GL082	8.97	11.27	7.15	33.64	22.10	10.28	3.07	1.49	0.74	0.39	0.22	0.17	0.08	0.06	0.07	0.06	0.15	0.01	0.01	0.00	0.00	0.02	0.00	0.04
2758892	2015GL083	7.90	15.66	12.19	28.88	20.27	6.69	3.73	1.71	0.99	0.62	0.50	0.37	0.26	0.09	0.05	0.03	0.04	0.00	0.00	0.00	0.00	0.00	0.00	0.00
2758893	2015GL084	13.96	29.34	17.07	20.03	10.58	3.19	3.54	1.35	0.57	0.18	0.09	0.02	0.02	0.00	0.01	0.02	0.03	0.00	0.00	0.00	0.00	0.00	0.00	0.00
2758894	2015GL085	15.27	17.41	9.52	27.01	16.33	6.74	2.84	1.29	0.80	0.46	0.31	0.34	0.11	0.13	0.28	0.16	0.28	0.10	0.06	0.04	0.06	0.07	0.06	0.32
2758895	2015GL086	16.64	27.74	11.51	14.81	9.48	3.40	7.26	3.67	1.97	1.08	0.64	0.53	0.32	0.26	0.24	0.17	0.18	0.02	0.01	0.00	0.01	0.02	0.00	0.04
2758896	2015GL087	13.15	20.66	10.91	20.73	16.11	8.37	4.02	1.90	0.92	0.43	0.37	0.48	0.16	0.14	0.26	0.22	0.22	0.06	0.03	0.01	0.04	0.08	0.05	0.67
2758897	2015GL088	11.43	18.73	10.11	19.63	12.50	6.54	4.65	2.70	2.07	1.18	1.23	0.99	0.42	0.42	0.71	0.61	1.60	0.51	0.20	0.10	0.27	0.43	0.33	2.63
2758898	2015GL089	27.56	31.29	8.52	6.55	3.25	1.49	8.63	4.98	2.83	1.65	1.05	0.71	0.51	0.30	0.23	0.17	0.14	0.03	0.01	0.01	0.01	0.02	0.01	0.05
2758900	2015GL090	14.94	18.70	11.13	27.01	15.68	5.90	3.06	1.43	0.71	0.37	0.23	0.25	0.09	0.08	0.10	0.06	0.18	0.02	0.01	0.01	0.01	0.01	0.00	0.02

Appendix F. SWIR data: Terraspec® measurements results.

Sample ID	Station ID	Measurement type	TSA mineral 1	TSA weight 1	TSA mineral 2	TSA weight 2	TSA error	H_2O absorption feature	Al-OH absorption feature		
								Hull quotient depth	Wavelength (nm)	Hull quotient depth	Width (nm)
2232401	2015GL091	Alteration	Illite	0.618	Epidote	0.382	34.711	0.337	2199.2	0.23	30.1
2232401	2015GL091	Alteration	Illite	0.579	Epidote	0.421	43.607	0.386	2195.3	0.18	29.2
2232402	2015GL092	Alteration	Illite	0.612	Epidote	0.388	36.564	0.452	2198.3	0.19	32.1
2232403	2015GL093	Background	Illite	1	NULL	0	179.19		2197.9	0.10	30.4
2232403	2015GL093	Background	Illite	1	NULL	0	184.3		2197.3	0.10	30.4
2232404	2015GL094	Alteration	Illite	0.776	Phengite	0.224	15.809	0.46	2203.1	0.52	33.8
2232405	2015GL095	Alteration	Illite	0.618	Kaolinite	0.382	127.38		2206.1	0.14	31.6
2232405	2015GL095	Alteration	Illite	0.658	Kaolinite	0.342	188.62		2205.4	0.13	30.9
2232406	2015GL096	Alteration	Muscovite	0.813	Montmorillonite	0.187	27.846	0.22	2203.2	0.24	30.2
2232407	2015GL096	Alteration	Kaolinite	0.755	Montmorillonite	0.245	21.4		2208.5	0.32	27.3
2232408	2015GL097	Alteration	Illite	0.708	Kaolinite	0.292	38.17	0.274	2207.4	0.39	32.5
2232409	2015GL097	Alteration	Illite	1	NULL	0	27.779		2199.6	0.47	34.7
2232409	2015GL097	Alteration	Illite	1	NULL	0	23.894		2199.0	0.38	34.4
2232409	2015GL097	Alteration	Illite	0.807	Siderite	0.193	24.268		2200.4	0.34	34.1
2232412	2015GL098	Alteration	Kaolinite	0.711	Montmorillonite	0.289	30.742	0.445	2208.0	0.38	29.8
2232413	2015GL099	Alteration	Illite	1	NULL	0	48.866	0.273	2206.6	0.30	30.6
2232414	2015GL100	Alteration	Illite	0.695	Kaolinite	0.305	31.868	0.524	2204.1	0.42	34.9
2232415	2015GL101	Alteration	Kaolinite	0.639	Illite	0.361	50.918		2207.3	0.31	32.9
2232415	2015GL101	Alteration	Illite	0.694	Kaolinite	0.306	29.015		2205.4	0.41	34.4
2232415	2015GL101	Alteration	Kaolinite	0.835	Paragonite	0.165	37.741		2208.0	0.36	31.0
2232416	2015GL102	Alteration	Montmorillonite	0.545	Kaolinite	0.455	84.343		2207.8	0.26	30.4
2232416	2015GL102	Alteration	Montmorillonite	0.535	Kaolinite	0.465	93.061		2207.7	0.26	31.6
2232417	2015GL103	Alteration	Illite	0.586	Kaolinite	0.414	40.609	0.473	2206.8	0.35	34.8
2232418	2015GL104	Alteration	Illite	0.736	Halloysite	0.264	149.6	0.455	2207.4	0.36	27.8
2232419	2015GL105	Alteration	Siderite	0.623	Illite	0.377	114.73	0.319	2196.3	0.07	28.7
2232420	2015GL106	Alteration	Illite	0.578	Kaolinite	0.422	29.302	0.47	2206.8	0.44	34.0
2232421	2015GL107	Alteration	Montmorillonite	0.505	Kaolinite	0.495	181.01		2207.6	0.17	28.1
2232421	2015GL107	Alteration	Montmorillonite	0.55	Kaolinite	0.45	139.01		2207.5	0.15	29.6
2232421	2015GL107	Alteration	Kaolinite	0.572	Montmorillonite	0.428	55.338		2207.7	0.24	29.5
2232423	2015GL108	Alteration	Kaolinite	0.799	Montmorillonite	0.201	34.558		2208.4	0.34	30.0
2232423	2015GL108	Alteration	Kaolinite	0.812	Montmorillonite	0.188	35.898		2208.5	0.36	29.7
2232424	2015GL109	Alteration	Illite	0.719	Phengite	0.281	29.307	0.344	2205.6	0.54	33.7
2232425	2015GL110	Alteration	Illite	0.505	Kaolinite	0.495	113.58	0.384	2207.8	0.26	26.1
2232426	2015GL111	Alteration	Illite	0.617	Siderite	0.383	84.944	0.451	2197.9	0.26	32.0
2232427	2015GL112	Alteration	Illite	0.618	Epidote	0.382	81.061	0.466	2193.6	0.21	31.2
2232428	2015GL113	Alteration	Prehnite	0.589	Muscovite	0.411	300.22	0.332			
2232429	2015GL114	Alteration	Kaolinite	0.555	Illite	0.445	83.026	0.437	2207.2	0.26	31.9
2232430	2015GL115	Alteration	Illite	0.598	Kaolinite	0.402	69.996	0.381	2206.4	0.27	32.0
2232431	2015GL116	Alteration	Illite	0.609	Kaolinite	0.391	54.628	0.299	2208.5	0.32	25.3
2232432	2015GL117	Alteration	Illite	0.658	Phengite	0.342	64.363	0.274	2208.5	0.33	31.1
2232435	2015GL118	Alteration	Illite	0.643	Phengite	0.357	21.279	0.26	2204.7	0.47	33.6
2232436	2015GL119	Alteration	Illite	0.777	Kaolinite	0.223	26.143	0.378	2201.3	0.34	33.7
2232437	2015GL120	Alteration	Muscovite	1	NULL	0	25.379	0.211	2204.7	0.34	32.7
2232438	2015GL121	Alteration	Kaolinite	0.576	Illite	0.424	38.028	0.431	2207.2	0.34	33.2
2232439	2015GL122	Alteration	Illite	0.582	Kaolinite	0.418	87.567	0.305	2207.5	0.31	29.6
2232440	2015GL123	Alteration	Illite	0.602	Siderite	0.398	122.04	0.139	2206.7	0.09	29.4

Sample ID	Station ID	Measurement type	TSA mineral 1	TSA weight 1	TSA mineral 2	TSA weight 2	TSA error	H_2O absorption feature	Al-OH absorption feature		
								Hull quotient depth	Wavelength (nm)	Hull quotient depth	Width (nm)
2232441	2015GL124	Alteration	Illite	0.585	Kaolinite	0.415	49.649	0.453	2207.1	0.37	30.3
2232442	2015GL125	Alteration	Illite	0.681	Kaolinite	0.319	86.157	0.276	2197.6	0.19	33.5
2232443	2015GL126	Alteration	Illite	0.5	Kaolinite	0.5	44.827	0.381	2207.6	0.34	30.2
2232444	2015GL127	Alteration	Illite	0.756	Epidote	0.244	247.18	0.27	2196.8	0.14	27.4
2232446	2015GL128	Alteration	Kaolinite	0.626	Illite	0.374	40.21	0.343	2208.3	0.43	30.4
2232447	2015GL129	Alteration	Siderite	0.505	Illite	0.495	146.11	0.343	2206.6	0.19	27.2
2238654	2014GL001	Alteration	Illite	0.696	Phengite	0.304	82.789	0.179	2207.3	0.14	31.7
2238655	2014GL002	Alteration	Illite	0.776	Epidote	0.224	222.97	0.267	2197.3	0.08	27.9
2238655	2014GL002	Alteration	Illite	0.582	FeChlorite	0.418	48.472		2198.2	0.17	29.2
2238656	2014GL003	Alteration	Illite	1	NULL	0	84.578	0.339	2197.1	0.22	29.7
2238656	2014GL003	Alteration	Illite	0.774	Prehnite	0.226	104.23	0.357	2202.3	0.28	32.7
2238657	2014GL004	Alteration	Illite	0.504	FeChlorite	0.496	76.605	0.296	2197.1	0.21	27.1
2238658	2014GL005	Alteration	Illite	0.732	Prehnite	0.268	175.73	0.294	2196.9	0.14	28.3
2238659	2014GL006	Alteration	Epidote	1	NULL	0	71.079	0.244			
2238660	2014GL007	Alteration	Illite	1	NULL	0	82.97	0.285	2201.5	0.27	30.7
2238662	2014GL008	Alteration	FeChlorite	0.516	Illite	0.484	56.223	0.327	2198.6	0.15	30.0
2238663	2014GL009	Alteration	Illite	1	NULL	0	127.04	0.274	2196.8	0.17	27.3
2238664	2014GL010	Alteration	Illite	0.536	FeChlorite	0.464	54.507	0.225	2197.7	0.18	29.0
2238665	2014GL011	Background		0.557	Illite	0.443	93.688		2196.8	0.08	28.0
2238666	2014GL012	Alteration	FeChlorite	0.514	Illite	0.486	65.887		2197.4	0.15	27.2
2238667	2014GL012	Alteration	Illite	0.547	Epidote	0.453	69.403	0.224	2206.3	0.23	33.6
2238668	2014GL013	Alteration	Prehnite	0.815	Epidote	0.185	211.99	0.258			
2238669	2014GL014	Background	Illite	0.702	Epidote	0.298	510.01	0.171	2197.7	0.07	26.5
2238670	2014GL015	Alteration	Illite	1	NULL	0	175.4	0.222	2196.5	0.14	26.6
2238671	2014GL016	Background	Illite	0.529	FeChlorite	0.471	44.77		2196.8	0.21	29.4
2238674	2014GL017	Alteration	Illite	1	NULL	0	108.99	0.281	2197.8	0.17	28.9
2238675	2014GL018	Alteration	Illite	0.827	Epidote	0.173	108.98	0.258	2197.3	0.19	30.0
2238676	2014GL019	Alteration	Illite	0.576	FeChlorite	0.424	25.184	0.241	2201.0	0.22	29.9
2238677	2014GL020	Alteration	Illite	0.811	Epidote	0.189	170.22	0.276	2199.5	0.13	30.8
2238678	2014GL021	Alteration	Illite	0.649	Prehnite	0.351	142	0.282	2205.1	0.26	38.6
2238679	2014GL022	Alteration	Illite	0.545	Epidote	0.455	45.301	0.205	2201.6	0.15	29.3
2238680	2014GL023	Alteration	Illite	0.573	Kaolinite	0.427	161.14		2206.6	0.11	28.9
2238680	2014GL023	Alteration	Illite	0.609	Kaolinite	0.391	168.97		2206.4	0.12	29.5
2238681	2014GL024	Alteration	Illite	0.649	Phengite	0.351	87.957	0.314	2204.9	0.30	37.0
2238681	2014GL024	Background	Illite	1	NULL	0	470.78		2196.9	0.11	27.4
2238682	2014GL025	Alteration	Prehnite	0.521	Illite	0.479	188.32	0.295	2207.6	0.21	38.9
2238683	2014GL026	Alteration	Prehnite	1	NULL	0	130.18	0.247			
2238685	2014GL027	Background	Illite	1	NULL	0	162.99	0.338	2197.6	0.15	29.4
2238685	2014GL027	Alteration	FeChlorite	0.697	Illite	0.303	137.9				
2238686	2014GL028	Alteration	Illite	0.733	Epidote	0.267	82.61	0.328	2197.3	0.19	29.7
2238686	2014GL028	Alteration	IntChlorite	0.643	Illite	0.357	48.4	0.296	2197.0	0.12	26.7
2238687	2014GL028	Alteration	Illite	0.738	Epidote	0.262	243.16	0.206	2197.1	0.06	28.4
2238688	2014GL029	Alteration	Illite	0.811	Prehnite	0.189	50.899	0.276	2201.0	0.26	31.0
2238689	2014GL030	Alteration	Illite	0.754	Epidote	0.246	45.455	0.292	2197.5	0.30	32.0
2238689	2014GL030	Background	IntChlorite	0.692	Illite	0.308	72.922		2198.9	0.07	27.2
2238690	2014GL031	Alteration	Illite	0.527	Siderite	0.473	39.129	0.339	2205.2	0.32	30.3

Sample ID	Station ID	Measurement type	TSA mineral 1	TSA weight 1	TSA mineral 2	TSA weight 2	TSA error	H_2O absorption feature	Al-OH absorption feature		
								Hull quotient depth	Wavelength (nm)	Hull quotient depth	Width (nm)
2238690	2014GL031	Alteration	Illite	0.839	Epidote	0.161	57.523	0.288	2206.2	0.35	32.2
2238691	2014GL032	Background	Illite	1	NULL	0	290.57	0.254	2196.8	0.13	25.1
2238691	2014GL032	Background	Illite	0.776	Prehnite	0.224	82.033	0.312	2199.8	0.27	31.1
2238692	2014GL033	Alteration	Illite	0.716	Epidote	0.284	100.57	0.315	2207.8	0.28	36.8
2238693	2014GL034	Background	Illite	0.753	Prehnite	0.247	147.97	0.26	2197.7	0.21	26.6
2238694	2014GL035	Alteration	Illite	0.65	Prehnite	0.35	169.64	0.236	2200.0	0.20	30.9
2238697	2014GL036	Alteration	FeChlorite	0.59	Illite	0.41	48.56		2207.9	0.31	36.3
2238698	2014GL036	Alteration	Illite	0.742	IntChlorite	0.258	39.309	0.276	2199.6	0.28	29.8
2238699	2014GL037	Alteration	FeChlorite	0.644	Illite	0.356	53.085	0.253	2207.2	0.26	33.4
2238700	2014GL037	Alteration	Illite	0.67	Epidote	0.33	243.17		2207.5	0.18	38.2
2238701	2014GL038	Alteration	Illite	0.681	Prehnite	0.319	90.951	0.262	2197.0	0.22	28.1
2238702	2014GL038	Alteration	Illite	0.513	Phengite	0.487	63.623	0.355	2210.4	0.39	37.0
2238703	2014GL039	Alteration	Illite	0.674	Prehnite	0.326	142.51	0.327	2197.6	0.21	28.1
2238703	2014GL039	Alteration	Illite	0.674	Prehnite	0.326	105.34	0.318	2196.6	0.24	28.4
2238704	2014GL040	Alteration	Illite	0.509	Prehnite	0.491	175.01	0.281	2205.6	0.19	37.7
2238705	2014GL041	Alteration	Illite	0.544	FeChlorite	0.456	44.119		2201.1	0.28	32.5
2238706	2014GL041	Alteration	Illite	0.754	Ankerite	0.246	74.294	0.296	2201.3	0.14	28.7
2238708	2014GL042	Alteration	FeChlorite	0.534	Illite	0.466	92.554	0.182	2199.2	0.07	27.0
2238709	2014GL043	Alteration	Illite	0.544	FeChlorite	0.456	37.746	0.244	2200.7	0.22	32.5
2238710	2014GL044	Alteration	Illite	0.77	Prehnite	0.23	128.39	0.22	2196.7	0.20	27.8
2238711	2014GL045	Background	Illite	0.695	Prehnite	0.305	114.98		2197.5	0.21	27.2
2238712	2014GL046	Background	Illite	0.643	Kaolinite	0.357	109.18		2204.2	0.20	32.6
2238713	2014GL047	Alteration	Illite	0.627	Siderite	0.373	59.93	0.336	2198.8	0.26	29.2
2238714	2014GL048	Alteration	Illite	1	NULL	0	190.89	0.29	2197.9	0.11	28.6
2238715	2014GL049	Alteration	Illite	0.698	Prehnite	0.302	132.36	0.348	2196.9	0.22	27.9
2238716	2014GL050	Alteration	Illite	0.807	Prehnite	0.193	61.924	0.342	2197.3	0.31	30.6
2238717	2014GL051	Alteration	Illite	0.643	Prehnite	0.357	150.61	0.282	2208.9	0.25	35.9
2238717	2014GL051	Alteration	Illite	0.778	Prehnite	0.222	80.004	0.342	2198.1	0.25	30.1
2238720	2014GL052	Background	FeChlorite	0.547	Illite	0.453	113.54	0.274	2197.3	0.11	28.4
2238720	2014GL052	Alteration	FeChlorite	0.601	Illite	0.399	65.739		2206.8	0.20	34.3
2238721	2014GL053	Background	Illite	1	NULL	0	283.48	0.266	2197.3	0.14	28.2
2238721	2014GL053	Background	Illite	1	NULL	0	219.86	0.214	2197.5	0.11	27.7
2238722	2014GL054	Alteration	Illite	0.707	Prehnite	0.293	184.14	0.261	2196.7	0.19	27.4
2238722	2014GL054	Alteration	FeChlorite	0.583	Illite	0.417	116.54	0.283	2197.0	0.13	26.7
2238723	2014GL055	Alteration	Illite	0.665	Prehnite	0.335	226.27	0.206	2198.4	0.12	26.6
2238723	2014GL055	Alteration	Illite	0.647	Prehnite	0.353	102.88	0.266	2197.0	0.27	27.7
2238724	2014GL056	Background	Illite	1	NULL	0	169.34		2197.3	0.12	27.5
2238724	2014GL056	Background	Illite	1	NULL	0	169.92		2196.7	0.11	27.9
2238725	2014GL057	Background	Illite	0.66	Prehnite	0.34	173.24		2196.9	0.21	26.6
2238726	2014GL058	Background	Illite	1	NULL	0	244.08	0.274	2196.9	0.16	27.3
2238727	2014GL058	Alteration	Illite	0.677	Kaolinite	0.323	105.46		2204.3	0.19	31.9
2238728	2014GL059	Alteration	Illite	0.641	Prehnite	0.359	170.54	0.297	2197.5	0.19	25.7
2238728	2014GL059	Background	Illite	0.671	Prehnite	0.329	225.25		2196.9	0.13	26.3
2238729	2014GL060	Alteration	Illite	0.848	Epidote	0.152	157.43	0.256	2197.7	0.12	31.2
2238731	2014GL061	Alteration	Illite	1	NULL	0	272.79	0.319	2196.5	0.17	27.4
2238732	2014GL062	Background	IntChlorite	0.716	Illite	0.284	83.705		2199.6	0.05	27.8

Sample ID	Station ID	Measurement type	TSA mineral 1	TSA weight 1	TSA mineral 2	TSA weight 2	TSA error	H_2O absorption feature	Al-OH absorption feature		
								Hull quotient depth	Wavelength (nm)	Hull quotient depth	Width (nm)
2238733	2014GL063	Alteration	Illite	0.638	MgChlorite	0.362	109.26	0.173	2198.6	0.12	27.9
2238734	2014GL064	Alteration	Illite	1	NULL	0	162.68	0.225	2198.0	0.24	28.6
2238735	2014GL065	Background	Illite	0.56	Siderite	0.44	135.66		2197.5	0.10	29.7
2238736	2014GL066	Alteration	Illite	0.689	Prehnite	0.311	208.64	0.224	2196.4	0.15	27.2
2238737	2014GL067	Alteration	Illite	0.582	Prehnite	0.418	115.92	0.255	2198.6	0.23	26.3
2238738	2014GL067	Alteration	Illite	0.545	Epidote	0.455	95.005	0.266	2202.6	0.20	38.2
2238738	2014GL067	Background	Illite	0.658	Prehnite	0.342	134.72		2196.6	0.18	27.4
2238739	2014GL068	Background	Illite	1	NULL	0	148.12		2198.1	0.13	29.9
2238740	2014GL069	Alteration	Illite	0.671	Epidote	0.329	170.78	0.261	2209.1	0.25	34.4
2238743	2014GL070	Alteration	Illite	0.57	FeChlorite	0.43	67.572	0.269	2197.8	0.19	30.0
2238744	2014GL071	Background	Illite	0.617	MgChlorite	0.383	130.71		2197.5	0.22	28.3
2238745	2014GL072	Background	FeChlorite	0.585	Illite	0.415	71.316		2197.2	0.13	27.9
2238746	2014GL073	Alteration	Illite	0.552	Phengite	0.448	28.952	0.203	2206.9	0.53	34.0
2238747	2014GL073	Alteration	Illite	1	NULL	0	228.69	0.245	2196.6	0.15	28.0
2238748	2014GL074	Background	Illite	1	NULL	0	140.66		2199.1	0.14	30.8
2238749	2014GL075	Alteration	Illite	0.53	Prehnite	0.47	130.46	0.179	2217.1	0.29	40.8
2238749	2014GL075	Background	Illite	0.591	Prehnite	0.409	183.23		2196.6	0.14	24.6
2238750	2014GL076	Alteration	Prehnite	0.705	Epidote	0.295	296.99	0.131			
2238750	2014GL076	Background	Illite	0.529	Prehnite	0.471	193.26		2196.5	0.15	24.7
2238751	2014GL077	Alteration	Illite	0.737	Epidote	0.263	90.061	0.24	2203.0	0.29	37.6
2238752	2014GL078	Alteration	Muscovite	0.767	Epidote	0.233	99.013	0.364	2216.9	0.32	37.4
2238752	2014GL078	Alteration	Illite	0.795	Prehnite	0.205	82.073	0.239	2197.6	0.27	29.8
2238754	2014GL079	Alteration	Illite	0.594	Prehnite	0.406	187.06	0.153	2198.5	0.23	30.9
2238754	2014GL079	Alteration	FeChlorite	0.603	Prehnite	0.397	76.292	0.21			
2238755	2014GL080	Alteration	Illite	0.721	Prehnite	0.279	93.949	0.279	2198.0	0.17	29.1
2238756	2014GL080	Alteration	Illite	0.652	Prehnite	0.348	90.22	0.259	2197.1	0.21	28.2
2238756	2014GL080	Alteration	Prehnite	0.514	Illite	0.486	92.694	0.34	2203.1	0.28	37.7
2238757	2014GL081	Alteration	Illite	0.566	FeChlorite	0.434	59.453	0.278	2198.5	0.17	29.0
2238758	2014GL081	Alteration	Illite	0.741	Prehnite	0.259	89.542	0.382	2199.7	0.31	30.8
2238759	2014GL082	Alteration	Illite	0.677	Siderite	0.323	67.582	0.373	2199.9	0.24	31.8
2238760	2014GL083	Alteration	Illite	0.555	Siderite	0.445	122.57	0.386	2206.5	0.16	29.1
2238761	2014GL083	Alteration	Illite	1	NULL	0	144.81	0.274	2197.1	0.14	28.2
2238762	2014GL084	Alteration	Muscovite	0.806	Epidote	0.194	71.022	0.338	2208.8	0.35	35.8
2238763	2014GL085	Background	Illite	0.721	Prehnite	0.279	76.172	0.363	2198.1	0.28	27.8
2238766	2014GL085	Alteration	Illite	0.756	Ankerite	0.244	85.784	0.204	2197.8	0.17	29.3
2238767	2014GL086	Alteration	Muscovite	0.843	Epidote	0.157	78.212	0.168	2204.4	0.22	37.2
2238767	2014GL086	Background	Illite	0.691	Prehnite	0.309	179.45		2196.6	0.15	26.4
2238768	2014GL087	Alteration	Muscovite	0.738	Epidote	0.262	83.908	0.304	2211.1	0.31	36.4
2238768	2014GL087	Background	Illite	0.594	Siderite	0.406	111.32		2197.3	0.09	28.9
2238769	2014GL088	Alteration	Illite	0.816	Epidote	0.184	120.21	0.262	2200.8	0.22	35.6
2238770	2014GL089	Alteration	Prehnite	0.606	Illite	0.394	104.41	0.24	2200.9	0.18	41.2
2238771	2014GL090	Alteration	Illite	1	NULL	0	202.42		2199.2	0.27	29.5
2238771	2014GL090	Background	Illite	0.587	Prehnite	0.413	213.81		2196.2	0.12	25.5
2238772	2014GL091	Alteration	Prehnite	0.632	Illite	0.368	120.21	0.288			
2238773	2014GL092	Background	Illite	0.703	Prehnite	0.297	134.98		2197.3	0.15	27.5
2238774	2014GL093	Alteration	Prehnite	0.585	Illite	0.415	118.33	0.183	2198.8	0.20	36.4

Sample ID	Station ID	Measurement type	TSA mineral 1	TSA weight 1	TSA mineral 2	TSA weight 2	TSA error	H_2O absorption feature	Al-OH absorption feature		
								Hull quotient depth	Wavelength (nm)	Hull quotient depth	Width (nm)
2238775	2014GL094	Alteration	Illite	0.547	Siderite	0.453	68.596	0.34	2202.4	0.25	30.6
2238775	2014GL094	Alteration	Illite	0.647	Epidote	0.353	66.869	0.356	2204.4	0.28	29.3
2238777	2014GL095	Alteration	Illite	0.651	Phengite	0.349	65.914	0.272	2201.5	0.37	36.2
2238777	2014GL095	Alteration	Illite	0.74	Prehnite	0.26	140.11	0.325	2196.4	0.15	27.7
2238779	2014GL097	Alteration	Illite	0.823	Halloysite	0.177	55.204	0.346	2202.8	0.27	33.2
2238780	2014GL098	Alteration	Illite	0.775	Prehnite	0.225	88.783	0.381	2202.6	0.34	35.4
2238780	2014GL098	Background	Illite	1	NULL	0	120.68		2197.7	0.14	30.4
2238781	2014GL099	Background	Illite	0.701	Prehnite	0.299	90.685	0.295	2197.9	0.20	27.9
2238782	2014GL100	Background	Illite	1	NULL	0	195.01		2199.1	0.14	30.3
2238783	2014GL101	Alteration	Phengite	0.55	Illite	0.45	68.533	0.374	2211.9	0.32	36.7
2238784	2014GL102	Alteration	Illite	0.718	Epidote	0.282	150.81	0.286	2201.8	0.30	35.4
2238784	2014GL102	Background	Illite	1	NULL	0	189.23		2198.9	0.15	29.1
2238785	2014GL103	Alteration	Illite	1	NULL	0	69.267	0.312	2200.1	0.25	31.9
2238785	2014GL103	Alteration	Siderite	0.527	Illite	0.473	64.719	0.274	2206.8	0.23	34.9
2238786	2014GL104	Background	Illite	0.672	Prehnite	0.328	164.12	0.223	2198.1	0.13	26.8
2238789	2014GL105	Alteration	Prehnite	0.679	Epidote	0.321	320.49	0.161			
2238790	2014GL106	Alteration	Muscovite	0.804	Epidote	0.196	67.216	0.26	2206.5	0.33	39.5
2238791	2014GL107	Alteration	Prehnite	0.505	Epidote	0.495	521	0.205			
2238791	2014GL107	Background	Illite	0.592	Prehnite	0.408	222.08		2196.2	0.12	25.4
2238793	2014GL109	Alteration	Illite	0.683	Epidote	0.317	97.624	0.188	2198.7	0.17	28.7
2238794	2014GL110	Background	Illite	1	NULL	0	380.61		2199.2	0.06	29.0
2238795	2014GL111	Alteration	Illite	0.675	Prehnite	0.325	141.95	0.429	2208.0	0.26	34.8
2238796	2014GL112	Alteration	Illite	0.701	Prehnite	0.299	131.09	0.298	2198.4	0.23	26.7
2238797	2014GL113	Alteration	Muscovite	0.607	Prehnite	0.393	165.77	0.226	2217.8	0.23	38.9
2238798	2014GL114	Background	Illite	1	NULL	0	511.94	0.183	2198.4	0.07	28.3
2238800	2014GL115	Background	Illite	1	NULL	0	379.66		2197.2	0.09	26.6
2238801	2014GL116	Background	Illite	0.665	Prehnite	0.335	132.07	0.257	2197.2	0.17	26.5
2238802	2014GL117	Alteration	Phengite	0.541	Illite	0.459	44.223	0.156	2209.2	0.42	36.2
2238803	2014GL117	Background	Illite	1	NULL	0	373.1	0.233	2197.0	0.10	24.6
2238805	2014GL119	Alteration	Prehnite	0.599	Epidote	0.401	637.95	0.282			
2238806	2014GL120	Background	Illite	1	NULL	0	238.02		2196.6	0.07	26.0
2238807	2014GL121	Alteration	Illite	0.613	Phengite	0.387	36.788	0.098	2206.8	0.30	34.1
2238808	2014GL121	Alteration	Muscovite	1	NULL	0	22.95		2205.7	0.51	33.1
2238809	2014GL122	Background	Illite	0.603	Prehnite	0.397	215.7	0.226	2197.1	0.12	24.8
2238812	2014GL123	Background	Illite	0.661	Prehnite	0.339	243.74	0.365	2197.2	0.13	23.7
2238812	2014GL123	Alteration	Illite	1	NULL	0	151.7		2207.6	0.25	33.0
2238813	2014GL123	Alteration	Muscovite	1	NULL	0	26.164		2207.0	0.51	33.8
2238814	2014GL124	Alteration	Illite	0.76	Epidote	0.24	148.63	0.239	2200.0	0.21	29.7
2238815	2014GL125	Alteration	FeChlorite	0.717	Prehnite	0.283	63.005	0.193			
2238815	2014GL125	Background	Hornblende	0.811	Illite	0.189	55.082		2197.4	0.05	27.7
2238816	2014GL126	Alteration	Epidote	0.541	Illite	0.459	152.52	0.192	2206.7	0.16	38.6
2238816	2014GL126	Background	Illite	0.804	Epidote	0.196	245.57		2197.7	0.11	29.4
2238817	2014GL127	Background	Illite	1	NULL	0	479.56	0.163	2198.2	0.07	27.7
2238818	2014GL128	Background	Illite	1	NULL	0	236.83	0.139	2198.3	0.05	26.4
2238819	2014GL129	Alteration	Illite	0.542	Phengite	0.458	36.842	0.127	2205.7	0.48	34.7
2238820	2014GL130	Alteration	Epidote	1	NULL	0	144.8	0.142			

Sample ID	Station ID	Measurement type	TSA mineral 1	TSA weight 1	TSA mineral 2	TSA weight 2	TSA error	H_2O absorption feature	Al-OH absorption feature		
								Hull quotient depth	Wavelength (nm)	Hull quotient depth	Width (nm)
2238821	2014GL131	Alteration	Prehnite	0.518	Epidote	0.482	103.46	0.162			
2238821	2014GL131	Background	Illite	0.524	MgChlorite	0.476	236.76		2197.8	0.11	26.6
2238823	2014GL132	Background	Illite	0.582	MgChlorite	0.418	124.87	0.158	2200.7	0.20	32.5
2238823	2014GL132	Background	MgChlorite	0.652	Illite	0.348	93.578	0.122	2198.8	0.11	27.8
2238824	2014GL133	Alteration	Epidote	1	NULL	0	59.774	0.194			
2238825	2014GL134	Background	Illite	0.51	Hornblende	0.49	238.7	0.082	2198.9	0.09	25.8
2238826	2014GL135	Alteration	Muscovite	0.501	Epidote	0.499	192.85	0.154	2201.5	0.07	35.8
2238827	2014GL136	Alteration	Illite	0.506	MgChlorite	0.494	70.297	0.213	2200.1	0.21	30.1
2238828	2014GL137	Alteration	Epidote	1	NULL	0	362.96	0.133			
2238829	2014GL138	Background	Illite	0.625	Prehnite	0.375	190.5	0.206	2198.7	0.16	27.3
2238829	2014GL138	Background	Hornblende	0.6	Illite	0.4	115.65	0.091	2198.6	0.05	28.9
2238830	2014GL139	Alteration	IntChlorite	0.703	Epidote	0.297	64.341	0.15			
2238830	2014GL139	Alteration	MgChlorite	0.548	Muscovite	0.452	204.49	0.16	2204.4	0.16	40.0
2238831	2014GL140	Background	Prehnite	0.509	MgChlorite	0.491	137.72				
2238831	2014GL140	Background	MgChlorite	0.506	Muscovite	0.494	81.626		2201.9	0.12	36.8
2238832	2014GL141	Alteration	Prehnite	1	NULL	0	145.54	0.268			
2238835	2014GL142	Alteration	Epidote	0.834	Calcite	0.166	63.773	0.112			
2238836	2014GL143	Background	Muscovite	0.647	Epidote	0.353	250.09	0.066	2202.2	0.10	33.7
2238837	2014GL144	Alteration	IntChlorite	0.784	Illite	0.216	76.573		2201.6	0.09	36.8
2238838	2014GL145	Alteration	MgChlorite	0.774	Epidote	0.226	259.98	0.072			
2238839	2014GL146	Background	FeTourmaline	1	NULL	0	717.82		2204.8	0.06	26.1
2238840	2014GL147	Background	MgChlorite	0.661	Illite	0.339	143.05	0.085	2203.2	0.10	31.7
2238841	2014GL148	Background	MgChlorite	0.518	Illite	0.482	145.93	0.095	2201.9	0.17	32.3
2238842	2014GL149	Alteration	MgChlorite	0.738	Illite	0.262	107.46	0.072			
2238843	2014GL150	Background	MgChlorite	0.661	Illite	0.339	142.03	0.083	2200.3	0.13	37.0
2238844	2014GL150	Background	Epidote	0.774	Calcite	0.226	115.58	0.306			
2238846	2014GL151	Alteration	Illite	0.535	MgChlorite	0.465	78.122	0.209	2198.5	0.20	26.9
2238846	2014GL151	Alteration	Illite	0.511	Epidote	0.489	243.68	0.177	2200.1	0.15	31.4
2238847	2014GL152	Alteration	Prehnite	0.556	FeChlorite	0.444	44.207	0.221			
2238848	2014GL152	Alteration	IntChlorite	0.707	Epidote	0.293	57.873	0.078			
2238849	2014GL153	Alteration	FeChlorite	0.578	Siderite	0.422	39.484	0.22			
2238849	2014GL153	Background	Illite	0.74	Epidote	0.26	298.43		2197.6	0.28	27.3
2238851	2014GL155	Alteration	Muscovite	0.516	Epidote	0.484	232.79		2204.5	0.14	38.9
2238851	2014GL155	Background	Illite	0.588	Prehnite	0.412	263.68		2198.5	0.13	26.2
2238852	2014GL156	Alteration	Illite	0.596	Prehnite	0.404	288.39	0.209	2200.2	0.19	29.5
2238853	2014GL157	Alteration	Illite	0.657	Prehnite	0.343	103.06	0.385	2202.6	0.27	31.5
2238854	2014GL158	Background	Illite	0.559	MgChlorite	0.441	153.24	0.171	2197.8	0.14	26.8
2238855	2014GL159	Alteration	Illite	0.691	Phengite	0.309	67.88	0.31	2207.9	0.40	30.1
2238855	2014GL159	Alteration	Illite	0.509	Kaolinite	0.491	57.751	0.352	2206.6	0.45	32.6
2238855	2014GL159	Alteration	Kaolinite	0.643	Montmorillonite	0.357	37.541		2208.1	0.32	29.3
2238858	2014GL160	Alteration	Illite	0.66	Epidote	0.34	77.146	0.408	2207.3	0.28	29.1
2238858	2014GL160	Alteration	Illite	0.796	Prehnite	0.204	86.96	0.348	2199.4	0.32	32.4
2238859	2014GL161	Alteration	Illite	0.588	Phengite	0.412	19.032	0.247	2207.7	0.46	33.8
2238860	2014GL162	Alteration	Muscovite	1	NULL	0	29.815	0.176	2207.7	0.33	34.1
2238861	2014GL163	Alteration	Muscovite	0.764	Kaolinite	0.236	48.436	0.245	2206.8	0.37	29.2
2238862	2014GL164	Alteration	Illite	0.617	Phengite	0.383	22.072		2204.2	0.48	33.0

Sample ID	Station ID	Measurement type	TSA mineral 1	TSA weight 1	TSA mineral 2	TSA weight 2	TSA error	H_2O absorption feature	Al-OH absorption feature		
								Hull quotient depth	Wavelength (nm)	Hull quotient depth	Width (nm)
2238863	2014GL165	Alteration	Muscovite	1	NULL	0	121.9	0.075	2202.7	0.44	33.2
2238864	2014GL166	Alteration	Muscovite	0.515	Gypsum	0.485	52.819		2206.9	0.29	29.3
2238865	2014GL167	Alteration	Muscovite	0.847	Gypsum	0.153	70.184	0.28	2207.2	0.32	29.8
2238866	2014GL168	Alteration	Muscovite	1	NULL	0	69.033	0.176	2203.0	0.38	33.2
2238867	2014GL169	Alteration	Muscovite	1	NULL	0	82.794	0.182	2204.7	0.34	34.1
2238869	2014GL170	Alteration	Illite	0.628	Phengite	0.372	24.02	0.224	2204.1	0.49	32.7
2238870	2014GL171	Alteration	Muscovite	1	NULL	0	54.825	0.17	2202.3	0.48	32.5
2238870	2014GL171	Alteration	Illite	1	NULL	0	175.25	0.247	2206.4	0.34	32.9
2238870	2014GL171	Alteration	Phengite	0.53	Illite	0.47	40.872	0.299	2209.6	0.44	35.2
2238871	2014GL172	Alteration	Illite	0.596	Opal	0.404	84.294	0.314	2204.3	0.13	33.6
2238872	2014GL173	Alteration	Muscovite	0.842	Kaolinite	0.158	23.609	0.143	2207.9	0.42	30.7
2238873	2014GL174	Alteration	Kaolinite	0.586	Illite	0.414	157.51	0.311	2207.7	0.15	28.6
2238873	2014GL174	Alteration	Illite	0.615	Kaolinite	0.385	73.554		2206.4	0.24	32.6
2238874	2014GL175	Alteration	Muscovite	1	NULL	0	154.16	0.277	2201.4	0.40	31.9
2238875	2014GL176	Alteration	Kaolinite	0.623	Illite	0.377	28.528		2207.8	0.33	32.2
2238876	2014GL177	Alteration	Gypsum	0.533	Epidote	0.467	59.243		2219.1	0.10	23.7
2238876	2014GL177	Alteration	IntChlorite	0.665	Paragonite	0.335	73.212		2190.0	0.16	25.9
2238877	2014GL178	Alteration	Prehnite	0.557	Halloysite	0.443	275.53	0.332	2209.5	0.19	29.8
2238878	2014GL179	Alteration	Muscovite	1	NULL	0	17.916	0.109	2204.3	0.40	34.2
2238881	2014GL180	Background	MgChlorite	0.578	Illite	0.422	184.01	0.045	2200.5	0.12	35.2
2238882	2014GL181	Alteration	FeChlorite	0.764	Muscovite	0.236	23.089		2211.1	0.17	35.0
2238883	2014GL181	Alteration	FeChlorite	1	NULL	0	23.848		2208.7	0.05	31.5
2238884	2014GL182	Alteration	Epidote	0.571	Illite	0.429	446.48				
2238885	2014GL183	Background	MgChlorite	0.518	Illite	0.482	128.7	0.092	2198.3	0.18	26.0
2238885	2014GL183	Background	Hornblende	0.654	Illite	0.346	170.78	0.082	2200.0	0.11	28.7
2238887	2014GL185	Alteration	Epidote	0.523	Illite	0.477	123.41		2207.0	0.19	37.0
2238887	2014GL185	Alteration	Illite	0.662	MgChlorite	0.338	97.446		2199.5	0.22	27.9
2238888	2014GL186	Background	Hornblende	0.802	Epidote	0.198	245.04	0.058	2197.0	0.05	34.3
2238888	2014GL186	Background	Siderite	0.61	Illite	0.39	166.56	0.128	2196.9	0.05	28.2
2238889	2014GL187	Alteration	Illite	0.725	Prehnite	0.275	142.38		2201.4	0.22	31.6
2238890	2014GL188	Background	Illite	0.634	MgChlorite	0.366	88.865	0.216	2198.9	0.23	28.7
2238892	2014GL189	Background	Illite	0.528	Siderite	0.472	67.716		2198.9	0.11	27.9
2238893	2014GL190	Alteration	Illite	0.605	Siderite	0.395	66.954	0.252	2198.9	0.18	29.7
2238894	2014GL191	Background	FeChlorite	0.561	Illite	0.439	57.266		2198.9	0.18	27.4
2238895	2014GL192	Alteration	Illite	0.753	Epidote	0.247	229.74		2200.8	0.18	29.7
2238896	2014GL193	Alteration	Illite	0.615	Epidote	0.385	173.06	0.33	2202.0	0.26	35.4
2238896	2014GL193	Background	MgChlorite	0.554	Illite	0.446	227.21		2197.8	0.07	27.6
2238897	2014GL194	Alteration	Illite	0.693	Epidote	0.307	242.61	0.251	2204.8	0.19	40.0
2238898	2014GL195	Background	MgChlorite	0.579	Illite	0.421	86.793		2200.5	0.19	34.1
2238898	2014GL195	Background	Hornblende	0.68	Illite	0.32	125.69		2200.1	0.03	28.5
2238899	2014GL196	Alteration	MgChlorite	0.662	Illite	0.338	222.9	0.168			
2238899	2014GL196	Background	Hornblende	0.65	Illite	0.35	247.09		2198.9	0.05	23.7
2238900	2014GL197	Alteration	Prehnite	0.715	Epidote	0.285	211.84	0.14			
2238901	2014GL198	Alteration	Prehnite	0.554	MgChlorite	0.446	130.99	0.188			
2238904	2014GL199	Alteration	Epidote	0.648	Illite	0.352	99.484	0.237	2227.1	0.17	39.6
2238904	2014GL199	Alteration	Prehnite	0.537	Illite	0.463	215.11		2206.1	0.19	37.3

Sample ID	Station ID	Measurement type	TSA mineral 1	TSA weight 1	TSA mineral 2	TSA weight 2	TSA error	H_2O absorption feature	Al-OH absorption feature		
								Hull quotient depth	Wavelength (nm)	Hull quotient depth	Width (nm)
2238905	2014GL200	Alteration	Montmorillonite	1	NULL	0	186.44		2208.2	0.03	31.0
2238906	2014GL201	Alteration	Muscovite	1	NULL	0	157.98	0.273	2205.1	0.28	40.4
2238907	2014GL202	Alteration	Epidote	0.574	Illite	0.426	152.5	0.195	2207.5	0.16	36.9
2238907	2014GL202	Alteration	Muscovite	0.791	Epidote	0.209	130.73		2209.4	0.18	37.5
2238907	2014GL202	Background	Hornblende	0.761	Illite	0.239	127.1		2198.5	0.04	27.2
2238908	2014GL203	Alteration	Illite	0.501	IntChlorite	0.499	69.533	0.309	2204.8	0.23	29.5
2238908	2014GL203	Alteration	Epidote	0.771	Montmorillonite	0.229	46.711	0.372			
2238908	2014GL203	Alteration	Epidote	0.607	Halloysite	0.393	384.69	0.457	2208.0	0.21	27.2
2238908	2014GL203	Background	MgChlorite	0.505	Illite	0.495	128.83		2198.4	0.12	26.9
2238909	2014GL204	Background	Siderite	0.555	Illite	0.445	114.42	0.158	2197.9	0.04	29.5
2238910	2014GL205	Alteration	Illite	0.736	Epidote	0.264	117.49	0.284	2200.0	0.23	29.4
2238911	2014GL206	Background	Illite	1	NULL	0	295.71	0.173	2197.7	0.18	25.6
2238912	2014GL207	Alteration	IntChlorite	0.705	Illite	0.295	75.142	0.284	2206.7	0.12	34.2
2238913	2014GL208	Alteration	Illite	0.641	Epidote	0.359	145.4	0.242	2202.4	0.16	30.9
2238915	2014GL209	Alteration	Illite	0.565	Epidote	0.435	196.96	0.237	2197.3	0.21	24.5
2238916	2014GL210	Alteration	FeTourmaline	0.544	Epidote	0.456	317.48	0.145	2202.8	0.12	37.5
2238917	2014GL211	Alteration	Prehnite	0.652	Epidote	0.348	478.31	0.2			
2238917	2014GL211	Background	MgChlorite	0.592	Illite	0.408	135.18		2198.3	0.11	24.1
2238918	2014GL212	Alteration	Prehnite	0.542	Illite	0.458	269.28	0.267	2206.4	0.13	35.1
2238919	2014GL212	Alteration	Prehnite	0.592	MgChlorite	0.408	149.64	0.189			
2238920	2014GL213	Alteration	Epidote	0.762	Illite	0.238	140.44	0.209			
2238921	2014GL214	Alteration	FeChlorite	0.576	Prehnite	0.424	67.569	0.293			
2238922	2014GL215	Background	Illite	0.542	Prehnite	0.458	168.63		2198.2	0.22	29.8
2238923	2014GL216	Alteration	Prehnite	0.754	Epidote	0.246	110.1	0.178			
2238924	2014GL217	Background	Hornblende	0.591	Epidote	0.409	279.81				
2238927	2014GL218	Alteration	Prehnite	0.511	Illite	0.489	260.57	0.299			
2238928	2014GL219	Alteration	Prehnite	0.66	Epidote	0.34	446.39	0.214	2204.5	0.12	39.2
2238929	2014GL220	Alteration	Prehnite	0.705	Epidote	0.295	314.38	0.151			
2238929	2014GL220	Background	MgChlorite	0.614	Illite	0.386	139.11		2202.3	0.12	37.1
2238930	2014GL221	Background	Illite	0.704	Prehnite	0.296	72.565		2199.2	0.29	28.2
2238931	2014GL222	Alteration	Illite	0.618	Epidote	0.382	410.58	0.072	2201.4	0.08	32.7
2238931	2014GL222	Alteration	MgChlorite	0.614	Prehnite	0.386	174.63	0.084			
2238932	2014GL223	Background	MgChlorite	0.554	Illite	0.446	268.87	0.101	2198.4	0.12	28.5
2238932	2014GL223	Background	Muscovite	0.545	Prehnite	0.455	184.79	0.167	2198.3	0.21	26.9
2238933	2014GL224	Alteration	Prehnite	0.636	Muscovite	0.364	231.2	0.174			
2238934	2014GL225	Alteration	Prehnite	0.537	Muscovite	0.463	202.85	0.127	2200.9	0.16	35.5
2238935	2014GL226	Alteration	IntChlorite	0.574	Epidote	0.426	87.043	0.109			
2238935	2014GL226	Background	IntChlorite	0.601	Illite	0.399	115.18		2201.5	0.11	32.9
2238936	2014GL227	Background	Illite	1	NULL	0	237.51	0.123	2199.0	0.20	28.9
2238938	2014GL228	Background	Illite	0.51	Prehnite	0.49	241.71		2198.8	0.18	32.0
2238939	2014GL229	Background	Illite	0.516	MgChlorite	0.484	176.78	0.094	2199.7	0.23	34.1
2238939	2014GL229	Background	MgChlorite	0.568	Illite	0.432	160.08	0.081	2199.7	0.16	32.3
2238940	2014GL230	Background	MgChlorite	0.539	Illite	0.461	144.33	0.113	2199.9	0.15	29.1
2238940	2014GL230	Background	MgChlorite	0.537	Illite	0.463	157.82	0.072	2198.6	0.10	25.7
2238941	2014GL230	Alteration	Epidote	1	NULL	0	160.58	0.138			
2238941	2014GL230	Alteration	Epidote	1	NULL	0	142.13	0.177			

Sample ID	Station ID	Measurement type	TSA mineral 1	TSA weight 1	TSA mineral 2	TSA weight 2	TSA error	H_2O absorption feature	Al-OH absorption feature		
								Hull quotient depth	Wavelength (nm)	Hull quotient depth	Width (nm)
2238942	2014GL231	Background	MgChlorite	0.527	Illite	0.473	128.25		2199.1	0.14	25.2
2238942	2014GL231	Background	Illite	0.537	MgChlorite	0.463	183.41		2199.3	0.15	27.1
2238951	2015GL-V11-06	Alteration	Muscovite	0.682	Gypsum	0.318	24.49	0.364	2202.1	0.33	30.7
2238952	2015GL-V11-06	Alteration	Muscovite	1	NULL	0	60.927	0.097	2209.0	0.26	32.5
2238953	2015GL-V11-06	Alteration	Muscovite	1	NULL	0	44.282	0.109	2202.8	0.46	32.7
2238954	2015GL-V11-06	Alteration	Illite	0.621	Phengite	0.379	62.572	0.14	2202.3	0.49	30.6
2238955	2015GL-V11-06	Alteration	Muscovite	1	NULL	0	36.583	0.121	2203.8	0.41	33.6
2238956	2015GL-V11-06	Alteration	Muscovite	1	NULL	0	35.398	0.128	2202.4	0.36	30.8
2238957	2015GL-V11-06	Alteration	Illite	0.559	Dickite	0.441	51.453	0.351	2207.8	0.43	30.2
2238958	2015GL-V11-06	Alteration	Illite	0.77	Kaolinite	0.23	51.357	0.366	2207.9	0.39	28.6
2238959	2015GL-V11-06	Alteration	Muscovite	1	NULL	0	45.074	0.159	2201.8	0.38	31.0
2238960	2015GL-V11-13	Alteration	FeChlorite	0.518	Illite	0.482	35.934	0.333	2207.1	0.27	27.6
2238962	2015GL-V11-13	Alteration	Muscovite	1	NULL	0	106.88	0.257	2202.4	0.17	30.7
2238963	2015GL-V11-13	Alteration	Halloysite	0.682	Calcite	0.318	159.03	0.255	2208.1	0.24	28.3
2238964	2015GL-V11-13	Alteration	Muscovite	1	NULL	0	44.974	0.224	2206.6	0.26	32.5
2238965	2015GL-V11-13	Alteration	Muscovite	1	NULL	0	39.292	0.26	2206.2	0.23	29.9
2238966	2015GL-V11-13	Alteration	Muscovite	1	NULL	0	30.932	0.085	2204.3	0.25	30.5
2238967	2015GL-V11-13	Alteration	Kaolinite	0.572	Illite	0.428	37.024	0.349	2208.3	0.44	29.5
2238968	2015GL-V11-13	Alteration	Muscovite	1	NULL	0	94.037	0.23	2203.1	0.30	30.0
2238969	2015GL-V11-50	Alteration	Illite	0.67	Phengite	0.33	35.907	0.26	2203.5	0.32	32.4
2238970	2015GL-V11-50	Alteration	Illite	0.637	Phengite	0.363	19.883	0.197	2204.2	0.45	33.2
2238971	2015GL-V11-50	Alteration	Kaolinite	0.642	Illite	0.358	38.843	0.416	2208.3	0.45	30.2
2238974	2015GL-V11-50	Alteration	Kaolinite	0.586	Illite	0.414	57.309	0.274	2207.6	0.21	30.8
2238975	2015GL-V11-50	Alteration	Muscovite	0.555	Montmorillonite	0.445	75.272	0.322	2208.3	0.18	32.2
2238976	2015GL-V11-50	Alteration	Muscovite	1	NULL	0	45.529	0.125	2202.1	0.29	33.0
2238977	2015GL-V11-50	Alteration	Illite	0.573	Phengite	0.427	49.695	0.186	2205.3	0.22	32.7
2238978	2015GL-V11-50	Alteration	Kaolinite	0.547	Illite	0.453	56.758	0.327	2207.6	0.25	31.7
2238979	2015GL-V11-50	Alteration	Illite	0.583	Phengite	0.417	36.704	0.131	2204.3	0.45	33.5
2238980	2015GL-V11-50	Alteration	Kaolinite	0.641	Illite	0.359	36.589	0.367	2207.8	0.37	30.7
2238981	2015GL001	Alteration	Prehnite	0.508	Epidote	0.492	451.49	0.2			
2238982	2015GL002	Alteration	Muscovite	1	NULL	0	148.08	0.364	2204.7	0.33	38.7
2238983	2015GL003	Alteration	Illite	1	NULL	0	312.9	0.323	2196.7	0.11	27.2
2238985	2015GL003	Alteration	Siderite	0.641	Illite	0.359	136.97	0.37			
2238986	2015GL004	Alteration	Illite	1	NULL	0	112.15	0.357	2200.4	0.33	29.9
2238987	2015GL005	Alteration	Illite	0.566	Prehnite	0.434	142.74	0.34	2199.3	0.19	32.0
2238989	2015GL007	Alteration	Illite	0.668	Epidote	0.332	41.124	0.304	2200.9	0.27	30.4
2238990	2015GL008	Alteration	Illite	0.807	Epidote	0.193	127.83	0.36	2198.4	0.22	27.6
2238991	2015GL009	Alteration	Illite	0.578	Prehnite	0.422	117.26	0.309	2207.5	0.25	38.0
2238992	2015GL010	Alteration	Epidote	0.686	Montmorillonite	0.314	81.716	0.369	2206.4	0.08	28.1
2238993	2015GL010	Alteration	Illite	0.596	Siderite	0.404	64.226	0.327	2197.0	0.15	30.5
2238994	2015GL011	Alteration	Prehnite	0.738	Epidote	0.262	295.68	0.342			
2238994	2015GL011	Alteration	Illite	0.72	Prehnite	0.28	123.75	0.385	2205.4	0.27	36.5
2238997	2015GL011	Alteration	Epidote	0.516	Illite	0.484	32.653	0.31	2199.2	0.19	28.3
2238998	2015GL012	Background	Illite	0.646	Prehnite	0.354	273.83	0.31	2196.1	0.12	26.3
2238998	2015GL012	Background	Illite	0.674	Prehnite	0.326	254.72	0.291	2196.2	0.10	26.7
2238999	2015GL013	Alteration	Illite	0.722	Epidote	0.278	29.308	0.373	2200.4	0.27	31.0

Sample ID	Station ID	Measurement type	TSA mineral 1	TSA weight 1	TSA mineral 2	TSA weight 2	TSA error	H_2O absorption feature	Al-OH absorption feature		
								Hull quotient depth	Wavelength (nm)	Hull quotient depth	Width (nm)
2239000	2015GL014	Alteration	Illite	0.608	Epidote	0.392	145.04	0.334	2203.2	0.21	35.4
2242901	2015KB238	Alteration	Prehnite	1	NULL	0	366.46	0.285			
2242902	2015KB239	Alteration	Illite	0.556	Prehnite	0.444	207.2	0.252	2198.6	0.17	27.0
2242903	2015KB240	Alteration	Illite	0.698	Epidote	0.302	300.89	0.302	2199.3	0.14	27.1
2242904	2015KB241	Alteration	Prehnite	0.595	Illite	0.405	96.761	0.329	2201.1	0.20	38.4
2242905	2015KB242	Alteration	Illite	0.64	Prehnite	0.36	130.54		2198.2	0.21	25.6
2242906	2015KB243	Alteration	Illite	1	NULL	0	344.26	0.209	2200.2	0.03	27.6
2242906	2015KB243	Alteration	Epidote	0.805	Calcite	0.195	87.738	0.234			
2242907	2015KB244	Alteration	Illite	0.597	IntChlorite	0.403	43.809	0.298	2202.7	0.25	31.4
2242908	2015KB245	Alteration	Illite	0.528	MgChlorite	0.472	197.38		2208.2	0.20	28.2
2242909	2015KB246	Alteration	Prehnite	0.757	Epidote	0.243	216.51				
2242911	2015KB247	Alteration	Muscovite	0.558	IntChlorite	0.442	47.981	0.157	2208.1	0.17	34.4
2242912	2015KB248	Alteration	Illite	0.767	Epidote	0.233	389.18	0.335	2198.1	0.15	24.7
2242913	2015KB249	Alteration	Epidote	0.619	Illite	0.381	73.396	0.334	2202.7	0.19	35.7
2242914	2015KB250A	Alteration	Illite	0.789	Epidote	0.211	93.807	0.451	2196.6	0.23	33.1
2242914	2015KB250A	Alteration	Illite	0.741	Phengite	0.259	51.141	0.34	2206.5	0.41	31.7
2242914	2015KB250A	Alteration	Epidote	0.674	Halloysite	0.326	140.32	0.281	2208.8	0.17	23.2
2242916	2015KB251B	Alteration	Epidote	0.577	Illite	0.423	104.67		2205.5	0.13	34.1
2242917	2015KB252	Alteration	Prehnite	0.654	Epidote	0.346	197.54	0.233			
2242918	2015KB254	Alteration	Prehnite	0.528	Illite	0.472	176.32	0.305	2200.0	0.15	37.3
2242919	2015KB255	Alteration	Illite	0.592	Epidote	0.408	436.9	0.344	2197.3	0.14	25.2
2242921	2015KB256	Background	Illite	0.517	MgChlorite	0.483	147.71		2200.3	0.14	29.1
2242922	2015KB257	Alteration	Epidote	0.543	Phengite	0.457	148.23	0.228	2217.7	0.11	33.7
2242923	2015KB258	Alteration	Prehnite	0.501	FeChlorite	0.499	83.484	0.26			
2242923	2015KB258	Alteration	Illite	0.649	Prehnite	0.351	239.54	0.314	2197.7	0.13	25.8
2242924	2015KB259A	Alteration	Illite	0.555	Prehnite	0.445	176.68	0.284	2197.2	0.16	25.4
2242925	2015KB260	Alteration	Illite	0.818	Epidote	0.182	118.07	0.328	2199.2	0.22	29.7
2242925	2015KB260	Alteration	Prehnite	0.614	Illite	0.386	201.38	0.398	2207.5	0.14	36.3
2242926	2015KB261	Alteration	Prehnite	1	NULL	0	338.46	0.239			
2242927	2015KB263	Alteration	Hornblende	0.524	Epidote	0.476	137.64	0.102			
2242928	2015KB264	Alteration	Illite	0.796	Kaolinite	0.204	40.393	0.293	2207.3	0.29	31.7
2242929	2015KB265	Alteration	Illite	0.677	Epidote	0.323	526.94	0.403	2209.8	0.12	35.7
2242931	2015KB268	Alteration	Epidote	1	NULL	0	254.7	0.121	2208.7	0.05	32.4
2242931	2015KB268	Alteration	Illite	0.709	Epidote	0.291	219.39	0.31	2208.9	0.22	34.5
2242932	2015KB269	Alteration	Illite	0.523	Siderite	0.477	65.524	0.287	2202.3	0.18	33.9
2242933	2015KB270	Alteration	Dickite	0.721	Tourmaline	0.279	1235.75	0.337	2208.4	0.13	21.6
2242934	2015KB271	Alteration	FeChlorite	0.672	Illite	0.328	135	0.323	2208.7	0.10	31.3
2242935	2015KB272	Alteration	Muscovite	0.842	Brucite	0.158	176.72	0.116	2209.4	0.16	35.8
2242936	2015KB273	Alteration	Muscovite	0.711	Kaolinite	0.289	32.009	0.201	2206.9	0.37	29.4
2242937	2015KB274	Alteration	MgChlorite	0.654	Illite	0.346	133.24	0.219	2198.9	0.08	28.0
2242937	2015KB274	Alteration	Illite	0.548	Prehnite	0.452	259.97	0.217	2198.5	0.15	25.9
2242938	2015KB275	Alteration	Muscovite	1	NULL	0	34.489	0.33	2204.8	0.37	35.3
2242938	2015KB275	Alteration	FeChlorite	0.574	Illite	0.426	49.912	0.243	2201.8	0.24	31.0
2242939	2015KB276	Alteration	Illite	0.532	MgChlorite	0.468	117.67	0.331	2197.9	0.12	27.2
2242941	2015KB277	Alteration	Prehnite	0.604	Epidote	0.396	271.47	0.414			
2242942	2015KB278	Alteration	Epidote	0.697	Illite	0.303	97.559	0.334	2192.3	0.07	30.7

Sample ID	Station ID	Measurement type	TSA mineral 1	TSA weight 1	TSA mineral 2	TSA weight 2	TSA error	H_2O absorption feature	Al-OH absorption feature		
								Hull quotient depth	Wavelength (nm)	Hull quotient depth	Width (nm)
2242943	2015KB279	Alteration	Epidote	0.642	Kaolinite	0.358	205.94	0.123	2208.8	0.10	18.5
2242944	2015KB266A	Alteration	Illite	0.628	Kaolinite	0.372	38.416	0.402	2207.2	0.34	32.3
2242945	2015KB266B	Alteration	Illite	0.504	Kaolinite	0.496	180.51	0.282	2207.4	0.12	31.7
2242946	2015KB267	Alteration	Illite	1	NULL	0	40.898	0.397	2203.3	0.35	33.2
2245246	2015KB001	Alteration	Illite	1	NULL	0	259.34	0.454	2194.8	0.09	30.5
2245247	2015KB002	Alteration	Prehnite	0.561	Epidote	0.439	351.31	0.214			
2245248	2015KB004	Alteration	IntChlorite	0.634	Epidote	0.366	59.065	0.068			
2245249	2015KB005	Alteration	MgChlorite	0.581	Illite	0.419	96.25	0.213	2200.7	0.15	30.6
2245251	2015KB007	Alteration	IntChlorite	0.667	Epidote	0.333	49.57	0.112			
2245253	2015KB011	Background	Hornblende	0.623	Illite	0.377	219.55	0.085	2201.0	0.03	25.4
2245254	2015KB012	Alteration	Aspectral			1	10000	0.166	2198.5	0.14	29.9
2245255	2015KB015	Background	Aspectral			1	10000		2201.7	0.08	35.0
2245256	2015KB016	Background	Prehnite	0.519	Illite	0.481	169.7		2198.4	0.12	26.3
2245257	2015KB017	Alteration	Epidote	0.66	Prehnite	0.34	244.01	0.129			
2245258	2015KB019	Background	Muscovite	0.639	Prehnite	0.361	205.43	0.135	2198.8	0.15	26.8
2245259	2015KB020	Alteration	Illite	0.603	Phengite	0.397	113.44	0.306	2210.2	0.25	36.0
2245259	2015KB020	Alteration	Illite	0.518	Montmorillonite	0.482	93.922	0.275	2204.6	0.10	30.0
2245261	2015KB022	Alteration	Illite	0.556	Prehnite	0.444	153.62	0.213	2200.5	0.17	30.8
2245262	2015KB023	Alteration	IntChlorite	0.75	Illite	0.25	49.448	0.093	2202.8	0.09	34.0
2245263	2015KB024	Background	Muscovite	0.653	Prehnite	0.347	156.69	0.138	2198.8	0.14	26.2
2245264	2015KB025	Alteration	Illite	0.645	MgChlorite	0.355	80.94	0.259	2203.9	0.26	32.2
2245265	2015KB027	Background	Aspectral			1	10000	0.089	2198.1	0.05	25.6
2245266	2015KB028	Alteration	MgChlorite	0.723	Illite	0.277	148.9	0.14			
2245267	2015KB031	Alteration	Illite	0.548	Prehnite	0.452	202.07	0.145	2201.9	0.13	33.2
2245268	2015KB032A	Alteration	Prehnite	0.591	Epidote	0.409	327.89	0.141			
2245269	2015KB032B	Alteration	IntChlorite	0.763	Muscovite	0.237	37.404	0.153	2207.9	0.11	38.7
2245271	2015KB033	Alteration	Prehnite	0.597	Epidote	0.403	490.68	0.213	2201.6	0.13	37.8
2245271	2015KB033	Alteration	Prehnite	0.576	Illite	0.424	260.85	0.204	2201.7	0.13	40.0
2245272	2015KB034	Alteration	IntChlorite	0.679	Muscovite	0.321	43.512	0.143	2214.4	0.21	35.9
2245274	2015KB035	Alteration	IntChlorite	0.682	Epidote	0.318	107.16	0.195			
2245275	2015KB036	Alteration	Epidote	0.581	Phengite	0.419	272.07	0.043	2216.4	0.12	35.4
2245276	2015KB037	Alteration	Epidote	0.529	Illite	0.471	204.51	0.182	2205.2	0.11	36.5
2245277	2015KB009	Background	Illite	0.538	Prehnite	0.462	219.76	0.113	2199.5	0.12	25.9
2245278	2015KB038	Alteration	IntChlorite	0.765	Epidote	0.235	164.5	0.13			
2245279	2015KB040	Alteration	Epidote	0.514	Prehnite	0.486	215.51	0.143			
2245281	2015KB041	Alteration	IntChlorite	0.503	Epidote	0.497	67.298	0.108			
2245282	2015KB043A	Alteration	Epidote	1	NULL	0	312.83	0.023	2211.2	0.06	32.6
2245283	2015KB043B	Alteration	MgChlorite	0.559	Illite	0.441	123.29	0.26	2201.7	0.17	31.6
2245284	2015KB044	Alteration	IntChlorite	1	NULL	0	79.304	0.169			
2245285	2015KB045	Alteration	IntChlorite	0.559	Epidote	0.441	50.673	0.215			
2245286	2015KB046	Alteration	Prehnite	0.554	Epidote	0.446	350.68	0.176			
2245286	2015KB046	Alteration	IntChlorite	0.662	Epidote	0.338	71.177	0.149			
2245287	2015KB047	Alteration	Illite	0.512	Epidote	0.488	222.54	0.134	2201.8	0.09	26.7
2245289	2015KB049	Alteration	IntChlorite	0.708	Illite	0.292	123.82		2200.0	0.15	36.1
2245291	2015KB050	Alteration	Illite	0.511	Epidote	0.489	230.86		2202.2	0.08	36.6
2245292	2015KB051	Background	Prehnite	0.599	Illite	0.401	195.58				

Sample ID	Station ID	Measurement type	TSA mineral 1	TSA weight 1	TSA mineral 2	TSA weight 2	TSA error	H_2O absorption feature	Al-OH absorption feature		
								Hull quotient depth	Wavelength (nm)	Hull quotient depth	Width (nm)
2245293	2015KB052	Background	Illite	1	NULL	0	60.138	0.23	2198.8	0.21	33.2
2245294	2015KB053	Alteration	Prehnite	0.612	Epidote	0.388	350.85	0.148			
2245295	2015KB054	Alteration	Muscovite	0.665	Prehnite	0.335	178.93	0.178	2200.5	0.11	28.7
2245296	2015KB055	Alteration	Epidote	0.559	Prehnite	0.441	86.336	0.161			
2245297	2015KB056	Alteration	MgChlorite	0.567	Illite	0.433	231.58	0.136	2203.2	0.10	29.9
2245298	2015KB057	Alteration	IntChlorite	0.648	Epidote	0.352	105.54	0.146			
2245299	2015KB059	Background	MgChlorite	0.523	Illite	0.477	208.92	0.122	2198.5	0.11	26.1
2245301	2015KB060	Alteration	Epidote	0.629	Illite	0.371	146.95	0.296	2202.7	0.06	31.5
2245302	2015KB062	Alteration	Epidote	0.675	Illite	0.325	122.85	0.292	2201.8	0.13	34.9
2245303	2015KB063	Alteration	Epidote	0.779	Calcite	0.221	55.452	0.178			
2245304	2015KB064A	Alteration	Epidote	0.589	IntChlorite	0.411	53.699	0.165			
2245305	2015KB064B	Background	MgChlorite	0.584	Illite	0.416	185.74		2200.4	0.07	28.4
2245306	2015KB065	Alteration	Epidote	0.557	Gypsum	0.443	594.22		2217.0	0.00	17.0
2245307	2015KB066	Background	MgChlorite	0.547	Illite	0.453	236	0.131	2199.7	0.06	26.7
2245308	2015KB067	Alteration	IntChlorite	0.614	Epidote	0.386	58.877	0.16			
2245309	2015KB068	Alteration	Epidote	0.635	Illite	0.365	59.141	0.092	2205.3	0.20	37.2
2245309	2015KB068	Alteration	IntChlorite	0.547	Epidote	0.453	47.945	0.253			
2245311	2015KB069	Alteration	Hornblende	0.567	Epidote	0.433	88.346	0.188			
2245311	2015KB069	Alteration	Epidote	0.722	Calcite	0.278	91.141	0.143			
2245312	2015KB071	Alteration	Epidote	0.525	IntChlorite	0.475	40.053	0.123			
2245312	2015KB071	Alteration	Epidote	1	NULL	0	114.43	0.199			
2245313	2015KB070	Alteration	Hornblende	0.535	Epidote	0.465	160.61	0.271	2196.9	0.12	24.1
2245313	2015KB070	Alteration	Aspectral			1	10000	0.124	2200.6	0.05	26.6
2245314	2015KB072	Alteration	IntChlorite	0.607	Epidote	0.393	38.208	0.17			
2245314	2015KB072	Alteration	IntChlorite	0.769	Epidote	0.231	43.932	0.133			
2245315	2015KB073	Alteration	Prehnite	0.589	Epidote	0.411	519.02	0.242	2200.8	0.15	33.5
2245316	2015KB074	Alteration	Epidote	1	NULL	0	114.81	0.209			
2245316	2015KB074	Alteration	IntChlorite	0.58	Epidote	0.42	129.29	0.169			
2245317	2015KB075	Background	Illite	0.562	Prehnite	0.438	158.02	0.238	2199.6	0.18	30.8
2245318	2015KB076	Background	Illite	0.528	Prehnite	0.472	308.63	0.128	2198.6	0.10	24.0
2245319	2015KB077	Background	Muscovite	0.56	Prehnite	0.44	288.99	0.123	2199.4	0.08	23.8
2245321	2015KB078	Background	Prehnite	0.696	Illite	0.304	107.82	0.215			
2245322	2015KB079	Alteration	Hornblende	0.527	Epidote	0.473	68.961	0.111			
2245323	2015KB081	Background	Prehnite	0.568	Muscovite	0.432	138.68	0.169	2202.8	0.13	38.0
2245324	2015KB082	Alteration	MgChlorite	0.64	Illite	0.36	219.49	0.216	2201.7	0.14	36.5
2245325	2015KB026	Background	Illite	0.61	Prehnite	0.39	156.46	0.241	2198.3	0.15	27.4
2245326	2015KB083	Alteration	Epidote	0.525	Hornblende	0.475	159.47	0.107			
2245327	2015KB029	Alteration	Epidote	0.639	Illite	0.361	174.99	0.159	2199.4	0.08	31.1
2245328	2015KB030	Alteration	IntChlorite	1	NULL	0	344.81	0.085	2210.4	0.06	28.2
2245328	2015KB030	Alteration	FeChlorite	0.739	Prehnite	0.261	100.73	0.184	2205.6	0.10	38.0
2245329	2015KB084	Alteration	Epidote	0.59	Prehnite	0.41	380.79	0.186			
2245331	2015KB085	Alteration	FeChlorite	1	NULL	0	38.628	0.144	2217.4	0.06	34.7
2245332	2015KB086	Background	Muscovite	0.623	Prehnite	0.377	256.68		2203.8	0.15	35.9
2245333	2015KB087	Alteration	MgChlorite	0.552	Illite	0.448	235.83	0.13	2198.5	0.12	25.1
2245333	2015KB087	Alteration	Epidote	0.616	Prehnite	0.384	210.74	0.134			
2245334	2015KB088	Alteration	IntChlorite	0.562	Illite	0.438	31.814		2204.7	0.21	33.7

Sample ID	Station ID	Measurement type	TSA mineral 1	TSA weight 1	TSA mineral 2	TSA weight 2	TSA error	H_2O absorption feature	Al-OH absorption feature		
								Hull quotient depth	Wavelength (nm)	Hull quotient depth	Width (nm)
2245335	2015KB089	Background	Illite	0.597	Prehnite	0.403	213.45	0.201	2199.3	0.13	25.6
2245336	2015KB090	Background	Prehnite	0.529	Illite	0.471	174.16		2200.4	0.17	31.0
2245337	2015KB091	Background	Prehnite	0.639	Muscovite	0.361	205.2		2201.4	0.10	38.1
2245338	2015KB092	Background	Muscovite	0.535	Prehnite	0.465	164.48		2201.0	0.12	31.5
2245339	2015KB093	Alteration	IntChlorite	0.621	Illite	0.379	132.83	0.126	2208.9	0.04	30.1
2245341	2015KB094	Alteration	Illite	0.602	Prehnite	0.398	122.96	0.317	2200.8	0.20	31.8
2245342	2015KB095	Background	Illite	0.577	Prehnite	0.423	422.41	0.118	2201.6	0.08	28.9
2245343	2015KB096	Background	Hornblende	0.568	Illite	0.432	284.36	0.121	2198.6	0.06	25.2
2245344	2015KB097	Background	Muscovite	1	NULL	0	354.38	0.082	2201.8	0.05	24.8
2245345	2015KB098	Background	Siderite	0.586	Muscovite	0.414	143.5		2200.4	0.13	32.4
2245346	2015KB099	Background	Illite	0.511	Prehnite	0.489	160.35		2200.6	0.18	29.2
2245347	2015KB100	Alteration	Epidote	0.673	Illite	0.327	187.12	0.152	2202.6	0.07	34.7
2245348	2015KB101	Background	Illite	0.713	Siderite	0.287	51.849		2198.9	0.21	32.5
2245348	2015KB101	Background	Illite	1	NULL	0	506.26		2201.7	0.08	25.7
2245349	2015KB102	Alteration	Epidote	0.791	Calcite	0.209	78.279	0.187			
2245349	2015KB102	Alteration	Epidote	0.557	Halloysite	0.443	399.63	0.195	2207.7	0.09	23.8
2245351	2015KB103A	Alteration	MgChlorite	0.783	Epidote	0.217	103.68	0.301			
2245351	2015KB103A	Alteration	IntChlorite	0.744	Epidote	0.256	94.879	0.096			
2245353	2015KB105A	Background	Illite	0.609	Prehnite	0.391	266.57	0.239	2199.3	0.18	28.3
2245354	2015KB105A	Alteration	MgChlorite	0.506	Illite	0.494	234.38		2200.0	0.10	24.8
2245355	2015KB106	Alteration	Prehnite	0.549	Epidote	0.451	477.37	0.205	2200.9	0.11	36.1
2245356	2015KB107	Alteration	Illite	0.571	MgChlorite	0.429	81.609		2200.6	0.20	29.5
2245357	2015KB108	Background	MgChlorite	0.635	Illite	0.365	137.52		2200.2	0.10	32.2
2245358	2015KB109	Alteration	MgChlorite	0.674	Illite	0.326	116.29	0.113	2200.0	0.11	26.1
2245359	2015KB110	Alteration	Prehnite	0.625	Illite	0.375	200.12	0.198			
2245361	2015KB111	Alteration	Prehnite	0.711	MgChlorite	0.289	62.72	0.189			
2245362	2015KB112	Background	Illite	0.613	Prehnite	0.387	181.59	0.206	2200.2	0.19	28.8
2245363	2015KB113	Background	Illite	1	NULL	0	611.98	0.168	2207.7	0.04	30.0
2245364	2015KB115	Background	Illite	1	NULL	0	403.97	0.122	2200.7	0.03	26.4
2245365	2015KB116	Alteration	Siderite	0.584	Illite	0.416	106.5	0.185	2201.7	0.05	26.9
2245366	2015KB117	Background	Muscovite	1	NULL	0	369.63	0.152	2196.8	0.06	28.3
2245367	2015KB118	Background	Illite	1	NULL	0	464.94	0.158	2196.7	0.09	24.9
2245368	2015KB119	Background	Illite	1	NULL	0	88.229	0.22	2198.2	0.15	29.6
2245369	2015KB120	Alteration	Prehnite	1	NULL	0	75.689	0.281			
2245371	2015KB121A	Alteration	Illite	0.604	Siderite	0.396	95.667		2204.6	0.08	29.1
2245372	2015KB121B	Alteration	Illite	0.515	Siderite	0.485	118.94		2199.7	0.08	27.6
2245373	2015KB122	Alteration	IntChlorite	0.571	Epidote	0.429	45.023	0.202			
2245374	2015KB123	Alteration	Epidote	0.511	Muscovite	0.489	270.7	0.115	2201.6	0.13	36.3
2245375	2015KB124	Alteration	Illite	0.566	IntChlorite	0.434	40.734	0.415	2202.5	0.22	31.8
2245376	2015KB125	Background	Illite	0.522	Prehnite	0.478	163.45	0.194	2198.6	0.14	26.5
2245377	2015KB127	Background	Illite	0.665	Prehnite	0.335	182.11	0.196	2198.8	0.13	28.0
2245378	2015KB128A	Alteration	Prehnite	1	NULL	0	249.55	0.204			
2245379	2015KB128B	Alteration	Epidote	0.731	Prehnite	0.269	52.655	0.232			
2245381	2015KB129	Alteration	Illite	0.563	MgChlorite	0.437	81.982	0.274	2200.9	0.19	29.5
2245382	2015KB131	Alteration	Illite	0.598	Gypsum	0.402	359.17		2199.3	0.04	30.3
2245383	2015KB132	Alteration	Prehnite	0.541	Epidote	0.459	362.81	0.249	2199.3	0.12	35.7

Sample ID	Station ID	Measurement type	TSA mineral 1	TSA weight 1	TSA mineral 2	TSA weight 2	TSA error	H_2O absorption feature	Al-OH absorption feature		
								Hull quotient depth	Wavelength (nm)	Hull quotient depth	Width (nm)
2245384	2015KB133	Alteration	Prehnite	1	NULL	0	72.039	0.138			
2245385	2015KB134	Background	IntChlorite	0.543	Epidote	0.457	78.817				
2245386	2015KB135A	Background	Prehnite	0.609	Illite	0.391	220.02		2199.8	0.09	35.7
2245387	2015KB136	Alteration	IntChlorite	0.503	Epidote	0.497	76.896	0.14			
2245387	2015KB136	Alteration	Epidote	0.514	Illite	0.486	319.01	0.219	2199.5	0.06	29.0
2245388	2015KB137	Alteration	Prehnite	1	NULL	0	110.57	0.223			
2245389	2015KB138	Background	Illite	0.575	Prehnite	0.425	322.79		2198.6	0.10	26.9
2245389	2015KB138	Background	MgChlorite	0.512	Illite	0.488	206.28		2199.7	0.11	27.0
2245391	2015KB139	Alteration	Prehnite	1	NULL	0	106.03	0.248			
2245391	2015KB139	Alteration	Prehnite	1	NULL	0	114.81	0.234			
2245392	2015KB140	Background	Illite	0.618	Prehnite	0.382	112.22		2199.7	0.22	28.9
2245393	2015KB141	Background	Illite	0.538	MgChlorite	0.462	78.74		2200.4	0.12	27.7
2245394	2015KB142	Background	Illite	0.514	Prehnite	0.486	231.76		2198.9	0.16	30.6
2245395	2015KB143	Alteration	Illite	0.697	Prehnite	0.303	153.99	0.308	2201.2	0.12	29.7
2245396	2015KB144A	Alteration	Prehnite	1	NULL	0	59.769	0.239			
2245397	2015KB145	Alteration	FeChlorite	0.568	Prehnite	0.432	92.403	0.185			
2245398	2015KB146	Alteration	Prehnite	0.561	FeChlorite	0.439	68.188	0.217			
2245399	2015KB147	Alteration	Prehnite	0.643	Muscovite	0.357	249.4	0.24			
2245401	2015KB148	Alteration	Prehnite	0.656	Muscovite	0.344	149.54	0.213			
2245402	2015KB149C	Alteration	Prehnite	0.507	Muscovite	0.493	134.2	0.243	2199.5	0.17	30.5
2245403	2015KB149B	Alteration	Prehnite	0.622	Muscovite	0.378	234.86	0.21			
2245404	2015KB150	Alteration	Illite	0.596	Epidote	0.404	343.46	0.246	2197.1	0.09	25.4
2245405	2015KB151A	Alteration	Prehnite	0.555	Illite	0.445	197.88	0.274	2199.4	0.14	37.1
2245406	2015KB152A	Alteration	Epidote	0.601	Prehnite	0.399	252.65	0.178			
2245407	2015KB153	Alteration	Illite	0.567	Prehnite	0.433	266.77	0.21	2198.7	0.16	26.3
2245408	2015KB154	Alteration	Prehnite	0.507	FeChlorite	0.493	69.782	0.37			
2245409	2015KB155A	Alteration	FeTourmaline	0.51	Epidote	0.49	200.29	0.155	2202.9	0.13	37.1
2245409	2015KB155A	Alteration	IntChlorite	0.705	Illite	0.295	37.538	0.168	2202.2	0.14	32.5
2245411	2015KB155B	Alteration	Epidote	0.609	Prehnite	0.391	241.4	0.193	2197.3	0.15	29.1
2245411	2015KB155B	Alteration	Prehnite	1	NULL	0	80.529	0.193			
2245412	2015KB156	Alteration	Prehnite	0.848	Epidote	0.152	86.748	0.224			
2245413	2015KB157	Alteration	Prehnite	0.783	Epidote	0.217	112.34	0.159			
2245414	2015KB159	Alteration	Prehnite	0.618	Epidote	0.382	524.58	0.216	2198.6	0.13	27.3
2245415	2015KB160B	Alteration	Prehnite	0.551	MgChlorite	0.449	151.33	0.221			
2245416	2015KB161B	Alteration	Prehnite	1	NULL	0	122.33	0.144			
2245417	2015KB162	Alteration	FeChlorite	0.69	Prehnite	0.31	83.062	0.217			
2245418	2015KB163A	Alteration	Muscovite	0.622	Epidote	0.378	115.73	0.236	2211.4	0.15	35.9
2245419	2015KB163B	Background	Illite	0.524	Prehnite	0.476	130.52		2197.7	0.22	24.7
2245421	2015KB164	Alteration	Muscovite	0.659	Prehnite	0.341	208.13	0.196	2198.6	0.11	27.5
2245422	2015KB165	Alteration	Illite	0.598	Prehnite	0.402	131.8	0.215	2200.2	0.16	30.6
2245423	2015KB166A	Alteration	Prehnite	0.85	Epidote	0.15	128.58	0.202			
2245424	2015KB167	Alteration	Illite	0.597	MgChlorite	0.403	123.5		2201.3	0.21	34.3
2245425	2015KB168	Alteration	Prehnite	1	NULL	0	70.601	0.31			
2245426	2015KB169A	Alteration	Prehnite	1	NULL	0	181.48	0.234			
2245427	2015KB169B	Alteration	Epidote	0.735	Illite	0.265	89.723	0.264			
2245428	2015KB170	Alteration	Prehnite	1	NULL	0	67.594	0.274			

Sample ID	Station ID	Measurement type	TSA mineral 1	TSA weight 1	TSA mineral 2	TSA weight 2	TSA error	H_2O absorption feature	Al-OH absorption feature		
								Hull quotient depth	Wavelength (nm)	Hull quotient depth	Width (nm)
2245429	2015KB171	Alteration	Epidote	0.6	Illite	0.4	181.31	0.197	2198.2	0.16	29.7
2245429	2015KB171	Alteration	Epidote	0.763	Illite	0.237	97.047	0.262			
2245431	2015KB172	Alteration	Illite	0.538	Prehnite	0.462	228.75	0.339	2204.6	0.22	39.3
2245432	2015KB173	Alteration	Illite	0.685	Prehnite	0.315	139.78	0.367	2205.3	0.21	38.5
2245433	2015KB174	Alteration	Prehnite	0.52	Illite	0.48	143.47	0.304	2202.1	0.19	40.5
2245434	2015KB175	Alteration	Epidote	0.537	Prehnite	0.463	364.25	0.21	2197.7	0.09	24.8
2245435	2015KB176	Background	Illite	0.754	Epidote	0.246	463.21	0.122	2198.4	0.05	28.1
2245436	2015KB177	Alteration	MgChlorite	0.528	Illite	0.472	155.12	0.221	2201.3	0.12	32.4
2245437	2015KB178	Alteration	MgChlorite	0.547	Illite	0.453	218.95	0.25	2198.5	0.18	27.3
2245437	2015KB178	Alteration	Epidote	0.557	Illite	0.443	244.68	0.285	2199.5	0.17	35.0
2245438	2015KB179	Alteration	Muscovite	0.546	Prehnite	0.454	286.69	0.19			
2245439	2015KB180	Alteration	IntChlorite	0.646	Illite	0.354	96.882		2201.8	0.16	35.4
2245441	2015KB181	Alteration	Prehnite	0.806	Epidote	0.194	138.27	0.207			
2245442	2015KB182	Alteration	Illite	0.604	Epidote	0.396	126.75		2198.3	0.22	25.2
2245443	2015KB183	Alteration	FeChlorite	0.767	Prehnite	0.233	107.11	0.247			
2245444	2015KB184	Alteration	Epidote	0.634	Prehnite	0.366	216.07	0.313	2199.7	0.13	34.9
2245445	2015KB185A	Alteration	Phengite	0.67	Illite	0.33	51.375	0.257	2213.5	0.33	35.7
2245446	2015KB185B	Alteration	Phengite	0.613	Illite	0.387	165.55	0.25	2213.3	0.27	35.3
2245447	2015KB186	Alteration	Prehnite	0.578	Muscovite	0.422	181.47	0.248			
2245448	2015KB188	Alteration	Illite	0.556	Prehnite	0.444	104.54	0.288	2204.8	0.22	39.7
2245449	2015KB189	Alteration	MgChlorite	0.509	Illite	0.491	161.65	0.271	2203.5	0.18	38.0
2245451	2015KB190	Alteration	Illite	1	NULL	0	181.74	0.203	2197.6	0.19	27.5
2245452	2015KB191A	Alteration	Illite	0.587	Prehnite	0.413	121.89	0.332	2200.4	0.24	32.7
2245453	2015KB192	Alteration	Illite	0.63	Epidote	0.37	64.506	0.304	2198.3	0.23	28.6
2245454	2015KB193	Alteration	Illite	0.72	Prehnite	0.28	122.6	0.334	2199.6	0.25	29.5
2245455	2015KB195	Alteration	Illite	0.69	Kaolinite	0.31	83.167	0.44	2208.5	0.40	27.7
2245455	2015KB195	Alteration	Kaolinite	0.551	Illite	0.449	71.41	0.427	2207.4	0.27	32.3
2245456	2015KB196	Alteration	Illite	0.523	Prehnite	0.477	124.41	0.372	2202.1	0.23	34.8
2245457	2015KB197	Alteration	FeChlorite	0.592	Illite	0.408	63.679	0.346	2200.9	0.20	29.1
2245457	2015KB197	Alteration	Illite	0.667	Prehnite	0.333	107.79	0.321	2197.7	0.18	27.4
2245458	2015KB198A	Alteration	Illite	0.613	Epidote	0.387	180.95	0.217	2206.9	0.17	35.4
2245459	2015KB199	Alteration	Illite	0.664	Prehnite	0.336	93.141	0.367	2202.7	0.22	32.3
2245461	2015KB200	Alteration	Ankerite	0.75	Kaolinite	0.25	26.604	0.24	2208.5	0.14	24.0
2245461	2015KB200	Alteration	Kaolinite	0.804	Siderite	0.196	27.086	0.236	2208.5	0.31	29.7
2245462	2015KB201	Alteration	Siderite	0.58	Illite	0.42	113.98	0.351	2208.9	0.17	38.8
2245463	2015KB202	Alteration	Prehnite	1	NULL	0	204.72	0.274			
2245464	2015KB204	Alteration	Illite	0.645	Prehnite	0.355	130.68	0.38	2199.0	0.23	29.9
2245465	2015KB205	Alteration	Epidote	0.586	Illite	0.414	72.106	0.274	2197.4	0.17	24.1
2245466	2015KB206	Alteration	Prehnite	0.739	Epidote	0.261	236.04	0.268			
2245467	2015KB207	Alteration	Epidote	0.595	Prehnite	0.405	126.99	0.18			
2245468	2015KB208	Alteration	IntChlorite	0.659	Illite	0.341	55.824	0.215	2207.7	0.14	22.6
2245469	2015KB209	Alteration	Illite	0.561	Prehnite	0.439	243.96	0.292	2199.6	0.16	35.1
2245471	2015KB210	Alteration	Illite	0.579	Epidote	0.421	181.77	0.349	2197.6	0.22	25.9
2245472	2015KB212	Alteration	Illite	0.583	Siderite	0.417	81.532	0.351	2201.0	0.13	31.9
2245472	2015KB212	Alteration	Epidote	0.736	Illite	0.264	72.764	0.266			
2245473	2015KB213	Alteration	IntChlorite	0.735	Epidote	0.265	126.15	0.203			

Sample ID	Station ID	Measurement type	TSA mineral 1	TSA weight 1	TSA mineral 2	TSA weight 2	TSA error	H_2O absorption feature	Al-OH absorption feature		
								Hull quotient depth	Wavelength (nm)	Hull quotient depth	Width (nm)
2245474	2015KB214	Alteration	Epidote	0.782	Illite	0.218	56.401	0.266			
2245474	2015KB214	Alteration	Epidote	0.771	Ankerite	0.229	61.256	0.222			
2245475	2015KB215	Alteration	Muscovite	0.765	Epidote	0.235	70.499	0.264	2208.7	0.28	35.5
2245476	2015KB216	Alteration	Epidote	0.671	Illite	0.329	269.68	0.171	2207.1	0.09	36.2
2245477	2015KB217	Alteration	Epidote	0.537	Prehnite	0.463	89.084	0.266			
2245478	2015KB218	Alteration	Epidote	0.818	Calcite	0.182	69.965	0.175			
2245478	2015KB218	Alteration	Epidote	1	NULL	0	71.221	0.183			
2245479	2015KB219	Alteration	Prehnite	0.647	Muscovite	0.353	146.16	0.288			
2245481	2015KB221	Alteration	Prehnite	0.751	Epidote	0.249	286.4	0.309			
2245482	2015KB222	Alteration	Prehnite	0.77	Epidote	0.23	177.47	0.277			
2245483	2015KB224	Alteration	Illite	0.768	Prehnite	0.232	105.44		2197.9	0.16	30.0
2245484	2015KB225	Alteration	Prehnite	1	NULL	0	103.88	0.32			
2245485	2015KB226	Alteration	Illite	0.716	Epidote	0.284	282.52	0.236	2202.3	0.20	37.5
2245486	2015KB227	Alteration	Illite	0.604	Phengite	0.396	59.286		2208.6	0.48	30.9
2245487	2015KB228	Background	Illite	0.568	Prehnite	0.432	129.84		2198.0	0.21	25.3
2245488	2015KB229A	Alteration	Prehnite	0.848	Epidote	0.152	161.58	0.201			
2245491	2015KB230B	Alteration	Prehnite	0.631	Epidote	0.369	197.44	0.312			
2245492	2015KB231	Alteration	Illite	0.662	Epidote	0.338	194.18		2202.1	0.24	36.6
2245493	2015KB233A	Alteration	Illite	0.567	Epidote	0.433	144.44	0.236	2203.8	0.13	34.6
2245493	2015KB233A	Alteration	Epidote	1	NULL	0	503.29	0.054	2212.0	0.04	30.0
2245494	2015KB233B	Alteration	Illite	0.801	Epidote	0.199	191.8	0.337	2198.0	0.14	29.3
2245494	2015KB233B	Alteration	IntChlorite	0.618	Illite	0.382	50.104	0.224	2201.0	0.11	27.6
2245495	2015KB234	Alteration	Illite	0.558	Epidote	0.442	144.15	0.233	2208.4	0.14	31.6
2245496	2015KB235	Alteration	Illite	0.76	Prehnite	0.24	89.957	0.364	2199.8	0.28	29.2
2245497	2015KB236A	Alteration	FeChlorite	0.705	Illite	0.295	35.562	0.163	2205.3	0.26	33.7
2245498	2015KB236B	Alteration	IntChlorite	0.689	Illite	0.311	40.974	0.16	2208.3	0.11	26.2
2245499	2015KB237	Alteration	Epidote	1	NULL	0	101.69	0.196			
2247901	2015GL015	Alteration	Illite	0.82	Epidote	0.18	35.779		2198.0	0.30	31.5
2247902	2015GL015	Alteration	Illite	0.847	Epidote	0.153	56.049		2201.0	0.34	30.4
2247903	2015GL016	Alteration	Illite	0.774	Epidote	0.226	230.27		2197.3	0.23	26.8
2247904	2015GL016	Alteration	Illite	0.79	Epidote	0.21	94.486		2199.2	0.22	30.3
2247905	2015GL017	Alteration	Illite	1	NULL	0	265.34		2197.9	0.16	28.9
2247906	2015GL017	Alteration	Muscovite	0.821	Epidote	0.179	80.137		2207.3	0.28	37.4
2247906	2015GL017	Alteration	Illite	0.826	Epidote	0.174	148.7		2198.7	0.24	28.3
2247906	2015GL017	Background	Illite	0.627	Prehnite	0.373	297.2		2196.4	0.11	26.6
2247908	2015GL018	Alteration	Illite	1	NULL	0	125.71		2200.4	0.28	30.5
2247909	2015GL019	Alteration	Illite	0.642	Epidote	0.358	147.4		2197.2	0.22	26.4
2247910	2015GL020	Alteration	Prehnite	0.779	Epidote	0.221	262.81	0.343			
2247911	2015GL021	Alteration	Illite	0.61	Prehnite	0.39	236.41	0.347	2208.5	0.23	35.7
2247912	2015GL022	Alteration	Illite	0.624	Siderite	0.376	51.617	0.39	2199.7	0.27	32.3
2247913	2015GL023	Alteration	Illite	0.587	Prehnite	0.413	173.38	0.393	2198.9	0.29	32.7
2247914	2015GL024	Alteration	Illite	0.796	Epidote	0.204	69.743	0.345	2199.9	0.25	31.0
2247915	2015GL024	Background	Illite	1	NULL	0	342.77	0.185	2204.0	0.05	28.7
2247915	2015GL024	Background	Siderite	0.524	Illite	0.476	206.27	0.219	2199.7	0.06	29.2
2247916	2015GL025	Alteration	Illite	1	NULL	0	177.64	0.293	2197.9	0.13	26.9
2247916	2015GL025	Alteration	Illite	0.584	Prehnite	0.416	227.71	0.293	2197.0	0.14	25.8

Sample ID	Station ID	Measurement type	TSA mineral 1	TSA weight 1	TSA mineral 2	TSA weight 2	TSA error	H_2O absorption feature	Al-OH absorption feature		
								Hull quotient depth	Wavelength (nm)	Hull quotient depth	Width (nm)
2247917	2015GL026	Alteration	Epidote	1	NULL	0	464.63	0.266			
2247920	2015GL026	Alteration	Illite	0.597	Prehnite	0.403	165.03	0.337	2196.8	0.18	26.5
2247921	2015GL027	Alteration	Illite	0.648	Siderite	0.352	50.264	0.448	2198.7	0.32	29.2
2247922	2015GL028	Alteration	Illite	1	NULL	0	244.29	0.386	2206.9	0.13	27.5
2247923	2015GL029	Alteration	Illite	0.706	Prehnite	0.294	177.55	0.391	2197.8	0.20	28.6
2247924	2015GL030	Alteration	Illite	1	NULL	0	180.72	0.312	2197.1	0.11	28.0
2247925	2015GL031	Background	FeChlorite	0.624	Illite	0.376	82.468		2197.7	0.09	28.3
2247925	2015GL031	Background	Siderite	0.506	Illite	0.494	171.37		2199.5	0.07	29.3
2247925	2015GL031	Background	Illite	1	NULL	0	127.5		2199.3	0.11	30.8
2247926	2015GL032	Alteration	Illite	0.787	Prehnite	0.213	86.767		2199.6	0.23	31.2
2247926	2015GL032	Alteration	Illite	0.816	Epidote	0.184	196.54		2201.9	0.11	30.7
2247927	2015GL033	Alteration	Prehnite	0.538	Epidote	0.462	382.65	0.226			
2247928	2015GL034	Background	Illite	1	NULL	0	306.83	0.201	2199.4	0.04	26.9
2247928	2015GL034	Background	Illite	1	NULL	0	475.91	0.21	2197.1	0.07	26.9
2247929	2015GL035	Alteration	Prehnite	0.542	Muscovite	0.458	190.97	0.297			
2247931	2015GL036	Alteration	IntChlorite	0.523	Illite	0.477	42.581	0.315	2197.8	0.22	28.4
2247932	2015GL037	Alteration	Muscovite	0.688	Prehnite	0.312	90.239	0.256	2209.5	0.27	38.7
2247933	2015GL038	Alteration	Illite	0.525	Epidote	0.475	57.907	0.399	2200.9	0.21	30.6
2247934	2015GL038	Alteration	Illite	0.58	Epidote	0.42	174.79	0.366	2198.4	0.13	26.9
2247935	2015GL039	Alteration	Prehnite	0.804	Epidote	0.196	258.06	0.333			
2247936	2015GL040	Alteration	Illite	0.745	Ankerite	0.255	69.945	0.366	2208.3	0.33	32.3
2247937	2015GL041	Alteration	Epidote	0.517	Illite	0.483	68.6		2201.8	0.11	33.7
2247937	2015GL041	Background	Illite	1	NULL	0	214.44		2196.2	0.11	27.9
2247937	2015GL041	Background	Illite	0.663	Prehnite	0.337	229.59		2196.1	0.11	27.0
2247937	2015GL041	Background	Illite	1	NULL	0	554.82		2196.7	0.06	27.3
2247937	2015GL041	Background	Illite	0.721	Epidote	0.279	449.33		2196.8	0.08	27.8
2247938	2015GL042	Alteration	Illite	0.733	Prehnite	0.267	147.16	0.295	2198.5	0.19	27.2
2247939	2015GL043	Alteration	Illite	1	NULL	0	172.6	0.387	2200.8	0.24	33.1
2247940	2015GL044	Alteration	Illite	0.554	FeChlorite	0.446	48.388	0.292	2204.8	0.21	35.4
2247943	2015GL045	Background	Illite	0.678	Prehnite	0.322	86.108	0.405	2196.7	0.17	28.8
2247943	2015GL045	Background	Illite	0.682	Prehnite	0.318	149.75	0.382	2196.6	0.12	28.6
2247944	2015GL046	Background	Illite	1	NULL	0	355.27	0.278	2196.7	0.07	27.7
2247944	2015GL046	Background	Illite	1	NULL	0	542.69	0.263	2196.8	0.07	28.1
2247945	2015GL047	Alteration	Muscovite	0.839	Epidote	0.161	118.94	0.429	2202.5	0.23	34.5
2247946	2015GL048	Alteration	Illite	0.681	Siderite	0.319	69.087	0.332	2205.6	0.16	32.3
2247947	2015GL049	Alteration	Prehnite	0.509	Illite	0.491	252.23	0.339			
2247948	2015GL050	Alteration	Illite	0.695	Prehnite	0.305	79.421	0.381	2198.7	0.23	27.8
2247949	2015GL050	Background	FeChlorite	0.548	Illite	0.452	102.5		2198.2	0.11	26.3
2247950	2015GL051	Alteration	Muscovite	0.743	Epidote	0.257	34.736	0.368	2208.4	0.34	36.3
2758851	2015GL051	Alteration	Prehnite	0.594	Epidote	0.406	285.05	0.279			
2758852	2015GL052	Alteration	Illite	0.546	Prehnite	0.454	141.16	0.386	2206.2	0.22	37.3
2758854	2015GL053	Background	Illite	1	NULL	0	1553.71		2198.2	0.04	27.1
2758855	2015GL054	Alteration	Muscovite	0.694	Epidote	0.306	94.407	0.343	2203.1	0.17	35.2
2758856	2015GL055	Alteration	Illite	0.671	Prehnite	0.329	134.66	0.376	2196.4	0.18	27.5
2758857	2015GL056	Alteration	FeChlorite	0.759	Prehnite	0.241	75.626	0.251			
2758858	2015GL057	Background	Illite	0.745	Epidote	0.255	299.85		2196.6	0.08	27.0

Sample ID	Station ID	Measurement type	TSA mineral 1	TSA weight 1	TSA mineral 2	TSA weight 2	TSA error	H_2O absorption feature	Al-OH absorption feature		
								Hull quotient depth	Wavelength (nm)	Hull quotient depth	Width (nm)
2758859	2015GL058	Alteration	Epidote	0.599	Illite	0.401	303.71	0.286			
2758860	2015GL059	Alteration	Muscovite	0.791	Epidote	0.209	43.108	0.349	2201.4	0.24	30.1
2758861	2015GL060	Background	Illite	1	NULL	0	264.94	0.245	2196.7	0.05	28.0
2758862	2015GL061	Background	Illite	0.508	Hornblende	0.492	192.13	0.218	2199.8	0.06	28.9
2758862	2015GL061	Background	Illite	0.619	Prehnite	0.381	317.86	0.258	2197.0	0.09	26.4
2758863	2015GL062	Alteration	Illite	0.541	Epidote	0.459	102.7	0.287	2200.4	0.23	29.6
2758866	2015GL063	Alteration	Illite	0.677	Epidote	0.323	410.66	0.317	2218.4	0.25	40.2
2758867	2015GL064	Alteration	Prehnite	1	NULL	0	175.1	0.363			
2758868	2015GL065	Alteration	Illite	1	NULL	0	25.735	0.391	2202.6	0.47	34.2
2758869	2015GL065	Alteration	Illite	0.644	Phengite	0.356	31.687	0.234	2205.8	0.30	34.3
2758870	2015GL066	Alteration	Illite	0.669	Opal	0.331	50.875	0.353	2207.8	0.25	32.1
2758871	2015GL067	Alteration	Prehnite	0.738	Epidote	0.262	244.45	0.301			
2758872	2015GL068	Background	Illite	1	NULL	0	201.62	0.238	2197.7	0.06	30.4
2758873	2015GL069	Alteration	Illite	0.717	Ankerite	0.283	46.613	0.342	2207.5	0.32	30.1
2758874	2015GL070	Alteration	Illite	0.563	Prehnite	0.437	134.01	0.282	2200.9	0.15	34.9
2758877	2015GL072	Background	Illite	0.646	Prehnite	0.354	150.42	0.339	2196.5	0.19	26.9
2758877	2015GL072	Background	Illite	1	NULL	0	315.48	0.343	2195.7	0.12	27.2
2758878	2015GL073	Alteration	Illite	0.732	Prehnite	0.268	142.4	0.334	2203.2	0.23	37.3
2758879	2015GL073	Alteration	Illite	0.826	Prehnite	0.174	70.029	0.408	2200.9	0.34	33.0
2758880	2015GL074	Alteration	Prehnite	0.602	Epidote	0.398	641.13	0.257	2202.5	0.13	38.9
2758881	2015GL075	Alteration	Illite	0.572	Prehnite	0.428	110.79	0.309	2196.6	0.26	25.7
2758882	2015GL076	Background	Illite	0.667	Prehnite	0.333	129.35	0.294	2196.9	0.15	26.8
2758882	2015GL076	Background	Illite	0.679	Prehnite	0.321	190.31	0.343	2196.3	0.14	27.1
2758883	2015GL077	Alteration	Illite	0.548	Phengite	0.452	73.802	0.301	2204.3	0.32	38.2
2758884	2015GL078	Background	Illite	1	NULL	0	491.3	0.197	2197.1	0.05	26.9
2758884	2015GL078	Background	Illite	0.591	Prehnite	0.409	174.45	0.244	2196.4	0.13	26.0
2758885	2015GL079	Alteration	Prehnite	0.612	Epidote	0.388	249.73	0.145			
2758886	2015GL080	Alteration	Muscovite	0.825	Epidote	0.175	39.95	0.358	2204.4	0.35	34.7
2758889	2015GL081	Alteration	Halloysite	1	NULL	0	715.82		2206.1	0.06	29.3
2758890	2015GL081	Alteration	FeChlorite	0.766	Illite	0.234	59.491	0.183	2206.8	0.11	32.7
2758891	2015GL082	Alteration	Illite	0.79	Epidote	0.21	290.4	0.281	2200.0	0.15	31.3
2758892	2015GL083	Alteration	Illite	0.71	Prehnite	0.29	201.18		2197.1	0.20	27.0
2758892	2015GL083	Alteration	Illite	0.701	Prehnite	0.299	163.96		2197.3	0.18	26.9
2758893	2015GL084	Background	Siderite	0.501	Illite	0.499	117.23	0.246	2197.5	0.11	29.1
2758893	2015GL084	Background	Siderite	0.567	Illite	0.433	100.88	0.199	2198.7	0.07	29.4
2758894	2015GL085	Alteration	MgChlorite	0.58	Illite	0.42	147.24	0.238			
2758895	2015GL086	Background	Illite	0.701	Prehnite	0.299	165.58		2197.2	0.14	28.3
2758895	2015GL086	Background	Illite	1	NULL	0	371.98		2198.0	0.08	27.6
2758896	2015GL087	Alteration	Illite	0.729	Epidote	0.271	195.64	0.247	2199.4	0.16	29.7
2758897	2015GL088	Alteration	Prehnite	0.699	Epidote	0.301	246.44	0.277			
2758898	2015GL089	Background	Illite	1	NULL	0	522.01		2197.0	0.08	28.4
2758898	2015GL089	Background	Illite	0.753	Epidote	0.247	460.59		2196.6	0.07	26.9
2758900	2015GL090	Alteration	Illite	0.775	Prehnite	0.225	110.4	0.279	2200.1	0.25	30.7